Netherlands Enterprise Agency

Morphodynamics for IJmuiden Ver Wind Farm Zone

>> *Sustainable. Agricultural. Innovative. International.*

Netherlands Enterprise Agency

RVO Approval for Publication

Document Characteristics

Version	Title	Date of Publication	Reference Contractor	Reference RVO
3.0	Morphodynamics for IJmuiden Ver Wind Farm Zone	July, 2023	11208404-002-HYE-0001	WOZ2220017

Approval

Approval for public disclosure	Position
Menno Hofstra	Project Manager RVO Offshore Wind Energy
Peter-Paul Lebbink	Programme Manager RVO Offshore Wind Energy

IJMUIDEN VER WIND FARM SITES I - VI (IJVWFS I - VI)

Certification Report Morphodynamics and Scour Mitigation

Netherlands Enterprise Agency

Report No.: CR-SC-DNV-SE-0190-08299-3 Morphodynamics IJmuiden Ver Wind Farm Sites I - VI (IJV) Wind Farm Zone
Date: 2023-07-03

Project name:	IJmuiden Ver Wind Farm Sites I - VI (IJVWFS I - VI)	DNV Energy Systems
Report title:	Certification Report Morphodynamics and Scour Mitigation	Renewables Certification DNV Denmark A/S
Customer:	Netherlands Enterprise Agency, Croeselaan 15, 3521 BJ Utrecht, The Netherlands	Tuborg Parkvej 8 2900 Hellerup
Customer contact:	Matté Brijder (RVO)	Denmark
Date of issue:	2023-07-03	Tel: +45 39 45 48 00
Project No.:	10268766	
Report No.:	CR-SC-DNV-SE-0190-08299-3 Morphodynamics IJmuiden Ver Wind Farm Sites I - VI (IJV) Wind Farm Zone	

Applicable contract(s) governing the provision of this Report: 202007034 / WOZ2200210

Objective:

The objective of this report is to confirm that DNV as an independent third party has verified that the result of a morphodynamic and scour mitigation study carried out for IJmuiden Ver Wind Farm Sites I - VI (IJVWFS I - VI) can be used for design of the future offshore wind according to DNV-SE-0190:2023.

Prepared by:	Verified by:	Approved by:
Asp, Erik 2023.07.03 10:47:29 +02'00'	Hunt, Helena Jane Digitally signed by Hunt, Helena Jane Date: 2023.07.03 12:31:31 +02'00'	2023.07.05 09:52:23 +02'00'
Erik Asp Senior Principal Engineer	Helena Hunt Principal Engineer	Johan Olaison Project Sponsor

DNV Distribution:

☐ OPEN. Unrestricted distribution, internal and external.

☐ INTERNAL use only. Internal DNV document.

☒ CONFIDENTIAL. Distribution within DNV according to applicable contract.*

☐ SECRET. Authorized access only.

*Specify distribution: DNV Renewables Certification

Keywords:

Offshore wind, IJmuiden Ver Wind Farm Sites I - VI (IJV) Wind Farm Zone, Site Conditions Assessment

Rev. No.	Date	Reason for Issue	Prepared by	Verified by	Approved by
0	2023-05-16	Draft issue	EAH	HEHU	xxx
1	2023-06-06	Second issue	EAH	HEHU	JOOLA
2	2023-06-23	Third issue	EAH	HEHU	JOOLA
3	2023-07-03	Forth issue	EAH	HEHU	JOOLA

Table of contents

1 EXECUTIVE SUMMARY

The IJmuiden Ver Wind Farm Sites I - VI (IJVWFS I - VI) are located in the Dutch Sector of the North Sea, approximately 62 km from the west coast of the Netherlands. As part of the tender preparations, the Netherlands Enterprise Agency (Rijksdienst voor Ondernemend Nederland, RVO) requested a morphology and scour mitigation study of the investigation area at IJVWFS I - VI.

DNV was assigned to verify those bathymetric, scour and scour mitigation studies and their use within a Design Basis for Offshore Wind Power Plants in accordance with DNV-SE-0190.

2 CERTIFICATION SCHEME

Document No.	Title
DNV-SE-0190:2023-03	Project certification of wind power plants

The morphology and scour mitigation studies have been evaluated based on Section 2.3.2 Site Assessment of DNV-SE-0190.

3 SCOPE OF EVALUATION

The scope and interface of the evaluation covered by the report is the morphodynamics and scour mitigation investigations which are a part of the site conditions assessment for the assets wind turbines, offshore substations and power cables.

The appendix to this report comprises the detailed DNV evaluation which include references to standards, list of documentation and the conclusion of the DNV evaluation.

4 CONDITIONS

The conditions identified during the technical evaluation are listed in the appendices. The conditions are assigned to the certification phases in which they need to be considered and evaluated.

The conditions listed in the following shall be addressed as part of the certification process.

For the design phase the following condition shall be addressed:

- The final scour mitigation strategy will have to be defined by the designer, for the actual foundation and cable design to be used.

For the operation and maintenance phases the following condition shall be addressed:

- The seabed levels within the wind farm area shall be monitored and remedial actions taken before the seabed levels are compromised.

5 OUTSTANDING ISSUES

No outstanding issues have been identified.

6 CONCLUSION

DNV has found that the morphology study is complete, carried out according to industry best practice, is plausible, and that

- Lowest Sea Bed Level (LSBL) for the period 2022-2072
- Best Estimate Bathymetry (BEB) for the period 2022-2072
- Highest Sea Bed Level (HSBL) for the period 2022-2072

as defined in the documents listed in Section A4 are derived in line with the requirements following Section 2.3.2 of the DNVGL-SE-0190 and can be used as basis for determining design seabed levels for IJmuiden Ver Wind Farm Sites I - VI (IJVWFS I - VI). The conditions in Section 4 shall be observed.

Although the actual scour prediction and mitigation strategies must be defined by the designer for the actual foundation and cable concepts, DNV has found the presented methods to be in line with industry practice.

APPENDIX A
Morphological and Scour mitigation investigations

Evaluation of morphological and scour mitigation investigations for IJmuiden Ver Wind Farm Sites I - VI (IJVWFS I - VI)

A1 Description of verified component, system or item

Within the wind farm area, a morphology and scour mitigation study has been performed. The study's results and the morphodynamic site conditions are documented by the customer and build the basis for the verification described in the current report.

A2 Interface to other systems/components

Currently, no interfaces to other systems/components are present.

A3 Basis for the evaluation

Applied codes and standards:

Document No.	Revision	Title
DNV-ST-0437	2021-11	Loads and site conditions for wind turbines
IEC 61400-3-1	2019	Wind Turbines – Part 3: Design requirements for offshore wind turbines

A4 Documentation from customer

List of reports:

Ref.	Document No.	Revision	Title
/1/	11208404-002-HYE-0001	3.0 2023-03-24	Morphodynamics for IJmuiden Ver Wind Farm Zone
/2/	11208404-002-HYE-0002	2.1 2023-03-24	Scour and scour mitigation for IJmuiden Ver Wind Farm Zone

A5 Evaluation work

/1/ presents the bathymetrical/morphodynamic assessment for the planned IJmuiden Ver Wind Farm Sites I - VI (IJVWFS I - VI). /1/ contains information regarding:

- Description of morphodynamic features in the wind farm zone
- An analysis of the morphodynamics
- Extrapolation of historical morphodynamic activities for the estimation of future seabed levels

The bathymetry in IJV is characterized by several north-south oriented sand banks with heights ranging from a few meters up to 10 m. In the southwest (Site II), a deeper channel occurs where the Holocene layer is absent. The maximum depth of this channel is 10 m lower than the rest of IJV. Most of Sites I-VI are covered by dynamic sand waves.

The sand waves typically migrate towards the north-northeast with migration rates with typical rates between 0.4 m/year and 2.7 m/year. The sand waves have lengths between 170 m and 620 m and are 0.9 m to 3.5 m high (5% and 95% non-exceedance values for Sites I-VI).

The eastern megaripples have migration speeds that are so large that many megaripples will pass each foundation during the lifetime of the wind farms. Therefore, only their dimensions were determined, and their representative statistical values were included as an uncertainty band for predicted bed levels.

The sand waves have been analyzed in 3 steps based on the historical and recent seabed bathymetries

a. Determination of transect locations
b. Sand wave dynamics (sand wave migration speed and sand wave migration direction)
c. Sand wave dimensions

Future migration

In /1/ future predictions are made over the period 2022 until 2072, based on (i) existing historical bathymetry data available from the NLHO (Royal Netherlands Navy - Hydrographic Office, 1980-2021) and (ii) data provided by RVO; measured by GEOxyz (2021) for sites I-IV and Fugro (2022 for Sites V and VI).

The future bathymetries (BEB, LSBL and HSBL) and corresponding bed level changes have been estimated by artificial shifting the mobile seabed components of the most recent 2022 bathymetry.

- Lowest Seabed Level (LSBL) is the estimated cumulative lower enveloped of the predicted seabed combined with the downward uncertainty over a given period
- Best Estimate Bathymetry (BEB) is the estimated cumulative predicted seabed over a given period
- Highest Seabed Level (HSBL) is the estimated cumulative higher enveloped of the predicted seabed combined with the upward uncertainty over a given period

To account for a) survey, b) megaripples and c) spatial resolution uncertainty + spatial varying sand wave shape uncertainty have been added to the uncertainty. DNV has reviewed these uncertainty bands and found them to be on the safe side.

DNV has a) reviewed the study, b) has found that the study is carried out according to industry best practice and c) agrees on the following main data provided along with /1/:

Unexploded Ordnances (UXO's)

In addition to the future predictions /1/ also present a hindcast of the seabed levels for the period 1945 to 2022 to detect bandwidths as a vertical demarcation for the location of Unexploded Ordnances (UXO's). DNV has reviewed and found the Best (BEOL), Lowest (LOL) and Highest (HOL) object levels are correctly modelled.

Scour Mitigation Strategies

In /2/ different scour mitigation strategies are presented. DNV has found that the methods are in line with industry practice.

Scour Depths

/2/ presents scour depths between 8.3 m- 13.9 m (95% non-exceedance values of the maximum scour depths around 10, 12 m and 14m monopiles during the lifetime) DNV has found that the estimated scour depths are plausible and are in line with industry practice.

A6 Conditions to be considered in other certification phases

The conditions identified during the technical evaluation are listed in the following.

For the design phase the following condition shall be addressed:

- The final scour mitigation strategy will have to be defined by the designer, for the actual foundation and cable design to be used.

For the operation and maintenance phases the following condition shall be addressed:

- The seabed levels within the wind farm area shall be monitored and remedial actions taken before the seabed levels are compromised.

A7 Outstanding issues

There are no outstanding issues.

A8 Conclusion

DNV has found that the morphology study is complete, carried out according to industry best practice, is plausible, and that

- Lowest Sea Bed Level (LSBL) for the period 2022-2072
- Best Estimate Bathymetry (BEB) for the period 2022-2072,
- Highest Sea Bed Level (HSBL) for the period 2022-2072

as defined in the documents listed in Section A4 are derived in line with the requirements following Section 2.3.2 of the DNV-SE-0190 and the related “Basis for the evaluation” listed in Section A3 can be used as basis for determining design seabed levels for IJmuiden Ver Wind Farm Sites I - VI (IJVWFS I - VI). The conditions in Section A6 shall be observed.

Although the actual scour prediction and mitigation strategies must be defined by the designer for the actual foundation and cable concepts, DNV has found the presented methods to be in line with industry practice.

About DNV

DNV is the independent expert in risk management and assurance, operating in more than 100 countries. Through its broad experience and deep expertise DNV advances safety and sustainable performance, sets industry benchmarks, and inspires and invents solutions.

Whether assessing a new ship design, optimizing the performance of a wind farm, analyzing sensor data from a gas pipeline or certifying a food company's supply chain, DNV enables its customers and their stakeholders to make critical decisions with confidence.

Driven by its purpose, to safeguard life, property, and the environment, DNV helps tackle the challenges and global transformations facing its customers and the world today and is a trusted voice for many of the world's most successful and forward-thinking companies.

Deltares

Morphodynamics for IJmuiden Ver Wind Farm Zone

Morphodynamics for IJmuiden Ver Wind Farm Zone

Author(s)
Tom Roetert
Vassia Dagalaki
Anne de Beer
Jelmer IJntema

Morphodynamics for IJmuiden Ver Wind Farm Zone

Client	Rijksdienst voor Ondernemend Nederland
Contact	Menno Hofstra
Reference	202201045
Keywords	Seabed morphodynamics, sediment transport, IJmuiden Ver, Offshore wind

Document control	
Version	3.0
Date	24-03-2023
Project nr.	11208404-002
Document ID	11208404-002-HYE-0001
Pages	265
Classification	
Status	final

Author(s)		
	Tom Roetert	Anne de Beer
	Vassia Dagalaki	Jelmer IJntema

Summary

Deltares was awarded the contract for a morphodynamic assessment of the IJmuiden Ver Investigation Area (IJV IA) located in the IJmuiden Ver Wind Farm Zone (IJV). The study area is located approximately 62 km west of the coast of North Holland and has a foreseen capacity of 6,000 MW. IJV comprises six Sites (I-VI), of which the coordinates are subject to change, with a total surface area of 613 km^2.

The aim of this morphodynamic assessment is to characterise various bedforms and seabed dynamics and to quantify future seabed level changes over the period 2020 to 2072. The results will aid wind farm developers in their choice and design of wind turbine foundations and cable routes.

The bathymetry in IJV is characterised by a number of north-south oriented sand banks with heights ranging from a few metres up to 10 m. In the southwest (Site II), a deeper channel occurs where the Holocene layer is absent. The maximum depth of this channel is 10 m lower than the rest of IJV. Most of Sites I-IV are covered by dynamic sand waves. In Sites V-VI, only a few sand waves are present. In general, the sand wave crests are oriented perpendicular to the sand banks.

The median grain size of IJV decreases from south to northeast, ranging between 0.026 mm and 0.290 mm (silt to medium sand) between one and five metres below the seabed. In the southwest deepest part of IJV, as well as locally over the sand waves troughs and crests, coarser grain sizes occur at the seabed. Fines content is 1-2% with maximum values of 10%. There is no trend in grain size or fines content with depth.

Non-erodible layers in the subsurface are only present close to the seabed locally in IJV, for example in the southwest of Site II. The non-erodible layers are unlikely to affect the seabed morphodynamics because they are either too deep or too sparsely spread to be exposed by the seabed dynamics.

Numerical model results indicate that the sediment transport patterns are largely tide-dominated, with meteorological conditions having only a transient effect. Model results indicate a net sediment transport direction across IJV towards the north-northeast, in line with the direction of the dominant flood tidal currents. This direction of transport generally agrees with the observed migration direction of sand waves from the data analysis.

To analyse seabed dynamics a detailed analysis is presented focussing on sand waves present in IJV. Sand wave dynamics are determined by using a 2D cross-correlation technique. The sand waves typically migrate towards the north-northeast with migration rates between 0.4 m/year and 2.7 m/year. Migration rates are in general similar for Sites I-VI. For Site V migration rates are different due to the small number of sand waves present. No sand waves were detected in Site VI.

A Fourier analysis was applied to define sand wave dimensions. In IJV, the sand waves have lengths between 170 m and 620 m and are 0.9 m to 3.5 m high (5% and 95% non-exceedance values for Sites I-VI). The highest sand waves are observed in Sites I-II, while the longest sand waves are found in Site V. Analysis of large-scale seabed variations shows that the seabed may be considered effectively static over the lifetime of the wind farm. Analysis of high-resolution data and repeat survey lines indicates that temporal variations in megaripple dimensions have been small (5 to 10 cm).

Based on a morphodynamic analysis, a future Best Estimate Bathymetry (BEB), Lowest Seabed Level (LSBL) and a Highest Seabed Level (HSBL) are estimated. The LSBL and HSBL are the predicted lowest and highest future seabed levels, respectively, for the period 2022 to 2072, including uncertainty bands. Predicted seabed level changes vary between -3.12 m and +5.22 m (99.9% non-exceedance values for Sites I-VI). Maps of the predicted seabed level changes over the period 2020 to 2072 are presented in Figure 1. The highest bed level changes are predicted for Sites I-II, where the highest mobile sand waves are found. The lowest for bed level changes are predicted for Sites V-VI.

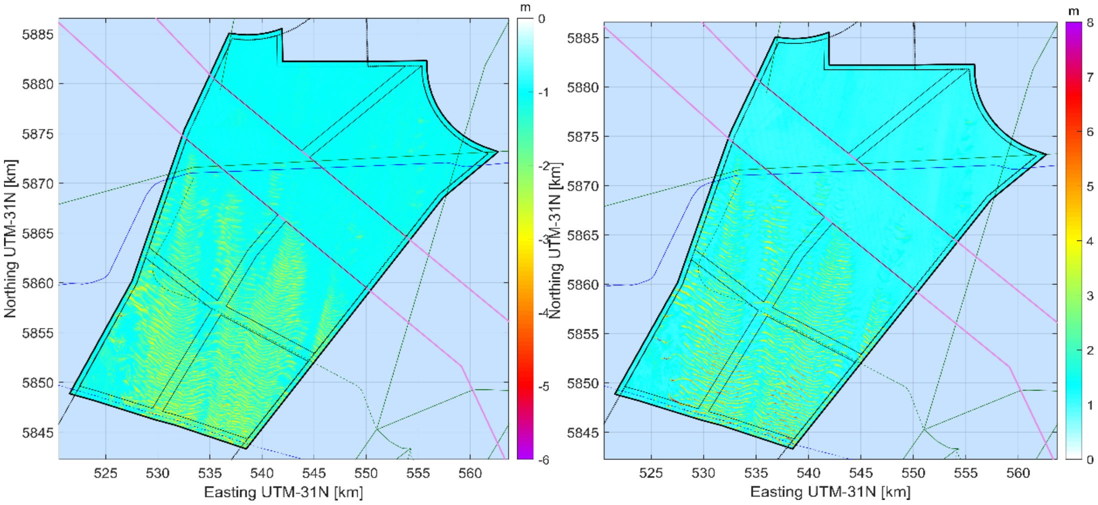

Figure 1: Overview of the predicted seabed level changes over the period 2022 to 2072 showing the difference between the present seabed and the lowest (LSBL, left plot) and highest (HSBL, right plot) predicted seabed levels.

In addition to future seabed levels, hindcast seabed levels for the period 1945 to 2022 was constructed to assess the possible levels at which Unexploded Ordnances (UXO's), which were dumped in the North Sea during the Second World War, are located. To take into account the full range of possible object levels, the Lowest Object Level, the Highest Object Level and the Best-Estimate Object Level over the period 1945 to 2022 are calculated. These levels respectively represent the lower, best and upper estimate of the lowest seabed level over the period 1945 to 2022.

Morphodynamic activity, such as sand wave migration, may pose a threat to foundations and cables if not considered in the design and general wind farm planning. For example, cables might become exposed and foundation fixation levels might decrease as a result of seabed lowering. To mitigate this increased initial cable burial depths and foundation pile lengths or scour protection extents are required.

The predicted seabed level changes presented in this study follow from the applied morphological analysis techniques, describing the (uncertainty of the) physics and the natural variability of the analysed morphological system. No additional safety margins for design purposes have been applied.

Samenvatting

Rijksdienst voor Ondernemend Nederland (RVO) heeft Deltares opdracht gegeven om een morfodynamische analyse van de zeebodem uit te voeren voor het IJmuiden Ver onderzoeksgebied (IJV IA). Het studiegebied ligt ongeveer 62 km ten westen van de Noord-Hollandse kust en heeft een heeft een capaciteit van ongeveer 6,000 MW. IJV bestaat uit 6 deelgebieden (I-VI), waarvan de coördinaten aan verandering onderhevig zijn, met een totale oppervlakte van 613 km^2

Het doel van de morfodynamische analyse is om de verschillende bodemvormen in kaart te brengen en de mogelijke bodemveranderingen in de periode 2020 tot 2072 te kwantificeren, zowel in opwaartse als neerwaartse richting. Met deze resultaten kunnen de windparkontwikkelaars vervolgens de ondersteuningsconstructies en kabeltracés ontwerpen alsmede de optimale locaties hiervan bepalen.

De bathymetrie in IJV wordt gekenmerkt door een aantal noord-zuid georiënteerde zandbanken met hoogtes van enkele tot 10 m. In het zuidwesten (Site II) komt een diepere geul voor waar de Holocene laag afwezig is. De maximale diepte van deze geul is 10 m dieper dan de rest van IJV. Het merendeel van Sites I tot IV is bedekt met dynamische zandgolven. In Sites V en VI zijn slechts enkele zandgolven aanwezig. In het algemeen staan de kammen van de zandgolven loodrecht op de zandbanken.

De mediane korrelgrootte van IJV neemt af van zuid naar noordoost varieert tussen 0.026 mm en 0.290 mm (slib tot middelzwaar zand) tussen één en vijf meter onder de zeebodem. In het zuidwestelijk gelegen diepste deel van IJV, alsmede plaatselijk over de zandgolftroggen en -kammen, komen grovere korrelgroottes voor op de zeebodem. Het gehalte aan fijne deeltjes bedraagt 1-2% met maximumwaarden van 10%. Er is geen trend in korrelgrootte of fijnstofgehalte met de diepte.

Niet-erodeerbare lagen in de ondergrond van IJV zijn alleen plaatselijk in IJV dicht bij de zeebodem aanwezig, bijvoorbeeld in het zuidwesten van Site II. Het is onwaarschijnlijk dat de niet-erodeerbare lagen de morfodynamiek van de zeebodem beïnvloeden, omdat ze ofwel te diep ofwel te dun verspreid liggen om door de zeebodemdynamiek te worden blootgelegd.

Numerieke modelresultaten geven aan dat de sedimenttransportpatronen grotendeels door het getij worden gedomineerd, waarbij meteorologische omstandigheden slechts een tijdelijk effect hebben. De modelresultaten wijzen op een netto sedimenttransportrichting over IJV naar het noordnoordoosten, in lijn met de richting van de dominante getijdenstromingen. Deze transportrichting komt over het algemeen overeen met de waargenomen trekrichting van zandgolven uit de data-analyse.

Om de dynamiek van de zeebodem te analyseren is een gedetailleerde analyse gepresenteerd die gericht is op de zandgolven in IJV. De dynamiek van de zandgolven wordt bepaald met behulp van een 2D-kruiscorrelatietechniek. De zandgolven migreren typisch naar het noordnoordoosten met migratiesnelheden tussen 0.4 m/jaar en 2.7 m/jaar. De migratiesnelheden zijn over het algemeen vergelijkbaar voor Sites I-VI. Voor Site V zijn de migratiesnelheden anders door het kleine aantal aanwezige zandgolven. In Site VI zijn geen zandgolven waargenomen.

Een Fourier analyse is toegepast om de dimensies van de zandgolven te bepalen. In IJV hebben de zandgolven lengten tussen 170 m en 620 m en zijn ze 0.9 m tot 3.5 m hoog (5% en

95% niet-overschrijdingswaarden voor Sites I-VI). De hoogste zandgolven zijn waargenomen in Site I-en II, terwijl de langste zandgolven in Site V gevonden zijn. Uit de analyse van grootschalige variaties in de zeebodem blijkt dat de zeebodem gedurende de levensduur van het windmolenpark als effectief statisch kan worden beschouwd. Uit de analyse van gegevens met hoge resolutie en herhaalde onderzoekslijnen blijkt dat de temporele variaties in de afmetingen van de megabodem klein zijn (5 tot 10 cm).

Op basis van een morfodynamische analyse zijn een toekomstige Best Estimate Bathymetry (BEB), Lowest Seabed Level (LSBL) en een Highest Seabed Level (HSBL) voorspeld. De LSBL en HSBL zijn de respectievelijke voorspelde laagste en hoogste toekomstige zeebodemniveaus voor de periode 2022 tot 2072, inclusief onzekerheidsmarges. De voorspelde veranderingen van het zeebodemniveau variëren van -3.12 m tot +5.22 m (99,9% niet-overschrijdingswaarden voor de locaties I-VI). Kaarten van de voorspelde veranderingen van het zeebodemniveau voor de periode 2020 tot 2072 zijn weergegeven in Figuur 1. De grootste bodemveranderingen worden voorspeld voor Sites I-II, waar de hoogste mobiele zandgolven zijn gevonden. De kleinste veranderingen in de zeebodem worden voorspeld voor Sites V-VI.

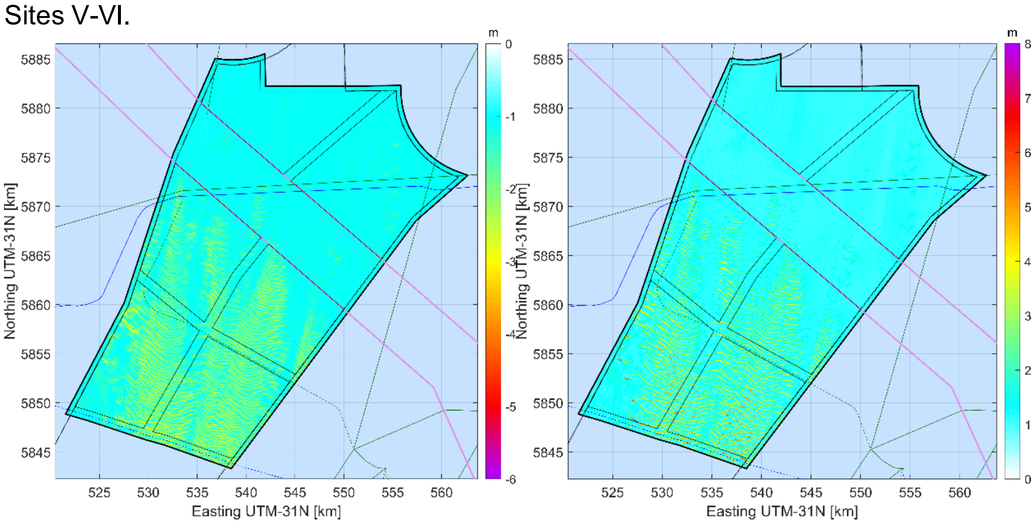

Figuur 1: Overzicht van de voorspelde veranderingen van het zeebodemniveau in de periode 2022-2072, met het verschil tussen de huidige zeebodem en het laagste (LSBL, linker plot) en het hoogste (HSBL, rechter plot) voorspelde zeebodemniveau.

Naast de toekomstige zeebodemniveaus is een hindcast gemaakt voor zeebodemniveaus over de periode 1945 tot 2022 om de mogelijke niveaus te bepalen waarop zich niet-ontplofte explosieven (UXO's) bevinden die tijdens de Tweede Wereldoorlog in de Noordzee zijn gedumpt. Om rekening te houden met het volledige bereik van mogelijke objectniveaus, zijn het laagste, het hoogste en het best geschatte objectniveau voor de periode 1945-2022 berekend. Deze niveaus vertegenwoordigen respectievelijk de laagste, hoogste en beste schatting van het laagste zeebodemniveau in de periode 1945-2022.

Morfodynamische activiteit zoals zandgolfmigratie kan een bedreiging vormen voor funderingen en kabels indien hiermee geen rekening wordt gehouden bij het ontwerp en de algemene planning van het windmolenpark. Zo kunnen kabels bloot komen te liggen en kan de inklemmingsdiepte van funderingen afnemen als gevolg van de verlaging van de zeebodem. Om dit op te vangen zijn grotere initiële begraafdiepten voor kabels en funderingspalen of een grotere omvang van de schuurbescherming nodig.

De in deze studie gepresenteerde voorspelde veranderingen in zeebodemniveau vloeien voort uit de toegepaste morfologische analysetechnieken en beschrijven de (onzekerheid van de) fysica en de natuurlijke variabiliteit van het geanalyseerde morfologische systeem. Er zijn geen extra veiligheidsmarges voor ontwerpdoeleinden toegepast.

About Deltares

Deltares is an independent institute for applied research in the field of water and the subsurface. Throughout the world, we work on smart solutions, innovations and applications for people, environment and society. Our main focus is on deltas, coastal regions and river basins. Managing these densely populated and vulnerable areas is complex, which is why we work closely with governments, businesses, other research institutes and universities at home and abroad. Our motto is ‘Enabling Delta Life’.

As an applied research institute, the success of Deltares can be measured by how much our expert knowledge can be used in and for society. At Deltares, we aim to use our leading expertise to provide excellent advice and we carefully consider the impact of our work on people and planet.

All contracts and projects contribute to the consolidation of our knowledge base. We always apply a long-term perspective when developing solutions. We believe in openness and transparency. Many of our software, models and data are freely available and shared in global communities.

In the offshore wind energy sector, Deltares is specialised in metocean conditions, wave loads, operational forecasting systems, foundation stability, scour, bed protection, nature inclusive design, cable and foundation integrity and last but not least seabed morphodynamics, geology, survey and monitoring techniques. Deltares is also involved in several research projects related to offshore wind such as EU-FP7-MERMAID, FLOW (2011-2015), GROW (2016-onwards) and TKI-Wind op Zee (JIP WindJack, JIP OSCAR, JIP WiFi, TKI-Chaincutter, JIP HaSPro, JIP SiMoN, JIP-GBS, JIP HyPE-ST, JIP ECO FRIEND, JIP CALM and JIP HybridEnerSeaHub of which many are initiated and coordinated by Deltares. Deltares’ capability statement on offshore wind can be downloaded here: https://www.deltares.nl/en/issues/offshore-engineering/.

As part of the research agenda of Deltares, new techniques for analysing and modelling sand wave migration and sediment transport have been developed. Recent examples are a continuous field measurement technique for sand waves, an improved morphodynamic module for the Delft3D model (based on Lesser et al. (2004)) and new techniques to use satellite imagery (Luijendijk et al., 2018) for detecting shoreline dynamics and bathymetric changes. These techniques are continuously being validated, developed and, therefore, further improved.

Deltares is based in Delft and Utrecht, the Netherlands. We employ over 800 people from 40 countries. We have branch and project offices in Australia, Indonesia, New Zealand, the Philippines, Singapore, the United Arab Emirates and Vietnam. Deltares also has an affiliated organisation in the USA.

Contents

Glossary

BEB	Best-estimate bathymetry, on average the best estimate of future seabed levels. Locally this level can differ from the actual measured seabed level for a specific year
Bed load transport	Transport of sediment along the stream bed
BEOL	Best-Estimate Object Level; the best estimate lowest seabed level over the period 1945 up to the most recent measurement
BH	Borehole
Composite bathymetry	Bathymetry compiled from different individual bathymetries. Overlap between surveys is kept to a minimum whilst exact date of measurement is kept
CPT	Cone penetration test
DINO-database	Data and Information of the Netherlands Subsurface
DCSM-FM	Dutch Continental Shelf Model – Flexible Mesh. The Deltares numerical model applied in this assessment
EMODnet	European Marine Observation and Data network
ETRS89 UTM-31N	The horizontal coordinate system used in this study
Fines content	The percentage of finer material (<3 mm) found in a sediment sample
geological units	Soil layers below the seabed surface. Timescales of formation are in the order of centuries
Grain size	Size of the sediment particles (diameter) with specific metrics used (e.g. d_{50} corresponds to the median grain size)
HKW	Hollandse Kust (west) Wind Farm Zone
HOL	Highest Object Level, the upper envelope of the lowest level expected over the period from 1945 up to the most recent measurement
HSBL	Highest SeaBed Level, the highest level to be expected over the considered future period
IHO	International Hydrographic Office
kPa	Kilo pascal, undrained shear strength of clays. Strengths correspond to various definitions with clays <10 kPa referred to as extremely low strength clays
Large-scale bathymetry	The seabed underlying the sand waves and megaripples. Formation of this is a process of centuries to millennia
LAT	Lowest astronomical tide
LOL	Lowest Object Level, the lowest level expected over the period from 1945 up to the most recent measurement
LSBL	Lowest SeaBed Level, the lowest level to be expected over the considered future period
MBES	MultiBeam Echo Sounder. Measurement equipment for measuring bathymetries
Megaripples	Small scale bed features with lengths of several metres and heights up to a few decimetres. Timescales of dynamics are in the order of months
Morphodynamics	Interaction and adjustment of the seabed and hydrodynamic processes as a result of the motion of sediment. In this assessment morphodynamics are considered over period of months (spring-neap cycles) to decades (period of interest 2020-2072)

NEL	Non-erodible layers. Layers for which no natural erosion is expected
NLHO	Netherlands Hydrographic Office
Offshore Wind Energy Act	Law in which offshore wind in the Netherlands is regulated
Residual sediment transport	Net sediment transport over a period consisting of a similar amount of ebb and flood tides
RMSE	Root Mean Square Error
Sand waves	Bed features with lengths of hundreds of metres and heights up to a few metres. Timescales of dynamics are in the order of years
SBES	Single Beam Echo Sounder. Measurement equipment for measuring bathymetries
Scour	Erosion of sediments around an obstacle. Obstacles can be foundations, pipelines and cables but also wrecks.
SBP	Sub-bottom profiler
SDE+ grant	Subsidy for sustainable energy transition
Spring-neap cycle	Period over which one spring (highest difference between lowest and highest water level) and one neap (smallest difference between lowest and highest water level) tide occur
Suspended load transport	Transport of sediment in the water column
THU	Total Horizontal Uncertainty. The horizontal uncertainty related to bathymetry measurements
TNO	the Netherlands Organisation for applied scientific research
TVU	Total Vertical Uncertainty. The vertical uncertainty related to bathymetry measurements
UHRS	Ultra high resolution seismic
Uorb,cr	Critical orbital velocity for which sediment is mobilised as induced by waves motion
UXO	Unexploded ordnance. Historical remnants of war and bombs that did not explode
VC	Vibrocore
IJV	IJmuiden Ver
IJV IA	IJmuiden Ver Investigation Area
IJV WFZ	IJmuiden Ver Wind Farm Zone

1 Introduction

1.1 Background

In 2013 more than 40 organisations and the Dutch Government entered into the Energy Agreement for Sustainable Growth (Energieakkoord voor Duurzame Groei). An important part of this agreement includes scaling up of offshore wind power development. The Ministry of Economic Affairs and Climate Policy presented a road map outlining how the Government plans to achieve its offshore wind goals in accordance with the timeline agreed upon.

The roadmap to achieve this goal sets out a schedule of yearly tenders including the Borssele, Hollandse Kust, Ten noorden van de Waddeneilanden and IJmuiden Ver (IJV) Wind Farm Zones. The Dutch Government has developed a systematic framework under which offshore Wind Farm Zones are designated. Any locations outside these Wind Farm Zones are not eligible to receive a permit. Within the designated Wind Farm Zones, the government decides the specific sites where wind farms can be constructed using a so-called Wind Farm Site Decision (‘Kavelbesluit’). This contains conditions for building and operating a wind farm on a specific site. The Dutch transmission system operator TenneT will be responsible for grid connection.

Winners of the site development tenders will be granted a permit to build a wind farm according to the Offshore Wind Energy Act (Wet Windenergie op zee) and are offered for a grid connection to the mainland. The Ministry provides a set of site data, which can be used for the preparation of bids for these tenders. This morphodynamic study is part of the site data.

This assessment focusses on the IJV Investigation Area (IA) which is located approximately 62 km west of the coast of North Holland. IJV consists of six wind farm Sites (I-VI), of which the coordinates are subject to change, and will have a combined capacity of 6,000 MW. In total, three 2 GW converter stations are planned connecting the wind farm to the onshore power grid. IJV is indicated in Figure 1.1 with red and black polygons, whereas existing and under construction wind farms are indicated by green and blue polygons, respectively.

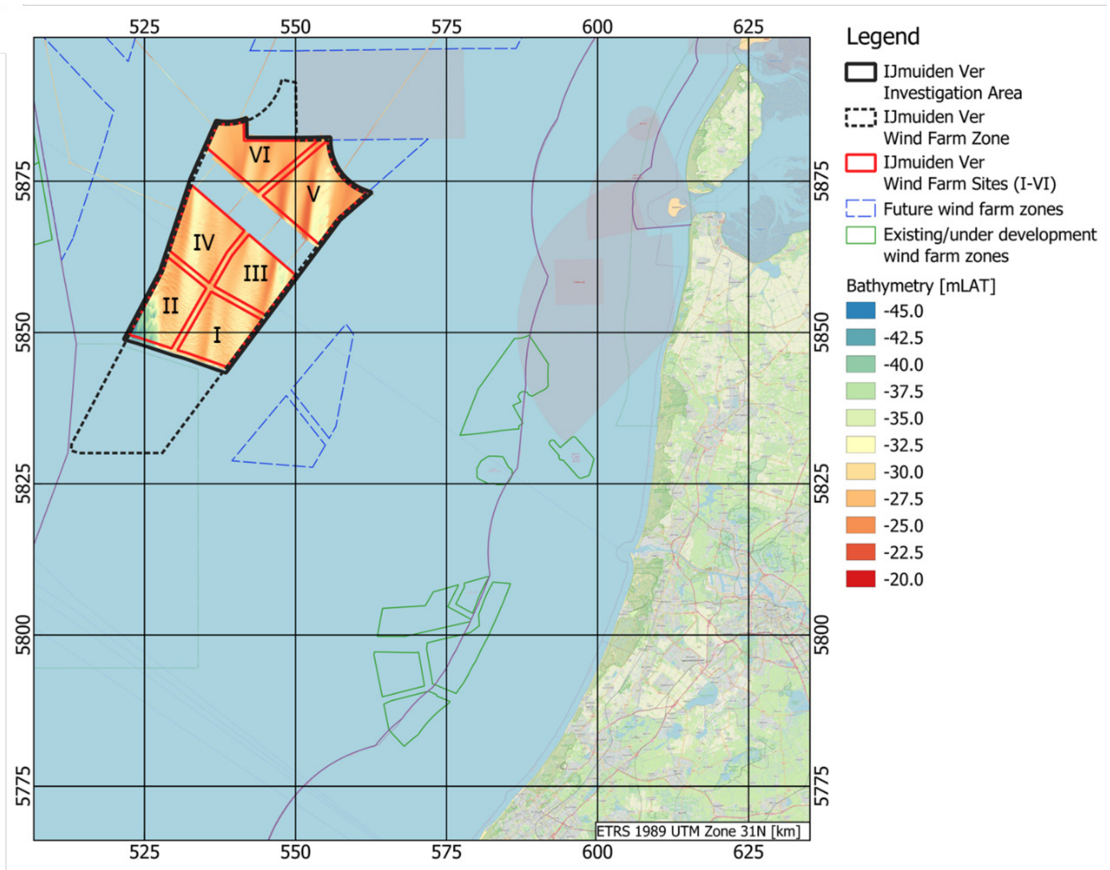

Figure 1.1: Location of IJV (black polygon), IJV individual Sites (I-VI, red polygons) and neighbouring existing (green polygons) and future (blue polygons) Wind Farm Zones off the Dutch coast. Bathymetry data inside IJV is provided by GEOxyz (2021) for Sites I-IV and by Fugro (2022a) for Sites V-VI.

1.1 Previous studies for IJV

An overview of IJV was performed by Arcadis Nederland BV and Geo-Engineering.org GmbH (2019), where the geology and morphology were investigated using data sources that were available at that time. The metocean conditions for IJV were derived by DHI (2019).

This study presents a detailed investigation of the morphodynamics in IJV and forms, together with Deltares (2023), the scour and scour protection study for IJV. The analysis is based on the geophysical (Fugro, 2022a; GEOxyz, 2021) and geotechnical investigations (Fugro, 2022b, 2022c, 2022d, 2022e, 2022f, 2022g) as well as historical geophysical (Royal Netherlands Navy - Hydrographic Office, 1980-2021) and geotechnical (Valerius et al., 2015) information.

More information about site studies for IJV is available here.

1.2 Objectives and deliverables

The objective of this study is to provide RVO and companies tendering for IJV with detailed information on the predicted morphodynamics in the IJV IA over the period 2020 to 2072 (1945-2022 for the hindcast). The analysis is based on a data-driven approach supported by the results of sediment transport modelling. The report contains the following information:

- A detailed description of morphodynamic features in IJV;
- A description of the shallow geological and sedimentological site conditions to a depth of 20 m below the seabed to understand the existing morphology and to predict future behaviour;
- An analysis of the morphodynamics in IJV;

- Simulated sediment transport rates in IJV based on hydrodynamic and wave modelling to increase system understanding, validate findings from the data-driven analysis and support the selection of appropriate uncertainty ranges for the predicted bed levels;
- Extrapolation of seabed dynamics for the estimation of future seabed levels (2020 to 2072) and hindcast of historic seabed levels (1945 to 2022). Levels are determined every five years with an increased resolution during the foreseen installation years.

To support the morphodynamic analysis, the geological, geophysical and hydrodynamic conditions in IJV are analysed to ensure that all relevant physical processes are taken into account. The outcomes of this analysis are presented in:

- A descriptive report presenting the analysis and main results (this document);
- A webinar;
- A GIS archive and XYZ data with hindcasted and future seabed levels.

1.3 Structure of this report

This report is structured as follows. Chapter 2 describes the available data. An overview of the area including a description of processes is given in Chapter 3. The methodology for the morphodynamic analysis is discussed in Appendix A. Results of the analyses are discussed in Chapter 4 (data-driven analysis), Chapter 5 (numerical modelling) and Chapter 6 (assessment of future and historic seabed levels). The report is completed with conclusions and recommendations in Chapter 7.

The attached appendices include figures from the hydrodynamic modelling, the geological analysis and the bathymetry composites in Appendices B, C and D, respectively. Additional transects over the area are presented in Appendix E. An overview of data accompanying this report is provided in Appendix F.

2 Overview of the available data

2.1 Introduction

In this section background information applied in this study is summarised. First, in Section 2.2 the available bathymetry data is discussed, followed by the geotechnical and other geophysical data relevant to this study in Section 2.3. Hydrodynamic and wave measurement data is introduced in Section 2.4.

As per the requirements of RVO, and similar to previous studies by Deltares (2015, 2016a, 2016c, 2019b, 2020d, 2022a), all geographical coordinates are based on the ETRS1989 horizontal datum, which is based on the GRS80 ellipsoid, and the UTM-31N projection (EPSG 25831). Vertical levels are relative to Lowest Astronomical Tide (LAT), unless mention is made of a different specific level[1].

2.2 Bathymetry data

The two main sources of bathymetric data for this study comprise (i) existing historical bathymetry data available from the NLHO (Royal Netherlands Navy - Hydrographic Office, 1980-2021) and (ii) data provided by RVO; measured by GEOxyz (2021) for Sites I-IV and measured by Fugro (2022a) for Sites V-VI and additional survey lines.

An overview of the number of surveys available for IJV is presented in Figure 2.1. The presented figure includes both historic seabed surveys and data provided by RVO. The area of analysis is extended to also cover possible dynamics of bedforms migrating into IJV (important during the extrapolation of data).

At IJV and its surroundings, 12 surveys were conducted between 1976 and 2022 each covering part of the analysis area. Furthermore, 11 repeat survey lines were completed in 2021 and 2022. The availability of a large number of surveys improves both the temporal and spatial coverage in the analysis of seabed dynamics. The surveys are summarised in Table 2.1. The table includes detailed information on the surveys such as measurement dates, data density and the survey related THU (Total Horizontal Uncertainty) and TVU (Total Vertical Uncertainty). For the THU and TVU reported mean values plus two times the standard deviation are presented. If not available, IHO standards are presented (International Hydrographic Organization, 2020).

Other data sources such as GEBCO and data from admiralty charts are not used in the analysis because of limited spatial coverage and large uncertainties in bed levels. For the numerical modelling, bathymetry data was taken from the NLHO for the Dutch continental shelf and from United Kingdom Hydrographic Office (1977-2021) for the United Kingdom continental shelf. EMODNet data near IJV on the Dutch continental shelf is not included in the analysis as it is already covered by the NLHO data.

[1] A different datum (MSL) is used for the figures relevant to the methodology and results of the numerical modelling analysis.

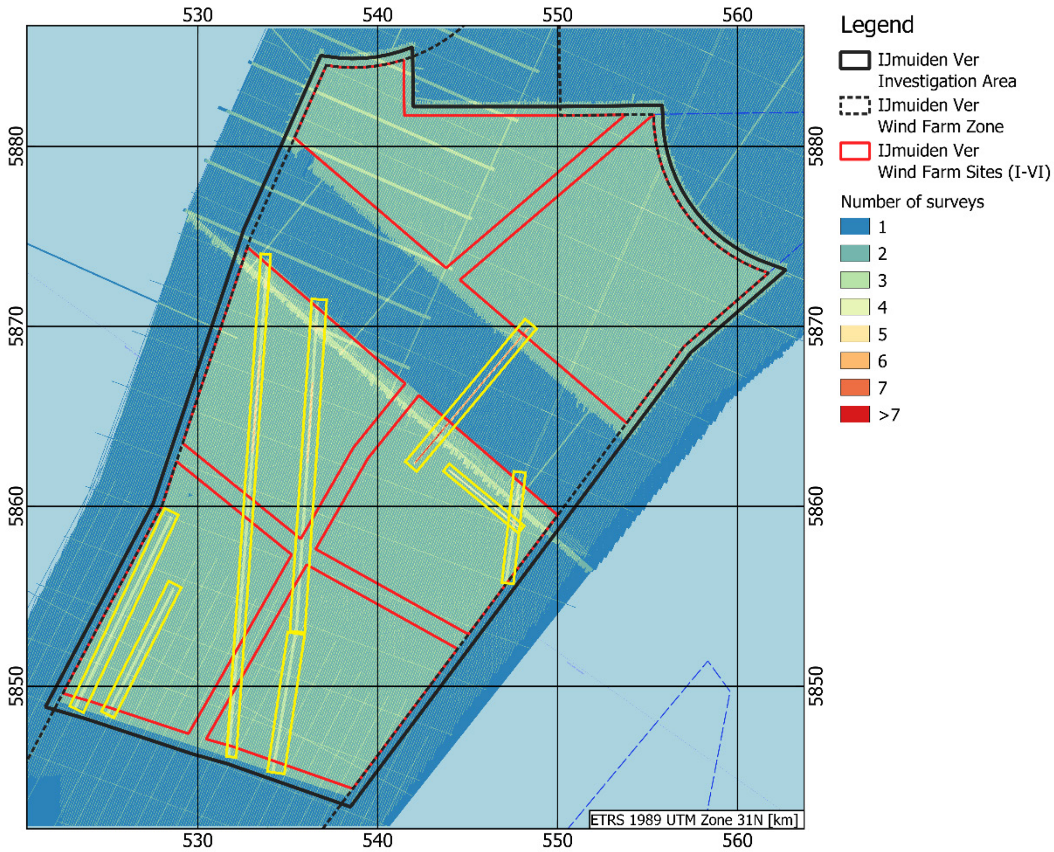

Figure 2.1: Overview of the number of surveys available for IJV. The area of IJV mostly contains two to three surveys for the period 1976 to 2022. The additional survey lines in the area are highlighted with yellow rectangles.

Table 2.1: Historical bathymetry surveys available in and around the study area. Column Survey method indicates the seabed mapping system. Columns THU and TVU present respectively the THU and TVU. Data density is specified as Low (SBES (Single-Beam Echo Sounder) with data points spacing greater than 100 m), Average (SBES with spacing of approximately 100 m between sailed lines), High (MBES (Multi-Beam Echo Sounder) data with a 5 m by 5 m resolution) and Very High (MBES data with a 0.5 m by 0.5 m resolution).

Survey ID	Start date (day-month-year)	End date (day-month-year)	Data density	Survey method	THU [m]	TVU [m]
NLHO data (Deltares inhouse database)						
15563	01-02-1976	30-04-1976	Low	SBES	20.00	1.00
15564	01-03-1976	31-05-1976	Low	SBES	20.00	1.00
15562	12-03-1976	15-04-1976	Low	SBES	20.00	1.00
402	01-01-1992	28-02-1992	Average	SBES	5.00	0.50
10464	01-05-2002	31-08-2002	Average	SBES	5.00	0.50
11544	01-08-2003	30-11-2003	Average	SBES	5.00	0.50
10625	01-08-2003	30-11-2003	Average	SBES	5.00	0.50
18168	08-09-2013	30-03-2014	High	MBES	5.00	0.50
18668	24-08-2014	14-03-2015	High	MBES	5.00	0.50
19241	01-08-2015	12-01-2016	High	MBES	5.00	0.50

RVO measured data IJV (Fugro, 2022a; GEOxyz, 2021)						
2D campaign Sites I-IV	08-04-2020	06-08-2020	Very High	MBES	1.67	0.18
2D campaign Sites V-VI	27-03-2022	02-07-2022	Very High	MBES	0.25	0.21
Repeat survey lines (TenneT and Fugro)						
TenneT Transect 01	07-09-2021	07-09-2021	Very High	MBES	2.00	0.25
TenneT Transect 02	07-09-2021	25-09-2021	Very High	MBES	2.00	0.25
TenneT Transect 03	07-09-2021	08-09-2021	Very High	MBES	2.00	0.25
TenneT Transect 04	07-09-2021	07-09-2021	Very High	MBES	2.00	0.25
TenneT Transect 05	07-09-2021	07-10-2021	Very High	MBES	2.00	0.25
GeoXYZ Repeat Line	11-04-2022	11-04-2022	Very High	MBES	2.00	0.25
TenneT Repeat Line	12-04-2022	12-04-2022	Very High	MBES	2.00	0.25
Repeat Line MBES 1st	11-04-2022	12-04-2022	Very High	MBES	2.00	0.25
Repeat Line MBES 2nd	20-05-2022	20-05-2022	Very High	MBES	2.00	0.25
Repeat Line MBES 3rd	07-06-2022	07-06-2022	Very High	MBES	2.00	0.25
Repeat Line MBES Last	29-08-2022	29-08-2022	Very High	MBES	2.00	0.25

2.3 Geotechnical and geophysical data

2.3.1 Geotechnical data

Geotechnical data is used to assess the composition of the top sediment layer in terms of grain sizes and the presence of non-erodible layers. Cone Penetration Tests (CPTs), boreholes, Vibrocores and grab samples were performed during multiple geotechnical campaigns. Here, geotechnical data is taken from Fugro (2022b, 2022c, 2022d, 2022e, 2022f, 2022g); GEOxyz (2021). In addition, geotechnical data in IJV was collected from the DINO-database, similar to data presented in Arcadis Nederland BV and Geo-Engineering.org GmbH (2019).

CPT logs provide geotechnical characteristics of the sediments to the penetration depth (e.g. tip resistance and sleeve friction values) allowing for the interpretation of the vertical profile properties of the sediment, mainly lithology and stiffness. Boreholes and Vibrocores were taken at various locations across IJV to provide a description of the sediments at different depths (lithology, sedimentary structures etc) and at some locations, the grain size distribution. To assess seabed composition in more detail, part of the Vibrocore data was taken at 19 transects and contain five Vibrocores per transect. The transect locations are indicated with red ovals in Figure 2.2.

For the sediment transport modelling and seabed characterisation, information on the median grain size (d_{50}) and the percentage of fines in the sediment is required, to assess spatial variability across IJV and influence on sediment transport patterns. Information on sediment grain sizes by Fugro (2022b, 2022c, 2022d, 2022e, 2022g); GEOxyz (2021) is supplemented with digital maps of median grain sizes of the sand fraction (63 – 2000 µm) and the fines content (i.e. percentage of grain sizes smaller than 63 µm) of the Dutch continental shelf with a spatial resolution of 200 m composed by TNO in 2007 (Maljers & Gunnink, 2007). The median grain size per node is based on interpolation of measured grain size distributions of both seabed sediment samples and sediment cores in the DINO-database of TNO.

An overview of all available data is presented in Figure 2.2 and Table 2.2.

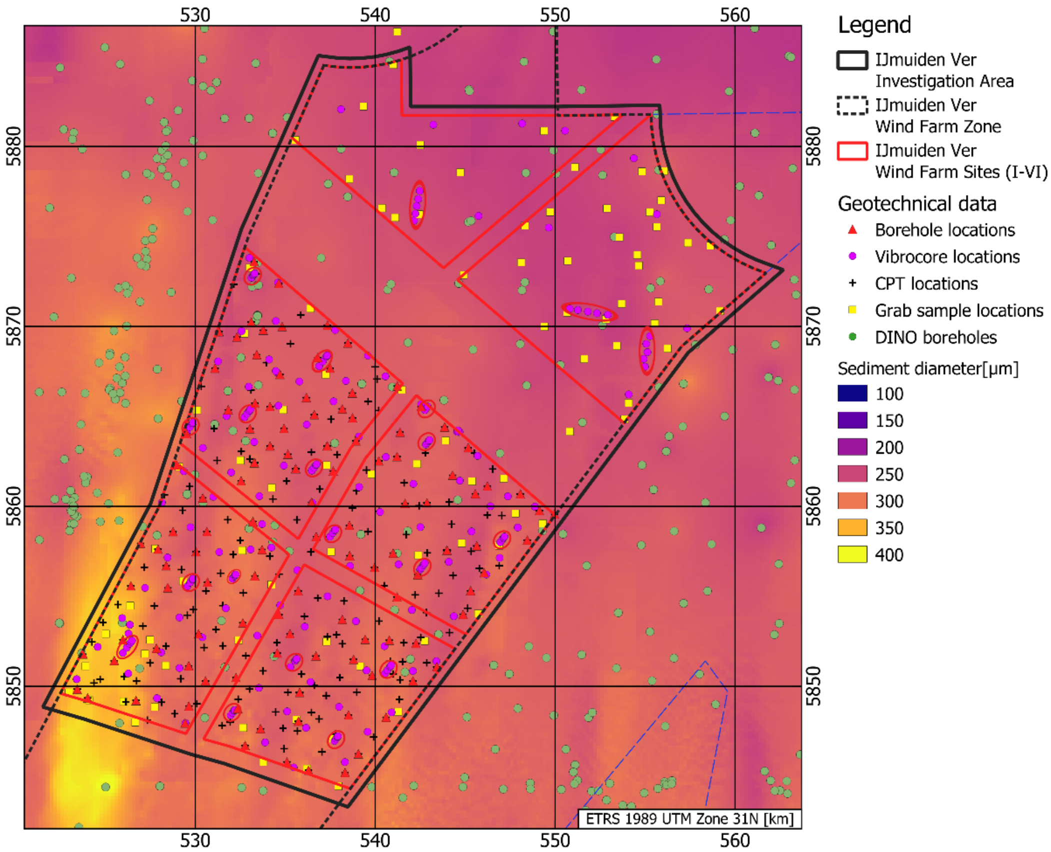

Figure 2.2: Overview of data used in the geotechnical analysis including an overview of the d_{50}. Red ovals indicate locations of the Vibrocore transects.

Table 2.2: Overview of the available geotechnical data for IJV. Distinction is made between Sites I-IV and Sites V-VI as measurements were conducted during different campaigns.

Type	Number of locations IJV I-IV	Number of locations IJV V-VI
Boreholes	114 (Fugro, 2022d, 2022e)	-
Vibrocores	164 (Fugro, 2022g)	25 (Fugro, 2022c)
CPT	354 (Fugro, 2022f)	25 (Fugro, 2022c)
Grab Samples	49 (GEOxyz, 2021)	42 (Fugro, 2022b, 2022c)
Grain size	DINOloket and interpolated maps (Grain size maps)	

2.3.2 Seismic and side scan sonar data

Using the reflection of acoustic waves by geological layers in the subsurface, sub-bottom profiler (SBP) and Ultra high resolution seismic (UHRS) data provides information on the geometry of the geological units' sub-seabed and a general indication of lithology. The data provided by Fugro (2022a); GEOxyz (2021) provides information on the upper tens of metres below the seabed. Based on the data, a first stage ground model of the main geological units was constructed by Fugro (2022a); GEOxyz (2021). The thickness of the top geological layer (the Southern Bight Formation) is shown in Figure 2.3. Based on previous morphodynamic assessments (e.g. on the nearby Hollandse Kust (west) Wind Farm Zone (Deltares, 2020d)), it is expected that most morphodynamic behaviour during the wind farms lifetime will take place in this formation.

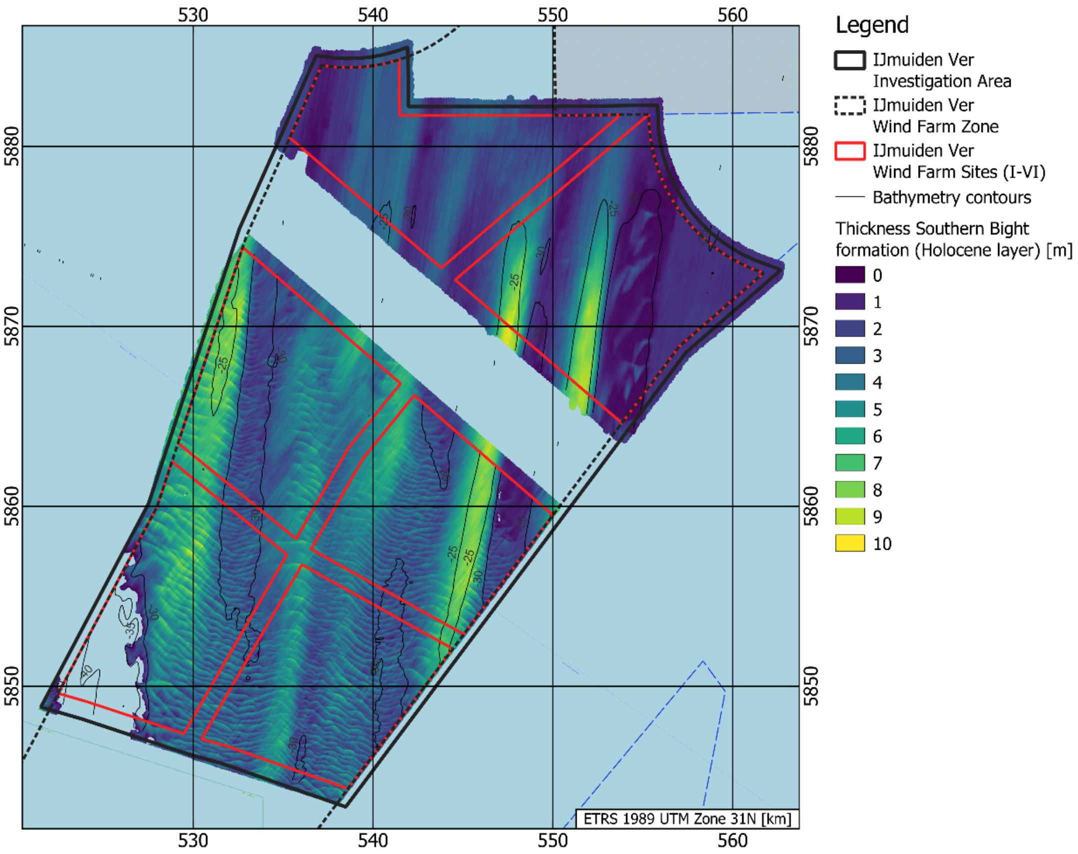

Figure 2.3: Thickness of the Southern Bight Formation in IJV (Fugro, 2022a; GEOxyz, 2021) with depth contours. The gap in the presented data at the southwest area of IJW (Site II) indicates local absence of the Southern Bight formation (Holocene layer). All remaining areas where no thickness of the Southern Bight Formation is presented (e.g. the shipping corridor south of Sites V-VI) are outside of the survey limits.

Side-scan sonar data (GEOxyz (2021) provides information on the reflectivity of the seabed, which is a function of its roughness and lithology. Its interpretation helps to constrain which areas are mobile or non-mobile.

2.4 Hydrodynamic data

In-situ measured hydrodynamic data are used for the validation of the numerical model. Two buoys were deployed in IJV (RPS, 2022b). The two buoys are referred to as Station A and Station B but are abbreviated in this report as IJVA and IJVB, respectively. The deployment date was 28th April 2022. The monitoring campaign will measure wind, waves, temperatures, pressures and currents for a period of two years. The current speed and direction are measured at various depths through the water column with a vertical spacing of 1 m. The locations of the measurements are illustrated in Figure 2.4. Table 2.3 presents the time periods for which measurement data are available for the present study.

Due to the short duration of available measurements in IJV, longer-term measurements at other locations close to IJV were considered for the validation of the hydrodynamic and wave models. These included multiyear water level and current measurements at the locations of HKWA buoy water level,measurements at K13a platform (sourced from MATROOS), as well as wave measurements at K13a and K14 platform locations (sourced from MATROOS).

The numerical models used (DCSM-FM 0.5 nm and DCSM-SWAN) are extensively calibrated, mainly against water level measurements and wave measurements, respectively. The validation carried out for this study is presented in detail in Appendix A. The following paragraphs summarize the findings on the models' performance based on the validation of the hydrodynamic and wave models.

First, the hydrodynamic model was validated using water level and depth-averaged current velocity magnitude and direction measurements. High correlation and limited scatter were found when comparing the measured and modelled water level measurements over all examined locations. A temporally uniform bed level difference of ~12 cm between the simulated and measured water levels was observed for the locations IJVA and IJVB. This offset is partially attributed to the measurements. Nonetheless, the effect of such difference on the sediment transports is expected to be small within the scope of this study.

Similarly, high correlation was found between the measured and modelled depth averaged current velocity and directions for all examined locations. An underprediction of the peak velocities (3.5 cm/s on average, based on the 2022 measurements) by the model was found. This underprediction is more pronounced for the dominant northeast directed peak flood velocities, compared to the southwest directed peak ebb velocities. Based on that, the model is expected to capture correctly the sediment transport asymmetry with an underprediction of the sediment transport rates.

The wave model was validated using measurements of significant wave height, peak wave period and mean wave direction. High correlation between the model results and observations for the significant wave height was found. At the same time an underestimation of the lower wave heights (Hs<1 m) by the model was observed, while for the intermediate and higher wave conditions which are more important for sediment transport at IJV, the performance of the model is significantly better. The modelled and measured data of the remaining wave parameters compare less well. For both though the model was able to follow the longer term measured trends. In general, it can be stated that all parameters reflect the conditions in the area of interest.

Table 2.3: Meta data on metocean measurement locations and associated measured parameters used for the validation of the hydrodynamic and wave models.

Loc	Latitude (N)	Longitude (E)	Water Depth (m LAT)	Period of available / used measurements	Characteristic time interval	Measured parameters
IJVA	52°53'08"	3°42'39"	32.1	01/05/2022-31/05/2022	~10 mins	Current speed, current direction, water level, wave parameters
IJVB	52°53'39"	3°41'07"	26.0	01/05/2022-31/05-2022	~10 mins	Current speed, current direction, water level, wave parameters
HKWA	52° 34' 10"	3° 44' 17"	23.4	01/02/2019-20/07/2019	~10 mins	Current speed, current direction, water level
K13a	53° 13' 3"	3° 13' 13"	29.3	01/01/2019-31/12/2021	~10 mins	water level, wave parameters
K14	53° 15' 59"	3° 37' 59"	28.4	01/01/2019-31/12/2021	~10 mins	wave parameters

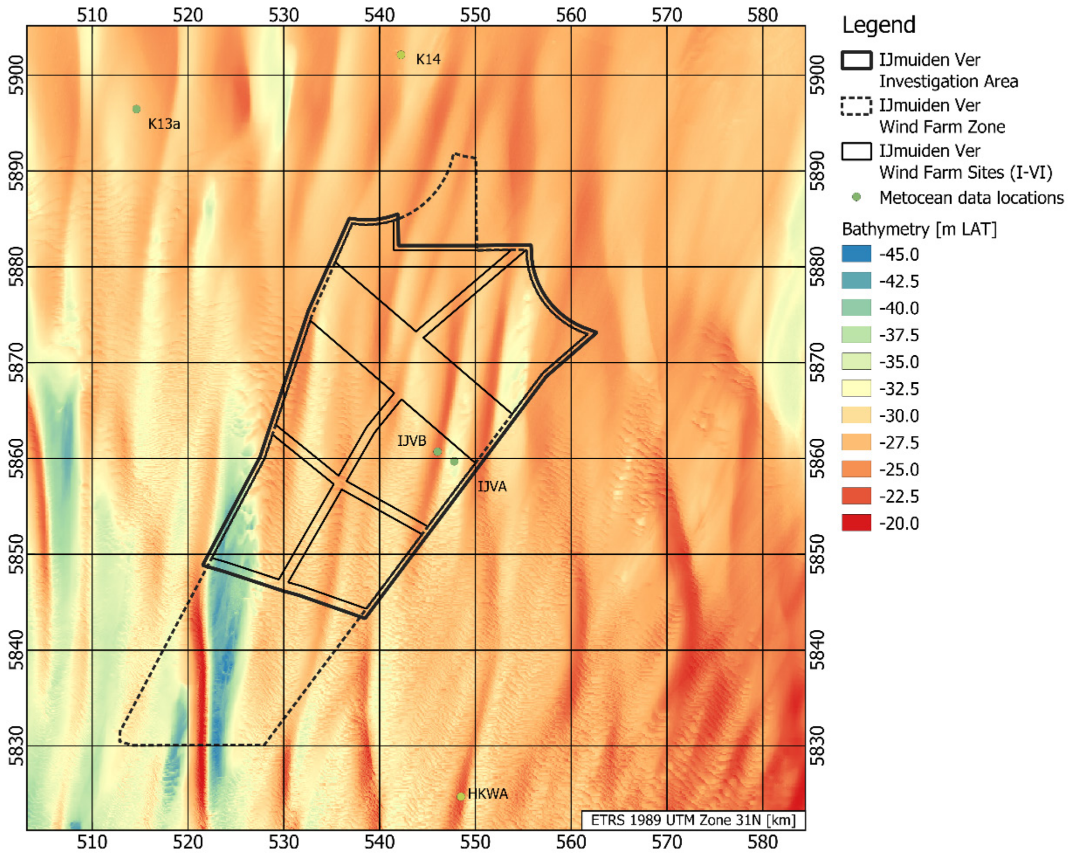

Figure 2.4: Locations of the metocean data. The bathymetry inside IJV OWF consists of the most recent datasets. Outside IJV OWF EMODnet bathymetry (EMODnet Bathymetry Consortium, 2020) is visualised – this dataset is not part of the morphodynamic analysis.

2.5 Summary of available data and gap analysis

For the purpose of the morphodynamic assessment several data sources have been analysed. Most important are the bathymetry, geotechnical and geophysical data, and hydrodynamic data. The quality and amount of geotechnical and hydrodynamic data are high and that these are sufficient to carry out the presented analysis.

The spatial and temporal coverage of available data is high for the purposes of this study, with three datasets covering the entire IJV over the period 2002 to 2022. For the locations of the repeat survey lines coverage is higher. It is noted though that some restrictions on the analysis apply: Except for the locations with the repeat survey lines, only interannual comparisons could be made for the entire IJV. Additionally, the period of available data (20 years) is shorter than the period of extrapolation (2020 to 2072). This might impact interpretation of the larger-scale dynamics. For example, dynamic behaviour of sand banks has a timescale of decades or centuries. Over a period of 20 years, any dynamic behaviour can be in the same order as the dataset uncertainties. To account for the increasing uncertainty in larger-scale bed level changes in the future due to potentially partially observed bed level change trends, a temporally increasing upward and downwards uncertainty range is applied at the bed level predictions. For more details on the uncertainty ranges applied, reference is made to Section 6.4.

For the areas surrounding IJV the spatial and temporal availability of the data is lower. For most areas at most two (of which only one is fully covering) bathymetry datasets were available. However, with regards to the expected dynamics within IJV, the impact of this limited temporal and spatial coverage on the bed level predictions in IJV is low.

The available geotechnical data is of high quality and spatial resolution. The large amount of available data aids in the description and understanding of the seabed and characterisation of its dynamic behaviour. The available metocean measurement data from the buoys is temporally limited. The start of the measurements coincided with the start of this study and therefore only one month of validated measurement data was available. As discussed in Appendices A.3.1.2 and A.3.2.2, it has some impact on the validation of the numerical models applied. To supplement these short in-situ measurement datasets, datasets of metocean conditions close to IJV are procured and used in the validation process (see Section2.4).

3 Overview of the area

3.1 Introduction

This study focusses on investigating erosion and sedimentation patterns in IJV as a result of the transport of sediment. The transport of sediment is a coupling between bathymetry, sediment characteristics and hydrodynamics in offshore environments. The focus is on IJV over the period of 2020 to 2072 (1945 to 2022 for the hindcasts).

In this chapter an overview of the area is given focusing on the bathymetry, seabed composition and hydrodynamics and relevant morphodynamic processes, both at a regional scale (North Sea) as well as close to IJV. A more detailed description of the local conditions in IJV is provided in the Chapters 4 and 5, focussing on the morphodynamics and sediment transport patterns, respectively. Coupling between the data analysis (trend analysis on erosion and sedimentation patterns) and numerical modelling (sediment transport patterns) for IJV is presented in Section 6.2.

Section 3.2 presents an overview of the area at the regional scale, based on available literature on bathymetry, geology, hydrodynamics and sediment transport. Section 3.3 gives a general background on the dynamics of the seabed, while Section 3.4 presents the overview of the study area.

3.2 Regional overview

3.2.1 Overview of bathymetry and bedforms

IJV is located at the southern part of the North Sea, a shallow marginal sea at the north European Continental Shelf. The North Sea is connected at the south and north to the Atlantic Ocean through the English Channel and the Norwegian Sea respectively. Although the average depth of the North Sea is 74 m, in the Southern North Sea the depth does not exceed 50 m (Nauw et al., 2015).

Several morphological features are present in the North Sea including areas with tidal sand ridges, sand waves, megaripples, channels and gravel deposits, tunnel valleys, iceberg grooves, pockmarks and other (Eisma et al., 1979; Nauw et al., 2015). According to Eisma et al. (1979), the majority of the features in the North Sea are relict features, with the exception of the features in and around the Southern Bight.

The Southern Bight is characterised by Holocene sands - planar beds, megaripples, sand waves and linear sand ridges, which interact with the flow conditions (Eisma et al., 1979; Huntley et al., 1994). Linear sand ridges, or sand banks are observed mainly east the Norfolk coast and in the Southern Bight. Their along crest length can range up to 65 km, their width up to 2km and their height up to 40 m above the surrounding seabed. They are frequently superimposed by sand wave and megaripple systems. Sand waves are found covering most of the southern Bight and occupying the area southwest of the Dogger Bank The sand waves in the southern Bight are up to 15 m high and several hundreds of metres long (Eisma et al., 1979; Huntley et al., 1994). Figure 3.2 from Damen et al. (2018) presents the spatial distribution of sand wave characteristics in the Dutch North Sea.

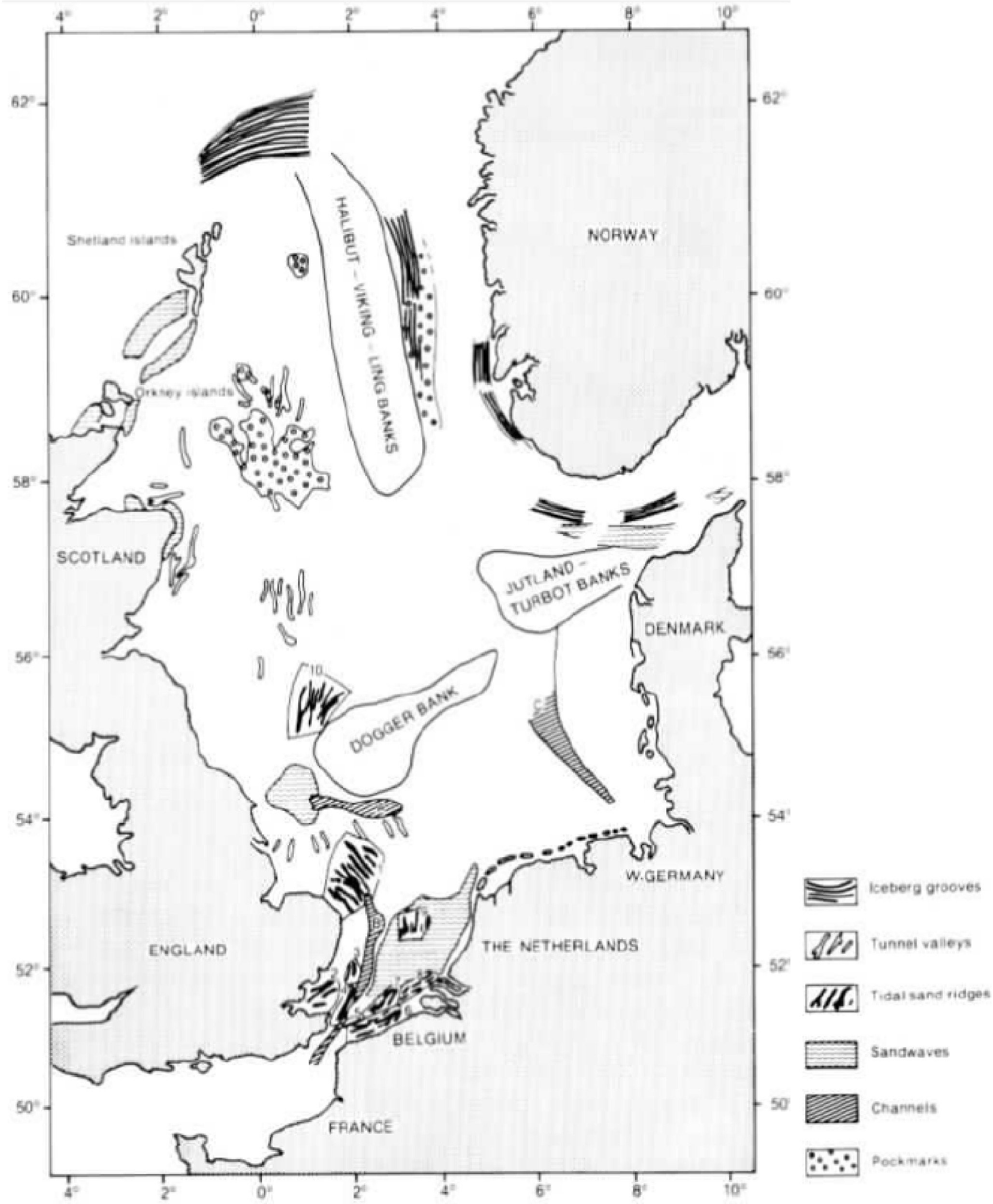

Figure 3.1: Morphological map of the North Sea (Eisma et al., 1979): 1-Norfolk Banks, 2-Thames Estuary Banks, 3-Gabbard Banks, 4-The Falls, , 5-Sandettie, 6-Flemish Banks, 7-Hinder Banks, 8-Zeeland Ridges, 9-Brown Bank Ridges, 10-East Bank Ridges, A-Outer Silver Pit, B-Deep Water Channel, C-Helgoland Channel.

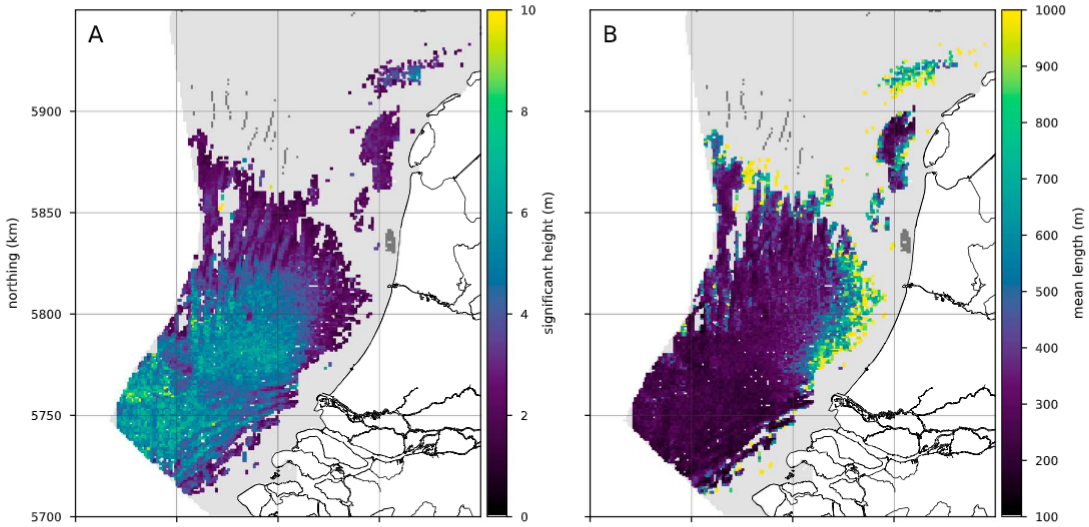

Figure 3.2: Sand wave characteristics (a) height and (b) length, aggregated per square kilometre and for high sand wave coverage (Damen et al., 2018).

3.2.2 Geology

Since one million years ago, glacial and interglacial periods have altered the landscape of the North Sea. The ice masses shifting on land and sea led to river diversion and sediment re-routing. The changes in ice volume during glacial-interglacial phases led to global changes in sea level, which affected the coastline configuration, as well as the location and the type of sediments accumulating.

During the early Middle Pleistocene between 1 and 0.5 Ma, the Dover Strait was closed, and England was connected to the European continent via a chalk land bridge (Hijma et al., 2012). The rivers draining to the area, Thames, Rhine, Meuse and the Baltic River System, transported sandy sediments to the area (Yarmouth Roads and Egmond Grounds Formation). During the Saalian glaciation (200 to 130 ka BP) the ice sheet protruded into the southern North Sea (Beets et al., 2005; Ehlers, 1990) and reached 56 degrees north latitude. IJV is located at the western edge of the maximum ice sheet extent (Cameron et al., 1993). West of the ice sheet margin deposition and erosion occurred in a periglacial environment.

South of the ice margin the Rhine and Meuse Rivers acted as meltwater drainage systems, draining in a south-westerly direction. Glaciolacustrine and glaciofluvial deposits are present in proximity to the ice sheet margin, overlying periglacial sediments. Glacial valley infill consists mostly of marine deposits. Saalian sediments in the southern North Sea were mostly eroded and reworked by the succeeding Eemian transgression.

After the Saalian glaciation the Rhine formed an incised valley that during the Eemian interglacial was transgressed by the sea. Fluvial sediments that filled the valley have not been described offshore, but the transgressive estuarine and shallow marine sediments of the Eem Formation occur in the study area and wider surroundings. After the peak of the interglacial, the sea level lowered and the study area became part of the deltaic plain of the Rhine (Arcadis Nederland BV & Geo-Engineering.org GmbH, 2019). The preserved deltaic sediments consist of significant clay and peat layers which are generally classified as the Brown Bank Member of the Eem Formation. The sandier sediments, depending on whether they are fluvial or tidal characteristics, form part of the Kreftenheye or Eem Formations, respectively.

Around 80 kyr ago (end of interglacial, beginning of the Weichselian), sea level lowered significantly, and incision by the Rhine resulted in large-scale erosion of the Eem Formation and Brown Bank Member of the Eem Formation. The southern part of the study area became part of the Rhine valley (Arcadis Nederland BV & Geo-Engineering.org GmbH, 2019) and fluvial sediments of the Kreftenheye Formation were deposited.

After the Rhine abandoned the area around 40 kyr ago and until the early Holocene, various types of sediment were deposited in the North Sea area belonging to the Boxtel Formation (Peeters et al., 2015). They consist of sediments deposited by brooks (sand, sandy loam), peat, thaw-lake deposits and wind-blown (aeolian) deposits (cover sand) in a periglacial environment. Based on the results of the geophysical investigations (Fugro, 2022a; GEOxyz, 2021) it is unclear if the Boxtel Formation occurs in IJV.

At the start of the Holocene sea level was still below -50 m LAT, but around 8.5 kyr ago sea level rose to around -20 m LAT (Hijma & Cohen, 2010). This resulted in rising groundwater levels and widespread peat formation, known as the Basal Peat Bed (Nieuwkoop Formation). Continued sea-level rise resulted in drowning of the peat landscape and the formation of initially back-barrier and estuarine settings and later a shallow-marine environment (Naaldwijk Formation).

After the shoreline migrated to the east of the study area, the sandy deposits were shaped into sand banks and sand waves (van Dijk & Kleinhans, 2005). These deposits are part of the Bligh Bank Member of the Southern Bight Formation.

3.2.3 Hydrodynamics

The tidal wave enters the North Sea from the Atlantic Ocean around Scotland and traverses the Sea in an anticlockwise direction around two amphidromic points and leaves the North Sea at the Norwegian coast again. Along the coast of the Netherlands the tidal wave propagates from southwest/west, towards the northeast/east. The two dominant tidal components (M2, S2) interact to create a 14-day spring neap tidal cycle. The interaction of the tidal components due to advection and friction (e.g. through the interaction with the bathymetry) generates internal tides and non-zero residual currents, which are locally important for sediment transports (Nauw et al., 2015; Sündermann & Pohlmann, 2011). Figure 3.3 presents the tidal residual circulation in the North Sea from Brettschneider (1967). It illustrates a southwest to north east residual flow in the South North Sea, offshore of the Dutch coast.

Apart from the tide, wind also creates wind driven circulation in the North Sea, controls the spectrum of wind waves and can lead to significant storm related water level changes (storm surges)(Otto et al., 1990; Sündermann & Pohlmann, 2011). The most prevalent westerly winds force an anti-clockwise (cyclonic) circulation around the North Sea (Sündermann & Pohlmann, 2011). Temperature and salinity variations induce a seasonal variation in stratification and density-driven currents, stronger during the summer and autumn months (Nauw et al., 2015; Otto et al., 1990). At the shallower parts of the North Sea, tidal mixing creates a mixed water column without significant heat stratification (Nauw et al., 2015). Seasonal salinity gradients are present at the areas with significant freshwater inflow (ROFIs).

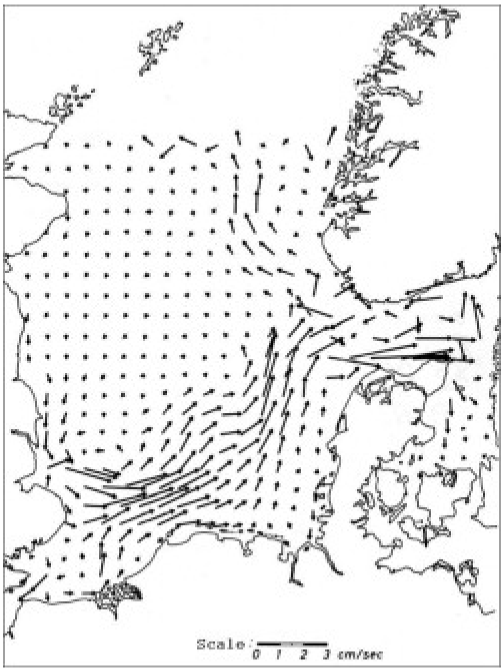

Figure 3.3: Residual currents of the M2-tide from (Brettschneider 1967) as presented in (Sundemann and Pohlmann, 2011).

3.2.4 Sediments and sediment transport

Surface sediment in the North Sea is mainly sand, with areas of mud to muddy sand (for example southeast and east of Dogger Bank), as well as several areas with gravel patches, observed frequently in UK waters (EMODnet Geology, 2019). Although the distribution of bed sediments dates back to the Pleistocene and Early Holocene era (Eisma & Kalf, 1987), currents in the Southern Bight are strong enough to move sand, sand banks and sand waves over time. Otto et al. (1990) observe that tidal asymmetry contributes to a net bed load and suspended sediment transport in the North Sea. Additionally, surface waves contribute to the sediment transport by raising bed material into suspension and transporting sediment in shallow waters (compared to the wavelength).

Eisma and Irion (1988) present a balance of the suspended sediment supply/loss from the North Sea. The authors estimate that the suspended sediment is incoming primarily from the English Channel and at lower rates from the North Atlantic, followed by inflow of sediment form erosion, river discharges, primary production and other sources. Suspended sediment is primarily deposited in the North Sea, typically at areas of lower velocities, including the Wadden Sea, river mouths, the Norwegian Channel/Skagerrak/northern Kattenga, the German Bight and other areas. A smaller amount of sediment is estimated to flow out of the North Sea. The authors report a near balance of sediment supply and loss/deposition, however uncertainties are noted with regards to individual estimates making up this balance.

Under the assumption of unrestricted large-scale sediment supply and non-changing hydrodynamic climate, a dynamic equilibrium in the sediment volumes locally in IJV over the lifetime of the OWF can be presumed. Comparisons of the available bathymetry data in IJV, as discussed in Sections 4.3.1.2 and 4.5, over a total period of 20 years, support this assumption, indicating that while sediment is transported over the OWF through bed load and suspended transport, long-term changes in the regional-scale bathymetry are limited and within the survey uncertainty bandwidths.

3.3 Seabed dynamics

For the dynamics of the seabed in the North Sea ample literature is available. This section discusses general findings on seabed dynamics, followed by specific literature on sand waves.

3.3.1 Bedform characterisation

Large parts of the sandy seabed of shallow seas, such as the southern North Sea, are characterised by rhythmic bedforms. These features are dynamic and are the result of the complex interaction between hydrodynamics, sediment transport and morphology. In this section a general description of these features and the relevant processes is given.

Typical parameters of geometry and dynamics that distinguish different types of bedforms (wavelength, wave height and mobility) are presented in Figure 3.4. The parameter values are based on expert judgement, existing literature and morphodynamic studies in comparable areas (e.g. Deltares, 2015, 2016a, 2016c, 2019b, 2020d, 2022a). In the last column of Figure 3.4, the potential threat to foundations and electricity cables is indicated per bedform.

Ripples are the smallest bedforms, in the order of centimetres, and the crest is oriented normal to the tidal current direction (i.e. flow-transverse, 90°). Because of their limited size, ripples cannot be observed on the regular offshore multibeam echo soundings and do not pose a threat to offshore wind farm constructions. Ripples are, however, relevant for the bed roughness and sediment transport in the area.

Megaripples have wavelengths of a few tens of metres and heights of a few decimetres up to 1 m and their crests are also generally oriented perpendicular to the tidal current direction, with a variation in their orientation over the lengths of sand waves (Malikides et al., 1989; van Dijk & Kleinhans, 2005). Because of their relatively short wavelength and high migration rates, a turbine foundation will experience many megaripples passing during the lifetime of a wind farm.

Sand waves have wavelengths between 100 and 1,000 metres, heights of several metres, and their crests are oriented approximately perpendicular to the tidal current direction (± 20°, Le Bot, 2001)). In the southern North Sea, sand waves are observed in water depths of more than 14 m (although sand waves occur at 7 – 9 m on the Belgian Continental Shelf (BSC) (Van Lancker & Jacobs, 2000)), with flow speeds of around 0.65 m/s and median grain sizes of 0.35 mm (Borsje et al., 2009). Sand waves may be superimposed by megaripples (e.g. van Dijk & Kleinhans, 2005).

Sand banks are the largest bedforms, with spacings up to kilometres and heights of several tens of metres. Offshore sand banks are oriented more or less parallel (up to 30°) to the main tidal current direction (Hulscher et al., 1993).

Sand waves, sand banks and to a lesser extent, megaripples have dimensions which are significant for foundation design. Where the sand banks often can be considered to be stationary for the lifetime of a wind farm, the sand waves typically migrate fast enough to cause (up to) metres of seabed variation, depending on the location on the sand wave relative to the foundation. For megaripples and ripples seabed variations at least in the order of the height of the megaripples are expected at the foundation location.

	Wavelength	Wave height	Mobility	Threat to foundations and cables
Ripples	O(0.1) m	O(0.01) m	Mobile and transient	Minimal
Megaripples	O(10) m	O(0.1) m	Mobile and transient	Small
Sand waves	**O(100) m**	**O(1) m**	**Mobile and persistent**	**Large**
Sand banks	O(1000) m	O(10) m	Stationary	Minimal

Figure 3.4: Morphodynamic seabed features in IJV and some typical characteristics. Capital "O(.)" indicates "In the order of". O(1) m indicates dimensions the order of metres (e.g. 1 or 15 m). Values are based on expert judgement, existing literature and morphodynamic studies in comparable areas (e.g. Deltares, 2015, 2016a, 2016c, 2019b, 2020d, 2022a).

3.3.2 Sand bank formation and physical processes of evolution

Offshore sand banks are generated and maintained by the horizontal deflection of the tidal current and varying current strengths over an undulating bed, whereby the highest flow velocities occur on the stoss side and the lowest flow velocities on the lee side. Therefore, the oscillating flow of tidal currents results in net sediment transport onto the bank (Hulscher et al., 1993; Huthnance, 1982), hence the growth of an initial undulation. In a morphodynamic modelling study, Idier and Astruc (2003) found that the orientation of sand banks is controlled by the current-driven sediment flux, whereas the wavelength is determined by the gravity-driven sediment flow (down-slope).

Numerical analyses of the sediment flux gradients show that the growth of sand banks to equilibrium height is mostly due to the hydrodynamic processes, although the saturation height slightly depends on the value of the bottom slope-effect coefficient (Idier & Astruc, 2003). For a water depth of 30 m, a steady velocity of 1 m/s and a grain size of 500 µm, their resulting equilibrium height was estimated to be 81% of the undisturbed water depth, although this may be a slight overestimate (Idier & Astruc, 2003). The saturation process is controlled by friction terms in the model, and not by gravity-driven sediment transport. The modelling saturation time is almost 8,000 years. For fully grown sand banks, a migration velocity of 11 m/yr occurred for a steady current of 1 m/s.

Due to the slow evolution of sand banks, empirical data on the migration rates of sand banks is scarce. Idier and Astruc (2003) summarise (see also Figure 3.5): "*Whereas the Norfolk Banks [Caston, 1972] moved toward the northeast direction by about 300 to 600 m during the last century (i.e., 3 to 6 m yr^{-1}), the Flemish Banks have only slightly moved during the last 300 years [Eisma et al., 1997] and the Hinder Banks seem to be stationary for the past 40 years. These various migration rates should be related to the intensity of steady currents*" (residual tidal currents or wind-induced current).

Observations at the Netherlands Continental Shelf revealed landward migration (no rates mentioned) and growth of an offshore bank and that bank dynamics were mostly caused by sand wave dynamics (Van Dijk et al., 2011). Elsewhere, sand banks were found to be more dynamic. Van Lanker and Jacobs (2000) reported a 20-38 m shift towards the northeast of the Baland Bank on the Belgium Continental Shelf in a 4-year period (5 – 9.5 m/yr). Morphodynamic analyses of sand banks on the French Continental Shelf revealed that coastward bank migration caused significant vertical bed level changes over a period of 30 years.

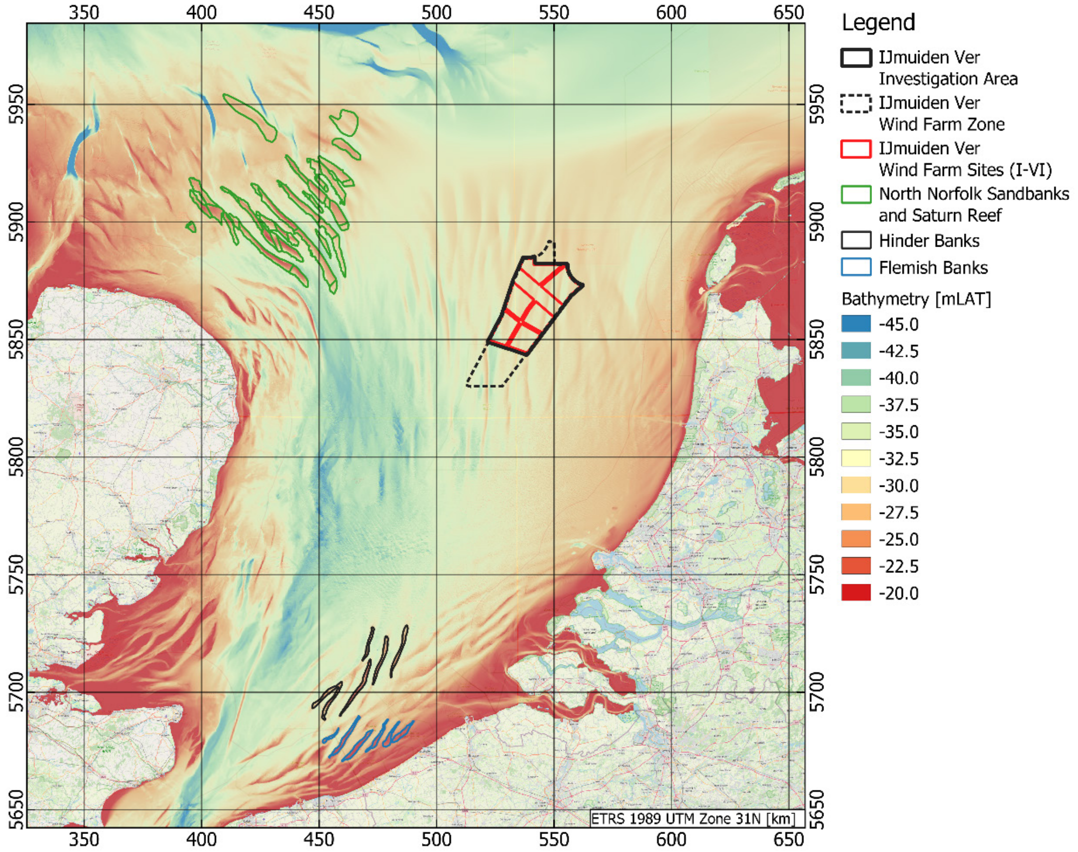

Figure 3.5: Overview of sand bank systems in the North Sea mentioned in Idier and Astruc (2003). The spatial information have been procured from data.gov.uk and marineregions.org. IJV OWF is also annotated on the figure. The bathymetry data presented on the background are sourced from EMODnet Bathymetry Consortium (2020).

3.3.3 Sand wave formation and physical processes of evolution

Sand waves are generated by the residual vertical circulation in the water column (Allen, 1980; Hulscher, 1996). Due to oscillating tidal flow over initially small perturbations of the seabed, residual vertical circulation cells are formed in the bottom boundary layer that transport sediment from the troughs to the crests, thereby initiating and maintaining sand waves (Allen, 1980) as shown in Figure 3.6. More recent modelling studies corroborated this process of formation.

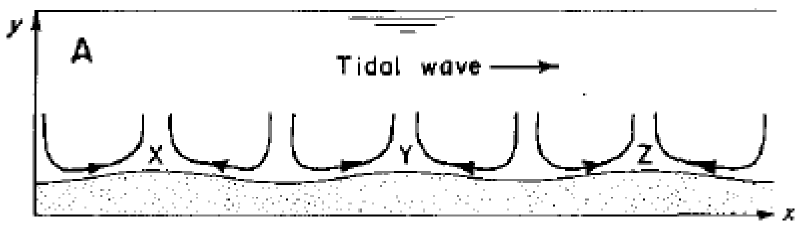

Figure 3.6: Isolines of net tide-integrated velocities due to oscillating tidal flow over perturbed bed that cause sand wave formation (from Allen, 1980).

In Besio and Rodriguez (2006) and Borsje et al. (2014) the influence of bed (growth) and suspended load (dampening) transport on the formation and evolution of sand waves was demonstrated using linear stability and process based, (e.g. Delft3d) models.

3.3.4 Typical sand wave characteristics

Sand waves have wavelengths in the order of hundreds of metres (Ashley, 1990; van Dijk & Kleinhans, 2005) and may migrate at a speed up to tens of metres per year (Dorst et al., 2009; van Dijk & Kleinhans, 2005; Van Santen et al., 2011). If sand waves are removed by dredging they may regenerate within a time period of years (Knaapen & Hulscher, 2002). The most recent and full-scaled overview of sand waves on the Dutch Continental Shelf is that of Damen et al. (2018), who presented the extent of the sand wave field and the spatial variation in sand wave morphology. They quantified the wavelengths (100 – 1000 m range), heights (1 – 10 m) and asymmetries of all sand waves on the Dutch Continental Shelf, with the longest (500-1000 m) and most asymmetric sand waves occurring off the Holland coast and at the northern edge of the field, and the highest sand waves (4 – 10 m) occurring in the southwestern offshore parts. Damen et al. (2018) correlated the sand wave morphology to environmental parameters (such as water depth, tidal current velocity, median grain size and significant wave height) and to process parameters (such as sediment transport mode (bedload versus suspended load), Shields parameters for both the tide and waves, and the residual sediment transport). They found that the occurrence of sand waves is related to sediment grain size, and the spatial variability in morphology is most likely controlled by sediment properties and transport mode.

3.3.5 Empirical studies on sand wave dynamics

Large-scale bathymetric patterns of offshore bedforms in the North Sea generally remain similar over decades. So, when two bathymetric maps, surveyed (more than) ten years apart, are compared, the plan-view bed patterns (sand banks and sand waves) are not much changed (see also Lankneus & Moor, 1991), apart from migration. In addition, bathymetric cross-sections of offshore sand banks with superimposed sand waves in the southern North Sea indicate that the large-scale bed morphology has remained similar over decades (e.g. Figure 3.24 Van Dijk, 2011).

In contrary to the similarity of the general pattern, quantitative studies of the geometry and dynamics of sand waves show that wavelengths, heights and shape may change over time on the scale of years or less, and that vertical bed dynamics are mainly due to sand wave migration (Van Dijk, 2011).

3.3.6 Changes of sand wave dimensions over time

Classical empirical studies on sand waves (e.g. McCave, 1971; Terwindt, 1971; Van Veen, 1935) reported on the occurrence, different shapes and dimensions of sand waves on continental shelves and hypothesised on their relationship with tidal currents and waves.

Sand wave lengths may change a few to tens of metres between surveys in time, but compared to their lengths of hundreds of metres, this change may be insignificant. The ranges in lengths of adjacent sand waves in one area at one time are larger than the changes in lengths of individual sand waves over time.

Sand wave heights may change following sand wave growth or decay, due to the perennial tidal flow, as described above, but also due to seasonal variations in environmental parameters (Buijsman & Ridderinkhof, 2008) or storms (Houthuys et al., 1994; Le Bot, 2001; Sterlini et al., 2009; Sterlini et al., 2012). The short-term differences in height (yearly or event-related) are only captured in high-temporal resolution monitoring data and may show other behaviour than the long-term changes (decades) and both may be in the orders of decimetres to metres (Le Bot, 2001).

In offshore locations on the Netherlands Continental Shelf, for example offshore Rotterdam at a water depth of 30 m below LAT, some sand waves decreased in height in the period 1999-2002 and then increased in height in the period 2002 – 2007 (e.g. site 1 in Van Dijk et al., 2011). Further offshore, at the North Hinder Traffic Separation Scheme in water depths of approximately 33 m below LAT, sand waves with an average wavelength of 270 m and an average wave height of 4.8 m, grew steadily in height (Van Dijk, 2011). Here, the crest heights of sand waves increased by approximately 2 m in the period between the early 1990s and 2006.

Seasonal variations in sand wave height were mapped by Buijsman and Ridderinkhof (2008) in a high temporal resolution time series between 1998 and 2005 of the tidal inlet Marsdiep (water depths around 24 m below MSL, average wavelength 190 m, average height 3 m), where sand waves were 0.5 m lower in spring (after storm season in winter) compared to autumn (prior to the storm season).

3.3.7 Variation in sand wave migration

On the Dutch, Belgian and French continental shelves in the southern North Sea, average sand wave migration rates vary between 0 and 20 m/yr: in most areas several metres per year with exceptions up to 20 m/yr (Dorst et al., 2011; Le Bot, 2001; van Dijk & Kleinhans, 2005; Van Dijk, 2008; Van Lancker & Jacobs, 2000).

Apart from the spatial variation in dynamic behaviour of sand waves (e.g. Dorst et al., 2011; Van Dijk & Egberts, 2008; van Dijk & Kleinhans, 2005), the migration direction and migration rates of sand waves may vary in time at one location. The migration direction of sand waves is generally in the direction of the residual current, but may reverse due to higher tidal constituents (Besio et al., 2004).

Migration rates depend on the residual current velocity but may also be controlled by wave action. This could be by the stirring of sediment, where waves add to the sediment transport and thereby increase migration rates (van Dijk & Kleinhans, 2005). In contrast, the directions of waves with respect to the residual tidal current may decrease migration rates if the wave and current directions are opposite to each other(Sterlini et al., 2012).

3.3.8 Sand wave variation due to storms

In general, the morphology of sand waves (lengths, heights, steepness and asymmetry), as well as their dynamics (growth, migration) can change over time, e.g. due to seasonal influences and occurrence of storms. Bathymetries measured are a snapshot in time and might not include these (short-term) intra-annual variability.

Direct field observations of the effects of wind-induced surface waves are scarce because hydrographic surveys are almost never performed immediately before and after a storm. In the literature, the effect of storm waves was observed at the Middelkerke Bank, Belgian Continental Shelf (Houthuys et al., 1994), where sand wave crests of 1 – 3 m high sand waves were lowered by 0.3 – 1.2 m after a series of storms (wind speeds of 20 – 40 m/s ≡ 8 – 12 Bft.) between October and November 1991. The sediment that was eroded from the crests was deposited on the direct lee sides and in the troughs of the sand waves, thereby smoothing the morphological profile. Water depths above the sand wave crests were 5 – 8 m (-Mean Lower Low Water Springs). Megaripples with heights of 0.2 – 0.5 m on the northwest flank of the bank disappeared after the storm.

Houthuys et al. (1994) did not find a depth-related difference in crest lowering (p.31). Our analysis of the cross sections, indicates that the bank profiles were unaffected in water depths more than approximately 13 to 17 m. Houthuys et al. (1994) also found that sand waves migrated towards the top of the bank. Sand wave migration towards the top of sand banks was also found in offshore wind farm studies at the Bligh Bank. Van Lancker and Jacobs (2000) arrived at a contradictive conclusion based on their data of the Baland Bank, one of the coastal banks off the Belgium coast in the period September 1996 – March 1998. They imply that the morphology was not determined by a series of storms from the northwest, but by an 8-day period of east-northeasterly winds of less than 6 Bft. They found that sediment was deposited in the troughs and on the stoss sides of the sand waves, and that a decrease in volume in the subsequent period was most severe for the shallow area and stable below 8 m depth.

Under high surface waves, sediment is stirred up and is transported by the tidal current. van Dijk and Kleinhans (2005) showed that the orbital motion at the bed below surface waves of H_s=3 m is sufficient to cause sediment transport at the bed at 25 m water depth for sediment grain sizes of up to 300 µm. Records of significant wave height in the shallow Southern Bight of the North Sea reveal that surface waves of 3 m occur several times per year, mostly during the winter season. During periods of fair-weather conditions, the height of sand waves may then again increase (Buijsman & Ridderinkhof, 2008; Terwindt, 1971). Therefore, both the magnitude and frequency of storms play a role in the reduction of sand wave heights. An additional factor affecting the migration rate of sand waves is the wind- and surge-driven current, which increases the sediment transport during storms and causes sedimentation in the waning stage of the storm (Papili et al., 2014).

A more recent observation, from a high-resolution survey of a track in a Dutch offshore wind farm site at 19 – 24 m water depth immediately before and after a storm, demonstrated that the bathymetry did not change, except for the minor lowering of megaripples by 2 to 3 cm (Deltares, 2019a). A storm from the southwest occurred on the 28th of March 2016 (maximum significant wave height of surface waves, H_{m0} = 5.5 m and peak waves periods T_p = 11 s) with surveys on the 18th of March and the 1st of April 2016. The observation contradicted the described effect of a single one-day storm on sand waves at 19 – 24 m water depth (19 m water above the crests) (Le Bot, 2001; van Dijk & Kleinhans, 2005). Other observations of the impact of storms on the seabed showed that they may also create (rather than erase) bedforms which are three-dimensional bedforms with wavelengths in the order of metres (Passchier & Kleinhans, 2005; Peters & Loss, 2012).

3.3.9 Summary

Tidal sand banks are formed by the horizontal deflection of the oscillating tidal current, whereas sand waves are generated by the vertical residual circulation in the water column. Sand banks are considered to be relatively stable in the majority of the literature, Sand waves are the bedforms of a size and dynamics that are most relevant in morphodynamic studies for offshore wind farms. The evolution and dynamics of sand banks and sand waves are controlled by hydrodynamic (e.g. tides, waves) and sediment transport processes, depending on the local conditions.

Sand waves on continental shelves reported in the literature typically have a long-term net migration rate of several to few tens of metres per year. However, the changes in length, height, steepness and asymmetry, and migration of individual sand waves are variable in time and may be opposite in subsequent periods between surveys. Net changes over a period of decades (dominated by the tidal flow) may therefore be more realistic because the short-term variations are averaged out. Short-term and seasonal changes may occur, mainly related to the occurrence of severe storms.

The findings from both literature and morphodynamic assessments for nearby wind farms are valid for IJV. It must, however, be stressed that only areas with similar seabed characteristics (e.g. sand wave dimensions, soil conditions, water depths and hydrodynamic conditions) should be compared.

3.4 Overview of the study area

3.4.1 Bathymetry and bedforms

IJV is located approximately 54 km off the west coast of the Netherlands. The area is divided into six (I, II, III, IV, V-VI) Sites. An overview of the seabed in and around IJV is presented in Figure 3.7. The area is characterised by a number of north-south oriented sand banks with heights of a few metres up to 10 m. In the southwest (Site II) a deeper channel occurs incising the Southern Bight formation (GEOxyz, 2021) with parts 10 m deeper than the rest of IJV (see also Figure 2.3). The majority of Sites I-IV are covered by dynamic sand waves. In Sites V-VI only a few sand waves occur. In general, the sand waves are oriented perpendicular to the sand banks.

IJV is crossed by a number of cables and pipelines of which some are abandoned. Between IJV Sites III, IV, V-VI a shipping corridor is present.

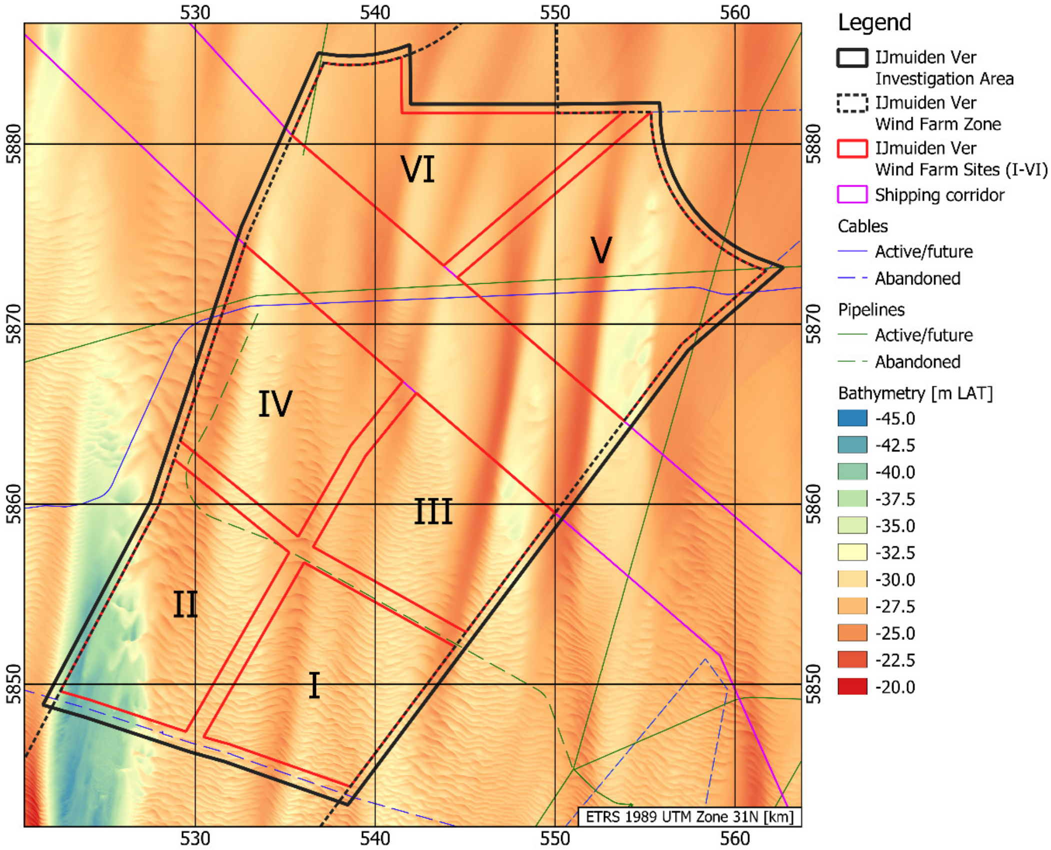

Figure 3.7: Overview of the seabed in and around IJV including Sites I, II, III, IV, V-VI.

3.4.2 Seabed composition and geology

Sediment dynamics are governed by the type of sediment available on the seabed. The geological evolution of IJV and its surroundings has been discussed extensively in Arcadis Nederland BV and Geo-Engineering.org GmbH (2019); Fugro (2022a); GEOxyz (2021). This section focusses on the current sediment characteristics and geology of IJV and its surroundings.

As described in Section 3.2.2 and in Arcadis Nederland BV and Geo-Engineering.org GmbH (2019) the geology in the southern North Sea and in extension IJV is formed by cycles of glaciation, deglaciation and sea-level changes. In the upper 100 m of the seabed sands, silty sands and clats are found, deposited during the Pleistocene and Holocene periods. The Pleistocene deposits observed underlying the Holocene deposits, belong mainly in the Eems and the Brown Bank Formations. As part of those formations, clay deposits of higher thickness in the form of glacial infill is observed. At the east of the IJV OWF Yarmouth Roads Formation sub crops the Holocene layers.

The vertical distribution of grain sizes at IJV which is important for assessing the morphodynamics of the seabed over a longer period of time (years to decades) is discussed in detail in Section 4.2.2.An overview of the seabed sediment median grain size is presented in Figure 2.2 and is composed from geotechnical data obtained for the Netherlands Continental Shelf (Maljers & Gunnink, 2007). The figure shows areas with larger sediment grain size towards the southwest of IJV where the Holocene layer is absent. For the remainder of IJV, grain sizes slightly decrease towards the north. Comparison with Figure 3.7 shows that the areas with smaller sediment grain sizes relate to areas where sand waves are absent. Similar findings on a relationship between grain sizes and the presence or absence of bedforms were presented in Damen et al. (2018).

3.4.3 Hydrodynamics

At IJV, a combination of several processes is ultimately driving the sediment dynamics. These governing processes include hydrodynamics (such as tides and wind-driven flow) and waves. Some of these processes are driven by atmospheric dynamics and meteorology (such as wind patterns, pressure fields, precipitation, etc.), which impose seasonal patterns, as well as occasional extreme events.

Figure 3.8 presents the magnitudes and directions of the modelled depth-averaged tidal velocities, averaged over the period 1979-2018 (DHI, 2019), while a current rose from a reference location (within the shipping lane between Sites III-IV and V-VI - with depth of ca. 25 m MSL) is presented in Figure 3.9. Average current magnitudes range between 0.37 and 0.45 m/s, with the lowest velocities simulated in Sites V-VI. Under normal conditions, the main current direction is north-northeast ranging from 10 to 27 ^{o}N, with the most northwards directions observed at the southwest area of Site II. DHI (2019) note that flood currents (towards the northeast) are usually stronger than ebb currents in IJV, indicating that the main direction of the residual currents is also similar to that of right panel in Figure 3.8.The influence of the bathymetry and more specifically the presence of sand banks on the currents can be observed in the spatial variability of magnitudes and directions direction: at the top of the sand banks the simulated current decrease in magnitude, while their direction is shifted more towards the northeast. When considering the current conditions over time for the reference location (Figure 3.9), the current signal is mostly towards the north-northeast and towards the south-southwest with depth-averaged current speeds up to approximately 0.8 m/s (approximately for 99% of the normal hydrodynamic conditions).

Figure 3.10 presents the maximum annual wave heights in and around IJV, averaged over the period 1979-2018 as well as the associated mean wave periods (DHI, 2019). A wave rose from a reference location (within the shipping lane between Sites III-IV and V-VI with depth of ca. 25 m MSL) is presented in Figure 3.11. The average annual maximum significant wave height ranges between 5.5 and 6.1 m, with the lowest values simulated in Sites I-II and the higher values in Site VI. The mean period associated with the mean annual maximum significant wave height ranges between 7.3 m (at the southwest of Site II) and 8.7 m (in Site VI). The influence of bathymetry and more specifically the presence of sand banks on wave conditions is illustrated in the spatial patterns of Figure 3.10: both the mean annual maximum significant wave heights and associated mean periods, increase over the peaks of the sand bars, while east and southeast of the sand banks ‘shadow zones’ of decreased wave heights and periods are observed. As presented in Figure 3.11, for IJV waves generally approach from the north-northwest or south-southwest with significant wave heights up to 4.5 m (approximately 99% of the normal wave conditions.

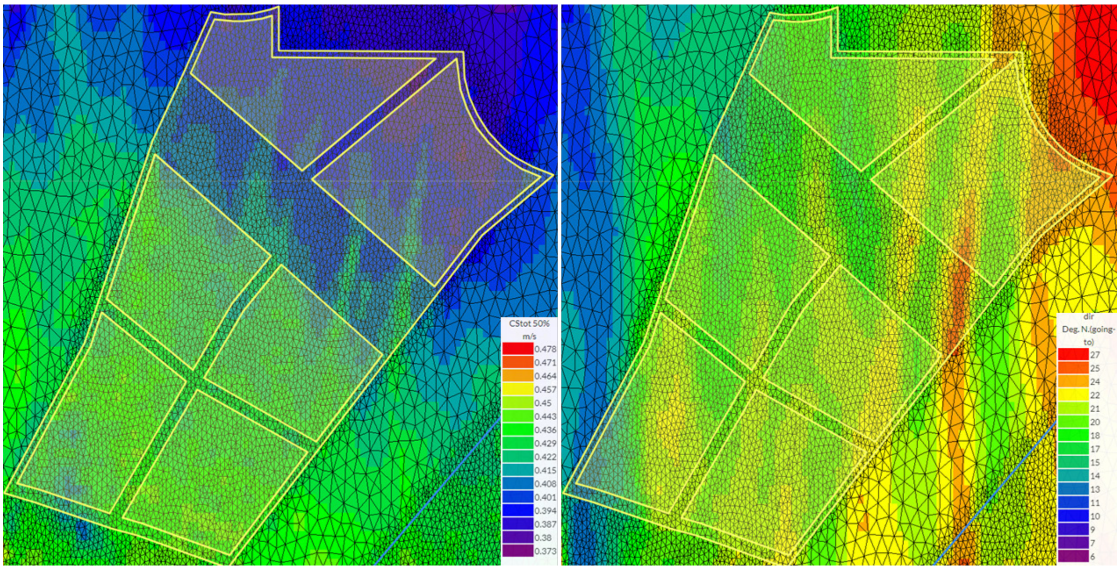

Figure 3.8: Map plot of simulated current magnitudes (left panel) and directions (right panel) in and around IJV WFZ, averaged over the period 1979-2018 from DHI (2019). Convention for currents is going to relative to north. The boundaries of IJV IA and the individual Sites are marked with yellow polygons.

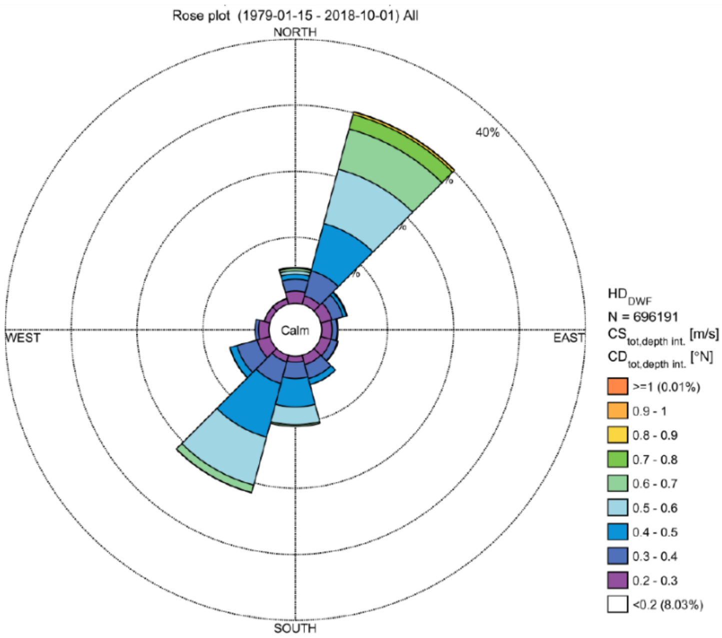

Figure 3.9: Rose plot showing depth-averaged current speeds for IJV as derived from DHI (2019). Convention for currents is going to relative to north.

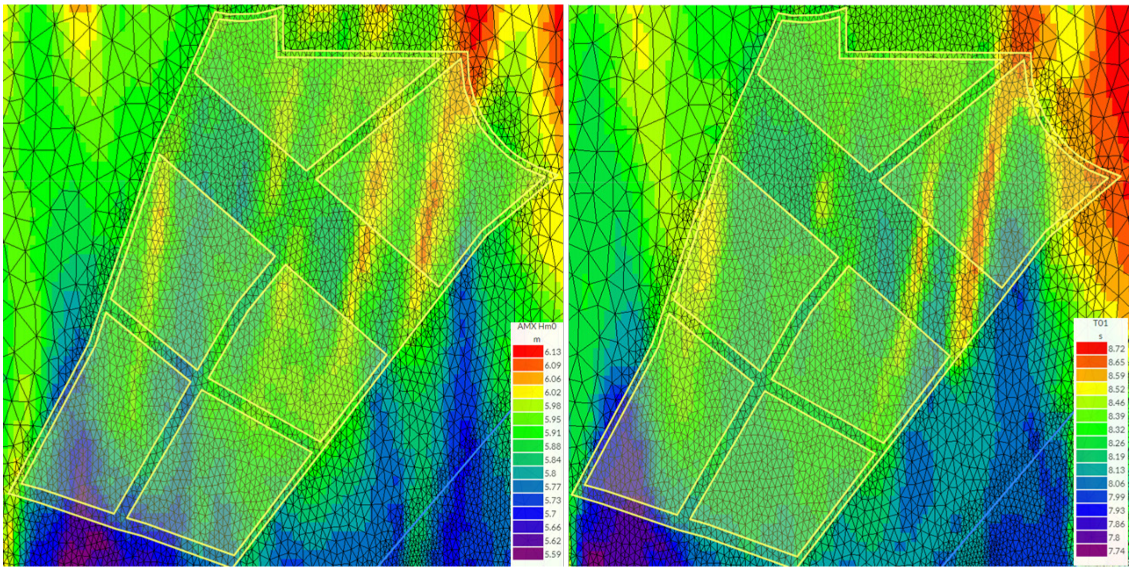

Figure 3.10:Map plot of simulated annual max significant wave height (H_{m0}, left panel) and associated mean wave period (T_{01}, right panel) in and around IJV WFZ, averaged over the period 1979-2018 from DHI (2019). The boundaries of IJV IA and the individual Sites are marked with yellow polygons.

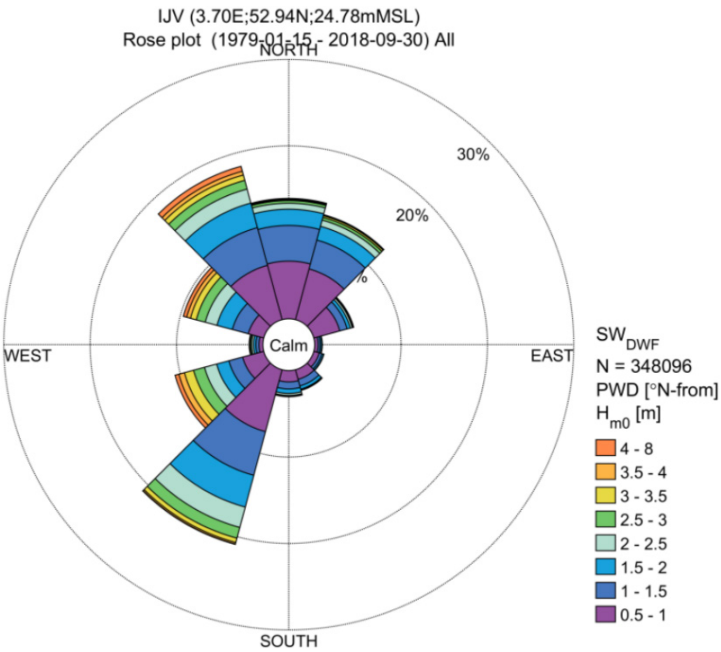

Figure 3.11:Rose plot showing significant wave heights for IJV as derived from DHI (2019). Convention is coming from relative to north.

For IJV the hydrodynamic conditions are important input parameters for the numerical modelling of sediment transport but also for the observed sediment transport patterns. The numerical modelling presented in this study focusses on the modelling of sediment transport patterns to support the data-driven analysis.

3.5 Temporal and spatial scales of the analysis

The morphodynamic activity at IJV is expressed but also caused/influenced by several factors acting on different spatial and temporal scales. For example, the interaction of tide with the bathymetry leads to the migration of sand banks over thousands of metres and hundreds to thousands of years. The same process contributes to the migration of sand waves and megaripples over years/decades or hours/days respectively, as the amount of volume that needs to be transferred is significantly smaller compared to the sand banks. Additionally, storms that occur over hours/days may also induce a morphodynamic response of the bedforms and larger-scale seabed. At the same time, the geological and geotechnical variations of the seabed sediments, present at the spatial scale of tens to thousands of metres may enhance or restrict the morphodynamic response to the hydrodynamic conditions.

The analysis methodology, presented in Appendix A, is structured to investigate each of the morphodynamics components separately and subsequently assemble the results the bed level extrapolation for the morphodynamic predictions. The focus of the analysis is on the sand wave migration and the relevant processes, as this is regarded as potentially the main driver of bed level change in the OWF during the project lifetime. To this end, the available surveys are analysed to obtain migration rates, while numerical modelling is used to investigate the driving processes over inter- and intra-annual timescales. The shorter and longer-term morphodynamic processes are evaluated to the extent possible through data analysis and numerical modelling (e.g. through numerical modelling of storm impact, megaripple analysis, or large-scale seabed change trends analysis). The aspects of those longer or shorter term morphodynamic processes that are not sufficiently included in the above analysis are then estimated. For those uncertainty ranges are defined, based on the available data, literature and expert judgement, and applied to the predictions (e.g. uncertainties in vertical seabed level trends).

The resolution used in the numerical modelling and data analysis is selected based on the relevant spatial scales of the processes/factors. For data analysis a resolution of 5 m is selected to represent sand wave dynamics in detail and include megaripples. For numerical modelling a larger resolution is used to sufficiently include the sand banks and large-scale seabed variations excluding though sand waves and smaller bedforms. Geotechnical and geological information are analysed in their original resolution but included highly schematised in the numerical modelling. Any aspects of the morphodynamic processes that are not sufficiently represented by the selected resolutions for the analyses are evaluated and included as uncertainty ranges in the predictions (e.g. grid resolution uncertainty).

Finally, the results of the analysis are reported on different scales, considering also the spatial division of the IJV IA to Sites I-VI. Intermediate findings and final results are generally reported on the IJV IA (e.g. trends of large-scale seabed change, comparison of numerical modelling and data analysis results). However, when results present significant variability over the IA (e.g. sand wave dynamics and bed level predictions), more detailed descriptions of the results are provided, per Site or per group of Sites (see also Section 7.2 Site-specific conclusions). An overview of the different spatial scales used to report the intermediate and final results can be found in the introductions of the following three chapters.

4 Results of data-driven analysis

4.1 Introduction

In this chapter the results of the data-driven analysis for determining the seabed mobility are presented. The aim of the data-driven analysis is to define historic trends in IJV and to provide the basis for the extrapolation of future seabed levels. Results are based on applying the methodology discussed in Appendix A.2 using the data presented in Sections 2.2, 2.3 and 2.4 within the context presented in Chapter 3.

In this chapter, the review and processing of geophysical and geotechnical data is discussed in Section 4.2, providing information both on the IJV IA and on individual Sites scales. The morphodynamic overview and splitting of different types of bedforms are presented in Section 4.3. The results of the sand wave analysis, large-scale seabed analysis and the smaller scale bedform analysis are presented in Sections 4.4, 4.5 and 4.6, respectively. The trends of largescale bed level change is discussed for the IJV IA area, while the variation of sand wave and megaripple characteristics over the different Sites is discussed. An analysis of the repeat survey lines is presented in Section 4.7. The chapter finishes with a summary of the analysis in Section 4.7.2.

4.2 Review and processing of available data

4.2.1 Review and processing of bathymetry data

In Section 2.2 and Figure 2.1 an overview of the available bathymetry data is presented. For the entire analysis area, a total of 34 surveys is available. All available data is interpolated to a 5x5 m resolution for the remainder of the analysis and checked for anomalies. Reference is made to Appendix A.2.2.1 for the justification and implications of the selected resolution. Although the resolution of the older bathymetries and the SBES bathymetries measured by the NLHO is limited to about 10-100 m, the datasets were found to (partly) resolve sand waves and are therefore valuable in determining long-term sand wave dynamics.

No significant offsets were found for the available surveys. And differences between surveys, except for the dynamics of sand waves and megaripples, is confined within the TVU values (see Table 2.1). The bathymetry data collected in 1976 was excluded from this analysis as the spatial coverage and quality of the data is very low (see Appendix D.1). The survey data from 1992 was excluded from the cross-correlation and Fourier analysis (to obtain migration dynamics and dimensions) because of limited spatial coverage. However, the data is included in defining large-scale seabed trends in Section 4.5. The repeat survey lines are used to indicate intra-annual variability in seabed levels with a specific focus on megaripple dynamics.

The available surveys only cover part of the analysis area, and so composite bathymetries were created. Surveys separated by the smallest possible timespan are grouped and, to the extent possible, the entire area is covered. This process resulted in five composite bathymetries, but only three are used fully in this study as discussed in the previous paragraph. Table 4.1 presents an overview of the distribution of the available surveys and composites including names used in the remainder of this report. It should be noted that local discontinuities may exist across bathymetry patches which are accounted for in the remainder of this analysis.

Table 4.1: *Overview of composite bathymetries including sources. Numbers correspond to Appendix D.*

Number	Name of bathymetry	Bathymetry sources
1	Bathymetry 1976	15563, 15564, 15562(Royal Netherlands Navy - Hydrographic Office, 1980-2021)
2	Bathymetry 1992	2561 (Royal Netherlands Navy - Hydrographic Office, 1980-2021)402 (Royal Netherlands Navy - Hydrographic Office, 1980-2021)
3	Bathymetry 2002-2003	10464, 11544, 10625 (Royal Netherlands Navy - Hydrographic Office, 1980-2021)
4	Bathymetry 2013-2016	18168, 18668, 19241 (Royal Netherlands Navy - Hydrographic Office, 1980-2021)
5	Bathymetry 2020-2022	2020 survey (GEOxyz, 2021); 2022 survey (Fugro, 2022a).

The original time stamp per survey, defined as the day halfway through the period in which the specific patch was surveyed, is retained and applied in the further analysis. An overview of the survey extents of the 2020-2022 bathymetry is presented in Figure 4.1. The other composite bathymetries are presented in Appendix D. Appendix D also includes a combination of Table 2.1 and Table 4.1 indicating which bathymetry is included in which composite.

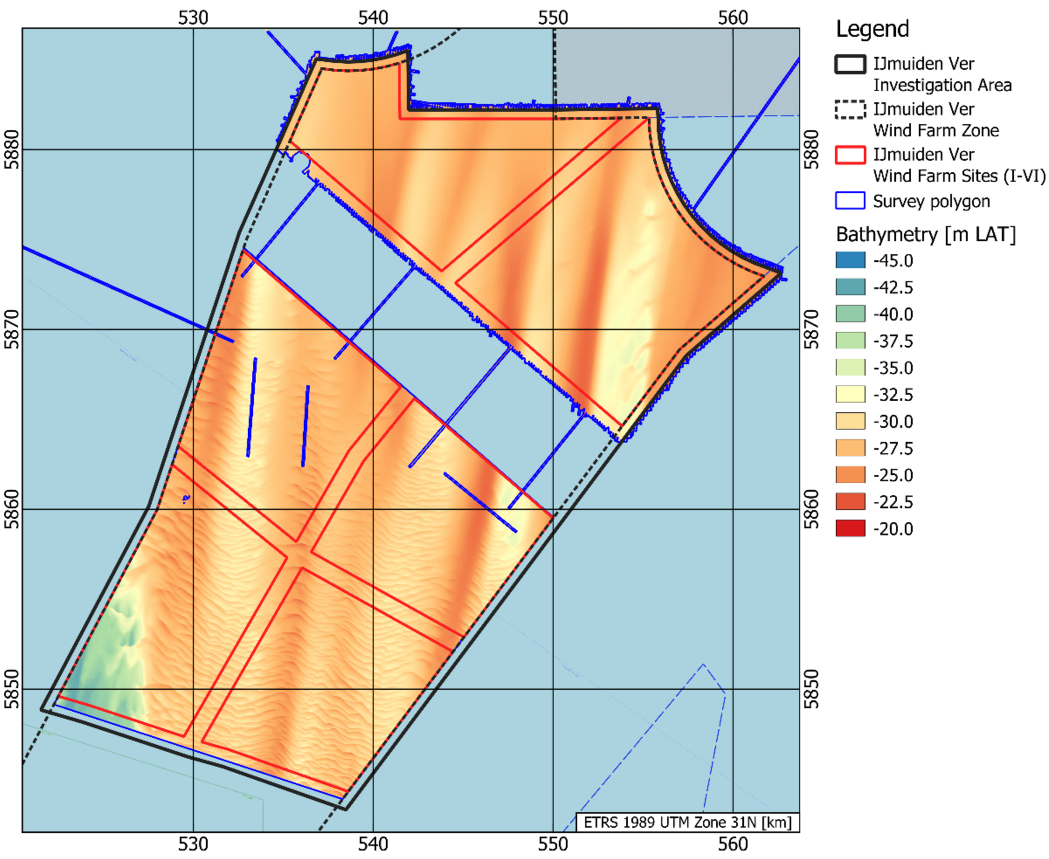

Figure 4.1: Overview of the composite 2020-2022 bathymetry, with blue polygons indicating extent of the various bathymetries used (see Table 4.1).

4.2.2 Review and processing of geophysical and geotechnical data

For IJV the available geotechnical and geophysical data, such as sub-bottom profiler data, is presented in Section 2.3 and shown in Figure 2.2 and Figure 2.3. For IJV sufficient CPT, borehole, Vibrocore and grab sample locations are available (Fugro, 2022b, 2022c, 2022d, 2022e, 2022f, 2022g; GEOxyz, 2021). Furthermore, the reports by Arcadis Nederland BV and

Geo-Engineering.org GmbH (2019), GEOxyz (2021) and Fugro (2022a) and their description of the local geology supports this analysis.

In this section the geological characteristics of IJV are analysed. The goals of the analysis are two-fold: first, to establish how the composition of the substrate in the area may affect future seabed level variations and second, to evaluate the added value of Vibrocores to investigate future wind farm morphodynamics. In the next sections the following is presented:

1. grain size distribution within the upper five metres (4.2.2.1);
2. overview of Vibrocores along seven transects (4.2.2.2);
3. presence, thickness and depth of non-erodible layers within the upper 20 metres (4.2.2.3).

4.2.2.1 Grain size distribution

The available borehole, Vibrocore and grab sample data indicate limited lateral and vertical variability of sediment grain sizes in the area within the first few metres below the seabed (Fugro (2022b, 2022c, 2022d, 2022e, 2022g); GEOxyz (2021). To illustrate this, the median sand grain size distribution and the fines content is shown for the first metre below the seabed. Figures showing the sand grain size distribution and the fines content between one and five metres below the seabed are presented at intervals of 1 m in Appendix C.1 and C.2.

Median grain size

The interpolation of geotechnical data as depicted in Figure 2.2, indicates fine to medium sand as the median grain size for the top sediment layer in IJV. The overview of d_{50} for the first metre below the seabed is shown in Figure 4.2 together with a combined non-exceedance curve in Figure 4.3.

Spatially the median sediment diameter decreases from south (Site I-II) to north (Site V-VI) from about 0.250 to 0.180 mm. In the southwest of Site II, in the deepest part of IJV, grain size increases to 0.350 to 0.400 mm. At this location the Holocene layer is absent. Locally spots occur with coarser grain sizes corresponding to the sand wave crests and troughs. Within the first metre below the seabed most locations display values between 0.180 and 0.300 mm. The finest grain sizes occur in Sites V-VI of IJV. At the seabed, grain sizes vary between 0.204 and 0.281 mm.

Between one and five metres below the seabed grain sizes vary from 0.026 to 0.290 mm (silt to medium sand). No clear trend in grain size was found with increasing depth, although median grain sizes indicate slightly finer material farther below the seabed (Table 4.2 and Appendix C.1). Non-exceedance curves for various depth classes are shown in Figure 4.4.

Median grain sizes per Site are presented in Table 4.3. It is found that with depth the median grain size decreases slightly. The spatial pattern with slightly larger grain sizes in Sites I-II compared to Sites V-VI is found for all depth classes. It is stressed that the spatial distribution of grain sizes farther below the seabed is more scattered than at the seafloor. This might relate to less uniformly distributed sediment in the seabed. However, the relative position of a geotechnical sample with respect to a bedform, e.g. on top of a megaripple or in a sand wave trough has influence on this spatial pattern. The depth to the formation underlying the, more uniformly distributed (see Section 4.2.2.2), Holocene Formation varies per sample. It is furthermore found that in Sites V-VI the grain sizes become significantly finer, although the amount of data for these Sites is limited compared to Sites I-IV (see Table 2.2).

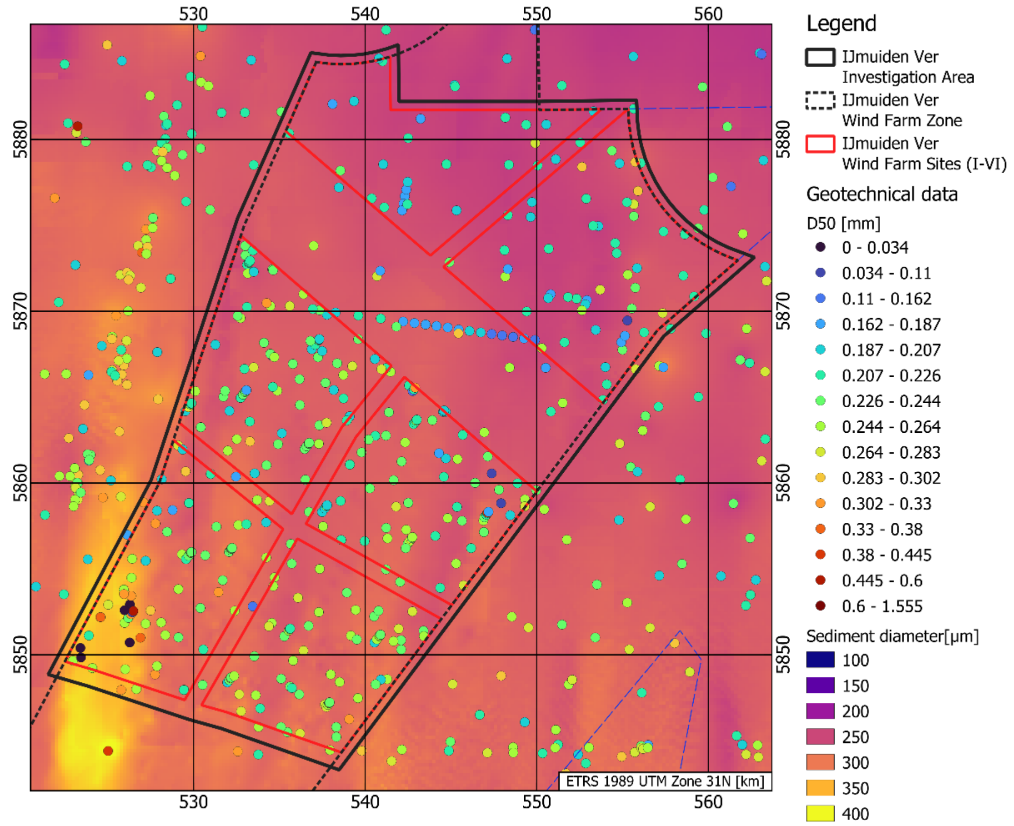

Figure 4.2: Overview of the median grain size in the first metre below the seabed based on borehole, Vibrocore and grab sample data.

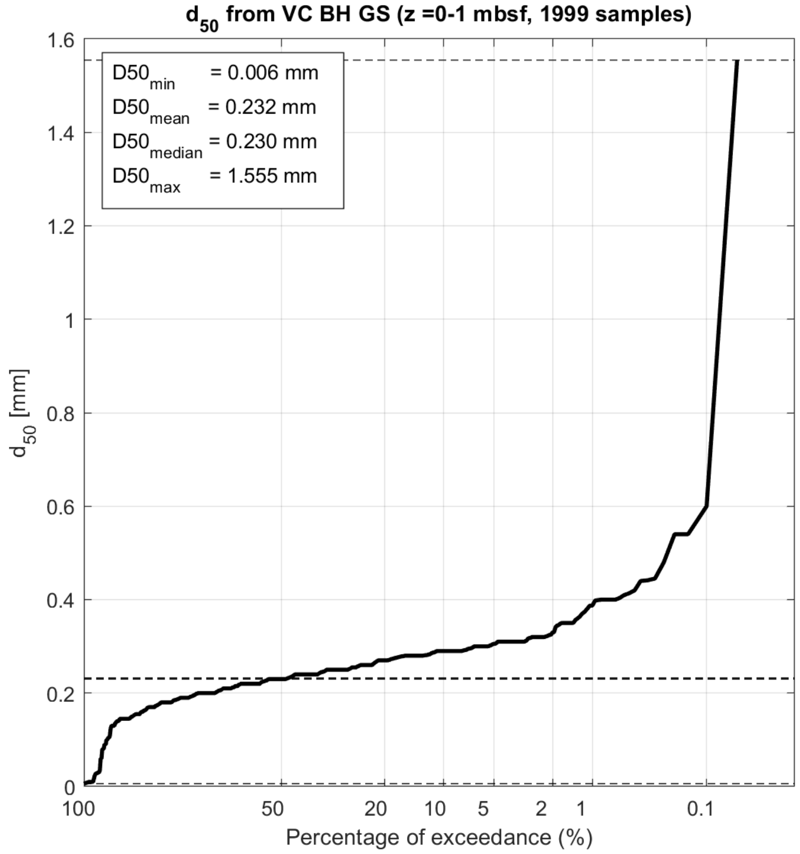

Figure 4.3: Non-exceedance curve of average grain size in the first metre below the seabed based on borehole, Vibrocore and grab sample data.

Table 4.2: *Median grain size d_{50} for the upper 5 m of the IJV seabed.*

d_{50} (mm)	**Boreholes (Fugro, 2022d, 2022e)** and DINOloket			**Vibrocores (Fugro, 2022c, 2022g)**			**Grab samples (Fugro, 2022b; GEOxyz, 2021)** and DINOloket		
Depth Class	5%	50%	95%	5%	50%	95%	5%	50%	95%
0 m	0.257	0.257	0.268	0.220	0.240	0.280	0.204	0.241	0.281
0-1 m	0.155	0.236	0.269	0.180	0.240	0.280	0.171	0.239	0.300
1-2 m	0.028	0.225	0.288	0.120	0.220	0.280			
2-3 m	0.096	0.203	0.265	0.090	0.210	0.270			
3-4 m	0.060	0.187	0.266	0.040	0.210	0.260			
4-5 m	0.026	0.181	0.280	0.020	0.210	0.290			

Table 4.3: *Median grain size d_{50} in mm for the upper 5 m of the IJV seabed per Site for all sources combined.*

Depth Class	**Site I**	**Site II**	**Site III**	**Site IV**	**Site V**	**Site VI**	**Sites I-VI**
0 m	0.250	0.256	0.240	0.240	0.214	0.212	0.240
0-1 m	0.240	0.248	0.230	0.230	0.214	0.210	0.240
1-2 m	0.239	0.235	0.210	0.220	0.194	0.192	0.220.
2-3 m	0.230	0.220	0.205	0.200	0.176	0.115	0.210
3-4 m	0.220	0.220	0.200	0.200	0.162	0.114	0.210
4-5 m	0.220	0.210	0.205	0.200	0.077	0.103	0.210

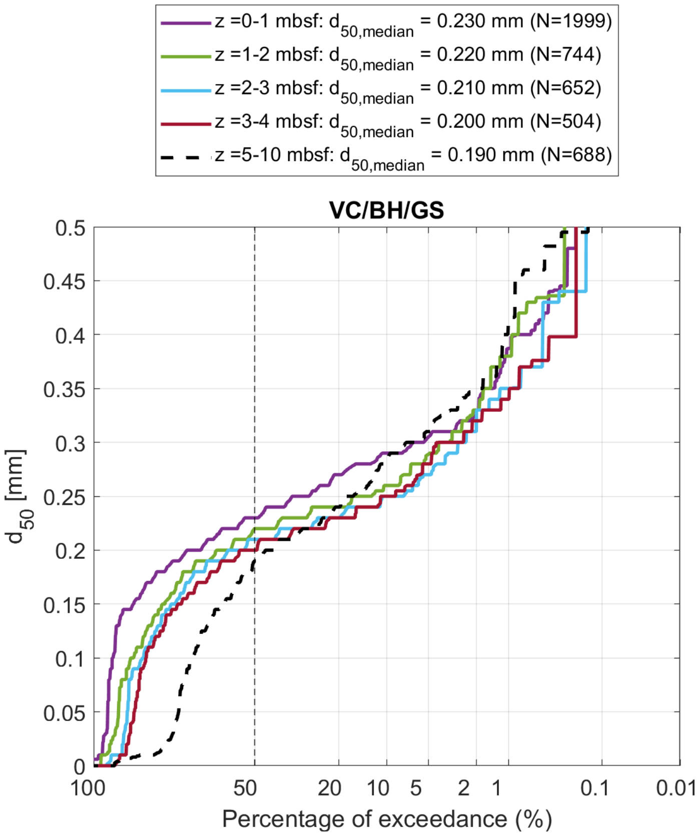

Figure 4.4: Overview of grain size distribution for various depth classes.

Fines content

Fines are classified as grain sizes with a diameter less than 0.063 mm. At the seabed the interpolation by TNO predicts fines close to 0% as shown in Figure 4.5. From the geotechnical data of Fugro (2022b, 2022c, 2022d, 2022e, 2022g); GEOxyz (2021) most locations show fines contents around 1-2% within the first metre below the seabed. Locally a few outliers up to 10% occur. The overview of fines for the first metre below the seabed is shown in Figure 4.5 and a combined non-exceedance curve is presented in Figure 4.6.

Between one and five metres below the seabed the average fines content is between 0 and 89%. No clear trend is found with increasing depths although median values for fines percentages indicate slightly finer farther below the seabed (Table 4.4 and Appendix C.2).

Median values for fines percentages per Site are presented in Table 4.5. It is found that with depth the percentage of fines slightly increases. The spatial pattern with slightly lower percentages in Sites I-II compared to Sites V-VI is found for all depth classes. It is stressed that the spatial distribution of grain sizes farther below the seabed is more scattered than at the seafloor. It is furthermore found that in Sites V-VI the grain sizes become significantly finer, although the amount of data for these Sites is limited compared to Sites I-IV (see Table 2.2). Detailed analysis of Sites V-VI showed however that half of the samples consisted of a significant percentage of fines whilst the percentages for the other half showed values similar to Sites I-IV.

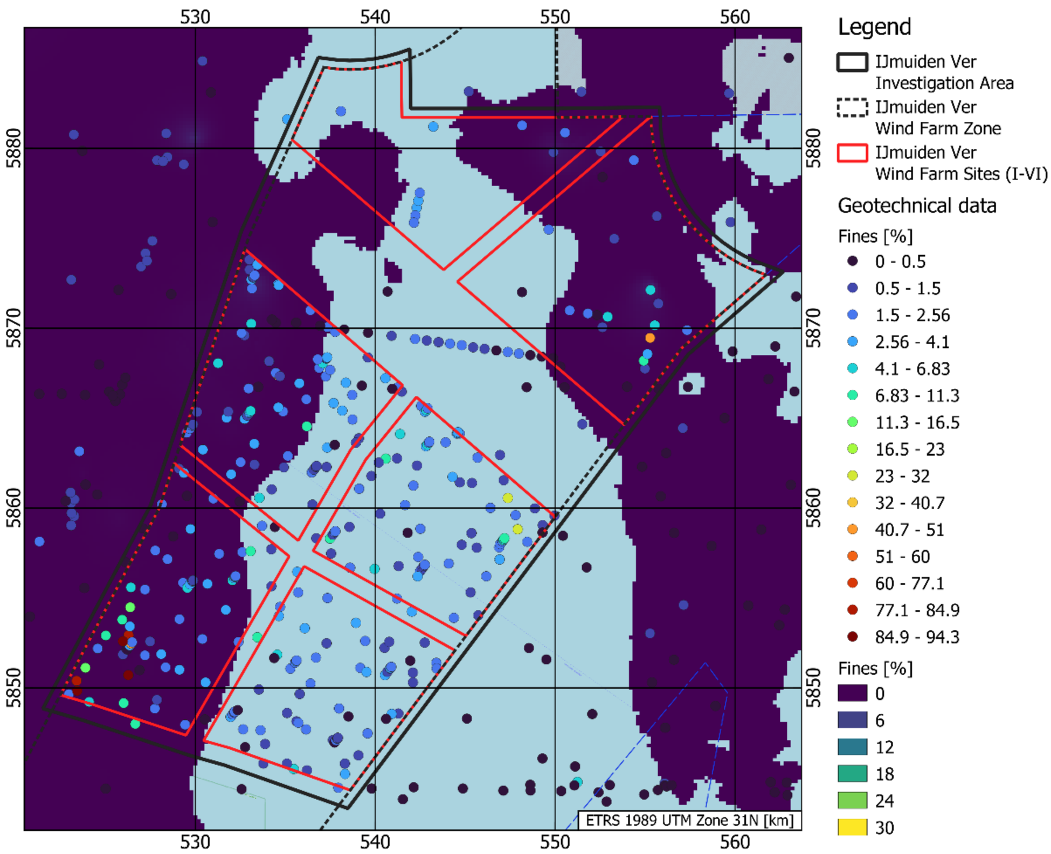

Figure 4.5: Overview of fines content in the first metre below the seabed based on borehole, Vibrocore and grab sample data. For the light blue areas no data was available from Maljers and Gunnink (2007).

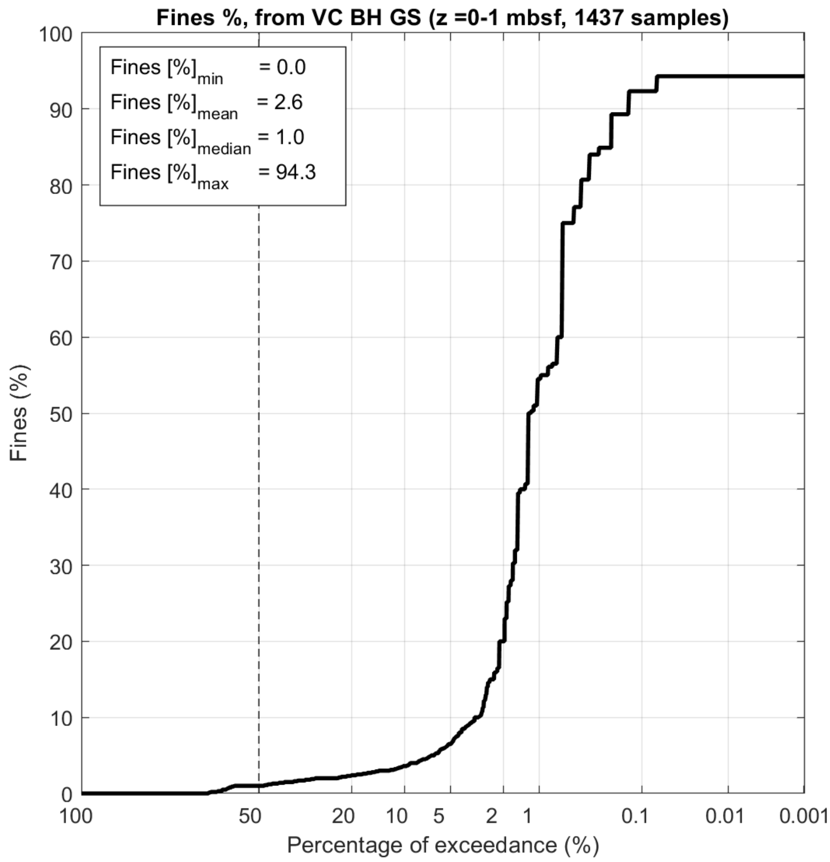

Figure 4.6: Non-exceedance curve of the fines content in the first metre below the seabed based on borehole and Vibrocore data.

Table 4.4: Percentage of fines in the upper 5 m of the IJV seabed.

Fines [%]	**Boreholes (Fugro, 2022d, 2022e) and DINOloket**			**Vibrocores (Fugro, 2022c, 2022g)**			**Grab samples (Fugro, 2022b; GEOxyz, 2021) and DINOloket**		
Depth Class	5%	50%	95%	5%	50%	95%	5%	50%	95%
0 m	1.2	1.2	1.4	0.7	1.9	8.5	1.2	1.6	9.3
0-1 m	0.2	1.7	4.5	0.7	2.0	8.5	0.0	1.3	5.9
1-2 m	0.2	2.4	8.1	0.8	2.3	14.1			
2-3 m	0.6	2.6	14.6	0.9	2.6	22.7			
3-4 m	0.8	2.8	50.9	1.0	3.0	66.2			
4-5 m	0.4	3.0	89.4	1.0	3.0	80.0			

Table 4.5: Percentage of fines for the upper 5 m of the IJV seabed per Site for all sources combined.

Depth Class	**Site I**	**Site II**	**Site III**	**Site IV**	**Site V**	**Site VI**	**Sites I-VI**
0 m	1.5	2.2	1.5	1.6	1.0	1.5	1.6
0-1 m	1.6	2.3	1.8	1.7	1.7	2.0	1.8
1-2 m	2.0	2.4	2.6	2.3	2.0	2.0	2.3
2-3 m	2.2	2.9	2.9	2.5	4.0	12.0	2.6
3-4 m	2.4	3.5	3.2	2.8	12.0	11.0	2.9
4-5 m	2.2	4.1	3.4	3.0	38.0	16.0	3.1

4.2.2.2 Vibrocore analysis

Vibrocore data by Fugro (2022c, 2022g) was analysed to investigate the spatial distribution of sediments over a number of transects. The digital files were processed and the relevant parameters of lithology, d_{50}, and fines and gravel content, were visualised. In these transects, which are drawn perpendicular to the sand wave crests, the bathymetry and geological horizons interpreted by Fugro (2022a); GEOxyz (2021) at the location of the sections is also included. Figure 2.2 shows the location of all the Vibrocores transects. Figure 4.7 shows two Vibrocore transects in the northeast and southwest of Site II. All other Vibrocore sections are provided in Appendix C.3.

The transect in the top panel of Figure 4.7 shows a clear vertical transition between the Southern Bight and Naaldwijk formations. Whereas the Southern Bight Formation is uniformly sandy, the Naaldwijk Formation at this location consists of clay. For the majority of the other transects a similar transition occurs. The bottom panel in Figure 4.7 shows a transect from the far southeast of IJV. At this location the Southern Bight Formation is mostly absent (see also Figure 2.3). In contrast to other transects the sediment distribution in the sand wave showed less uniformity with mostly medium sands present.

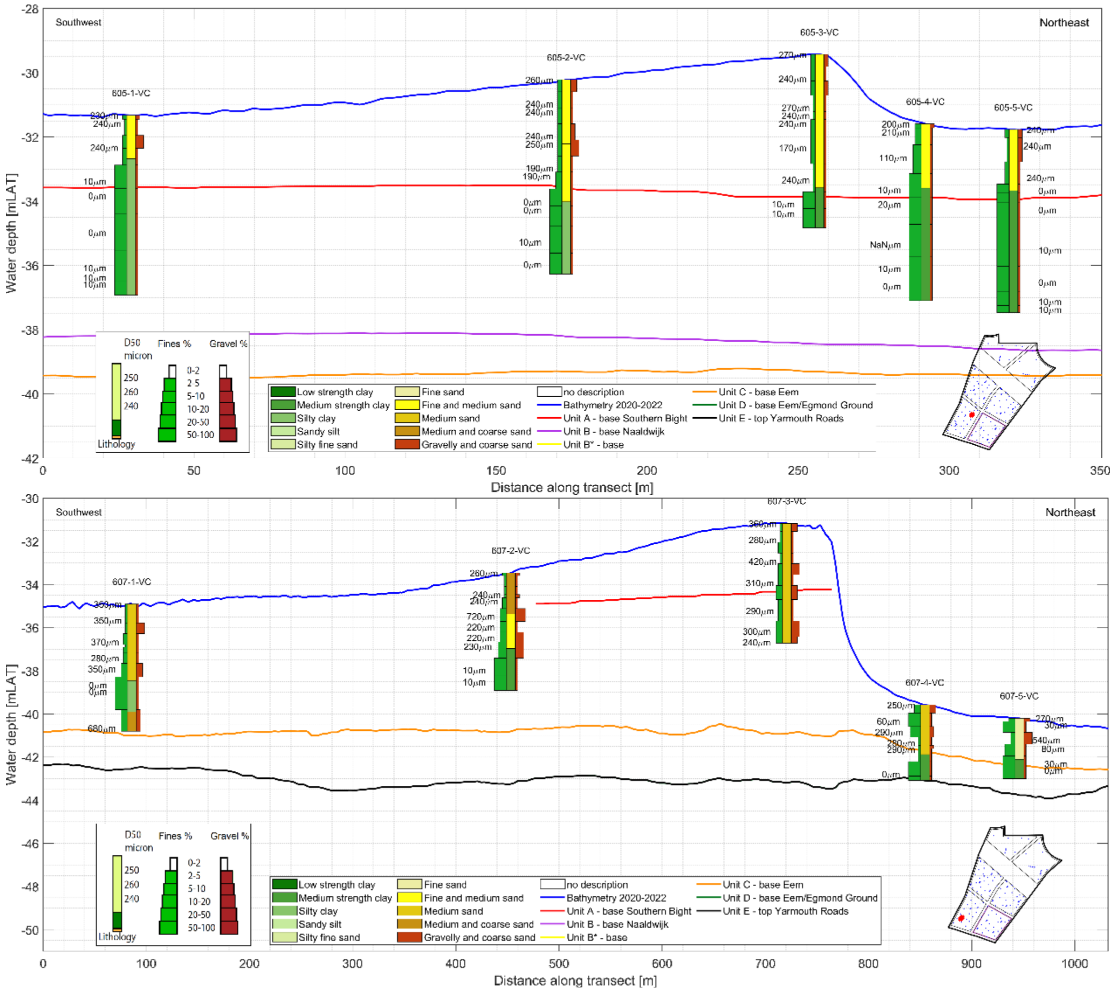

Figure 4.7: Vibrocore transects located in the northeast of Site II (top panel) and southwest of Site II (bottom panel) of IJV.

All Vibrocores penetrate the Southern Bight Formation (Bligh Bank Member). Most of them reach the Naaldwijk Formation and some of them the Eem Formation. The maximum thickness of the Bligh Bank Member is at the crests of the sand waves and minimum or zero in the troughs. Based on all sections the following general characteristics were observed:

- sediments of the Bligh Bank Member are fine-to-medium sand with little or no fines;
- sediments of the Naaldwijk Formation are highly heterogeneous ranging from clay to coarse sand. These sediments are near the seabed at the sand waves troughs;
- the Eem Formation consist of very fine sediments; although only one Vibrocore recovered Eem Formation.

Within the Southern Bight Formation, the following patterns were recognised:

- the crests of the sand waves are slightly coarser than the troughs;
- sediments are very much uniform, especially in the sand waves within the Bligh Bank Member and much less uniform below the Bligh Bank Member.

4.2.2.3 Occurrence of non-erodible layers and impact on seabed dynamics

In this section the occurrence of non-erodible layers in the top 20 metres of the seabed is presented and discussed. Analyses of borehole, CPT and Vibrocore data obtained in IJV (Fugro, 2022c, 2022d, 2022e, 2022f, 2022g), gives additional information on the potential presence of cohesive material at the seabed. In general, layers of medium to high strength clay (e.g., with an undrained shear strength larger than about 100 kPa) with sufficient thickness (e.g., in the order of a few metres) may limit morphodynamic development, if present near the seabed.

Arcadis Nederland BV and Geo-Engineering.org GmbH (2019), GEOxyz (2021) and Fugro (2022a) provided an overview of the different geological units. Based on the presented geological units it is expected that within the upper 20 metres of the seabed at IJV non-erodible layers are present below the Southern Bight Formation specifically in the Naaldwijk and Eem Formations. Although these layers are present in the upper 20 metres of the seabed, they are, for the most part, not present at the seabed.

Based on analyses of borehole and Vibrocore data presented in previous sections, IJV is characterised as sand-dominated with very limited potential for non-erodible layers to be present within the uppermost metres of the seabed. It is therefore expected that the influence of non-erodible layers on the seabed dynamics is limited. However, there are a limited number of locations (22 out of 8360 samples) where layers of cohesive material are identified relatively close to the seabed. For example, at three of the Vibrocore transects presented in Appendix C.3, clay was found in the Naaldwijk Formation. For the rest of the transects the sediment distribution in the Naaldwijk Formation and underlying layers show more variation.

4.3 Morphodynamic overview of the area and splitting of bedforms

4.3.1 Morphodynamic overview

Sections 4.3.1.1 and 4.3.1.2 present a general overview of the morphology of the area and the observed seabed variability, respectively.

4.3.1.1 General overview

The bathymetry of IJV and its surroundings is shown in Figure 4.8. IJV has a non-uniform morphology with variation in bed levels between -43 and – 22 m relative to LAT. Bed levels are deeper towards the southwest of IJV, reaching the minimum value in Site II.

In IJV a number of north-south oriented sand banks occur, traversing all Sites. The sand banks vary in height and steepness, and are most pronounced in Site V and just to the southwest outside IJV. In the southwest of IJV, in Site II, a deep channel occurs with depths 10 m below the surrounding seabed. At this location no Holocene formation is present (see Figure 2.3).

The area is partly covered by sand waves (see Section 4.4), which are present in Sites I-IV and partly in V, while absent from Site VI. Most of the sand waves in the area do have steeper sides faced north-northeast Some sand waves, especially on the eastern slope of the sand banks, were found to be have slopes with similar steepness (Figure 4.9).

IJV is partly covered by megaripples of various dimensions (see details in Section 4.6). The spatial extent correlates largely with the presence of sand waves and the presence of the slightly coarser grain sizes at the seabed (see Figure 4.2). Although the spatial resolution of the transect presented in Figure 4.9 is much larger than average megaripple lengths (see Section 4.6), the presence of the megaripples can be seen in the data as small variations around the sand wave signal mostly in the sand wave troughs. Because of limited spatial resolution of the original 2013-2016 data, this transects show a smoother pattern.

No direct indications of large-scale human interventions, such as dredging were observed, except for some platforms and a number of cables and pipelines crossing the area (most specifically Sites II, VI, V, VI). It is noted that such an intervention might have taken place and was not picked up by measurements. For example, an intervention might have taken place shortly after the seabed was measured and might have restored to the original situation before a second measurement of the seabed was performed.

Any shipwrecks and exposed pipelines or cables on the seabed are expected to influence seabed dynamics only locally (about 100 m from the object) and therefore mainly influence megaripples. The influence of nearby wind farms on seabed morphodynamics in IJV is considered to be negligible.

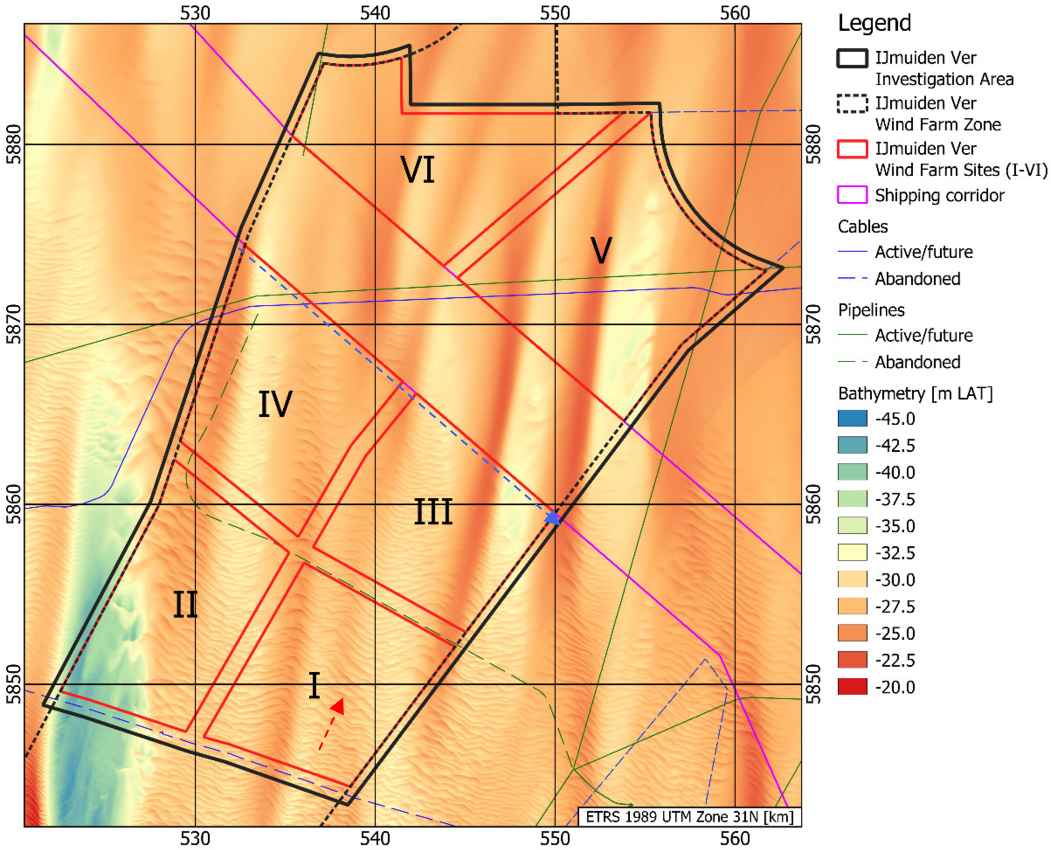

Figure 4.8: Overview of IJV analysis area including present and future infrastructure and the most recent composite bathymetry, i.e. for every grid point the most recent bathymetry measurement is displayed. The blue and red dashed line indicate locations of the transects displayed in Figure 4.9.

Figure 4.9 presents an example of seabed levels for three different bathymetries along two transect in IJV (blue and red dashed arrows in Figure 4.8). The first transect (red dashed line in Figure 4.8) is drawn from south-southwest to north-northeast (top plot in Figure 4.9). Clearly visible are the asymmetrical sand waves migrating towards the right (north-northeast). Small variations in sand wave troughs and crests are assumed to be a result of either measurement inaccuracies, limited survey resolution, megaripples, shape alterations or the transect not drawn in exactly the direction of migration.

The second transect (blue dashed line in Figure 4.8) is drawn from west-northwest to east-southeast (bottom plot in Figure 4.9). Visible are the large sand banks with lengths of more than 500 m and heights up to 10 m. Over the period 2002 to 2020, variations in bed levels, except from the dynamic sand waves and megaripples, have been limited.

In Appendix E.1 west-east seabed profiles over the entire IJV using the repeat survey lines are presented.

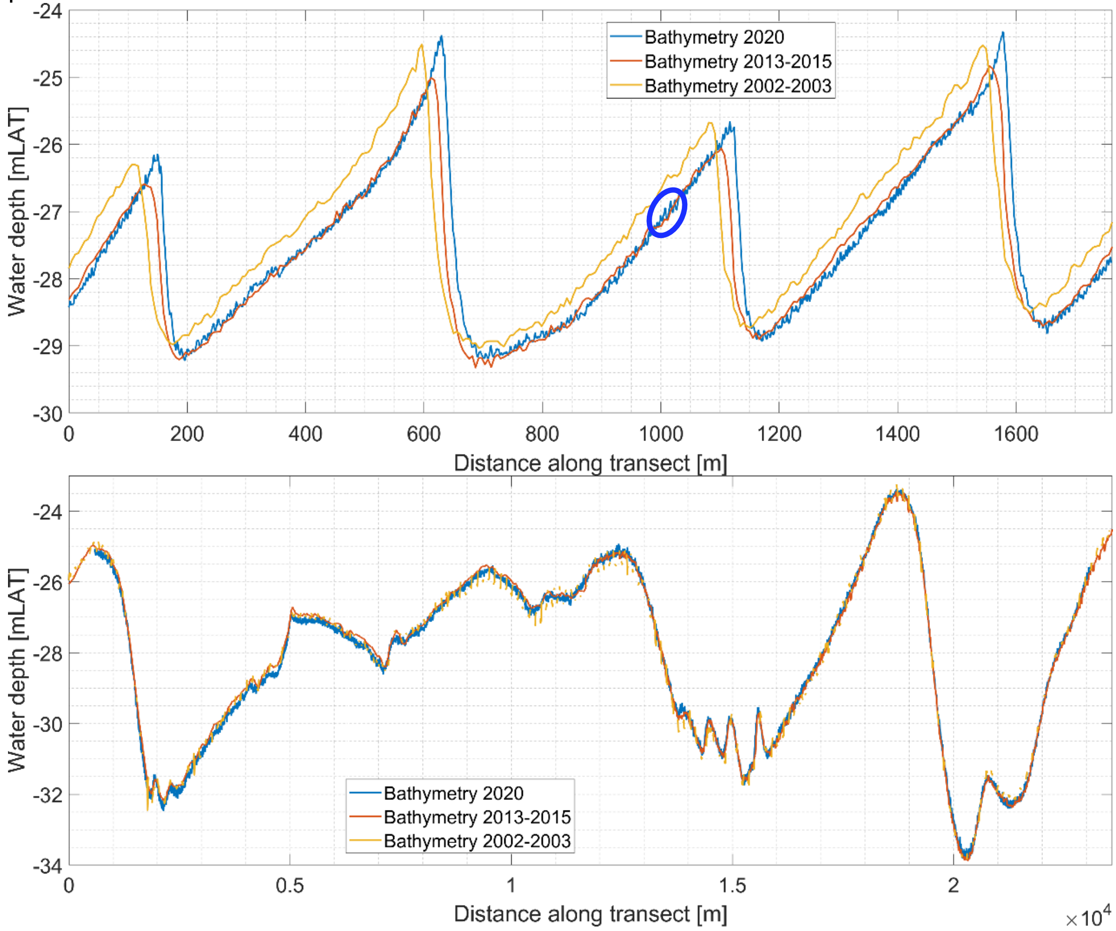

Figure 4.9: Example of seabed levels along a transect in IJV taken from three composite bathymetries. Locations of the transects are indicated in Figure 4.8 by a red dashed line and a blue dashed line. Transects are drawn from south-southwest to north-northeast (top plot) and from west-northwest to east-southeast (bottom plot). Small variations in the seabed profile of maximum a few decimetres indicate the presence of megaripples. The blue circle in the top plot indicates this variation.

4.3.1.2 Seabed variability

The basis of the data-driven analysis is the observed differences between available bathymetries. From these observed differences the appropriate analysis methodology is chosen. Figure 4.10 shows the difference in bed levels between the 2013-2016 and 2020-2022 bathymetries in IJV.

Comparison of the presence of sand waves (Figure 4.1 and Figure 4.8) to the areas with observed mobility showed resemblance. This variability is especially visible at Sites I-IV. For the other areas (Sites V-VI), where (almost) no sand waves are present, only small differences are found. These differences are most likely a result of uncertainties in the available bathymetry data. For example, in Site VI and the northern part of Site IV in Figure 4.10 negative values (blueish patch indicating slight seabed level lowering) are found. Neglecting influences of sand waves (reddish lines in Sites I-IV), Figure 4.10 shows positive values (reddish patch indicating slight seabed level increase) in Sites I-IV. The extents of the patches do match exactly with the extents of the surveys incorporated in the 2013-2016 bathymetry as depicted in Appendix D.4. This highlights uncertainties related to historic bed level measurements.

The uncertainties are further elaborated in the large-scale seabed dynamics section (Section 4.5). This difference in mobility is further discussed in the sand wave analysis (Section 4.4.2) and the numerical modelling (Chapter 5).

Overall, mean differences between bathymetries (2002-2003, 2013-2015 and 2020-2022) are between -0.05 and +0.05 m with standard deviations of 0.21 (comparison between 2020-2022 and 2013-2016) to 0.39 (comparison between 2020-2022 and 2013-2016). In total 95% of the observed changes fall between -0.80 and +0.80 m over the period 2002 to 2022. This bandwidth is mostly covered by the TVU values presented in Table 2.1 (0.18-0.21 m for the 2020-2022 bathymetry and 0.50 m for the 2002-2003 and 2013-2016 bathymetries) which are 0.68 to 0.71 m for the period 2002-2003 to 2020-2022. It is noted though that the presented bandwidth does include seabed level changes as a result of sand wave migration. This is discussed further in Section 4.5.

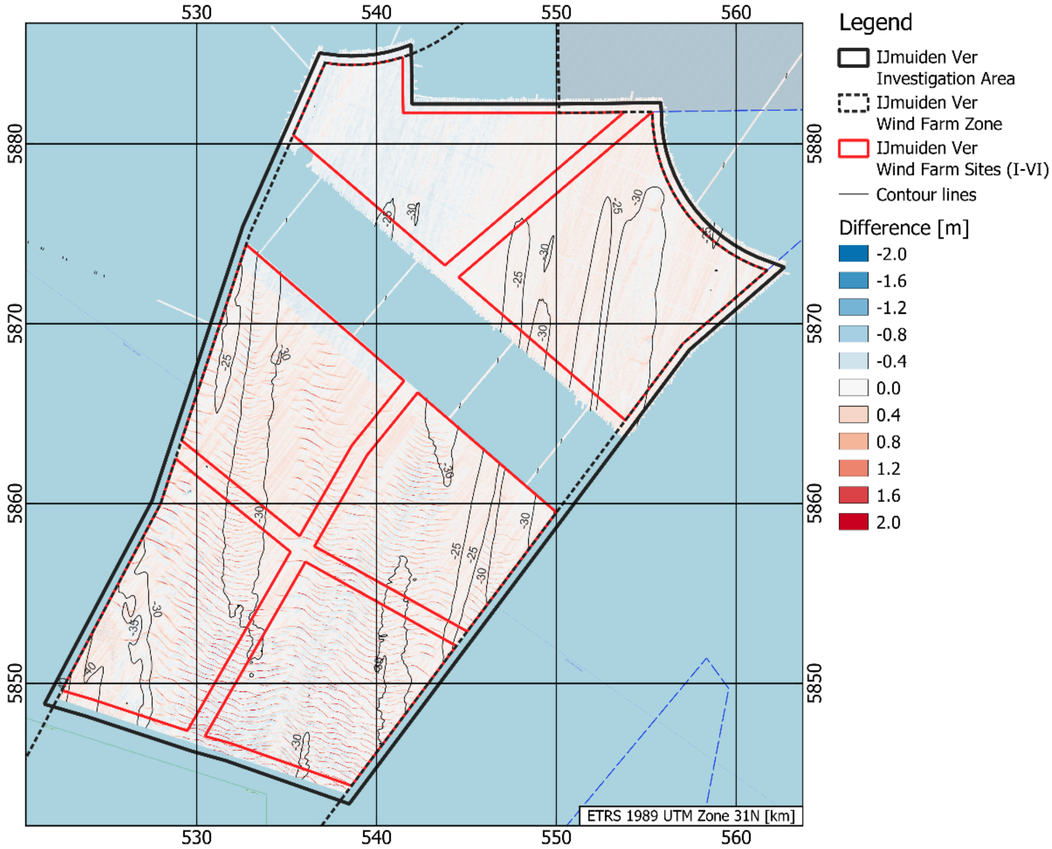

Figure 4.10:Differences in bed levels between the 2013-2016 and 2020-2022 bathymetry with positive values indicating accretion and negative values erosion.

4.3.2 Spatial distribution of bedforms

For IJV the bathymetry has three major components; the large-scale bathymetry (including sand banks), the sand waves and the megaripples. The large-scale seabed is analysed by filtering the bathymetry, the dimensions of which are based on bedform characteristics. For areas with sand waves an ellipsoid filter is applied with a certain length/width ratio. In this way, averaging over the sand waves has a limited impact on the large-scale bathymetry, while a filter size of 1,100 m is longer than the longest observed sand wave lengths in IJV, ensuring that all sand waves are filtered out.

Results of the bedform separation for the most recent bathymetry are presented in Figure 4.11 to
Figure 4.13. The figures depict the filtered large-scale bathymetry, the sand wave fields and the megaripple fields, respectively. The original unfiltered bathymetry is shown in Figure 4.8.

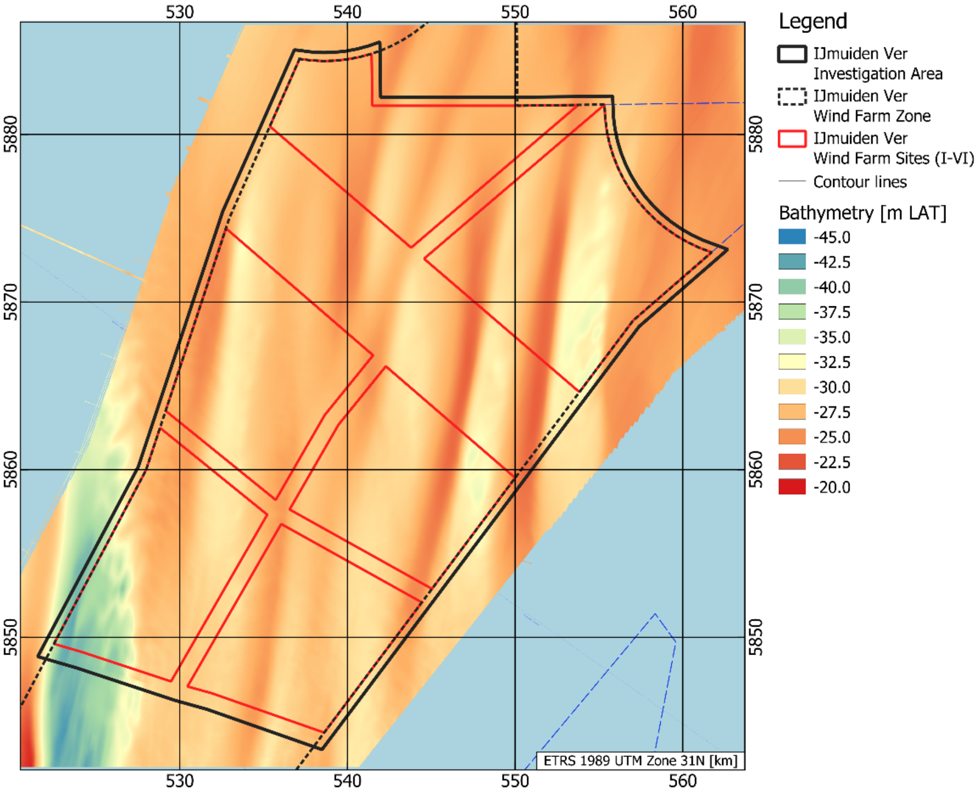

Figure 4.11:Overview of split bathymetries highlighting the large-scale bathymetry (sand banks) by removal of sand waves and megaripples.

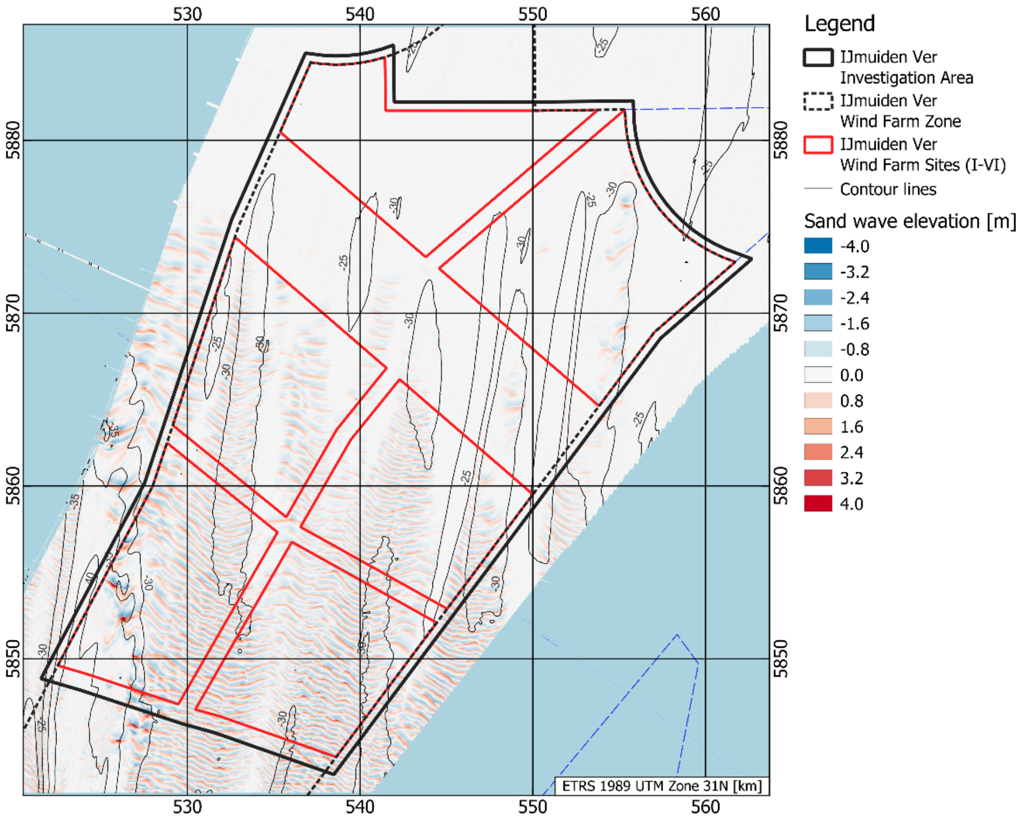

Figure 4.12:Overview of split bathymetries highlighting the sand wave fields.

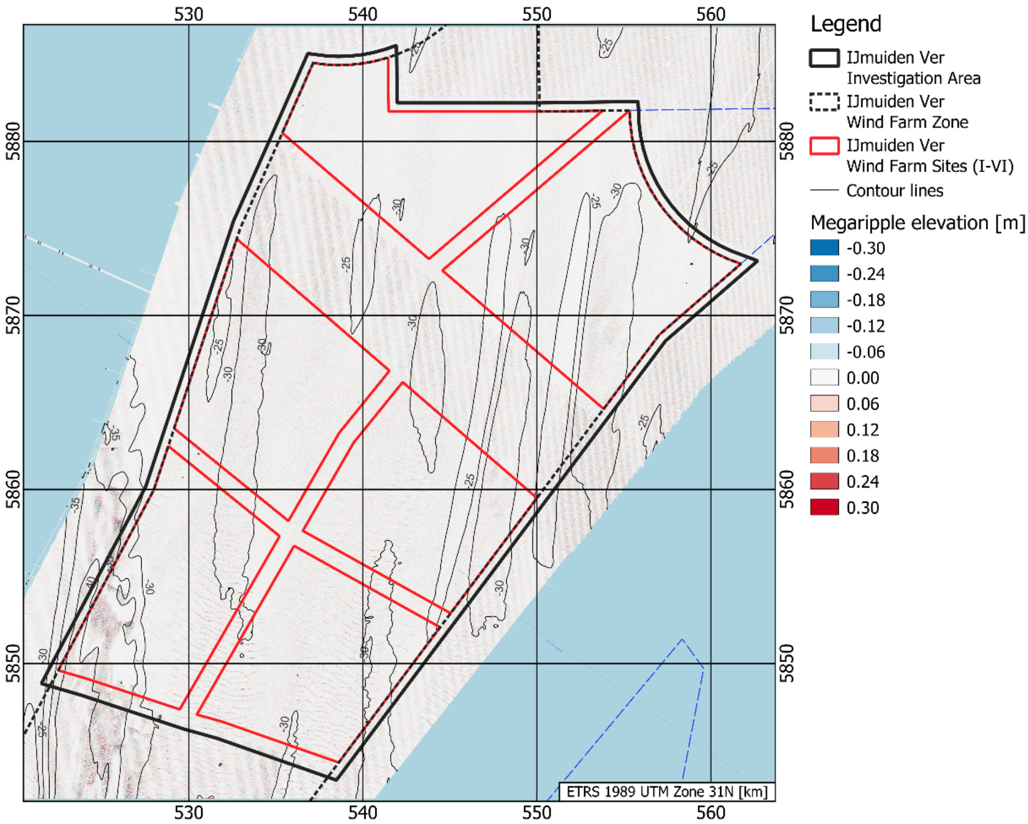

Figure 4.13:Overview of split bathymetries highlighting the megaripple fields.

4.4 Sand wave analysis

The general overview of seabed dynamics presented in Section 4.3 shows that sand waves are the most prominent bedforms causing seabed level changes. For the analysis of sand wave dynamics, three steps are performed.

- analysis locations are determined (Section 4.4.1);
- determination of sand wave dynamics in Section 4.4.2 and;
- sand wave dimensions in Section 4.4.3.

4.4.1 Sand wave analysis locations

For the analysis of sand wave dynamics all available mobile bathymetries were compared. Initially, locations are defined on top of the sand wave crests with a mutual spacing of 40 m. Each individual sand wave is analysed by a number of locations indicating spatial variability across the area of interest. An overview of the locations used is presented in Figure 4.14.

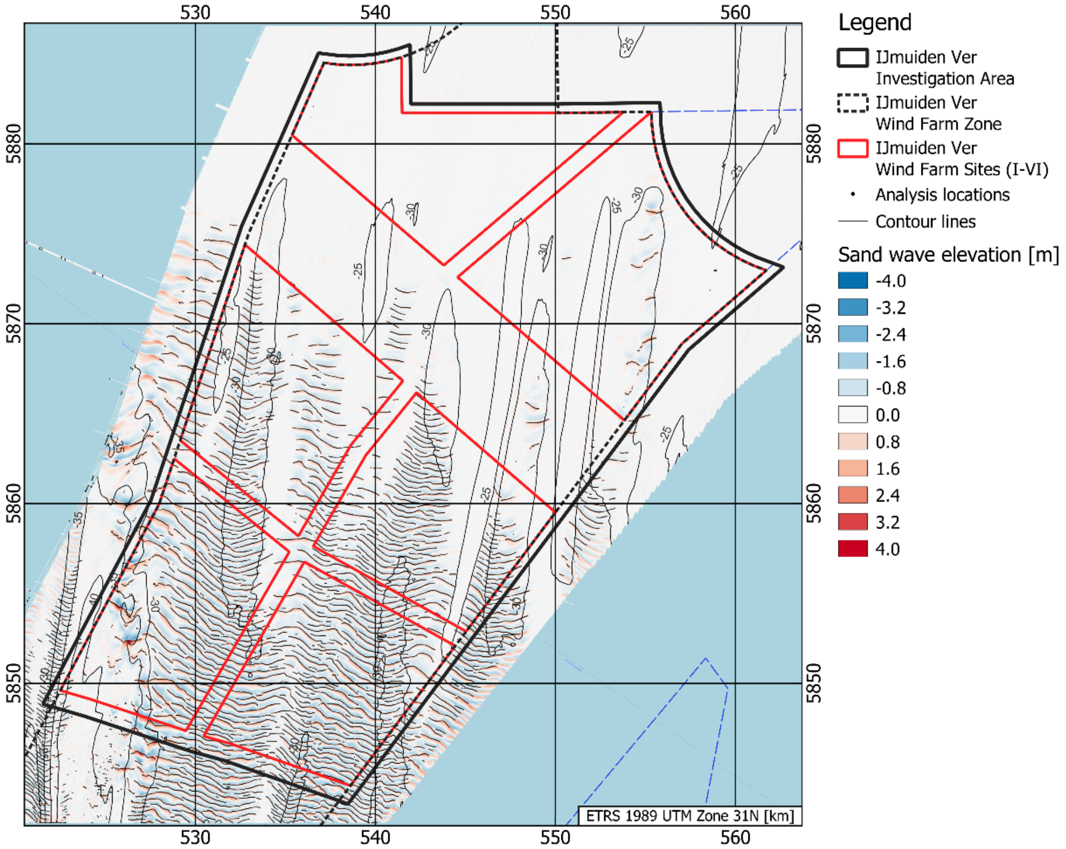

Figure 4.14:Overview of the analysis locations (black dots) used on top of the sand wave field. Due to the high density of analysis locations the dots appear as black lines (along the sand wave crests in the northwest to southeast direction).

4.4.2 Sand wave dynamics

The dynamics of the sand waves are determined by applying the methodology discussed in Appendix A.2.4.2. The 2D cross-correlation technique is applied to all possible combinations (55 in total) of composite bathymetries. This analysis yielded a mean, lower and upper bound value for the migration rates and directions per analysis location used in the data extrapolation.

The non-exceedance curves for the mean sand wave migration directions and rates are depicted in Figure 4.15. The spatial overview of mean migration directions and rates are shown in Figure 4.16 and Figure 4.17, respectively. The migration directions indicate that the sand waves migrate predominantly towards the north-northeast with a mean direction of 8 degrees north, with some local variations. Typical sand wave migration rates in IJV vary from 0.4 m/year to over 2.7 m/year, with local rates up to 6 m/year.

Spatial variation observed in IJV is largely related to the presence of the sand banks. No clear differences between individual Sites were found. The sand waves on the western slopes of the sand banks have the highest migration rates. The areas with limited seabed mobility occur on the eastern slopes of the sand banks. Locally, just southwest outside IJV, migration of sand waves is to the south-southwest. This area is indicated with a red circle in Figure 4.17. Observations will be compared to results from the numerical modelling in Section 6.2.

An overview of migration rates and direction per Site is presented in Table 4.6. The table includes the 5%, 50% and 95% non-exceedance values. The rates and directions ranges are similar for Sites I-IV. Among those, Site II presents the largest variation in terms of the observed rates and directions, related to the large bedforms present at the southwest side of the Site. The statistics of sand wave migration for Site V are quite different, due to the limited amount of bedforms present. No sand waves were detected in Site VI, thus no statistics are available for that Site.

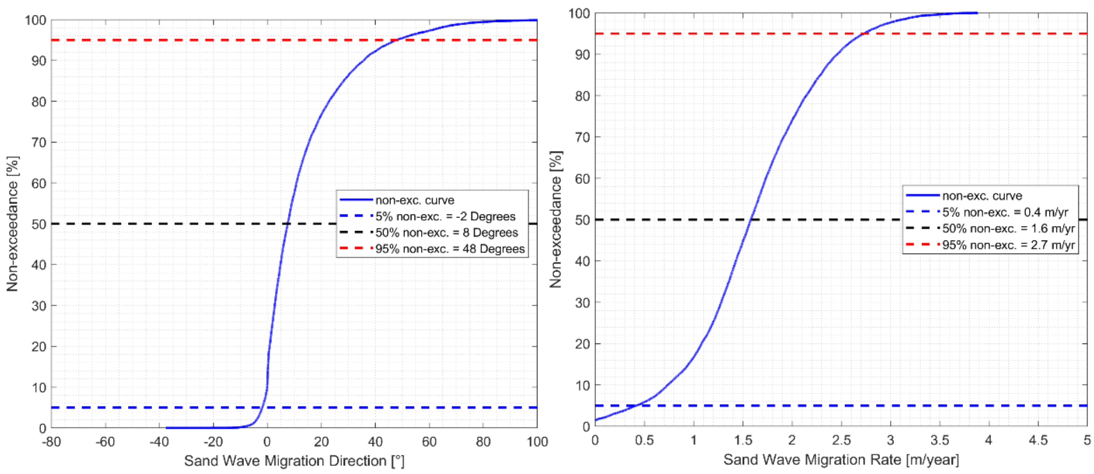

Figure 4.15:Non-exceedance curves for sand wave migration directions (left) and migration rates (right) for IJV Sites I-VI.

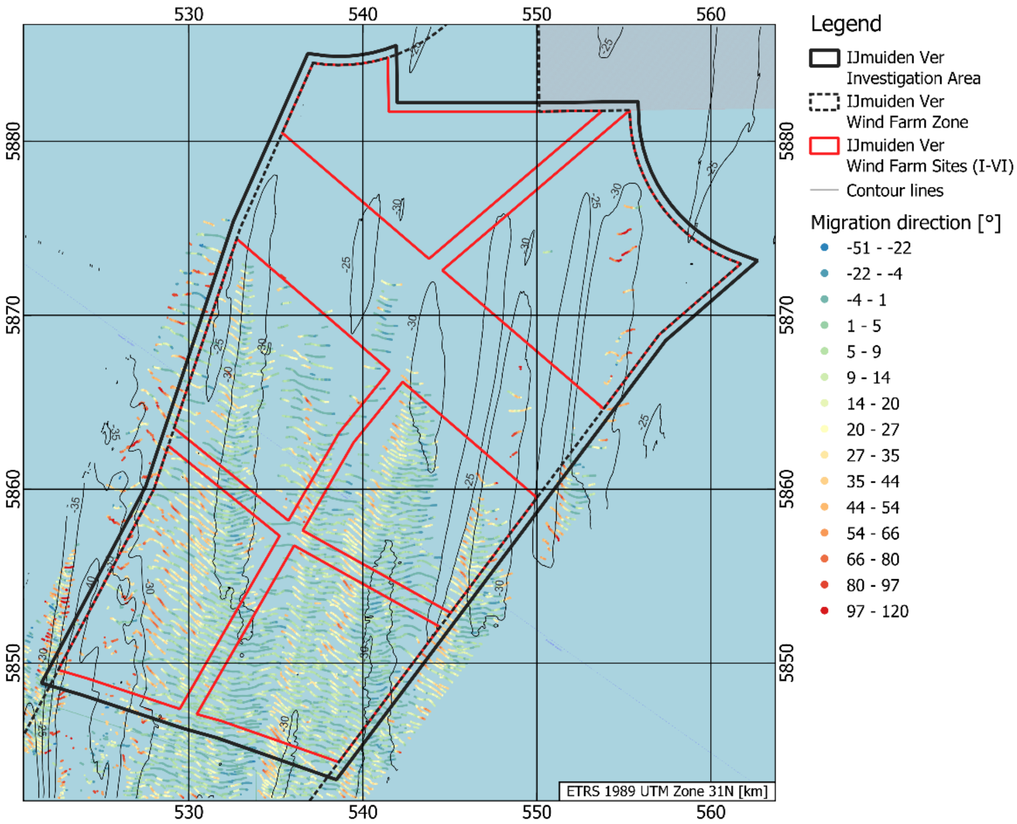

Figure 4.16:Spatial overview of the mean sand wave migration directions. Convention is clockwise relative to north.

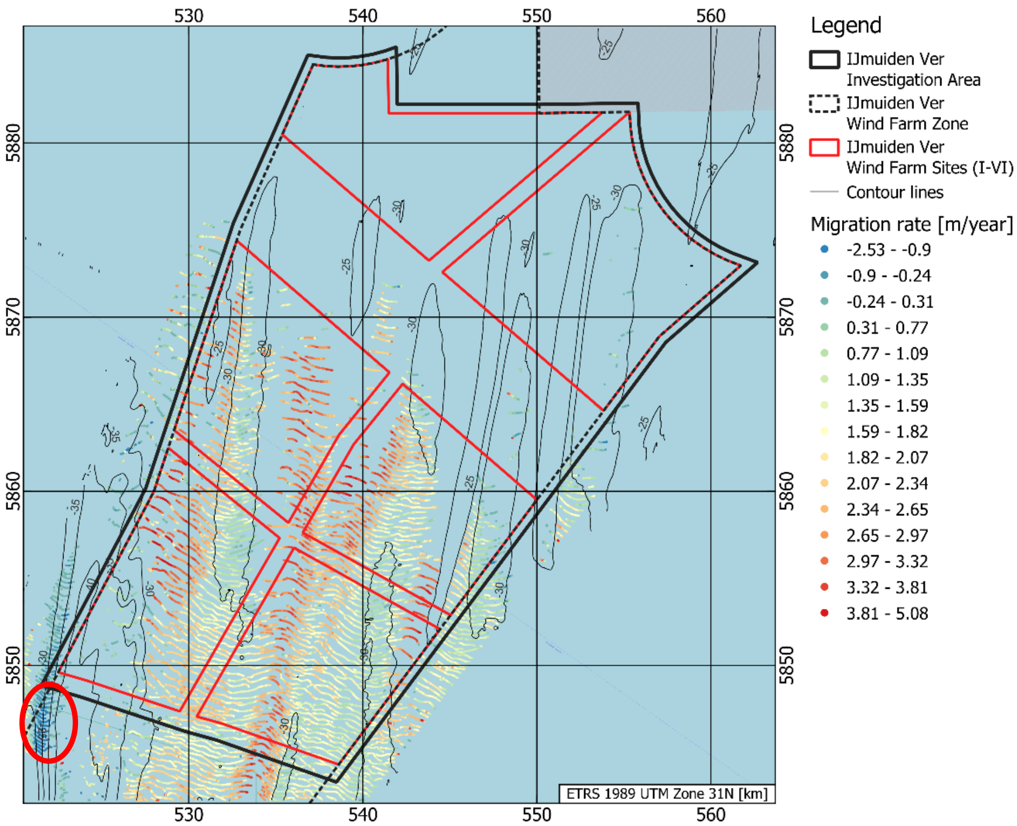

Figure 4.17:Spatial overview of the mean sand wave migration rates. The red circle indicates the area where sand waves migrate towards the south-southwest.

Table 4.6: *5%, 50% and 95% non-exceedance values for sand wave migration directions and rates per Site in IJV.*

Site	Sand wave migration rate [m/year]			Sand wave migration direction [°]		
	5%	50%	95%	5%	50%	95%
I	0.89	1.61	2.80	-2	5	35
II	0.15	1.43	2.69	-1	13	63
III	0.60	1.67	2.64	-3	7	40
IV	0.33	1.66	2.71	-3	8	43
V	-0.42	0.04	0.72	4	50	108
VI	-	-	-	-	-	-
I-VI	0.42	1.58	2.73	-2	8	48

4.4.3 Sand wave dimensions

The dimensions of the sand waves are determined by applying the methodology discussed in Section A.2.4.3. The Fourier approximation is applied to all composite bathymetries yielding sand wave heights and lengths. The non-exceedance curves for the sand wave heights and lengths in IJV as obtained from the recent 2020-2022 bathymetries are depicted in Figure 4.18. The spatial overviews of the sand wave heights and lengths are shown in Figure 4.19 and Figure 4.20, respectively. The spatial overviews include sand wave heights and lengths from the 2013-2016 bathymetry for areas not covered by the 2020-2022 bathymetry.

The sand wave heights vary between 0.9 m and 3.5 m in IJV and sand wave lengths between 170 m and 620 m (5% and 95% non-exceedance values). No clear spatial trend in sand wave dimensions was found in IJV, although the highest sand waves were found on top of the sand banks. The presence, dimensions and dynamics of sand waves are dependent on local sediment and hydrodynamic conditions.

An overview of sand wave heights and lengths per Site is presented in Table 4.7. The table includes the 5%, 50% and 95% non-exceedance values. The sand waves in Sites I-II are slightly higher compared to the rest of IJV with highest sand waves found in the southwest of Site II. The variation in Site V is caused by the limited amount of bedforms present. The longest sand waves are observed in Site V, while similar length statistics are found for Sites I-IV.

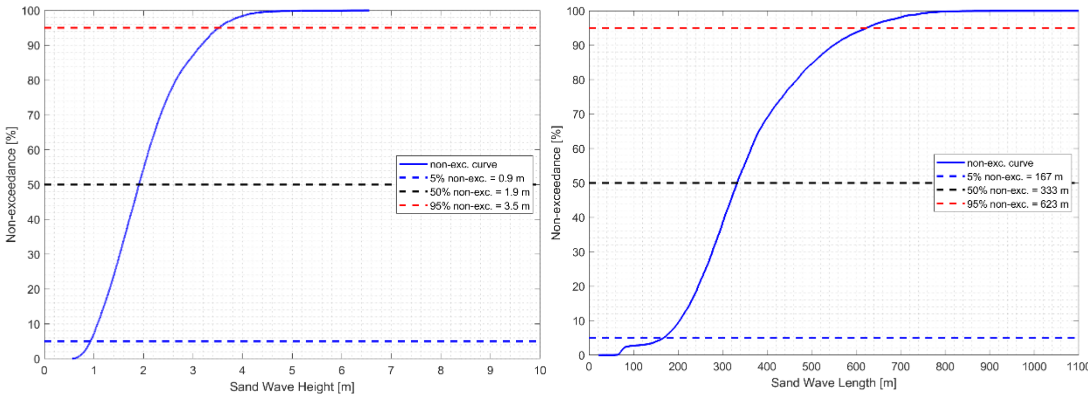

Figure 4.18:Non-exceedance curve for sand wave heights (left) and lengths (right) as derived from the 2020-2022 bathymetry for IJV Sites I-VI.

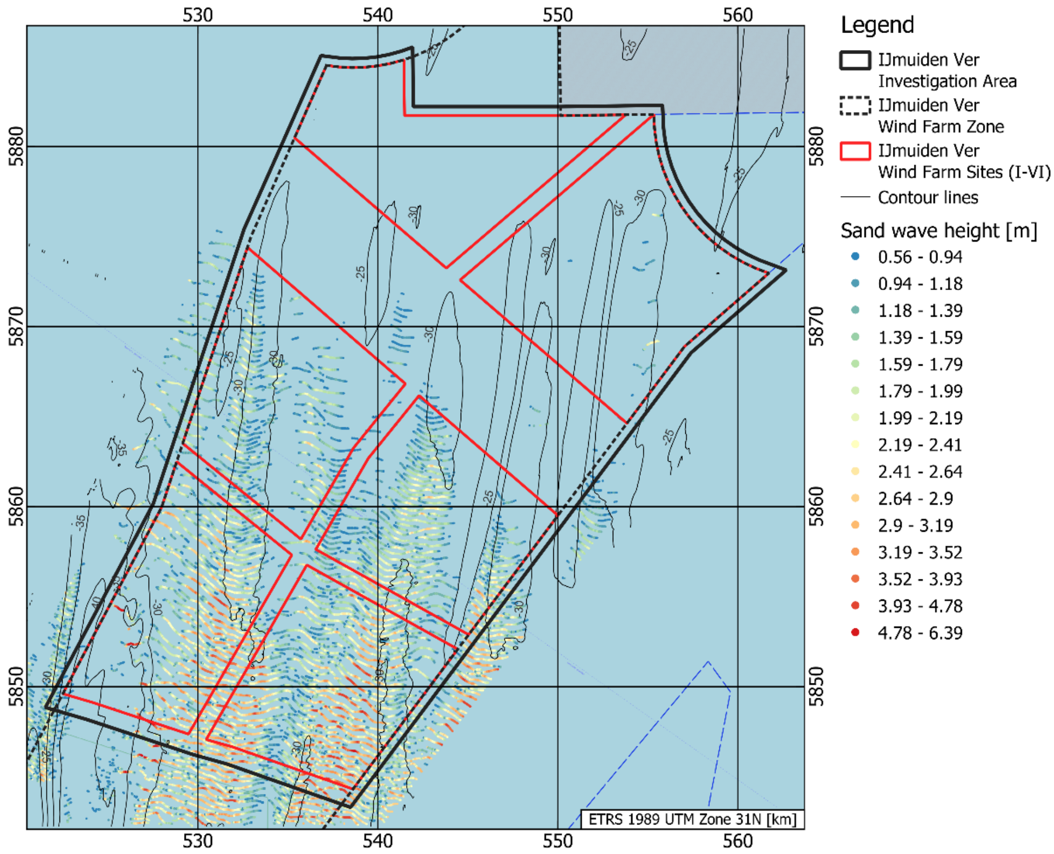

Figure 4.19:Spatial overview of sand wave heights using the 2020-2022 and 2013-2016 bathymetries.

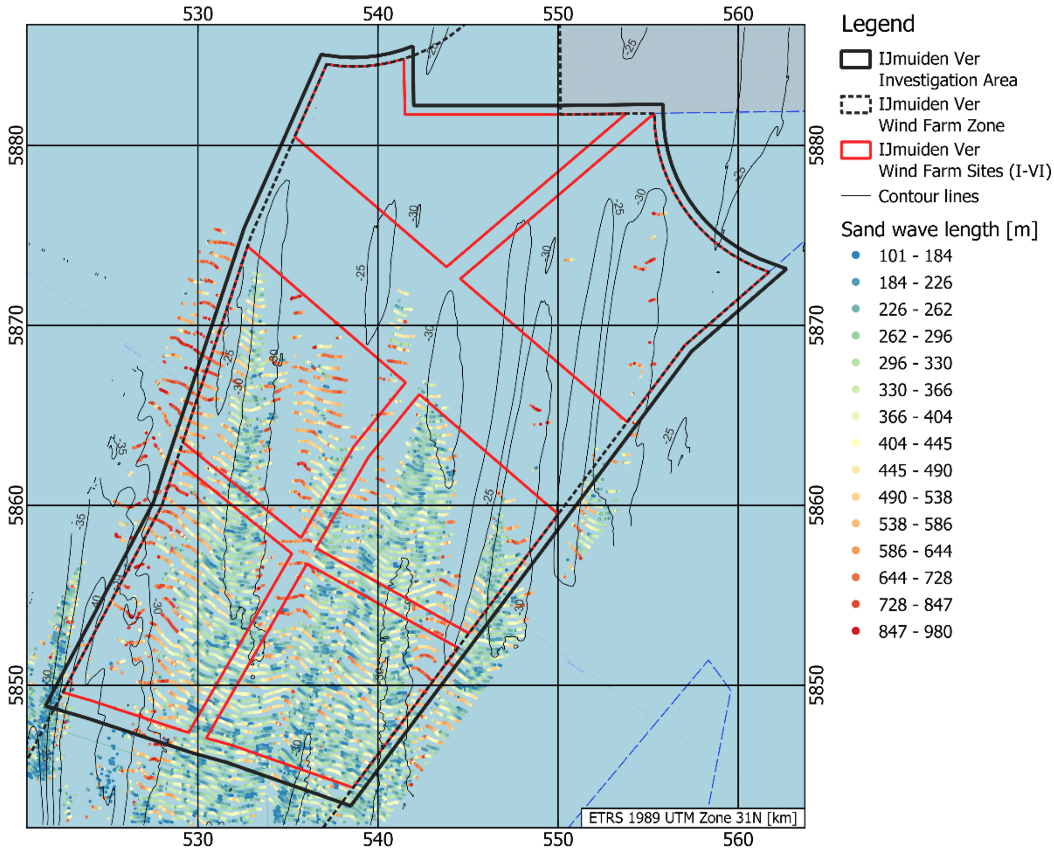

Figure 4.20:Spatial overview of sand wave lengths using the 2020-2022 and 2013-2016 bathymetries.

Table 4.7: 5%, 50% and 95% non-exceedance values for sand wave heights and lengths per Site in IJV.

Site	Sand wave height [m]			Sand wave length [m]		
	5%	**50%**	**95%**	**5%**	**50%**	**95%**
I	1.03	2.22	3.79	141	310	532
II	1.05	2.17	3.63	182	357	659
III	0.88	1.61	2.56	179	317	550
IV	0.79	1.46	2.33	189	403	689
V	0.71	1.16	2.41	381	625	787
VI	-	-	-	-	-	-
I-VI	0.93	1.91	3.51	167	333	623

To investigate the retention of sand wave shape in IJV over periods of multiple years, sand wave lengths and heights were compared between the 2013-2016 and 2020-2022 composite bathymetries. The comparison yielded relatively high correlations with correlation values of 0.98 and 0.92 (values of 1.0 indicate full correlation) for the sand wave height and length, respectively (Figure 4.21 and Figure 4.22). The 2002-2003 composite bathymetry was not used for this comparison because of the spatial coverage of the data. Calculated bed form dimensions for this bathymetry did not yield a similar level of detail.

Although correlations are relatively good, some differences can be observed as for both the sand wave length and height no full linear relationship is present (indicated by the dotted red line and the equation in the bottom right in both Figure 4.21 and Figure 4.22). It is assumed that these differences arise from the applied methodology, the quality of the available data and slight alterations of sand wave shapes/dimensions. For clarity, squares with only one or two entries are highlighted purple in the figures.

After checks on the presumed outliers it was concluded that these relate to uncertainties in the applied methodology (especially for sand wave lengths) and in the data resolution (for the sand wave heights). For example, on the edges of the sand wave fields defining the start and end points of sand wave fields was quite sensitive. Although a dedicated method was introduced for this, see Appendix A.2.4.3, this gave some outliers in the presented comparison.

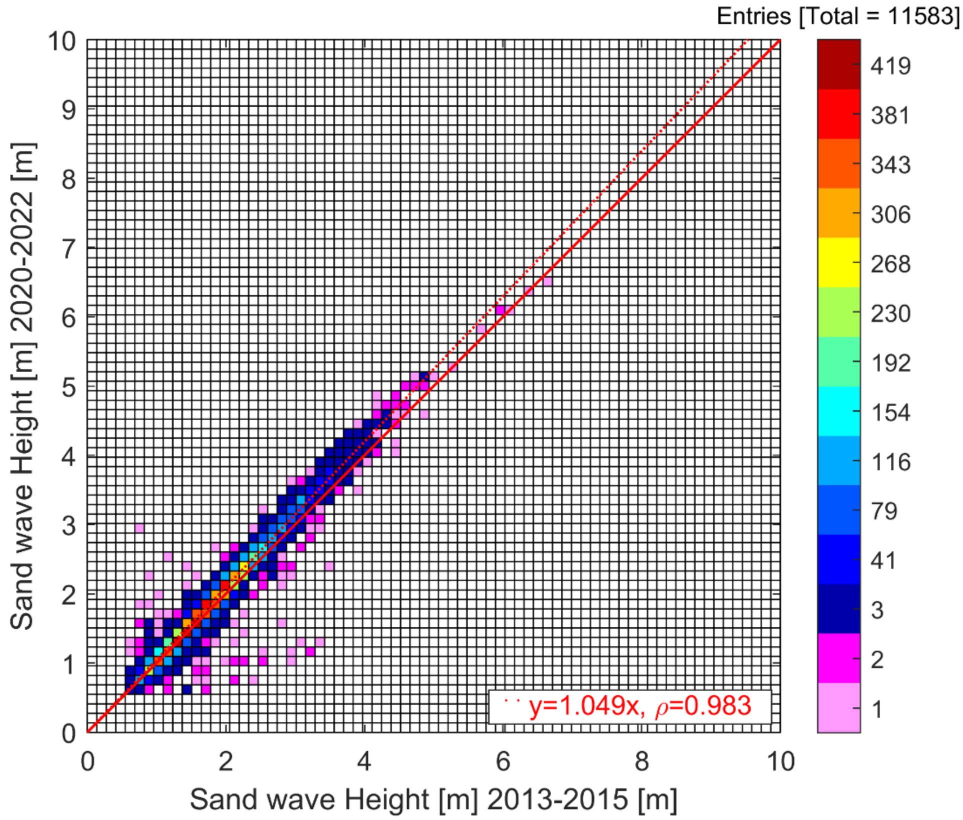

Figure 4.21:Cross-correlation density scatter plot for sand wave heights in 2013-2016 and 2020-2022.The red line indicates the linear relationship of the data.

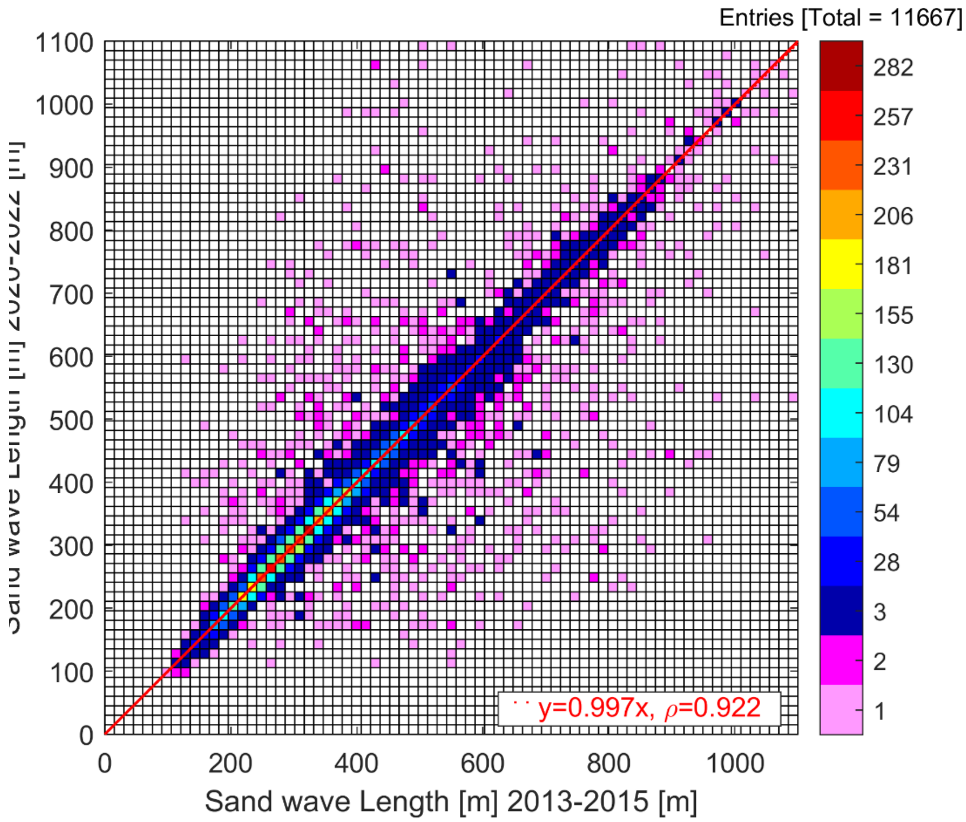

Figure 4.22:Cross-correlation density scatter plot for sand wave length in 2013-2016 and 2020-2022. The red line indicates the linear relationship of the data.

To further highlight the correlation between sand wave heights and lengths over time, Table 4.8 highlights the mean and standard deviation values for the sand wave height and length comparison between the 2013-2016 and 2020-2022 composite bathymetries. It can be seen that the mean differences for both height and length are very small (0.08 m and -1.6 m respectively). The standard deviation for sand wave lengths is higher (52.8 m) but still falls well below the 5% non-exceedance values for sand wave lengths (see Table 4.7). For sand wave heights the standard deviation is 0.12 m, which is also much smaller than the 5% non-exceedance values presented in Table 4.7.

Similar values were found when considering each individual Site, except for the length comparison in Site V. As highlighted in the previous paragraph the applied method introduces some uncertainties when determining sand wave lengths for individual sand waves or sand waves at the edges of sand wave fields. Site V is characterised by a number of these individual sand wave fields. Visual inspection showed that changes in sand wave lengths in Site V were limited.

Table 4.8: Mean and standard deviation values for the comparison of sand wave heights and lengths from the 2013-2016 and 2020-2022 composite bathymetries specified.

Comparison 2013-2016 and 2020-2022	Mean [m]	Standard deviation [m]
Sand wave height	0.08	0.12
Sand wave length	-1.6	52.8

It is therefore concluded that changes in sand wave heights and lengths are limited over the period 2013-2022. Visual inspections of bed forms in the 2002-2003 composite bathymetry did yield similar results. Furthermore, less than 5% of the data points in Figure 4.21 and Figure 4.22 only has one or two entries (this includes outliers, although not solely). However, the time period for which high quality data is available (2013-2022) is relatively short compared to the period of extrapolation 2020-2072. Also, some small differences in heights and lengths were found, which could be related to uncertainties in the applied methodology, in the available data or changes in bedform dimensions.

To capture these differences an additional uncertainty is added to the seabed predictions as described in Appendix A.4.5.1. Based on the found correlation, the uncertainty related to sand wave reshaping is quantified as 0.20 m for areas with sand waves and 0.32 m for the sand wave crest. These values correspond to one and two standard deviations away from the mean difference as specified in Table 4.8. The downward uncertainty at the sand wave crest location is quantified as 0.25 m (0.6 * 0.20 + 0.4 * 0.32). This value is smaller compared to the upward uncertainty because of the sand wave shape at the crest which is often sharp peaked (see Figure 4.9). Changes in sand wave lengths are incorporated in this uncertainty when assuming volume balance in the sand waves, i.e. a shortening sand wave will cause it to increase in height. If the sand wave fields would have changed significantly over the considered period, it is not likely that individual sand waves would have restored to almost exactly the same dimensions.

4.5 Large-scale seabed dynamics

The dynamics of the large-scale seabed are determined by applying the methodology discussed in Appendix A.2.5. The analysis is based on temporal difference plots between the various surveys. For each of the comparisons only locations measured at least three times are taken into account.

To indicate the long-term seabed trends two comparisons are made. The first is shown in Figure 4.23 and depicts the vertical trend (dz/dt) of all the bathymetries. The second is shown in Figure 4.24 and depicts the dz/dt trend of all the large-scale bathymetries. The limits of the colour bar, ±0.05 m/year, are chosen to resemble realistic natural variations and not the span of the data. This choice clearly illustrates that vertical seabed variations are limited and fall within uncertainties of the historic seabed levels.

Most prominent are the vertical trends at the locations of the sand waves in Figure 4.23. These trends are not (or much less) observed in Figure 4.24 for the large-scale bathymetries. The vertical bed level differences of maximum ±2cm/year are observed over a period of 20 years which implies that large-scale seabed lowering or rise is insignificant and hence the morphodynamics in IJV are mainly driven by sand wave migration. The reddish (Sites I-IV) and blueish (Site VI) areas in IJV are most likely related to offsets in the historic data.

In 4.3.1.2 the differences between the 2002-2003, 2013-2015 and 2020-2022 composite bathymetries were discussed. These differences (including median and standard deviation values) did indicate changes (95% bandwidth) roughly in the same order as the total TVU. These differences however did include the effect of sand waves, which can be quite significant. Table 4.9 highlights the mean and standard deviation values for the differences between the three composite bathymetries with and without sand waves. It is concluded that mean differences between bathymetries are very small, do not show a trend in time, and that there is little difference when including or excluding sand waves. This indicates that over time (20 years since 2002) no significant loss in sediment is observed. The standard deviations obtained from the differences are significantly lower when excluding sand waves (factor 1.5 to 2) from the composite bathymetries. This highlights the effect of sand waves, with non-linear seabed level changes over time due to horizontal migration of (asymmetrical) bedforms. When excluding sand waves, i.e. comparing the large-scale bathymetries, 95% bandwidth of differences fall well within the total TVU ranges (-0.5 to +0.45 m compared to 0.68 to 1.00 m). When considering the individual Sites similar values were found.

Table 4.9: Mean and standard deviation values of differences between composite bathymetries with and without sand waves.

Dataset comparison	Differences measured bathymetries		Differences large-scale bathymetries		Total TVU [m]
	Mean [m]	Standard Deviation [m]	Mean [m]	Standard Deviation [m]	
2020-2022 to 2013-2016	0.06	0.21	0.07	0.08	0.68-0.71
2020-2022 to 2002-2003	-0.01	0.39	-0.01	0.21	0.68-0.71
2013-2016 to 2002-2003	-0.06	0.29	-0.07	0.22	1.00

The earlier assumption (Section 4.3.1) that the large-scale bathymetry, obtained after filtering out the rhythmic bedforms, can be considered static is thus confirmed. However, to cover for uncertainties in the vertical seabed level trends, i.e. changes in the same order as survey related uncertainties, a yearly increase and decrease of the large-scale seabed of 0.01 m is used as an uncertainty in the extrapolation of seabed levels as discussed in Chapter 6 and Appendix A.4.5. These values are comparable to one standard deviation as observed from the data comparison. For example, over the period 2002-2022 (20 years) a standard deviation of 0.21 m was found. In the uncertainty band a value of 20 times 0.01 m (0.20 m) is included for large-scale seabed level changes.

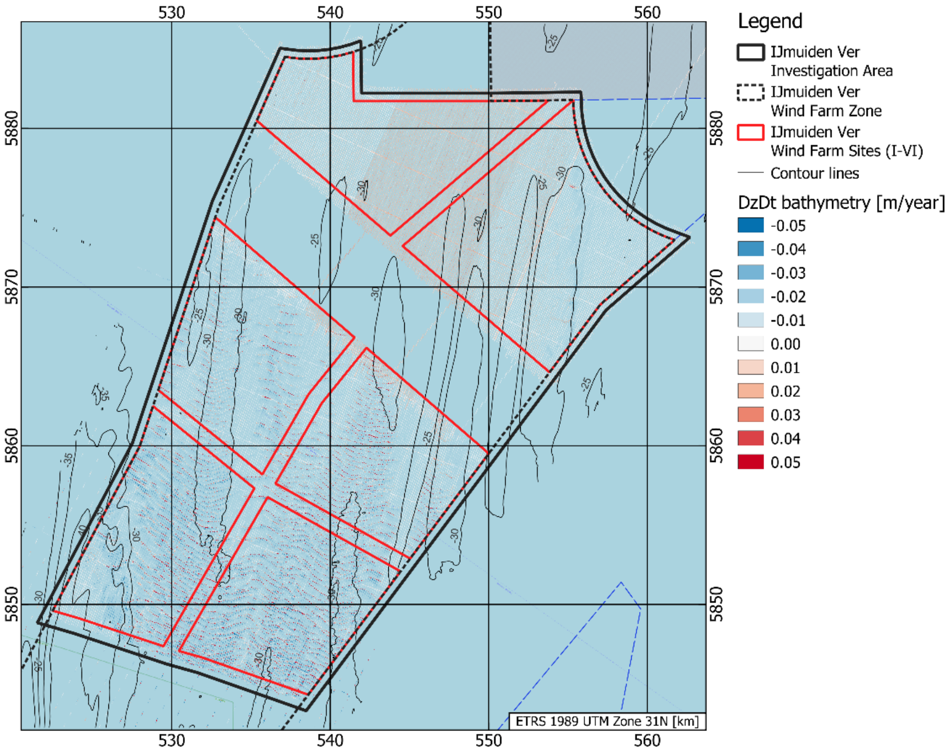

Figure 4.23:Yearly vertical seabed variations based on all bathymetries over the period 1992 to 2022.

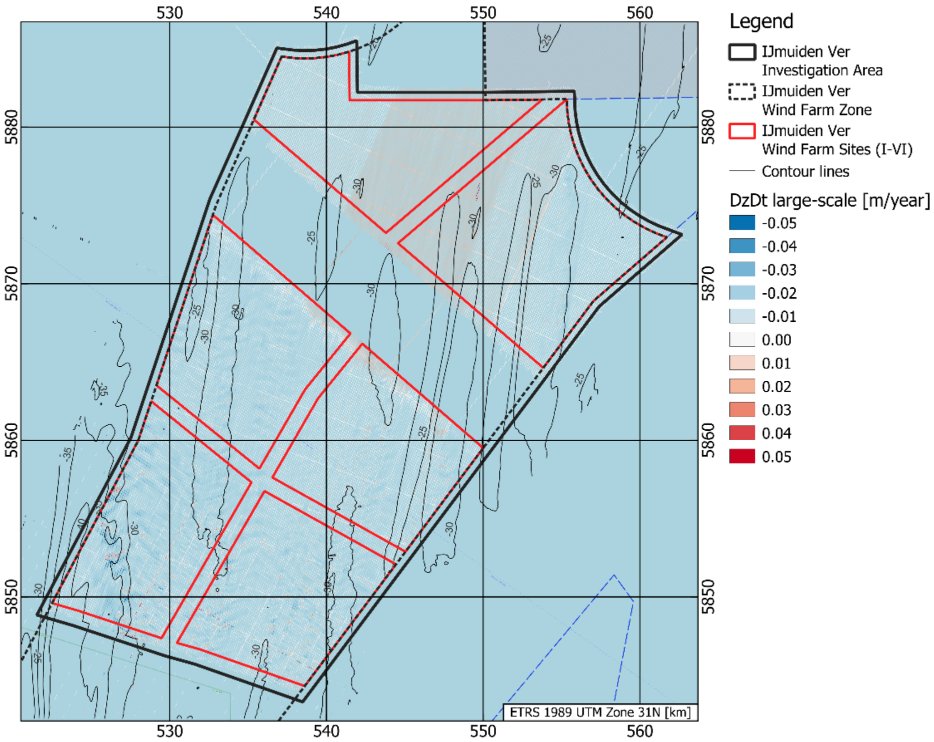

Figure 4.24:Yearly vertical seabed variations based on all large-scale bathymetries over the period 1992 to 2022.

4.6 Megaripple dynamics

As explained in Section 3.5 and Appendix A.2.6, megaripples have rapid migration rates so that many megaripples will pass each foundation throughout the lifetime of the wind farm.

Therefore, it was decided not to predict megaripple migration, but to analyse their dimensions and to use this information in the prediction of future bed levels (see also Chapter 6).

The presence and elevation of megaripples is illustrated by Figure 4.25 indicating the megaripple elevation around the sand waves for a transect in IJV (similar transect as Figure 4.9). The megaripple heights (total amplitude) for this specific transect vary between 0.05 and 0.20 m. At the locations of the sand wave crests megaripple heights increase. This is caused by the filtering methodology used where the sharp crest of the sand wave is partially taken up in the megaripple signal.

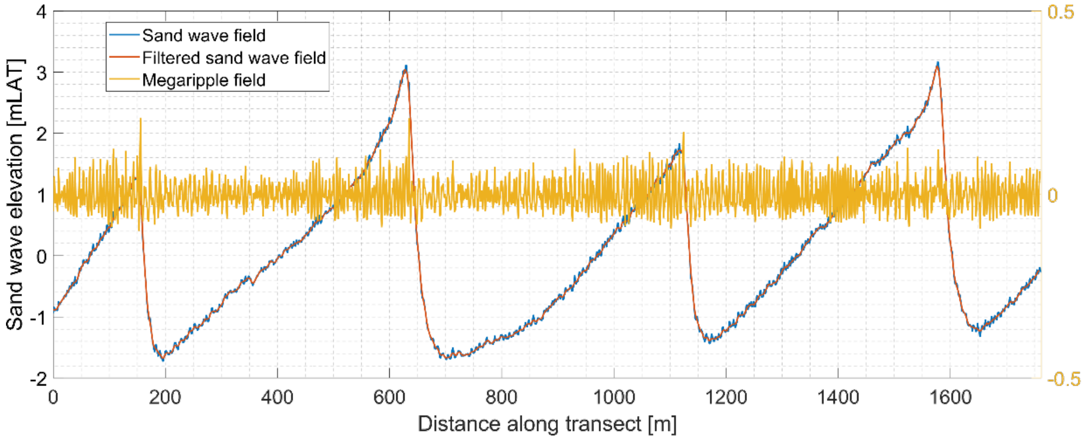

Figure 4.25:Presence and elevation of megaripples along a transect (similar to Figure 4.9) using the 2020-2022 bathymetry. The blue line indicates the derived mobile seabed, the red line the sand wave field and the yellow line the megaripple field.

Megaripples are present throughout IJV, although they are less prominent in areas without/ limited sand waves (Sites V-VI). The largest megaripples are observed towards the southwest of IJV, in Site II. A zoomed-in plot of the megaripples of that area is shown in Figure 4.26. These locations correspond to the areas without the Holocene formation. In this part of Site II, megaripples with lengths up to 30 m and heights up to 0.8 m occur.

Based on the limited availability of high-quality data no overall conclusion on the temporal variability of megaripple dimensions could be made. However, megaripple variation could be obtained from the repeat survey lines, which are discussed in Section 4.7.

To cover any temporal variation in megaripple dimensions an uncertainty of 0.10 (for seabed lowering) and 0.15 (for seabed rise) m is used as the uncertainty in the extrapolation of seabed levels as discussed in Chapter 6 and Appendix A.4.5. This value is based on findings of temporal variations in the repeat survey lines (see Section 4.7) and from similar assessments for seabed dynamics on the Netherlands Continental Shelf such as Hollandse Kust West (Deltares, 2020c).

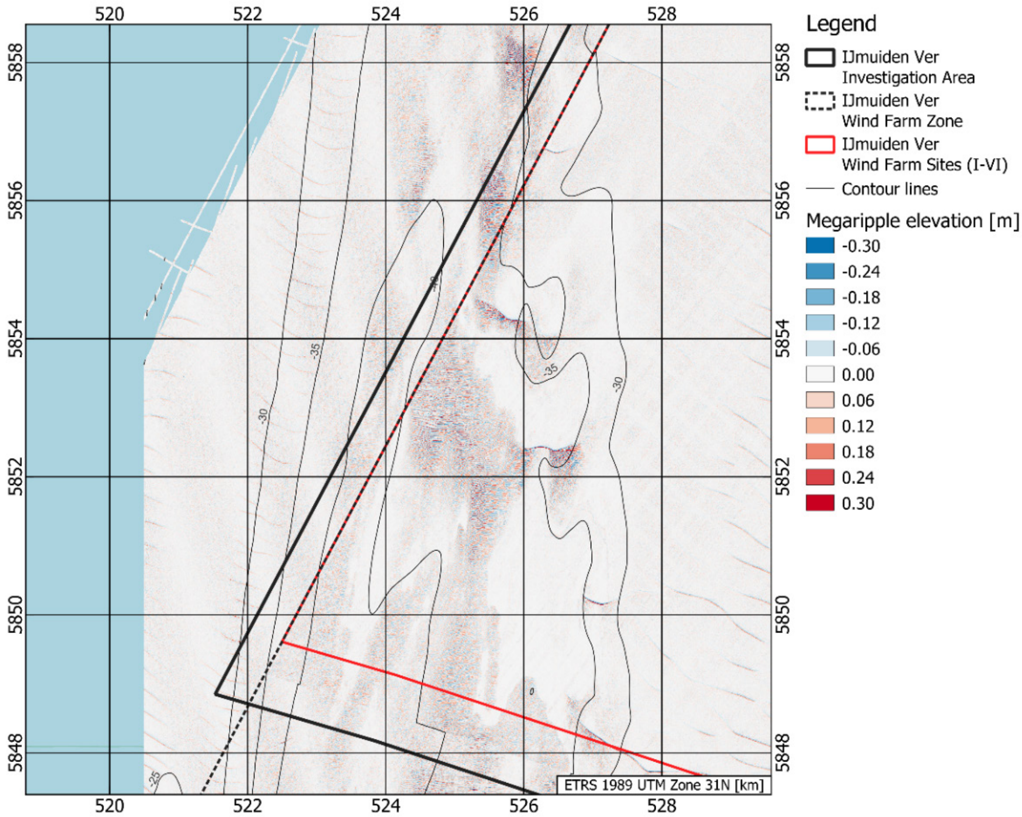

Figure 4.26:Spatial zoomed-in overview of the southwest of IJV where the highest megaripples occur.

4.7 Analysis of repeat survey lines

During the survey campaigns in IJV since 2020, a number of survey lines were repeated (see Table 2.1). In total 12 repeat lines were conducted for (part of) seven transects (see numbering in Figure 2.1). In this section, the seabed profiles along these transects are discussed in Section 4.7.1. Profiles of sand waves and megaripples are discussed in Section 4.7.2. Seabed profiles along all repeat survey lines are presented in Appendix E.2.

4.7.1 Seabed profiles

The repeat survey lines provide high-resolution information on the water depths over a relatively short time period (2020-2022). Within this period, sand wave migration is limited (as discussed in Section 4.4.2). To illustrate this, seabed profiles are extracted from the available survey data along the repeat survey lines. Three examples are shown in Figure 4.27. All other seabed profiles are included in Appendix E.2.1.

The seabed profiles along the repeat survey lines indicate limited migration of sand waves over the period 2020-2022 (see for example middle panel in Figure 4.27). Compared to the 2002-2003 and 2013-2016 bathymetries, migration is observed in the direction of the steepest slope (towards the right – approximately north). For the bottom panel observed dynamics are limited and, in the case of the 2002-2003 bathymetry, related to uncertainties in measurements. From these seabed profiles it is concluded that intra-annual variations over the period 2020-2022 in sand wave dynamics and dimensions, and large-scale seabed dynamics, are limited.

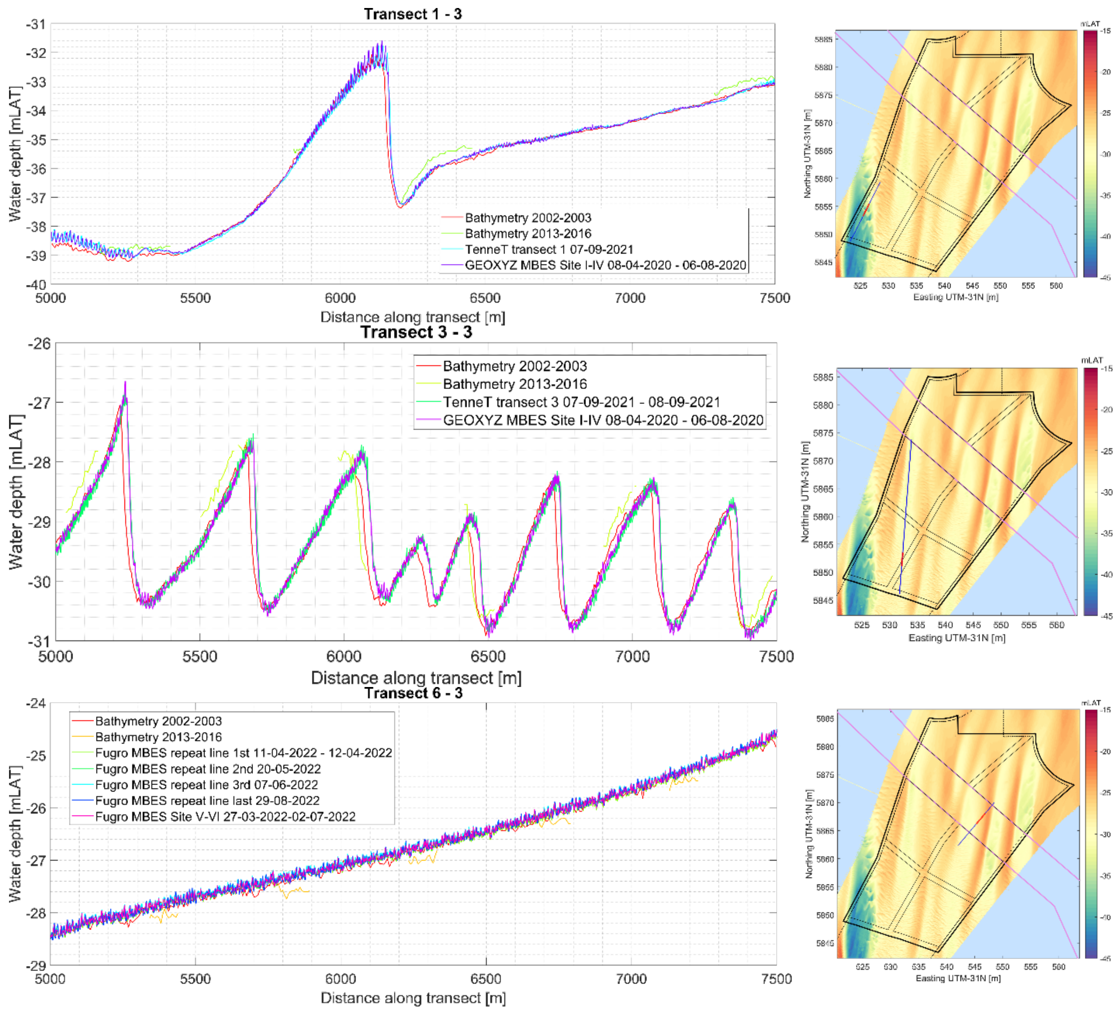

Figure 4.27:Seabed profiles along part of repeat survey lines 1, 3 and 6. Location of the profiles are indicated by red lines in the right panels.

4.7.2 Sand wave and megaripple profile

The previous section indicated that sand wave and large-scale seabed dynamics are limited over the period 2020-2022. Most value from the repeat survey lines can be gained from studying the megaripple dynamics. As discussed in Section 4.6, megaripples are highly dynamic and quickly adapt to (changing) hydrodynamic conditions. To assess these dynamics, multiple, closely spaced in time, high resolution measurements are required.

Data along the repeat survey lines is analysed and split into three signals; the sand waves, the megaripples and the large-scale seabed. The splitting is performed along the seabed profiles by using dedicated filtering techniques. An example is shown in Figure 4.28, representing two measurements for the same transect as the top panel of Figure 4.27. Other profiles are presented in Appendix E.2.2.

Although measurements are more than one year apart there is a clear resemblance between the sand wave and megaripple signals. Clear patches of megaripples occur superimposed on top of the sand wave. Outside the sand wave, limited megaripples are observed.

Further insight about the megaripple dimensions can be obtained from non-exceedance curves representing the total megaripple height per measurement. Figure 4.29 presents the non-exceedance curve of megaripple heights for transect 1 and 6. Other non-exceedance curves are presented in Appendix E.2.3.

Repeat survey lines 1 and 6 have been monitored (partly) twice and six times, respectively, over the period 2020-2022. The largest differences between the two non-exceedance curves are the heights of the megaripples. Megaripples along transect 1, located in the southwest of IJV, are significantly higher compared to transect 6. This was also found in the megaripple analysis (see Figure 4.26). Although the majority of IJV megaripples do not exceed 0.4 m in height, the megaripples in the southwest of IJV range up to 1.0 m.

The non-exceedance curves for transect 6, bottom panel in Figure 4.29, show some variation over time. Repeat survey lines indicate increasing megaripple heights over the period of April to August 2022. Similar observations were made for transect 3 and 4 (see Appendix E.2.3) where megaripples were higher in August and September than April. Observed differences are about 5-10 cm which correspond with findings for Hollandse Kust West (Deltares, 2020c). The chosen uncertainty related to megaripples of 0.10 m as defined in Section 4.5, is therefore maintained.

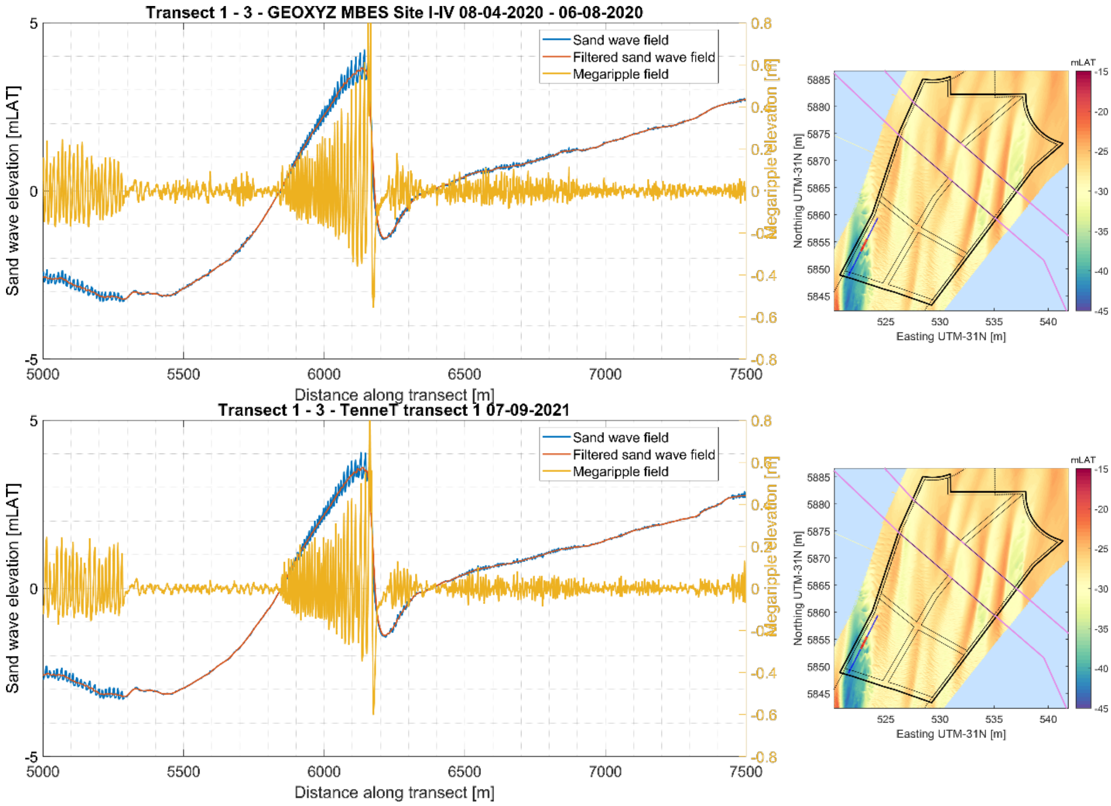

Figure 4.28:Split seabed profiles along part of repeat survey line 1. The top and bottom panels show data from two different measurements.

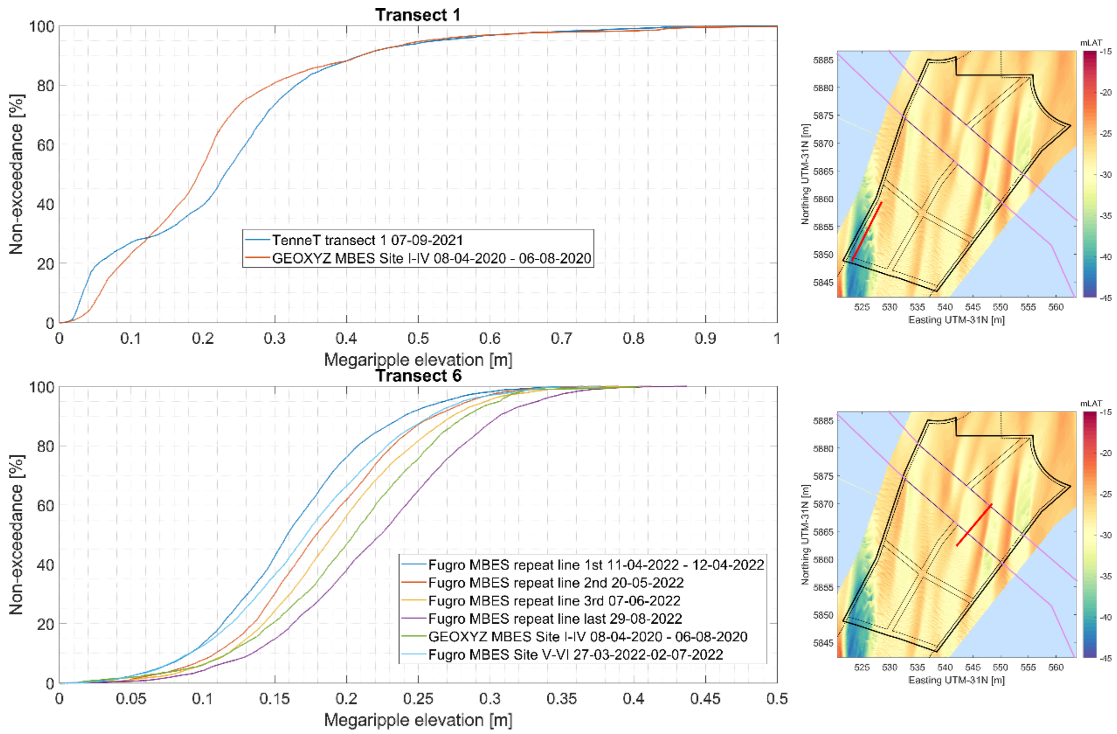

Figure 4.29:Non-exceedance curves of megaripple heights for repeat survey lines 1 (top) and 6 (bottom).

4.8 Summary

A morphodynamic analysis focussed on sand waves, large-scale seabed changes (sand banks) and megaripples in IJV is presented. It is estimated that within IJV sand waves migrate towards the north-northeast with a mean best estimate direction of 13°N. Typical migration rates range between 0.4 m/year and 2.7 m/year, with local rates up to 6 m/year. Migration statistics are similar for Sites I-VI. For Site V statistics are different due to the small number of sand waves present. No sand waves were detected in Site VI. Spatially, the sand waves on the western slopes of the sand banks have the highest migration rates.

In IJV, sand wave heights and lengths (90% interval) show a large range between 0.9 m and 3.5 m and 190 m and 728 m, respectively. There is no clear spatial trend in sand wave dimensions, although sand waves are higher in Sites I-II. The longest sand waves are found in Site V, the distribution of lengths is similar between Sites I-V.

Differences in large-scale bathymetry between the different surveys did not show a consistent pattern in either deposition or erosion over the Sites. Also, available literature discussing this specific area does not provide quantitative information. Therefore, it is assumed that over the wind farm lifetime, no significant large-scale changes will occur.

The analysis of large-scale seabed dynamics is subject to uncertainties, especially when considering older surveys. This is addressed as an uncertainty in the seabed predictions by including a yearly increasing value of 0.01 m/year, uniformly over Sites I-VI, both upward and downward.

Analysis shows that megaripples in IJV have wavelengths up to 30 m and amplitudes up to 1.0 m. Throughout IJV, areas with very small megaripples are present, corresponding with the areas without sand waves and the areas where clay is present at the seabed (Sites V-VI). The highest megaripples occur towards the southwest of IJV (Site II). Temporal variations in megaripple dimensions were small. However, megaripple occurrence and dimensions are highly variable in time, as they are highly dynamic. Hence, the megaripple dynamics have been incorporated as an uncertainty parameter in predicting seabed levels.

5 Results of numerical modelling

5.1 Introduction

As described in Appendix A.3, the validated hydrodynamic numerical model was extended to simulate the sediment transport patterns across IJV. The aim of the sediment transport simulations is to build on the presented data, the methodology and the background to IJV in Chapters 2 and 3 and Appendix A as well as to support the data-driven analysis in Chapter 4.

The results of the simulations are presented and discussed in the following sections. Tidal flow and sediment transport patterns derived over one arbitrary spring tide and one arbitrary neap tide over IJV IA are presented in Section 5.2 (tide-only forcing). Subsequently, in Section 5.3, sediment transport patterns over the representative spring-neap tidal cycle in a year are presented (tide-only forcing). The variability of sediment transports over the different Sites is discussed. The intra-annual and interannual variations of sediment transport under both tidal and meteorological forcing are described in Sections 5.4 and 5.5, respectively. Section 5.6 compares bed load and suspended sediment transport on an annual scale, while Section 5.7 explores the sensitivity of the sediment transport to changes in the median sediment diameter. Finally, the impact of average and extreme wave conditions on the sediment transport over the different Sites is discussed in Sections 5.8 and 5.9, respectively.

The numerical simulations provide insight into the effect of the underlying bathymetry and different forcing conditions on the general sediment transport patterns and their spatial and temporal variability. However, the exact sediment transport loads/rates cannot be relied upon without careful calibration/validation, which is beyond the scope of this study. As the absolute values do not have an established and direct relationship to the migration rates of sand waves, the focus is on the general (directional and magnitude) patterns of sediment transport. Along with the insight on the underlying processes that drive the sand wave migration, these patterns are used to validate the migration rates and directions determined using the surveys (Chapter 4).

It is noted that the numerical model is used to model the larger scale sediment transport patterns over the area of interest. The numerical model is not detailed enough to explicitly simulate the sand wave dynamics (migration, changes in shapes etc).

5.2 Tidal flow and net sediment transport

To build a system understanding and assess the relative importance of the various forcing mechanisms with respect to flow and sediment transport, results are first presented in this section from simulations with tide-only forcing.

The left panel of Figure 5.1 presents tidal ellipses at several locations in IJV. These tidal ellipses reflect the modelled depth-averaged tidal current velocities and directions over an arbitrary day during a spring tide (1st September 2019). The figure shows a wide directional variation of velocities during this spring tide. The tidal axis is generally directed in a north-northeast-south-southwest direction. Flood velocities (north-northeast) are generally more concentrated in terms of direction compared to ebb velocities (south-southwest). Along the tidal axis a weak asymmetry towards the north-northeast direction is observed, with flood velocities reaching higher peaks than ebb velocities across IJV.

The tide-driven total[2] sediment transport is presented in the right panel of Figure 5.1 as transport ellipses over the same spring tide. Compared to the presented flow ellipses, asymmetries in the transport magnitudes are much stronger. For most locations, higher transport peaks are observed in the flood direction (north-northeast). This is correlated with the asymmetry observed in the flow velocities, with amplified related to the non-linear relationship between flow velocity and sediment transport. Higher transport peaks in the ebb direction (south-southwest) are observed locally at the southwest edge of the area, outside of IJV during the neap tide.

Overall, larger transport magnitudes are observed at the southwest of the area in Figure 5.1. This is partly due to the locally steeper bed level gradients in the south west. Across IJV, some variation in the predicted sediment transport is observed, linked to the presence of sand banks traversing the area at a small angle relative to the tidal axis; sediment transport is locally increased in magnitude along the west slopes of the sand banks and decreased along the east slopes.

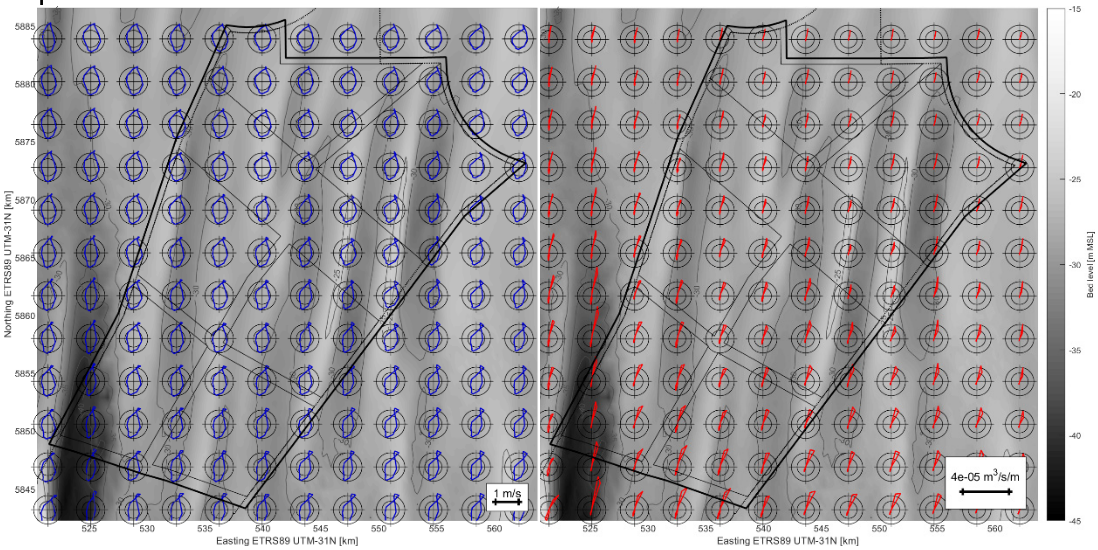

Figure 5.1: Left panel: Depth-averaged flow velocity magnitude and direction presented as tidal ellipses for one spring tide in the simulation period (1st September 2019). The scale of the velocity magnitudes is annotated in the bottom right corner. Right panel: Total sediment transport ellipses for the same spring tide. The scale of the total transport magnitude is annotated in the bottom right corner. Other lines indicate extents of the OWF Sites (black lines) and bed level contours (grey lines).

[2] The term total sediment transport refers to the sum of bed load and suspended sediment transports.

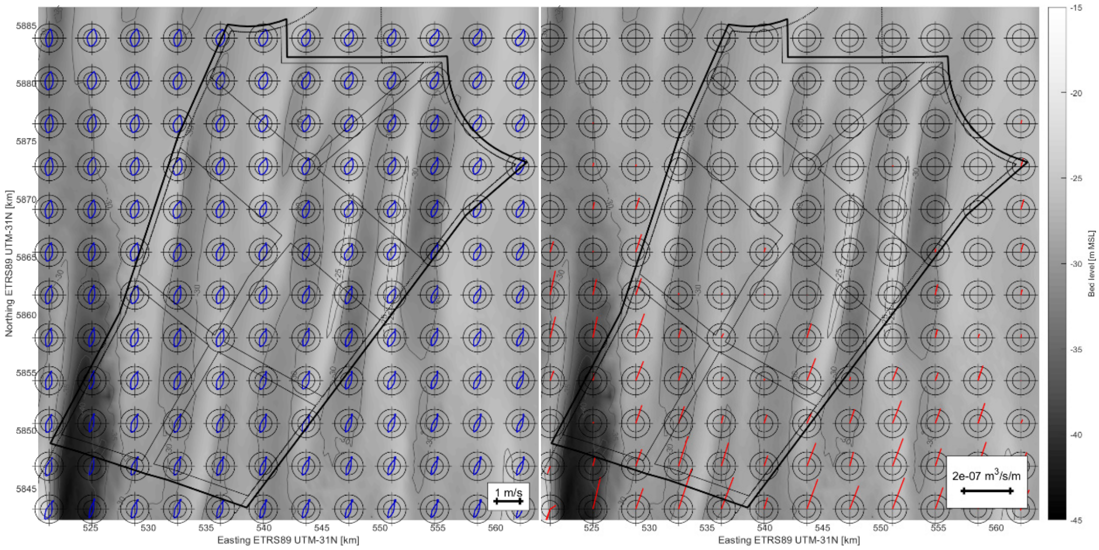

Figure 5.2: Left panel: Depth-averaged flow velocity magnitude and direction presented as tidal ellipses for one neap tide in the simulation period (25th August 2019). The scale of the velocity magnitudes is annotated in the bottom right corner. Right panel: Total sediment transport ellipses for the same neap tide. The scale of the total transport magnitude is annotated in the bottom right corner. Other lines indicate extents of the OWF Sites (black lines) and bed level contours (grey lines).

Depth-averaged tidal velocities have smaller amplitudes during the neap tide of 25th August 2019. For this arbitrary neap tide, the left panel of Figure 5.2 shows almost symmetrical flood and ebb peak velocities, a tidal axis generally directed in a north-northeast-south-southwest direction and more concentrated flood velocities (north-northeast) compared to ebb velocities (south-southwest). Sediment transport (right panel of Figure 5.2) during this period is significantly lower than observed during the spring tide. Sediment transport is higher in the south part of IJV and is generally north-northeast-directed.

5.3 Sediment transport over the representative spring-neap tidal cycle

The total sediment transport, predicted by the transport model, with tidal forcing only, are aggregated over the complete representative spring-neap cycle (about 15 days, see Appendix A.3.3.2 and Figure A.23) to obtain a map of the residual sediment transport vectors and magnitudes (Figure 5.3). The residual total sediment transport in and around IJV are mostly directed towards the north-northeast. Southeast- and south-directed transport are observed locally at the southwest corner of IJV (Site II), over the eastern steep slope of the sand bank. The presented magnitudes decrease gradually towards the north (towards Sites V-VI), with the largest total residual transport observed at the southwest part of IJV (Site II). In addition, some spatial variation in the residual transport is observed connected to the presence of sand banks/slopes in the wind farm area. Sediment transport increases with the increasing bed levels at the southwest edge of IJV as well as along the western slope of the sand banks. Transport is reduced along the east slope of the sand banks and reaches a minimum at the 'downstream' trough. In places, sediment transport is locally deflected towards the east over the sand bank crests (with the exception of the westernmost sand bank in IJV where transport is deflected towards the south after crossing the crest).

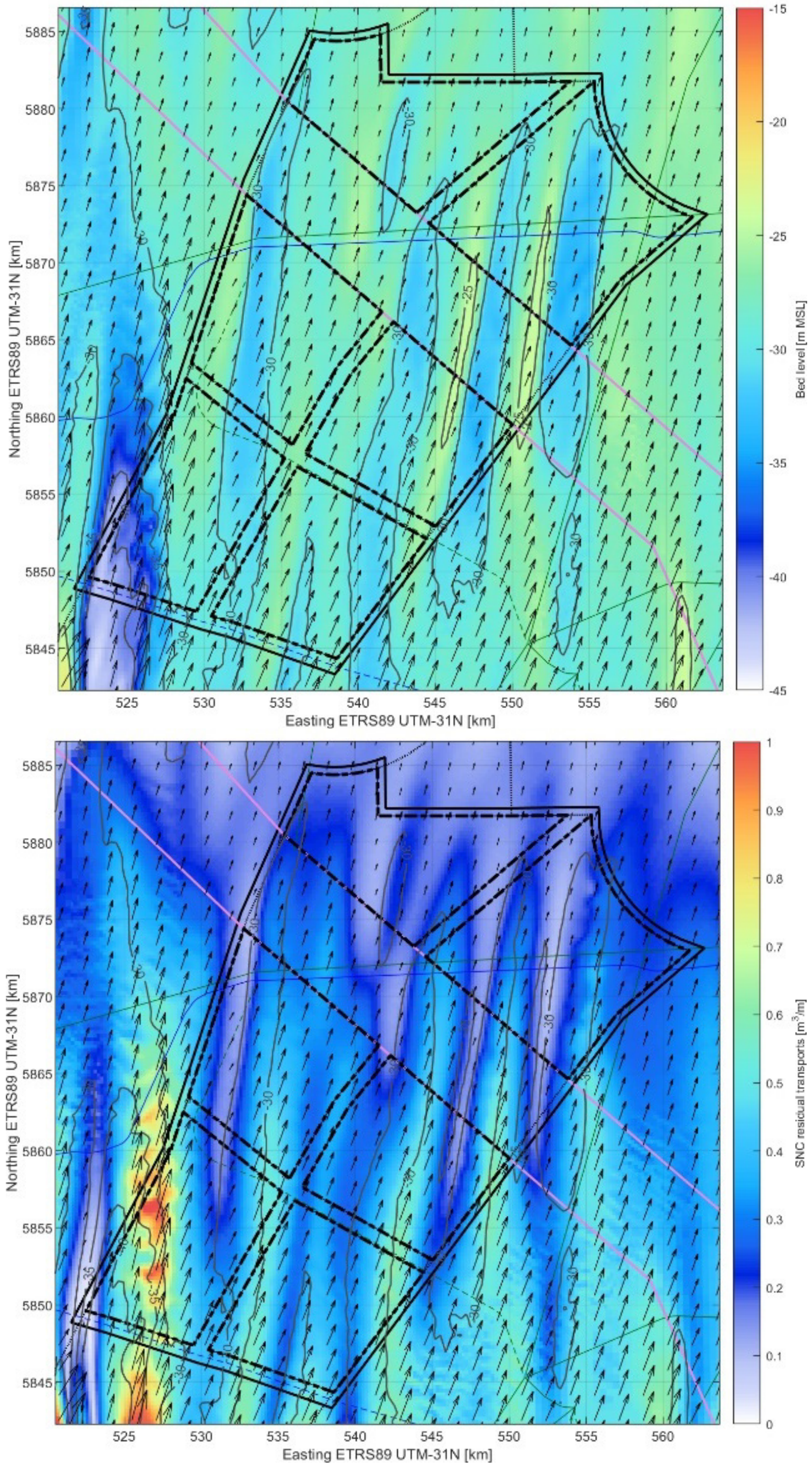

Figure 5.3: Predicted residual total sediment transport vectors for a representative spring-neap tidal cycle (27th May to 11th June 2019). The vectors are displayed over the bed levels (top panel) and over the predicted magnitudes (bottom panel) to illustrate spatial variation in sediment transport magnitudes and directions. Other lines indicate extents of the OWF Sites (black lines), navigation channel (pink lines), existing cables and pipelines (green and blue lines).

5.4 Intra-annual variability

To assess the intra-annual variability of residual total sediment transport across IJV due to the effect of meteorological conditions (wind and atmospheric pressure), maps of residual sediment transport over all 24 spring-neap tidal cycles in a single year were derived from the respective numerical model results. Figure 5.4 presents the residual sediment transport maps over two spring-neap cycles in 2019 and illustrates the effect of meteorological forcing on the residual sediment transport patterns across IJV.

The left panel in Figure 5.4 shows that for the period 1st January 2019 to 15th January 2019 southwest-directed winds reinforce the southwest directed residual tidal transports (e.g., see Figure 5.3). In contrast, for the period of 1st April 2019 to 15th April 2019 (right panel in Figure 5.4), the northwest-directed winds reinforce the residual sediment transport in the same direction as the wind across the entire area of interest.

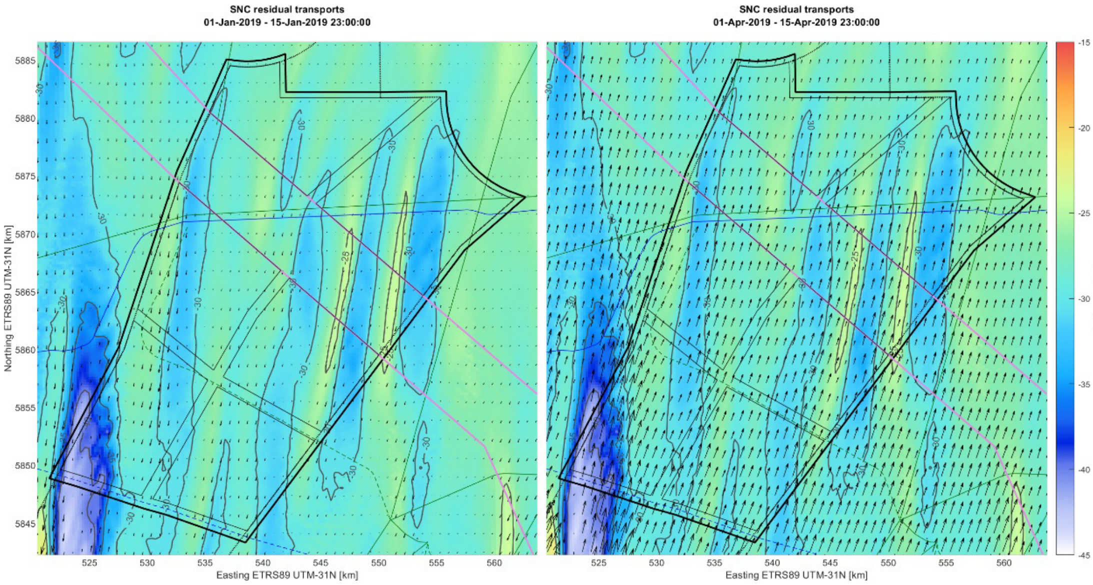

Figure 5.4: Predicted residual total sediment transport vectors for two spring-neap tidal cycles. The vectors are displayed over the bed level. Left panel: period 1st January 2019 to 15th January 2019. Right panel: 1st April 2019 to 15th April 2019. Other lines indicate extents of the OWF Sites (black lines), bathymetry contours (grey lines), navigation channel (pink lines), existing cables and pipelines (green and blue lines).

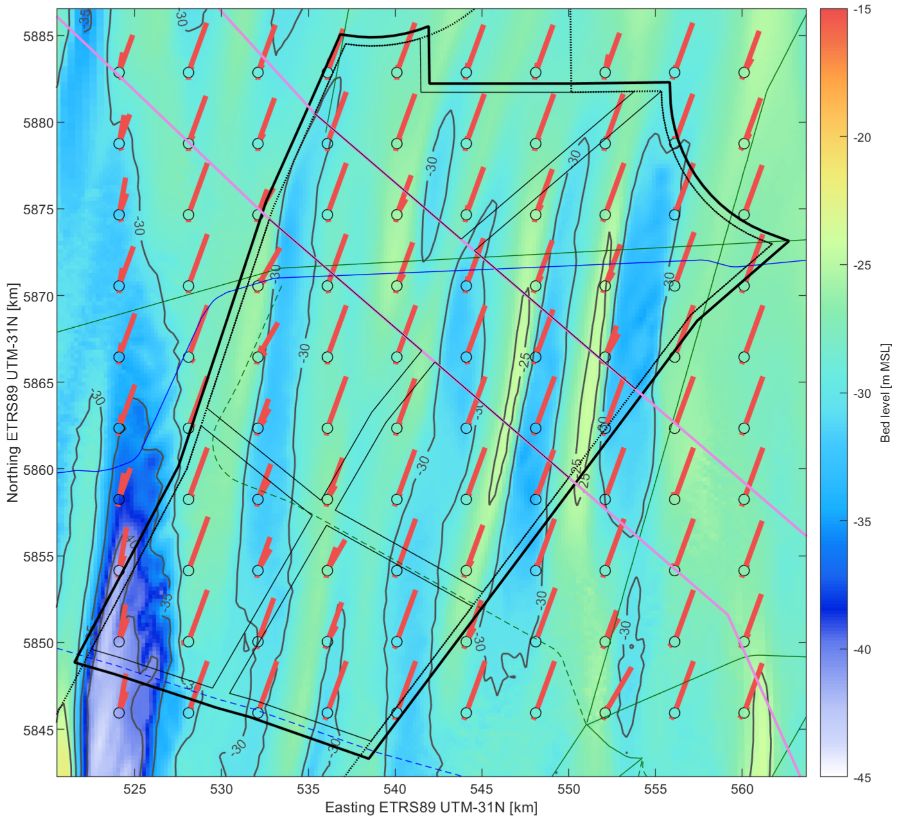

Figure 5.5: Directional roses of all the 2019 spring-neap cycle residual total sediment transport across IJV. The roses are presented over the bed level. Other lines indicate extents of the OWF Sites (black lines), bathymetry contours (grey lines), navigation channel (pink lines), existing cables and pipelines (green and blue lines).

The directional distribution of spring-neap cycle aggregated sediment transport in 2019 is shown in Figure 5.5. At each point (marked with a black circle) the residual transports are plotted directionally with a 10° bin resolution, according to the direction that sediment is transported towards. The length of the individual bars represents the frequency of occurrence of this particular direction for the spring-neap cycle residual sediment transport in 2019. Overall, the directions of residual sediment transport follow the tidal axis (as presented in Figure 5.3), with limited directional spreading. A strong directionality of the residual sediment transport towards the north-northeast is observed uniformly across IJV. Over the total area, south-southwest directed residual sediment transport is observed, with low frequency over the year, reflecting the effect of south directed strong wind events.

5.5 Interannual variability

To assess the interannual variability of sediment transport in IJV, maps of residual total sediment transport over five different years (2017-2021) were derived from the numerical model results from runs that included both tidal and meteorological forcing. Figure 5.6 presents residual total sediment transport maps over 2019. The directional distribution and spatial variation in magnitudes of the sediment transports across IJV are very similar to those presented in Section 5.3, which were calculated over the representative spring-neap tidal cycle. This illustrates that the effect of meteorological conditions on the directions of residual sediment transport is transient; meteorological forcing can deflect the tide-driven sediment transport (as seen in Figure 5.4) but the duration and frequency of such events is small compared to the continuous presence of tidal currents. The annual residual sediment transport in 2019 was driven primarily by tidal forcing.

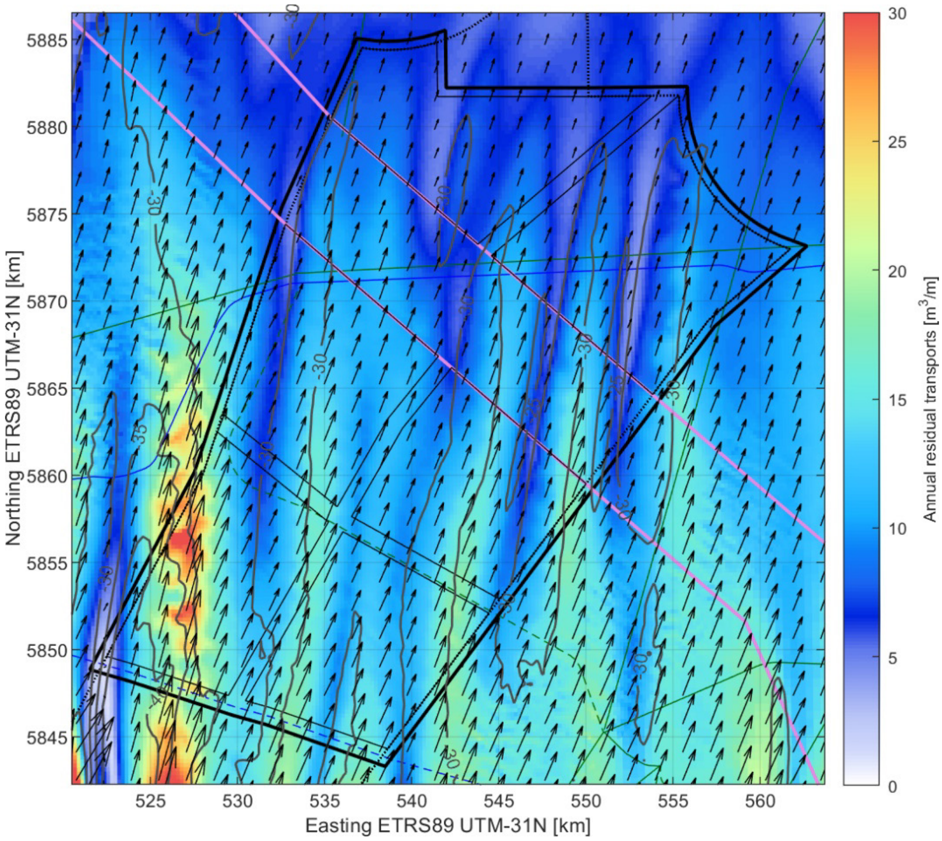

Figure 5.6: Residual total sediment transport vectors over the year 2019 including the effects of meteorological forcing. The vectors are displayed over the bed level. Other lines indicate extents of the OWF Sites (black lines), bathymetry contours (grey lines), navigation channel (pink lines), existing cables and pipelines (green and blue lines).

The respective maps of the remaining five years (2017-2018, 2020-2021) are in Appendix B. Residual transport over the four simulated years in IJV are very similar in magnitude and direction to those presented in Figure 5.6. This indicates that the long-term behaviour of the system in terms of tide and wind-driven sediment transport can be represented by the annual derived values.

5.6 Bed load and suspended sediment transport

As described in Appendix A.3.3.1, the sediment transport model simulates two different modes of transport; bed load and suspended sediment. In Section 3.3, the effect of these different modes on sand wave formation is discussed. In previous numerical studies, bed load was found to contribute to the growth of sand waves while suspended load has a dampening effect on the sand waves (i.e. suspended sediment transport is limiting sand wave growth and with increased suspended sediment transport, sand waves are lower). This dampening effect is further discussed in Borsje et al. (2014) and Van Gerwen et al. (2018). Similarly, an assumption is made that bed load transport has a larger contribution to sand wave migration compared to suspended sediment transport. Therefore, although the numerical model does not explicitly resolve sand waves, the model results are assessed separately for the two modes of transport to complement the data analysis regarding the sand wave dynamics in IJV.

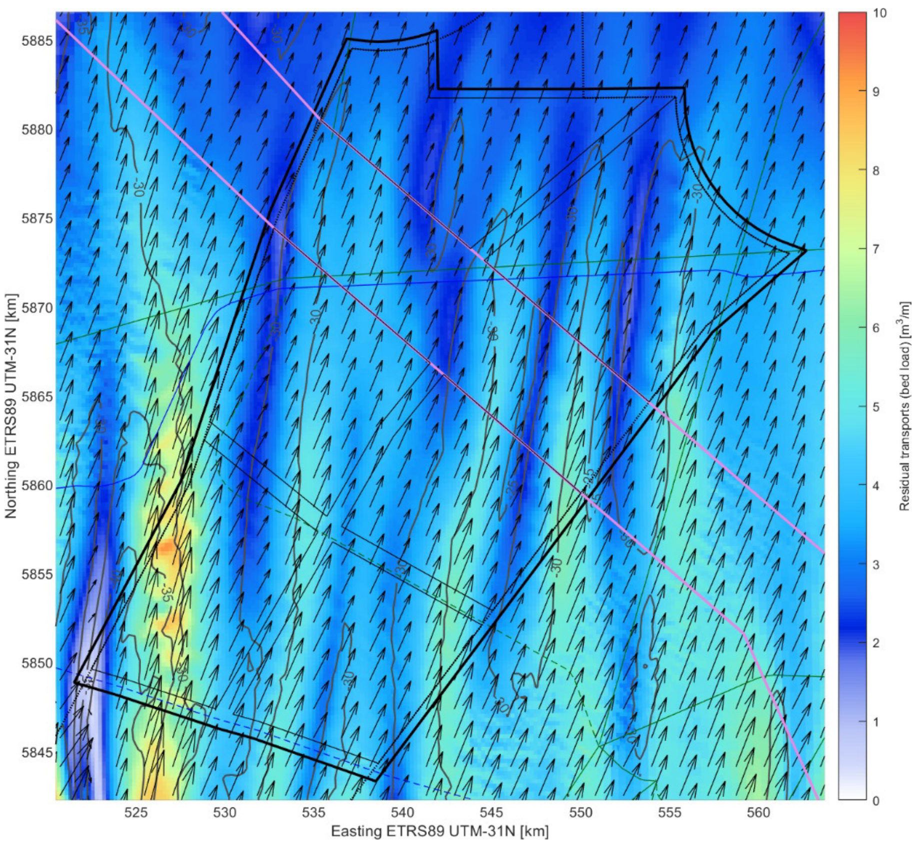

Figure 5.7: Residual bed load sediment transport vectors for the year 2019 (under tidal and meteorological forcing). The vectors are presented over the residual bed load sediment transport magnitudes. Other lines indicate extents of the OWF Sites (black lines), bathymetry contours (grey lines), navigation channel (pink lines), existing cables and pipelines (green and blue lines).

In this section, the relative contributions of bed load and suspended sediment transport to the total sediment transport is described based on the numerical modelling results presented in previous sections. The residual bed load and suspended sediment transports for the year 2019 are presented in Figure 5.7 and Figure 5.8, respectively. In general, suspended sediment consists of finer particles that are light enough to be entrained into the flow and maintained in suspension for considerable periods of time due to turbulence. In contrast, coarser particles that are heavier will be predominantly transported as bedload, by sliding, rolling and hopping along the seabed (van Rijn, 1984a, 1984b). Residual bed load sediment transport magnitudes are generally smaller (ranging from 0.5 to 10 m^3/m) while suspended residual sediment transport reaches significantly larger values (locally exceeding 25 m^3/m, at the southwest end of IJV). The directions of the two modes of transport are similar across the entire area of IJV and the overall patterns follow the patterns of total annual residual sediment transport (see Section 5.5).

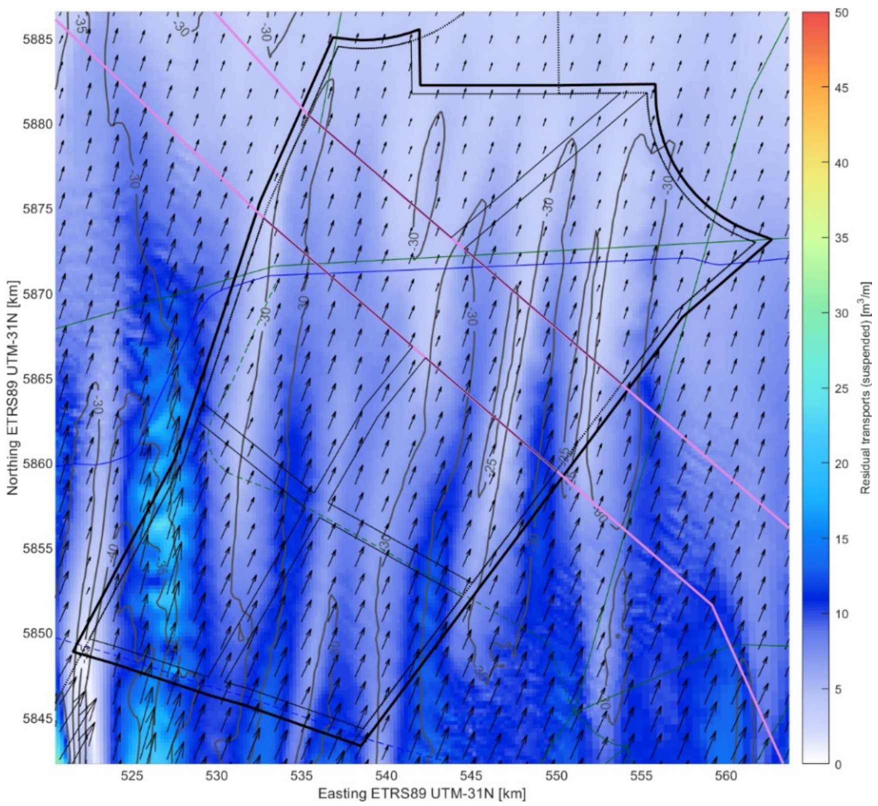

Figure 5.8: Residual suspended sediment transport vectors for the year 2019 (under tidal and meteorological forcing). The vectors are presented over the residual suspended sediment transport magnitudes. Other lines indicate extents of the OWF Sites (black lines), bathymetry contours (grey lines), navigation channel (pink lines), existing cables and pipelines (green and blue lines).

5.7 Sensitivity to sediment diameter (d_{50})

The sediment transports presented in the previous sections are predicted under the assumption of a uniform sandy top layer with a d_{50} of 250μm. In reality, lateral and vertical variability of sediment grain sizes occur in the area as discussed in Section 4.2.2. To assess the sensitivity of residual sediment transport to sediment diameter the hindcast simulation of the year 2019 was repeated two times assuming a d_{50} of 200μm and a d_{50} of 300μm. Figure 5.9 and Figure 5.10 present the predicted residual bed load and suspended sediment transports for the two d_{50} values, respectively.

Compared to bed load sediment transport, suspended residual transport is more sensitive to changes in the sediment diameter. For a d_{50} of 200μm residual suspended sediment transport reaches up to 45 m^3/m at the southwest edge of IJV, with an average value of 15 m^3/m. For the larger d_{50} value (300μm), maximum residual suspended sediment transport reduces to 20 m^3/m, while average residual suspended sediment transport reduces to 5 m^3/m. In contrast, the larger d_{50} leads to a small increase in the residual bed load transport (about 1 m^3/m). This indicates that although the total residual sediment transport decreases when an increased sediment size is considered, a larger percentage of the total transport becomes mobile as bed load rather than as suspended load.

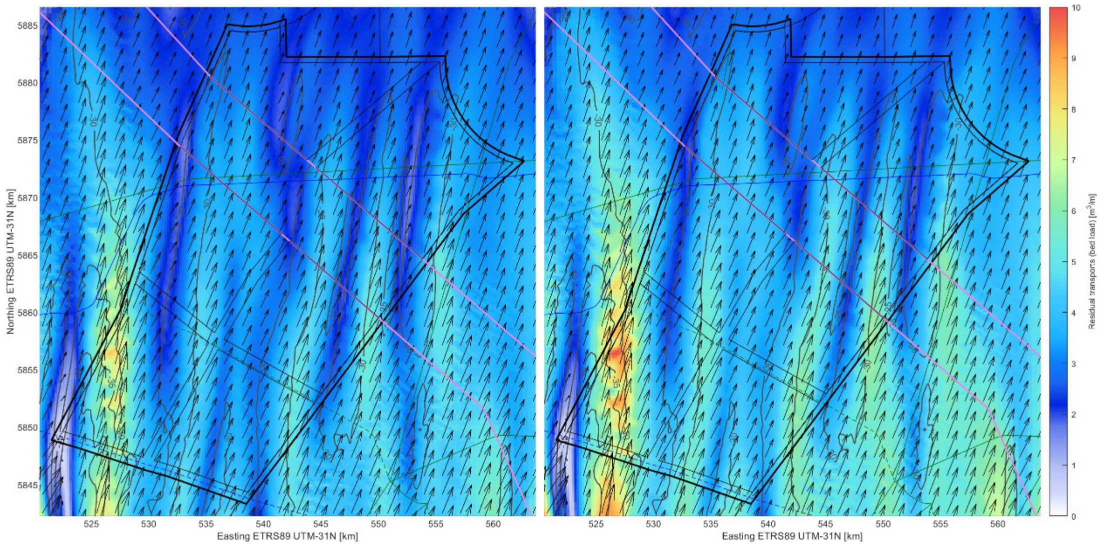

Figure 5.9: Residual bed load sediment transport vectors for the year 2019 (under tidal and meteorological forcing) for d_{50}=200µm (left panel) and d_{50}=300µm (right panel). The vectors are presented over the residual bed load sediment transport magnitudes. Other lines indicate extents of the OWF Sites (black lines), bathymetry contours (grey lines), navigation channel (pink lines), existing cables and pipelines (green and blue lines).

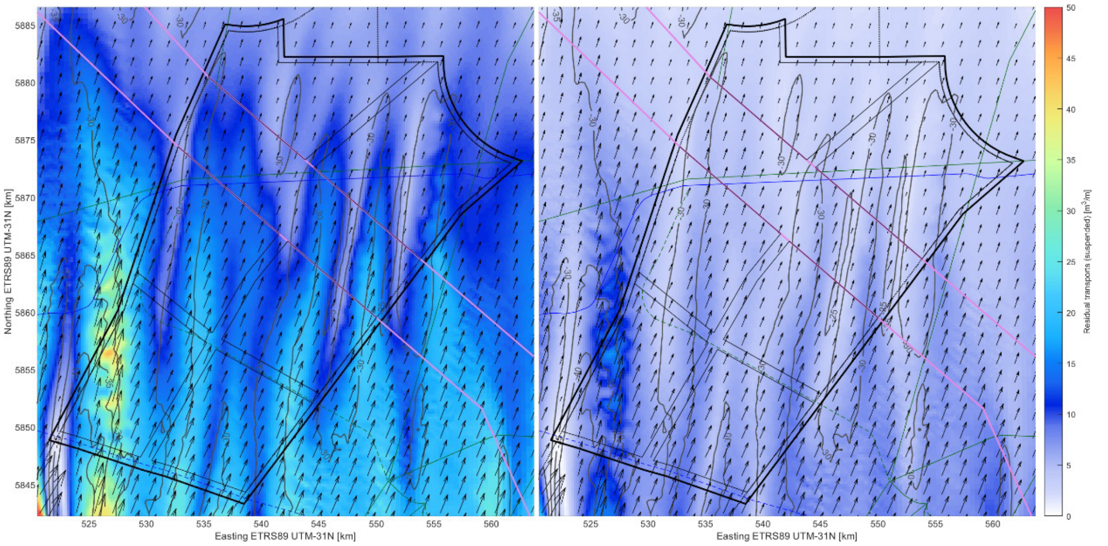

Figure 5.10: Residual suspended sediment transport vectors for the year 2019 (under tidal and meteorological forcing) for d_{50}=200µm (left panel) and d_{50}=300µm (right panel). The vectors are presented over the residual suspended sediment transport magnitudes. Other lines indicate extents of the OWF Sites (black lines), bathymetry contours (grey lines), navigation channel (pink lines), existing cables and pipelines (green and blue lines).

5.8 Impact of average wave conditions

The impact of average wave conditions on seabed mobility in IJV is evaluated using the hindcast simulation of the calendar year 2019 that includes tidal and meteorological data including wave forcing (see Appendix A.3). Figure 5.11 and Figure 5.12 present the predicted residual total and bed load sediment transport over the simulation period.

The comparison of the vectors of residual transport over 2019 between the simulations that include and exclude wave forcing (Figure 5.6 against Figure 5.12 and Figure 5.7 against Figure 5.12) show that waves have a negligible influence on the direction of the sediment transported as bed load or total transport; the results from each two simulations are similar. This is an expected outcome since typically currents are the main driver of transport of sediment and hence will dictate the transport directions. Waves predominantly influence the availability of sediment to be transported by the currents, by exerting an oscillatory shear stress on the seabed. Therefore, waves will generally influence the magnitudes of sediment transport rather than the direction. The largest increase in magnitudes is observed at the shallower areas (the peak of the sand banks).

Under the combined effect of tide, meteorological conditions and waves, sediment transports (total and bed load) are on average highest over Site II. They are simulated decreasing over the IJV IA towards the north, with the lowest values on average occurring over Sites V-VI.

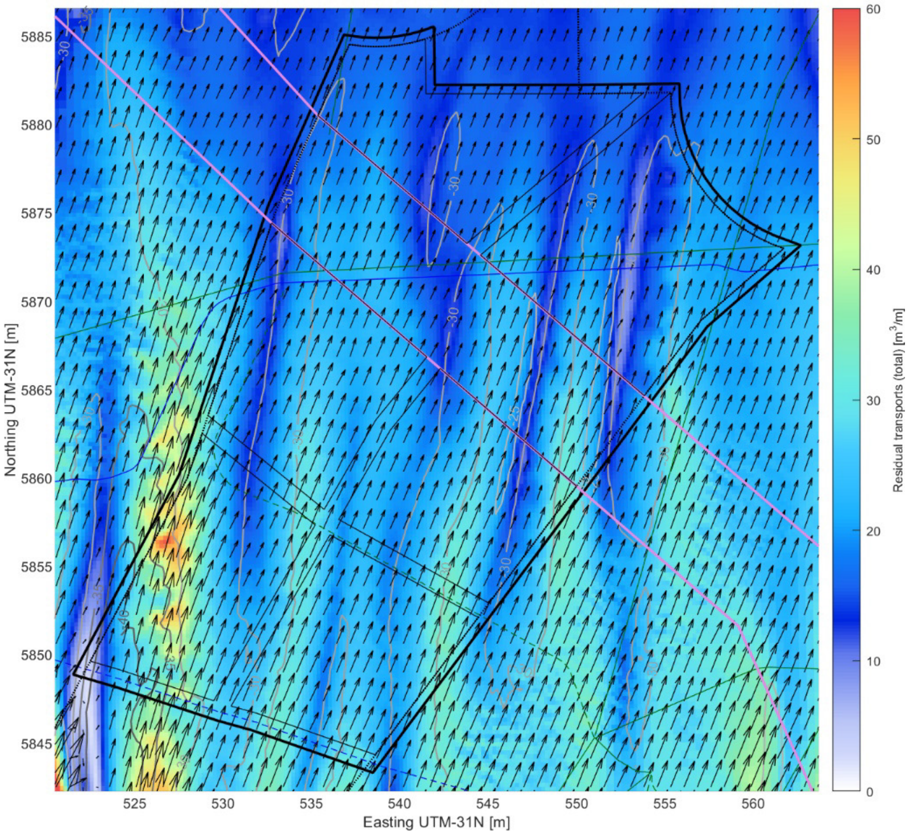

Figure 5.11:Residual total sediment transport vectors for the year 2019 (under tidal, meteorological and wave forcing). The vectors are presented over the residual total sediment transport magnitudes. Other lines indicate extents of the OWF Sites (black lines), bathymetry contours (grey lines), navigation channel (pink lines), existing cables and pipelines (green and blue lines).

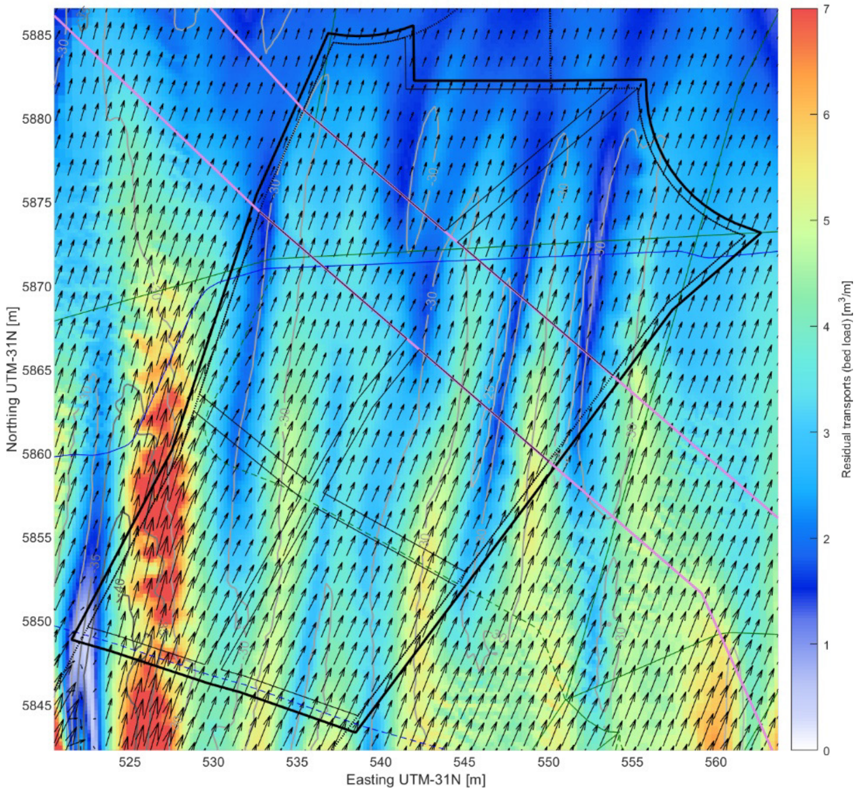

Figure 5.12:Residual bed load sediment transport vectors for the year 2019 (under tidal, meteorological and wave forcing). The vectors are presented over the residual bed load sediment transport magnitudes. Other lines indicate extents of the OWF Sites (black lines), bathymetry contours (grey lines), navigation channel (pink lines), existing cables and pipelines (green and blue lines).

5.9 Impact of extreme wave conditions

To assess the impact of extreme events on the sediment transport patterns across IJV, sediment transport output was used from the coupled flow-wave-sediment transport simulations for the synthetic RP50 and RP100 storms (see Appendix A.3.3.3 for more details on the coupled model setup and the storm synthesis). The simulated total sediment transport over the period 29th October 2006 to 4th November 2006, capturing the initial build up and ramping down of the storms, were aggregated to obtain a map of the residual total sediment transport. These were compared to the residual total sediment transport maps under tide-only forcing as well as under tidal and meteorological forcing (without waves) over the same period. Figure 5.14 and Figure 5.15 illustrate this comparison for the synthetic storms with RP50 and RP100, respectively. For reference, Figure 5.13 presents the residual total sediment transport over the storm period under tide-only forcing.

The residual total transport under tide-only forcing (Figure 5.13) are generally directed north over the area of interest. Sediment transport magnitudes are higher along the western slopes of the sand banks in the project area.

Figure 5.14 and Figure 5.15 show that the sediment transport patterns and magnitudes for the other two forcing combinations (tide and meteorological, waves tide and meteorological) are similar between the RP100 and RP50 storms. However, larger magnitudes are predicted for the most severe RP100 condition compared to the RP50 condition for the simulation including waves, especially along the western slopes of the sand banks at depths shallower than approximately –30 m MSL.

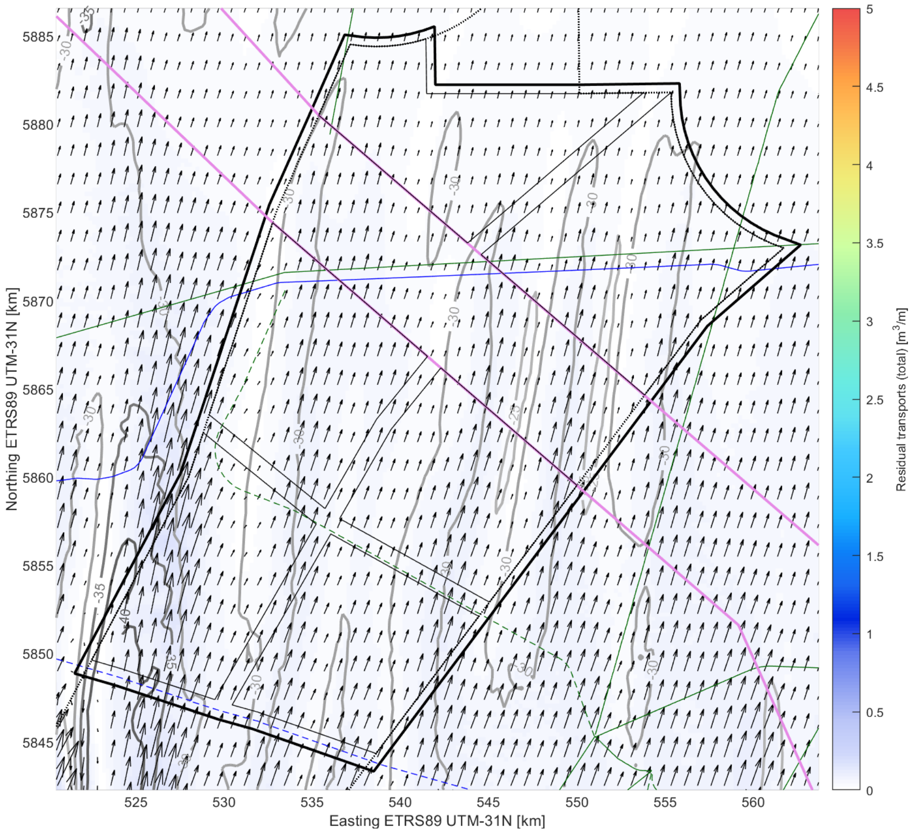

Figure 5.13:Vectors of residual total sediment transport during the storm period under tide-only conditions. The vectors are displayed over the computed residual total transport magnitudes. Other lines indicate extents of the OWF Sites (black lines), bathymetry contours (grey lines), navigation channel (pink lines), existing cables and pipelines (green and blue lines).

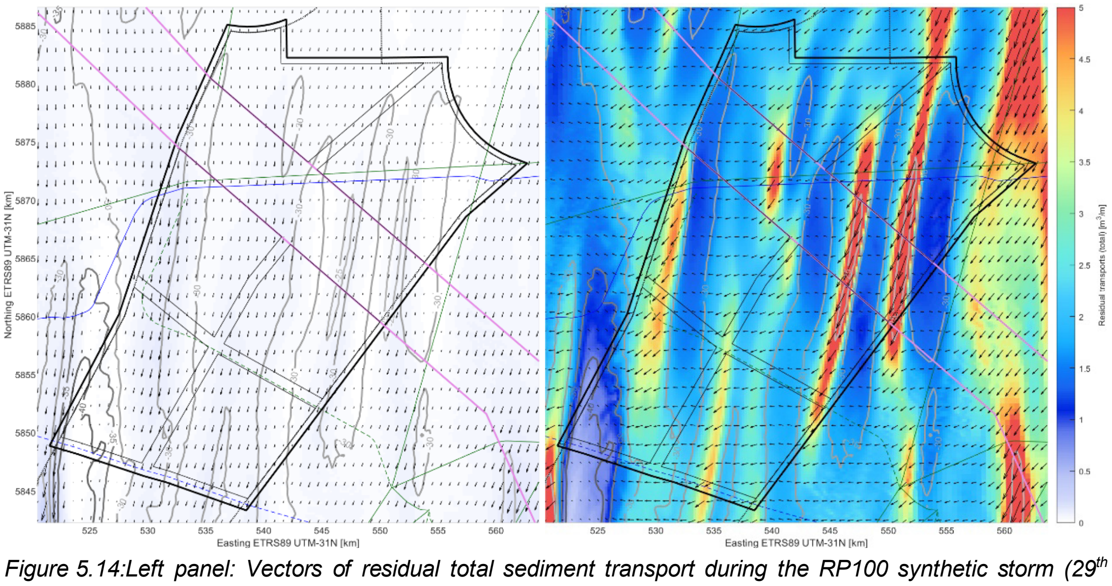

Figure 5.14:Left panel: Vectors of residual total sediment transport during the RP100 synthetic storm (29th October to 4th November 2006) under tidal and meteorological forcing. Right panel: Vectors of residual total sediment transport during the same storm under waves, tidal and meteorological forcing. The vectors are displayed over the computed residual transport magnitude. Other lines indicate extents of the OWF Sites (black lines), bathymetry contours (grey lines), navigation channel (pink lines), existing cables and pipelines (green and blue lines).

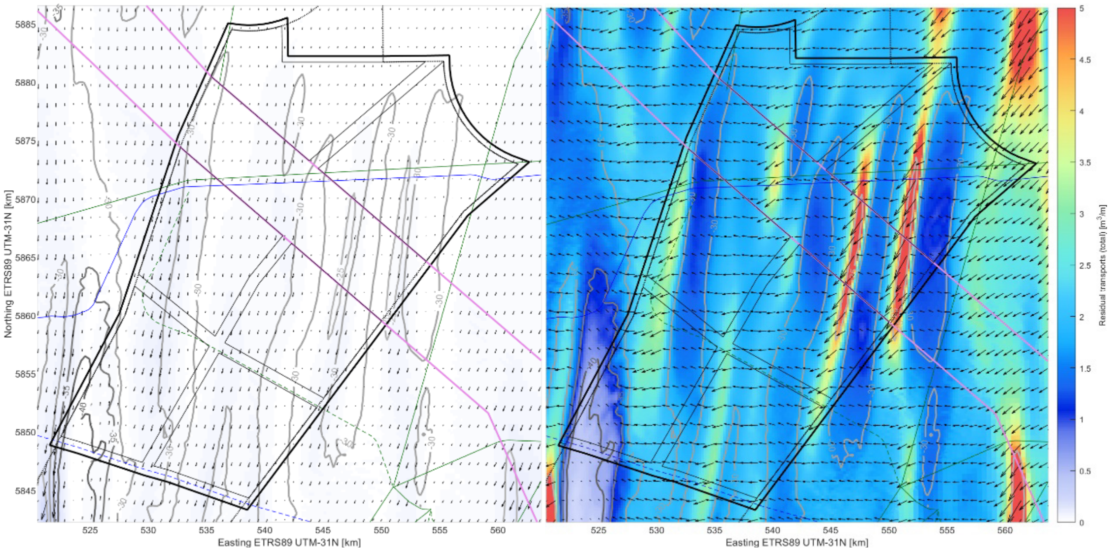

Figure 5.15:Left panel: Vectors of residual total sediment transport during the RP50 synthetic storm (29th October to 4th November 2006) under tidal and meteorological forcing. Right panel: Vectors of residual total sediment transport during the same storm under waves, tidal and meteorological forcing. The vectors are displayed over the computed residual transport magnitude. Other lines indicate extents of the OWF Sites (black lines), bathymetry contours (grey lines), navigation channel (pink lines), existing cables and pipelines (green and blue lines).

In the case of tidal and meteorological forcing, and in contrast to tide-only forcing, southwest directed winds appear to force strong wind-driven currents that, in turn, force the residual transport in the same direction (left panels in Figure 5.14 and Figure 5.15).

When waves are included in the simulations (right panels in Figure 5.14 and Figure 5.15), the residual total sediment transport increases significantly in magnitude, due to the increased sediment stirring from the bed. The increase in residual sediment transport is more pronounced along the western slopes of the sand banks, where velocities are higher, and the effect of the waves is more significant due to shallower water depths. The highest sediment transports during storm conditions are observed over Sites III and V. In addition, residual sediment transport is deflected more towards the west; an effect which is more pronounced for the areas with lower residual transport magnitudes.

Storm impact on the seabed was assessed as the cumulative change in the initial sediment layer thickness, on the bed during the period 29th October 2006 to 4th November 2006. Model results for both RP100 and RP50 synthetic storms show only local bed level differences up to 1 cm after the storm (Figure 5.16), which are small compared to the expected future bed level changes due to sand wave migration. When a smaller d_{50} (100µm instead of 250µm) is used to estimate the storm impact in areas comprised of finer grain sizes, the maximum derived bed level changes in IJV range up to 5 cm (Figure 5.17). The largest bed level decrease is expected in Sites II, III, IV and V. Some deposition is expected over the east-ascending slope in Site II, while Sites I and VI are expected to be least affected by storms.

Due to the coarse resolution of the grid, local features such as sand waves and megaripples are not represented in the modelled bathymetry schematisation. The interpreted changes in bed level due to extreme storms should therefore be interpreted as changes in the large-scale bathymetry and not changes related to sand wave characteristics. Generally, during extreme events sand wave crests may be lowered by several decimetres for the larger sand waves in shallower water as discussed in Section 3.3.8. Sand wave heights are expected to recover under normal current and wave conditions when they will return to their dynamic equilibrium dimensions and shape.

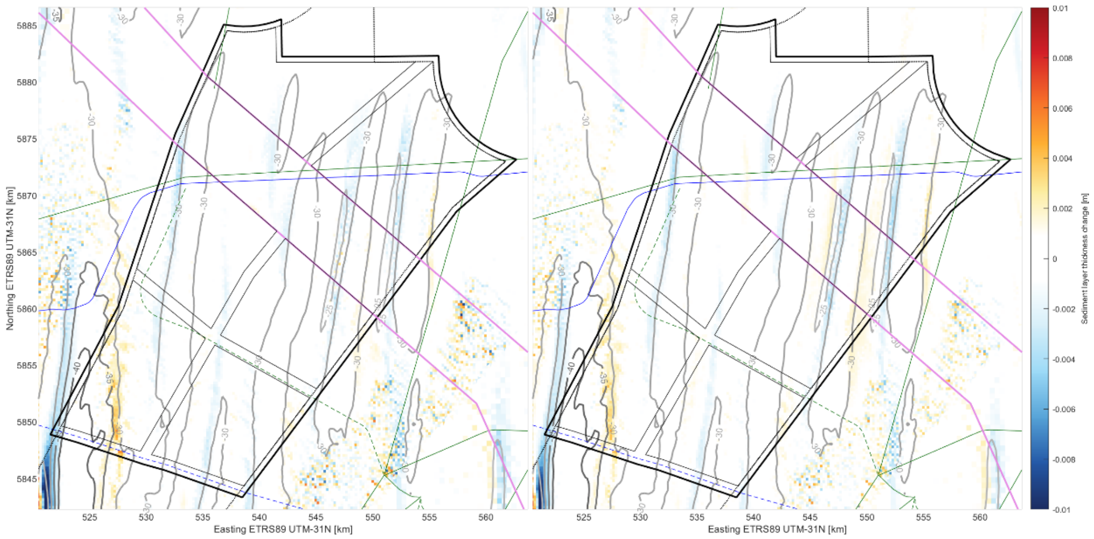

Figure 5.16:Bed level changes [m] during the synthetic RP100 storm (left panel) and RP50 storm (right panel), from 29th October-2006 to 4th November-2006. Storms are simulated using the coupled flow-wave-sediment-transport model (d_{50}=250µm). Other lines indicate extents of the OWF Sites (black lines), bathymetry contours (grey lines), navigation channel (pink lines), existing cables and pipelines (green and blue lines).

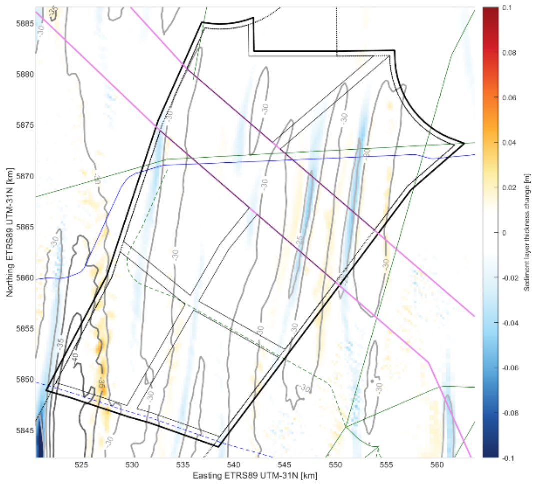

Figure 5.17:Bed level changes [m] during the synthetic RP100 storm, from 29th October-2006 to 4th November-2006 using d_{50}=100µm. Other lines indicate extents of the OWF Sites (black lines), bathymetry contours (grey lines), navigation channel (pink lines), existing cables and pipelines (green and blue lines).

6 Results assessment of future and historic seabed levels

6.1 Introduction

This chapter presents the results of the assessment of future and historic seabed levels. The chapter starts in Section 6.2 with a comparison between the results of the data-driven analysis and the numerical modelling over the IJV IA area. Validation of the extrapolation methodology is presented in Section 6.3. Extrapolated future seabed levels and corresponding classification zones are presented in Sections 6.4 and 6.5. The results are firstly presented for the entire IJV IA area, and subsequently an overview of the predicted bed level change statistics is provided per Site. The historic seabed levels are presented in Section 6.6, for the entire IJV IA and summarised per Site. Risks and possible mitigation measures related to seabed level variations are presented in Section 6.7. Finally, considerations on incorporating morphodynamics in the cable route design are provided in Section 6.8. The methodology to derive the future and historic seabed levels is discussed in Appendix A.4.

Extrapolated future and historic seabed levels are delivered in a database along with this report. These predictions will be used to support the design, installation and maintenance of the infrastructure in IJV. The full list of deliverables is presented in Appendix F.

Results in this report are presented with centimetre resolution. However, it should be noted that morphological predictions for the timescales considered in this study cannot be predicted this accurately and should always be interpreted with some uncertainty margin.

The predicted seabed level changes presented in this study follow the applied morphological analysis techniques, describing the (uncertainty of the) forecasts and the natural variability of the analysed morphological system, and the quantity and quality of available data. No additional safety margins for design purposes have been applied.

6.2 Comparison between the results of the data-driven analysis and numerical modelling

The data-driven analysis performed on the available bathymetry datasets yielded historical trends of seabed dynamics in IJV. The results are limited in temporal spread; the number of surveys available over the period between the first dataset and the final dataset is limited compared to the period over which data is available. Numerical modelling was performed to assess the long-term and intra-annual sediment transport patterns. These simulated patterns were compared to results of the data-driven analysis.

The numerical results provide insight into the governing processes and sediment transport patterns across IJV. Residual sediment transport across IJV varies in magnitude and direction under the effect of meteorological and wave conditions. However, the effect of tidal asymmetry is dominant when analysing longer periods and the annual residual sediment transport does not vary significantly in the considered five-year period. In addition, both annual residual bed load and suspended sediment transport present similar directional patterns.

Figure 6.1 presents the comparison between the spatial variation in the migration directions with the residual bed load transport variations across IJV. Across IJV sand wave migration generally aligns with the north-northeast direction of residual sediment transport. Some noise or local differences are present in the data analysis results with individual sand waves appearing to migrate east or west, which is not captured in the numerical modelling results. At the southwest of the area a number of sand waves appear to be migrating southwards based on the data. These sand waves are moving along the eastern steeper side of a sand bank. Along the same slope, the residual sediment transport appears to be deflected southeast and eventually southwards (see also Figure 5.3).

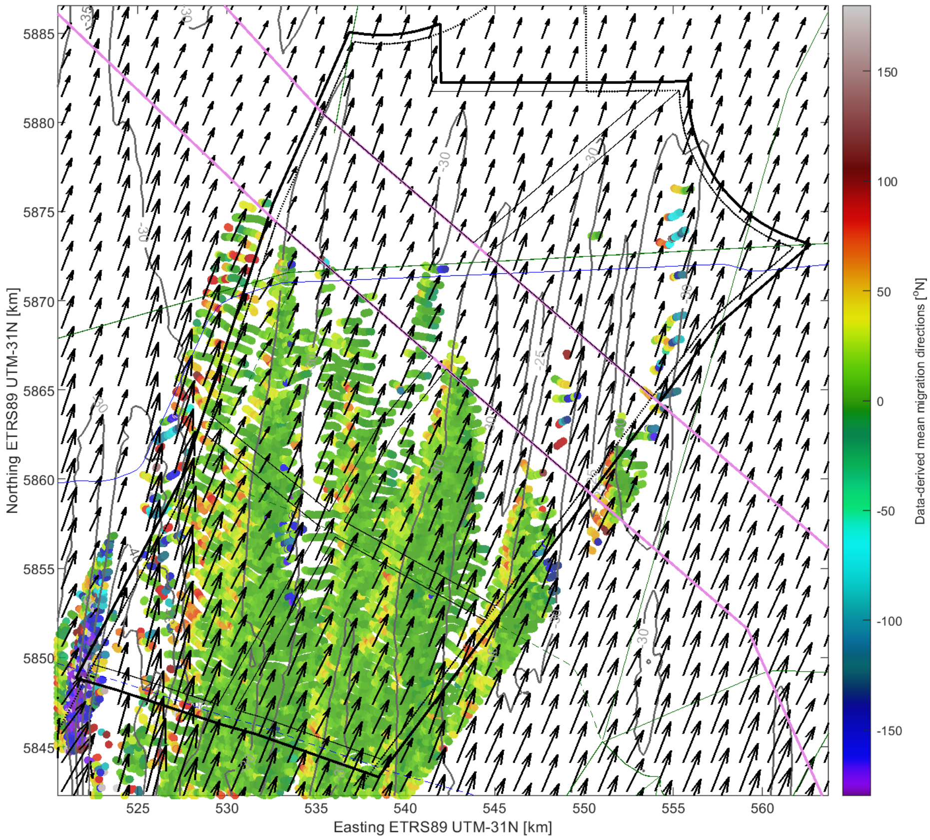

Figure 6.1: Vectors of modelled residual bed load transport over the year 2019. The vectors are displayed over data-derived mean sand wave migration directions [°N] across IJV. Other lines indicate extents of the OWF Sites (black lines), bathymetry contours (grey lines), navigation channel (pink lines), existing cables and pipelines (green and blue lines).

Figure 6.2 presents the comparison between the spatial variation in the residual bed load transport magnitude (denoted as vectors) and the data-derived migration rates across IJV (denoted as coloured dots). For the purposes of the comparison the latter are transformed to annual sand wave migrated volume taking into account the local sand wave dimensions (length and height as defined in Section 4.4.3). Based on the data-driven analysis, larger sand wave migrated volumes are observed on the western slopes of the sand banks traversing IJV, while on the eastern slopes, less volume is transported. The effect of these variations in the underlying bathymetry is also visible in the modelled residual transport, with the lowest values in sediment transport (length of vectors) observed at the eastern slope of the sand banks (reference is also made to Figure 4.17 and Figure 5.9).

Despite the good agreement of the data-derived annual transported volumes with the annual residual bed load magnitudes (Figure 5.9), the numerically modelled sediment transport magnitudes are not used to validate the data. This is because the numerical model used in this study has not been calibrated on (bed load) sediment transport measurements, while the seabed conditions (sediment supply and properties) are largely schematised. The numerical model uses a relatively coarse grid, and the sand waves and smaller bedforms are not included in the bathymetry schematisation. In addition, the proportion of bed load transport that contributes to the sand wave migration versus that being transported out of IJV is not known.

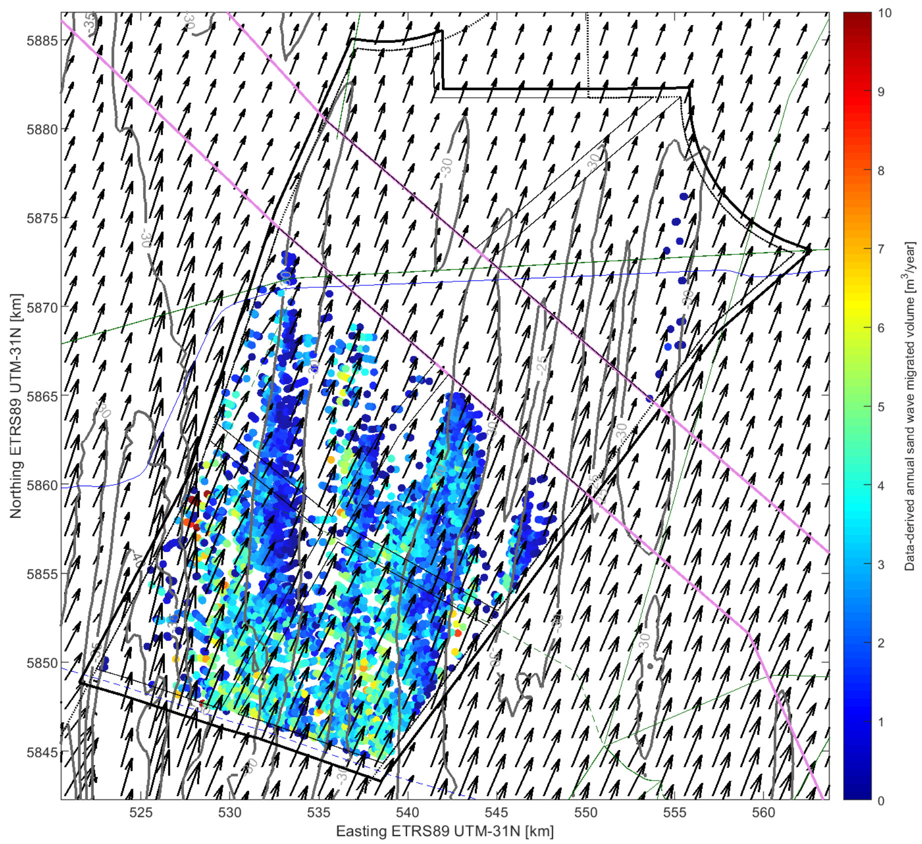

Figure 6.2: Vectors of modelled residual bed load transport over the year 2019. The vectors are displayed over data-derived mean annual sand wave migrated volumes across IJV. Other lines indicate extents of the OWF Sites (black lines), bathymetry contours (grey lines), navigation channel (pink lines), existing cables and pipelines (green and blue lines).

For the reasons above, a direct relationship between the absolute values of bed load sediment transport and the migration rates (or migrated volumes) of sand waves is not established in this study. The comparison is based on the general patterns of residual bed load transport magnitude of change, rather than the absolute values).

The comparison of the results from the data-driven approach and the numerical simulations shows that the annual residual sediment transport (mainly driven by the tidal asymmetry) accounts for the general patterns in the observed seabed dynamics. In general, it is found that the directions and magnitudes of residual sediment transport within IJV and the overall area are well aligned with the results of the data-driven analysis. In the following section, the migration directions and rates output from the data-driven analysis are used in the extrapolation of seabed levels.

6.3 Validation of extrapolation methodology

In the previous section the trends in seabed dynamics determined in Chapters 4 and 5 are validated using the numerical modelling results. To proceed with the extrapolation of the data, the methodology, which is described in Appendices A.4.4 and A.4.5 needs to be validated. The validation is done by means of the steps described in Appendix A.4.3.

In this section the 2013-2015 bathymetry is hindcasted using the 2020-2022 bathymetry as a starting point combined with the trends derived in Chapter 4. It is noted that the trends used to hindcast the 2013-2015 bathymetry were obtained by comparing historical bathymetries including the measured 2013-2015 bathymetry. Because of this, the validation is not completely independent, i.e. the validation case is already used in the calibration. However, because of the limited availability of bathymetry data, all datasets were used in determining the historical seabed trends.

The hindcasted best-estimate bathymetry for 2013-2015 is compared to the measured 2013-2015 bathymetry in Figure 6.3. Clearly visible are the red and blue patches. These patches align with the extents of the individual surveys used in the composite 2013-2015 bathymetry as shown in Appendix D.4. To exclude these differences the difference between the large-scale components of the 2020-2022 and 2013-2015 composite bathymetries is subtracted from the results presented in Figure 6.3. The corrected outcome is presented in Figure 6.4 showing much less differences than Figure 6.3. The effects at the edges and at the interfaces of individual surveys are a result of the applied filtering process to obtain the large-scale seabed component.

The Root Mean Square Error, only considering the individual Sites I-VI, is 12.8 cm when using the uncorrected comparison. This value is well below the combined TVU of the 2020-2022 (0.18-0.21 m) and the 2013-2015 (0.50 m) bathymetries. This total TVU is 0.68-0.71 m indicating that at any given location a difference between the measured 2020-2022 and the 2013-2015 bathymetry can be of this magnitude as a result of uncertainties in the measurements. The RMSE when considering the corrected bathymetry is 8.4 cm.

Chapter 4 highlighted that the majority of bedform dynamics in IJV are a result of the migration of sand waves. The dynamics over the period 2013-2022 are highlighted in Figure 4.10 showing the significant local influence of sand wave dynamics on seabed level changes. The locations of these sand waves are still present in Figure 6.4 although much less pronounced compared to Figure 4.10. The presence of the sand waves in Figure 6.4 indicates that the hindcasted 2013-2015 best-estimate bathymetry is not a perfect match with the measured 2013-2015 bathymetry. This can be explained by the following three reasons:

1. There is a difference in quality of the data, with the 2020-2022 bathymetry having a much higher resolution than the 2013-2015 bathymetry. This has consequences for the accurate representation of megaripples and sand wave slopes;
2. The historic trends are based on the period 2002-2022 and not solely 2013-2022. During the extrapolation the full period is used to combine both short and long term trends in seabed dynamics;
3. A small difference in the actual migration rate over the period 2013 to 2022 and the best-estimate migration rate as determined over the period 2002 to 2022 can lead to significant differences at the steep slopes of the sand waves. For example, with a slope of seven degrees, a difference of 0.2 m/year over the period 2013-2022 can lead to a vertical difference of 17 cm.

The comparison presented uses the hindcasted 2013-2015 best-estimate bathymetry which is, as explained in Section 6.4.1, the best approximation of a bathymetry in a given year but can differ locally. For this reason the full bandwidths in migration rates and directions and uncertainties are incorporated to capture future seabed levels. The validation of the extrapolation methodology is shown in Table 6.1. This table shows the RMSE for the comparison between the 2013-2015 lowest seabed level (LSBL), best-estimate bathymetry (BEB) and highest seabed level (HSBL) and the measured 2013-2015 bathymetry (both corrected and uncorrected). Furthermore specific percentiles in the differences are given.

A number of observations are made. First, the RMSE for the BEB is lower than the RMSE for the LSBL and HSBL hindcasted levels. Furthermore, the LSBL and HSBL including uncertainties are almost in all cases respectively below or above the measured 2013-2015 bathymetry. Finally, when considering the BEB > 99.99% of the values is within the combined

TVU of 0.68 to 0.71 m. For the corrected hindcasted 2013-2015 BEB the majority of the absolute differences with the measured bathymetry is smaller than 0.20 m.

Based on the limited differences in the validation case and the measured bathymetry fully captured between the lower and upper bounds of the hindcasted seabed levels, it is concluded that the methodology applied in this chapter can be used to extrapolate future seabed levels. It is stressed that this validation only covers a period of 7-9 years whilst the extrapolation is performed over a period of 52 years. Over time, small uncertainties can grow to values significant to impact predicted future seabed levels.

Table 6.1: Overview of the RMSE and different percentile for the comparison of the hindcasted and measured 2013-2015 bathymetries.

Hindcasted bathymetry	RMSE	0.01% [m]	1% [m]	5% [m]	50% [m]	95% [m]	99% [m]	99.99% [m]
BEB 2013-2015	0.13	-0.46	-0.22	-0.14	0.07	0.24	0.31	0.60
LSBL 2013-2015	0.16	-1.62	-0.49	-0.29	-0.07	0.10	0.17	0.31
$LSBL_{unc}$ 2013-2015	0.63	-2.23	-1.10	-0.88	-0.60	-0.31	-0.22	-0.08
HSBL 2013-2015	0.31	-0.24	-0.11	-0.03	0.20	0.49	1.18	2.64
$HSBL_{unc}$ 2013-2015	0.85	0.18	0.32	0.41	0.80	1.19	1.92	3.37

Table 6.2: Overview of the RMSE and different percentile for the comparison of the corrected hindcasted and measured 2013-2015 bathymetries.

Hindcasted bathymetry	RMSE	0.01%	1%	5%	50%	95%	99%	99.99%
BEB 2013-2015	0.08	-0.61	-0.21	-0.13	-0.00	0.13	0.20	0.52
LSBL 2013-2015	0.19	-1.72	-0.57	-0.34	-0.13	0.01	0.07	0.26
$LSBL_{unc}$ 2013-2015	0.69	-2.33	-1.18	-0.94	-0.67	-0.38	-0.32	-0.18
HSBL 2013-2015	0.25	-0.27	-0.06	-0.01	0.13	0.38	1.10	2.56
$HSBL_{unc}$ 2013-2015	0.79	0.24	0.37	0.43	0.73	1.09	1.84	3.29

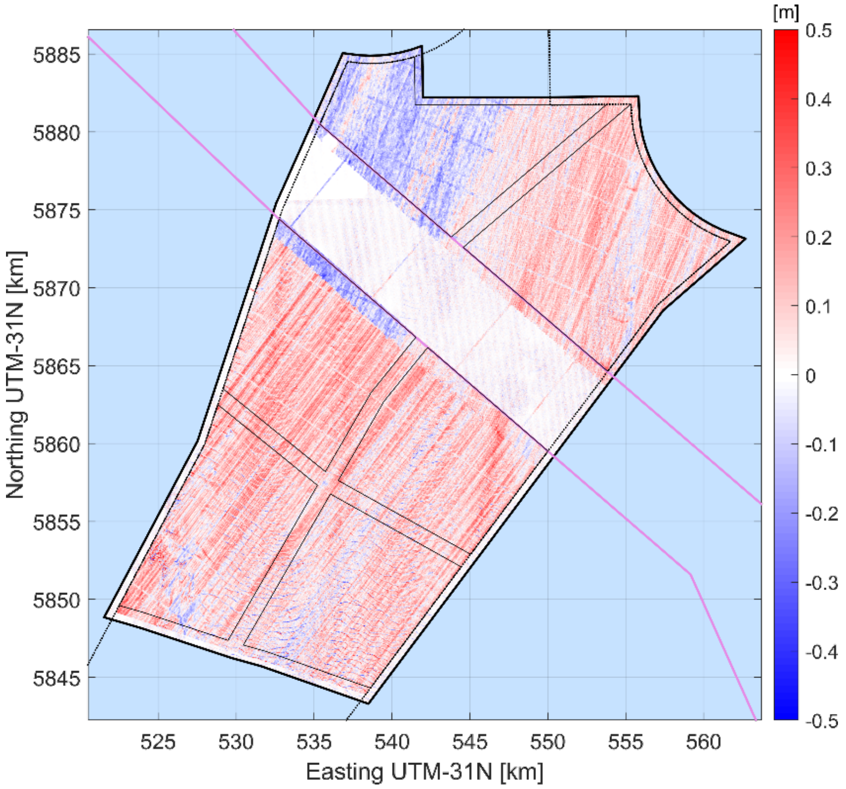

Figure 6.3: Difference between the hindcasted best-estimate bathymetry of 2013-2015 and the measured 2013-2015 bathymetry.

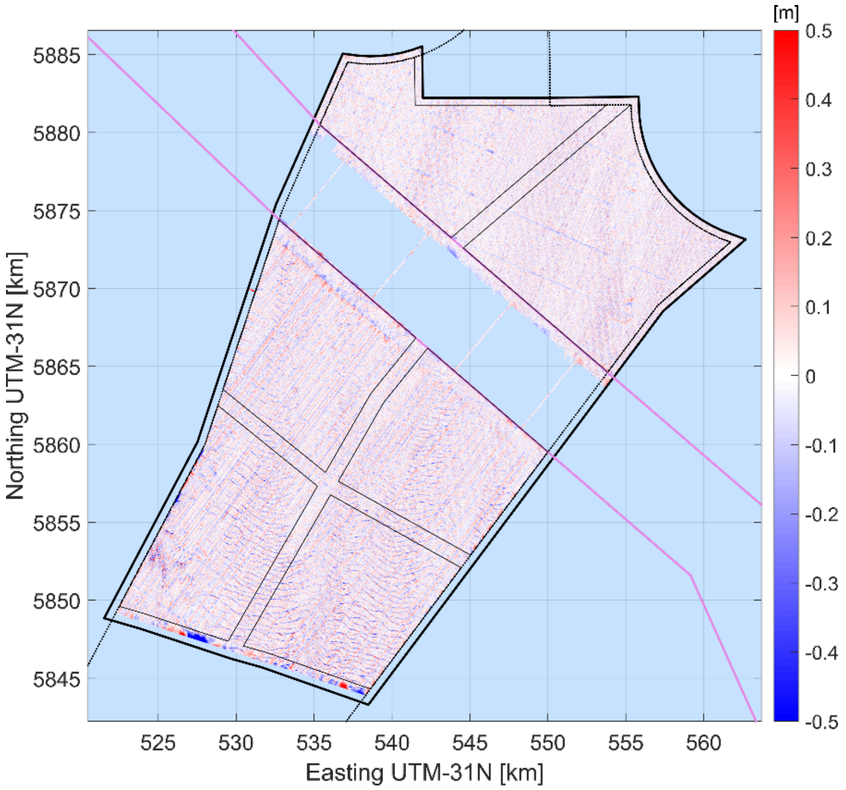

Figure 6.4: Difference between the hindcasted best-estimate bathymetry of 2013-2015 and the measured 2013-2015 bathymetry minus the difference between the 2020-2022 and the 2013-2015 large-scale bathymetries.

6.4 Future seabed levels

This section presents predictions of future seabed levels using extrapolation of the seabed trends determined in Chapters 4 and 5, and validated in Section 6.2 using the numerical modelling results, and the methodology described in Appendices A.4.4 and A.4.5.

In this section the future best-estimate bathymetry (BEB) for the year 2025 and the lowest seabed level (LSBL), highest seabed level (HSBL) and maximum slope for the period 2022 to 2072 are presented. This section is concluded with a table presenting results for the individual Sites. The provided future seabed levels comprise the following, with a more detailed overview presented in Appendix A.4.6.1:

i) BEB every 5 years over the period 2022 to 2072 (e.g. 2035);
ii) LSBL, HSBL and maximum seabed slopes every 5 years over the period 2022 to 2072 (e.g. 2035).

The basis for prediction of future seabed levels is the bathymetries captured by Fugro (2022a); GEOxyz (2021).

6.4.1 BEB in 2025

The BEB is predicted using the best estimate local migration direction and its associated local mean migration rate (see Section 4.4.2). Figure 6.5 shows a difference plot between the predicted BEB of 2025 and the measured 2020-2022 bathymetry. In the difference plot the migration of the sand wave field is manifest as local rise and lowering of the bathymetry.

The BEB should have, on average, the smallest overall error; when compared to the actual 2025 bathymetry the BEB_{2025} is expected to have the smallest area-averaged total difference. At specific locations it may differ significantly, but the observed differences are not expected to exceed the limits provided by the LSBL and HSBL given that the original assumptions for this analysis are satisfied.

The BEB only provides a very rough indication of the possible seabed development during the lifetime of the wind farm and should not be treated as a firm design parameter. For design, the LSBL and HSBL provide better information (maximum expected potential seabed level variations at each grid point). However, the BEB does provide a valuable estimate of the seabed to compute the most probable O&M costs (e.g. related to expected cable re-burial length).

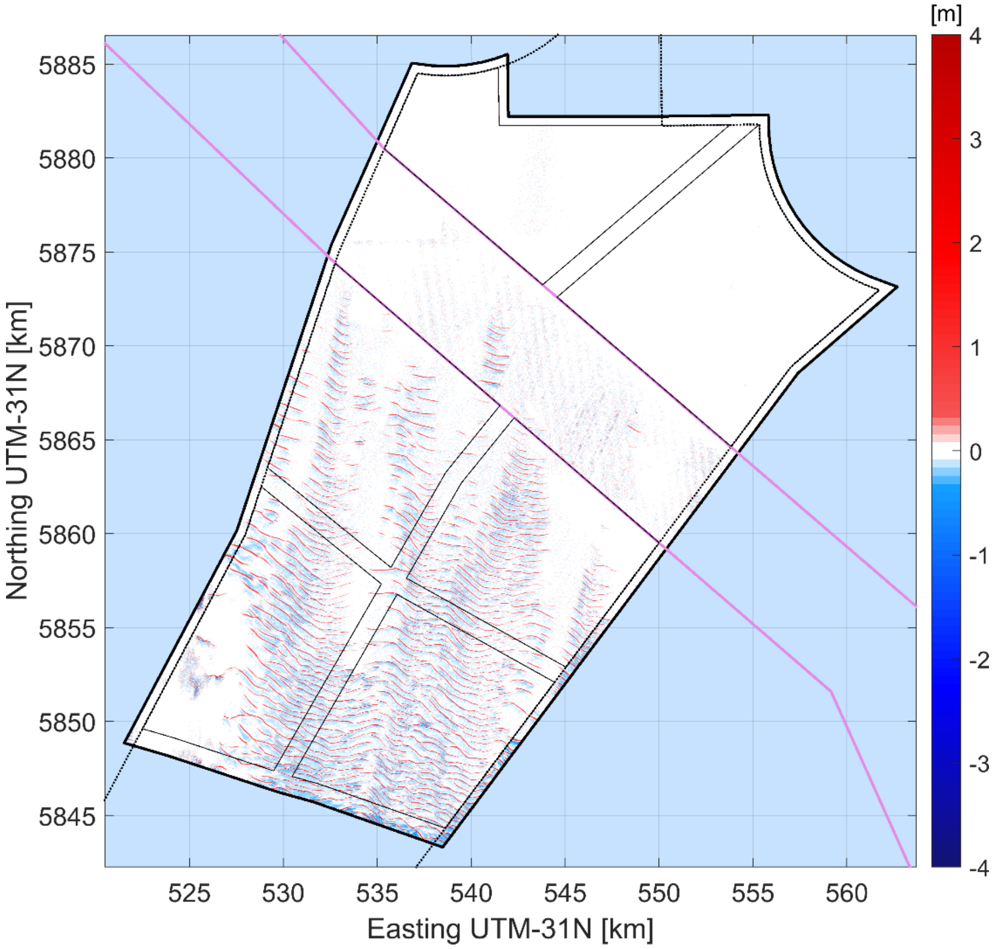

Figure 6.5: Difference between a predicted best estimate of the 2025 bathymetry and the measured 2020-2022 bathymetry. Other lines indicate extents of the OWF Sites (black lines) and the navigation channel (pink lines).

6.4.2 LSBL in 2022 to 2072

The LSBL is the estimated cumulative lower envelope of the predicted seabed levels combined with the downward uncertainty over a given period. The result for the period 2020-2022 to 2072 is presented in Figure 6.6. The overall bathymetry of the LSBL is similar to the latest bathymetry, but it is typically a few metres deeper with slightly less pronounced sand waves. The deepest parts are found in the southwest of IJV.

Calculating the difference between the LSBL and the 2020-2022 bathymetry, provides the maximum predicted seabed lowering, as shown in Figure 6.7. The current sand wave crests of the 2020-2022 bathymetry have the largest predicted lowering in seabed level of up to 3.58 m, as the 99.9%-non exceedance value for IJV Sites I-VI. The maximum predicted seabed lowering occurs in the vicinity of the highest sand waves in Sites I-II, whereas Sites V-VI describe lower predicted seabed lowering. Section 6.4.5 provides a detailed overview per Site.

The seabed close to possible scour protections and cable crossings will most likely lower more than the LSBL because of local scour and edge scour. Buried electricity cables that cause no flow disturbance will only incur this scour effect if the cables are exposed on the seabed.

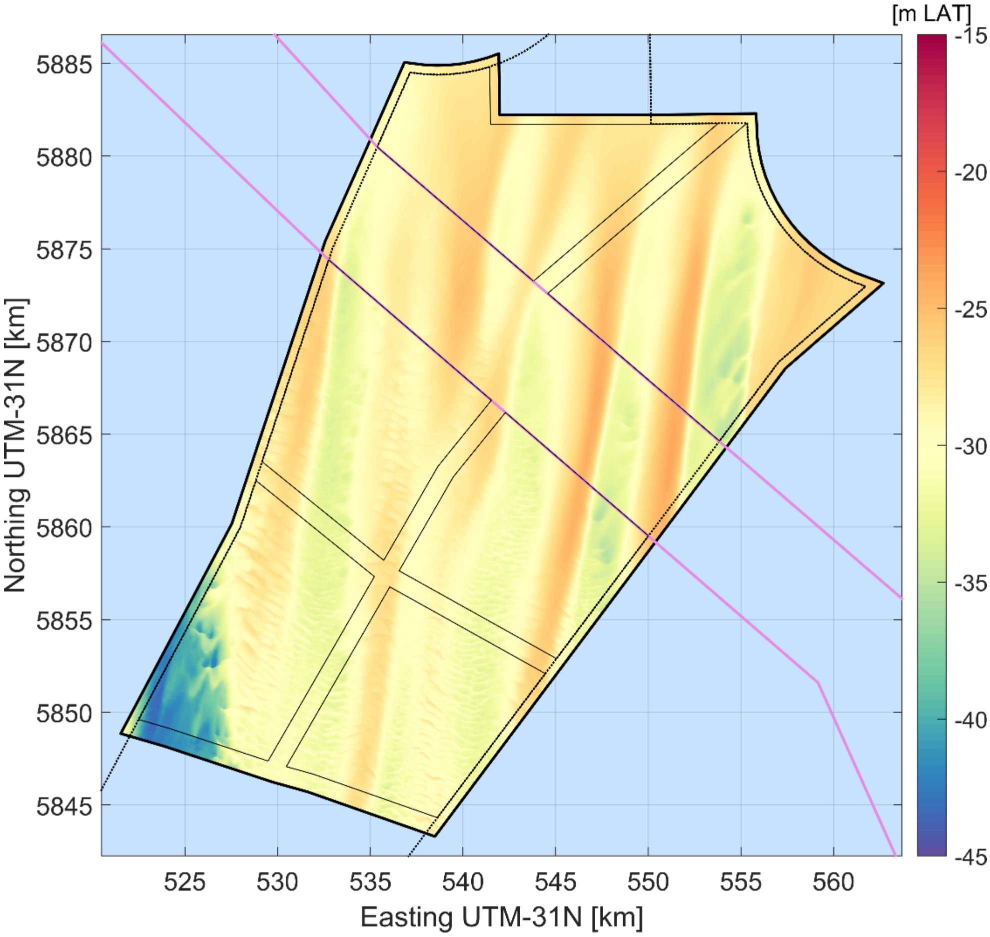

Figure 6.6: The predicted LSBL for the period 2022 to 2072. The LSBL is estimated as the lower envelope of the sand wave and megaripple variability over the period 2020 to 2072 combined with the large-scale bathymetry and the downward uncertainty. Other lines indicate extents of the OWF Sites (black lines) and the navigation channel (pink lines).

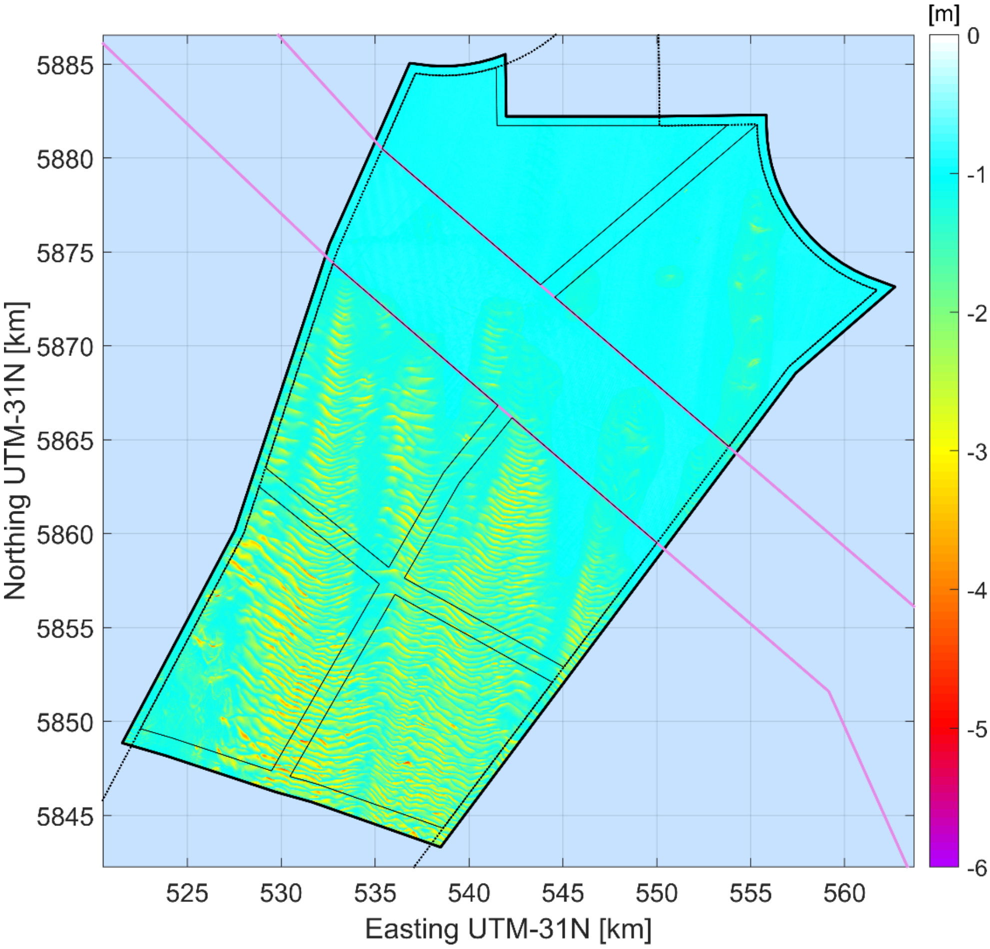

Figure 6.7: The maximum predicted seabed lowering calculated as the difference between the most recent bathymetry and the LSBL over the period 2022 to 2072 (Figure 6.6). Other lines indicate extents of the OWF Sites (black lines) and the navigation channel (pink lines).

For the downward uncertainty band, four sources are described in Appendix A.4.5 and in Sections 4.4 to 4.7. The downward uncertainty and grid resolution uncertainty for the lower envelope of seabed levels are shown in Figure 6.8 and Figure 6.9 and defined as:

i) 0.20 m (survey inaccuracy);
ii) Spatially and temporally varying;
iii) 0.20 m for the sand wave field and 0.25 m for the sand wave crest locations; and
iv) 0.10 m for the megaripple uncertainty and 0.01 (yearly) multiplied by 52 years = 0.52 m for the uncertainties in vertical seabed level trends.

The sum of the sources i, ii, iii and iv reaches a maximum of 1.07 m for the downward uncertainty over the period 2020 to 2072. Note that the contribution of the grid resolution as a result of using the 5x5 m resolution is accounted for separately in the seabed predictions (i.e. it is not part of the uncertainty band).

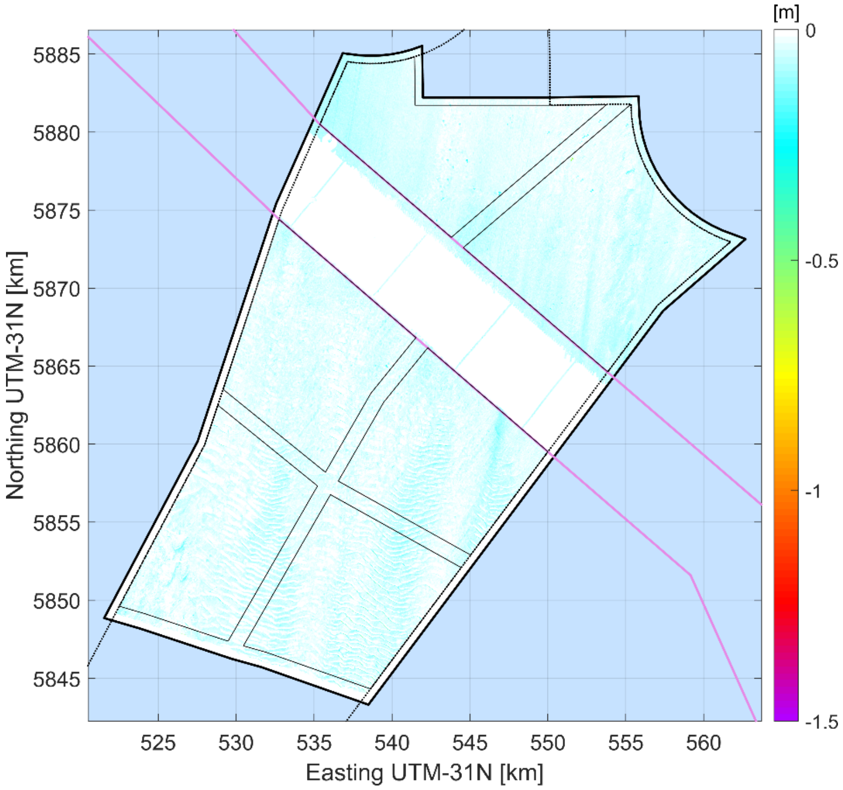

Figure 6.8: Overview of the downward uncertainty excluding the grid resolution as applied in the LSBL 2022 to 2072. Other lines indicate extents of the OWF Sites (black lines) and the navigation channel (pink lines).

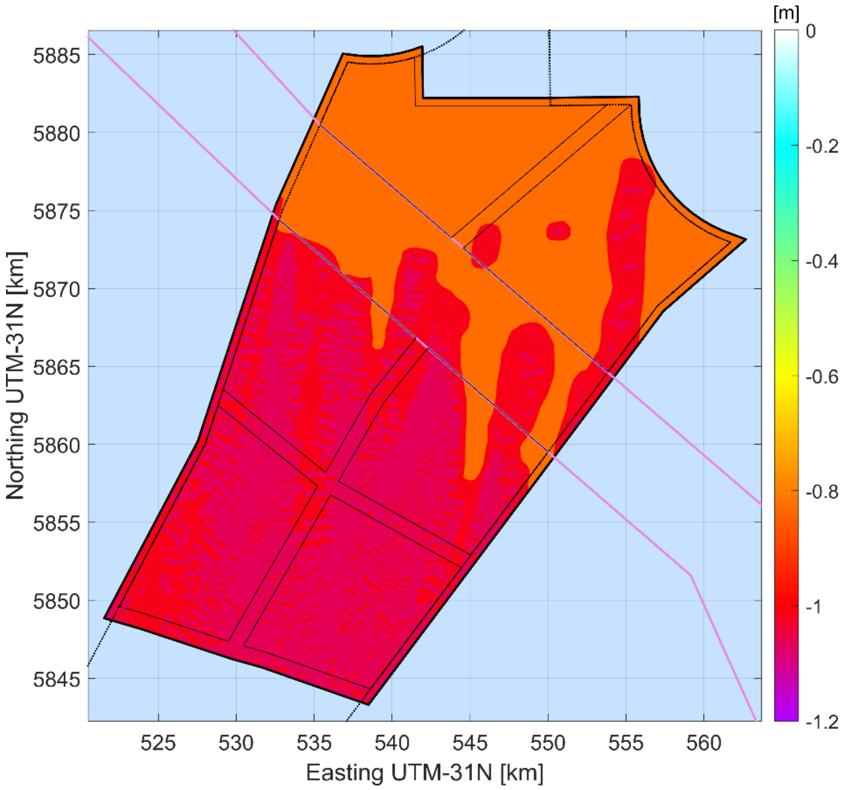

Figure 6.9: Overview of the downward grid resolution uncertainty contribution as applied in the LSBL 2022 to 2072. Other lines indicate extents of the OWF Sites (black lines) and the navigation channel (pink lines).

Finally, the LSBL is compared with the base of the Holocene formation as discussed in Section 2.3 and 4.2.2, to check whether the LSBL may penetrate it in the future. By subtracting the elevation of the base of the Holocene formation from the LSBL, the remaining layer thickness is calculated. Figure 6.10 indicates that the minimum remaining layer thickness between the LSBL and the base of the Holocene formation is, in most cases, above 0 m.

Penetration of the base Holocene occurs either locally in between the sand waves or locally in Sites V-VI. In those areas, the Holocene layer has been detected as a thin veneer (Section 2.3). Ultimately, the size and depth of this penetration is considered too small to adjust the LSBL due to the presence of non-erodible layers. It is noted that the available information from the ground model has some uncertainty at the edges (as discussed in Section 2.3). The remaining layer thickness might therefore be different when assessing location-specific geotechnical measurements.

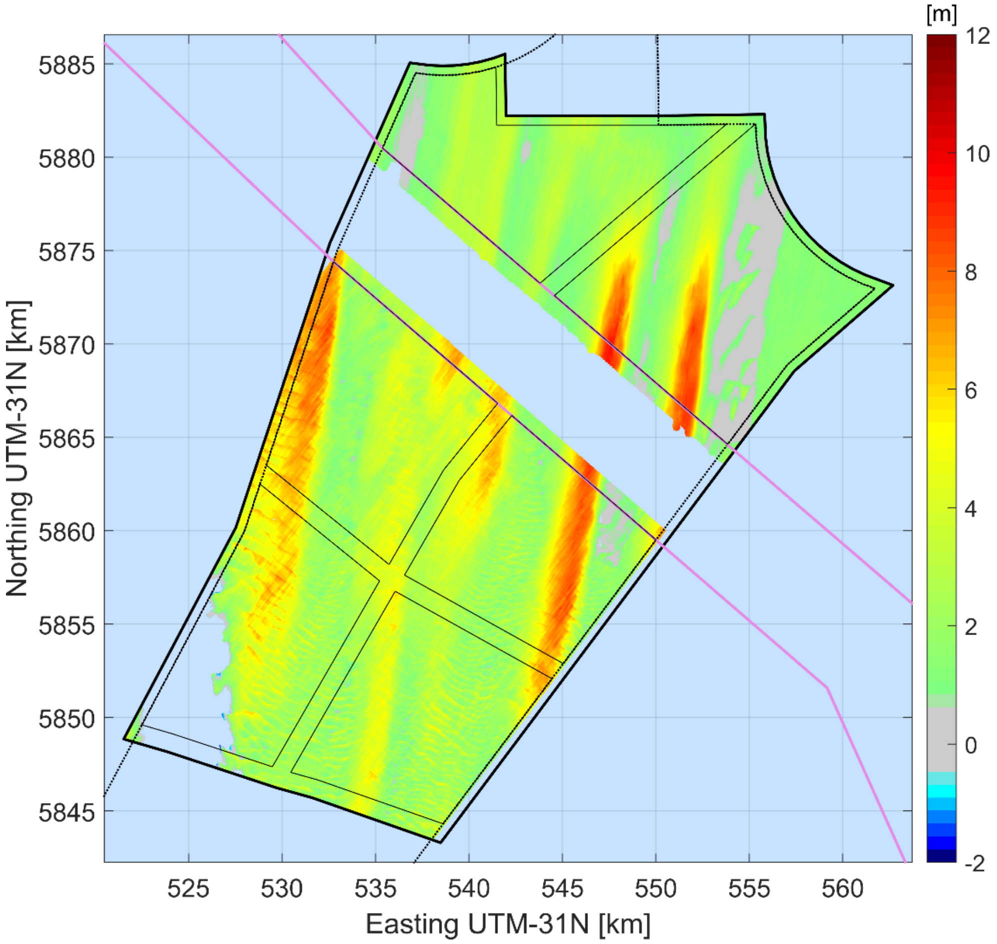

Figure 6.10:Remaining layer thickness between the LSBL and the base of the Holocene formation. The blue areas indicate zones in which no measurements of the Holocene layer are available. Other lines indicate extents of the OWF Sites (black lines) and the navigation channel (pink lines).

6.4.3 HSBL in 2022 to 2072

The HSBL is the estimated cumulative upper envelope of the predicted seabed levels combined with the upward uncertainty over a given period. The result for the period 2022 to 2072 is presented in Figure 6.11. The overall bathymetry of the HSBL is similar to the 2019 bathymetry, but it is typically a few metres shallower with more pronounced sand waves. The shallowest parts occur over the full IJV area but more specifically in the northeast.

Calculating the difference between the HSBL and the 2019 bathymetry provides the maximum predicted seabed level rise, as shown in Figure 6.12. The current sand wave troughs of the 2019 bathymetry have the largest predicted rise of up to 5.46 m, as the 99.9%-non exceedance value for IJV Sites I-VI. The largest maximum predicted seabed level rise is in the vicinity of the largest sand waves, in Sites I, II-III. The crests of the sand waves and areas with limited seabed mobility have a zero predicted rise when excluding the uncertainty band. Sites V-VI have lower predicted seabed level rise values.

The seabed close to scour protections and cable crossings will most likely not rise significantly, because local scour will counteract this. Buried electricity cables that cause no flow disturbance will not have this “beneficial” scour effect and will therefore experience a rising seabed if a sand wave crest passes over. This might be relevant for the maximum cable temperature (“thermal bottleneck effect”).

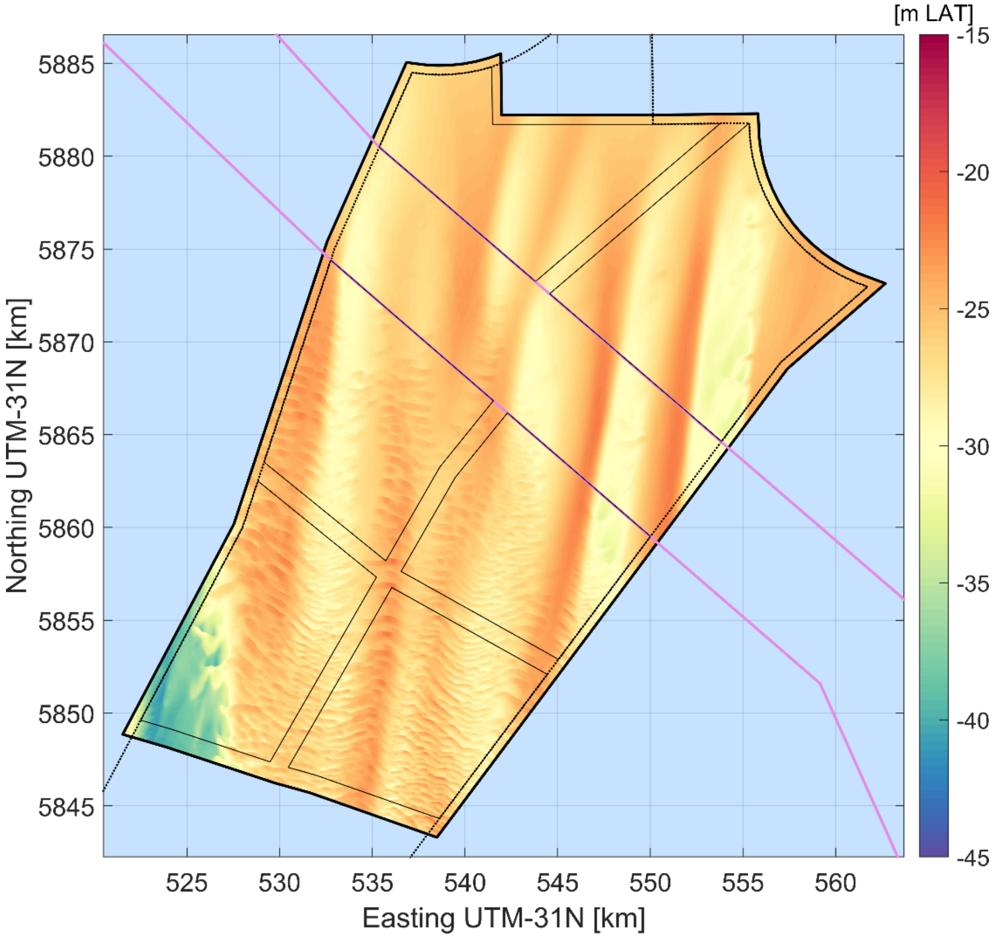

Figure 6.11:The predicted HSBL for the period 2022 to 2072. The HSBL is estimated by the upper envelope of the sand wave and megaripple variability over the period 2022 to 2072 combined with the large-scale bathymetry and the upward uncertainty. Other lines indicate extents of the OWF Sites (black lines) and the navigation channel (pink lines).

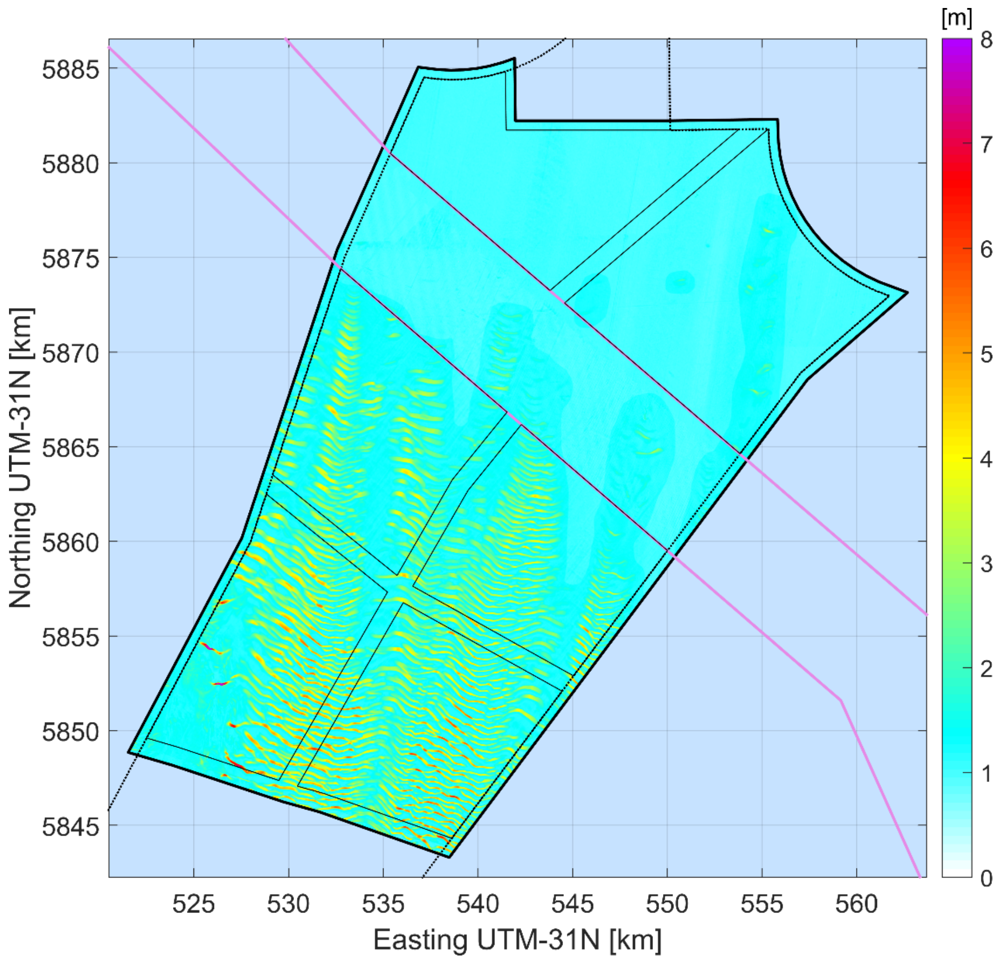

Figure 6.12:The maximum predicted seabed rise calculated as the difference between the latest bathymetry and the HSBL over the period 2022 to 2072 (Figure 6.11). Other lines indicate extents of the OWF Sites (black lines) and the navigation channel (pink lines).

For the upward uncertainty band, four sources are described in Appendix A.4.5 and in Sections 4.4 to 4.7. The upward uncertainty and grid resolution uncertainty for the upper envelope of seabed levels are shown in Figure 6.13 and Figure 6.14 and defined as:

i) 0.20 m;
ii) Spatially and temporally varying;
iii) 0.20 m for the sand wave field and 0.32 m for the sand wave crest locations; and
iv) 0.15 m for the megaripple uncertainty and 0.01 (yearly) multiplied by 52 years = 0.52 m for the uncertainties in vertical seabed level trends.

The sum of the sources i, ii, iii and iv reaches a maximum value of 1.19 m for the upward uncertainty over the period 2020 to 2072. Note that the contribution of the grid resolution as a result of using the 5x5 m resolution is accounted for separately in the seabed predictions (i.e. it is not part of the uncertainty band).

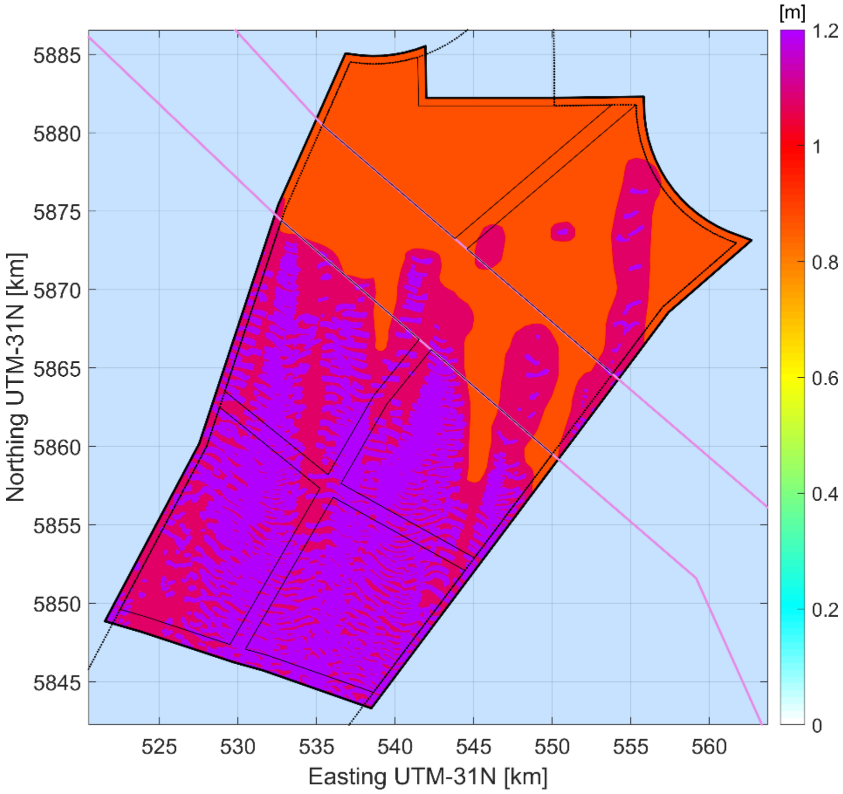

Figure 6.13: Overview of the upward uncertainty excluding the grid resolution and large-scale uncertainties as applied in the HSBL 2022 to 2072. Other lines indicate extents of the OWF Sites (black lines) and the navigation channel (pink lines).

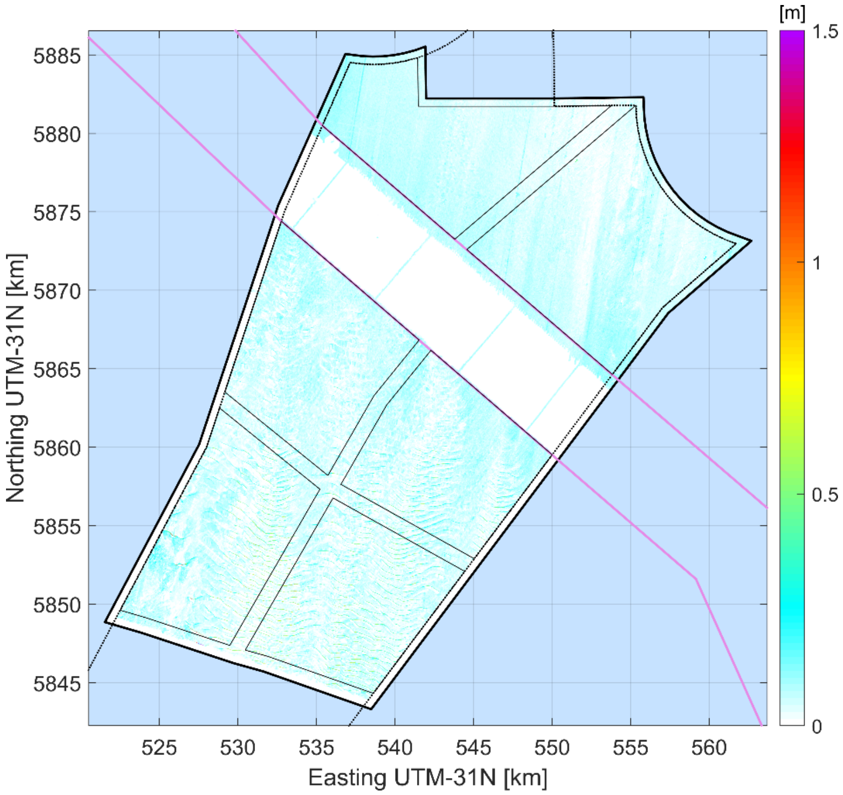

Figure 6.14: Overview of the upward grid resolution uncertainty contribution as applied in the HSBL 2022 to 2072. Other lines indicate extents of the OWF Sites (black lines) and the navigation channel (pink lines).

6.4.4 Maximum seabed slopes in 2025

Maximum slope fields for IJV were derived from the bathymetry. Slopes are derived from the large-scale bathymetry (limited slopes so not directly visible) and sand wave field; because of their scale and dynamics the megaripples are not considered. The predicted maximum slope field for the year 2025 is shown in Figure 6.15. The overall maximum slope generally varies between 0 and 3 degrees, with local maxima at the locations of the sand waves (especially in the southwest part of IJV), not including local anomalies such as shipwrecks. Larger maximum slopes occur on the steeper parts of the sand waves.

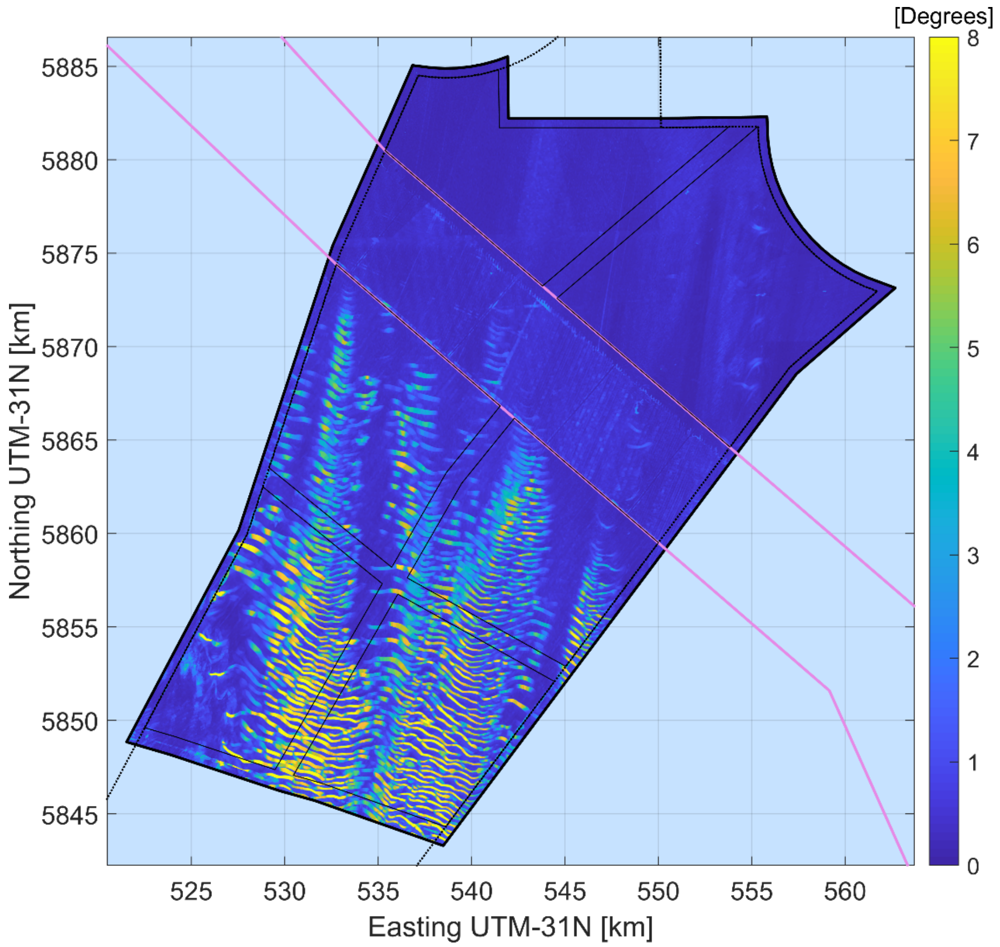

Figure 6.15:The predicted maximum slope field for the year 2025. The maximum slope field is the summation of the upper envelope of all expected slopes for the year 2025. Other lines indicate extents of the OWF Sites (black lines) and the navigation channel (pink lines).

6.4.5 Overview per Site

Table 6.3, Table 6.4, Table 6.5 and Table 6.6 present an overview of several percentiles associated with the predicted bed levels for the individual Sites as well as over the combined area (excluding the navigational corridor). The 0.1%, 1%, 5%, 50%, 95%, 99% and 99.9% non-exceedance values of the maximum predicted seabed lowering and rise including and excluding uncertainties over the period 2022-2072 are presented.

Sites I-II present the largest seabed level lowering and rise over the 2022-2072 period, both locally, as well as over the full area. This is attributed to the higher migrating sand waves present in those areas. In contrast, sand waves are limited or absent from Sites V-VI. In those areas the predicted lowering and rise are thus significantly lower. The predicted changes are mainly affected by the movement of megaripples and uncertainty bands applied.

Table 6.3: *Overview of the different percentile values associated with the maximum predicted seabed lowering (excluding uncertainties) for the period 2022-2072. The percentiles are presented for each individual Site of IJV as well as for the combined area of all Sites.*

	Maximum predicted seabed lowering 2022-2072 (excluding uncertainties)						
	$p_{99.9\%}$	$p_{99\%}$	$p_{95\%}$	$p_{50\%}$	$p_{5\%}$	$p_{1\%}$	$p_{0.1\%}$
Site I	-2.63	-2.14	-1.74	-0.69	-0.09	-0.05	-0.01
Site II	-2.78	-2.34	-1.89	-0.5	-0.09	-0.05	-0.02
Site III	-2.14	-1.76	-1.39	-0.31	-0.09	-0.05	-0.01
Site IV	-2.18	-1.78	-1.31	-0.27	-0.10	-0.07	-0.04
Site V	-0.35	-0.24	-0.19	-0.12	-0.06	-0.04	-0.03
Site VI	-0.86	-0.40	-0.25	-0.13	-0.07	-0.05	-0.03
Sites I-VI	-2.51	-1.98	-1.46	-0.2	-0.07	-0.05	-0.02

Table 6.4: *Overview of the different percentile values associated with the maximum predicted seabed lowering (including uncertainties) for the period 2022-2072. The percentiles are presented for each individual Site of IJV as well as for the combined area of all Sites.*

	Maximum predicted seabed lowering 2022-2072 (including uncertainties)						
	$p_{99.9\%}$	$p_{99\%}$	$p_{95\%}$	$p_{50\%}$	$p_{5\%}$	$p_{1\%}$	$p_{0.1\%}$
Site I	-3.70	-3.21	-2.80	-1.74	-1.15	-1.11	-1.07
Site II	-3.85	-3.40	-2.95	-1.55	-1.13	-1.09	-1.06
Site III	-3.21	-2.83	-2.46	-1.35	-0.96	-0.91	-0.88
Site IV	-3.25	-2.84	-2.36	-1.31	-1.12	-0.97	-0.90
Site V	-1.17	-1.06	-1.01	-0.94	-0.88	-0.86	-0.85
Site VI	-1.92	-1.44	-1.25	-0.97	-0.89	-0.87	-0.85
Sites I-VI	-3.58	-3.04	-2.52	-1.22	-0.90	-0.88	-0.86

Table 6.5: *Overview of the different percentile values associated with the maximum predicted seabed rise (excluding uncertainties) for the period 2022-2072. The percentiles are presented for each individual Site of IJV as well as for the combined area of all Sites.*

	Maximum predicted seabed rise 2022-2072 (excluding uncertainties)						
	$p_{99.9\%}$	$p_{99\%}$	$p_{95\%}$	$p_{50\%}$	$p_{5\%}$	$p_{1\%}$	$p_{0.1\%}$
Site I	4.64	3.82	3.00	0.27	0.06	0.04	0.02
Site II	5.82	3.70	2.86	0.33	0.07	0.04	0.02
Site III	3.23	2.48	1.87	0.23	0.08	0.05	0.03
Site IV	2.98	2.43	1.87	0.24	0.09	0.07	0.05
Site V	0.31	0.26	0.21	0.13	0.07	0.05	0.03
Site VI	1.10	0.41	0.27	0.14	0.06	0.04	0.03
Sites I-VI	4.27	3.20	2.14	0.17	0.07	0.05	0.03

Table 6.6: Overview of the different percentile values associated with the maximum predicted seabed rise (including uncertainties) for the period 2022-2072. The percentiles are presented for each individual Site of IJV as well as for the combined area of all Sites.

	Maximum predicted seabed rise 2022-2072 (including uncertainties)						
	$p_{99.9\%}$	$p_{99\%}$	$p_{95\%}$	$p_{50\%}$	$p_{5\%}$	$p_{1\%}$	$p_{0.1\%}$
Site I	5.83	5.01	4.19	1.43	1.16	1.13	1.10
Site II	7.01	4.89	4.05	1.45	1.16	1.12	1.10
Site III	4.42	3.67	3.06	1.33	1.05	1.00	0.96
Site IV	4.17	3.62	3.06	1.34	1.16	1.03	0.97
Site V	1.18	1.13	1.08	1.00	0.94	0.92	0.90
Site VI	2.23	1.55	1.33	1.02	0.94	0.92	0.90
Sites I-VI	5.46	4.39	3.33	1.25	0.96	0.93	0.91

6.5 Classification of seabed levels

In this section, the LSBL and HSBL and the corresponding estimated seabed level lowering and rise are classified into zones corresponding to certain bandwidths of changes in seabed levels. Figures are presented for the period 2020 to 2072. The classification is based on Table A.4 in Appendix .4.6 and is for illustration purposes only. The actual classification is dependent on the design of the support structures and the properties of electricity cables and should be adjusted accordingly once this information is available.

The classification zones are:

i) for a seabed lowering for the period 2020 to 2072;
ii) for a seabed rise for the period 2020 to 2072; and
iii) for a combined seabed lowering and rise for the period 2020 to 2072.

Figure 6.16 describes how the classification zones are dependent on the LSBL, HSBL and the predicted seabed level changes. These classification zones are described in Appendix A.4.7 and the caption of Figure 6.16.

The asymmetrical shape of LSBL and HSBL indicates that the sand waves will have migrated in a north-northeast direction with similar migration rates. The largest seabed level changes are found on and adjacent to the location of the sand wave crests in the 2020-2022 bathymetry.

The classification of the zones differs for seabed lowering and rise (Table A.4). This implies that for each data point, two classifications apply: one for the predicted seabed lowering and one for the predicted seabed rising. For each point, the highest absolute value is displayed in the combined map (with absolute seabed changes over 5 m being the most severe).

An overview of the classification zones for IJV is shown in Figure 6.17. A zoom plot of the area around a transect in the southeast of IJV is shown in Figure 6.18. Spatial distributions of the classification zones for seabed lowering and seabed rise are shown in Figure 6.19 and Figure 6.20. As can be seen from the figures, the majority of the areas are across the Sites are classified as Zone 2 (1-3 m of predicted change) for both lowering and rising. The highest predicted changes are related to the presence of mobile sand waves. The majority of the locations with the highest predicted lowering (>5m) are present in Sites I, II, III, and VI, while the locations with the highest predicted rise are mainly in Sites I-II. Sites V-VI are predicted less morphodynamically changing, with a higher number of locations classified as Zone 1 (0-1 m of predicted change) for both lowering and rising.

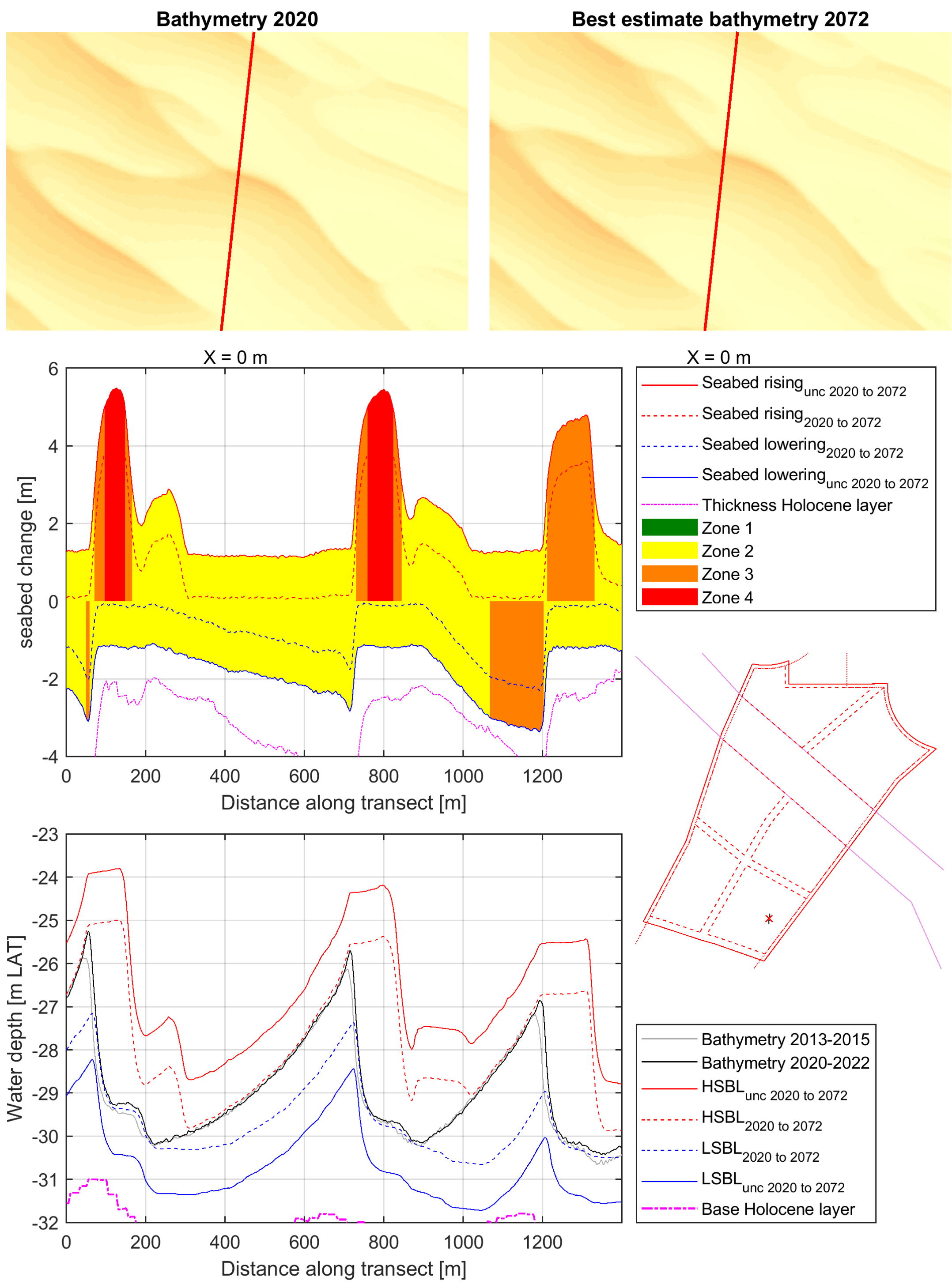

Figure 6.16:Overview of classification zones for a transect in IJV. Top plots: Zoom plot of location of transect on top of the most recent bathymetry (left) and on top of the BEB$_{2072}$ (right). Middle plot: Seabed rising and lowering relative to the 2020-2022 bathymetry (dashed red/blue lines). The maximum rising and lowering, including the uncertainty bands, are indicated by the solid red/blue lines. Middle right plot: location of transect in IJV. Bottom plot: 2020-2022 bathymetry (solid black line), together with the upper envelope of the migrated bathymetries (dashed red line), the lower envelope of the migrated bathymetries (dashed blue line), the LSBL (solid blue line) and the HSBL (solid red line). The crests and troughs of sand waves are levelled because these are already at their highest and lowest levels. The purple line indicates the base of the Holocene layer as this is often indicated as the layer with morphodynamic activity.

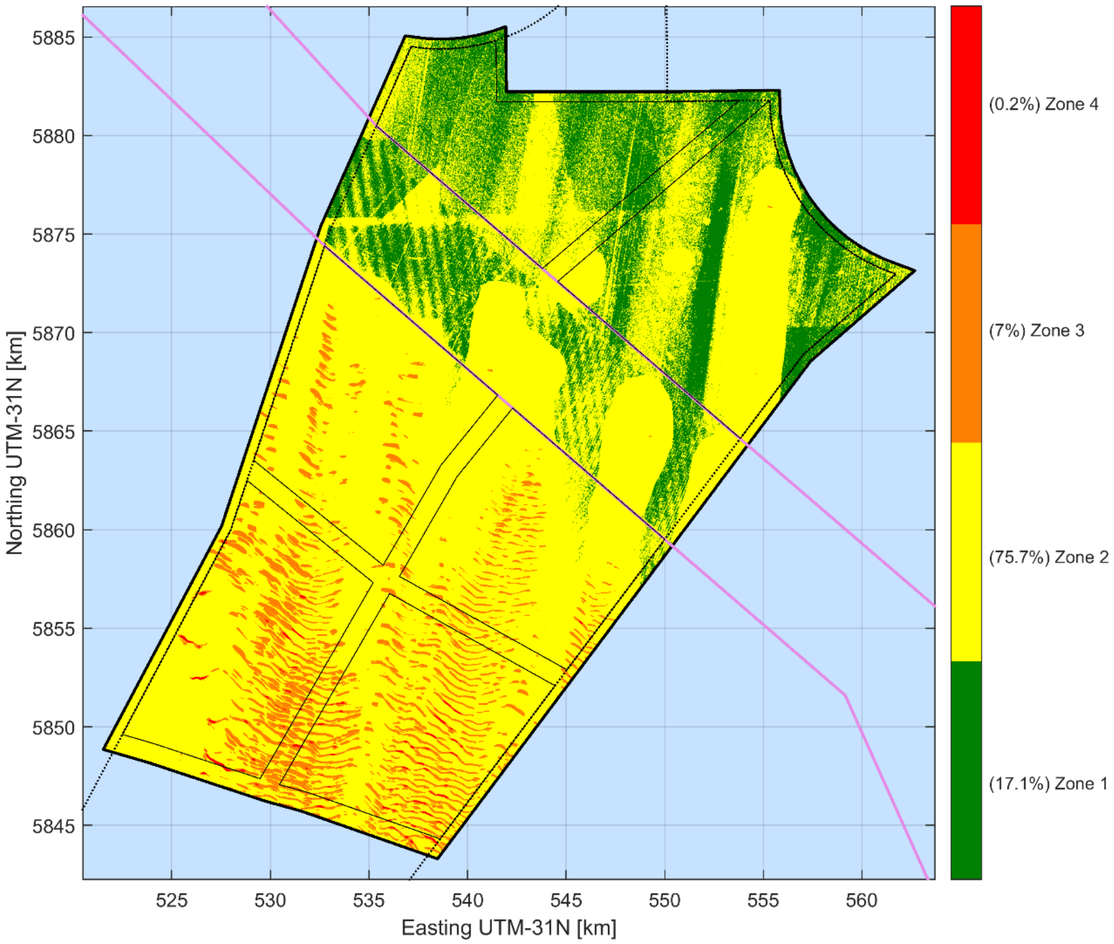

Figure 6.17:Overview map of classification zones for the combined highest and lowest seabed levels in IJV. Other lines indicate extents of the OWF Sites (black lines) and the navigation channel (pink lines).

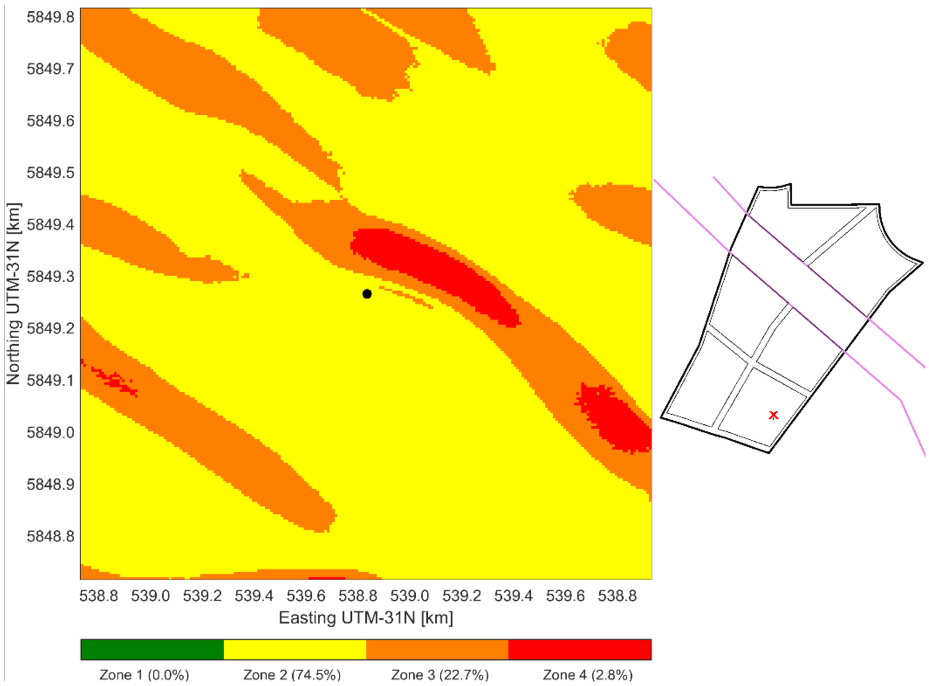

Figure 6.18:Zoom plot of classification zones for the combined highest and lowest seabed levels in the southeast of IJV.

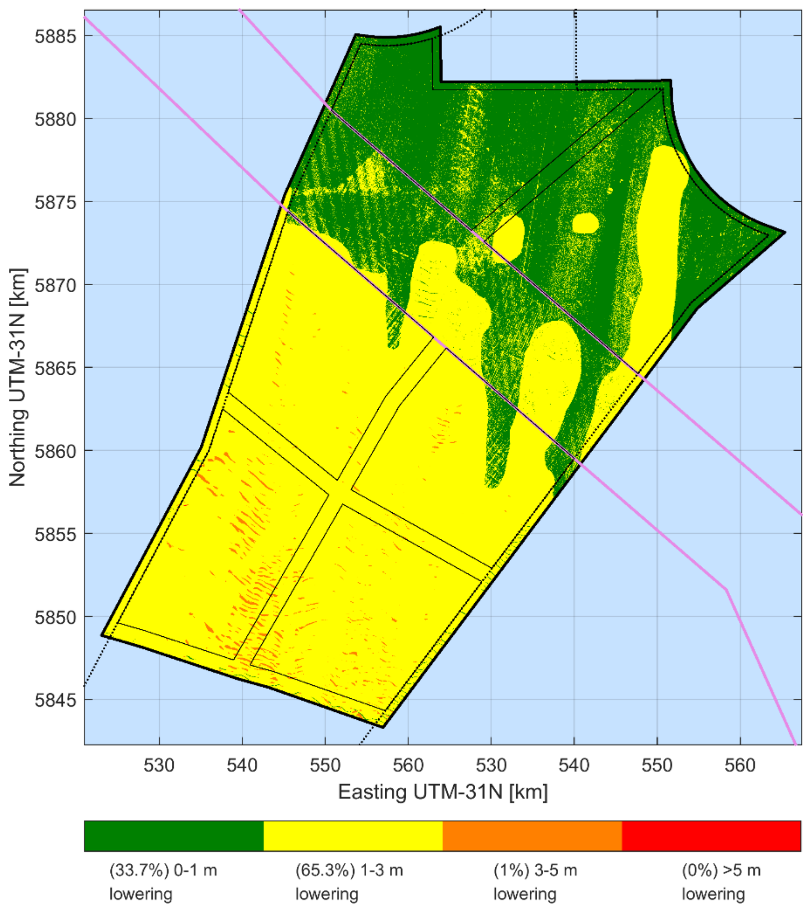

Figure 6.19:Overview of classification zones of seabed rise in IJV. Pink lines indicate the navigation channel.

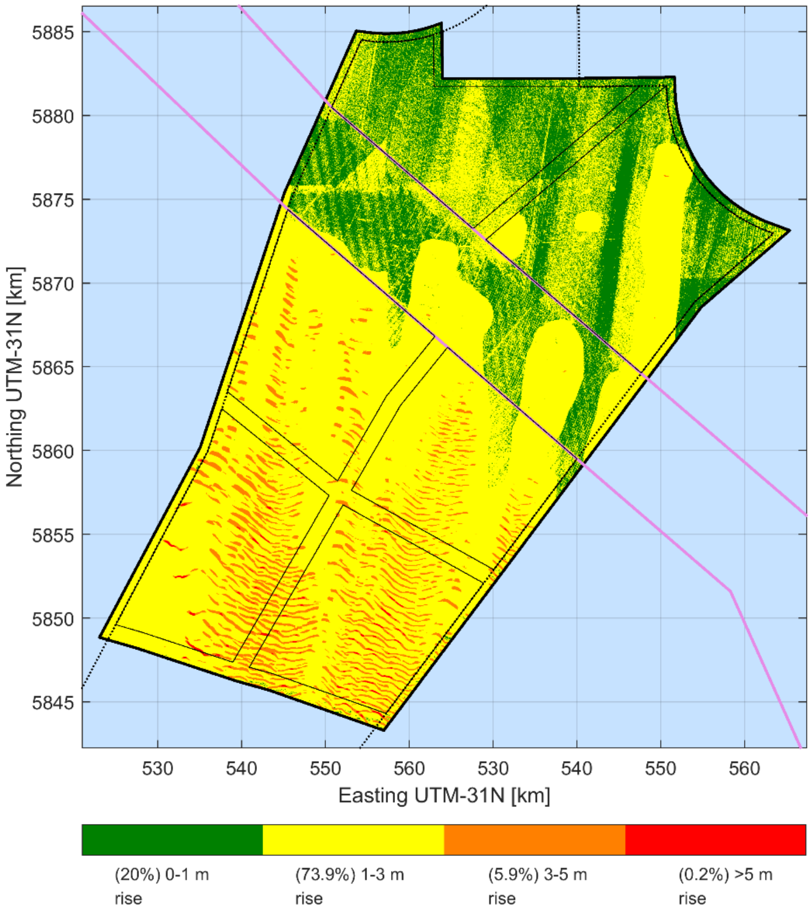

Figure 6.20:Overview of classification zones of the seabed rise in IJV. Other lines indicate extents of the OWF Sites (black lines) and the navigation channel (pink lines).

6.6 Historic seabed levels

This section presents historic seabed levels resulting from the extrapolation of seabed trends determined in Chapter 4 and 5, validated against numerical modelling in Section 6.2 and the methodology described in Appendix A.3.3.3.

They are presented to provide a prediction of the lowest seabed levels over the period since World War II relevant to the determination of possible locations of Unexploded Ordnances (UXO's). It is assumed that relatively small objects such as UXO's cause no/negligible flow disturbance themselves and will only cause local scour that can result in partial settlement of the object. These objects will not, however, affect the processes responsible for sand wave dynamics, and will experience coverage if a sand wave passes over them.

An UXO is never expected to migrate upwards and a typical UXO will self-bury to about half its height. Since this process has a faster timescale than sand wave migration, an UXO will most likely stay at the lowest seabed level it has experienced between 1945 and the present day. Quantification of the initial penetration of UXO's into the seabed is not part of the scope of this study. If significant penetration occurred during impact, then at locations that mainly experienced seabed rise the actual vertical level of the UXO's may be overestimated.

In this chapter the Best Estimate Object Level (BEOL), Lowest Object Level (LOL) and Highest Object Level (HOL) for the period 1945 to 2022 are presented, with more detail presented in Appendix A.4.6.2. The basis of the prediction of historic seabed levels is the bathymetries collected by Fugro (2022a); GEOxyz (2021). This section concludes with a table presenting the results for individual Sites within IJV.

6.6.1 LOL from 1945 to 2022

The LOL is the estimated cumulative lower envelope of the extrapolated seabed levels combined with the downward uncertainty over a given period. The result for the period 1945 to 2022 is presented in Figure 6.21. The overall bathymetry of the LOL is similar to the 2020-2022 bathymetry, but it is typically a few metres deeper with less pronounced sand waves. The deepest parts are found towards the southwest of IJV.

Calculating the difference between the LOL and the 2020-2022 bathymetry, the maximum predicted differences in seabed level are shown in Figure 6.22. The current sand wave crests are subject to the largest predicted differences in seabed level with values up to -4.72 m as the 99.9%-non exceedance value, across IJV. This indicates that since 1945 the seabed was at some point lower than the present seabed. The highest predicted seabed change is close to the highest sand waves, mainly within Sites I-II. The deepest troughs of the sand waves and areas with limited seabed dynamics have a zero predicted difference when excluding the uncertainty band. Sites V-VI are predicted to have the lowest seabed change.

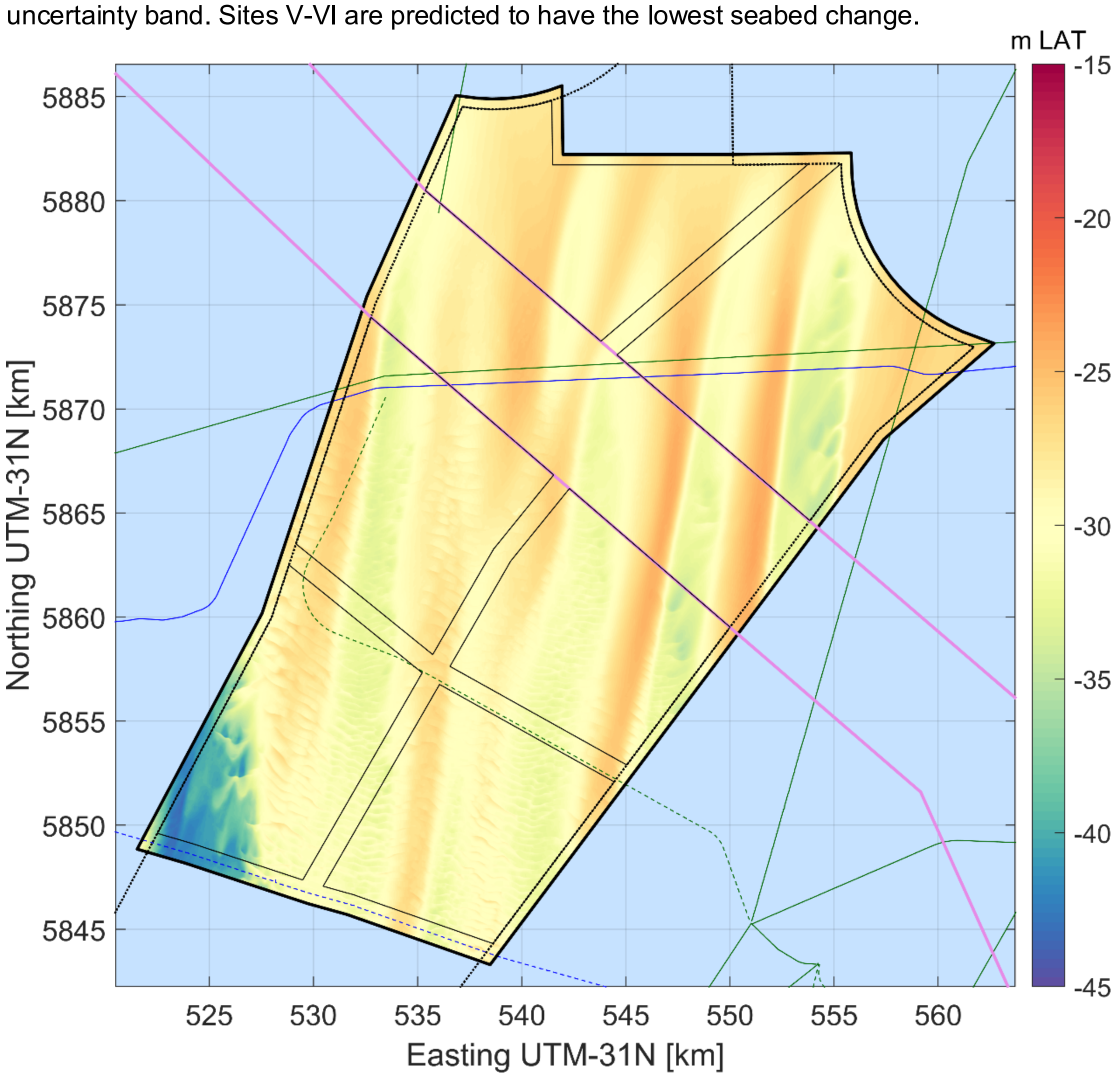

Figure 6.21:The predicted LOL for the period 1945 to 2022. The LOL is estimated by the lower envelope of the sand wave and megaripple variability over the period 1945 to 2022 combined with the large-scale bathymetry and the downward uncertainty. Other lines indicate extents of the OWF Sites (black lines) and the navigation channel (pink lines).

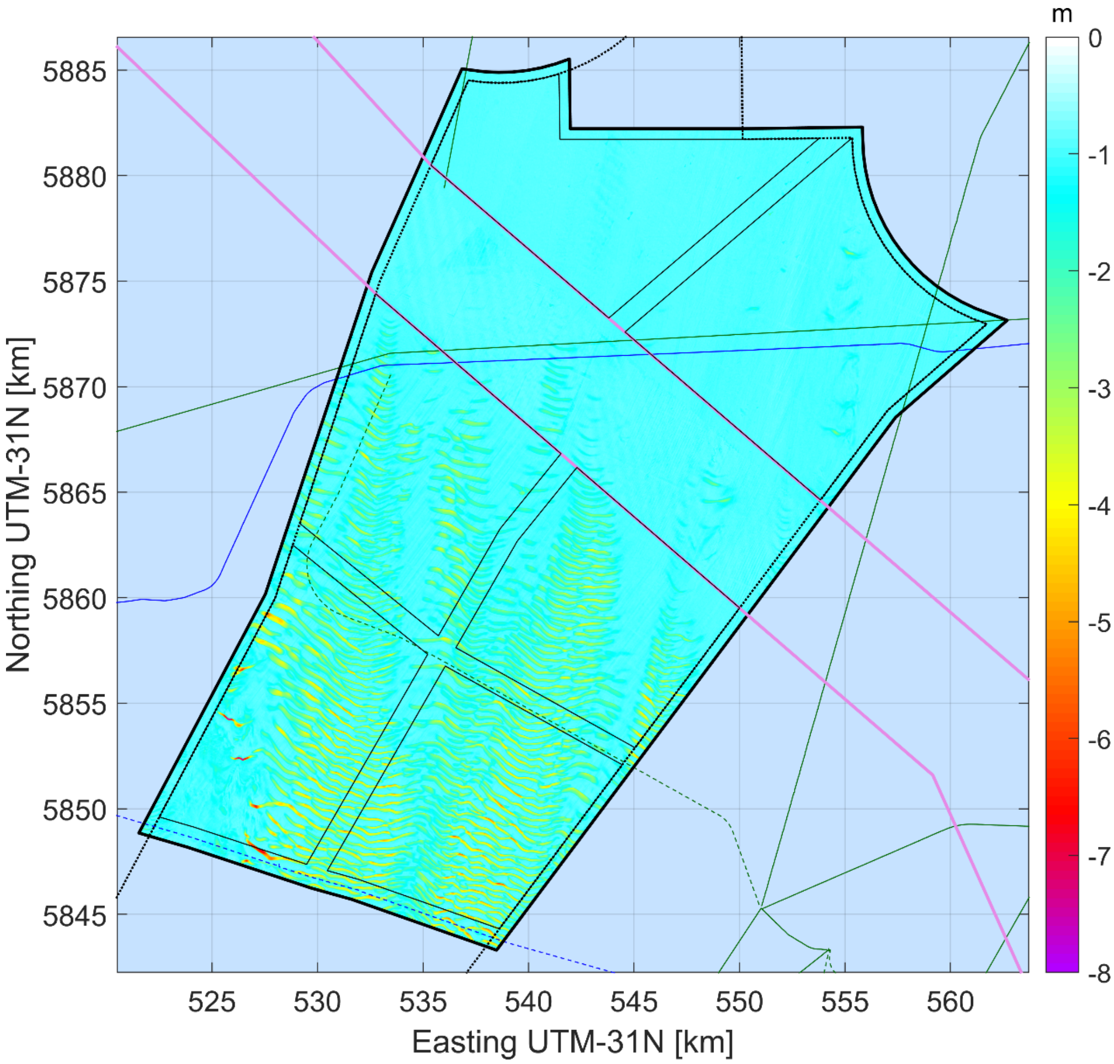

Figure 6.22:The maximum predicted seabed level differences between the 2020-2022 bathymetry and the LOL over the period 1945 to 2022 (Figure 6.21). The negative values indicate that at some point between 1945 and 2022 the seabed was lower than the present seabed. Other lines indicate extents of the OWF Sites (black lines) and the navigation channel (pink lines).

For the downward uncertainty band four sources are described in Appendix A.4.5 and in Sections 4.4 to 4.7. The downward uncertainty and grid resolution uncertainty for the lower envelope of seabed levels are shown in Figure 6.23 and Figure 6.24 and defined as:

i) 0.20 m (survey inaccuracy);
ii) Spatially and temporally varying;
iii) 0.20 m for the sand wave field and 0.25 m for the sand wave crest locations; and
iv) 0.10 m for the megaripple uncertainty and 0.005 (yearly trend) multiplied by 77 years = 0.385 m for the uncertainties in vertical seabed level trends.

The sum of the sources i, ii, iii and iv reaches a maximum value of 0.935 m for the downward uncertainty over the period 1945 to 2022. Note that the contribution of the grid resolution as a result of using the 5x5 m resolution is accounted for separately in the seabed predictions (i.e. it is not part of the uncertainty band).

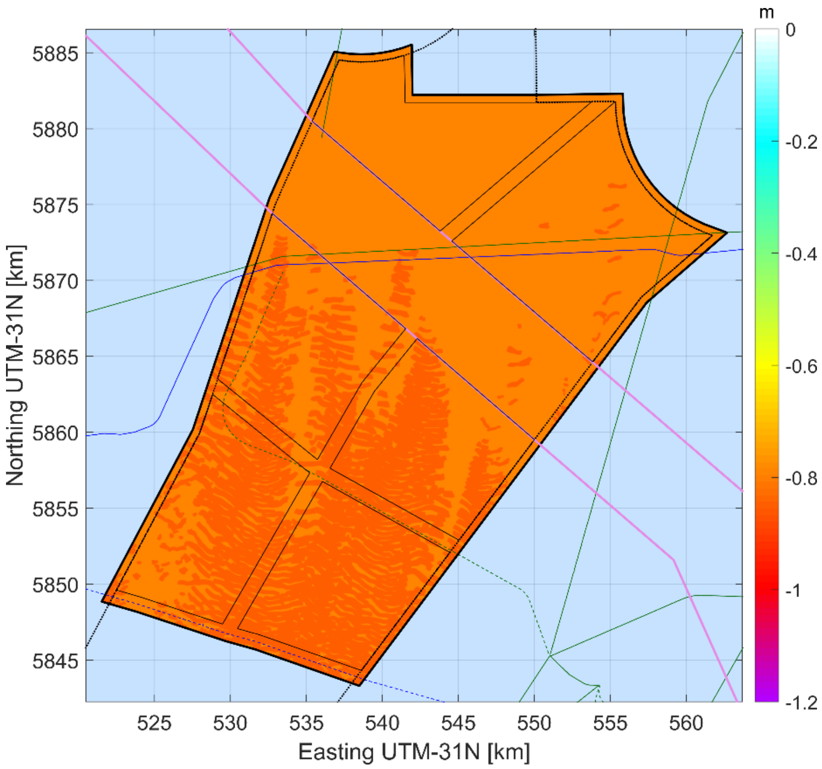

Figure 6.23:Overview of the downward uncertainty excluding the grid resolution and large-scale uncertainties as applied to the LOL 1945 to 2022. Other lines indicate extents of the OWF Sites (black lines) and the navigation channel (pink lines).

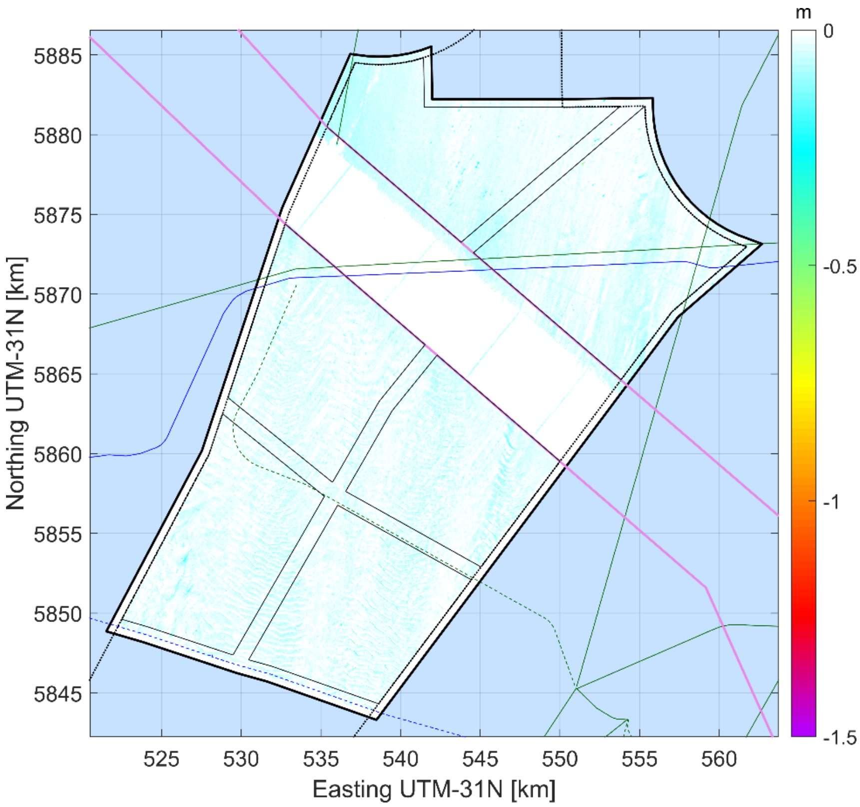

Figure 6.24:Overview of the grid resolution uncertainty contribution (bottom plot) as applied to the LOL 1945 to 2022. Other lines indicate extents of the OWF Sites (black lines) and the navigation channel (pink lines).

6.6.2 HOL from 1945 to 2022

The HOL is the estimated cumulative upper envelope of the extrapolated seabed levels combined with the upward uncertainty over a given period. Compared to the LOL only the lower bound migration rates are considered. The result for the period 1945 to 2022 is presented in Figure 6.25. The overall bathymetry of the HOL is similar to the 2020-2022 bathymetry, but it is typically a few metres deeper than the 2020-2022 bathymetry, but shallower than the LOL.

Calculating the difference between the HOL and the 2020-2022 bathymetry, the distribution of the minimum predicted differences in seabed levels can be estimated, as shown in Figure 6.26. The largest differences between the HOL and the latest bathymetry are at the locations of the sand waves with values up to -3.20 m as the 99.9%-non exceedance value, across IJV, when excluding uncertainties (+0.30 with uncertainties). This indicates that since 1945 the seabed was at some point lower than the present seabed. The largest differences are found in the vicinity of the highest sand waves, in Sites I-II. The deepest troughs of the sand waves and areas with limited seabed mobility have a zero predicted difference when excluding the uncertainty band. The smallest differences between the HOL and the latest bathymetry are in Sites V-VI.

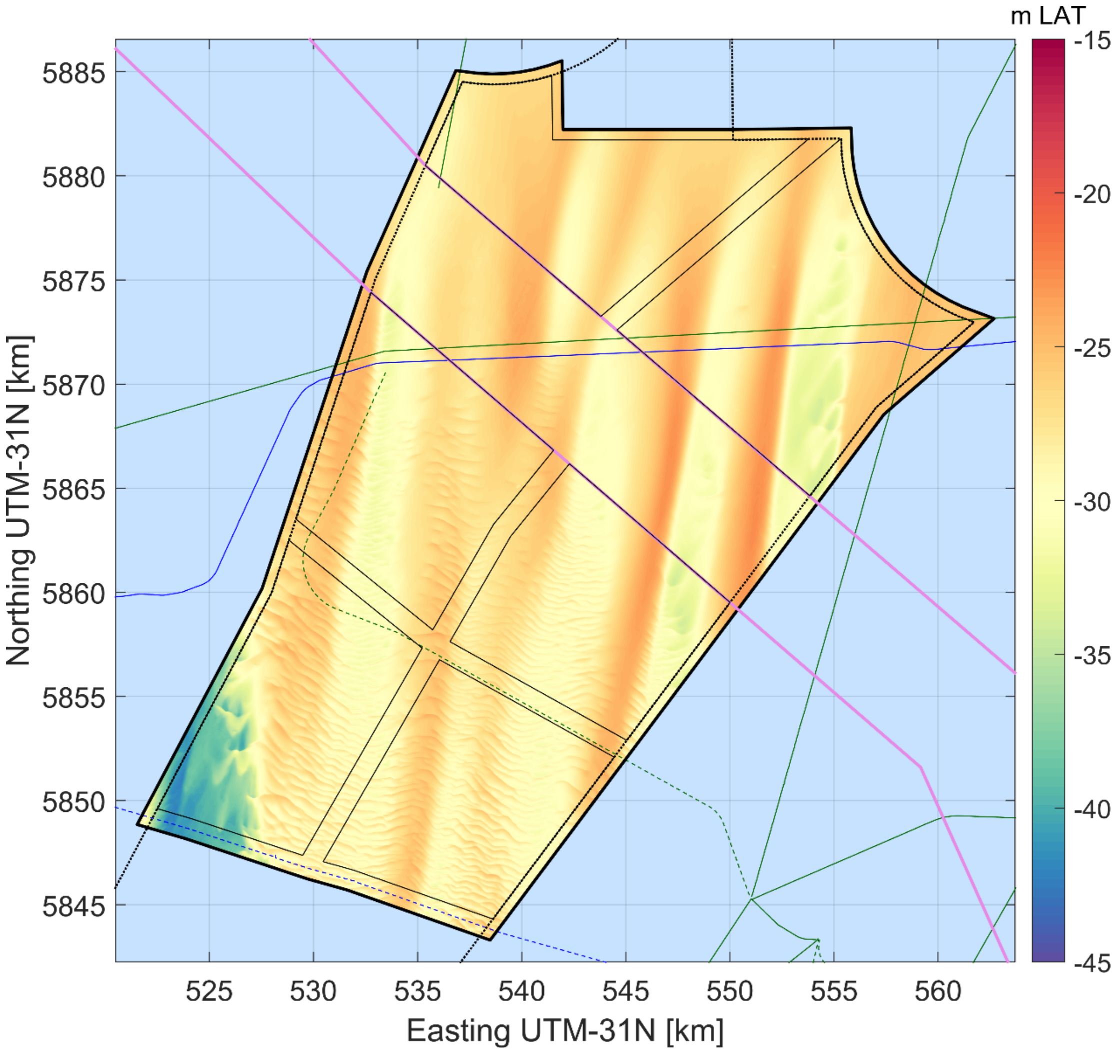

Figure 6.25:The predicted HOL for the period 1945 to 2022. The HOL is estimated by the upper envelope of the sand wave and megaripple variability over the period 1945 to 2022 combined with the large-scale bathymetry and the upward uncertainty. Other lines indicate extents of the OWF Sites (black lines) and the navigation channel (pink lines).

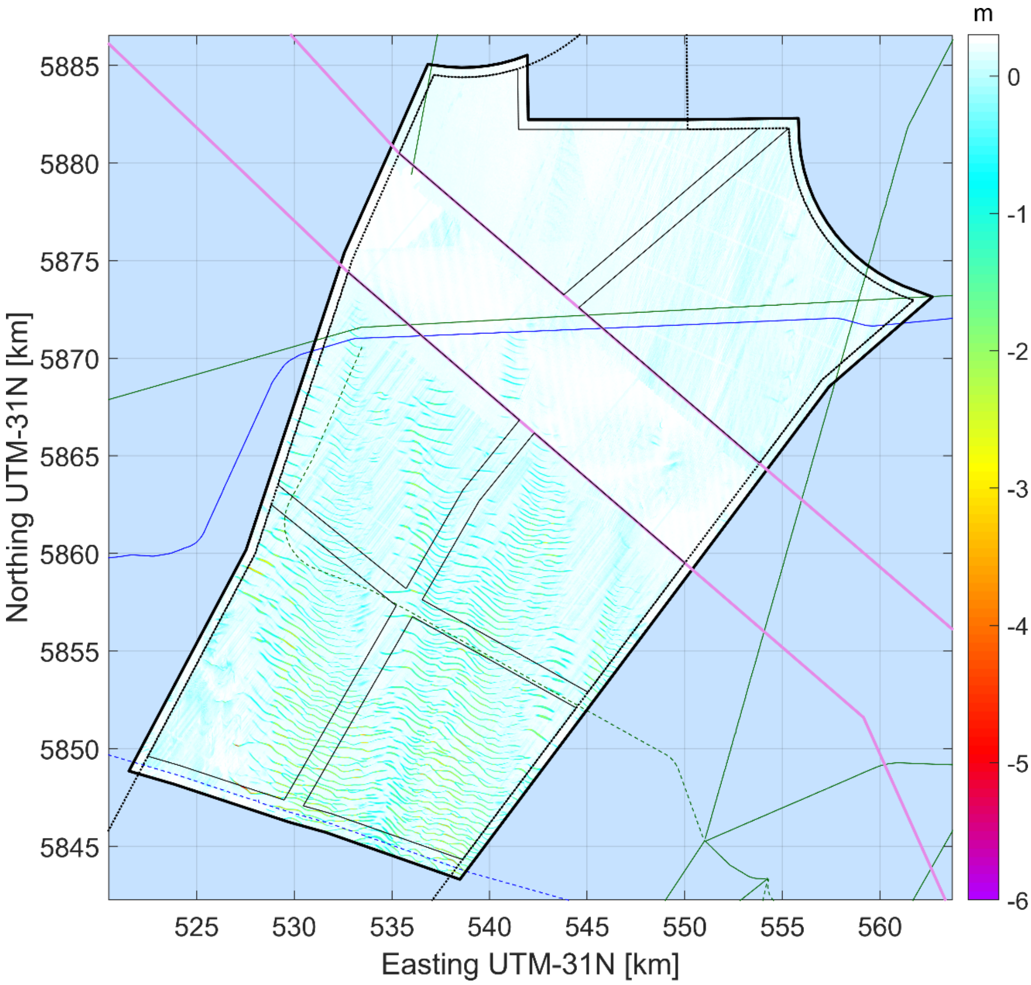

Figure 6.26:The minimum predicted seabed level differences between the 2020-2022 bathymetry and the HOL (Figure 6.25). The negative values indicate that at some point between 1945 and 2020 the seabed was lower than the present seabed. Other lines indicate extents of the OWF Sites (black lines) and the navigation channel (pink lines).

For the upward uncertainty band four sources are described in Appendix A.4.5 and in Sections 4.4 to 4.7. The upward uncertainty and grid resolution uncertainty for the upper envelope of seabed levels are shown in Figure 6.27 and Figure 6.28 and defined as:

i) 0.20 m;
ii) Spatially and temporally;
iii) Not applicable; and
iv) 0.10 m for the uncertainties in megaripple dimensions.

For the upper estimate of the lower envelope of seabed levels sources iii) and the vertical seabed level variations are not considered because the upper estimate of the lowest levels is not subject to sand wave reshaping (e.g. growth) and large-scale seabed trends (upwards).

The sum of the sources i, ii, iii and iv reaches a maximum value of 0.30 m for the upward uncertainty over the period 1945 to 2022. Note that the contribution of the grid resolution as a result of using the 5x5 m resolution is accounted for separately in the seabed predictions (i.e. it is not part of the uncertainty band).

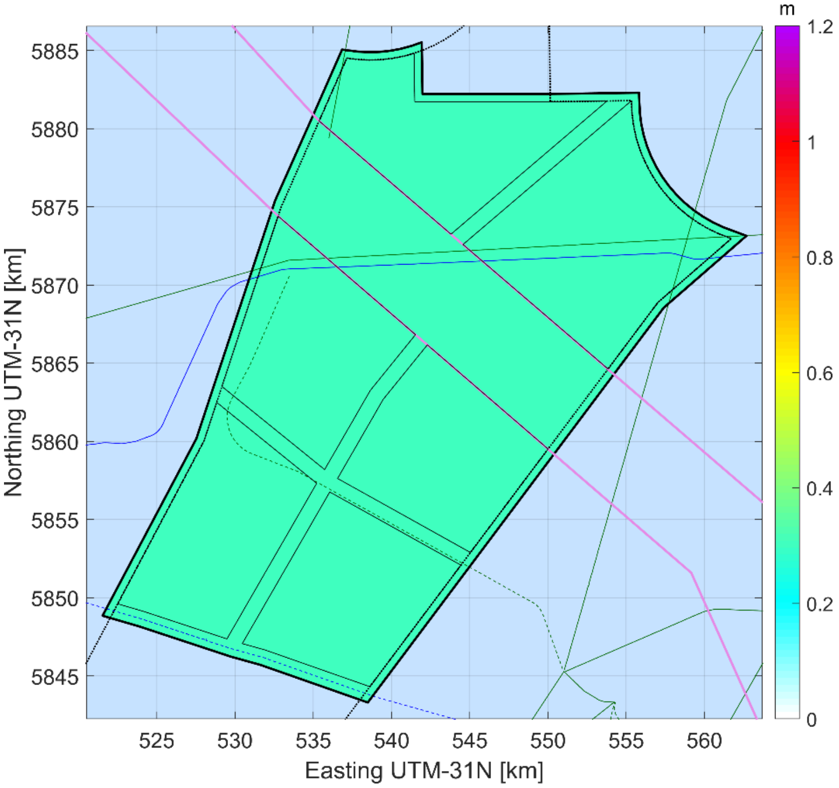

Figure 6.27:Overview of the upward uncertainty excluding the grid resolution uncertainty as applied to the HOL 1945 to 2022. Other lines indicate extents of the OWF Sites (black lines) and the navigation channel (pink lines).

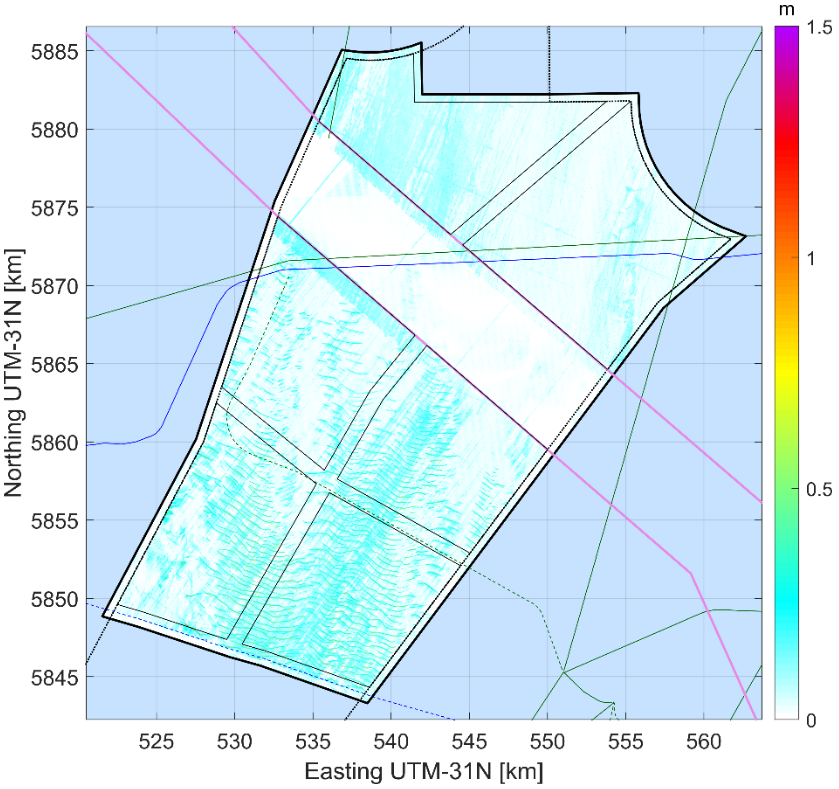

Figure 6.28:Overview of the upward grid resolution uncertainty contribution (bottom plot) as applied to the HOL 1945 to 2022. Other lines indicate extents of the OWF Sites (black lines) and the navigation channel (pink lines).

6.6.3 Overview per Site

Table 6.7 to Table 6.10 present an overview of several percentiles associated with the hindcast bed levels for the individual Sites as well as over the combined area (excluding the navigational corridor). The 0.1%, 1%, 5%, 50%, 95%, 99% and 99.9% non-exceedance values of the maximum and minimum seabed level differences (differences between LOL or HOL and the latest measured bathymetry) including and excluding uncertainties over the period 2022-1945 are presented.

Sites I-II present the largest differences between LOL or HOL and the latest measured survey over the period 2022-1945, both locally, as well as over the full area. This is attributed to the higher migrating sand waves present in those areas. In contrast, sand waves are limited or absent from Sites V-VI. In those areas the predicted bed level differences between LOL or HOL and the latest measured survey are thus significantly lower.

Table 6.7: Overview of the different percentile values associated with the maximum predicted differences between the cumulative lower envelope of bed levels (excluding uncertainties) for the period 2022-1945 and the latest measured bathymetry. The percentiles are presented for each individual Site of IJV as well as for the combined area of all Sites.

	Maximum difference from latest measured bathymetry, 2022-1945 (excluding uncertainties)						
	$p_{99.9\%}$	$p_{99\%}$	$p_{95\%}$	$p_{50\%}$	$p_{5\%}$	$p_{1\%}$	$p_{0.1\%}$
Site I	-4.21	-3.39	-2.67	-0.44	-0.07	-0.05	-0.03
Site II	-5.20	-3.37	-2.53	-0.28	-0.07	-0.05	-0.03
Site III	-3.02	-2.37	-1.84	-0.23	-0.09	-0.06	-0.04
Site IV	-2.67	-2.16	-1.58	-0.22	-0.09	-0.06	-0.04
Site V	-0.37	-0.26	-0.21	-0.13	-0.07	-0.05	-0.03
Site VI	-1.09	-0.41	-0.27	-0.16	-0.09	-0.06	-0.04
Sites I-VI	-3.86	-2.86	-1.94	-0.18	-0.08	-0.06	-0.04

Table 6.8: Overview of the different percentile values associated with the maximum predicted differences between the cumulative lower envelope of bed levels (including uncertainties) for the period 2022-1945 and the latest measured bathymetry. The percentiles are presented for each individual Site of IJV as well as for the combined area of all Sites.

	Maximum difference from latest measured bathymetry, 2022-1945 (including uncertainties)						
	$p_{99.9\%}$	$p_{99\%}$	$p_{95\%}$	$p_{50\%}$	$p_{5\%}$	$p_{1\%}$	$p_{0.1\%}$
Site I	-5.05	-4.23	-3.51	-1.27	-0.89	-0.85	-0.83
Site II	-6.04	-4.21	-3.37	-1.09	-0.88	-0.85	-0.82
Site III	-3.87	-3.21	-2.68	-1.03	-0.90	-0.86	-0.83
Site IV	-3.51	-3.01	-2.43	-1.02	-0.89	-0.86	-0.83
Site V	-1.16	-1.05	-0.99	-0.91	-0.85	-0.84	-0.82
Site VI	-1.92	-1.22	-1.06	-0.94	-0.87	-0.85	-0.83
Sites I-VI	-4.70	-3.71	-2.78	-0.97	-0.87	-0.85	-0.83

Table 6.9: Overview of the different percentile values associated with the minimum predicted differences between the cumulative higher envelope of bed levels (excluding uncertainties) for the period 2022-1945 and the latest measured bathymetry. The percentiles are presented for each individual Site of IJV as well as for the combined area of all Sites.

	Minimum difference from latest measured bathymetry, 2022-1945 (excluding uncertainties)						
	$p_{99.9\%}$	$p_{99\%}$	$p_{95\%}$	$p_{50\%}$	$p_{5\%}$	$p_{1\%}$	$p_{0.1\%}$
Site I	-3.65	-2.84	-1.86	-0.12	-0.06	-0.04	-0.02
Site II	-3.50	-2.61	-1.03	-0.13	-0.05	-0.03	-0.02
Site III	-2.60	-1.82	-0.85	-0.13	-0.06	-0.04	-0.02
Site IV	-2.41	-1.52	-0.46	-0.13	-0.06	-0.04	-0.03
Site V	-0.27	-0.20	-0.15	-0.07	-0.04	-0.03	-0.02
Site VI	-0.37	-0.29	-0.23	-0.11	-0.05	-0.03	-0.02
Sites I-VI	-3.23	-2.09	-0.61	-0.11	-0.05	-0.03	-0.02

Table 6.10: Overview of the different percentile values associated with the minimum predicted differences between the cumulative higher envelope of bed levels (including uncertainties) for the period 2022-1945 and the latest measured bathymetry. The percentiles are presented for each individual Site of IJV as well as for the combined area of all Sites.

	Minimum difference from latest measured bathymetry, 2022-1945 (including uncertainties)						
	$p_{99.9\%}$	$p_{99\%}$	$p_{95\%}$	$p_{50\%}$	$p_{5\%}$	$p_{1\%}$	$p_{0.1\%}$
Site I	-3.35	-2.54	-1.56	0.18	0.24	0.26	0.28
Site II	-3.20	-2.31	-0.73	0.17	0.25	0.27	0.28
Site III	-2.30	-1.52	-0.55	0.17	0.24	0.26	0.28
Site IV	-2.11	-1.22	-0.16	0.17	0.24	0.26	0.27
Site V	0.03	0.10	0.15	0.23	0.26	0.27	0.28
Site VI	-0.07	0.01	0.07	0.19	0.25	0.27	0.28
Sites I-VI	-2.93	-1.79	-0.31	0.19	0.25	0.27	0.28

6.7 Risks and possible mitigation measures

A number of different bed level definitions are derived in this section so to be used by the developer when considering different design choices.

Morphodynamic activity such as sand wave migration may pose a threat to foundations and cables if not considered in the design and general wind farm planning. It is beyond the scope of this study to provide specific design recommendations, but in the following sections a few general points are highlighted. However, they should not be considered exhaustive. The design of cable routes and foundations in morphodynamically active environments is discussed in more detail in section 6.8 and Deltares (2022b).

When defining the initial conditions for the design basis, the LSBL and HSBL at the time of foundation installation should be taken into consideration since the seabed may have changed relative to the 2020-2022 bathymetry. Also, future morphodynamic variations should be considered when predicting the variations which may occur during the lifetime of the wind farm.

6.7.1 Cables

Within the current offshore wind industry, 70-80% of insurance claims are related to failures of cables (https://www.deltares.nl/en/news/launch-major-joint-industry-project-reliable-offshore-cables/). On average, in Europe, one export cable and about ten inter-array cables fail every year. Cable failures pose one of the highest risks as they can cause blackout of the entire wind farm. In addition, cable monitoring and repair require expensive marine operations. One of the causes of cable failure is morphodynamic activity such as sand wave migration. Typical failure mechanisms are:

i) Manufacturing faults;
ii) Insufficient cable burial depth;
iii) Overheating;
iv) Internal stresses;
v) Free spanning; and
vi) Dragging anchors or fishnets, dropped objects.

As bedforms migrate, a cable located near the sand wave crest may experience significant seabed lowering, which may make the cable vulnerable to anchors or other threats. In contrast, if a sand wave crest passes over a cable that was formerly in a sand wave trough, it may experience a significant increase in the burial depth, which could cause local temperature increases around the cable. Depending on the specifications of the cable and environmental requirements, this may be a problem ('thermal fatigue').

It is known that cables exposed on the seabed may experience local scour, which in some cases may be sufficient to undermine the cable, causing a free span. When combined with sand wave migration the risk of free spanning increases. A free span of a cable may, besides causing a local stress build up, may cause vortex induced vibrations.

6.7.2 Foundations

Seabed level changes may pose problems to the foundations of the wind turbines or sub-stations. Large seabed changes may cause problems with respect to:

i) Geotechnical stability due to reduced support;
ii) Stability of scour protection; and
iii) Resonance related effects (such as fatigue).

If a foundation is installed on a sand wave crest it may experience a significant lowering, which combined with (for example) scour may cause insufficient geotechnical bearing capacity due to reduced support from the surrounding soil. A prevention method is installation of scour protection systems. However, if the scour protection is not sufficiently flexible and able to adjust to seabed variations it may become unstable and in the worst case fail to protect the foundation. Therefore, locations with large predicted seabed lowering are best avoided.

As the fixation level of the pile changes due to morphodynamic activity, the dynamics of the combined system including foundation and tower may change. In a worst case the natural frequency of the system changes which may lead to an undesired amplification of harmonic loading.

6.7.3 Summary

Risks related to morphodynamic and mobile seabed are summarised in Table 6.11: Other potential risks are not addressed apart from those related to the use of jackup platforms during the installation of wind turbines. This section is indicative only and is not intended to be complete or comprehensive.

Morphodynamic risks are related to large-scale seabed variations (due to natural processes, unrelated to the presence of infrastructure); risks related to a mobile seabed are related to local interaction between the hydrodynamics, the structure and the mobile seabed. The table below shows that potential risks can be mitigated by either a careful selection of the location with respect to predicted seabed lowering, taking appropriate mitigation measures, or by a combination of both.

Table 6.11: Overview of potential risks to cables and pile foundations (and a jackup platform if used for the installation) related to a morphodynamic mobile seabed. This table is indicative only and not intended to be complete or comprehensive.

Structure type	Potential risks related to morphodynamics of the seabed	Potential risks related to mobile seabed (sediments)
Pile Foundation (PL)	Significant risk for change in eigen-frequency if piles are installed at unfavourable locations and morphodynamics are not taken into account in the structure and/or scour protection design. When installed at carefully selected locations the risks can be low to negligible.	Scour around the foundation might change the eigen-frequency of the pile. Pile foundations can potentially be designed for the expected scour depth in IJV, but a scour protection might be more cost-efficient, especially for larger turbines and larger pile diameters.
Jackup Platform (JU)	Negligible risk due to limited duration of jack-up operations (relative to the timescale of morphodynamic processes)	Low risk for short-term operations (of a few days), significant risk for longer operations (weeks to months) depending on the leg and spud can type and penetration depth. Scour protection might be required also for temporary operations.
Gravity Base Foundation (GB)	Low risk if installed in sand wave troughs; for other locations seabed preparation (e.g. dredging until LSBL) is recommended. Note that wide foundations such as GB may interfere with the morphodynamic processes responsible for sand wave growth and migration, causing a faster morphodynamic response of the seabed. This should be considered when placing GB in areas other than the sand wave troughs.	Significant risk if the GB is not protected against scour. This risk can be managed by installing a scour protection, possibly in combination with seabed preparation.
Suction Caisson Foundation (SC)	Low risk if installed in sand wave troughs; for other locations extension of the suction cans or seabed preparation (e.g. dredging) is recommended.	Scour can pose a significant risk to SC, but they can be designed with more streamlined shapes to reduce scour. Also, the length of the suction cans can be increased. Otherwise a scour protection is recommended that does not interfere with the suction process during installation of the suction cans.
Cable (CB)	Negligible risk in areas with a stable seabed; low risk in areas with a (slightly) rising seabed if thermal characteristics of the cable are taken into account in cable design; significant risk on cable exposure in areas with a lowering seabed and a small initial cable burial depth.	As long as the cable is buried sufficiently deep (for other potential threats such as anchor dragging, dropped objects etc.) the risks are low to negligible. Special attention should be given to the areas just around the scour protections of the wind turbine foundations, where due to edge scour (mainly E of the scour protection) the cables may become exposed after some years. Also, cable crossings require special attention.

6.8 Cable routing in morphodynamic environments

The predicted seabed level changes over the period 2020 to 2072 can be as high as several metres. The effect of incorporating seabed dynamics in the cable routing is considered to be highly relevant. This section provides considerations on incorporating morphodynamics in the cable route design.

6.8.1 Sand wave migration

Cables crossing a sand wave field, which spatially migrates with different speeds, may experience local stress build-up due to an uneven strain. When combined with (for example) thermal stresses, this may become critical. It is known that cables exposed on the seabed may experience local scour, which in some cases may be sufficient to undermine the cable, causing a free span. When combined with sand wave migration, the risk of free spanning increases. A free span of a cable may, besides a local stress build up, also experience vortex induced vibrations (VIV). An example of how sand waves could influence burial depth is shown in Figure 6.29, which depicts the interaction between pipelines and sand waves (similarity to cables).

A cable connection between two wind turbines may cross a sand wave field. The increased risk of failure could be overcome by diverting the cables around the most morphodynamically active areas of the sand wave field. However, the increased cable length would likely incur extra costs. Therefore, in addition to the cable bending radius and the burial depth, the diversion should not lead to extreme increases in cable lengths.

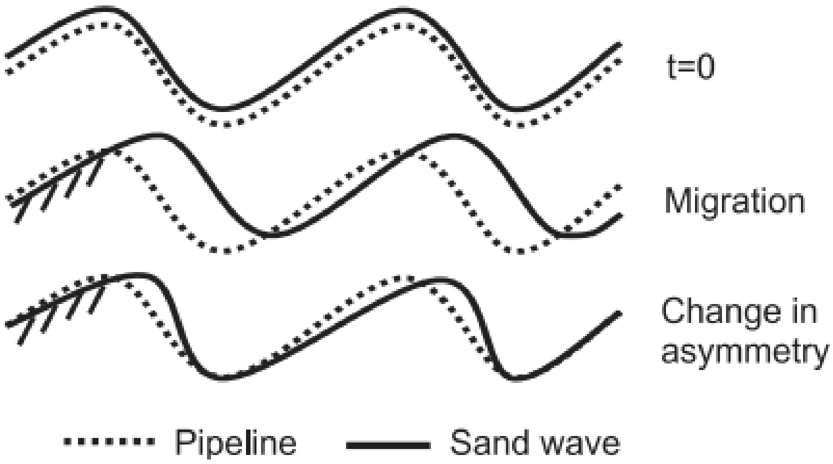

Figure 6.29:Effect of migrating sand waves on the burial depth of pipelines that shows that pipelines can become exposed both due to migration of sand waves and due to changing sand wave shapes (Morelissen et al., 2003); this figure is also valid for the interaction between cables and sand waves.

Sand wave migration poses a great threat to cable failure. In sand wave fields with relatively slowly migrating sand waves (such as IJV) the net bed level change over the design life of the wind farm will be either positive (bed level rise) or negative (bed level lowering) depending on the location of the cable sections beneath the sand waves.

Cable sections below or near the crest of a sand wave or below the stoss side of a sand wave will typically experience a net lowering of the seabed over the design life of the wind farm (see Figure 6.30). Alternatively, cable sections near a sand wave trough will most typically experience a rising seabed throughout the duration of their design life. Cable sections initially constructed on the lee side of a crest or the stoss side of a trough may experience both rising and falling bed levels. The net seabed level change at the latter sides will typically be much lower than those buried directly under a crest or trough point. These possible modes of seabed level change are summarised in Figure 6.30.

If sand wave migration is slow, e.g. a quarter wavelength over the cable design lifetime, the maximum seabed lowering and rise occur along the steeper parts of the stoss and lee side, respectively.

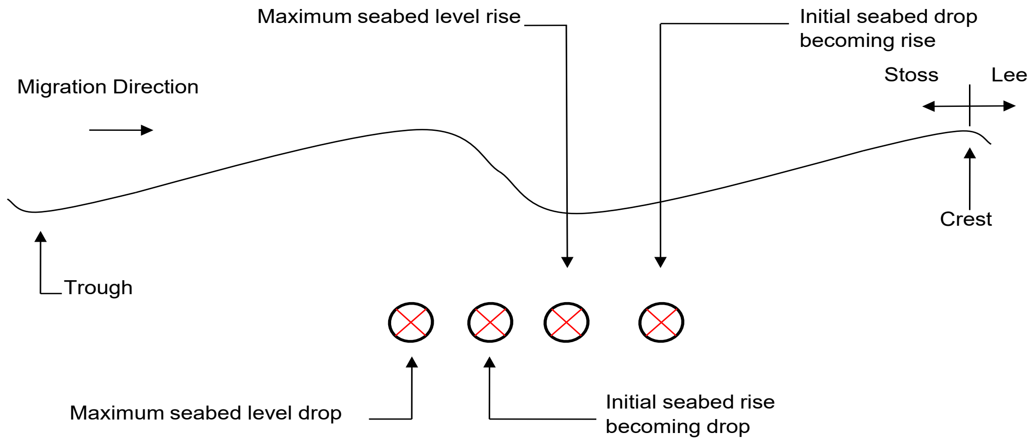

Figure 6.30:Schematisation of general sand wave dynamics above a buried cable relative to its horizontal position.

To quantify the morphological evolution of the seabed over the lifetime of a wind farm, the minimum seabed level observed during a certain period has to be determined. The results presented in Chapter 6 is used below in an example of cable routing optimisation for Site I in IJV.

6.8.2 Cable routing

To better understand the interaction between cable routing and the morphodynamic environment, this section addresses both the large-scale (which turbine needs to connect to which turbine) and the small-scale (optimising a specific cable connection) cable routing. The methods and outcomes presented are further discussed in Roetert et al. (2017).

6.8.2.1 Overall wind farm cable layout

In a wind farm located far offshore, the turbines are often connected to one or more offshore high voltage stations (OHVS) via cable strings. The aim of the “overall” cable routing is to connect all these turbines to the OHVS, taking into account several routing constraints:

- Power cable capacity, translated to a maximum number of turbines connected via one string;
- Cable length should be minimised;
- Minimising crossings of navigational channels, pipelines, cables and other existing infrastructure in or on the seabed;
- Wind farm Site boundaries;
- Wrecks and other obstacles (e.g. potential archaeological finds);
- Unexploded ordnances (UXO’s); and
- Locations with unfavourable geological characteristics.

In most presently available cable routing methods, morphodynamic behaviour of the seabed is not taken into account for the overall wind farm cable routing. In such cases the cable routing is conducted based only on present materials (cable and turbine capacities) and obstructions (UXO’s, complicated soil layers and Site boundaries). By addressing the morphodynamic behaviour of the seabed (further discussed in Roetert et al. (2017), highly dynamic areas can be highlighted as additional time-varying constraints to the overall wind farm cable routing, reducing risks of cable failure due to sand wave migration. Risks of cable failure are calculated from internal risks, such as overheating, and external risks caused by either dragged or dropped objects, such as anchor drops, fishing net drag and spudcan positioning errors. Each risk is quantified as a probability of cable failure per year for a certain penetration depth.

To demonstrate the results of a cable routing assessment, a hypothetical simulation was performed with turbine locations as illustrated in Figure 6.31. This figure shows 67 randomly placed turbines in IJV with a spacing of at least 1,275 m taking into account present constraints such as cables and pipelines. The layout in reality will be determined in a wind resource and energy yield assessment taking wake effects into account. With an assumed maximum number of six turbines per cable string, the turbines were connected via 12 strings to the OHVS (TenneT Platform) while minimizing total cable length.

6.8.2.2 Cable routing of individual inter-array cables

Following determination of the overall cable routing, the risk of cable failure due to sand wave migration can be further reduced by optimising each inter-array cable connection separately. To analyse effects of inter-array cable routing, each connection is optimised in the vertical (into the bed) and horizontal (pathways between the turbines) planes. The effectiveness of both methods largely depends on the bedforms present between two turbines. In case multiple sand waves need to be crossed, optimisation in the vertical plane is the most effective approach since routing cables around these sand waves incurs significant additional cable length. By contrast, when a power cable is more or less parallel to sand wave crests, the risks of cable failure can be reduced greatly by routing cables through sand wave troughs via a horizontal optimisation.

Figure 6.31 shows two connections that were chosen for further optimisation taking into account the morphodynamic environment.

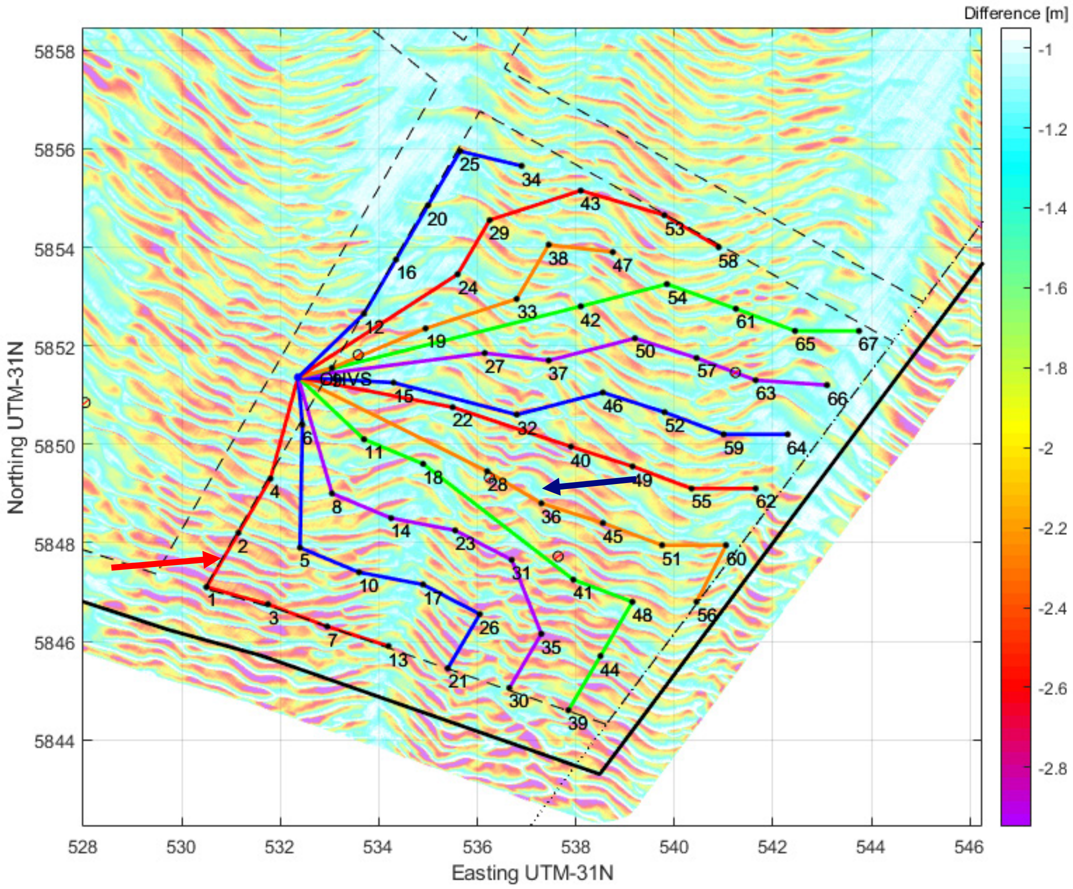

Figure 6.31:Wind farm layout for random turbine locations in IJV Site I. The red and blue arrows denote the example inter-array cable optimised in the vertical (red) and horizontal (blue) planes. Red hatched areas indicate constraining areas.

The individual inter-array cable routing starts with determining an optimal initial burial depth for the cable in the vertical plane, while assuming a fixed position in the horizontal plane (e.g. two turbines are connected via a straight line). For a chosen connection (red arrow in Figure 6.31), the vertical optimised cable position is depicted in Figure 6.32, which has been chosen to illustrate the effect of migrating sand waves on cable burial depth. Since this connection has to cross multiple sand waves, routing cables around the sand waves is not cost-efficient, and instead, the initial burial depth is varied.

Figure 6.32 clearly shows the predicted seabed lowering (difference between blue and black line in top plot) due to sand wave migration and the added uncertainty band. If seabed morphodynamics is not taken into account, it is assumed that power cables are buried with a certain constant burial depth (dashed red line); here 1 m. In Figure 6.32 it is observed that the power cables is almost fully exposed assuming the LSBL and a 1 m burial depth. In this scenario it can become prone to cable failure. Optimising the initial burial depth (green line in the bottom plot) ensures that minimum cable coverage (straight blue line in the bottom plot) is guaranteed over the wind farm lifetime. This minimum cable coverage is based on permit requirements and cable characteristics.

For this specific example, the optimised cable burial depth is approximately 0.5 m below the LSBL. However, this position is subject to the trade-off between cable length and dredging efforts. This is considered the scenario with the least cable reburial. A second option is that more risk of failure is accepted at hotspots, which are identified from a morphodynamic assessment, and are monitored, and maintenance performed when necessary. This might save on dredging efforts but gives rise to more risk of exposure, and hence failure.

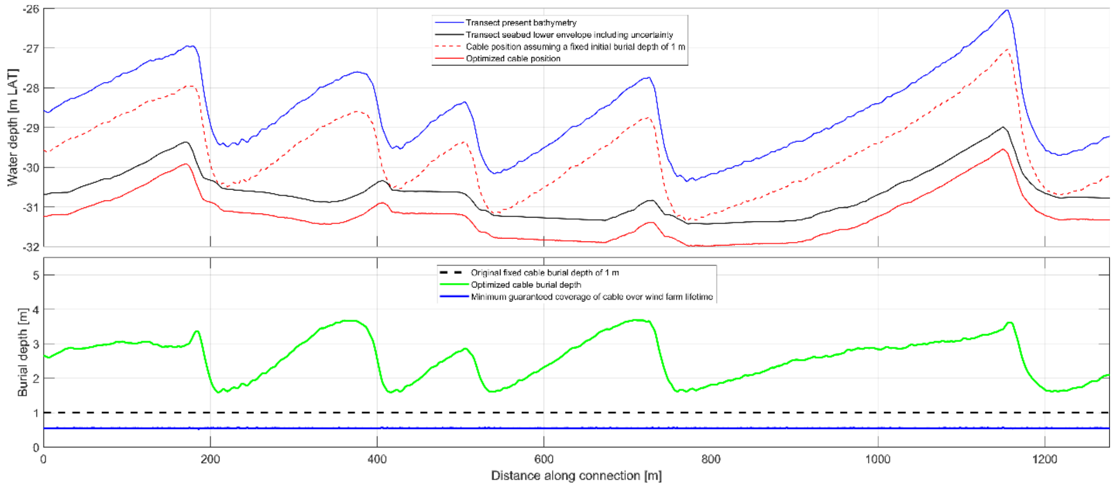

Figure 6.32:Optimised cable position in the vertical plane between two turbines. The top plot depicts the present bathymetry (blue line), lowest seabed level over time including uncertainty (black line), the cable position assuming a constant burial depth (dashed red line) and the optimised cable position (red line). The bottom plot depicts the original fixed cable burial depth (dashed black line), the optimised cable burial depth (green line) and the minimum guaranteed cable coverage over the period considered, which is here assumed at 0.5 m (fixed blue line). The location of the transect is indicated by a red arrow in Figure 6.31.

Sand wave dynamics can lead to differences in bed level changes over a cable transect. In IJV, where seabed dynamics are a result of sand wave migration, these differences can be up to 3.4 m within certain cable strings. When assuming a fixed initial burial depth (e.g. the average of the optimised initial burial depth depicted in Figure 6.32), cable segments experiencing a relatively small seabed lowering or rise (order of 0 to 1 m) are always subject to larger burial depth requirements, potentially resulting in higher risks of overheating and high cable installation costs. By contrast, cable segments that may be subject to a large seabed lowering have an increased risk of failure due to limited burial depth or even cable exposure. By introducing a varying initial burial depth, risks are minimised per segment, instead of averaged over the total cable length. Also, cable burial can be performed faster in segments where smaller burial depths need to be achieved.

Vertical optimisation across IJV is shown in Figure 6.33, which shows each connection between two turbines by means of the required initial burial depth. The redder cable stretches indicate parts which need to be buried deeper. The spatial overview indicates that for most of IJV the benefit of vertical optimisation is limited. In sand wave areas some benefit can be gained by taking into account seabed morphodynamics.

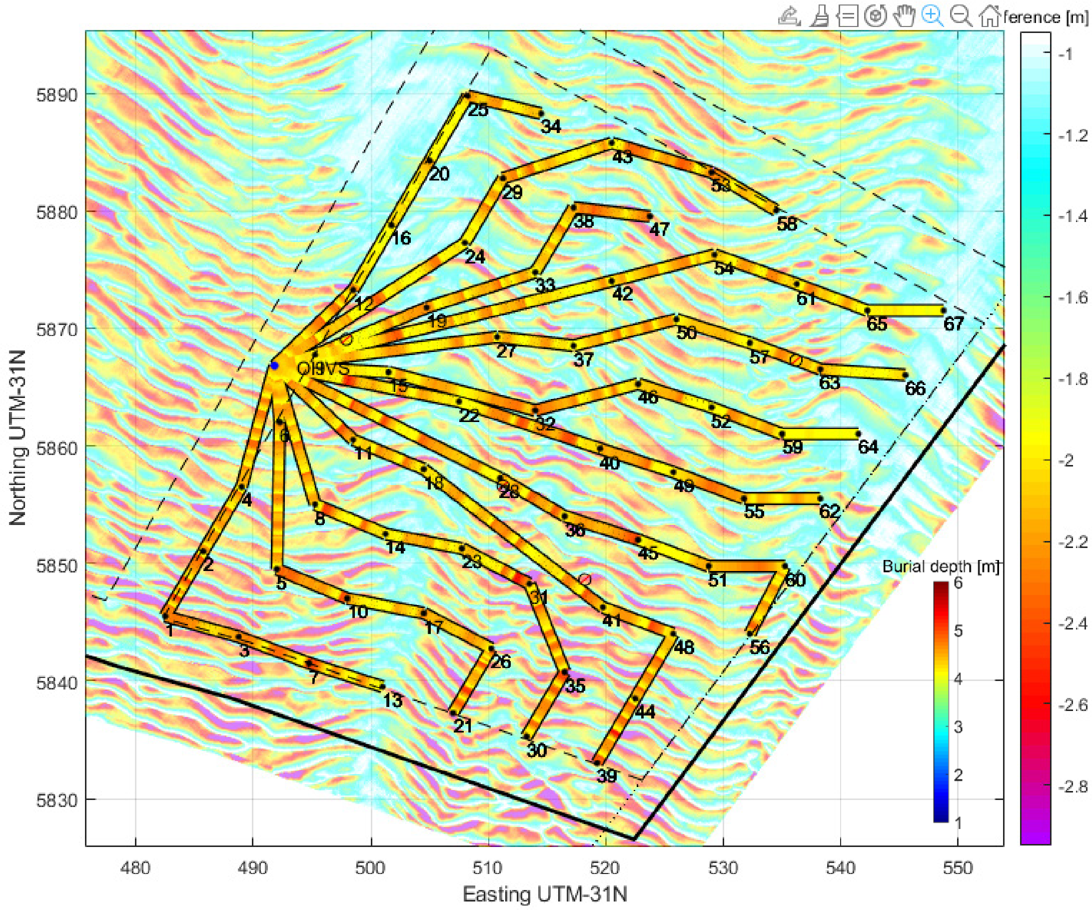

Figure 6.33:Spatial overview of vertical cable route optimisation. Each string connecting two turbines is visualised by means of the required initial burial depth. Red parts indicate cable stretches which need to be buried deeper. The colour bar for the required cable burial depth is displayed in the bottom right of the figure.

The second part of inter-array cable routing is to find the optimal route in the horizontal plane by diverting the cable around areas that require large burial depths, taking into account cable bending radii, cable lengths and dredging efforts. The following constraints should be assessed and taken into account as additional risks when assessing the optimal route:

- Avoiding existing infrastructure such as navigation channels, pipelines and cables;
- Wind farm Site boundaries;
- Locations with unfavourable geological characteristics; and
- Known edge scour locations; for IJV the most severe edge scour is expected at the north-northeast-side.

In the case of a power cable that is more or less parallel to sand wave crests, the risks of cable failure can be reduced greatly by routing cables through sand wave troughs or areas with little morphodynamic activity, without increasing cable lengths and dredging efforts significantly. For the chosen connection (blue arrow in Figure 6.31), the horizontally optimised cable position is depicted in Figure 6.34. The optimal route is based on certain assumptions regarding the trade-off between cable length and dredging volumes, combined with the risk of possible cable failure (Roetert et al., 2017). Changing these assumptions would potentially lead to a (slightly) different optimal route.

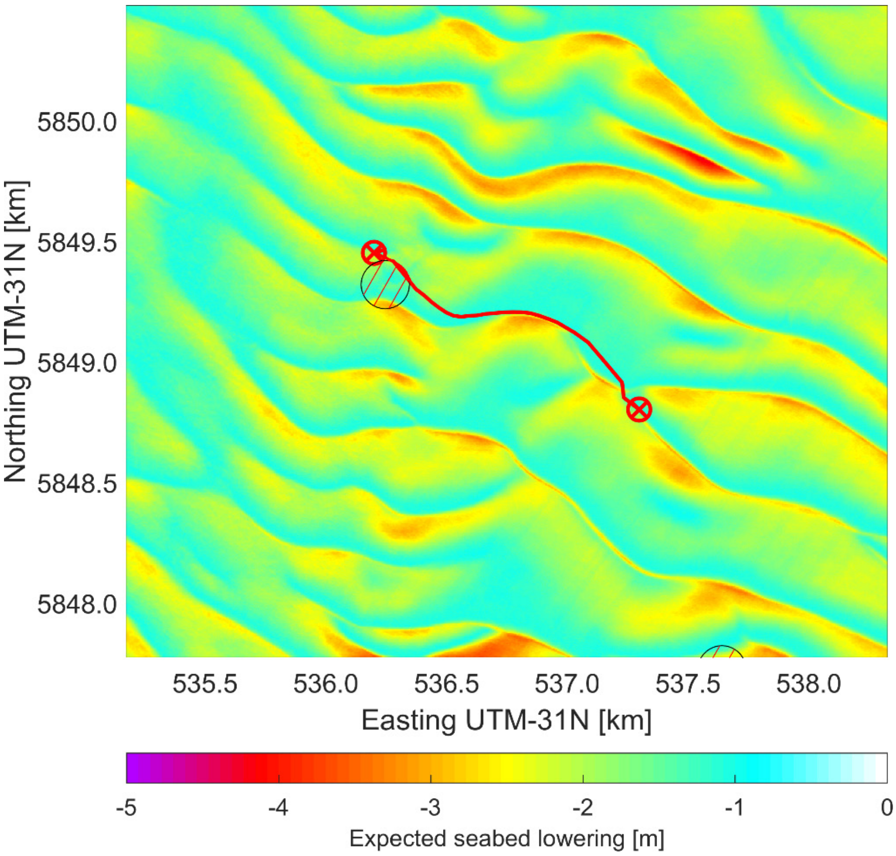

Figure 6.34:Optimised cable position in the horizontal plane between two turbines. The thick red line indicates the optimal route. The red hatched area close to the northeast turbine marks a restricted area (e.g. an area around a UXO object).The colour map indicates the predicted seabed lowering over the period 2020 to 2072. The location of the transect is indicated by a blue arrow in Figure 6.31.

Clearly visible is the optimal cable routing around an area with increased seabed lowering. It is advised that the dynamic behaviour of the seabed should be taken into account in cable route design.

7 Conclusions and recommendations

7.1 Conclusions

IJV is located 60 km east of the coast of North Holland and consists of six wind farm Sites (I-VI) and will have a combined capacity of 6,000 MW. The objective of this study is to provide RVO, and companies tendering for IJV, with detailed information on the morphodynamics in the IJV IA over the period of construction and operation. The analysis is based on a data-driven approach supported by results of sediment transport modelling.

The overall objective of this study is to assess the future and historic seabed levels in the IJV IA and individual Sites for various years (every five years over the period 2022 to 2072) and periods (2022 to 2072 and 1945 to 2022) to support the design, installation and maintenance of wind turbines, inter-array cables, substations and their support structures. Data and literature have been analysed to characterise the seabed features and assess the historic and potential future seabed dynamics. Analysis of field measurements and numerical predictions supported an understanding of the dynamics informing the future seabed level predictions using data-driven methods.

Available high-resolution bathymetric surveys between 2013 and 2022, and older surveys between 1976 and 2003, allowed division of the seabed into distinct morphodynamic features. These are megaripples, sand waves and underlying large-scale bathymetry. The analysis is supported by available geotechnical measurements and data on the composition of the top sediment layer.

Sand waves within IJV typically migrate towards the north-northeast with a mean best estimate direction of 13° relative to north. Typical migration rates range from 0.4 m/year to 2.7 m/year, with local rates up to 6 m/year. Migration statistics are similar for Sites I-VI. For Site V statistics are different due to the small number of sand waves present. No sand waves were detected in Site VI. Spatially, the sand waves on the western slope of the central sand bank have the highest migration rates.

Sand wave heights and lengths vary between 0.9 m and 3.5 m, and 170 m and 620 m, respectively. Generally, the highest sand waves are on top of the sand banks. As can be seen in Table 7.1, the highest sand waves are observed in Sites I-II. The distribution of sand wave lengths is similar between Sites I-V, with the longest sand waves are found in Site V.

Table 7.1: Selected non-exceedance values for the sand wave dimensions and migration rates for the different Sites across IJV.

Site	Sand wave height [m]		Sand wave length [m]		Migration rate [m/yr] in best estimate direction	
	$p_{50\%}$	$p_{95\%}$	$p_{50\%}$	$p_{95\%}$	$p_{50\%}$	$p_{95\%}$
I	2.22	3.79	310	532	1.61	2.80
II	2.17	3.63	357	659	1.43	2.69
III	1.60	2.56	317	550	1.67	2.64
IV	1.46	2.33	403	689	1.66	2.71
V	1.16	2.41	625	787	0.04	0.72
VI	-	-	-	-	-	-
I-VI	1.91	3.51	333	623	1.58	2.73

Differences in large-scale bathymetry between different surveys did not show a consistent pattern in either deposition or erosion. Therefore, it is assumed that over the wind farm lifetime no significant large-scale changes occur. However, the analysis of large-scale seabed dynamics is subject to uncertainties, especially when using older surveys. This is addressed as an uncertainty in the seabed predictions by including a yearly increasing value of 0.01 m/year, both vertically upward and downward, applied uniformly over all Sites.

The average grain size across IJV decreases from south to north and east, ranging between 0.026 mm and 0.29 mm (silt to medium sand) between one and five metres below the seabed. In the southwest deepest part of IJV (Site II), as well as locally over the sand waves troughs and crests (Sites I-IV), coarser grain sizes occur at the seabed. In general grain sizes decrease slightly from south (Sites I-II) to north (Sites V-VI). Fines content ranges from 0-3% in the uppermost 2 metres of the seabed. Values over 10% where found locally in Sites V-VI deeper than 4 metres below the seabed. There is no clear trend in grain size or fines content with depth below the seabed. Although median grain sizes indicate a slight decrease with depth in IJV, the spatial distribution is more scattered. The results imply that non-erodible layers in the subsurface of IJV are not likely to affect the seabed morphodynamics, because they are too deep (based on observed and expected seabed dynamics) or too sparsely spread to be exposed by the seabed dynamics.

Analysis of Vibrocores indicates the presence of various geological layers in IJV in the top six metres. The Holocene Southern Bight Formation is fine to medium sand with little or no fines becoming progressively finer towards the base of the Bligh Bank Member, as the scale of the observed sand waves. Sediment at the sand wave crests is slightly coarser than in the troughs. A gravel rich layer, which is interpreted as the base of the active layer, occurs a few decimetres beneath the seabed in the sand wave troughs for most of the surveyed locations.

Analysis of the high-resolution data and repeat survey lines shows that megaripples in IJV have wavelengths up to 30 m and heights up to 1.00 m. Throughout IJV, areas with very small megaripples are present, which correspond with areas without sand waves and areas where clay is present at the seabed (Sites V-VI). The highest megaripples are located towards the southwest of IJV (Site II). Temporal variations in megaripple dimensions are small (5 to 10 cm), although based on limited information. It is possible that megaripple occurrence and dimensions are highly variable in time. They are highly dynamic and so the megaripples dynamics have been incorporated as an uncertainty parameter in predicting seabed levels.

The numerical simulations provide information on the governing processes and sediment transport patterns across IJV. Residual sediment transport varies in magnitude and direction under the effect of meteorological, wave conditions and extreme events. However, overall, the effect of tidal asymmetry is the dominant driver when analyzing over longer periods. The annual residual sediment transport does not vary significantly over the simulated five-year period. In general, it is found that the modelled spatial patterns of sediment transport magnitudes and directions are well aligned with the observed sand wave migration rates and directions.

Future seabed levels are estimated by displacing the seabed based on historic trends. These trends are denoted as lower bound, mean and upper bound migration direction and rate resulting from the probabilistic distributions for each analysis location. The use of the local probability distributions provides a quantitative approach to capturing the spatial and temporal variability in the sand wave migration and subsequently the extrapolation of future and historic seabed levels. Although spatial and temporal variability is included in the migration rates and directions, local extremes can still be present, and this variability might change in the future. Possible changes can be a result of the variability in the system and because of limited spatial (mostly three to four surveys for IJV) and temporal (limited in terms of high-resolution bathymetry data) spread in available bathymetric data which can influence future seabed level predictions.

By superimposing the displaced sand waves and megaripples to the large-scale bathymetry, future and historic seabed levels are predicted. To account for additional uncertainties such as grid resolution and shape uncertainty, their variability is subsequently included in various predicted bed level definitions. A Best Estimate Bathymetry (BEB), a Lowest Seabed Level (LSBL) and a Highest Seabed Level (HSBL) are estimated. The BEB represents the predicted bathymetry for a certain year with the smallest expected average error. The LSBL and HSBL represent the predicted lowest and highest seabed levels, respectively, for the period 2022 to 2072, including uncertainty bands.

The predicted LSBL describes a bathymetric shape similar to the existing static part of the bathymetry, but typically a few metres lower. Comparison of the LSBL with the 2020-2022 bathymetry shows a predicted maximum seabed lowering of approximately -3.58 m (99.9% non-exceedance value for IJV Sites I-VI). As expected, the greatest lowering is at the location of the existing sand wave crests, while the smallest lowering is in the areas where no bedforms are present. The highest predicted seabed level lowering (99.9% non-exceedance value) thus occurs in Sites I-II, where the highest mobile sand waves are present. In contrast Sites V-VI where sand waves are mostly absent present the lowest extreme percentiles of predicted seabed lowering

The HSBL shows a bathymetric shape similar to the existing static part of the bathymetry, but typically several metres higher. Comparison of the HSBL with the 2020-2022 bathymetry shows a predicted maximum difference of 5.46 m (99.9% non-exceedance value across IJV). In contrast to the seabed lowering, the largest potential rise of the seabed is along the sand wave slopes, with minimal rises at the locations of the present sand wave crests. The highest predicted seabed level rise (99.9% non-exceedance value) occurs in Sites I-II, while Sites V-VI present the lowest extreme percentiles of seabed rise.

A hindcast of seabed level was completed to assess the possible levels at which Unexploded Ordnances (UXO's) are located. Important assumption in this method are that an UXO will never move upwards and a typical UXO will self-bury to about half its height. To take into account the full range of possible object levels, the Lowest Object Level, the Highest Object Level and the Best-Estimate Object Level over the period 1945 to 2022 are calculated. These levels respectively represent the lower, best and upper estimate of the lowest seabed level over the period 1945 to 2022.

Predictions and hindcasts of future and historic seabed levels over IJV IA, are delivered in a database along with this report. These predictions can be used to support the design, installation and maintenance of wind turbines, inter-array cables, substations and their support structures in IJV. An overview of the data is presented in Appendix F.

The expected seabed level changes presented in this study used applied morphological analysis techniques, describing the (uncertainty of the) forecasts and the natural variability of the analyzed morphological system. No additional safety margins for design purposes have been applied. The effect of future human interventions such as beach nourishments or dredging operations is not considered in the predicted seabed level changes.

7.2 Site-specific conclusions

In the following paragraphs an overview of the main findings of this analysis is presented for the different Sites. The aim of this section is to highlight the variability in the characteristics and predicted morphodynamics in IJV and to provide detailed information on the varying morphodynamics dedicated on specific Sites. Three groups of Sites (I-II, III-IV, V-VI) are distinguished. The conclusions presented in the following sections are not exhaustive and should always be considered along with Section 7.1.

7.2.1.1 Sites I-II

The bathymetry in Sites I-II is characterised by a number of north-south oriented sand banks with heights ranging from a few metres up to 10 m. In the southwest of Site II, a deeper channel occurs where the Holocene layer is absent. The maximum depth of this channel is 10 m lower than the rest of IJV.

Sites I-II are characterised by the highest sand waves, with 50% of the heights exceeding 2 m at the analysed locations (Table 7.1). Within the two Sites, the highest sand waves are observed on top of the sand banks as well as at the east side of the channel formation southwest in Site II. The sand wave lengths range between 141 and 659 m, similar to sand wave lengths in most other Sites. In Sites I-II, sand waves migrate towards the north-northeast with a mean best estimate direction of 5° and 13° relative to the north, respectively. Typical migration rates range between 0.15 m/yr and 2.80 m/yr (minimum and maximum $p_{5\%}$ and $p_{95\%}$ of the individual Sites).

Similar to the rest of the Sites, no trends of large-scale seabed level changes were observed in the available data. The uncertainty in the long-term large-scale seabed level changes is incorporated in the predictions by including a yearly increasing value of 0.01 m/year, both vertically upward and downward.

Megaripples overlay other bed forms present in Sites I-II. The largest megaripples are observed southwest of Site II, where megaripples with lengths up to 30 m and heights up to 1.00 m occur. Although the observed variation in megaripple dimensions is limited, megaripple occurrence and dimensions are expected to be highly variable in time. Megaripple dynamics have been incorporated as an uncertainty parameter in predicting seabed levels.

Median grain size diameters range between 0.210 and 0.248 mm for the first five metres below the seabed in Sites I-II. Locally spots of coarser grain sizes at sand wave crests/troughs are observed. Additionally, in the channel formation southwest of Site II, where the Holocene layer is absent, the grain sizes increase up to 0.400 mm. Fines content ranges between 1.5-2.4% in the uppermost 2 metres of the seabed. There is no clear trend in grain size or fines content with depth below the seabed. Although median grain sizes indicate a slight decrease with depth in IJV, the spatial distribution is more scattered. The results imply that non-erodible layers in the subsurface of IJV are not likely to affect the seabed morphodynamics, because they are too deep (based on observed and expected seabed dynamics) or too sparsely spread to be exposed by the seabed dynamics.

Sites I-II present the largest predicted seabed level lowering and rising due to the high sand waves present. The maximum predicted seabed lowering over 2022-2072 is approximately -3.70 m and -3.85 m for Sites I and II, respectively (99.9% non-exceedance values), observed mainly at the location of existing sand wave crests. The maximum predicted seabed rise over 2022-2072 is approximately 5.83 m and 7.01 m for Sites I and II, respectively (99.9% non-exceedance values), observed mainly along the sand wave slopes.

For the future and hindcast predictions, upward and downward uncertainty estimates from different sources (data collection, grid resolution, sand wave reshaping, megaripple dynamics, and large-scale seabed variations related uncertainties) are applied. No additional safety margins for design purposes have been applied. The effect of future human interventions such as beach nourishments or dredging efforts is not considered in the predicted seabed level changes.

7.2.1.2 Sites III-IV

The bathymetry in Sites III-IV is characterised by a number of north-south oriented sand banks with heights ranging from a few metres up to 10 m, overlaid by sand waves and megaripples. Sand wave heights of 1.60 and 1.46 m (50% non-exceedance value) are observed in Sites III and IV, respectively (Table 7.1). Within the two Sites, the highest sand waves are observed on top of the sand banks. Sand wave lengths range between 179 and 689 m, similar to sand wave lengths in most other Sites. The sand waves migrate towards the north-northeast with a mean best estimate direction of 7°-8° relative to the north. Typical migration rates range between 0.33 m/yr and 2.71 m/yr (minimum $p_{5\%}$ and maximum $p_{95\%}$ of migration rates for the individual Sites).

Similar to the rest of the Sites, no trends of large-scale seabed level changes were observed in the available data. The uncertainty in the long-term large-scale seabed level changes is incorporated in the predictions by including a yearly increasing value of 0.01 m/year, both vertically upward and downward.

Megaripples overlay other bed forms present in Sites III-IV. Although the observed variation in megaripple dimensions is limited, megaripple occurrence and dimensions are expected to be highly variable in time. Megaripple dynamics have been incorporated as an uncertainty parameter in predicting seabed levels.

Median grain size diameters range between 0.200 and 0.240 mm for the first five metres below the seabed in Sites III-IV. Locally, spots of coarser grain sizes at sand wave crests/troughs are observed. Fines content ranges between 1.5-1.8% in the uppermost 2 metres of the seabed. There is no clear trend in grain size or fines content with depth below the seabed. Although median grain sizes indicate a slight decrease with depth in IJV, the spatial distribution is more scattered. The results imply that non-erodible layers in the subsurface of IJV are not likely to affect the seabed morphodynamics, because they are too deep (based on observed and expected seabed dynamics) or too sparsely spread to be exposed by the seabed dynamics.

For Sites III and IV, the maximum predicted seabed lowering over 2022-2072 is approximately -3.21 m and -3.25 m, respectively (99.9% non-exceedance values), observed mainly at locations of existing sand wave crests. The maximum predicted seabed rise over 2022-2072 is approximately 4.42 m and 4.17 m for Sites III- and IV, respectively (99.9% non-exceedance values), observed mainly along the sand wave slopes.

For the future and hindcast predictions, upward and downward uncertainty estimates from different sources (data collection, grid resolution, sand wave reshaping, megaripple dynamics, and large-scale seabed variations related uncertainties) are applied. No additional safety margins for design purposes have been applied. The effect of future human interventions such as beach nourishments or dredging operations is not considered in the predicted seabed level changes.

7.2.1.3 Sites V-VI

The bathymetry in Sites V-VI is characterised by a number of north-south oriented sand banks with heights ranging from a few metres up to 10 m. In Site V a number of sand waves overlaid by megaripples are observed, while in Site VI no sand waves are observed. The sand waves have heights of 1.16 m (50% non-exceedance value, Table 7.1). Sand wave lengths range between 381 and 787 m, longer compared to sand waves in the other Sites. The sand waves migrate towards the north-northeast with a mean best estimate direction of 50° relative to the north. Typical migration rates range between -0.42 m/yr and 0.72 m/yr ($p_{5\%}$ and $p_{95\%}$ of migration rates for the individual Site, negative values indicate migration a direction opposite of the prevailing direction).

Similar to the rest of the Sites, no trends of large-scale seabed level changes were observed in the available data. The uncertainty in the long-term large-scale seabed level changes is incorporated in the predictions by including a yearly increasing value of 0.01 m/year, both vertically upward and downward.

Megaripples overlay sand banks and sand waves present in Sites V-VI. Their dimensions are smaller compared to megaripples observed in other Sites. Although the observed variation in megaripple dimensions is limited, megaripple occurrence and dimensions are expected to be highly variable in time. Megaripple dynamics have been incorporated as an uncertainty parameter in predicting seabed levels.

Median grain size diameters range between 0.077 and 0.214 mm for the first five metres below the seabed in Sites V-VI. Locally spots of coarser grain sizes at sand wave crests/troughs are observed. Fines content ranges between 1.0-2.0% in the uppermost 2 metres of the seabed. It is found that in Sites V-VI the grain sizes become significantly finer with increasing depth below the seafloor. Additionally, half of the samples from Site V-VI consisted of a significant percentage of fines whilst the percentages for the other half showed values similar to Sites I-IV. The results imply that non-erodible layers in the subsurface of IJV are not likely to affect the seabed morphodynamics, because they are too deep (based on observed and expected seabed dynamics) or too sparsely spread to be exposed by the seabed dynamics.

Sites V-VI present the lowest predicted seabed level lowering and rising due to the absence/ scarcity of sand waves. For Sites V and VI, the maximum predicted seabed lowering over 2022-2072 is approximately -1.17 m and -1.92 m, respectively (99.9% non-exceedance values), observed mainly at the location of existing sand wave crests. The maximum predicted seabed rise over 2022-2072 is approximately 1.18 m and 2.23 m for Sites V andVI, respectively (99.9% non-exceedance values), observed mainly along the sand wave slopes.

For the future and hindcast predictions, upward and downward uncertainty estimates from different sources (data collection, grid resolution, sand wave reshaping, megaripple dynamics, and large-scale seabed variations related uncertainties) are applied. No additional safety margins for design purposes have been applied. The effect of future human interventions such as beach nourishments or dredging operations is not considered in the predicted seabed level changes.

7.3 Recommendations

The understanding of the seabed dynamics in IJV is significantly enhanced by this study. However, based on the outcomes in relation to the potential foundation and cable locations, it is recommended to carry out an additional bathymetry survey prior to installation, at locations with significant dynamics at the seabed (e.g. Sites I-IV). For areas with limited seabed dynamics (e.g. the majority of Sites V-VI), the uncertainties are smaller, and the benefit of future surveys is limited. Also, the relative complexity of the seabed including the sand wave dynamics, and initial slopes and bed levels in the vicinity of planned foundations, are best assessed using this new survey.

Future survey data, both geophysical and geotechnical will be of great value to further enhance our understanding of seabed mobility in the entire IJV, both spatially and temporally, and hence improve predictions of future bed levels. It is expected that advances in technology will lead to further reduction of uncertainties associated with the predicted future bed levels in IJV and surroundings. The quality of the results of this study will also benefit from a ground model developed from any future soil investigations.

To avoid uncertainties and inaccuracies due to a lack of data in areas where bedforms which occur outside IJV would be migrating into the offshore windfarm it is advised to extend the surveyed area outside IJV into specific areas because of the long period of operation (up to 2072) and significant seabed mobility present at some locations. With only limited survey coverage at the Site boundaries, the total range of possible seabed changes could be underestimated. Given the observed seabed mobility, extending the surveyed area south of Sites I-II and east of Sites I-III is advised with a distance of approximately 300 m (maximum migration rate of 6 m/year multiplied by the period of 50 years between 2022 to 2072). Alternatively, the band of high uncertainty along the edge of the offshore wind farm area can be accounted for, when planning the locations of the foundations and cables. For example, the additional extension of the surveyed area can be limited only to the actual areas potentially affected.

In a morphodynamically active area, such as the IJV WFZ (Sites I-IV in particular), it is recommended to utilise the results of the morphodynamic assessment throughout the entire design process. By using these results, areas of significant seabed lowering could potentially be avoided and areas that are predicted to be subject to limited/no future change or seabed rise could if possible be targeted for the development of windfarm infrastructure.

References

Allen, J. R. L. (1980). Sand waves: a model of origin and internal structure. *Sedimentary geology, 26*(4), 281-328.

Arcadis Nederland BV, & Geo-Engineering.org GmbH. (2019). Geological Desk Study IJmuiden Ver Wind Farm Zone, reference 180017, Netherlands Enterprise Agency. Retrieved from https://offshorewind.rvo.nl/files/view/efaf435f-3607-46b1-9eab-bf14c88461d4/1637047931202111_ijv_gp_report.pdf

Ashley, G. M. (1990). Classification of large-scale subaqueous bedforms: a new look at an old problem-SEPM bedforms and bedding structures. *Journal of Sedimentary Research, 60*(1).

Battjes, J. A., & Janssen, J. (1978). Energy loss and set-up due to breaking of random waves *Coastal Engineering 1978* (pp. 569-587).

Beets, D. J., Meijer, T., Beets, C. J., Cleveringa, P., Laban, C., & Van der Spek, A. J. F. (2005). Evidence for a Middle Pleistocene glaciation of MIS 8 age in the southern North Sea. *Quaternary International, 133*, 7-19.

Besio, G., Blondeaux, P., Brocchini, M., & Vittori, G. (2004). On the modeling of sand wave migration. *Journal of Geophysical Research: Oceans, 109*(4), 1-13.

Besio, G., & Rodriguez, M. A. L. (2006). Sediment transport patterns in the neighbourhood of cylindrical porous structures: The "Mar de Trafalgar" offshore wind farm. *Coastal Engineering*, 2318-2329.

Booij, N., Ris, R. C., & Holthuijsen, L. H. (1999). A third-generation wave model for coastal regions: 1. Model description and validation. *Journal of Geophysical Research: Oceans, 104*(C4), 7649-7666.

Borsje, B. W., de Vries, M. B., Bouma, T. J., Besio, G., Hulscher, S. J. M. H., & Herman, P. M. J. (2009). Modeling bio-geomorphological influences for offshore sandwaves. *Continental Shelf Research, 29*(9), 1289-1301.

Borsje, B. W., Kranenburg, W. M., Roos, P. C., Matthieu, J., & Hulscher, S. J. M. H. (2014). The role of suspended load transport in the occurrence of tidal sand waves. *Journal of Geophysical Research: Earth Surface, 119*(4), 701-716.

Brettschneider, G. (1967). *Anwendung des hydrodynamisch-numerischen verfahrens zur ermittlung der m (ind. 2)-mitschwingungsgezeit der nordsee*: Institut FUER MEERESKUNDE DER UNIVERSITAET HAMBURG.

Buijsman, M. C., & Ridderinkhof, H. (2008). Long-term evolution of sand waves in the Marsdiep inlet. I: High-resolution observations. *Continental Shelf Research, 28*(9), 1190-1201.

Cameron, D., Van Doorn, D., Laban, C., & Streif, H. (1993). *Geology of the southern North Sea basin.* Paper presented at the Coastlines of the southern North Sea.

Carrère, L., Lyard, F., Cancet, M., Guillot, A., & Roblou, L. (2012). *A new global tidal model taking taking advantage of nearly 20 years of altimetry.* Paper presented at the Proceedings of meeting" 20 Years of Altimetry.

Charnock, H. (1955). Wind stress on a water surface. *Quarterly Journal of the Royal Meteorological Society, 81*(350), 639-640.

Damen, J. M., van Dijk, T. A. G. P., & Hulscher, S. J. M. H. (2018). Spatially varying environmental properties controlling observed sand wave morphology. *Journal of Geophysical Research: Earth Surface, 123*(2), 262-280.

Deltares. (2015). Morphodynamics of Borssele Wind Farm Zone WFS-I and WFS-II; Prediction of seabed level changes between 2015 and 2046. Ref: 1210520-000-HYE-0004; final report, dated 26 June 2015. Retrieved from: https://offshorewind.rvo.nl/file/view/33453652/report-morphodynamical-desk-study-wfs-i-ii-deltares.

Deltares. (2016a). Morphodynamics of Borssele Wind Farm Zone WFS-IV, WFS-III and WFS-V; Prediction of seabed level changes between 2015 and 2046. Ref: 1210520-000-HYE-0012; final report, dated 25 January 2016. Retrieved from

http://offshorewind.rvo.nl/file/view/42115002/report-morphodynamics-bwfs-iv-iii-v-deltares-2016
Deltares. (2016b). Morphodynamics of Hollandse Kust (zuid) Wind Farm Zone; Prediction of seabed level changes between 2016 and 2051. Retrieved from http://offshorewind.rvo.nl/file/view/47910422/report-morphodynamics-of-hollandse-kust-zuid-wind-farm-zone-deltares
Deltares. (2016c). Morphodynamics of Hollandse Kust (zuid) Wind Farm Zone; Prediction of seabed level changes between 2016 and 2051. Ref: 1230851-000-HYE-0003; final report, dated 22 December 2016. Retrieved from http://offshorewind.rvo.nl/file/view/47910422/report-morphodynamics-of-hollandse-kust-zuid-wind-farm-zone-deltares
Deltares. (2019a). Morphodynamics and scour mitigation for Hollandse Kust (noord) Wind Farm Zone. Retrieved from https://offshorewind.rvo.nl/file/view/55040006/Report+-+Morphodynamics+and+Scour+Mitigation+-+Deltares
Deltares. (2019b). Morphodynamics and scour mitigation for Hollandse Kust (noord) Wind Farm Zone. Ref: 11202796-000-HYE-0002; final report, dated 15 March 2019. Retrieved from https://offshorewind.rvo.nl/files/view/e8cfe3eb-6356-475e-b2fd-624e90e34257/1554977804hkn_20190409_deltares_morphodynamics%20and%20scour%20mitigation-f.pdf
Deltares. (2020a). D-Morphology, 1D/2D/3D, D-Morphology in Delta Shell User Manual. Released for Delft3D FM Suite 2020. draft version; dated 15 March 2020. Retrieved from: https://content.oss.deltares.nl/delft3d/manuals/D-Morphology_User_Manual.pdf
Deltares. (2020b). Hollandse Kust (west) Field Measurement Campaign - Validation Report - April 2020. Reference: 11203488-001-HYE-0001; final report dated 18 December 2020.
Deltares. (2020c). Morphodynamics for Hollandse Kust (west) Wind Farm Zone. Retrieved from https://offshorewind.rvo.nl/file/view/55040638/Report+-+Morphodynamical+Investigation+-+Deltares
Deltares. (2020d). Morphodynamics for Hollandse Kust (west) Wind Farm Zone. Ref: 11204811-002-HYE-0001; final report, dated 6 July 2020. Retrieved from https://offshorewind.rvo.nl/file/view/55040638/Report+-+Morphodynamical+Investigation+-+Deltares
Deltares. (2022a). Morphodynamics for Ten noorden van de Waddeneilanden Wind Farm Zone. WOZ2210243. Ref: 11206714-002-HYE-0001; final report, dated 14 February 2022. Retrieved from https://offshorewind.rvo.nl/file/download/4985a940-cf31-4070-aa69-d33ff78c677c/tnw_20220224_deltares_morpho_report-f.pdf
Deltares. (2022b). Scour and scour mitigation for the IJmuiden Ver Wind Farm Zone. WOZ202201045. Ref: 11208404-002-HYE-0002; draft report, dated 14 September 2022.
Deltares. (2023). Scour and scour mitigation for IJmuiden Ver Wind Farm Zone. WOZ2220017. Ref: 11208404-002-HYE-0002. Retrieved from https://offshorewind.rvo.nl/files/view/5704b803-1954-4d8f-a3d7-77c0d0c423ec/ijv_20230207_deltares_scour-and-scour-mitigation-report-f.pdf
DHI. (2019). Metocean desk study and database for Dutch Wind Farm Zones Feasibility level study for IJmuiden-Ver, Ten Noorden van de Waddeneilanden & Hollandse Kust (west). Ref: 11822658; final report, dated: 12 March 2019. Retrieved from https://offshorewind.rvo.nl/files/view/a352572e-de9f-4cbd-b8a1-24d5394152a8/1554278436hkw-tnw-ijv_20190401_metocean_feasibility_dhi_report-portfolio-f.pdf
Dienst Hydrografie. (2007). Memorie Noordzee reductiematrix 2006 (in Dutch). Ministerie van defensie, Koninklijke Marine
Dorst, L. L., Roos, P. C., & Hulscher, S. J. M. H. (2011). Spatial differences in sand wave dynamics between the Amsterdam and the Rotterdam region in the Southern North Sea. *Continental Shelf Research, 31*(10), 1096-1105.
Dorst, L. L., Roos, P. C., Hulscher, S. J. M. H., & Lindenbergh, R. C. (2009). The estimation of sea floor dynamics from bathymetric surveys of a sand wave area. *Journal of applied geodesy, 3*(2), 97-120.

Ehlers, J. (1990). Reconstructing the dynamics of the north-west European Pleistocene ice sheets. *Quaternary Science Reviews, 9*(1), 71-83.
Eisma, D., & Irion, G. (1988). Susupended matter and sediment transport. In, Pollution of the North Sea: an assessment. W. Salomons, BL Bayne, EK Duursma and U. Förstner: Springer Verlag, Berlin.
Eisma, D., Jansen, J., & van Weering, T. C. (1979). Sea-floor morphology and recent sediment movement in the North Sea. *The Quarternary history of the North Sea*, 217-231.
Eisma, D., & Kalf, J. (1987). Dispersal, concentration and deposition of suspended matter in the North Sea. *Journal of the Geological Society, 144*(1), 161-178.
EMODnet Bathymetry Consortium. (2020). EMODnet Digital Bathymetry (DTM 2020). EMODnet Bathymetry Consortium. Retrieved from https://doi.org/10.12770/bb6a87dd-e579-4036-abe1-e649cea9881a
EMODnet Geology. (2019). Harmonised multiscale map of the seabed substrate
Fugro. (2022a). Geophysical Results Report. Geophysical Survey at the IJmuiden Ver Wind Farm Sites V and VI (IJ56) | Dutch Sector, The Netherlands, F192961_REP_007 01, Issue 01, Dated: 22-September-2022. Retrieved from https://offshorewind.rvo.nl/files/view/efaf435f-3607-46b1-9eab-bf14c88461d4/16370479312021111_ijv_gp_report.pdf
Fugro. (2022b). IJmuiden Ver Wind Farm Sites V and VI –Dutch Sector, North Sea Field and Environmental Data Report Environmental Sampling Locations, F192961_REP_009, Issue 03, Dated: 30-August-2022
Fugro. (2022c). IJmuiden Ver Wind Farm Sites V and VI –Dutch Sector, North Sea Geotechnical Data – Investigation Data Seafloor In Situ Test Locations and Sample Locations, F192961_REP_008, Issue 02, Dated: 19-September-2022
Fugro. (2022d). IJmuiden Ver Wind Farm Zone –Dutch Sector, North Sea Geotechnical Data – Investigation Data Geotechnical Borehole Locations – High Priority Area, F172957/03, Issue 03, Dated: 13-June-2022
Fugro. (2022e). IJmuiden Ver Wind Farm Zone –Dutch Sector, North Sea Geotechnical Data – Investigation Data Geotechnical Borehole Locations – Low Priority Area, F172957/04, Issue 02, Dated: 24-June-2022
Fugro. (2022f). IJmuiden Ver Wind Farm Zone –Dutch Sector, North Sea Geotechnical Data – Investigation Data Seafloor In Situ Test Locations, F172957/01, Issue 06, Dated: 18-March-2022. Retrieved from https://offshorewind.rvo.nl/files/view/03baced5-aac2-4cd0-ad0f-d5c362cfb87b/ijv_20220714_fugro_seafloor-in-situ-testlocations_report-f.pdf
Fugro. (2022g). IJmuiden Ver Wind Farm Zone –Dutch Sector, North Sea Geotechnical Data – Investigation Data Seafloor Sample Locations, F172957/02, Issue 06, Dated: 22-April-2022
GEOxyz. (2021). Final Survey Report, Geophysical Survey - Ijmuiden Ver Wind Farm Zone, Document number: BE3445H-634-FR-03-3.0, Revision : 3.0, Dated: 01-May-2021. Retrieved from https://offshorewind.rvo.nl/files/view/efaf435f-3607-46b1-9eab-bf14c88461d4/16370479312021111_ijv_gp_report.pdf
Hasselmann, K., Barnett, T., Bouws, E., Carlson, H., Cartwright, D., Enke, K., . . . Kruseman, P. (1973). Measurements of wind-wave growth and swell decay during the Joint North Sea Wave Project (JONSWAP)
Hijma, M. P., & Cohen, K. M. (2010). Timing and magnitude of the sea-level jump preluding the 8200 yr event. *Geology, 38*(3), 275-278.
Hijma, M. P., Cohen, K. M., Roebroeks, W., Westerhoff, W. E., & Busschers, F. S. (2012). Pleistocene Rhine–Thames landscapes: geological background for hominin occupation of the southern North Sea region. *Journal of quaternary science, 27*(1), 17-39.
Houthuys, R., Trentesaux, A., & De Wolf, P. (1994). Storm influences on a tidal sandbank's surface (Middelkerke Bank, southern North Sea). *Marine Geology, 121*(1), 23-41.
Hulscher, S. J., de Swart, H. E., & de Vriend, H. J. (1993). The generation of offshore tidal sand banks and sand waves. *Continental Shelf Research, 13*(11), 1183-1204.

Hulscher, S. J. M. H. (1996). Tidal-induced large-scale regular bed form patterns in a three-dimensional shallow water model. *Journal of Geophysical Research: Oceans, 101*(C9), 20727-20744.
Huntley, D., Huthnance, J., Collins, M., Liu, C.-L., Nicholls, R., & Hewitson, C. (1994). Hydrodynamics and sediment dynamics of North Sea sand waves and sand banks *Understanding the North Sea System* (pp. 83-96): Springer.
Huthnance, J. M. (1982). On one mechanism forming linear sand banks. *Estuarine, Coastal and Shelf Science, 14*(1), 79-99.
Idier, D., & Astruc, D. (2003). Analytical and numerical modeling of sandbanks dynamics. *Journal of Geophysical Research: Oceans, 108*(C3).
International Hydrographic Organization. (2020). Standards for Hydrographic Surveys 6th edition. IHO publication No. 44. Retrieved from https://iho.int/uploads/user/pubs/Drafts/S-44_Edition_6.0.0-Final.pdf
Knaapen, M. A. F., & Hulscher, S. J. M. H. (2002). Regeneration of sand waves after dredging. *Coastal Engineering, 46*(4), 277-289.
Lankneus, J., & Moor, G. (1991). Present-day evolution of sand waves on a sandy shelf bank. *Oceanologica acta, Special issue*.
Le Bot, S. (2001). *Morphodynamique de dunes sous-marines sous influence des marées et des tempêtes: processus hydro-sédimentaires et enregistrement: exemple du Pas-de-Calais.* Lille 1.
Lesser, G. R., Roelvink, J. A., Van Kester, J. A. T. M., & Stelling, G. S. (2004). Development and validation of a three-dimensional morphological model. *Coastal Engineering, 51*(8-9), 883-915.
Luijendijk, A., Hagenaars, G., Ranasinghe, R., Baart, F., Donchyts, G., & Aarninkhof, S. (2018). The State of the World's Beaches. *Scientific reports, 8*.
Lyard, F., Lefevre, F., Letellier, T., & Francis, O. (2006). Modelling the global ocean tides: modern insights from FES2004. *Ocean Dynamics, 56*(5-6), 394-415.
Malikides, M., Harris, P., & Tate, P. (1989). Sediment transport and flow over sandwaves in a non-rectilinear tidal environment: Bass Strait, Australia. *Continental Shelf Research, 9*(3), 203-221.
Maljers, D., & Gunnink, J. (2007). Interpolation of measured grain-size fractions. Retrieved from https://publicwiki.deltares.nl/display/OET/Dataset+documentation+TNO+NCP+grain+size+maps
McCave, I. N. (1971). Sand waves in the North Sea off the coast of Holland. *Marine Geology, 10*(3), 199-225.
Morelissen, R., Hulscher, S. J. M. H., Knaapen, M. A. F., Németh, A. A., & Bijker, R. (2003). Mathematical modelling of sand wave migration and the interaction with pipelines. *Coastal Engineering, 48*(3), 197-209.
Nauw, J., de Haas, H., & Rehder, G. (2015). A review of oceanographic and meteorological controls on the North Sea circulation and hydrodynamics with a view to the fate of North Sea methane from well site 22/4b and other seabed sources. *Marine and Petroleum Geology, 68*, 861-882.
Otto, L., Zimmerman, J., Furnes, G., Mork, M., Saetre, R., & Becker, G. (1990). Review of the physical oceanography of the North Sea. *Netherlands journal of sea research, 26*(2-4), 161-238.
Papili, S., Wever, T., Dupont, Y., & Van Lancker, V. (2014). Storm influence on the burial of objects in a shallow sandy shelf environment. *Marine Geology, 349*, 61-72.
Passchier, S., & Kleinhans, M. G. (2005). Observations of sand waves, megaripples, and hummocks in the Dutch coastal area and their relation to currents and combined flow conditions. *Journal of Geophysical Research: Earth Surface, 110*(F4).
Peeters, J., Busschers, F. S., & Stouthamer, E. (2015). Fluvial evolution of the Rhine during the last interglacial-glacial cycle in the southern North Sea basin: a review and look forward. *Quaternary International, 357*, 176-188.
Peters, S. E., & Loss, D. P. (2012). Storm and fair-weather wave base: A relevant distinction? *Geology, 40*(6), 511-514.

Roetert, T. J., Raaijmakers, T. C., & Borsje, B. W. (2017, June 25-30). *Cable route optimization for offshore wind farms in morphodynamic areas.* Paper presented at the The 27th International Ocean and Polar Engineering Conference, San Francisco, CA, USA.

Rogers, W. E., Hwang, P. A., & Wang, D. W. J. J. o. P. O. (2003). Investigation of wave growth and decay in the SWAN model: three regional-scale applications. *33*(2), 366-389.

Royal Netherlands Navy - Hydrographic Office. (1980-2021). Online availaility of data of the Netherlands Hydrographic Service. Retrieved from https://english.defensie.nl/topics/hydrography/documents/letters/2020/06/24/online-availability-of-data-from-the-hydrographic-service

RPS. (2022a). TN328326 Supply of Metocean Data for IJmuiden Ver Investigation Area, Monthly Measurement and Validation Report (MMF03707.000, 100-CN-REP-2007 Rev 1)

RPS. (2022b). TN328326 Supply of Metocean data for IJmuiden Ver Investigation Area. Monthly Measurement and Validation Report - IJV May 2022. MMF03707.000 100-CN-REP-2007 Rev 1, Dated: 12-August-2022. Retrieved from https://offshorewind.rvo.nl/files/view/746f5bd3-c5c8-4884-af52-2e4b1f63c212/ijv-rps-metocean-data-and-report-may-2022-1.zip

Sterlini, F., Hulscher, S. J. M. H., & Hanes, D. M. (2009). Simulating and understanding sand wave variation: A case study of the Golden Gate sand waves. *Journal of Geophysical Research: Earth Surface, 114*(F2).

Sterlini, F. M., van Dijk, T. A. G. P., IJzer, S., & Hulscher, S. J. M. H. (2012). *Seasonal changing sand waves and the effect of surface waves.* Paper presented at the 5th International Short Conference on Applied Coastal Research (SCACR 2011), Aachen, Germany.

Sündermann, J., & Pohlmann, T. (2011). A brief analysis of North Sea physics. *Oceanologia, 53*(3), 663-689.

Terwindt, J. H. J. (1971). Sand waves in the Southern Bight of the North Sea. *Marine Geology, 10*(1), 51-67.

United Kingdom Hydrographic Office. (1977-2021). ADMIRALTY Marine Data Portal - Seabed Mapping Service. from https://seabed.admiralty.co.uk/

Valerius, J., Van Lancker, V., Van Heteren, S., Leth, J. O., & Zeiler, M. (2015). Trans-national database of North Sea sediment data. Data compilation by Federal Maritime and Hydrographic Agency (Germany); Royal Belgian Institute of Natural Sciences (Belgium); TNO (Netherlands) and Geological Survey of Denmark and Greenland (Denmark)., Tech. rep., 2015.

Van Dijk, T. A. G. P., C. Van der Tak, W.P. De Boer, M.H.P. Kleuskens, P.J. Doornenbal, R.P. Noorlandt and V.C. Marges. . (2011). The scientific validation of the hydrographic survey policy of the Netherlands Hydrographic Office, Royal Netherlands Navy. *Deltares, Report 1201907-000-BGS-0008: 165 pp.* doi: http://publications.deltares.nl/1201907_000.pdf

Van Dijk, T. A. G. P., & Egberts, P. J. P. (2008). *The variability of sand wave migration in the North Sea.* Paper presented at the Proceedings of the 3rd international workshop on Marine Sand waves and River Dune Dynamics, Leeds (UK), University of Leeds.

van Dijk, T. A. G. P., & Kleinhans, M. G. (2005). Processes controlling the dynamics of compound sand waves in the North Sea, Netherlands. *Journal of Geophysical Research: Earth Surface, 110*(F4).

Van Dijk, T. A. G. P., Lindenbergh, R.C., Egberts, P.J.P. (2008). Separating bathymetric data representing multi-scale rhythmic bedforms: a geostatistical and spectral method compared. *Journal of Geophysical Research, 113*(F04017). doi: 10.1029/2007JF000950

Van Gerwen, W., Borsje, B. W., Damveld, J. H., & Hulscher, S. J. M. H. (2018). Modelling the effect of suspended load transport and tidal asymmetry on the equilibrium tidal sand wave height. *Journal of Coastal Engineering, 136*, 56-64.

Van Lancker, V., & Jacobs, P. (2000). *The dynamical behaviour of shallow-marine dunes.* Paper presented at the Proceedings of the International Workshop on Marine Sandwave Dynamics/TRENTESAUX A., GARLAN T.,(eds.).-Lille: University of Lille 1, 2000.

van Rijn, L. C. (1984a). Sediment Transport, Part I: Bed Load Transport. *110*(10), 1431-1456. doi: doi:10.1061/(ASCE)0733-9429(1984)110:10(1431)
van Rijn, L. C. (1984b). Sediment Transport, Part II: Suspended Load Transport. *110*(11), 1613-1641. doi: doi:10.1061/(ASCE)0733-9429(1984)110:11(1613)
van Rijn, L. C. (1990). Sediment Transport in combined Currents and Waves. Euromech 262, Sand Transport, Wallingford, United Kingdom.
Van Rijn, L. C. (2007a). Unified view of sediment transport by currents and waves. I: Initiation of motion, bed roughness, and bed-load transport. *Journal of Hydraulic Engineering, 133*(6), 649-667.
Van Rijn, L. C. (2007b). Unified view of sediment transport by currents and waves. II: Suspended transport. *Journal of Hydraulic Engineering, 133*(6), 668-689.
Van Rijn, L. C. (2007c). Unified view of sediment transport by currents and waves. III: Graded beds. *Journal of Hydraulic Engineering, 133*(7), 761-775.
Van Santen, R. B., De Swart, H. E., & Van Dijk, T. A. G. P. (2011). Sensitivity of tidal sand wavelength to environmental parameters: A combined data analysis and modelling approach. *Continental Shelf Research, 31*(9), 966-978.
Van Veen, J. (1935). Sand waves in the North Sea. *Hydrogr. Rev, 12*(1), 21.
Wu, J. (1982). Wind-stress coefficients over sea surface from breeze to hurricane. J. Geophys. Res., 87 (C12), 9704-9706.
Zijl, F., & Groenenboom, J. (2019). Development of a sizth generation model for the NW European Shelf (DCSM-FM 0.5nm), Model setup, calibration and validation
Zijlema, M., Van Vledder, G. P., & Holthuijsen, L. J. C. E. (2012). Bottom friction and wind drag for wave models. *65*, 19-26.

A Methodology

A.1 Introduction

In this appendix the methodology for performing the seabed mobility assessment in IJV is presented. The analyses comprise of three main steps:

1. Data-driven analysis to derive historic seabed level trends;
2. Numerical modelling to derive sediment transport patterns to validate the results of the data-driven analysis and the impact of extreme events on the seabed;
3. Extrapolation of historic trends to future and historic seabed levels.

This chapter gives an overview of the approach for the data-driven analysis, the numerical modelling and the data extrapolation in Appendices A.2, A.3 and A.3.3.3 respectively.

A.2 Methodology for data-driven analysis

A.2.1 Overview

The focus of the data-driven analysis is to use the data presented in Chapter 2. The data-driven analysis presented here focuses on the dynamics of the seabed. The methodology for performing the data-driven analysis in this study consists of five distinct steps of which some contain sub steps. These steps are the following:

1. the data presented in Chapter 2 is reviewed and processed. From this a general overview of the site conditions is presented based on the processed bathymetry surveys and available geotechnical information;
2. an overview of the area from a morphodynamic point of view is given and the seabed is split in separate layers, each containing information on a single type of bedform;
3. a dedicated sand wave analysis is presented focussing on determining sand wave dynamics and dimensions;
4. a dedicated analysis on the dynamics of the large-scale seabed (i.e. the seabed underlying the smaller scale bedforms) is presented;
5. the smallest scale bedforms are analysed to be included as part of the uncertainty band;

It is noted that the above steps 1 to 5 can be applied to offshore environments with relatively mild climates such as the North Sea. In case larger-scale bed features such as coastal sand banks show horizontal displacement over a period of years to decades a similar approach as discussed under step four is applied. Each of these steps including sub steps is elaborated separately in the remainder of this section.

A.2.2 Step 1: Review and processing of available data

To prepare the data-driven analysis, the bathymetrical and geotechnical data presented in Chapter 2 is first reviewed and processed. This section discusses the methodology for processing the bathymetrical data and geotechnical data in Sections 2.2 and 2.3 respectively.

A.2.2.1. Review and processing of bathymetrical data

All available bathymetry data presented in Section 2.2 is interpolated (by means of inverse distance weighting) or resampled to a resolution of 5x5 m for the analysis presented in the remainder of this report. The resampling is done by either taking a single point each 5 metre from the original dataset or in case this is not possible (e.g. with a 2x2 m resolution) by means of inverse distance weighting. A resolution of 5x5 m is used to enhance computational efficiency while still maintaining sufficient resolution to resolve sand waves.

The 5x5 m resolution used is deemed sufficient to achieve the goal of this study and derive historic seabed trends and extrapolate those into future seabed levels. It is noted that smaller scale bedforms, such as megaripples are not fully resolved with the 5x5 m resolution (mostly 2-3 points per megaripple). These smaller scale bedforms are however very dynamic, spatially and temporal changing in dimensions and dynamics (see Section 4.6) and cannot be tracked between subsequent surveys. Characteristics are included in the extrapolation of seabed levels (see also Section 4.6).

It is stressed that the information lost as a result of thinning out the data (e.g. crests and troughs of smaller scale bedforms such as megaripples) is taken into account in the analysis as the grid resolution uncertainty. To determine the grid resolution uncertainty the original bathymetry resolution is used. Background to this is given in Appendix A.4.5.1 where the grid resolution uncertainty is described.

No interpolation of missing data is performed as this could lead to over- or underestimation of seabed dynamics. All surveys were checked for errors in the vertical reference levels, e.g. in case a survey is on average significantly deeper than all other surveys, and if required this was corrected. If found that surveys are subject to too large uncertainties or too limited spatial resolution, then those are excluded from the analysis.

As a basis for checking errors in the vertical reference levels, the most recent data was used. The average difference between surveys gives a good indication of possible vertical referencing errors. This is under the assumption that average values rule out differences as a result of sand wave migration and that large-scale morphodynamics are negligible over the period between the two surveys.

Often the available surveys do not cover the entire area of interest. To make the data-driven analysis more efficient, i.e. less comparisons of individual surveys, composite bathymetries are created. In essence, individual bathymetries are grouped for more efficient data processing as discussed specifically for the area of interest in Section 4.2.1.

Bathymetry surveys separated by the smallest possible timespan are grouped and, to the extent possible, the entire area is covered. Overlap between surveys in a single composite bathymetry is kept minimal. The original time stamp per survey, defined as the day halfway through the period in which the specific patch was surveyed, is retained and applied in the further analysis.

Anomalies influencing (local) seabed morphodynamics, such as shipwrecks and pipeline free spans, are only partly considered in the morphodynamic analysis in this report. For the seabed predictions, the anomalies are assumed to be fixed objects and sand waves can migrate over them freely. Even though only partly included in this study, it must be stressed that the effect of e.g. shipwrecks may significantly change over time and care should be exercised if constructing close to such objects. However, effects will be spatially limited to the vicinity of the structure and normally not more than up to ten times the size of the object.

A.2.2.2. Review and processing of other geophysical and geotechnical data

All available geophysical, other than bathymetrical data, and geotechnical data presented in Section 2.3 is reviewed and processed such that a description of the top sediment layer is created to support the understanding of the dynamics of the seabed. The collected data was used to extract the sequencing of the geological layers over the considered area and more specifically the thickness and spatial distribution of the top sediment characteristics. This review and processing of the relevant geophysical and geotechnical data is used to describe areas with similar expected seabed dynamics. No additional interpretation of the geophysical data other than to check the derived geological layers is performed.

The goals of the analyses are twofold: first, to establish how the composition of the substrate in the area may affect future seabed level variations and second, to evaluate the added value of the geotechnical campaign with Vibrocores to investigate future morphodynamics. Specifically, the analysis focused on the presence of non-erodible layers within the upper 20 m of the substrate and the grain size variation within the upper 5 metres. Non-erodible layers are clay, silt, or peat layers characterised by high stiffness and resistance to erosion.

The analysis is based on data from the recent measurement campaign by presented in Section 2.3 and uses the following methodology:

Borehole analysis
The available boreholes were analysed for presence of NEL, for the average sand grain size (D50) and for the percentage of fines.

Vibrocore analysis
Lithological description, fines, sand and gravel fraction and D50 are visualized to produce cross-sections at locations with multiple Vibrocores measurements, e.g. over a single bedform. These cross-sections were analysed to investigate lateral and vertical variations in grain size. In addition, the Vibrocore data was compared to sand wave morphology and migration rate to investigate the possible effect of grain size variations on sand wave migration.

For all other Vibrocore locations available data is used for determination of the grain size diameter across IJV. It should be noted that the grain size analysis, specifically the D50 values, were calculated based on the bulk sediment sample, including gravel, shells and fines. The produced values are considered an overestimation of the sand D50. The D50 value of the sand fraction would have produced more interesting results for the goal of the project.

A.2.3 Step 2: Morphodynamic overview of the area and splitting of bedforms

Based on the review and processing of data a short description of the seabed composition and expected dynamics is given. This basic understanding is used to distinguish between the various morphodynamic processes in the area of interest. From the general description of seabed dynamics in Section 3.3 it was found that different types of bedforms can be present each having distinct morphodynamic characteristics.

For the further analysis, the different types of bedforms are separated to be analysed individually. Separate layers are created for the sand waves, the large-scale underlying seabed. To start the migrating part of the bathymetry has been separated from the underlying, large-scale bathymetry. For this purpose, a coarse spatial filtering of the bathymetry was applied on the available surveys. The filter size was chosen such that the mobile bedforms (i.e. sand waves and megaripples) could be removed, while the underlying bathymetry remains unaltered in shape and is not noticeably smoothened by the filtering process. The similar process is repeated for splitting the sand waves and the megaripples.

The specific orientation and dimensions of the filter are obtained following an iterative process analysing multiple orientations and multiple sizes of the filter. Results are analysed by comparing gradients present in the underlying large-scale bathymetry indicating still present sand wave information. Furthermore, the mobile bathymetries are checked by the extent to which the large-scale seabed was present. A perfect mobile bathymetry should depict only bedforms fluctuating around zero. The filtering for which splitting of bedforms provided the best results is used to derive the layers with the various bedforms in IJV. These layers form the basis for the data-driven analysis as well as for the assessment of future and historic seabed levels as discussed in Appendix A.3.3.3 and Chapter 6.

In the remainder of this document the definitions of the various spatial bathymetrical data fields as explained in Table A.1 are used.

Table A.1: Definitions of various bathymetrical data fields used in this study.

Short name	Description	Large-scale seabed	Sand waves	Megaripples
Bathymetry	Full measured bathymetry including all bedforms	√	√	√
Large-scale bathymetry	Filtered bathymetry with the large-scale seabed only	√	X	X
Mobile bathymetry	Filtered bathymetry with sand waves and megaripples only	X	√	√
Sand wave field	Filtered bathymetry with sand waves only	X	√	X
Megaripple Field	Filtered bathymetry with megaripples only	X	X	√

A.2.4 Step 3: Analysis of sand wave dynamics

To derive historical trends of seabed dynamics a data-driven analysis is performed for each bedform type discussed in Section 3.3 and Figure 3.2. This section focusses on the analysis of sand waves which are considering their timescales of migration (order of years) and their dimensions (several metres high) of biggest importance to the foundation fixation levels and cable burial depths. In this, the following three sub steps are included:

i) Determination of sand wave analysis locations;
ii) Determination of sand wave dynamics;
iii) Determination of sand wave dimensions.

It is noted that the below steps can be applied to offshore environments with relatively mild climates such as the North Sea. In case larger-scale bed features such as coastal sand banks show horizontal displacement over a period of years to decades a similar approach as discussed under step two is applied.

In the analysis the sand wave field is used for the first two steps as this excludes noise in the signal as a result of the presence of the smaller scale bedforms. For the third step the mobile bathymetry is used as this describes the full sand wave heights. Each of the sub steps is further elaborated in more detail in the remainder of this section.

A.2.4.1. Sand wave analysis locations

In the sand wave analysis, an approach specifically focussing on quantifying the dynamics and characteristics of the individual sand waves is applied. To start, sand wave crests are identified, and a number of analysis locations are defined along these crests spaced with a distance of approximately 50 to 100 metre. The detection of crests is performed in a similar way as presented in Appendix A.2.4.3. First a grid for the analysis area from the available bathymetry data is created with the columns roughly perpendicular to the sand waves. From this grid each column is analysed and local maxima (crests) and minima (troughs) were extracted.

This way, each individual sand wave is analysed by a number of locations indicating spatial variability along such a sand wave. The analysis locations defined are used for the further sand wave analysis.

A.2.4.2. Sand wave dynamics

For the analysis of sand wave dynamics, the mobile bathymetries of all available composite bathymetries are analysed by comparing all bathymetries to each other. For every possible comparison all analysis locations are analysed indicating both spatial and temporal (only when the number of surveys at a given location is larger than two) variability across the area of interest.

The sand wave dynamics are evaluated using a 2D cross-correlation. This technique computes local morphodynamics by using the horizontal translations of bedforms from bathymetrical surveys. An example of this technique is presented in Figure A.1, for an area around an analysis location. The size of the considered area is chosen such that at least a significant part of one sand wave is covered. It is also important to limit the area such that sand wave dynamics can be assessed locally. The figure indicates the shift between the two surveys (black and blue polygons) by means of the red arrow.

The presented method is proven to be such that even bathymetries with lower spatial resolution (e.g. a resolution of approximately 50x50 m) can be used to assess sand wave dynamics. Often older bathymetries have this limited resolution but do provide information on the long-term sand wave dynamics.

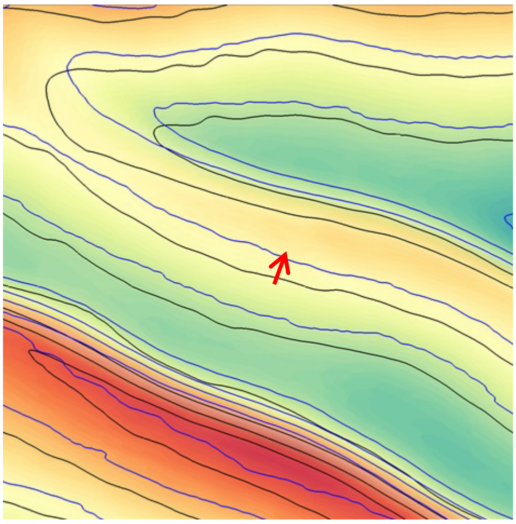

Figure A.1: Example of the 2D cross correlation. The red arrow indicates the highest correlation found between an older (black contour lines) and a more recent bathymetry (blue contour lines and presented as the figure background) with the arrow length indicating migration distance and the orientation migration direction.

Based on the above presented method the sand wave migration direction, direction of the arrow, and the sand wave migration distance, length of the arrow, are estimated for the entire analysis area. The sand wave migration rate is derived by dividing the migrated distance as derived from a comparison by the difference in measurement dates of the two bathymetries in comparison.

This resulted in a single value for the direction and rate per analysis location per survey comparison. It is noted that no values are found if one or both surveys contain insufficient data for the specific analysis location. To capture the full temporal variability of sand wave dynamics at each of the analysis locations, local variations over time are quantified. More specifically, for each analysis location the distribution of the migration directions and rates of all the neighbouring locations within a selected distance is calculated. The distance is selected such that the enclosed area is small enough to maintain local information but at the same time it should contain enough points to determine probability distributions.

Sand waves migrating in opposite direction might cause issues when determining the spread in migration directions. Averaging the migration direction for sand waves migrating in opposite migration directions can result in a resulting average migration direction perpendicular to the true direction of migration. This can occur when determining the spread in migration directions for a single analysis location or when interpolation is performed between several analysis locations.

To cover for sand waves migrating in opposing directions first a prevailing direction of migration is determined. Since sand waves are characterised by a steeper lee slope oriented in the direction of migration, the most prevailing direction of this lee slope is considered. All sand waves migrating roughly opposite of this direction are considered to have a negative migration rate, hence the direction of migration is flipped 180 degrees. For example, when the prevailing direction of migration is 20°N and a sand wave is migrating with two metres per year towards 190°N this, the sand wave is considered to migrate with a rate of minus two metres per year towards 10°N.

To include present spatial and temporal variation of migration directions and rates, a lower and upper bound migration direction are introduced, two times the standard deviation to the left and to the right of the mean migration directions and rates. Including these variations reduces uncertainties in the temporal evolution of sand wave migration directions and rates. The resulting bandwidths including mean values are used in the assessment of future and historical seabed levels.

A.2.4.3. Sand wave dimensions

For the analysis of the sand wave characterization in terms of wave height, a Fourier analysis is used (Van Dijk, 2008). This characterisation is used to check if sand waves retain heights over time. During the Fourier analysis transects are drawn at the previously defined sand wave analysis locations in the direction of sand wave migration. The length of these transects is chosen such that it at least covers a single sand wave. For each transect the crest and trough points are automatically determined as shown in Figure A.2. A Fourier series was fitted to the identified extremes by solving an overdetermined system of equations (Van Dijk, 2008). The sand wave heights and lengths are hence deduced from the corresponding Fourier series.

For the sand wave heights, the vertical difference between the average amplitude of two subsequent troughs is compared to the crest height. The sand wave length is calculated from the horizontal distance between two sand wave troughs. The sand wave heights and lengths are hence easily deduced from the corresponding Fourier series. This analysis is performed for all composite bathymetries.

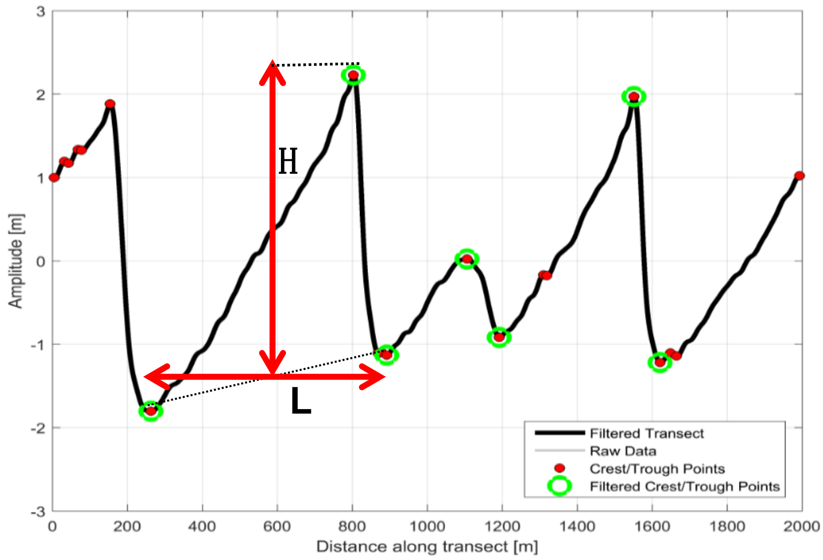

Figure A.2: Example of Fourier analysis on one transects from SW (left) to NE. The plot indicates the Fourier approximations of a sand wave signal (black line). Red dots indicate crest and trough point and the green circles indicate which points have been selected for analysis. The H indicates the sand wave height as calculated. It is noted that the raw data line is covered by the filtered transect (black line).

To investigate how well the sand waves retain their shape over periods of multiple years, sand wave dimensions obtained from one composite bathymetry are compared to sand wave dimensions from a second bathymetry. The correlation between bedform dimensions of two composite bathymetries is indicated by the Pearson Product-Moment Correlation coefficient (PMCC) in which a value of 1 would mean a total linear correlation. It is noted that patched bathymetries with limited spatial resolution (i.e. not able to fully resolve sand wave heights) and comparisons with limited temporal spread (e.g. less than a couple of years) are not considered when determining how well sand waves retain their shapes.

A.2.5 Step 4: Analysis of large-scale seabed dynamics

The analysis of large-scale seabed dynamics (such as sand banks or other large-scale patterns) is based on temporal difference plots between the patched surveys. Large-scale seabed changes associated with overall lowering or rising of (larger parts of) the seabed, can be quantified by computing differences between surveys. Here bathymetrical surveys are interpolated to a common grid and the vertical seabed changes (dz) are computed per grid point and divided by the time difference between the two surveys (dt).

The vertical dynamic trend was determined using a linear least squares technique. This means that a best fit is determined with linear regression based on all bed levels in the stacked time series per node (Figure A.3). To ensure that the analysis is not influenced by the dynamic rhythmic bedforms, such as sand waves and megaripples, the spatially filtered Large-scale Bathymetry is applied in the analysis.

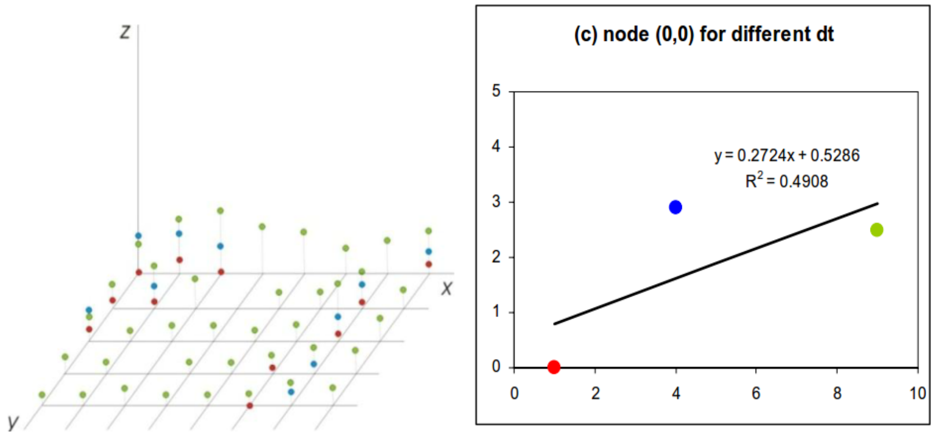

Figure A.3: Illustration of bathymetries which differ in location, density, method and period of surveying (left). At each node, the timeseries is calculated into a trend in vertical bed dynamics in m/year (right) (after Van Dijk, 2011).

In order to determine the large-scale seabed dynamics, a comparison is made which is an dz/dt overview of the area based on all available composite bathymetries. Possible vertical offsets in seabed levels are corrected as part of the data review and processing. It may be noted that for the composite bathymetries the original time stamp is used for computing the yearly variation.

A.2.6 Step 5: Analysis of smaller scale bedforms

As explained in Section 3.3, megaripples (and ripples) have migration rates that are so large that many megaripples will pass at each foundation throughout the lifetime of wind farms. Therefore, megaripple dynamics are not analysed and only information on their dimensions and to use this information in the prediction of bed levels (see also Appendix A.3.3.3). This is further stimulated by the fact that megaripple occurrence and dimensions are highly variable in time.

For determining dimensions of the megaripples, the megaripple field on a one by one-metre resolution is used. For this only the bathymetries with high spatial resolution can be used as coarser spaced bathymetries do not contain detailed information on megaripple dimensions. Furthermore, due to the high variability in space and time of megaripples it is not possible to be correlated between surveys.

Note that as an artefact of the filtering around the sand wave crest, the crest can be visible in the megaripple field (largest amplitudes in the extracted megaripple field). As these artefacts vary spatially, it is deemed not possible to distinguish between a sand wave crest and possible megaripples located on top of the sand wave crest. i.e. filtering the megaripples out gives an underestimation of sand wave heights, while disregarding the megaripples crests during filtering can give an overestimation of the sand wave height in the sand wave field. Therefore, the unfiltered mobile bathymetry is applied in the assessment of future and historic seabed levels. The additional uncertainty in spatial and temporal variation of megaripples is covered in as an uncertainty in the seabed predictions.

A.3 Methodology for numerical modelling

To increase our understanding of the system and to support the data-driven analysis, a numerical model was setup in Delft3D-Flexible Mesh (FM), to simulate hydrodynamics and sediment transports over IJV. The basis of this Delft3D-FM model is the DCSM-FM model which is refined in this case for IJV. The depth-averaged model was validated against current and water level measurements over multiple months for a number of locations. Moreover, a detailed wave model was set up to predicts the effects of waves on sediment transport rates during normal conditions and extreme storm events. Similar to the hydrodynamic model, the wave model was validated against in-situ timeseries for a period of multiple months in a number of locations.

Following the validation of the hydrodynamic models, the built-in sediment transport module was applied to simulate the sediment transports over IJV. The sediment transport model is run to verify and better understand the driving forces and their variability related to possible sand wave migration, for which the methodology is discussed in Appendix A.3.3. Based on the numerical model results, insights are gained in the variability of sediment transport patterns over various timescales (during a single tide, over a spring-neap tidal cycle, intra-annually, inter-annually). To this end, the contribution of bed load and suspended sediment transport to the total transport is assessed separately. Additionally, the sensitivity of residual sediment transports to changes in the assumed sediment diameter is assessed.

Next, the hydrodynamic model was coupled with the wave model to account for the effects of waves on the seabed mobility. In the coupled runs, information was exchanged between the hydrodynamic and wave models resulting in a two-way wave-current interaction. First, hindcast simulation of a single full calendar year was performed. This served to assess the spatial and temporal variability of sediment transport rates IJV, where normal wave conditions are expected to have an influence on the sediment transport rates. In that sense, the coupled runs complement spatially the hindcast sediment transport runs that exclude waves.

Moreover, the hydrodynamic model was coupled with the wave model to simulate sediment transport patterns during extreme storm events. To this end, synthetic storm events of typical design conditions (RP50 and RP 100) were simulated by imposing associated forcing conditions to the hydrodynamic and wave models.

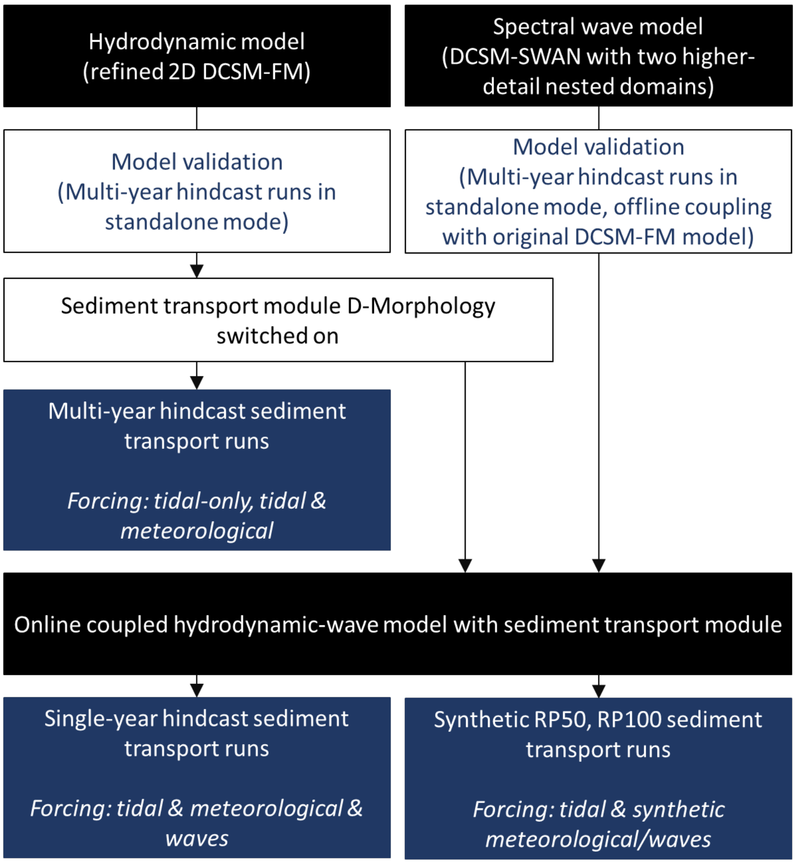

Figure A.4: Overview of numerical modelling approach.

Appendix A.3.1 describes the setup and validation of the hydrodynamic model based on Deltares' Delft3D Flexible Mesh software. Subsequently, Appendix A.3.2 describes the setup and validation of the wave model, which is based on the phase-averaged SWAN model. Finally, the coupling of the two models to allow for sediment transport simulations is presented in Appendix A.3.3.

A.3.1 Hydrodynamic model

A.3.1.1. Model setup

The model was based on the two-dimensional Dutch Continental Shelf Model (DCSM-FM 0.5 nm, version fhdflowfm2d-noordzee_0_5nm-j17_6-v1), property of Rijkswaterstaat, which runs in operational mode to provide tide-surge probability forecasts in the North Sea area. DCSM-FM 0.5 nm is extensively calibrated and validated mainly against water level measurements carried out in the North Sea over several years (Zijl & Groenenboom, 2019).

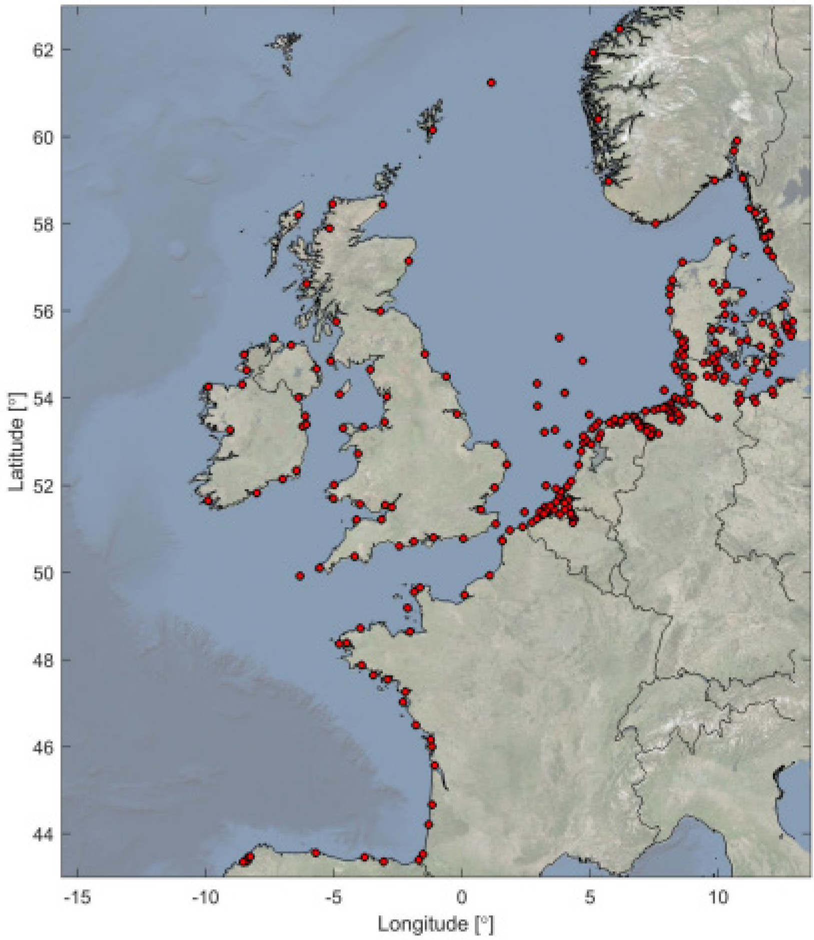

Figure A.5: Overview of the tide gauge locations used for model calibration & validation [(Zijl & Groenenboom, 2019)]

Grid schematization

The model domain covers the northwest European continental shelf, specifically the area between 15° W to 13° E and 43° N to 64° N and includes the North Sea and adjacent shallow areas such as the Wadden Sea and the Eastern and Western Scheldt. The large spatial extent of the model is essential to accurately predict the flow patterns in the North Sea. It uses a flexible mesh with resolution increasing with decreasing water depth from ca. 4 nm to ca. 0.5 nm in the south North Sea. Two additional consecutive refinements were applied to increase the grid resolution to ~200 m in IJV area, ensuring that flow and sediment transport are resolved accurately.

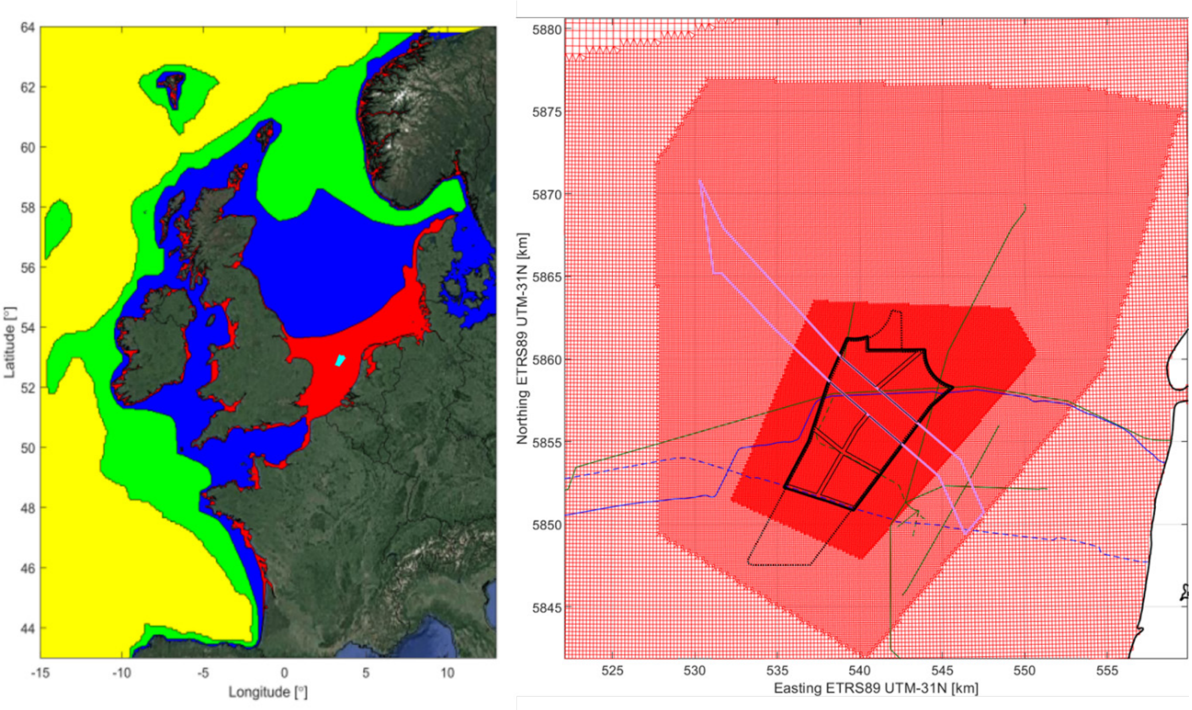

Figure A.6: On the left, overview of the DCSM-FM 0.5 nm model network with the colours indicating the grid size: yellow ~4 nm; green ~2 nm; blue ~1 nm, red ~0.5 nm. The location of IJV is marked with cyan box. Figure adapted from Zijl and Groenenboom (2019). On the right, an overview of the refined area around IJV can be seen. The black polygon denotes the designated IJV OWF area. The pipelines and export cables are shown with blue/green lines.

Bathymetry schematization

The depth schematization in the model is based on data from EMODnet supplemented with GEBCO 30’’ bathymetry data and is presented in Figure A.7. For the bathymetry in the refined area, a composite of the most recent surveys was used (see Section 2.2 for an extract of the data for IJV). The data was supplemented with data from the Royal Netherlands Navy - Hydrographic Office (1980-2021) on the Dutch continental shelf. The bathymetry data was smoothed (see Section 4.3.2) such that the large-scale bathymetric variations are schematized in the bathymetry - excluding the sand waves and other smaller bedforms.

For the numerical model input, a conversion between the MSL and LAT vertical reference levels is needed that covers the entire North Sea, similar to the extent of the model domain. High resolution bathymetry datasets in the refined area are corrected from LAT to MSL using the spatially varying datum difference derived from Dienst Hydrografie (2007).

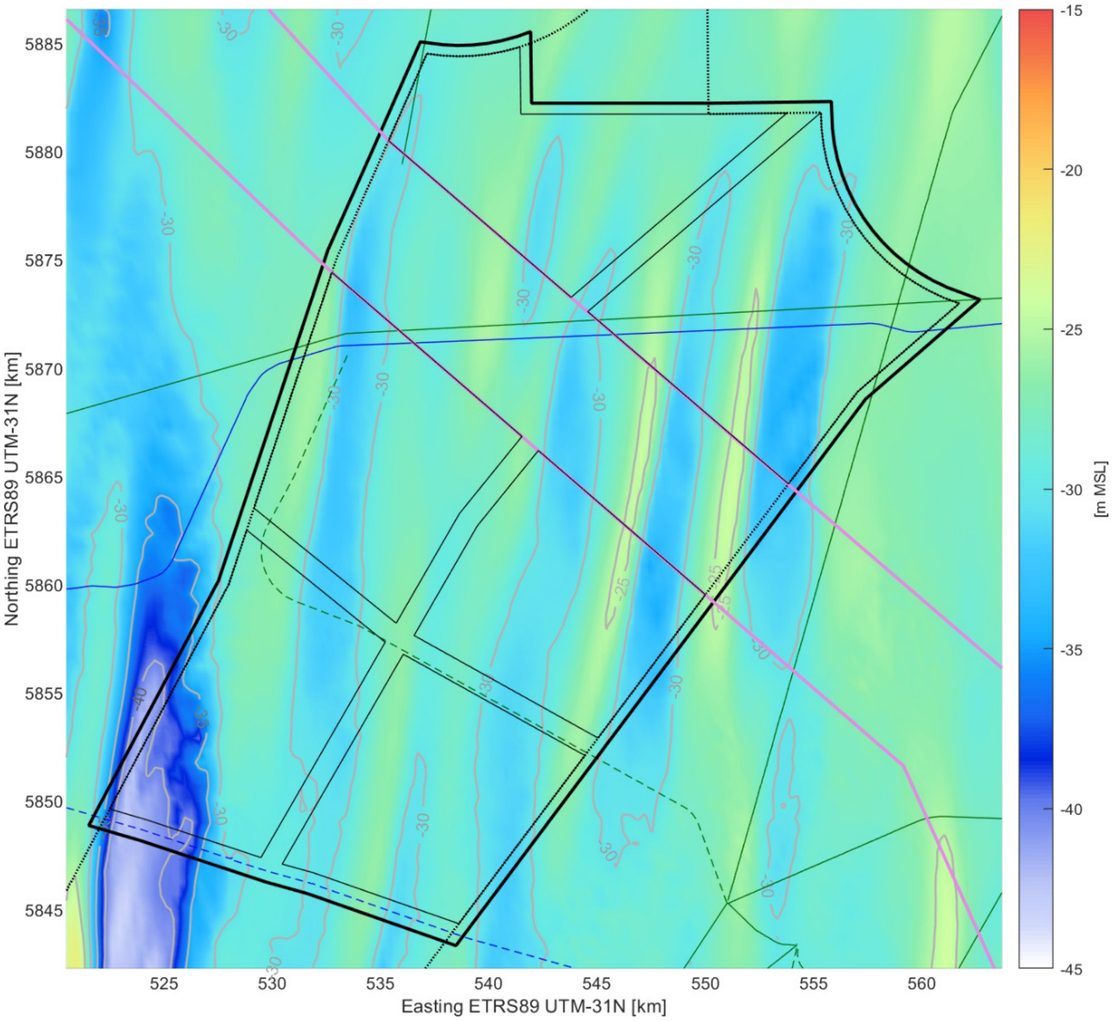

Figure A.7: Bathymetry schematization of the Delft3D -FM model at IJV.

The model is set up in depth-averaged (2D-horizontal) mode, which means that the computational grid is not discretized in the vertical. The aim of this study is to get further insight into the net sediment transport which is correlated to bedform dynamics including sand wave migration. Since thermal and density stratification is not a governing process for bedform dynamics in the North Sea, a 2D approach is justified.

Boundary conditions

At the northern, western and southern sides of the DCSM domain (Atlantic Ocean, see Figure A.6), open water level boundaries are defined. The tidal water levels at the open boundaries are derived by harmonic expansion using the amplitudes and phases of 32 harmonic components from FES2012. FES2012 provides the assimilated global tide on a 1/16° resolution (Carrère et al., 2012; Lyard et al., 2006). Besides tidal forcing at the boundaries, internal tide generation is also applied in the model.

For meteorological surface forcing of the model, time and space varying hourly neutral wind speeds (at 10 m height), and air pressure (at MSL) were used, derived from the ERA5 dataset. Data is available on a spatial resolution of 31 km, and a temporal output interval of 1 hour. To translate the 10-meter wind speed to surface stresses, the local wind speed dependent wind drag coefficient is calculated using the Charnock formulation (Charnock, 1955). To that end, a space and time varying Charnock coefficient is applied, also based on ERA5 dataset.

A.3.1.2. Calibration and validation

DCSM-FM 0.5 nm has been calibrated and validated extensively using shelf-wide water level measurements (Zijl & Groenenboom, 2019) as well as during previous projects.

For the purposes of the present assessment, additional measurements from two RPS LiDAR buoys (IJV-A buoy and IJV-B buoy), deployed by RPS group at IJV, are used to verify the performance of the refined hydrodynamic model. The two buoys were deployed at the end of April 2022, with the intention of measuring wind, waves, temperatures, pressures and currents for a period of two years. At the time of the current assessment, the measurements are still ongoing, while the measured data for the month of May 2022 were provided for this project validation.

The relatively short in duration IJV buoy data is supplemented with water level measurements from the platform K13a (25 km northwest of IJV, sourced from MATROOS) for the period 01/01/2019-31/12/2021. Additionally, water level and current measurements from the RVO measurement campaigns in the Hollandse Kust West OWF (sourced from offshorewind.rvo.nl) over the period 01/02/2019-20/07/2019 were used.

Current and water level measurements are available at the two locations (IJV-A buoy and IJV-B buoy), presented in Figure 2.4 for the time periods presented in Table 2.3. The hydrodynamic model has been run in hindcast mode for the years 2018-2021 (full year) as well as 2022 (January to July) to compare the modelled depth-averaged flow velocities and directions against the measurements. For 2022, the simulated period follows from the availability of ERA5 data that are used to force the model, at the time of the current measurement. It is noted that the ERA5 data used to force the model for May 2022 were not quality assured due to their proximity to the present. For more information regarding the measured data, the reader is referred to ((RPS, 2022b), Measurements - Watermanagement Centrum Nederland (WMCN) (rws.nl), (Deltares, 2020b)).

Figure A.8 presents a time series comparison of modelled water levels, depth-averaged flow velocities and flow directions against the hydrodynamic measurements for one spring-neap cycle in May 2022 for the location of the IJV-A buoy[3]. As can be seen in the figure, the water levels, and the current speeds and directions are simulated reasonably well by the model. The general range and variation during the spring neap tidal cycle are well captured. In the water levels a difference of ~12 cm is observed, during the entire month. This difference is likely partially linked to the MSL estimate used to derive the relative water level from absolute depth/pressure measurements (RPS (2022b) state that the MSL estimate was derived from only one week of data and will be updated during the course of the measurements). Nevertheless, the effects of such a difference in the measured/modelled water levels on the current/wave driven sediment transports are expected to be small within the scope of this study.

With regards to the current measurements, the tidal asymmetry in the velocity magnitudes and the directional distribution are well reflected in the model (middle and bottom panel in Figure A.8). Peak velocities are underpredicted by the model by an average 3.5cm/s and 15cm/s maximum. Peak velocities are more relevant to sediment transports and transport asymmetry as the sediment initiation of motion is more likely to occur during those periods. For May 2022 the difference between the modelled and measured peak flood and ebb velocities is 5 cm/s and 2.5 cm/s on average respectively, with flood velocities being generally higher compared to ebb velocities. Based on that the model is expected to capture the sediment transport asymmetry, with an underprediction of the residual sediment transport rates.

[3] It is noted that the measured current velocity at 60% of the water depth is used as the depth-averaged velocity for both IJV-A and IJV-B locations as velocity measurements for 30% to 50% of the water column are not considered acceptable in terms of quality (RPS, 2022a).

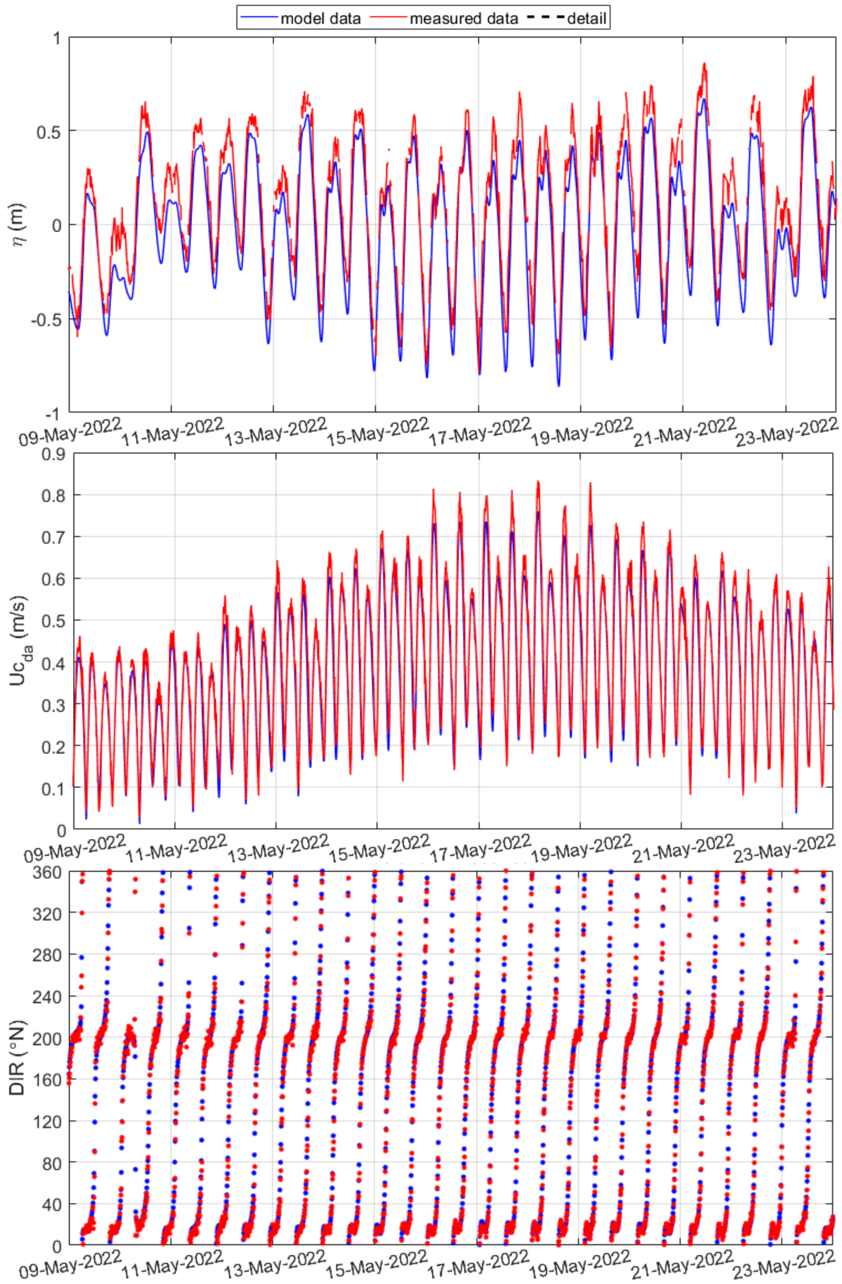

Figure A.8: Time series of measured (red) and modelled (blue) water level (top panel) and depth-averaged flow velocity (middle panel) and flow direction (bottom panel) at IJV-A buoy location over the period between 08-May-2022 and 24-May-2022.

Figure A.9, Figure A.10 and Figure A.11 present density scatter plots of the measured and modelled water levels, depth-averaged flow velocity magnitudes and directions at both measurement locations in IJV, K13a and HKW-A as well as the main statistics of the data comparisons such as the correlation coefficient (*ρ*), root-mean-square errors (*rmse)*, bias, standard deviation (*σ)* and finally the data population (*N)*. The comparisons with the available measurements show very good performance of the hydrodynamic model, with correlation coefficients above 0.9, low scatter index values and low RMSE for all measurement locations. Overall, the performance of the model was judged as satisfactory and no further changes were made to the current setup.

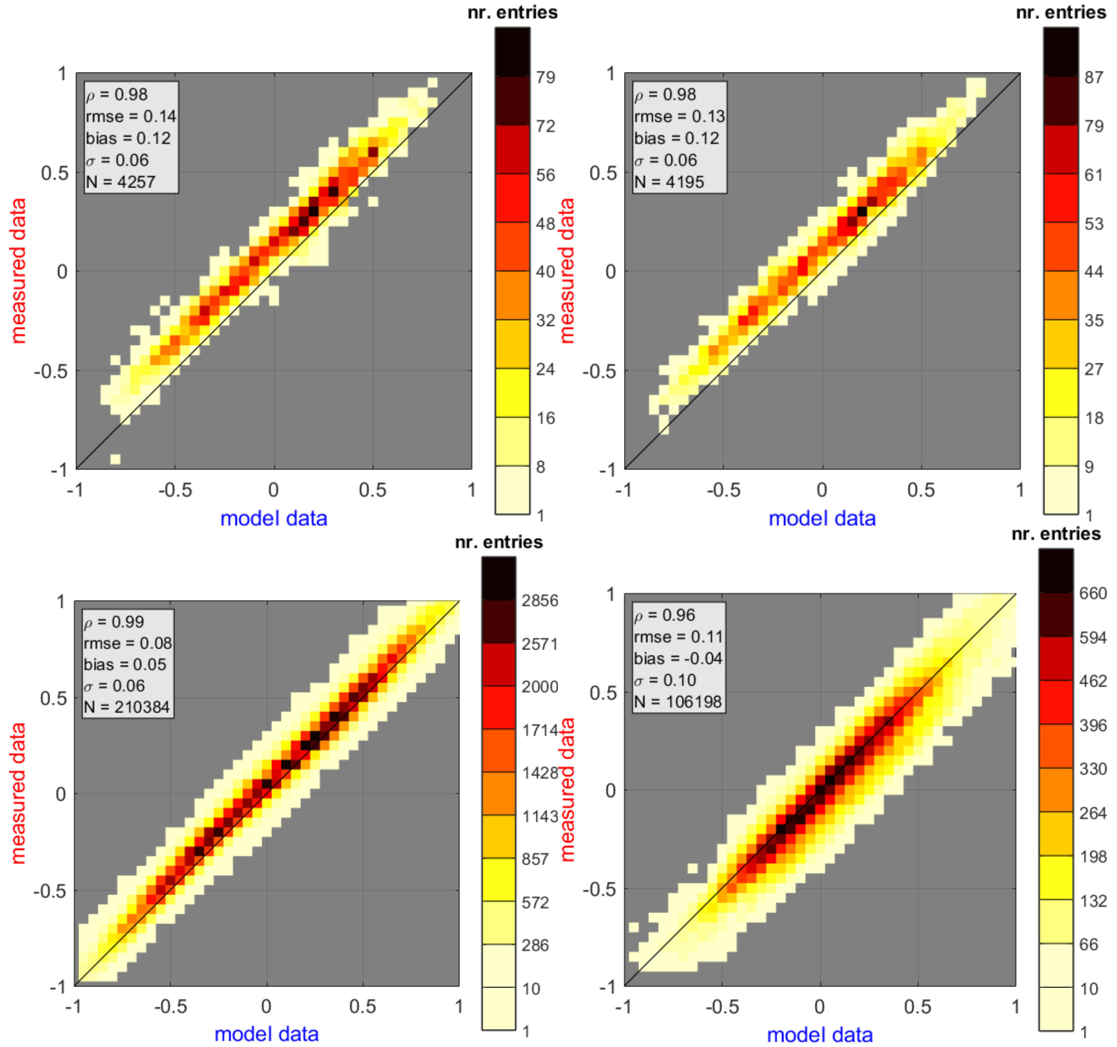

Figure A.9:Scatter plots of the modelled (horizontal axis) and measured (vertical axis) water level at IJV-A buoy (top left panel) and IJV-B buoy (top right), K13a (bottom left panel) and HKW-A (bottom right panel).

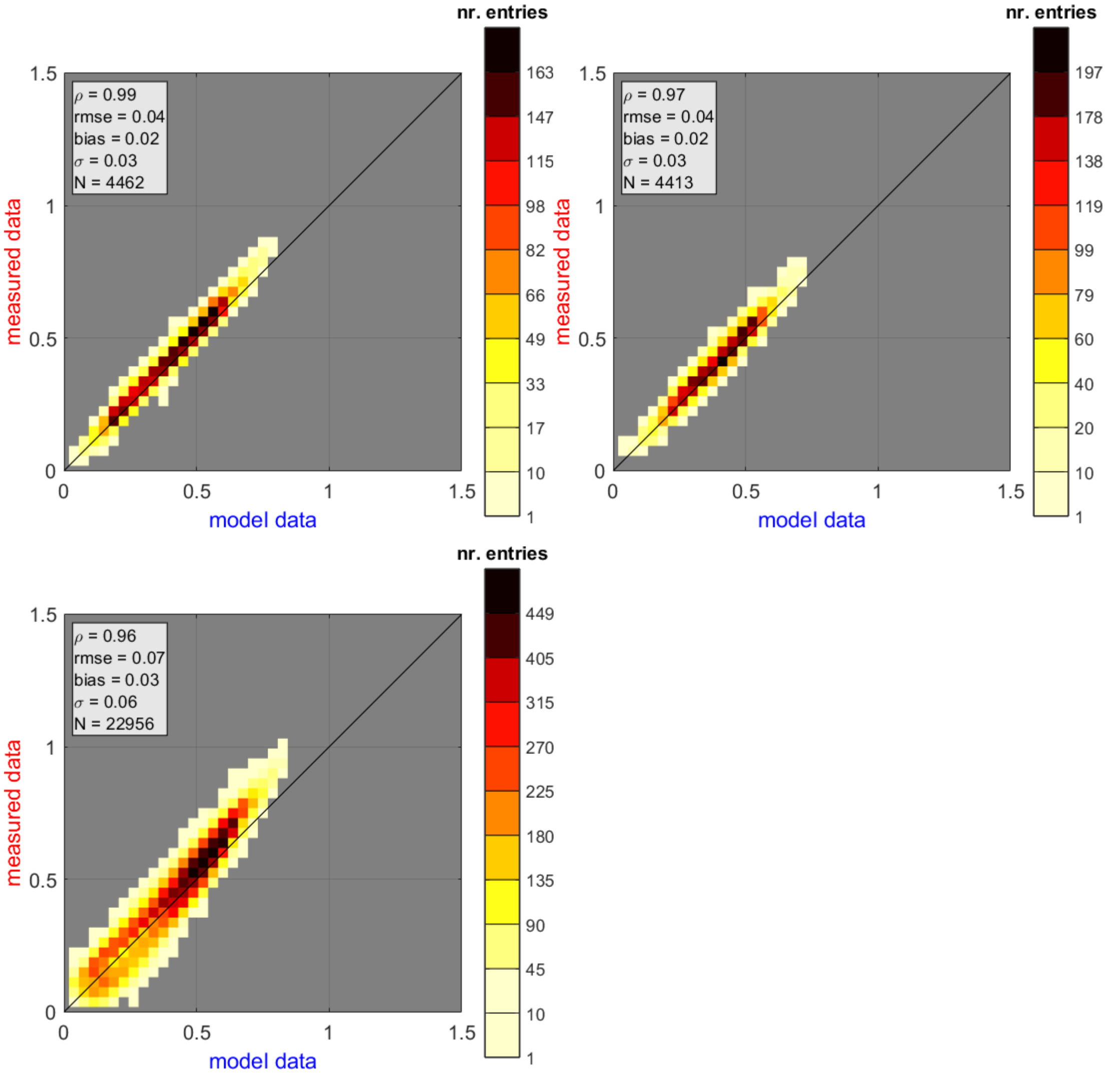

Figure A.10:Scatter plots of the modelled (horizontal axis) and measured (vertical axis) depth-averaged current magnitude IJV-A buoy (top left panel) and IJV-B buoy (top right), HKW-A (bottom left panel).

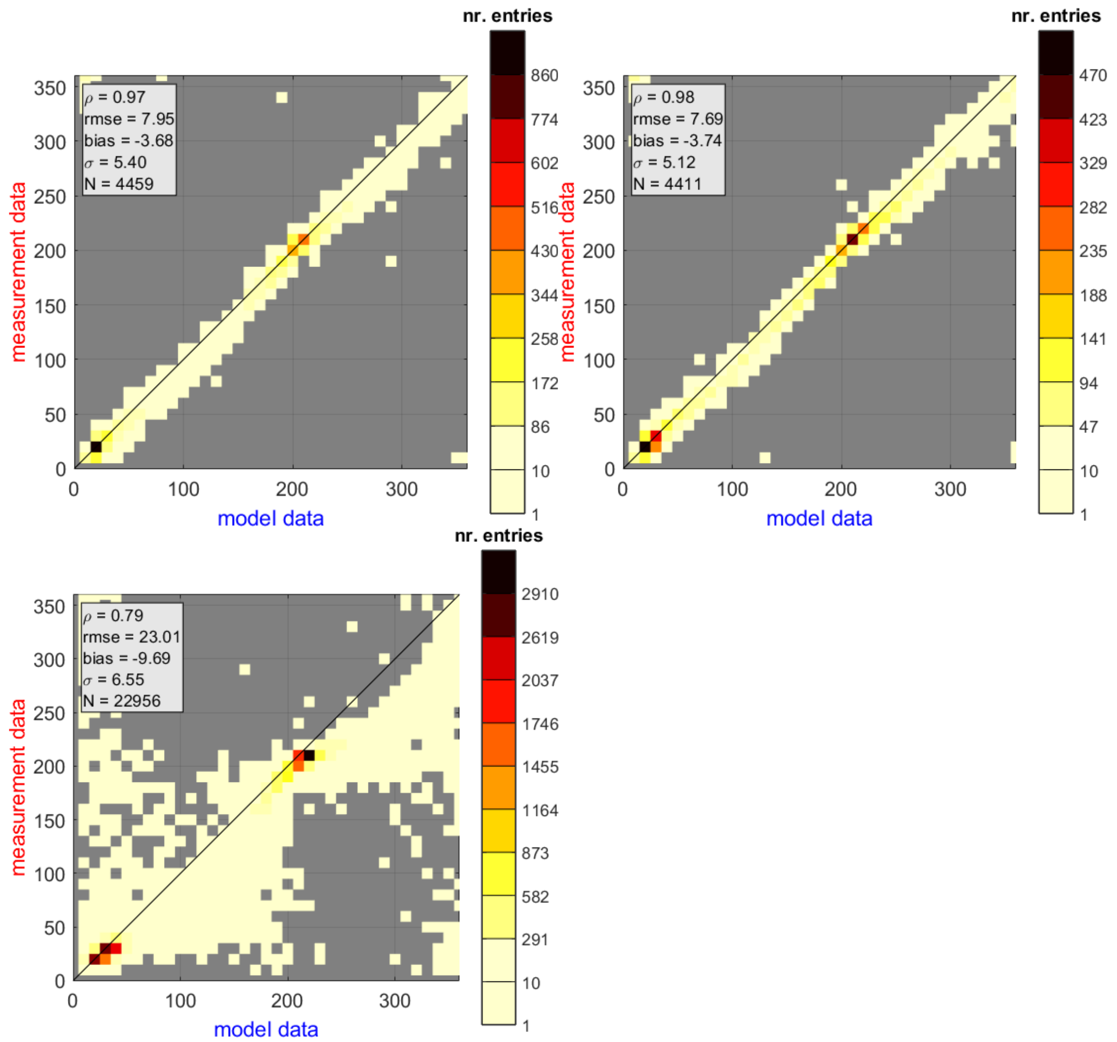

Figure A.11: Scatter plots of the modelled (horizontal axis) and measured (vertical axis) depth-averaged current direction IJV-A buoy (top left panel) and IJV-B buoy (top right), HKW-A (bottom left panel).

A.3.2 Wave model

A.3.2.1. Model setup

As a basis for the sediment modelling, a detailed wave model was setup in addition to the hydrodynamic model. For the wave modelling of IJV, the spectral wave model SWAN (version 41.20) was applied in non-stationary, third-generation mode to model wave generation, dissipation and propagation throughout the model domain. SWAN simulates the evolution of wave action density using the action balance equation (Booij et al., 1999). SWAN accounts for propagation in geographical space, depth- and current-induced refraction, shifting of the intrinsic radian frequency due to variation in mean current and depth, as well as the generation and dissipations of waves by wind and breaking respectively.

The SWAN software has been validated and verified successfully under a variety of field cases and is continually undergoing further development. For more information on SWAN, reference is made to the SWAN website.

The SWAN wave model was forced by ERA5 wind and offshore wave data and was calibrated and validated against in-situ wave measurements, taken from locations in and around IJV. The wave model was run in non-stationary mode i.e., taking evolution of the wave and wind conditions in time into account. The model uses a timestep of one hour, which is equal to the time step of the (ERA5) input wind fields and wave data.

Grid schematization
SWAN requires the specification of three types of grids:

1. a computational grid which defines the 2D geographical space of the grid points;
2. a directional grid which defines the directional range (usually 360°) and resolution;
3. a frequency grid which defines the range and resolution of the grid in frequency space.

The numerical wave model prepared for IJV is based on the large-scale Deltares' Dutch Continental Shelf Model (DCSM) SWAN model, which is extensively calibrated against observations at various locations in the North Sea. The DCSM model is forced by ERA5 wind data and ERA5 wave data is applied at its open North Atlantic boundaries.

To gradually transform the offshore conditions to IJV, two higher resolution domains are nested in the overall DCSM domain. The grid with the highest resolution is required to account for the variations in the local bottom gradients and depths in the area of interest. Furthermore, it allows for the computation of the wave model parameters on a similar resolution as in the computation of the flow wave parameters (see hydrodynamic model refinement, Appendix A.3.1.1). Consequently, IJV dedicated wave model consists of three model domains (see Figure A.12 and Figure A.13):

1. the large-scale DCSM domain with a grid resolution of approximately 3-4 km (green rectilinear grid);
2. the intermediate NestA domain with grid resolution of approximately 1 km (blue rectilinear grid) and;
3. the detailed NestB domain covering the area of interest with a grid resolution of approximately 220 m (red rectilinear grid).

Furthermore, the directional space covers the full circle (360°). The number of directional bins was set to 45, resulting in a directional resolution of 8°. Finally, the frequency space covers a range from 0.03 Hz to 0.6 Hz, allowing for wave period in the range of 1.67 – 33.33 seconds. The frequency resolution, f, is not constant since the distribution of the frequencies is logarithmic. The relative resolution, $\Delta f/f$, is constant and is equal to 0.1. Given the prescribed range of the frequency domain, this results in 32 frequency bins.

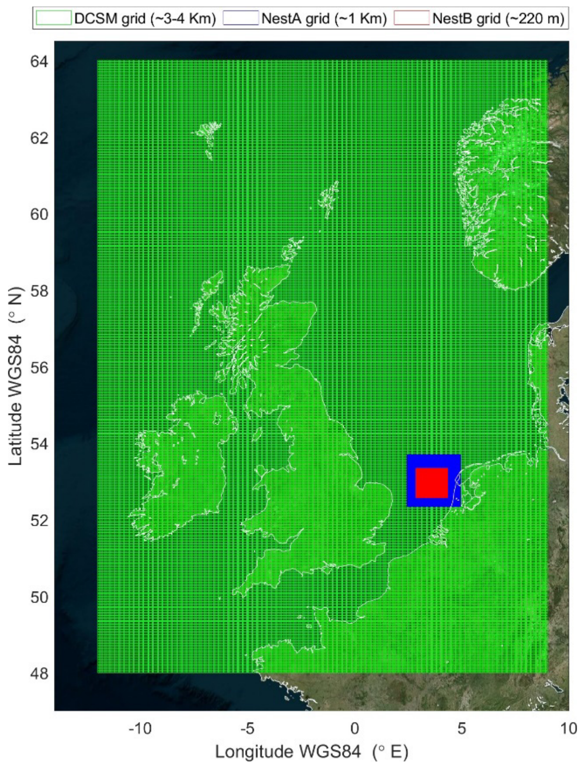

Figure A.12: IJV wave model domains. Green domain is the large-scale DCSM-SWAN, Blue domain is the intermediate NestA and Red domain is high resolution NestB.

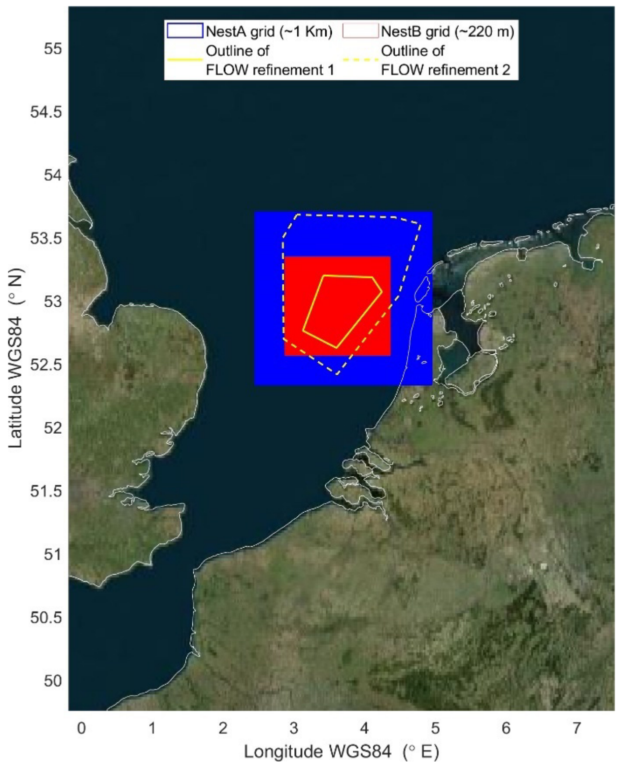

Figure A.13: IJV higher resolution wave model domains. Blue domain is the intermediate NestA and Red domain is high resolution NestB. The outlines of the two flow model refinement extents are shown with the yellow (dashed) lines.

Bathymetry schematization

The bathymetry schematization of the wave model is similar to the one used in hydrodynamic model (see Appendix A.3.1.1). The overall DCSM model bathymetry has been derived from a gridded bathymetric dataset (October 2016 version) from the European Marine Observation and Data Network (EMODnet). The resolution of the gridded EMODnet dataset is 1/8' x 1/8' (approx. 160 x 230 m). Note that although the Irish Sea is within the extent of the model's computational grid, the area is not modelled by locally excluding bathymetric information (see Figure A.14). This is done for computational efficiency. As a result, wave effects within this area are not captured by the model, however this has no influence on the area of interest.

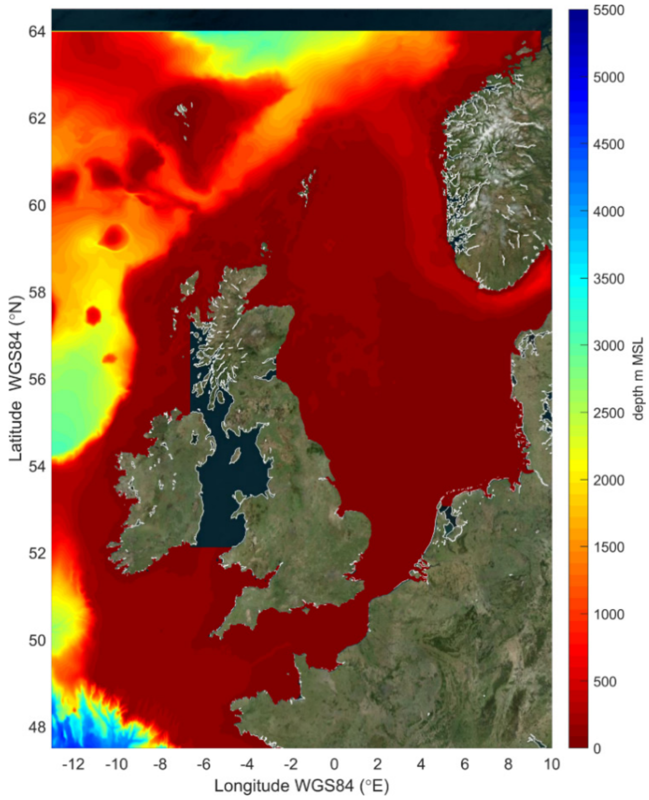

Figure A.14: Bathymetry (m MSL) in the overall DCSM-SWAN wave model (dataset from EMODnet).

For the two higher resolution nested domains, a composite of the most recent surveys was used (see Section 2.2). The data for the higher resolution domains was supplemented with surveys from the Royal Netherlands Navy - Hydrographic Office (1980-2021) on the Dutch continental shelf and from EMODnet Bathymetry Consortium (2020) for the remainder of the model domain. The bathymetric data was smoothed (Section 4.3.2) to exclude sand waves and smaller bedforms from the schematized bathymetry, while including the larger scale seabed variations. The data was corrected from LAT to MSL using the spatially varying datum difference derived from Dienst Hydrografie (2007).

Incoming boundary conditions

The SWAN model was forced at the open boundaries of the overall DCSM domain with parameterized wave spectra described by ERA5 time series of five wave parameters:

- Significant wave height, H_s,
- Peak wave period, T_p,
- Mean wave direction (coming from), MWD,
- Directional spreading, σ or m and
- Spectral shape, γ.

The spectral shape, γ, was assumed to be constant for all computations, being a JONSWAP shape (Hasselmann et al., 1973) with a value of $\gamma = 3.3$. The exact value of γ prescribed along the boundary is not critical since the model will automatically properly redistribute the wave energy in the frequency domain and in balance with the wind forcing. The amount of directional spreading present at the incoming boundaries was derived from the ERA5 time series for "wave spectral directional width". For numerical reasons, this value was capped at a maximum of $\sigma = 37.5°$ (one-sided directional spreading level from the mean direction). Also, for this boundary parameter, the exact value prescribed is not critical since the model will automatically properly redistribute the wave energy over the different directions in the computed domain. The remaining wave parameters (H_s, T_p and MWD) were taken directly from hourly ERA5 wave data (available every 0.25 degree in longitude and latitude) and assigned to the nearest grid point along the open boundary of the overall DCSM domain.

Land boundaries
No reflecting or transmitting boundaries were defined. All wave energy reaching an outer boundary or land boundary is assumed in the model to be fully absorbed at that location. At the sections bordering the Irish Sea waves propagate out of the computational domain uninfluenced as if they move into the Irish Sea.

Wind and hydrodynamic input
The wave model was forced spatially using the original hourly ERA5 wind fields. The spatially varying hourly water level and depth-averaged current fields from the original (not-refined) 2D DCSM-FM were used as input to all wave domains in the hindcast modelling. This means that the wave model simulates how the spatially distributed water levels and currents (speeds and directions) influence the wave propagation and evolution.

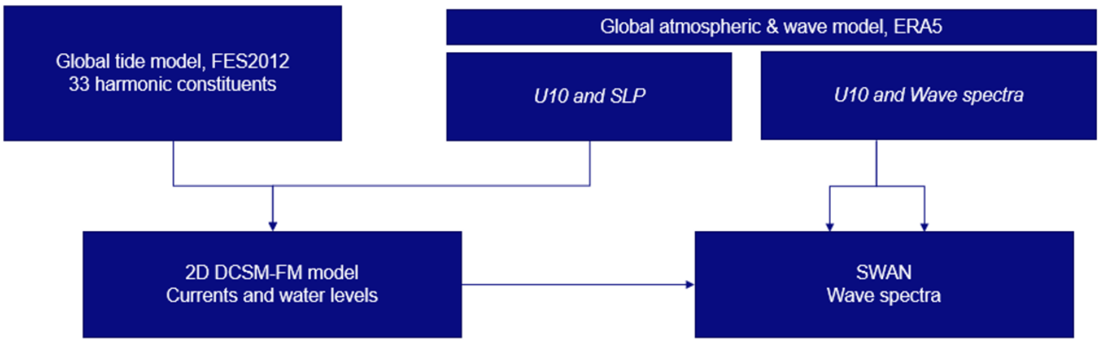

Figure A.15: Modelling approach of the wave standalone model. SLP stands for sea level pressure.

Numerical aspects and physical processes
All relevant physical processes were activated in SWAN for the wave modelling in this study. These physical processes were modelled based on specific formulations and associated parameters, which are summarized in Table A.2, together with the selected numerical settings.

Table A.2: Summary of applied settings in the wave model for numerical aspects and physics parameters.

Model parameter	Applied setting
Mode	Non-stationary
Accuracy	Changes of less than 1% in H_s and $T_{m0,1}$ at 99% of the grid points relatively to the previous iterations, a maximal number of 60 iterations
Integration scheme	BSBT (Backward Space Backward Time)
Generation	3rd generation including quadruplets
Wind drag	Wu (1982)
Bottom friction	JONSWAP formulation (Hasselmann et al., 1973) with c_{JON} = 0.038 m^2/s^3 (Zijlema et al., 2012)
Depth-induced wave breaking	Default Battjes-Janssen formulation (Battjes & Janssen, 1978)
White-capping	Formulations by Rogers et al. (2003)

A.3.2.2. Calibration and validation

The DCSM-SWAN model (overall domain) has been calibrated and validated extensively using shelf-wide wave measurements as well as during previous projects. As an example, Figure A.16 presents the density scatter and percentile comparison (QQ-plots) and the main statistics of the significant wave height wave height data comparisons such as the correlation coefficient, root-mean-square errors, bias and standard deviation in the period June 2006 – December 2020 for the wave buoy near platform K13a. Data comparisons for both the omni-directional dataset (centre panel Figure A.16) as well as for eight directional subsets (in Figure A.16 from top left, clockwise: NW, N, NE, E, SE, S, SW and W) are considered. Figure A.17 shows the corresponding omni-directional peak wave period and mean wave direction comparisons.

The data comparisons for both the omni-directional dataset as well as for eight directional subsets show a high correlation in conjunction with limited scatter between the model results and the observations for the significant wave height, Hs. High correlation is also observed in the mean wave directions, while for T_p the correlation is lower.

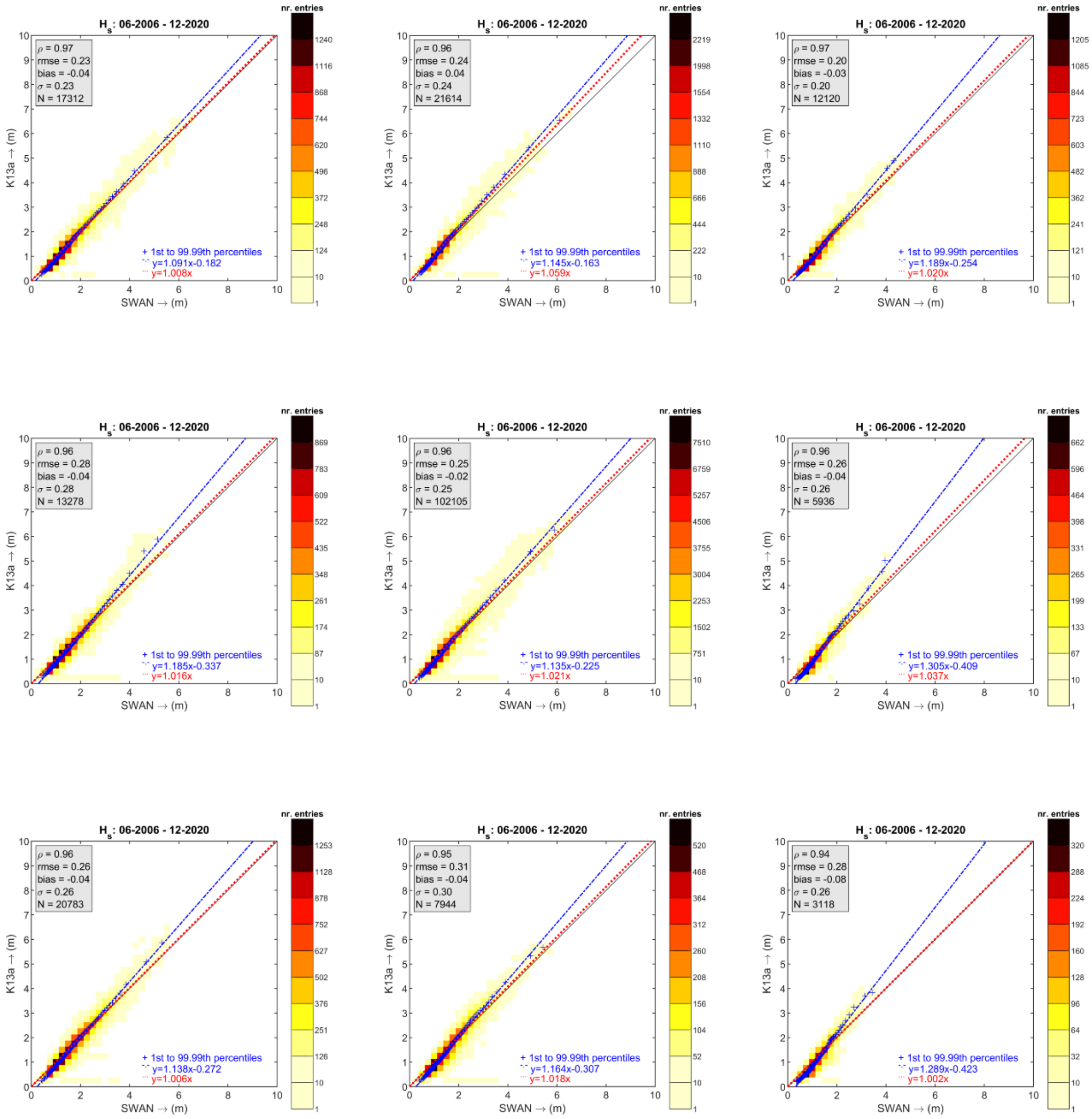

Figure A.16: Significant wave height density scatter comparisons between the buoy observations and DCSM-SWAN (large-scale domain) results at platform K13a. The panel in the middle shows the omni-directional comparisons and the panels surrounding it show the comparisons for the corresponding directional sectors (from top left, clockwise: NW, N, NE, E, SE, S, SW and W). The symmetric fit to the data is given by the red dotted line and the linear fit through the data percentiles (blue pluses) is given by the dashed blue line. The statistics of the comparisons are printed in the panels.

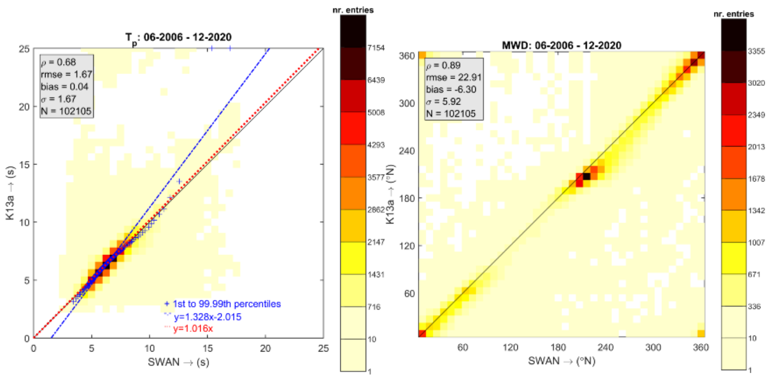

Figure A.17: Peak wave period (left) and mean wave direction (right) density scatter comparisons between the buoy observations and the DCSM-SWAN (large-scale domain) results at platform K13a.

The calibration and validation of the wave model prepared for the current assessment was focused on the higher resolution domains that have been nested in the large-scale DCSM-SWAN model. The performance of the high-resolution wave model domains was verified based on wave measurement from the two locations inside IJV (IJV-A and OJV-B buoy) as well as wave measurements available at the locations of the K13a and K14 platforms. To this end, the standalone wave model was run in hindcast mode for the years 2019-2021 covering the wave measurement available.

Model calibration

In the model calibration phase, consistency checks concerning the performance of the detailed domains were performed. For example, it was assessed whether any spurious effects or numerical instabilities occurred near the open boundaries of the nested domains. Since the nested domains performed well in transforming the offshore conditions to IJV (e.g., see Figure A.18) no calibration of the wave model was deemed necessary.

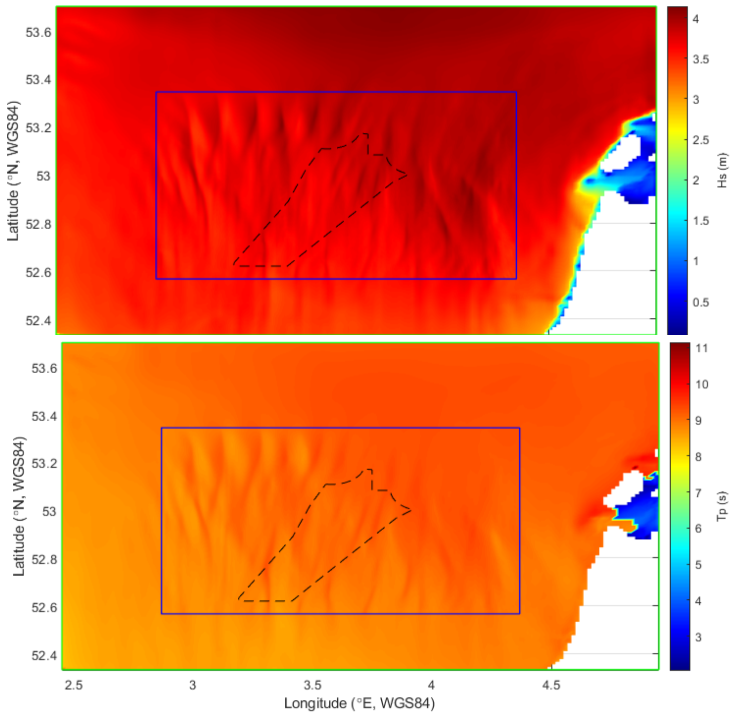

Figure A.18:Combined map output of NestA (within green polygon) and NestB domains (within blue polygon overlaying NestA map output) showing significant wave height (top panel) and peak wave period (bottom panel) for a random time during the hindcast period.

Model validation

The wave model has been run in hindcast mode for the periods 2019-2021 and 01/2022-06/2022 to be able to compare the modelled wave parameters against the measurements. For the hindcast wave simulations, the runs have been divided in intervals of 6 months (when applicable) with the first 48 hours simulated time considered as the spin-up period of the model[4]. First, the total time interval (e.g., 6 months) was modelled for the overall DCSM domain, generating the boundary input for the intermediate NestA domain. Accordingly, the total time interval was then modelled for the higher resolution domains NestA and NestB

[4] The spin-up period is the modelling interval which is required for the model to start up and initialise. This includes allowing the wave energy from the boundary to distribute over the total modelling domain. A spin-up period of 48 hours (2 days) is typically used. Results for the spin-up period may not be reliable and are discarded.

sequentially, with the boundary input for the highest resolution NestB domain generated by the NestA domain.

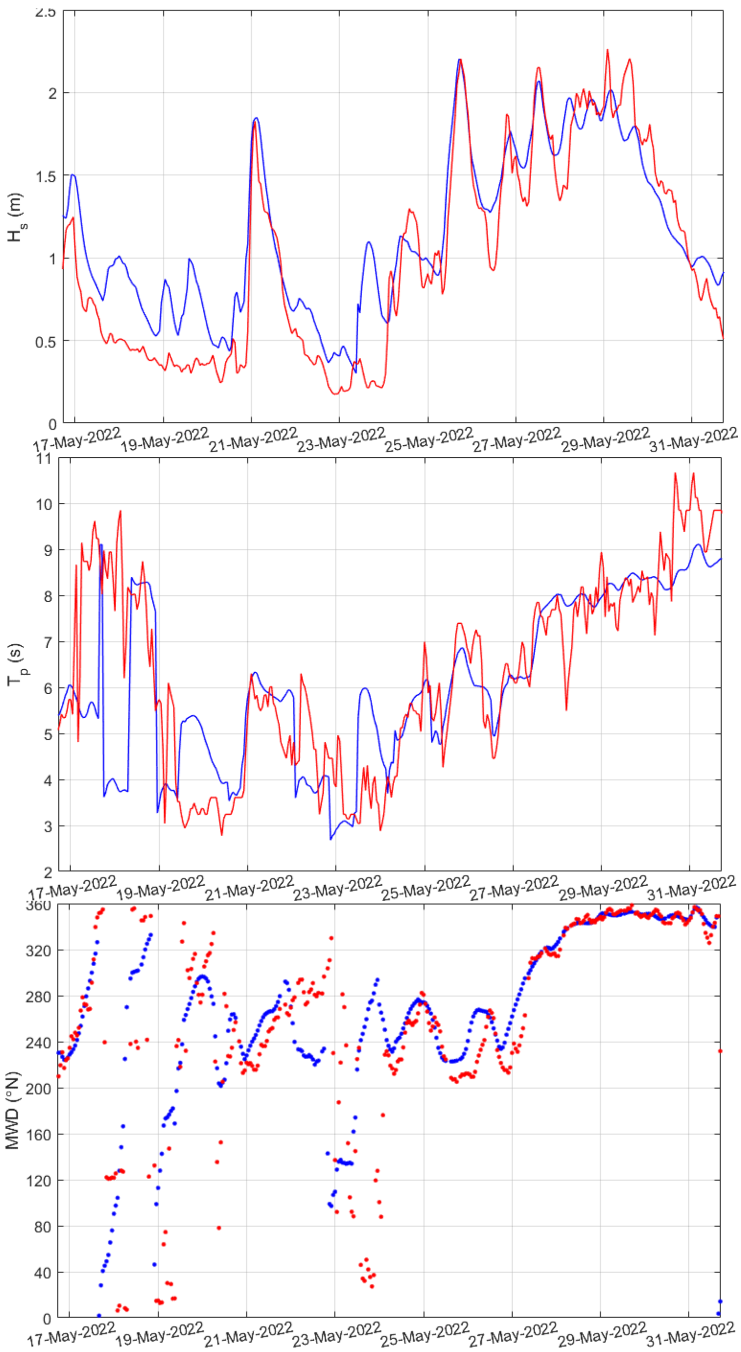

Figure A.19:Detailed timeseries plot of modelled versus measured significant wave height (top panel) and peak wave period (middle panel) and mean wave direction (bottom panel) for IJV-A buoy during a 15 day period.

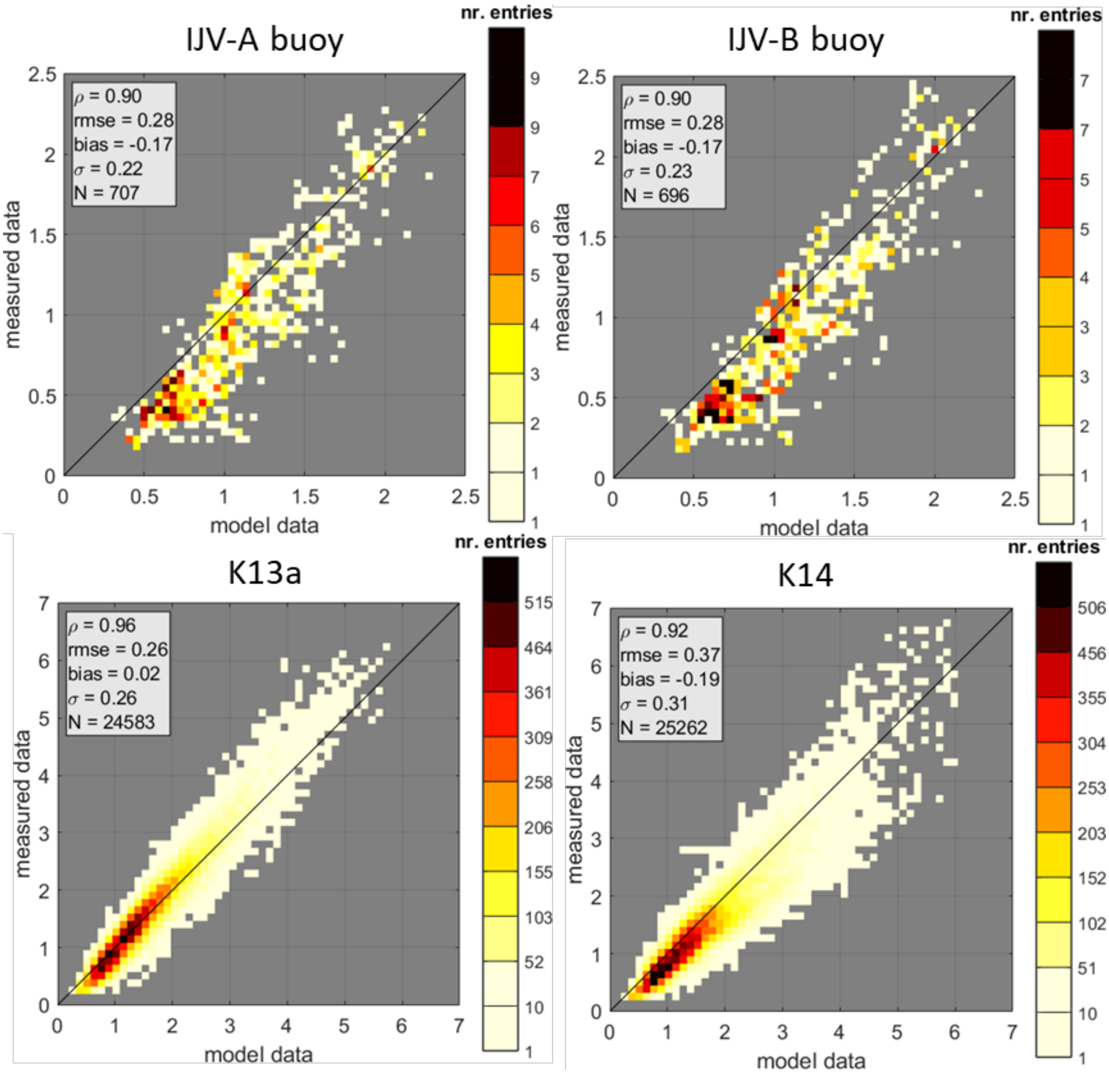

Figure A.20: Scatter density plots of modelled versus measured significant wave height at locations in the vicinity of IJV.

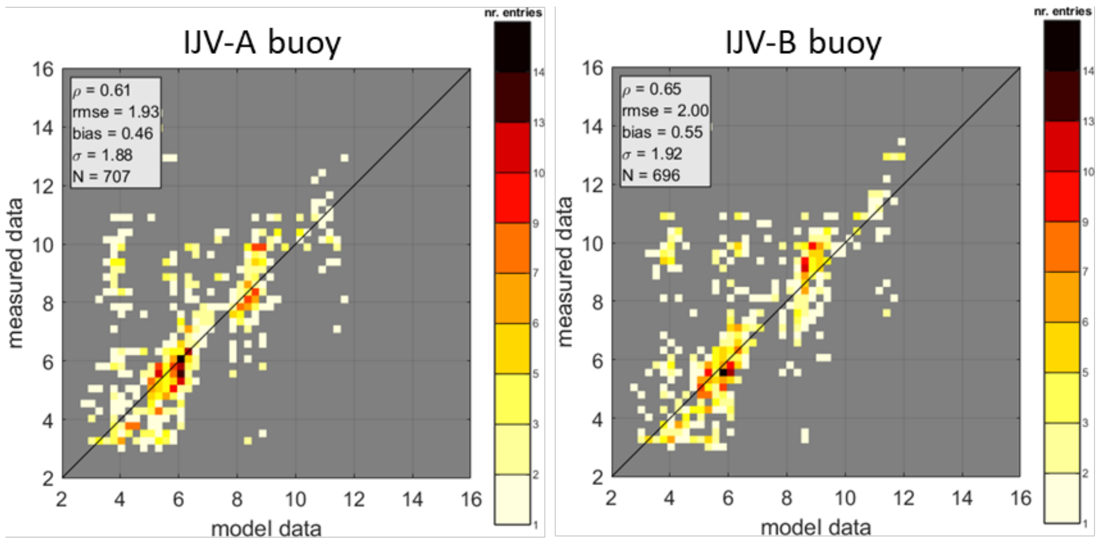

Figure A.21: Scatter density plots of modelled versus measured peak wave period at locations in the vicinity of IJV.

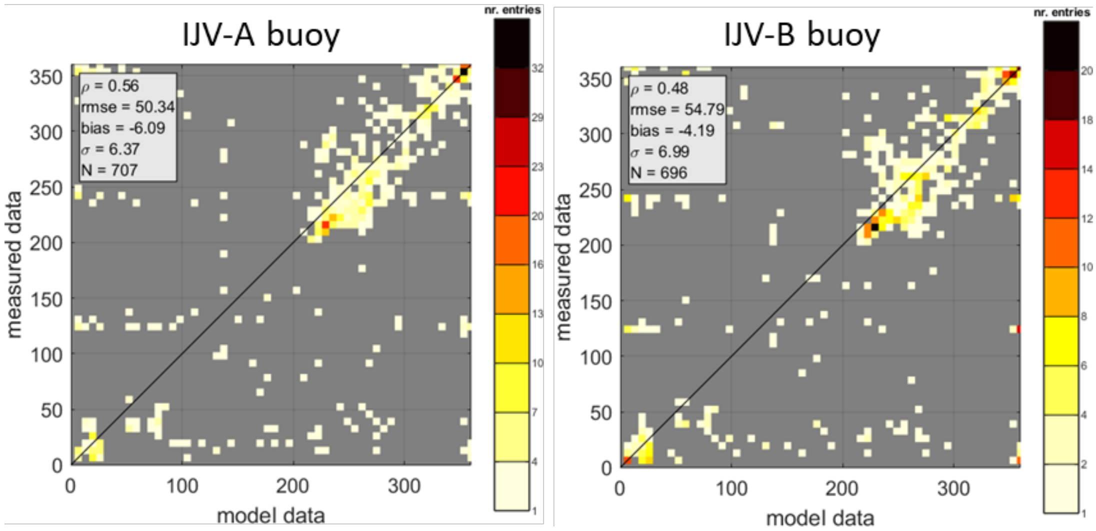

Figure A.22: Scatter density plots of modelled versus measured mean wave direction at locations in the vicinity of IJV.

Figure A.19 presents detailed timeseries from the available measurement period of the most relevant wave parameters (H_s, T_p and MWDR) for the location of the IJV-A buoy. Moreover, for the same parameters, Figure A.20, Figure A.21 and Figure A.22 present the density scatter and the main statistics of the data comparisons such as the correlation coefficient (*ρ*), root-mean-square errors (*rmse*), bias, standard deviation (*σ*) and finally the data population (*N*) for the locations IJV-A and IJV-B buoys as well as at the platforms K13a and K14. Note that for the locations IJV-A and IJV-B a month of measured wave heights is available, while at K13a and K14 longer term measurements (3 years) are available.

The validation plots show a high correlation in conjunction with limited scatter between the model results and the observations for the significant wave height, H_s. This is the case for all measuring stations. Both the timeseries plots and the density scatter plots show that the model tends to overestimate the lower wave heights (H_s<1 m). This tendency is more evident in the validation plots for IJV-A and IJV-B buoys, as for those locations measurements are available only during calm conditions (May 2022). When longer timeseries of wave measurements are considered (KP13a and KP14), which include a higher number of intermediate and higher wave conditions and are thus more relevant to sediment transport formulations, the overall predictive performance of the model increases.

The modelled and measured data of the remaining wave parameters compare less well. For T_p this is expected due to the discrete nature of this parameter. With regards to the MWD, the comparison between the modelled and measured data shows low correlation and large scatter. An inspection of the timeseries comparison shows that the modelled MWD fail to capture fast changes in wave directions but generally follow the longer-term measured trends. In general, it can be stated that both parameters reflect the conditions in the area of interest.

Overall, for the purposes of the current assessment, it is deemed that the wave model reflects the wave conditions in IJV with sufficient accuracy. The wave model is hence deemed to serve as a solid basis for sediment transport modelling in the area of interest.

A.3.3 Sediment transport modelling

The hydrodynamic model described in Appendix A.3.1 was extended to include sediment transport. This setup was used to model the sediment transports over different time periods under tidal forcing as well as tidal and meteorological forcing.

Appendix A.3.3.1 describes the inclusion of the sediment transport module in the hydrodynamic model setup. Appendix A.3.3.2 presents the selection of time periods to be analysed.

A.3.3.1. Flow-induced sediment transport model setup

The online morphology addition to Delft3D was used to simulate sediment transports in the flow domain at each computational time step (Lesser et al., 2004). The default settings have been applied in the sediment transport computation, which can be found in the D-Morphology User Manual (Deltares, 2020a). The TRANSPOR2004 transport equations were used to model the movement of non-cohesive sand fractions and are implemented in the Delft3D flow solver. The Delft3D implementation of this formulation follows the principle description of Van Rijn (2007a, 2007b, 2007c) separating the sediment transport into suspended and bed-load components. Suspended sediment transport is computed by the advection–diffusion equation and includes the effect of sediment in suspension on the fluid density. Bed load transports represent the transport of sand particles in the wave boundary layer in close contact with the bed surface and include an estimate of the effect of wave orbital velocity asymmetry. The built-in sediment transport model uses the Van Rijn (2007) sediment transport equations.

The bed was schematized to consist of a single sediment fraction with unlimited supply as the focus is on the modelling of sediment transport patterns rather than on morphodynamics. A set of hindcast simulations was performed (2017-2021), with an assumed median sediment diameter (D50) of 250μm which was deemed representative for the entire area. A single year (2019) was simulated with higher and lower assumed median diameter, 300μm and 200μm, uniformly over IJV to capture the residual sediment transport sensitivity to variations in the sediment diameter. It is noted that the purpose of the current numerical analysis is to build a system understanding in order to complement the data analysis, meaning that we are interested in the general patterns of sediment transport and in assessing the dominant forcing mechanisms, i.e., the focus is not on extracting accurate values of sediment transport rates. This also means that the exact values of median sediment diameters prescribed are not critical, as long as they are generally representative of the seabed composition at IJV.

Finally, the bed level was held constant over time (no bed updating) to prevent feedback between the flow and changing bed level. This was done to isolate the role of the changing flow on the sediment transport patterns that result from the interaction with the observed morphologic features.

A.3.3.2. Selection of analysed time-periods and sediment transport components

For seabed mobility, we focus on depth-averaged current velocities as it is the main driver for transport of bed sediment (van Rijn, 1990). As a first step the depth-averaged current velocities and total[5] sediment transport patterns over a single arbitrary spring (and neap) tide were assessed, omitting all other forcing from the model setup. However, given the relatively long period of interest (multiple years to decades), it is not suggested to represent hydrodynamics by a single tide. We therefore selected a representative spring-neap cycle that best represents the long-term tidal velocity signal in the horizontal tidal excursion. For this purpose, an analysis was setup to detect a single representative spring-neap-cycle from a time series of currents. This analysis is depicted in Figure A.23, which indicates a spring-neap-cycle that is most-representative for all spring-neap-cycles within the considered period (calendar year 2019), based on the horizontal tidal excursion (see label in Figure A.23). The selected spring-neap-cycle represents all other spring-neap-cycles which is a validated approach in sediment transport modelling (Lesser et al., 2004). The period from *27-May-2019 07:00::00* to *11-June-2019 00:30:00* is considered the most representative period. This period is subsequently simulated with the sediment transport model focusing on the tidal forcing.

[5] The term total sediment transport refers to the sum of suspended and bed load transports.

Furthermore, intra-annual and interannual variability in the sediment transport patterns are assessed through the 5-year sediment transport simulations (2017-2021). For these multi-year simulations, the model was forced using tidal conditions at the boundaries and meteorological (wind and atmospheric pressure) over the free surface as described in Appendix A.3.1.1. The contribution of both the bed load and suspended sediment transport load to the total transport patterns is presented and discussed. Finally, the sensitivity of the residual sediment transports to variations in the spatially uniform assumed sediment diameter is assessed.

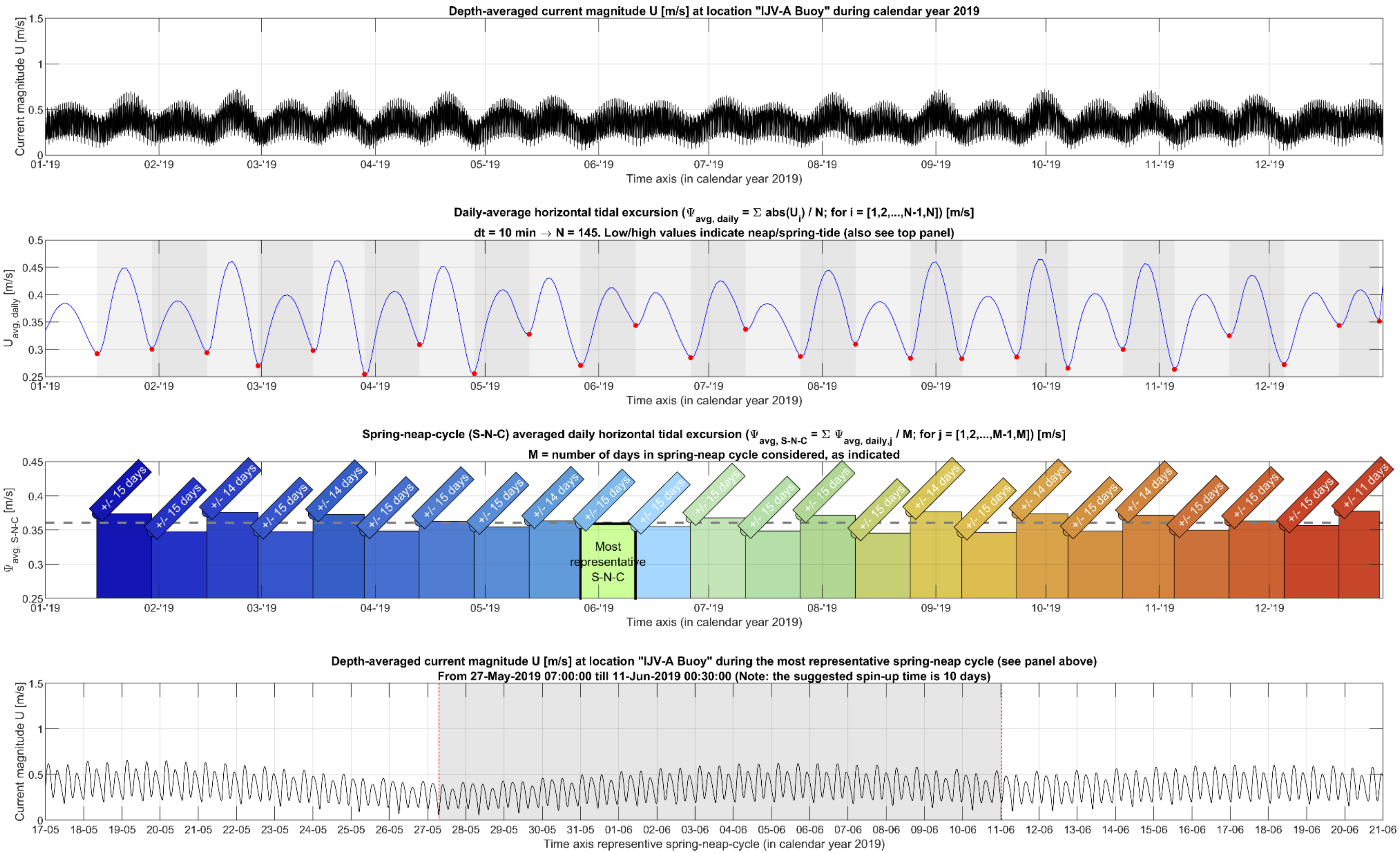

Figure A.23:Selection of the most representative spring-neap cycle. The selection is based on the cumulative absolute tidal excursion at IJV-A buoy location.

A.3.3.3. Wave and flow-induced sediment transport model set-up

To assess the influence of waves on sediment transport rates and the seabed in the area of interest coupled flow and wave simulations were performed. For the morphological assessment, the coupled wave and flow models eventually provide input for sediment transport modelling; note that the wave-induced near-bed shear stresses are the main agent for stirring of sediment (van Rijn, 1990).

Generally, the effects of waves near the seabed diminish with increasing water depth and become stronger closer to the shore. The largest extent of IJV is characterised by relatively large water depths typically exceeding 25 m relative to MSL. Consequently, it is deemed that for parts of IJV, storm conditions associated with extreme wave heights and wave periods are most relevant when accounting for the influence of waves on sediment transport rates. To evaluate this assumption the effects of normal and extreme wave conditions on the sediment transports in IJV are assessed by means of numerical simulations.

Effects of average wave conditions

Excluding the effects of waves to study the variability over the annual timescale is a suitable approach for IJV that is characterised by a relatively large water depth (see Appendix A.3.3.2). However, to assess the intra-annual variability in IJV, the aforementioned multi-year runs are complemented with sediment transport runs of a single calendar year (2019) with coupled wave and hydrodynamic simulations. Figure A.24 shows the coupling approach for the simulation of a single year-long sediment transport run due to combined waves and currents.

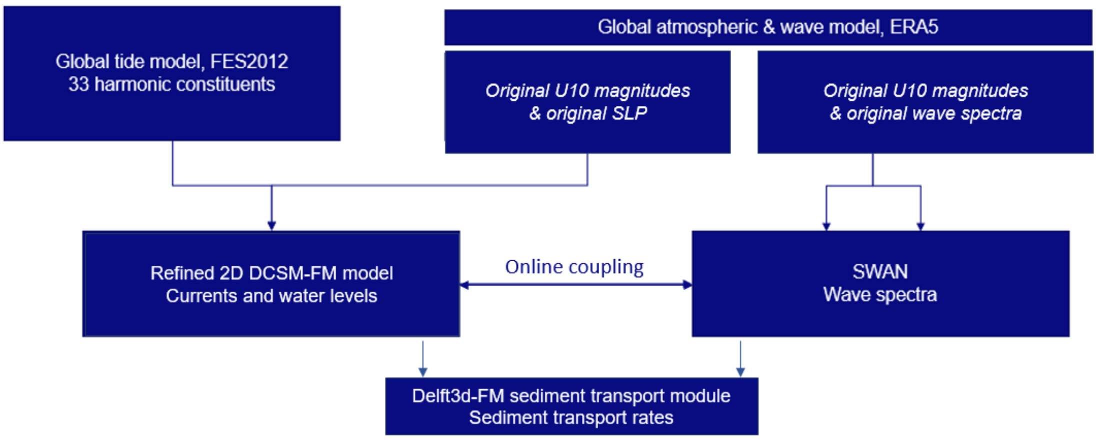

Figure A.24: Modelling approach of the coupled wave-flow sediment transport runs focused on normal conditions. SLP stands for sea level pressure.

A detailed description of the applied wave model was already presented in Appendix A.3.2 and the model results are discussed in Section 5.8.

Effects of extreme wave conditions

Sediment transport model runs that focus on the effects of extreme storm conditions were also performed. The extreme waves are expected to influence sediment transport rates in IJV. The model simulates storm conditions in IJV associated with return periods of 50 and 100 years.

These conditions are typically considered in the design of offshore infrastructure. The model runs are performed by coupling the non-stationary hydrodynamic and wave models discussed in Appendices A.3.1 and A.3.2. To simulate representative 50- and 100-year return period storm conditions, first an assessment of storm conditions for IJV was required. Once a representative storm event was identified based on the available information, appropriate modifications to the base hydrodynamic and wave models were applied and eventually synthetic 50- and 100-year storm conditions runs were prepared.

In the following, the assessment of representative storm conditions in IJV and the set-up of the synthetic storm conditions are discussed. The results of the sediment transport runs based on the synthetic storm events are presented in Section 5.8.

Selection of representative storm event in IJV
To assess the representative storm conditions in IJV, an analysis that combined the information summarized in the available metocean report for IJV (DHI, 2019) and wave timeseries from the Deltares' hindcast DCSM-SWAN model was made.

In more detail, significant wave height design values with return periods of 1, 50 and 100 years were retrieved from the metocean report (see Table A.3). These design values are determined based on extreme value analysis using modelled wave timeseries that cover the period 1979-2018 and correspond to a single output location that is deemed representative for the whole IJV (DHI, 2019).

Table A.3: Summary of design significant wave height based on the metocean report for IJV (DHI, 2019).

Location	WGS84/ UTM Zone 51N Coordinates	Significant wave height H_s in metres		
		RP 1 year	RP 50 years	RP 100 years
IJV reference location	547085, 5865482	5.7	7.7	8

Next, hourly wave timeseries produced by the Deltares' in-house DCSM-SWAN hindcast model were extracted for the IJV reference location and assessed. The available timeseries cover a period of more than 40 years from 1979 to 2020.

Combining these data, Figure A.25 shows the evolution of H_s, T_p and MWD relative to the design values (when applicable) during all storm events in the considered hindcast period that are characterised by a peak H_s exceeding the H_s with a return period of 1 year. The plotted timeseries are centred around the occurrence of the peak H_s with a presented time window of 2 days.

The lower panel in Figure A.25 shows that the predominant incoming wave directions during storms at IJV range between south, west and north directions (i.e., 200 – 360 °N). Given the geometry of the North Sea, the most extreme storm events considered here (i.e., RP50 and RP100) are associated with waves coming from the north direction. Consequently, only storms that are associated with incoming mean wave directions in the range of 320 to 40 degrees relative to North are further considered for the purposes of the current assessment.

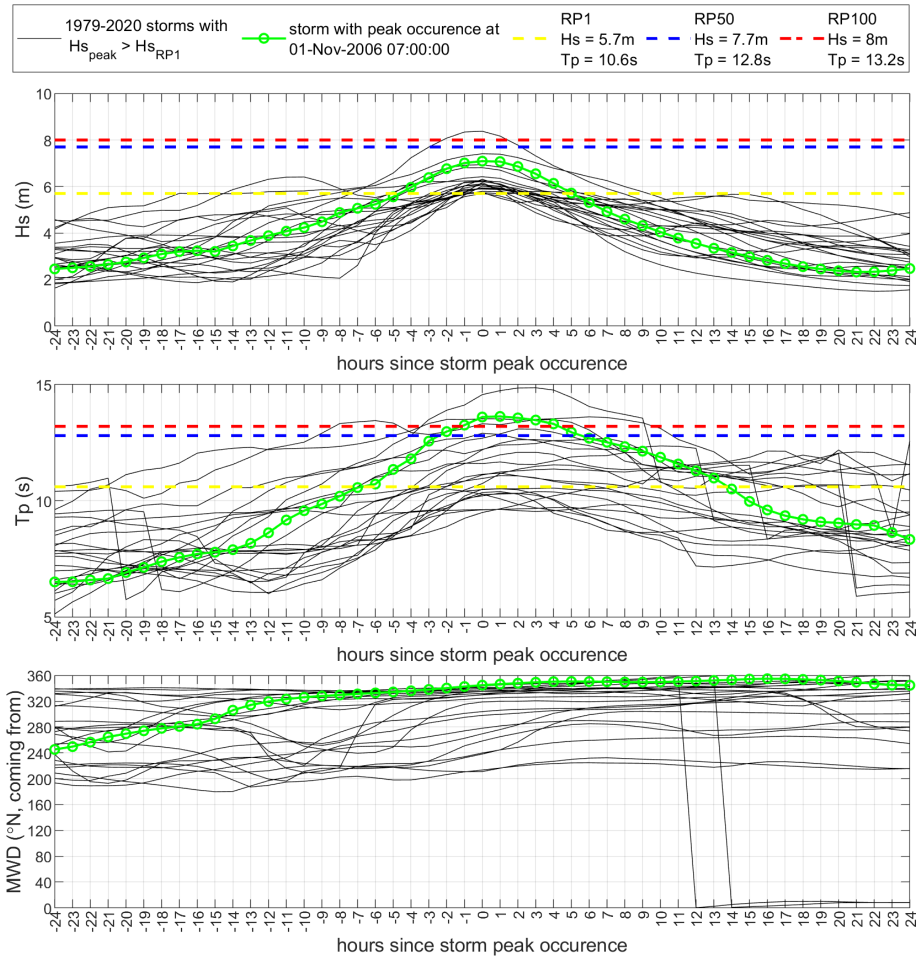

Figure A.25: 1979-2020 storms with peak significant wave height exceeding the RP1 value at IJV reference location. The most representative storm from the cluster of northern storms is highlighted with the green line.

The storm with peak occurrence on *01-Nov-2006 07:00:00* (highlighted with the green line in Figure 1) was qualitatively selected as the most representative storm for IJV with respect to the significant wave height profile of northern storms over the considered window of 2 days.

<u>*Set-up of synthetic design storm conditions*</u>
The available ERA5 timeseries (meteorological and incoming wave conditions) used to force the base hydrodynamic and wave models include the period that the most representative storm condition took place, i.e., the entire year of 2006. Therefore, the representative storm event can serve as the base case on which the synthetic storm conditions of RP50 and RP100 can be constructed.

The deviation of the significant wave height between the base case (actual storm of *01-Nov-2006 07:00:00*) peak occurrence and the design values is in the order of 5 and 10 percent for RP50 and RP100 respectively[6] (see Figure A.25).

[6] Note that it is not deemed necessary that the design and simulated significant wave heights at the occurrence of the storm's peak match exactly. While the coordinates of the reference location are the same between the DCSM-SWAN hindcast model and the hindcast model employed for the extraction of normal and extreme wave conditions for IJV, differences concerning the model's set-up or the exact depth at the reference location may apply.

To achieve the design values, the wind forcing of the coupled model was modified by increasing the wind magnitudes while keeping the directions unchanged. An increase of the wind magnitudes across the entire domain covered by the DCSM hydrodynamic and wave models would result in unrealistic flow and wave patterns at the area of interest and hence the wind field was modified only inside the extent of the intermediate wave domain (NestA) and thus also inside NestB. Accordingly, also the hydrodynamic model was forced with a modified wind field.

The duration of the coupled synthetic storm simulations (including the calibration runs) was 10 days starting on *27-Oct-2006 00:00:00*[7], with the first two days considered as spin-up time. The coupling interval between the hydrodynamic and wave models was set to 1 hour, i.e., same the timestep used in the non-stationary wave model. This means that the information exchange between the wave and flow models occurred every 1 hour of simulation time. Contrary to the base wave model (Appendix A.3.2), in the coupled model runs water level and current information were passed at each time step directly from the refined hydrodynamic model. Moreover, sediment transport rates are calculated by accounting for both flow and wave induced bed shear stress components. The modelling approach followed with the coupled model is presented in Appendix A.3.3.3.

The evolution of significant wave heights for the various calibration runs is presented in Figure A.26 relative to the design values. At the time of the peak occurrence, the synthetic storms with wind magnification factors of 1.0 and 1.1 are closest to the RP50 and RP100 design values. Therefore, these two synthetic storms are considered to represent RP50 and RP100 storm events that will be discussed in the following with regards to wave effects on sediment transport rates.

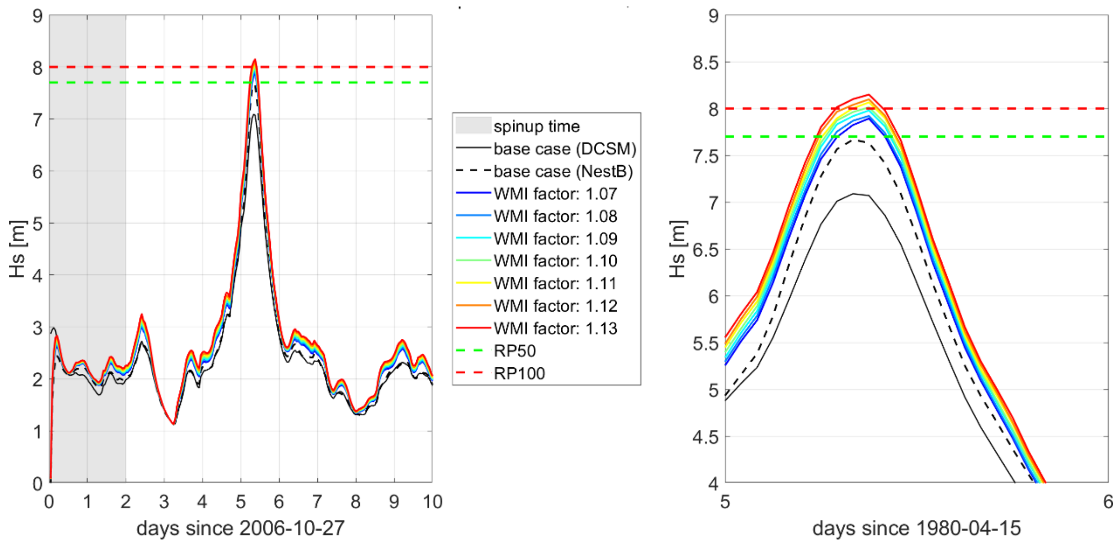

Figure A.26: Evolution of significant wave heights from calibration simulations employing various wind magnification factors (WMI). Left panel shows full simulation period and right panel shows a zoomed period around the peak occurrence. The synthetic storm simulations with factors of 1.0 and 1.1 are seen to approach closest the RP50 and RP100 design values.

[7] The mentioned date is referring to the ERA5 forcing time series used in the simulations. Since these timeseries are adjusted for the purposes of the current assessment (i.e., wind magnitude increase), it should be noted that the synthetic storm simulations are not hindcast simulations.

A.4 Methodology for the assessment of future and historic seabed levels

A.4.1 Overview

The focus of the assessment of future and historic seabed levels is to extrapolate the historic trends in seabed dynamics obtained from the data-driven analysis and numerical modelling. The methodology for the extrapolation of future (relevant for design, installation and maintenance) and historic (relevant to determine possible locations of Unexploded Ordnance's (UXO's) trends consists of the following five steps:

1. Coupling between results of the data-driven analysis and numerical modelling;
2. Validation of extrapolation methodology;
3. Extrapolation of historic trends;
4. Definition of uncertainties;
5. Assessment of future and historic seabed levels;
6. Classification of extrapolated seabed levels.

Each of these steps including sub steps is elaborated separately in the remainder of this section.

A.4.2 Comparison of results from data-driven analysis and numerical modelling

Basis for the assessment of future and historic seabed levels are the historic trends in seabed dynamics. For this, two types of analyses are presented, the data-driven approach and the numerical modelling.

A qualitative comparison is presented between the long-term data-derived sand wave migration rates over IJV and the annual derived sediment transports. Common patterns and differences in the spatial variation of directions are discussed taking into account the accuracy and limitations of each method.

For areas with large-scale erosion or sedimentation a qualitative comparison is made between these areas and magnitudes and directions derived from the numerical modelling.

A.4.3 Validation of extrapolation methodology

Extrapolation of historic trends is started with the validation of the applied methodology (as described in the next sections). In the validation of the extrapolation methodology a hindcast is made of a historic bathymetry measured. This historic bathymetry needs to be different from the starting bathymetry used in the extrapolation (often the most recent high-quality measurement.

The hindcasted bathymetry is thereafter compared to the measured historic bathymetry and differences are expressed in terms of a Root Mean Square Error (RMSE) and visual comparisons of the hindcasted and measured bathymetries.

A.4.4 Methodology for extrapolating historic trends

The assessment of future and historic seabed levels consists of extrapolating historic seabed level trends. The extrapolation is performed separately per type of bedform as each of these have a different dynamic behaviour. In general, two approaches are applied for extrapolating the seabed levels:

1. Extrapolation of vertical seabed level trends;
2. Extrapolation of horizontal migration of bedforms.

Based on the results of the data-driven analysis a decision is made for the most appropriate approach per bedform type. Bedforms for which no historic trends can be determined, such as the highly transient megaripples, are taken up as an uncertainty. It is noted that when considering historic bed levels the observed historic trends are reversed in the extrapolation. All approaches are discussed in more detail below.

A.4.4.1. Extrapolation of vertical seabed level trends

When the data-driven analysis indicates that a general downward or upward seabed level trend is present for the analysed bedform type, vertical seabed level trends are analysed and extrapolated. For this a similar approach is followed as discussed under Appendix A.2.5 resulting in linear regression lines for all nodes.

The uncertainty (goodness of fit) of a linear regression line is affected by the number of surveys and the distribution of the points. The standard error (SE) is used to assess the goodness of fit of the linear regression. Standard error indicates how far the data points are from the regression line on average. Lower values of standard error indicate a better fit to the available data. Additionally, standard error can be used to get an estimate of the 95% confidence/prediction interval. It is assumed that bed level variations at one location are Gaussian distributed. Hence, 95% of the datapoints are within a range that extends ±2*SE from the fitted line. The obtained values can be used to extrapolate large-scale seabed changes over time. e.g. a trend of 2 cm/year would result in a change of 60 cm over a period of 30 years.

A second methodology for extrapolating large-scale seabed changes is to assign a fixed value occurring over the period of interest. For example, a maximum value of 2 m can be assigned to a specific area of interest to illustrate expected large-scale changes. Often that maximum value is only reached after a number of years. To cater for this the value for the large-scale seabed changes grows logarithmic until the maximum is reached. i.e. each year the value increases until the maximum is reached, however this growth is larger for the first years compared to the last years of the period of growth.

It is noted that in some cases large-scale seabed changes are bound by lower and upper values. For example, a seabed can increase until a certain level is reached after which it is expected not to increase any further. For example, an abandoned tidal channel might fill in until it reaches a level similar to its surroundings. If applicable these bounds are applied to the large-scale seabed level changes possibly resulting in earlier reached lower values.

For areas which are subject to large-scale erosion and/or sedimentation (i.e. areas with seabed dynamics not resulting from bedform dynamics) with spatially and temporally varying trends observed seabed envelopes are included in the data extrapolation. Extrapolation of trends in these areas would result in overestimations of actual seabed trends.

It is noted that bathymetrical surveys are subject to uncertainties in vertical seabed levels. These uncertainties are smaller for the more recent surveys but can still be in the order of 0.10 to 0.30 m. This information, together with information on the quality of all available bathymetrical surveys is used to assess whether vertical seabed level trends are part of the uncertainty band or natural trends of the system.

A.4.4.2. Extrapolation of horizonal migration of bedforms

A second important contributor to vertical seabed level changes are the horizontal migration of bedforms with timescales and dimensions such that cable burial depths and foundation fixation points can be significantly influenced. Smaller scale bedforms are not considered in this approach as their variability in time is too high to track between bathymetrical surveys.

The future and historic bathymetries, as well as the corresponding bed level changes for the areas with dynamic bedforms are estimated by artificially shifting the bedforms. Starting point is a bathymetry covering as much of the area of interest as possible. This should at least over the area of interest but also an area outside to cover sand waves migrating into the area, i.e. information of future seabed levels in the area of interest might be currently outside the area of interest.

In most cases the available bathymetries are measured in different years and do not cover the entire analysis area. To cater for this an additional composite bathymetry is created. In case multiple bathymetries are available, the most recent highest quality bathymetries prevail, except for cases when this dataset is covering a small area or corridor (e.g. a survey with a width smaller than the length of the bedforms assessed).

To cover for the temporal differences in the composite bathymetry, each component is shifted using the mean migration direction and rate over this period. This is further explained in the extrapolation of an individual scenario below. For example, when a composite bathymetry is created from bathymetrical surveys measured in 1992, 2005 and 2020, the bathymetries measured in 1992 and 2005 are shifted over a period of 28 and 15 years respectively. This results in estimated seabed levels (based on shifting the 1992 and 2005 bathymetries) and a measured most recent bathymetry (2020). By combining these, with the measured most recent bathymetry prevailing, a composite bathymetry is created used as starting point in the data extrapolation.

The artificial shifting of the sand waves is done with the aid of the determined migration directions and rates bandwidths. These bandwidths contain a lower bound, mean and upper bound for both the migration direction and rate, resulting in 9 possible displacements fully describing the temporal variation in bedform dynamics.

First the bandwidths for all analysis locations are interpolated resulting in bandwidths for the entire grid used in the analysis. When combining the migration and directions, for every grid point the yearly shift in x and y direction is calculated. Based on the bandwidths three approaches for the extrapolation can be performed which are further explained below.

Extrapolation of an individual scenario

The first approach for extrapolation consists of shifting the composite bathymetry by means of a single scenario, i.e. a combination of a single migration direction and rate per grid point. This approach is used to determine best-estimate scenarios consisting of the extrapolation of the mean migration direction and rate. An example of this approach is shown Figure A.27 where per grid point (black dots) the displacement in x and y direction is shown by means of an arrow. This arrow indicates the direction of migration and the total displacement in that direction. This total displacement is calculating from multiplying the shift in x and y direction by the number of years for which the extrapolation is performed.

This approach results in grid points containing a certain bed level being extrapolated to a new x and y location. The resulting x, y and z locations are ultimately interpolated back to the original x and y locations resulting in an estimated seabed level for a specific scenario for a specific year which can be both below and above the most recent measured seabed level.

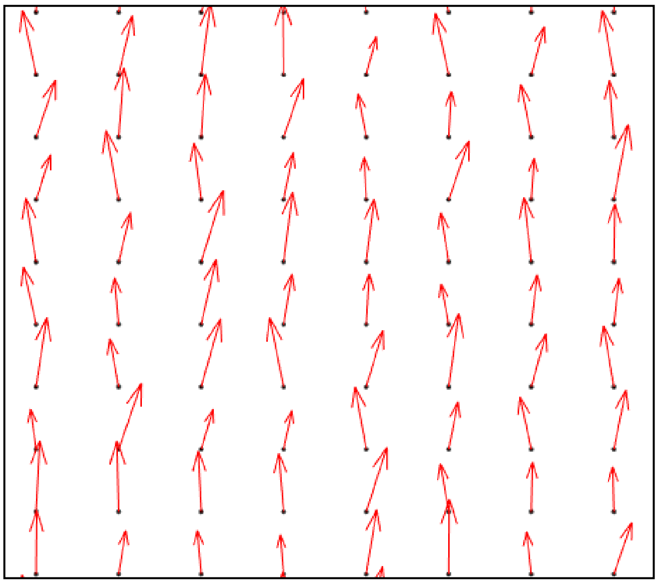

Figure A.27: Example of shifts per grid point (black dots) with the direction of the arrow indicating migration direction and the length of the arrow the migration rate (for illustration purposes, the grid resolution and scale of migration rates is not indicated in the figure).

Extrapolation of instantaneous seabed levels

The second approach for extrapolation consists of extrapolating the full bandwidth of shifts in x and y directions for a specific year. This is relevant when for a specific year the lower and upper envelope of expected seabed levels is requested. Examples are the year of installation for which an indication of expected seabed levels is required.

In this approach a polygon is drawn for each grid point which covers the area between the lower and upper bound migration direction and the minimum and maximum displacement away from the grid point (calculated by multiplying the lower and upper bound migration rate and the number of years for which the extrapolation is performed). This polygon describes the area where the analysed grid point (thick black dot) can be in the year assessed (e.g. the year of installation).

An example is shown in the left plot of Figure A.28 with the drawn polygon shaded blue and the analysed grid point as a thick black dot. It can be seen that a number of grid points (smaller blue dots) fall inside the polygon. In case the lower envelope of the expected seabed level for the year assessed is determined, all grid points inside the blue polygon with a bed level higher than the analysed grid point will be attributed with the original value of the analysed grid point. When determining the upper envelope of the expected seabed level for the year assessed the opposite is true: All grid points inside this blue polygon with values lower than the analysed grid point will be attributed with the original value of the analysed grid point.

In case opposite migration for a grid point is observed, the lower bound migration describes a negative migration rate, whereas the upper bound migration rate describes a positive migration rate. An example of the extent of this polygon is shown in the right plot of Figure A.28. It can be seen that the blue polygon covers an area on both sides of the grid point analysed.

This approach is performed for all grid points resulting in the lower or upper envelope of the expected seabed levels for the year assessed.

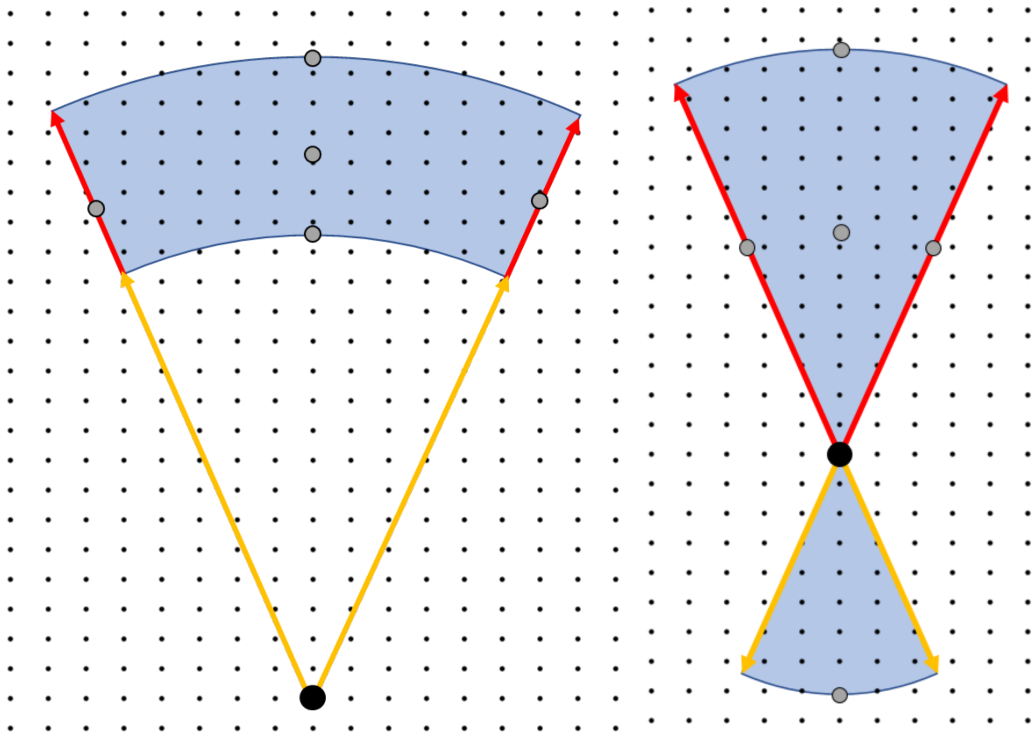

Figure A.28: Example of the extrapolation approach indicating a case where both the lower and upper bound migration direction have the same sign (left plot) and the case where opposite migration is observed (right plot). The analysed grid point is indicated by a thick black dot whereas the other grid points are indicated by smaller black dots. The lower bound displacement for the lower and upper bound migration directions are indicated with orange arrows, the upper bound displacements by the red arrows. The area between the lower and upper bound displacements between the lower and upper bound migration directions describe the area where the analysed grid point can be in the year assessed (e.g. the year of installation). All other scenarios, e.g. mean direction and mean displacement, are indicated by grey dots and always fall inside the blue polygon.

<u>Extrapolation of cumulative seabed levels</u>
The third approach for extrapolation consists of extrapolating the full bandwidth of shifts in x and y directions over a specific period. This is relevant when over a specific period the lower and upper envelope of expected seabed levels is requested. Examples are for the full lifetime of the wind farm relevant for determining initial cable burial depths.

The approach for this extrapolation is largely similar to the approach presented in Appendix A.4.4.2, except for the extent of the polygon in case no opposite migration is observed. For this approach the polygon covers the area between the lower and upper bound migration direction and between the analysed grid point and maximum displacement away from the grid point (calculated by multiplying the upper bound migration rate and the number of years for which the extrapolation is performed).

An example of this approach is shown in the left plot of Figure A.29 with the drawn polygon shaded blue and the analysed grid point as a thick black dot. This approach is performed for all grid points resulting in the lower or upper envelope of the expected seabed levels for the period assessed.

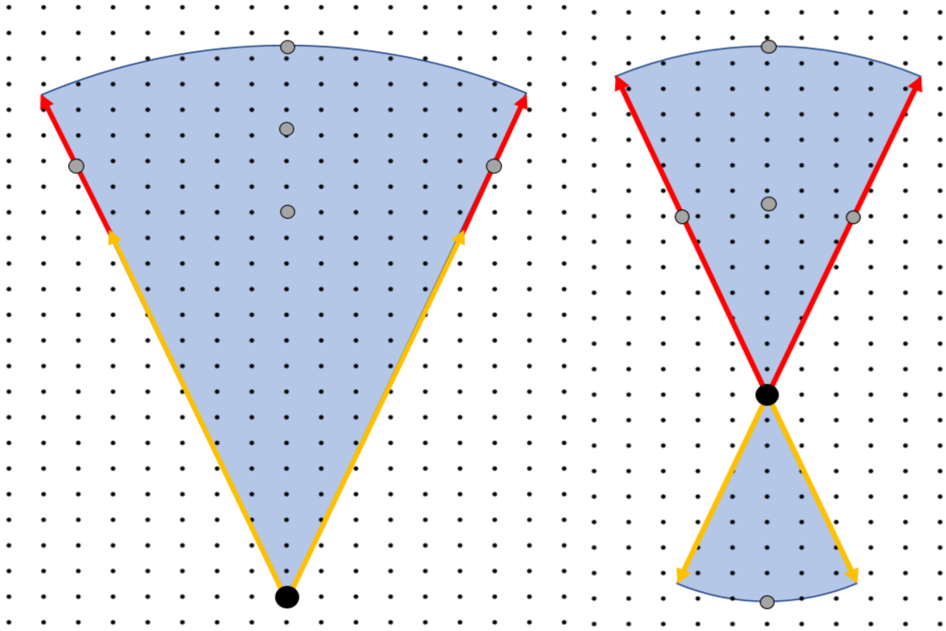

Figure A.29: Example of the extrapolation approach indicating a case where both the lower and upper bound migration direction have the same sign (left plot) and the case where opposite migration is observed (right plot). The analysed grid point is indicated by a thick black dot whereas the other grid points are indicated by smaller black dots. The lower bound displacement for the lower and upper bound migration directions are indicated with orange arrows, the upper bound displacements by the red arrows. The area between the analysed grid point and the upper bound displacement (left plot) and between the lower and upper bound displacements (right plot) between the lower and upper bound migration directions describe the area where the analysed grid point can be over the considered period (e.g. over the lifetime of the wind farm). All other scenarios, e.g. mean direction and mean displacement, are indicated by grey dots and always fall inside the blue polygon.

A.4.5 Definition of uncertainties

A.4.5.1. Sources of uncertainty

In the assessment of the future and historic seabed levels, various sources of uncertainty have to be taken into account both upward and downward, i.e. upward uncertainties are applied to the upper envelopes of extrapolated seabed levels whereas the downward uncertainties are applied to the lower envelopes of extrapolated seabed levels. The main sources of uncertainty in a data-driven morphological analysis based on measured bathymetrical data are:

1. Uncertainty due to data collection and differences in the collection of data;
2. Uncertainty due to the finite and limited grid resolution;
3. Uncertainty due to sand wave reshaping;
4. Uncertainties in megaripple dimensions and large-scale seabed variations.

Uncertainty due to data collection and differences in the collection of data

The bathymetries used are collected by means of Multi Beam Echo Sounding (MBES) or Single Beam Echo Sounding (SBES) (most often surveys from 15-30 years ago) The method used introduces uncertainties, which are larger for the SBES systems but still relevant for the MBES systems.

For instance, MBES data is less accurate further away from the ship where the angle between the seabed and the echo sounding device on the ship increases. After collection of the bathymetrical data, the raw echo sounding signals are processed before they can be applied for further analysis. Typical examples of such pre-processing are corrections for the movement of the ship during the measurements and tidal correction. Different methods of tidal correction may result in relatively large vertical differences between surveys in time.

For the extrapolation of bed levels, the most recent measured bathymetry is used as starting point. This most recent measured bathymetry is another composite bathymetry where for each location the most recent bathymetry measurement is taken. For each location the TVU value of that specific dataset is applied in the extrapolation. This uncertainty is ultimately incorporated in the total uncertainty band. For example, in case a bedform is migrating towards the area of interest, the TVU related to this should also be considered which can be different from the most recent measurement inside the area of interest.

Uncertainty due to the finite and limited grid resolution
Furthermore, the bathymetrical data is typically gridded to a raster of data points with a fixed resolution in x- and y-direction to be used in further analysis. Although a larger grid cell size can still be used to capture constant slopes accurately, it is expected to introduce errors in the bathymetry schematisation at the areas with changes in the slopes and larger slopes such as the troughs and peaks of the sand waves and megaripples.

The total uncertainty related to the grid resolution is quantified in two steps. First the spatial differences, both upward and downward are calculated from the difference between the grid used in the analysis and the full resolution bathymetry data (0.50 by 0.50 m for the most recent bathymetry). Second, the grid resolution uncertainty of the measured bathymetry is calculated. An example is shown in Figure A.30 (not drawn to scale), providing an example for a 0.50 by 0.50 m grid where assuming a slope of 5° (approximation of smaller scale bedform slopes in IJV), the expected loss in peak height (or trough depth) is estimated at 0.02 m. For a bathymetry with a resolution of 5 by 5 m this increases to 0.22 m.

For predictions (and hindcasts) the spatial varying grid resolution uncertainty is propagated through the area of interest together with the horizontal migration of bedforms. The fixed uncertainty related to the resolution of the bathymetry data is added as a fixed uncertainty.

The starting point for the downward and upward grid resolution contributions is formed by the most recent datasets measured. It is noted that this uncertainty is not absolute and reduces once seabed levels are extrapolated. For example, the initial seabed has a sand wave trough with an elevation of -2.0 m (relative to the large-scale seabed) and an upward grid resolution uncertainty of 0.8 m. This totals to an elevation of -1.2 m.

When a sand wave crest with an elevation of +3.0 m (relative to the large-scale seabed) and an upward grid resolution uncertainty of 0.2 m (which totals to 3.2 m) migrates over this trough location, the maximum seabed level for that given location will be equal to the 3.2 m. Hence the resulting contribution of the grid resolution uncertainty for that location reduces from 0.8 m to 0.2 m.

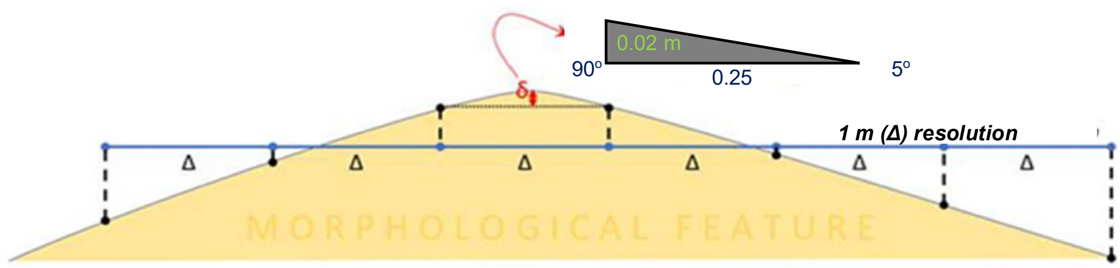

Figure A.30: Sketch to determine uncertainty related to the applied method. For a grid resolution of 0.5 by 0.5 m an uncertainty height of 0.02 m is found.

Uncertainty due to sand wave reshaping
To arrive at future and historic seabed levels, bedforms are migrated using different migration directions and migration rates. This approach assumes that the seabed is in a state of dynamic equilibrium, which implies that the bedforms will retain their shape and dimensions while they are migrating. However, bedforms might reshape e.g., steepen, change skewness or curvature as a result of changing (seasonal or event-driven) hydrodynamics.

This uncertainty is partly included in the extrapolation of seabed level using bandwidths in migration directions and rates. However, after considering uncertainties resulting from the applied methodology, some variation in bedform height can be present. This is determined from the temporal variations in sand wave dimensions as discussed in Appendix A.2.4.3.

If extrapolating bedforms over a long period (e.g. decades), bedforms can migrate into areas with different water depths, e.g. when migrating over a sand bank, causing dampening/growth of the bedforms or change shape under extreme events. To account for this, the bedform shape uncertainty is captured in two steps. First, areas containing the dynamic bedforms are defined. For these areas an uncertainty in bedform shape is taken into account in both the upward and downward uncertainty band.

Second, as shape alterations are mainly present at the crests of the bedforms because of steeper gradients and lesser water depth an additional uncertainty is considered within a radius of all crest locations. The uncertainty is subsequently propagated together with the bedforms over the bedform areas, under the assumption of an exponential growth, starting from zero values until the maximum uncertainty is reached after roughly 7 years. This 7-year period is taken as shape alterations do not occur instantly and the local morphodynamic system needs time to adapt to changing conditions (for example due to migration of sand waves). The length of the period is based on observations of (minor) shape alterations in areas subject to significant seabed mobility in the North Sea such as Hollandse Kust (west and zuid) Wind Farm Zones (Deltares, 2016b, 2020c).

Uncertainties in megaripple dimensions and large-scale seabed variations
Lastly, determining historic trends in seabed dynamics is associated with some uncertainties. For the horizontal migration of bedforms such as sand waves, this is largely covered by the bandwidth in migration rates and directions. Two main sources of uncertainty are addressed.

Uncertainties in vertical seabed level trends
Vertical seabed level trends are determined for areas without horizontal dynamics (for these areas a more sinusoidal vertical trend is expected) by performing a dz/dt analysis on the bedform layer analysed. This results in a yearly vertical trend which can be extrapolated. However, given uncertainties or offsets in vertical seabed levels, especially for the older bathymetry surveys, the yearly trend might fall inside this uncertainty band.

If the vertical seabed trend observed from the literature, data-analysis and numerical modelling, falls largely within the uncertainty bands a yearly uncertainty is added to the extrapolation of seabed levels. This uncertainty is applied uniformly over the area of interest both in downward and upward direction,

Uncertainties in historic trends of smaller scale bedforms
For smaller scale for which no historic trends could be determined, the inclusion in the extrapolation of seabed levels is treated in three parts. This is the case when bedforms are highly transient or subject to changes under extreme events.

First, the spatial distribution of megaripples is included in the prediction of future bathymetries as the unfiltered mobile bathymetry is used in the extrapolation. Second, the uncertainty induced from using a coarser grid in the analysis compared to the resolution of the measured data is quantified and included as described under ii).

Lastly, an important limitation is related to the temporal variation of the megaripples. The bathymetrical surveys are a snapshot recording at a single point in time while the occurrence and dimensions of the smaller scale bedforms such as megaripples may vary in time. Therefore, a fixed value is taken up in the uncertainty band to cover for this temporal variation. This value is determined from the analysis of smaller scale bedforms.

A.4.5.2. Summary of uncertainties

The total uncertainty band that is applied on the extrapolated future and historic seabed levels is based on the above denoted sources has similar components for the downward and upward direction and contains the following:

1. survey inaccuracy as specified for the bathymetry data used in the most recent measured bathymetry;
2. spatially and temporally varying results from the extrapolation of seabed levels using the most recent seabed measurement as starting point (grid resolution uncertainty);
3. fixed values for the sand wave area and sand wave crest locations. Spatially varying based on crest locations over time and based on found shape changes over time. Uncertainty is exponentially increasing over the first seven years (bedform reshaping uncertainties);
4. yearly increasing values for the uncertainties in vertical seabed level changes (if present) and a fixed value for the uncertainties in smaller scale bedform dimensions. Values based on results of data-driven analysis (uncertainties in large-scale seabed variations and megaripple uncertainties).

A.4.6 Future and historic seabed levels assessment

The historic trends, measured bathymetry, extrapolation approach and uncertainties can be combined to future and historic seabed levels. The method consists of the following components, in which the component for smaller scale bedforms such as megaripples is taken up in the sand waves and uncertainties:

1. Large-scale seabed;
2. Sand waves;
3. Uncertainties.

The evolution over time of both the lowest and highest seabed levels is not a linear process. A given location can expect both seabed lowering and seabed rise over a considered period in case a sand wave is migrating over. In this case it is possible that for the first years the highest seabed level rises, as the sand wave crest is migrating towards a certain location and remains constant for the remainder of the period. i.e. no new highest seabed level is observed as the sand wave crest is migrating away from the given location. In case a higher sand wave migrates past this specific location a new highest seabed level is recorded.

Note that at the boundary of the surveyed area, the results are less reliable due to lack of highest quality data. It must be stressed that this is related to the survey area, which often only covers the area of interest. However, when sand waves are migrating near the boundaries, data may not be available. The area that is potentially affected can be determined from the bedform migration rates at the boundaries multiplied by the total number of years in the extrapolation. The potential changes to the future and historic seabed levels will be larger when being closer to the boundary. It should be stressed that the affected area in general is outside of the area of interest and the majority of the results inside the area of interest can therefore be considered to be reliable.

The influence of future infrastructure, for example foundations and scour protections, is not considered in the extrapolated bandwidths because of uncertainties related to this. This influence can however be significant on local seabed level variations.

.
The following future and historic seabed levels are considered:

1. Future seabed levels:
    - Extrapolation of cumulative seabed levels over the periods 2023 to 2025 and for 2030 to 2065 with intervals of 5 year:
        - Lowest SeaBed Level cumulative;
        - Highest SeaBed Level cumulative;
        - Maximum seabed slope cumulative.
2. Historic seabed levels
    - Extrapolation of cumulative seabed levels over the period 1945 to 2022:
        - Best-Estimate Object Level;
        - Lowest Object Level;
        - Highest Object Level;

The composition of each of the above layers is elaborated in more detail below.

A.4.6.1. Future seabed levels

Future seabed levels assist in the design, installation and maintenance of the offshore wind farm. Future seabed levels can be used to track seabed level variations along cables or close to the foundations of the wind turbines. Each of the future seabed levels is compiled from a number of components including seabed trends, uncertainties and the top of any non-erodible layer. Lowest and highest seabed levels are expressed as cumulative, being the upper and lower envelope of seabed predictions over a given period.

Best-Estimate Bathymetry (BEB)
The BEB for a specific year is calculated by adding the following components:

1. Best estimate prediction of the large-scale seabed for that year (which can be similar to the starting large-scale seabed in case no clear vertical trend is observed);
2. Sand waves extrapolated by means of the mean migration direction and rate.

The BEB is expected to have the, on average, smallest overall error. In other words: when compared to the actual 2026 bathymetry the BEB_{2026} is expected to have the smallest area-averaged total difference. At specific locations it can differ significantly, but observed differences are not expected to exceed the limits provided by the LSBL and the HSBL given that the original assumptions for this analysis are satisfied.

The BEB is only provided to give a very rough indication of the possible seabed development during the lifetime of the wind farm and should not be treated as a firm design parameter. For this LSBL and HSBL provide better information (maximum expected potential seabed level variations at each grid point). However, the BEB does provide a valuable estimate of the seabed to compute the most probable O&M costs (e.g. related to expected cable re-burial length).

Lowest Seabed Level cumulative (LSBL)
The LSBL is the expected minimum seabed level for a specific period and is calculated by adding the following components:

1. Lower envelope of the large-scale seabed over the specific period (which can be similar to the starting large-scale seabed in case no clear vertical trend is observed);
2. Lower envelope of the cumulative extrapolation of sand waves for the specific period as explained in Appendix A.4.4.2;
3. Downward uncertainty band for the specific period;
4. Top of any non-erodible layer.

Highest Seabed Level cumulative (HSBL)
The HSBL is the expected maximum seabed level for a specific period and is calculated by adding the following components:

1. Upper envelope of the large-scale seabed for the specific period (which can be similar to the starting large-scale seabed in case no clear vertical trend is observed);
2. Upper envelope of the cumulative extrapolation of sand waves for the specific period as explained in Appendix A.4.4.2;
3. Upward uncertainty band for the specific period.

Maximum seabed slope cumulative
The maximum seabed slope cumulative is the expected maximum seabed slope for a period and is calculated by adding the following components:

1. Upper envelope of the slope of the large-scale seabed for the specific period (which can be similar to the starting large-scale seabed slope in case no clear vertical trend is observed);
2. Upper envelope of slopes from the cumulative extrapolation of sand waves for the specific period as explained in Appendix A.4.4.2 – note that for this smaller scale bedforms are not considered as their slopes are only present locally.

A.4.6.2. Historic seabed levels

Historic seabed levels are presented to provide an indication of the lowest seabed levels over the period since World War II relevant to determine possible locations of UXO's. It is assumed that relatively small objects such as Unexploded Ordnances (UXO's) cause no/negligible flow disturbance themselves and therefore will only cause local scour that can result in partial settlement of the object; these objects will, however, not affect the processes responsible for sand wave dynamics. Therefore, they will experience coverage if a sand wave crest passes over.

An UXO is expected to never travel upwards and a typical UXO will self-bury to about half its height. Since this process has a faster timescale than sand wave migration, an UXO will most likely stay at the lowest seabed level it has experienced between 1945 and now. Quantification of initial penetration of UXO's into the seabed is not part of the scope of this study. If significant penetration occurred during impact, then at locations that mainly experienced seabed rising the actual vertical level of the UXO's may be overestimated.

The following historic seabed levels are determined. It must be noted that historic trends are reversed when determining the historic seabed levels.

Lowest Object Level (LOL)
The LOL is the expected minimum seabed level since the World War II and is calculated by adding the following components:

1. Lower envelope of the large-scale seabed over the specific period (which can be similar to the starting large-scale seabed in case no clear vertical trend is observed);

2. Lower envelope of the cumulative extrapolation of sand waves for the specific period as explained in Appendix A.4.4.2;
3. Downward uncertainty band for the specific period;
4. Top of any non-erodible layer.

Best-Estimate Object Level (BEOL)
The BEOL is the expected best-estimate lowest seabed level since the World War II and is calculated by adding the following components:

1. Lower envelope of the large-scale seabed over the specific period (which can be similar to the starting large-scale seabed in case no clear vertical trend is observed);
2. Lower envelope of the cumulative extrapolation of sand waves for the specific period as explained in Appendix A.4.4.2;
3. Downward uncertainty band for the specific period.

Compared to the LOL and Figure A.29, the polygon covers the area between the lower and upper bound migration direction and between the analysed grid point and mean displacement away from the grid point (calculated by multiplying the mean migration rate and the number of years for which the extrapolation is performed).

Highest Object Level (BEOL)
The HOL is the expected maximum lowest seabed level since the World War II and is calculated by adding the following components:

1. Lower envelope of the large-scale seabed over the specific period (which can be similar to the starting large-scale seabed in case no clear vertical trend is observed);
2. Lower envelope of the cumulative extrapolation of sand waves for the specific period as explained in Appendix A.4.4.2;
3. Downward uncertainty band for the specific period.

Compared to the LOL and Figure A.29, the polygon covers the area between the lower and upper bound migration direction and between the analysed grid point and minimum displacement away from the grid point (calculated by multiplying the lower bound migration rate and the number of years for which the extrapolation is performed).

A.4.7 Classification of extrapolated seabed levels.

In the final step the LSBL and HSBL and the corresponding seabed level lowering and rising (calculated from the difference between the measured bathymetry and the LSBL and HSBL respectively) are classified into zones corresponding to certain bandwidths of changes in seabed levels. The classification of these zones is based on the expected seabed level lowering or rising or maximum slopes (see Table A.4).

Note that these classifications are for illustration purposes only. The actual classification is dependent on the design of the support structures and properties of electricity cables and should be adjusted accordingly once this information is available.

The classification of the zones differs for seabed lowering and rising (Table A.4). This implies that for each data point, two classifications apply: one for the expected seabed rising and one for the expected seabed lowering. For each point, the highest absolute value is displayed in the combined map (with absolute seabed changes over 5 m being the most severe. An example of this classification is shown in Figure A.31.

Table A.4: *Classification zones for bed level lowering and rise.*

Classification zones	Bed level lowering [m]	Bed level rising [m]
1	0 > dz ≥ -1.0	0 < dz ≤ 1.0
2	-1.0 > dz ≥ -3.0	1.0 < dz ≤ 3.0
3	-3.0 > dz ≥ -5.0	3.0 < dz ≤ 5.0
4	dz < -5.0	dz > 5.0

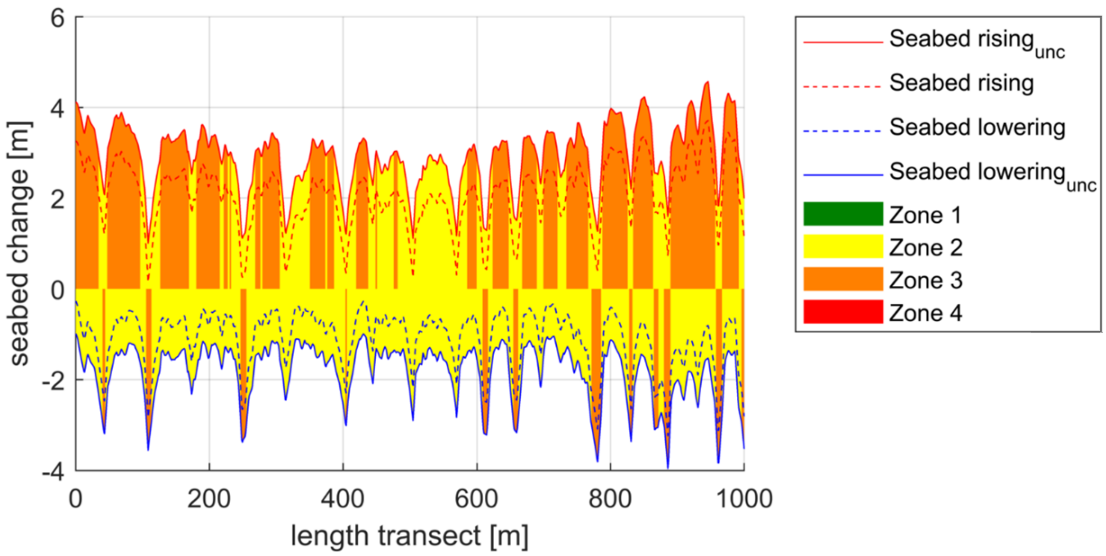

Figure A.31: Example of classification of seabed levels along a transect. The figure indicates the expected maximum seabed rising and lowering over a specific period translated to the four classification zones (e.g. all seabed changes larger than 5 m are classified as zone 4).

B Additional hydrodynamic model results

The following figure presents the residual total sediment transports of each of the years 2017-2018 and 2020-2021. Residual transport over the 4 simulated years in IJV are very similar in magnitude and direction to those presented in Figure 5.6. This indicates that the long-term behaviour of the system in terms of tide and wind-driven sediment transport can be well represented by the annual derived values.

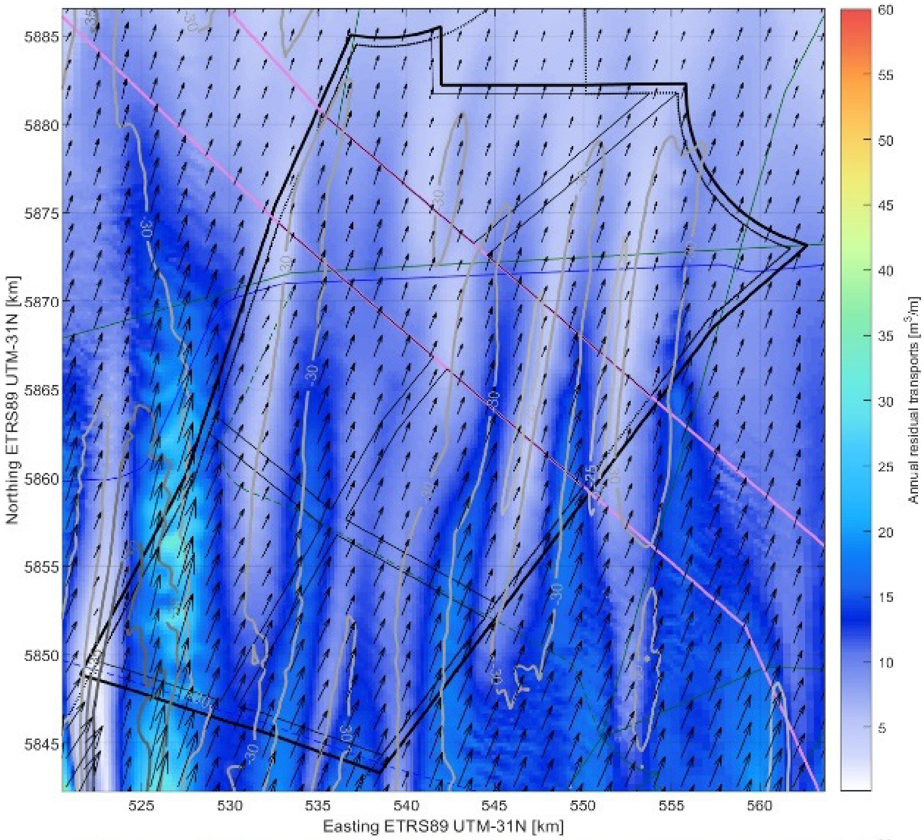

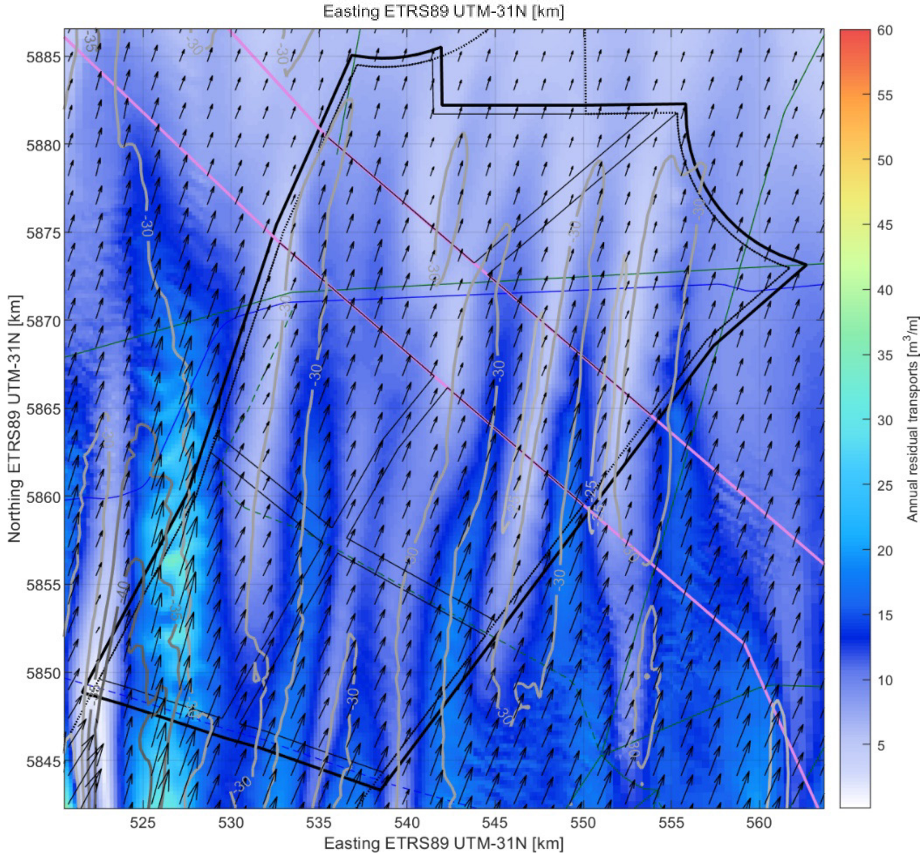

Figure B.1: Residual total sediment transport vectors over the year 2017 (top panel) and 2018 (bottom panel) including the effects of meteorological forcing. The vectors are displayed over the bed level. Other lines indicate extents of the OWF Sites (black lines), bathymetry contours (grey lines), navigation channel (pink lines), existing cables and pipelines (green and blue lines).

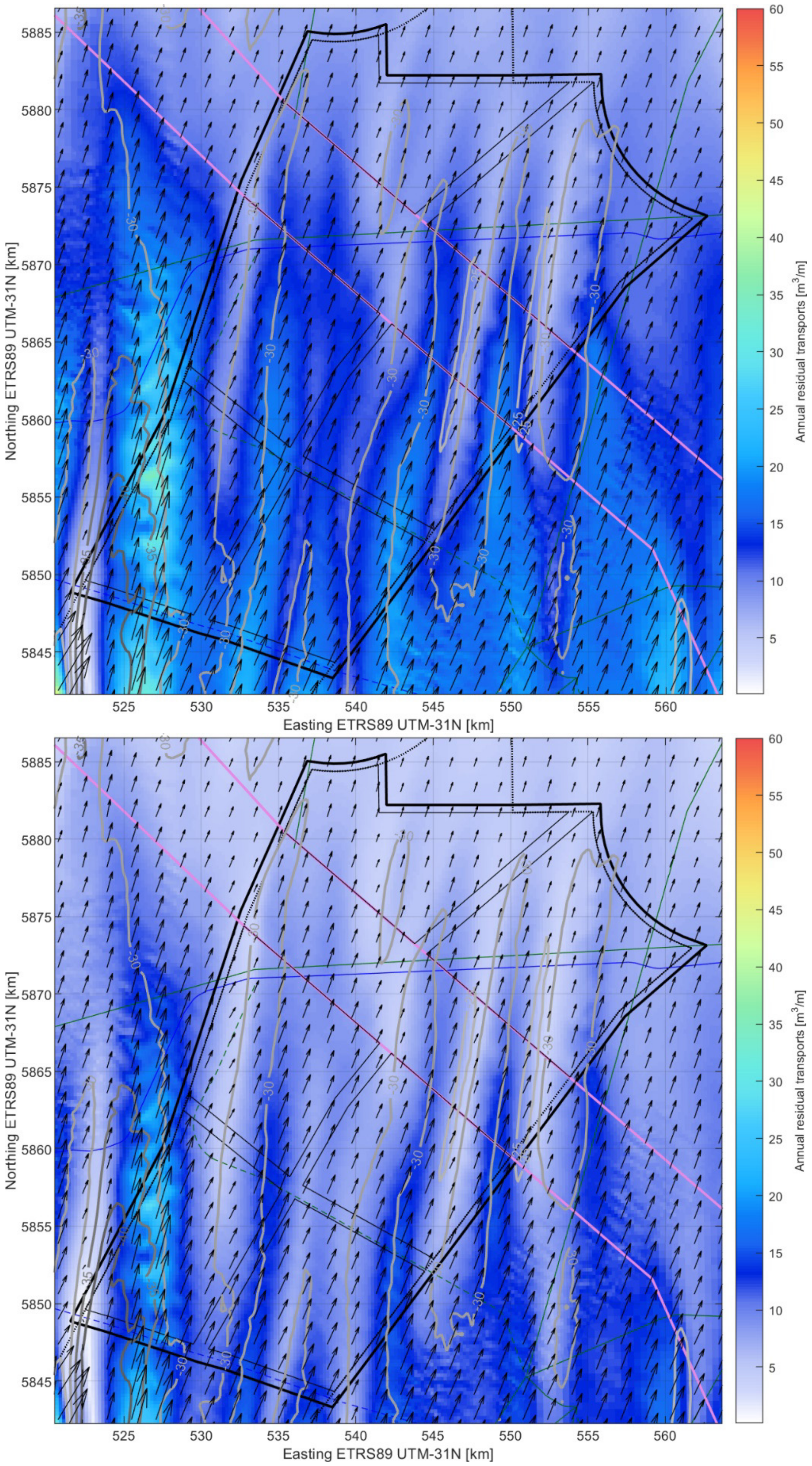

Figure B.2: Residual total sediment transport vectors over the year 2017 (top panel) and 2018 (bottom panel) including the effects of meteorological forcing. The vectors are displayed over the bed level. Other lines indicate extents of the OWF Sites (black lines), bathymetry contours (grey lines), navigation channel (pink lines), existing cables and pipelines (green and blue lines).

C Geological and geophysical analysis

This appendix provides additional figures of the geological and geophysical analysis presented in Section 4.2.2. First Appendix C.1 provides an overview of the grain size distribution for various depth classes followed by the fines percentages in Appendix C.2 and an overview of the Vibrocore sections Appendix C.3.

C.1 Grain size distribution

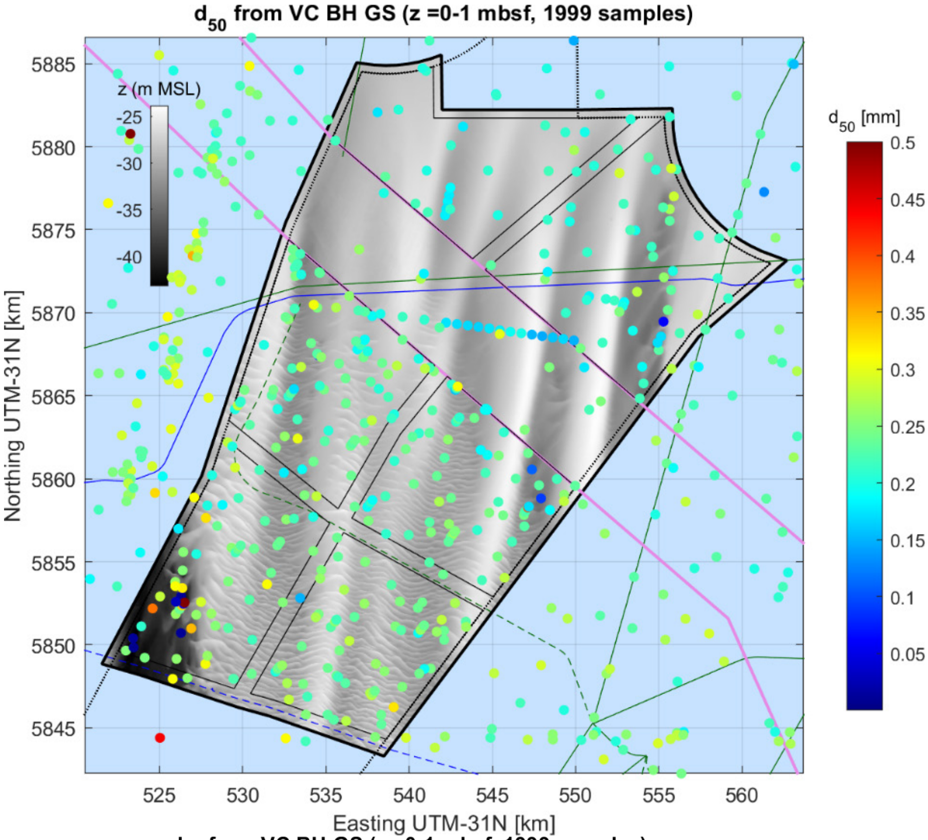

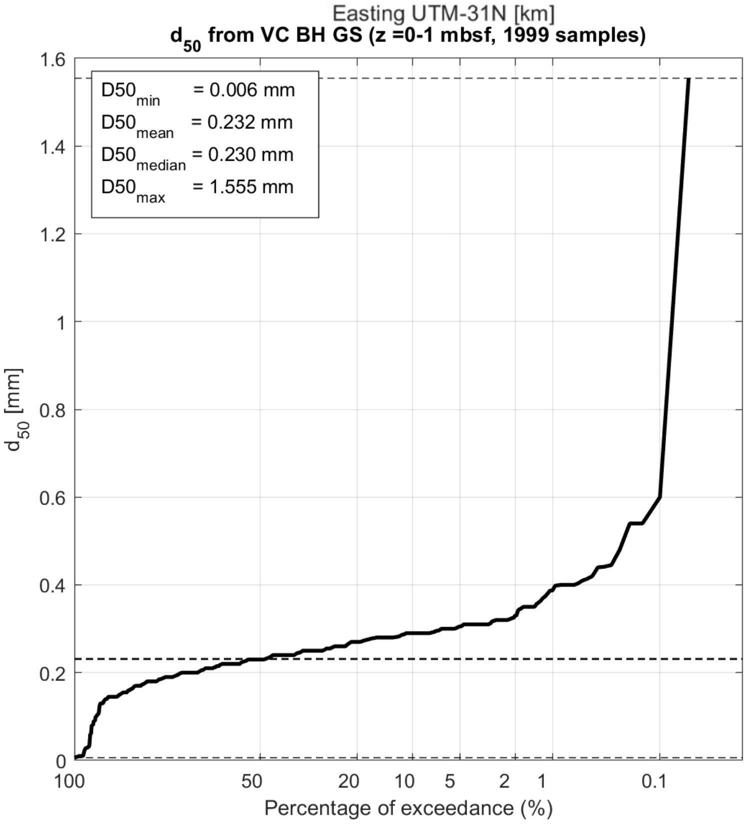

Figure C.1: Average grain size distribution in the first (0-1) metre below the seabed based on geotechnical data (boreholes, Vibrocores and grab samples) by Fugro (2022b, 2022c, 2022d, 2022e, 2022g); GEOxyz (2021) presented as spatial overview (top plot) and as non -exceedance curve (bottom plot).

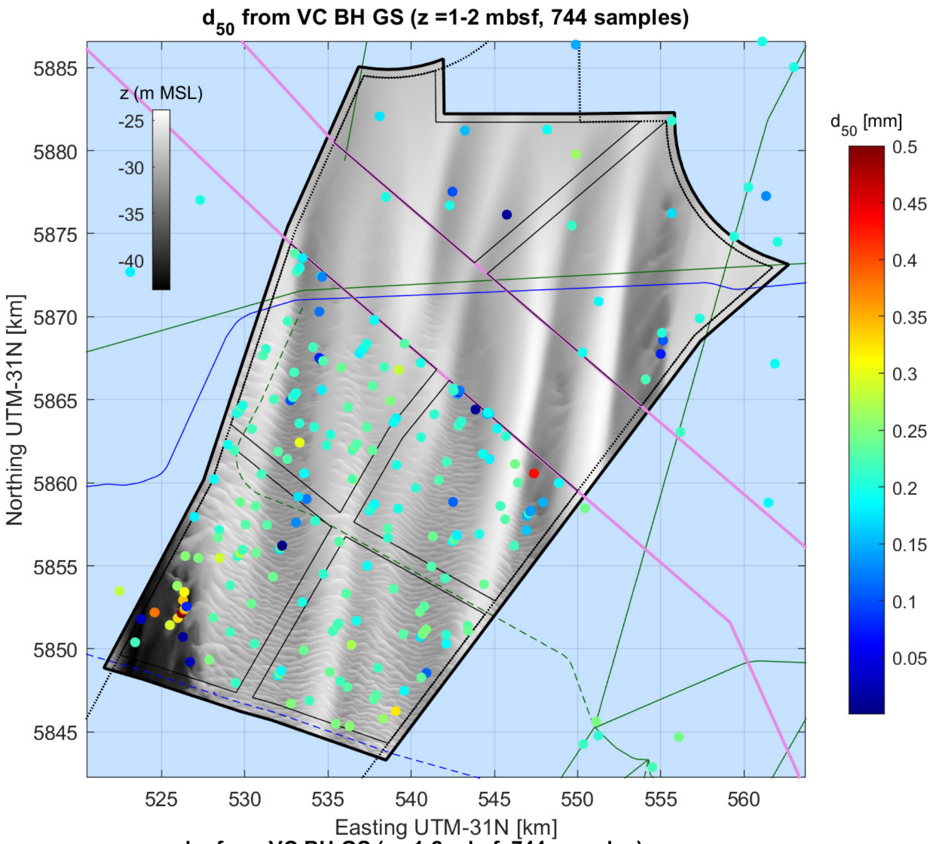

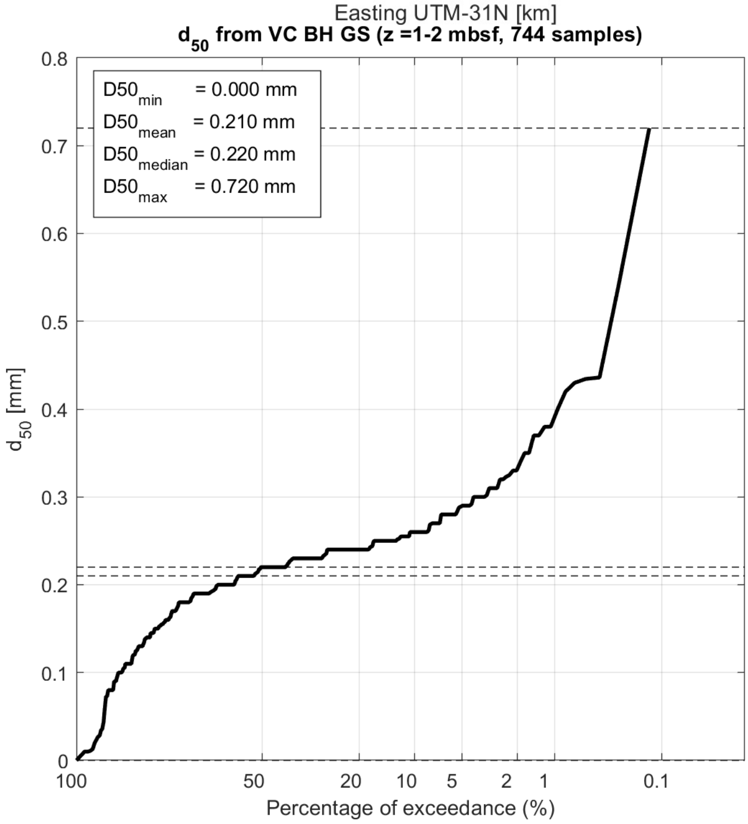

Figure C.2: Average grain size distribution in the second (1-2) metre below the seabed based on geotechnical data (boreholes and Vibrocores) by Fugro (2022c, 2022d, 2022e, 2022g) presented as spatial overview (top plot) and as non -exceedance curve (bottom plot).

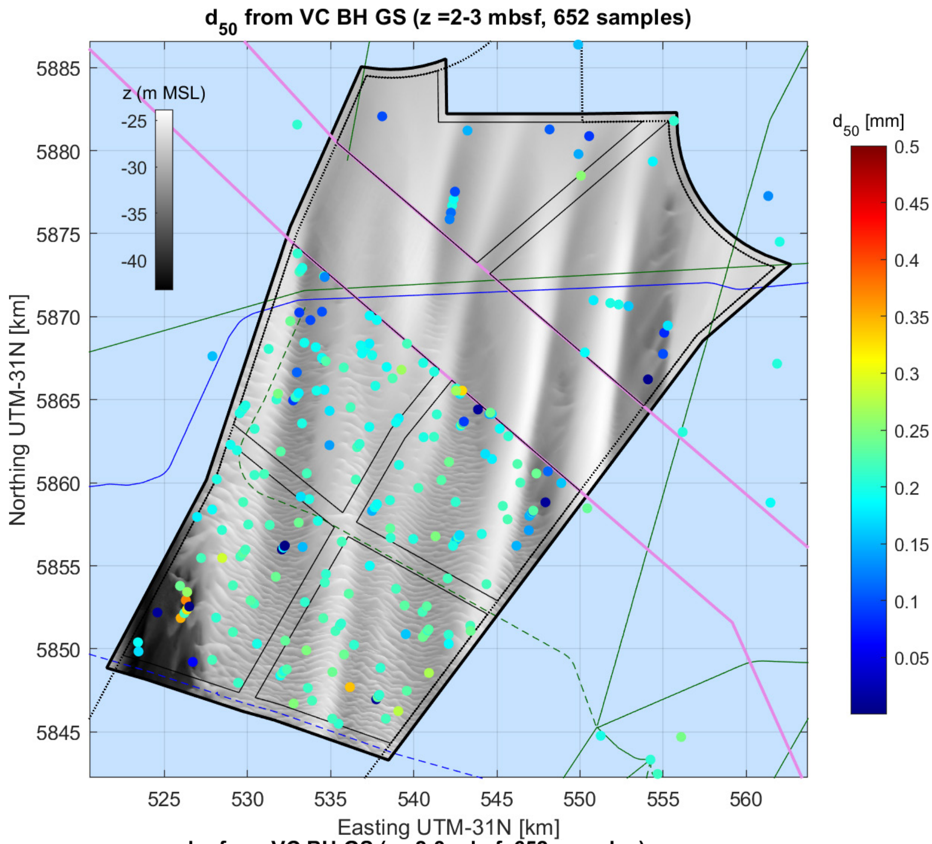

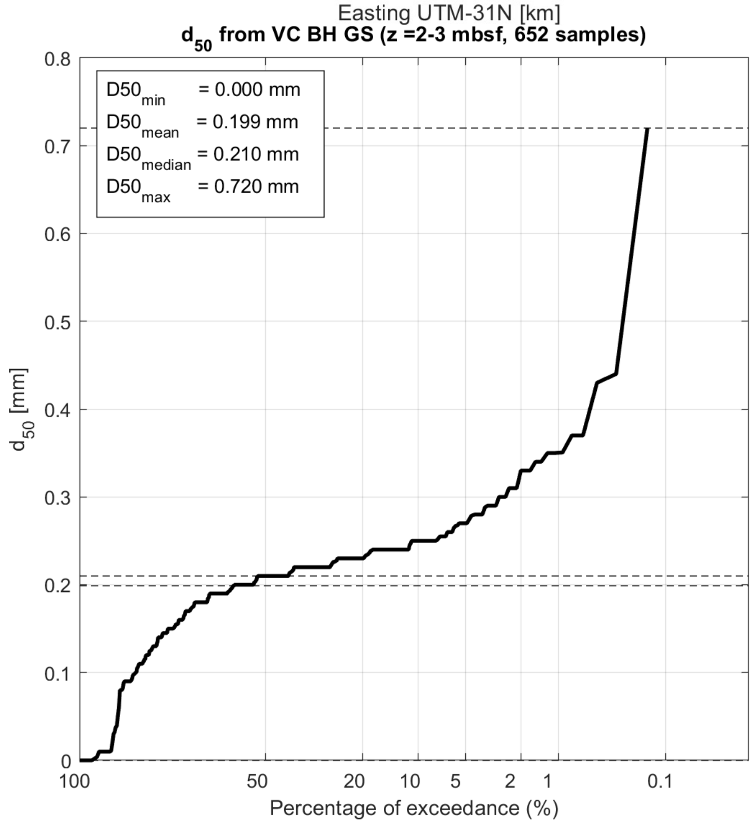

Figure C.3: Average grain size distribution in the third (2-3) metre below the seabed based on geotechnical data (boreholes and Vibrocores) by Fugro (2022c, 2022d, 2022e, 2022g) presented as spatial overview (top plot) and as non -exceedance curve (bottom plot).

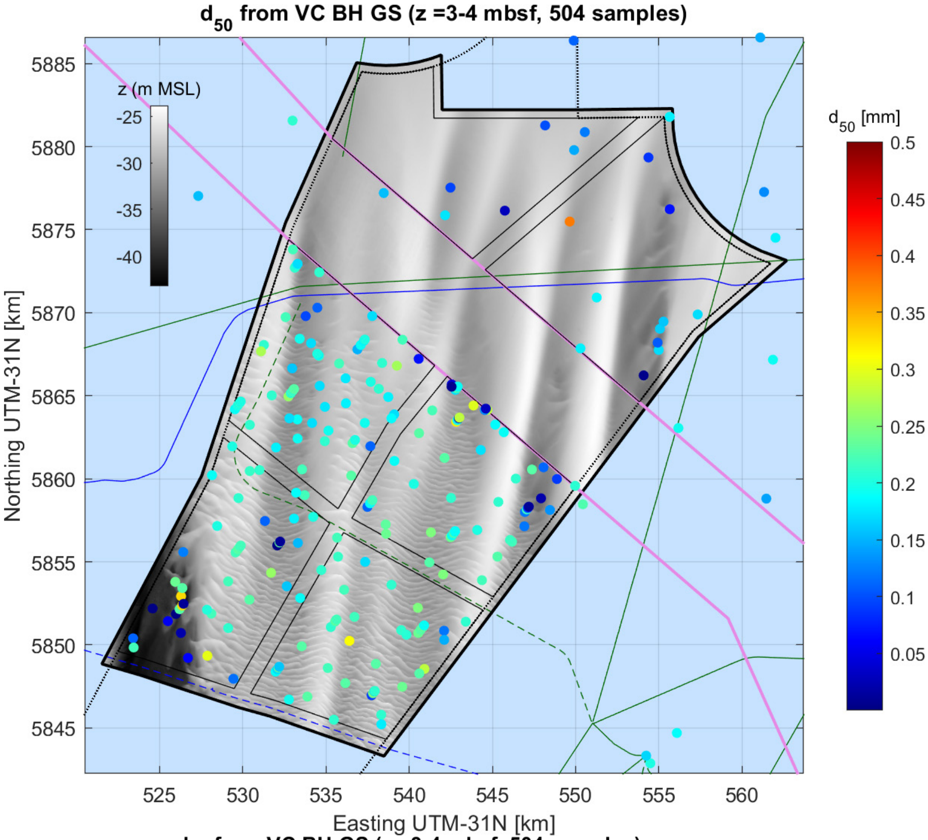

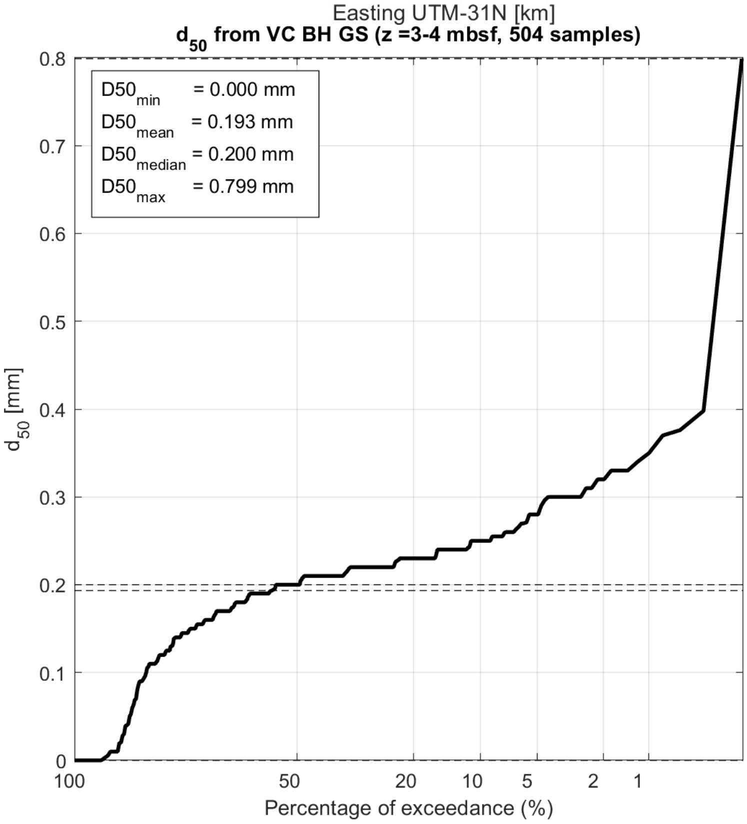

Figure C.4: Average grain size distribution in the fourth (3-4) metre below the seabed based on geotechnical data (boreholes and Vibrocores) by Fugro (2022c, 2022d, 2022e, 2022g) presented as spatial overview (top plot) and as non -exceedance curve (bottom plot).

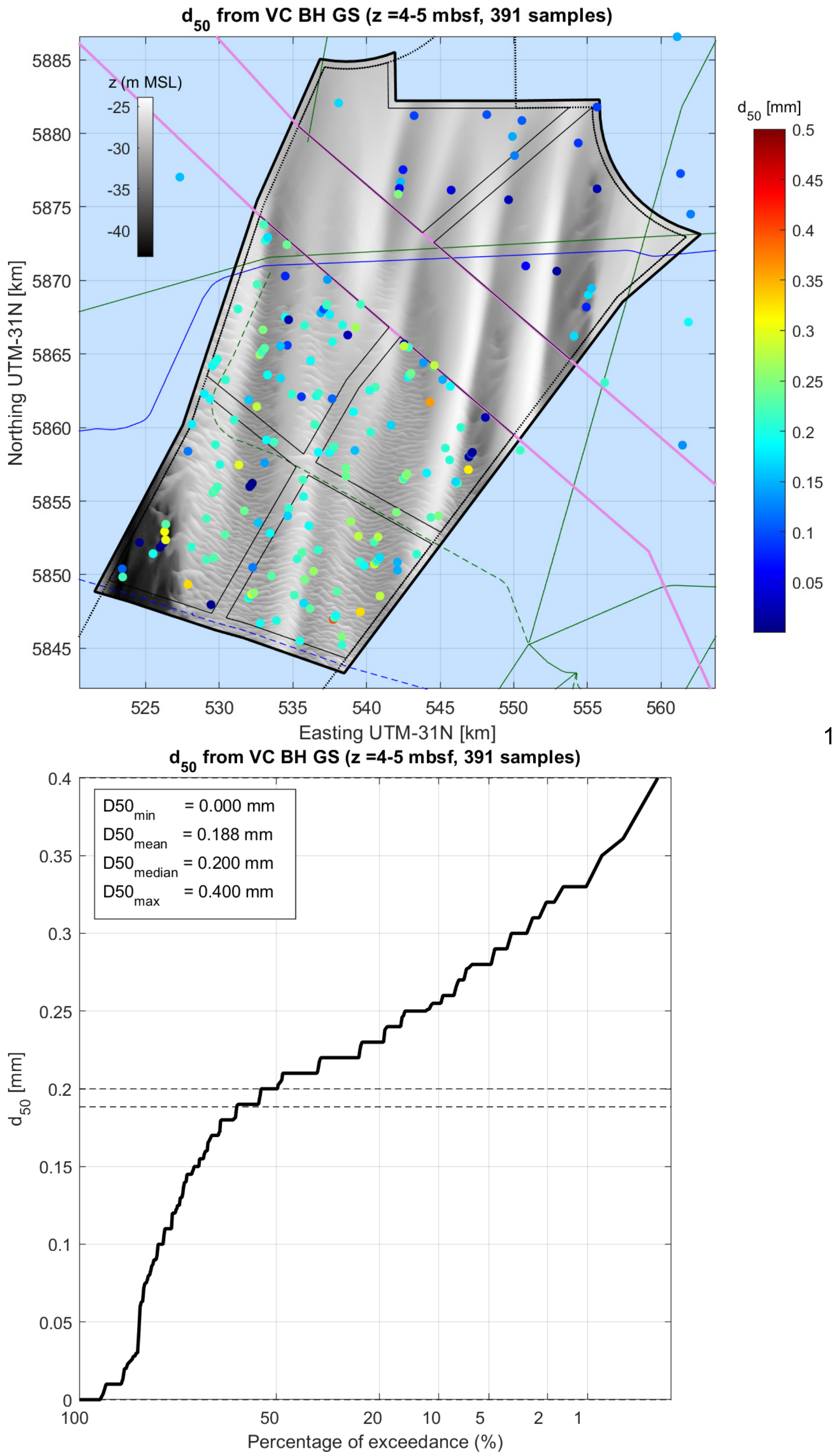

Figure C.5: Average grain size distribution in the fifth (4-5) metre below the seabed based on geotechnical data (boreholes and Vibrocores) by Fugro (2022c, 2022d, 2022e, 2022g) presented as spatial overview (top plot) and as non -exceedance curve (bottom plot).

C.2 Fines content

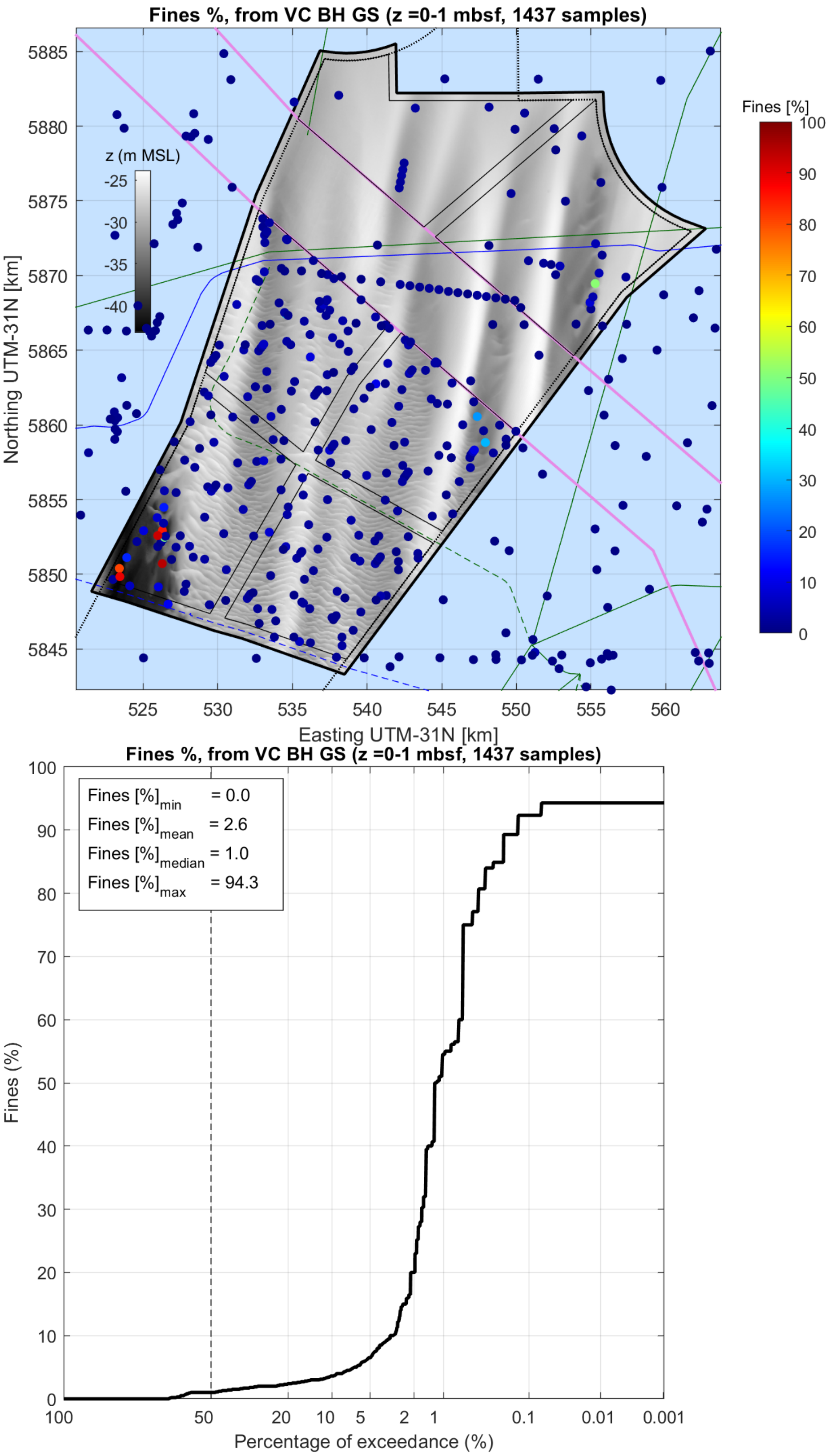

Figure C.6: Fines content in the first (0-1) metre below the seabed based on geotechnical data (boreholes, Vibrocores and grab samples) by Fugro (2022b, 2022c, 2022d, 2022e, 2022g); GEOxyz (2021) presented as spatial overview (top plot) and as non -exceedance curve (bottom plot).

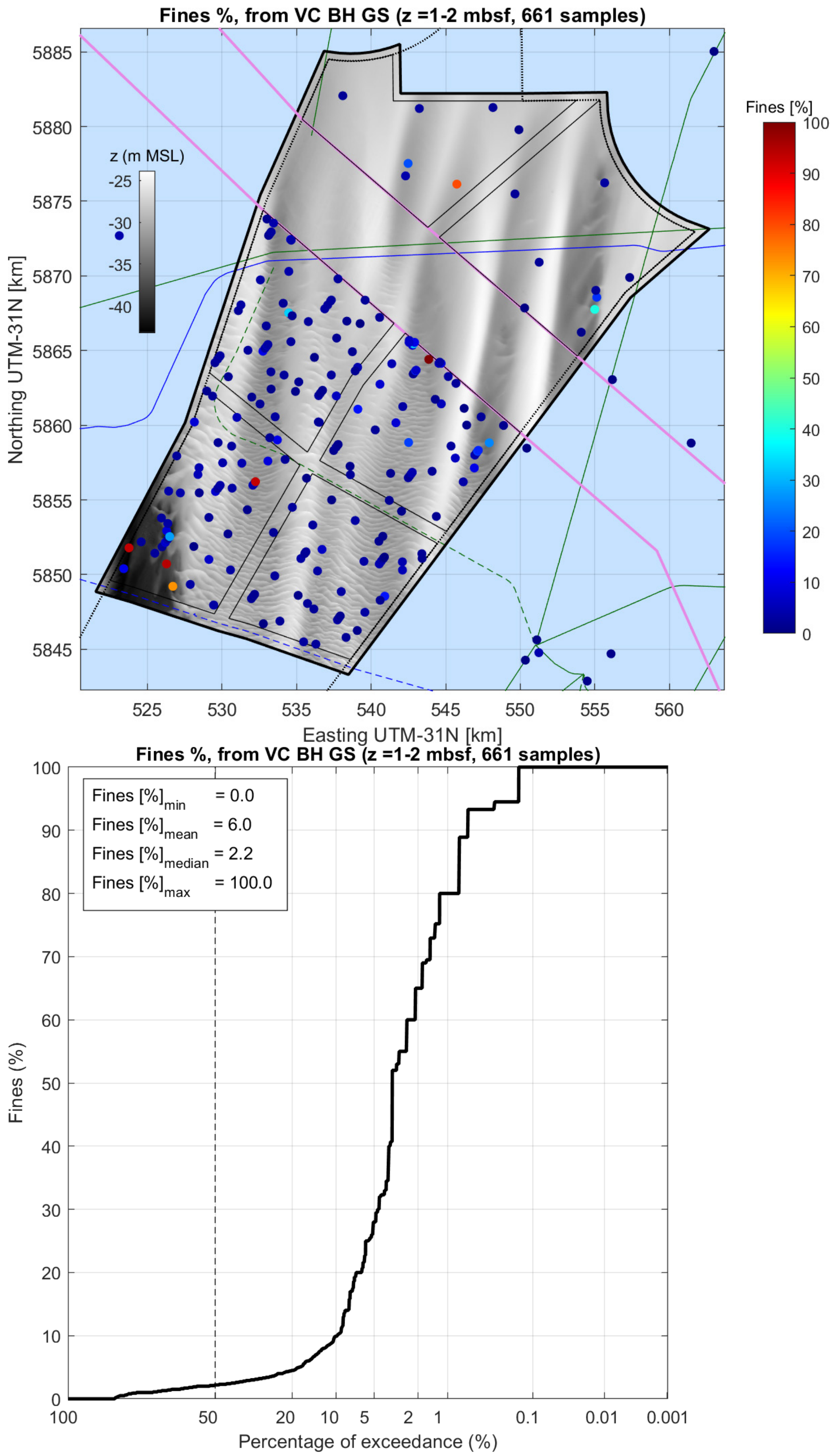

Figure C.7: Fines content in the second (1-2) metre below the seabed based on geotechnical data (boreholes and Vibrocores) by Fugro (2022c, 2022d, 2022e, 2022g) presented as spatial overview (top plot) and as non -exceedance curve (bottom plot).

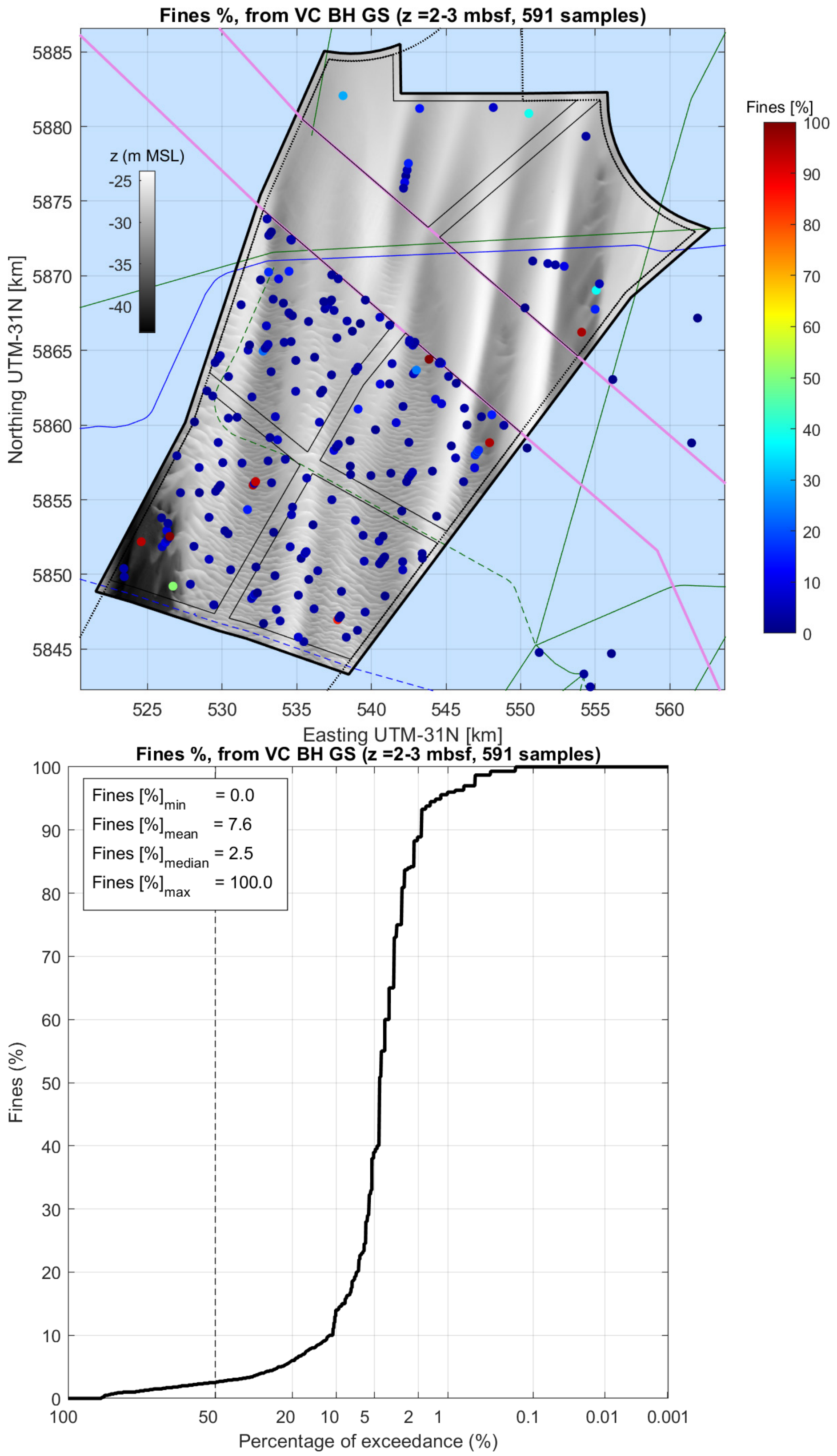

Figure C.8: Fines content in the third (2-3) metre below the seabed based on geotechnical data (boreholes and Vibrocores) by Fugro (2022c, 2022d, 2022e, 2022g) presented as spatial overview (top plot) and as non -exceedance curve (bottom plot).

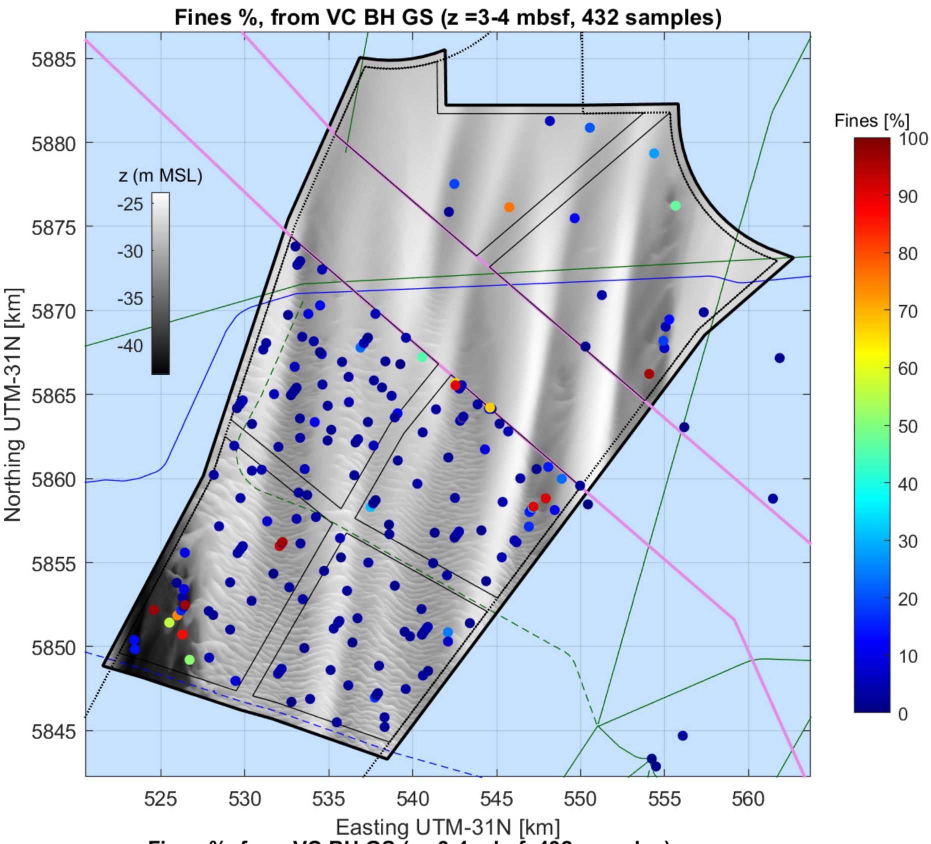

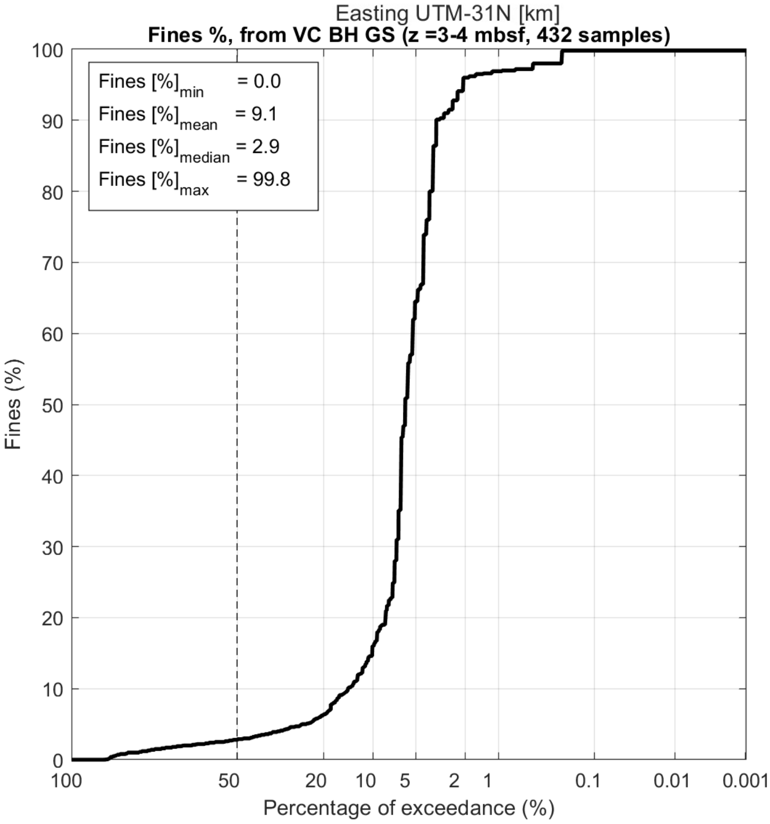

Figure C.9: Fines content in the fourth (3-4) metre below the seabed based on geotechnical data (boreholes and Vibrocores) by Fugro (2022c, 2022d, 2022e, 2022g) presented as spatial overview (top plot) and as non -exceedance curve (bottom plot).

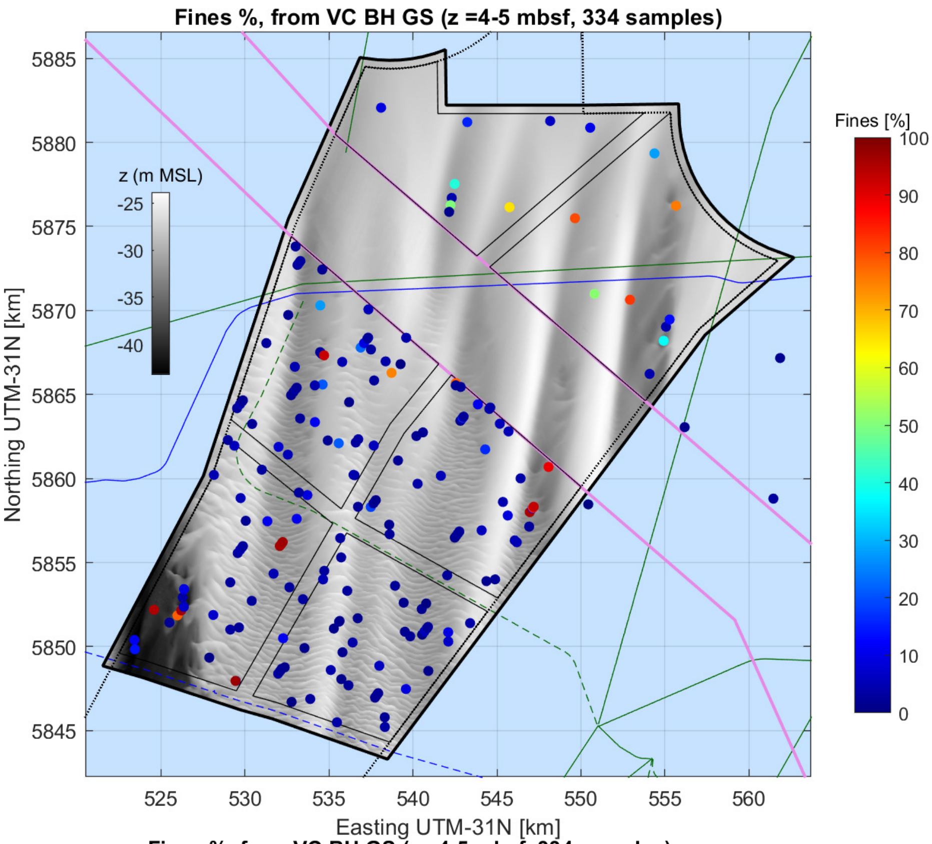

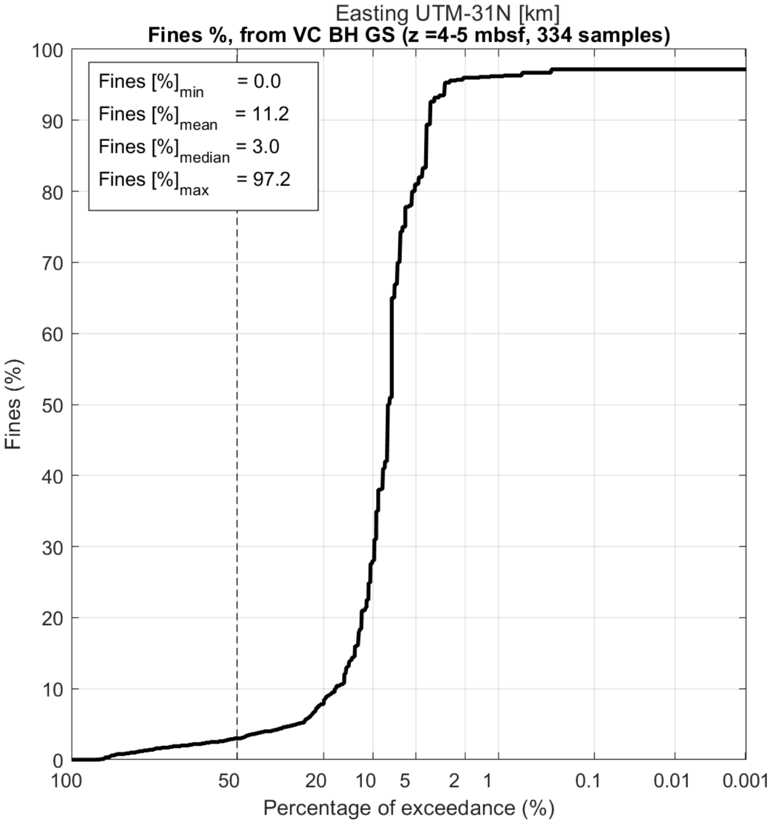

Figure C.10: Fines content in the fifth (4-5) metre below the seabed based on geotechnical data (boreholes and Vibrocores) by Fugro (2022c, 2022d, 2022e, 2022g) presented as spatial overview (top plot) and as non -exceedance curve (bottom plot).

C.3 Vibrocore transects

This appendix presents the 19 transects over several Vibrocore locations as discussed in Section 4.2.2.2.

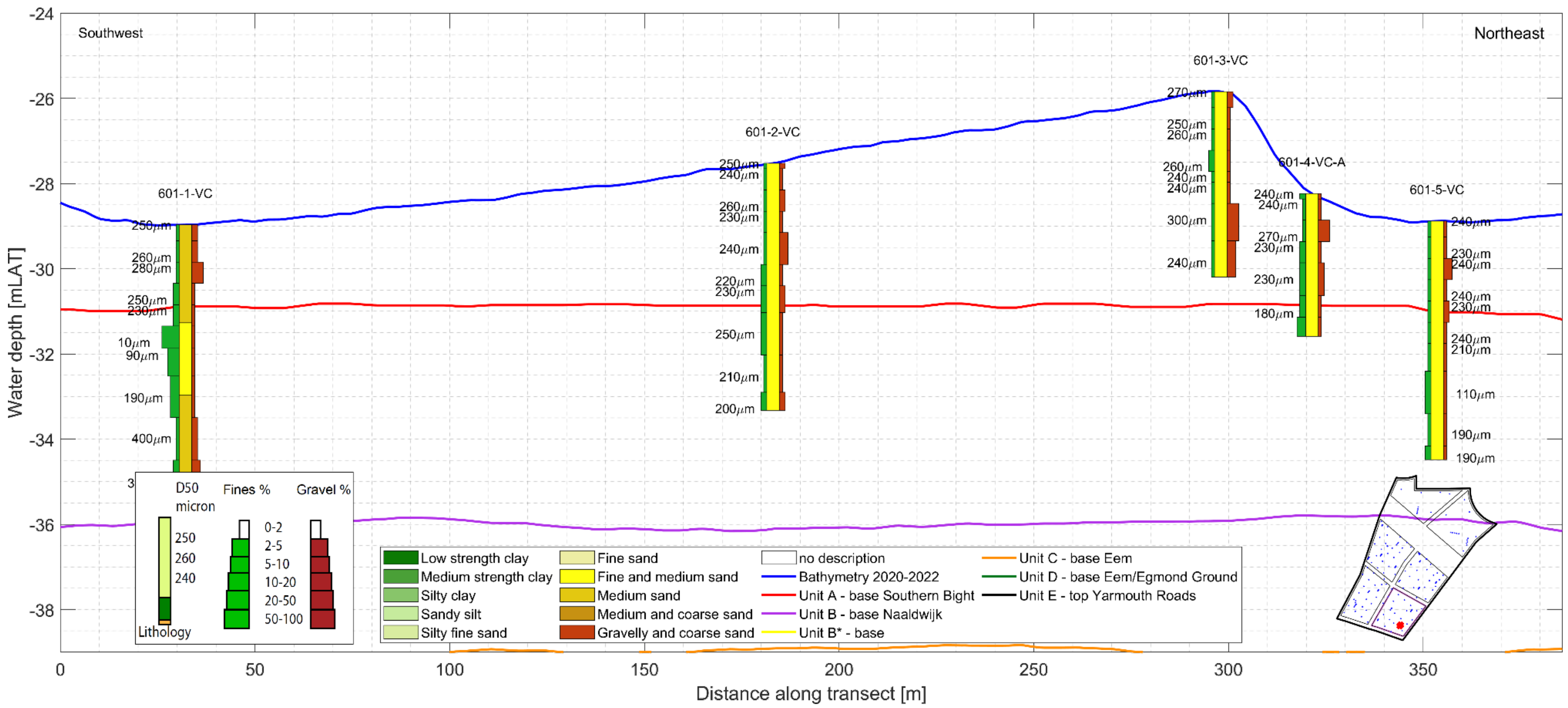

Figure C.11: Vibrocore transect 601.

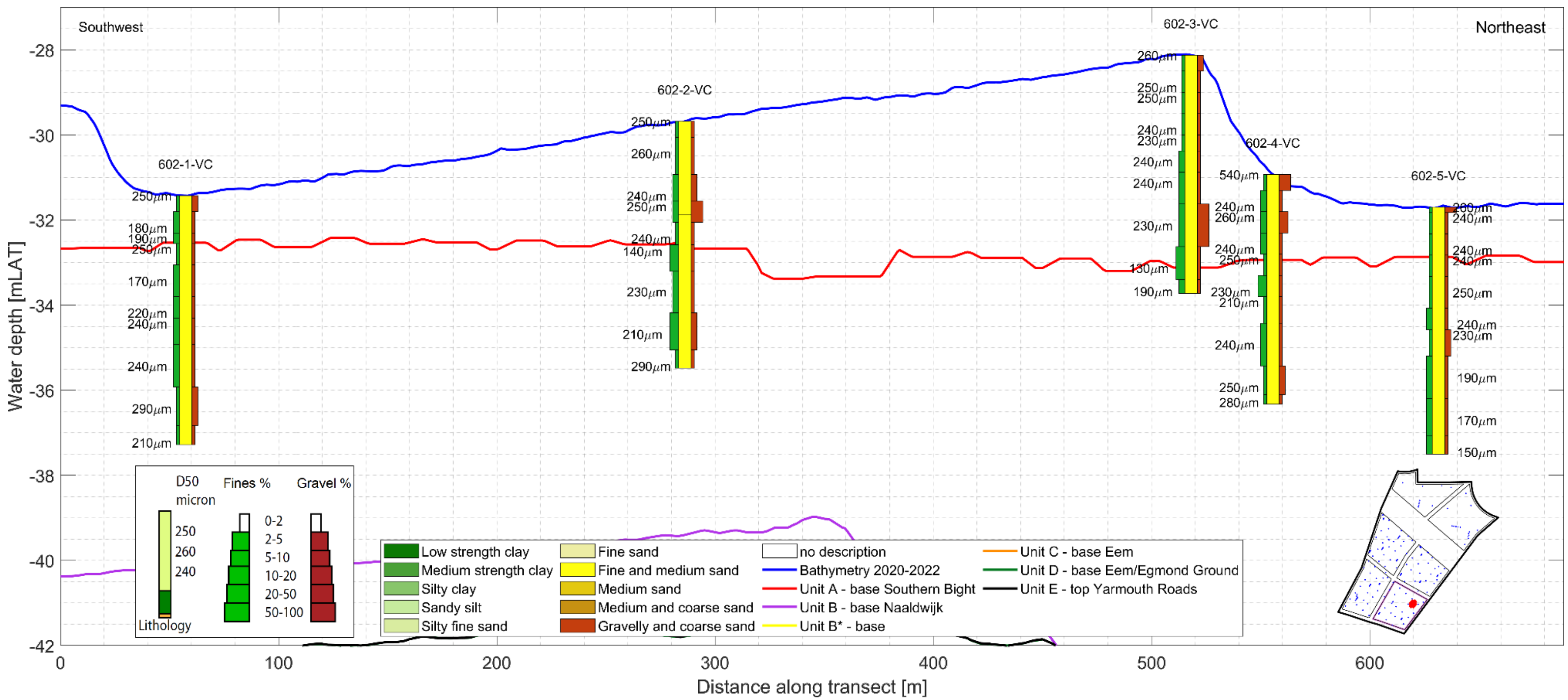

Figure C.12: Vibrocore transect 602.

Figure C.13: Vibrocore transect 603.

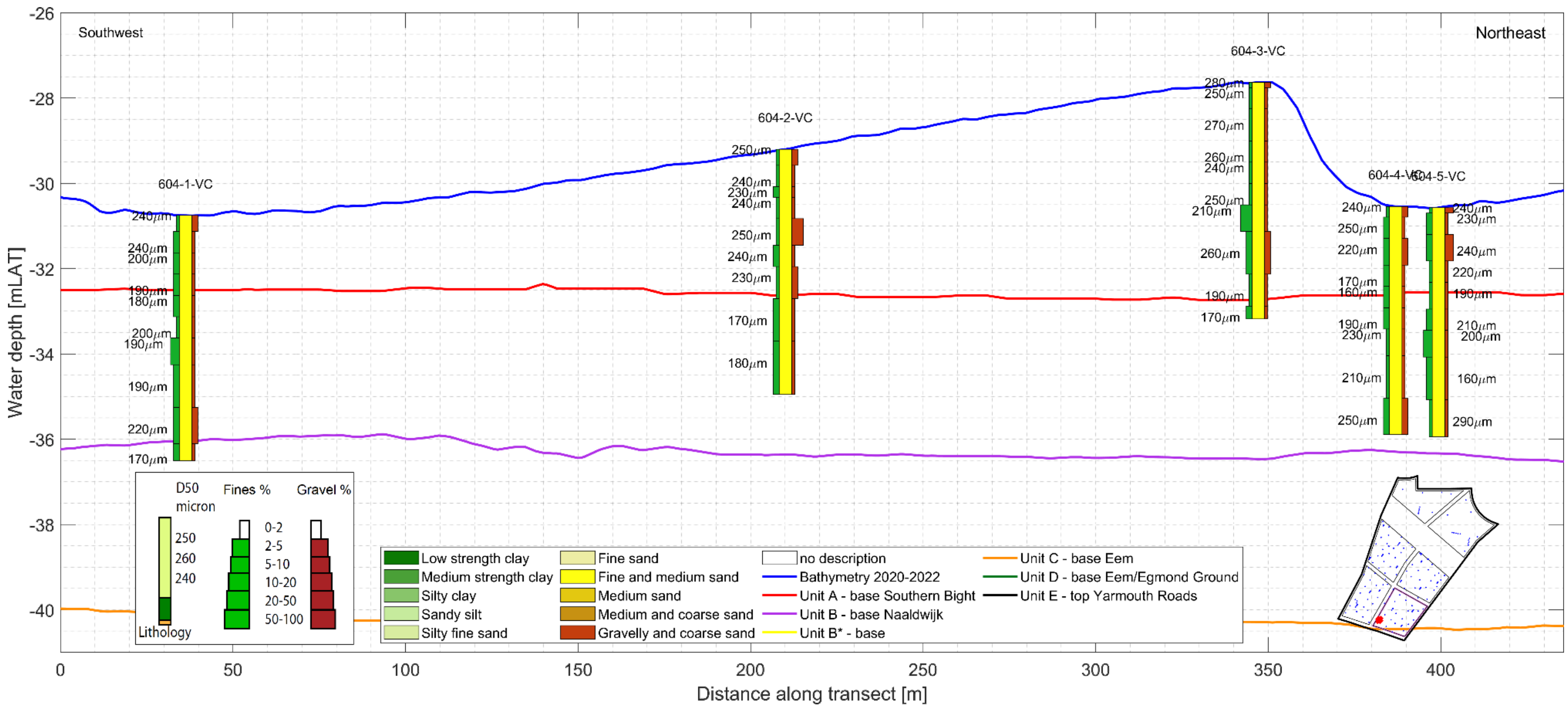

Figure C.14: Vibrocore transect 604.

Deltares

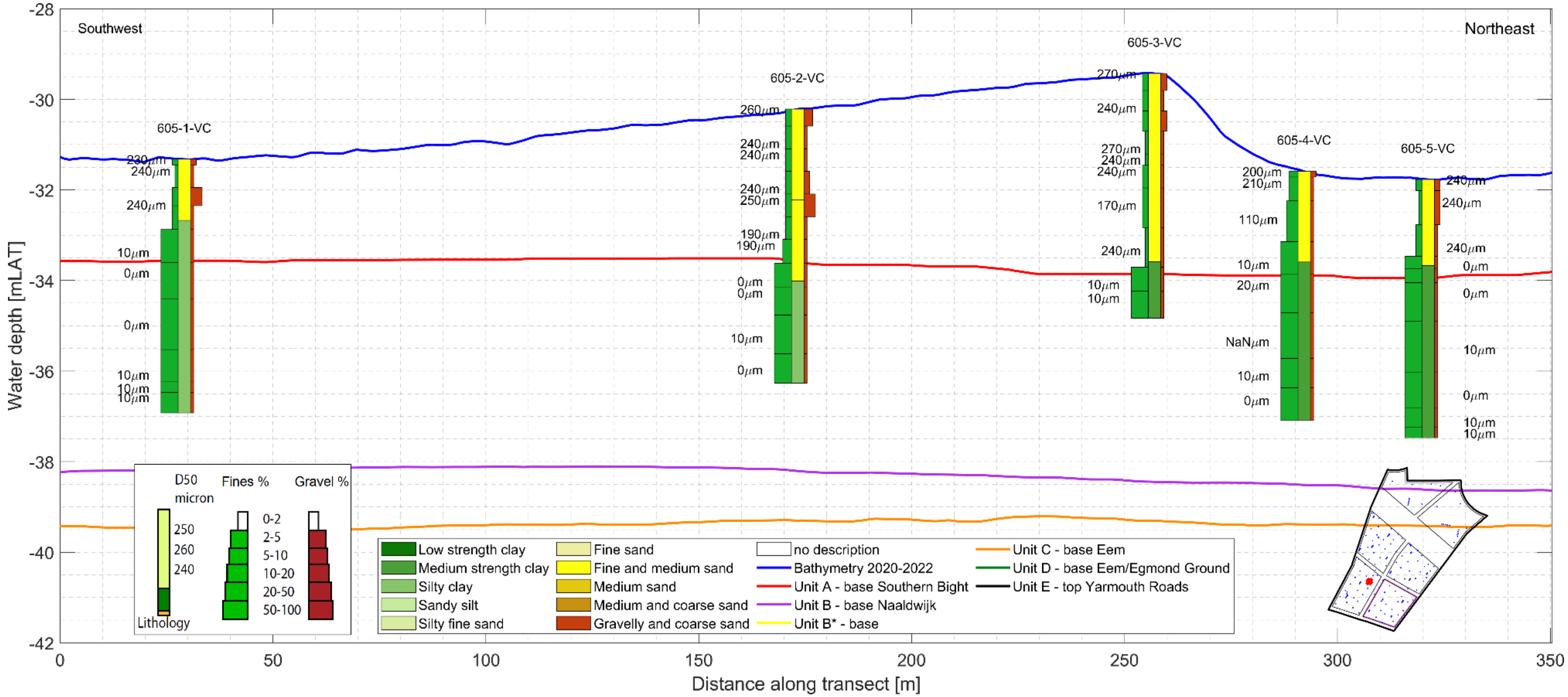

Figure C.15: Vibrocore transect 605.

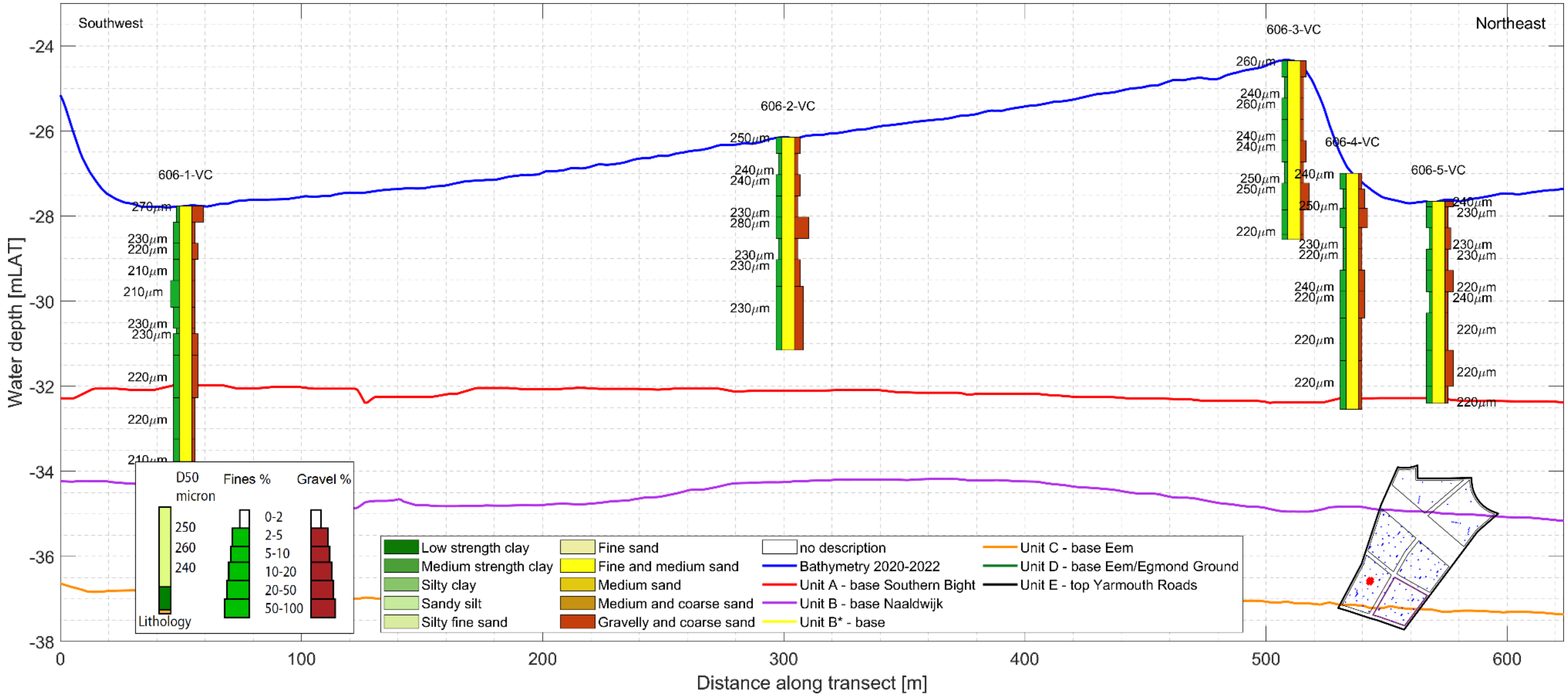

Figure C.16: Vibrocore transect 606.

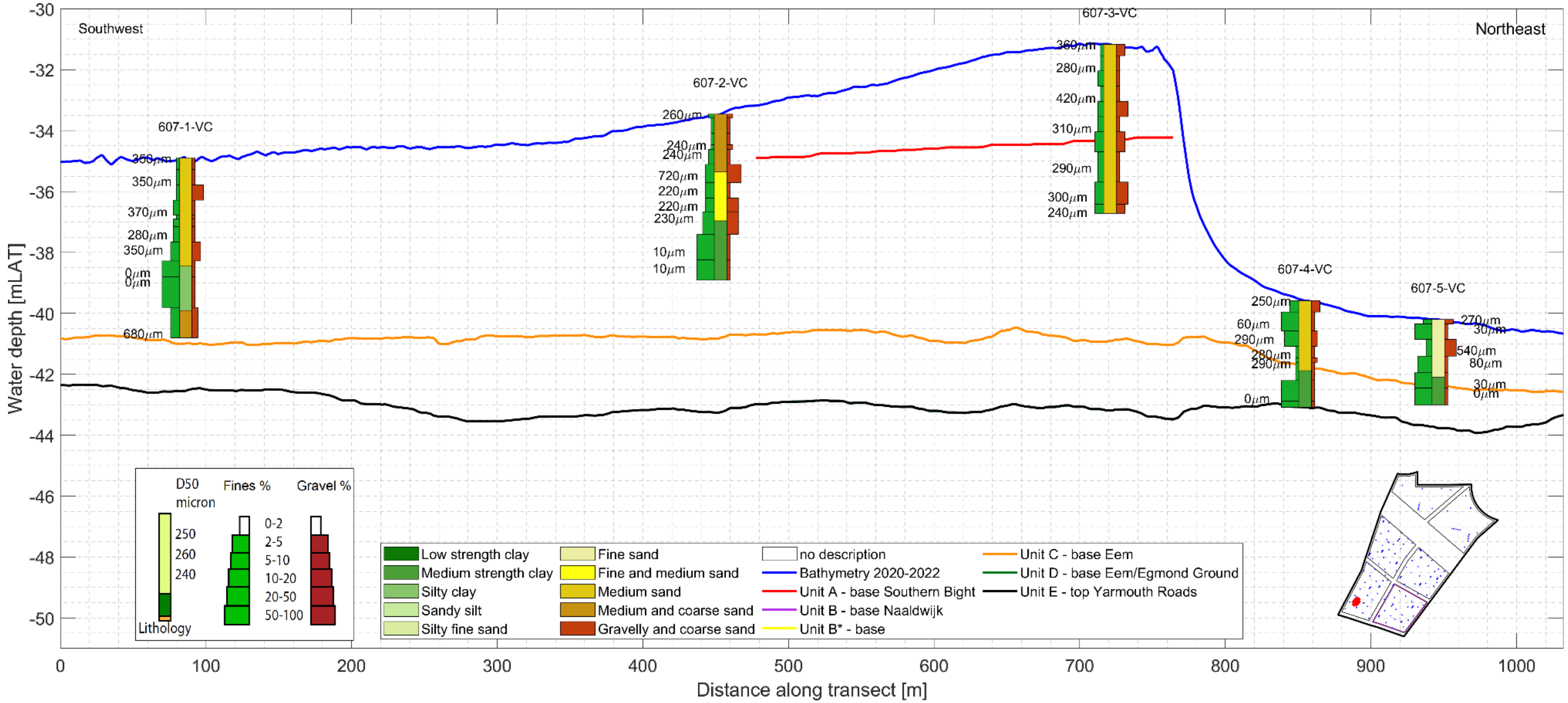

Figure C.17: Vibrocore transect 607.

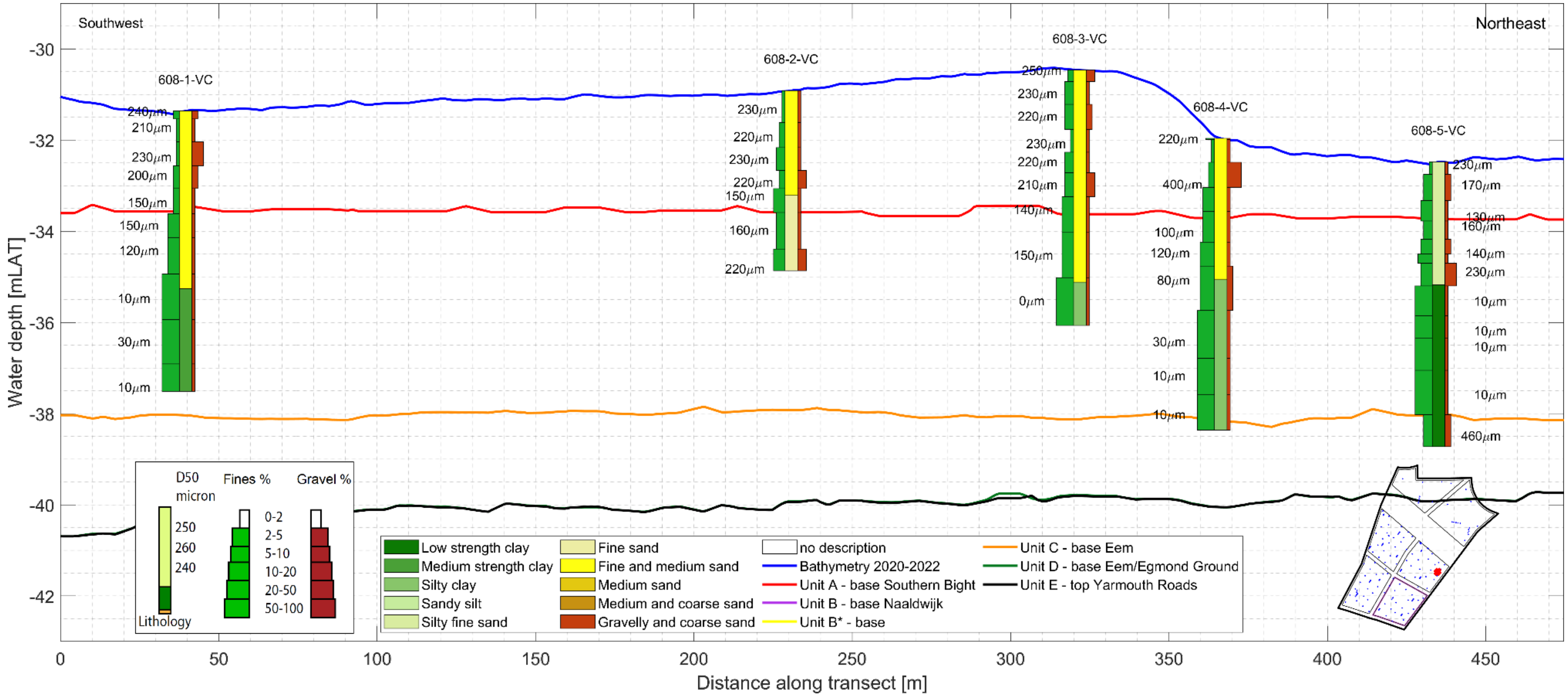

Figure C.18: Vibrocore transect 608.

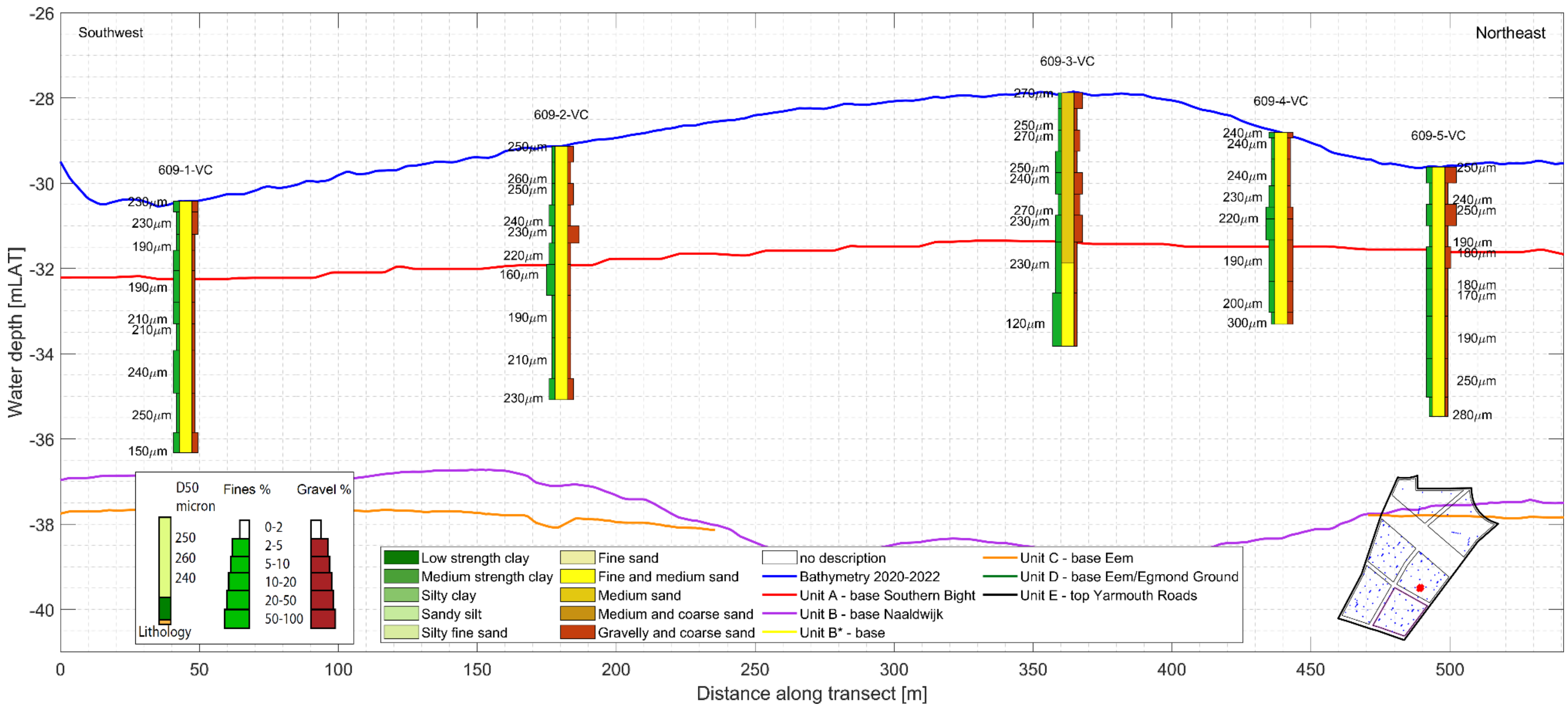

Figure C.19: Vibrocore transect 609.

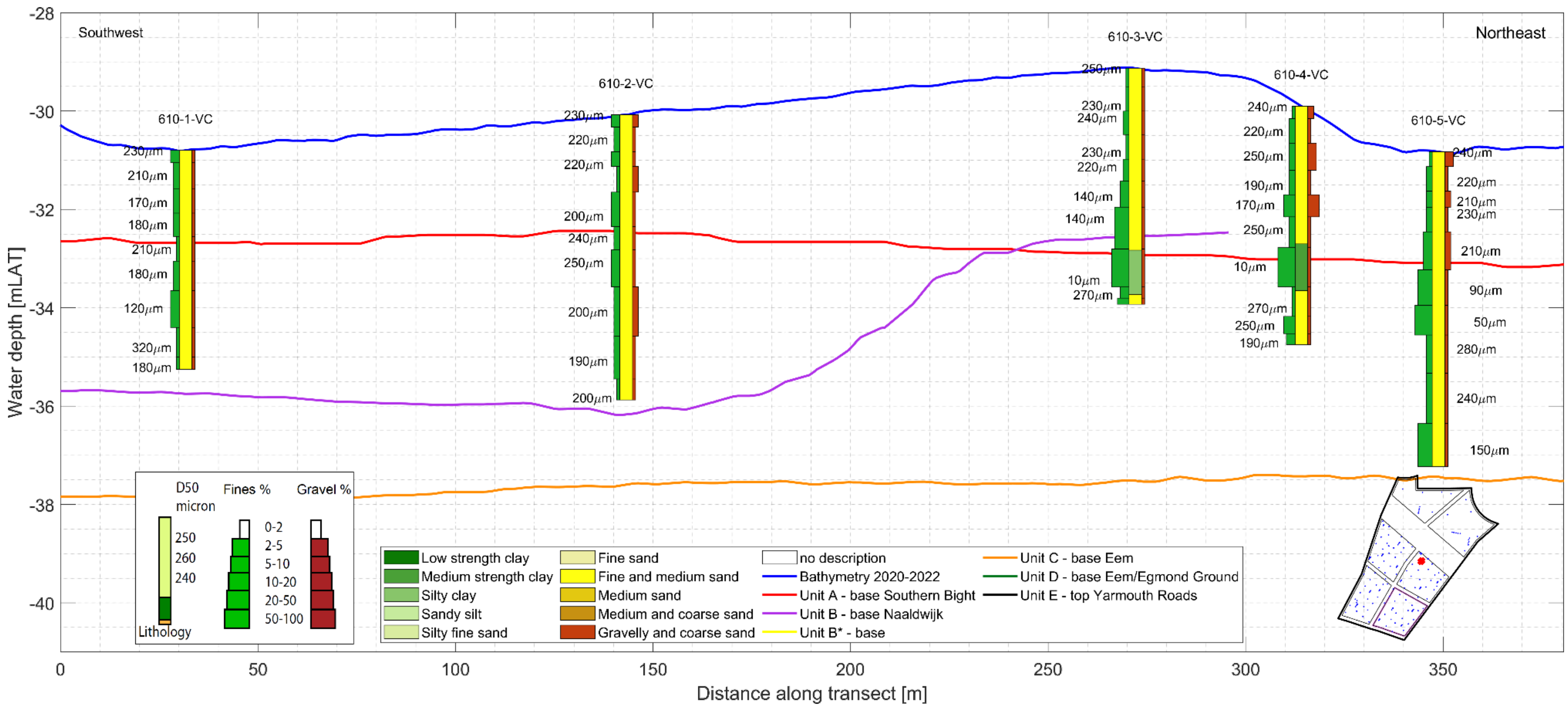

Figure C.20: Vibrocore transect 610.

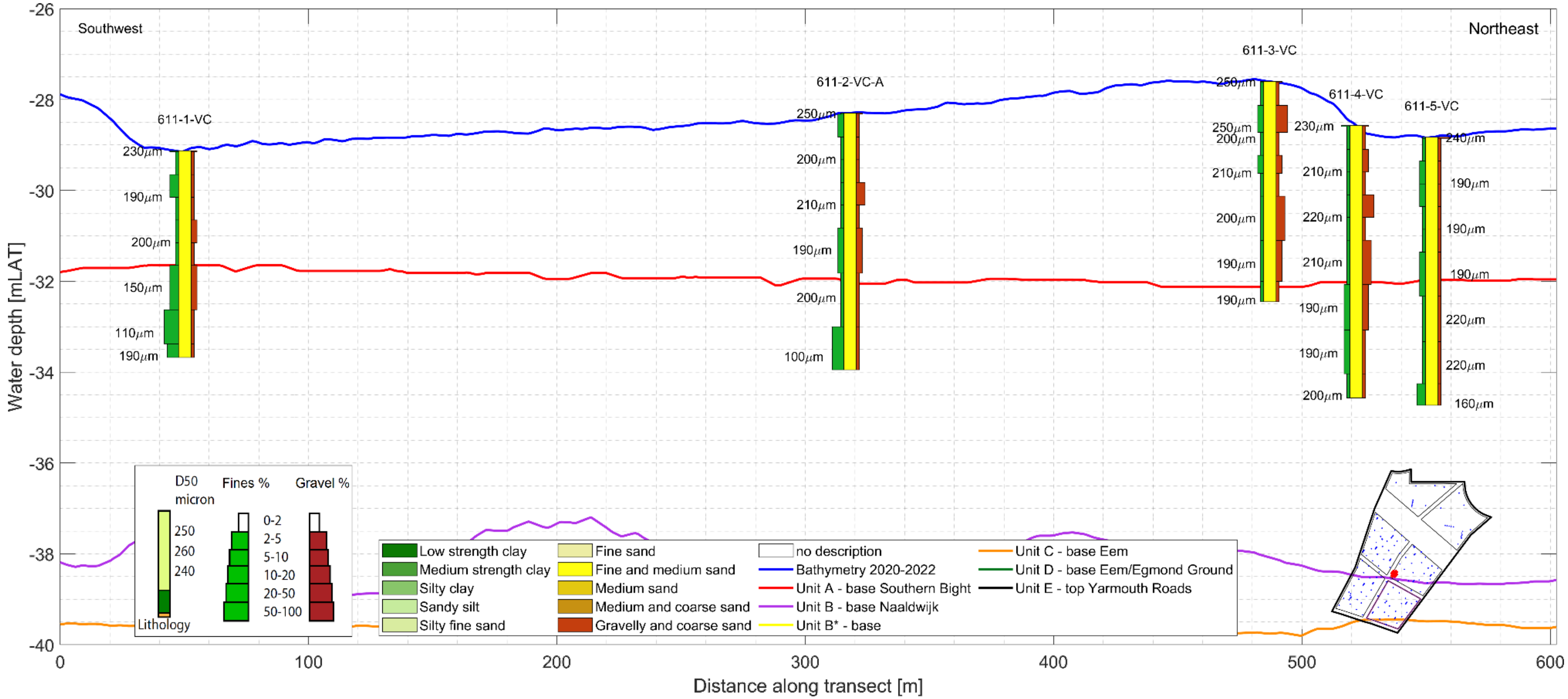

Figure C.21: Vibrocore transect 611.

Deltares

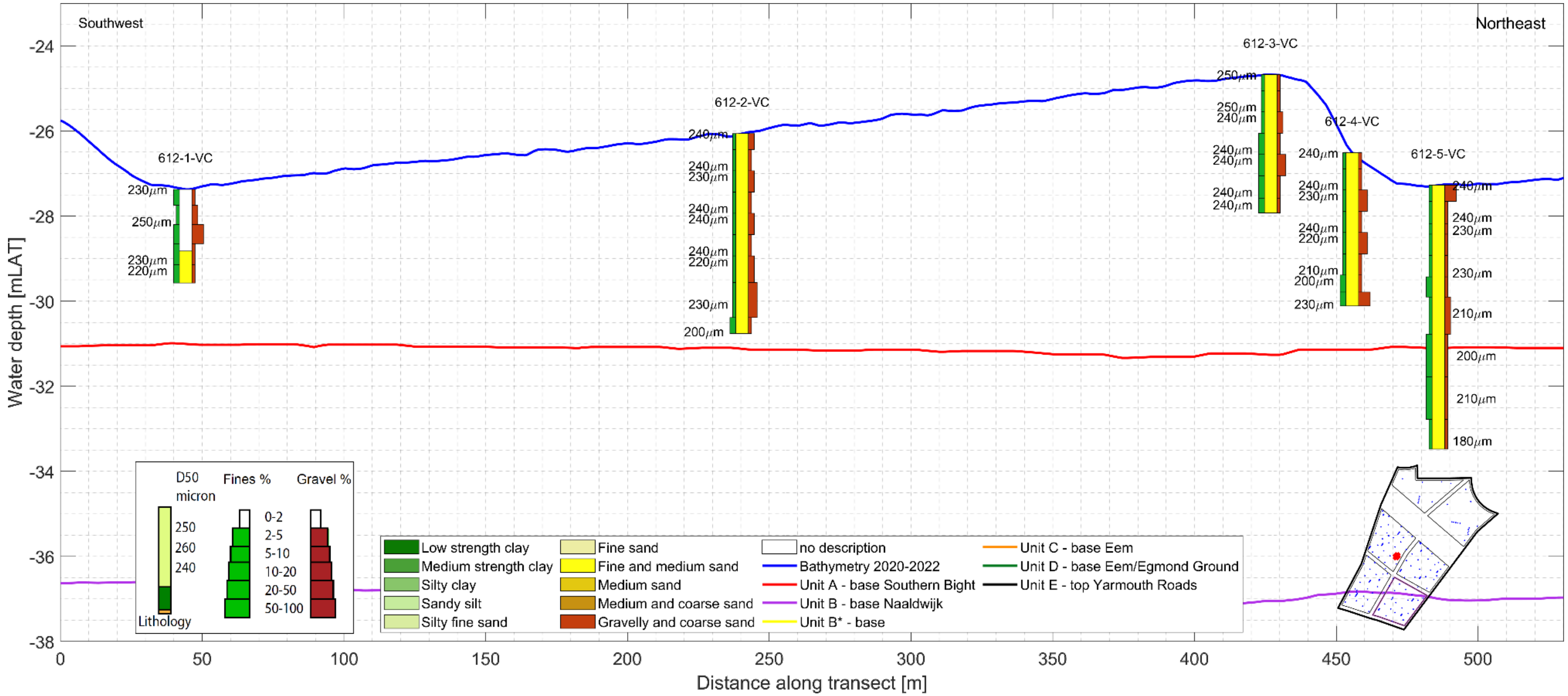

Figure C.22: Vibrocore transect 612.

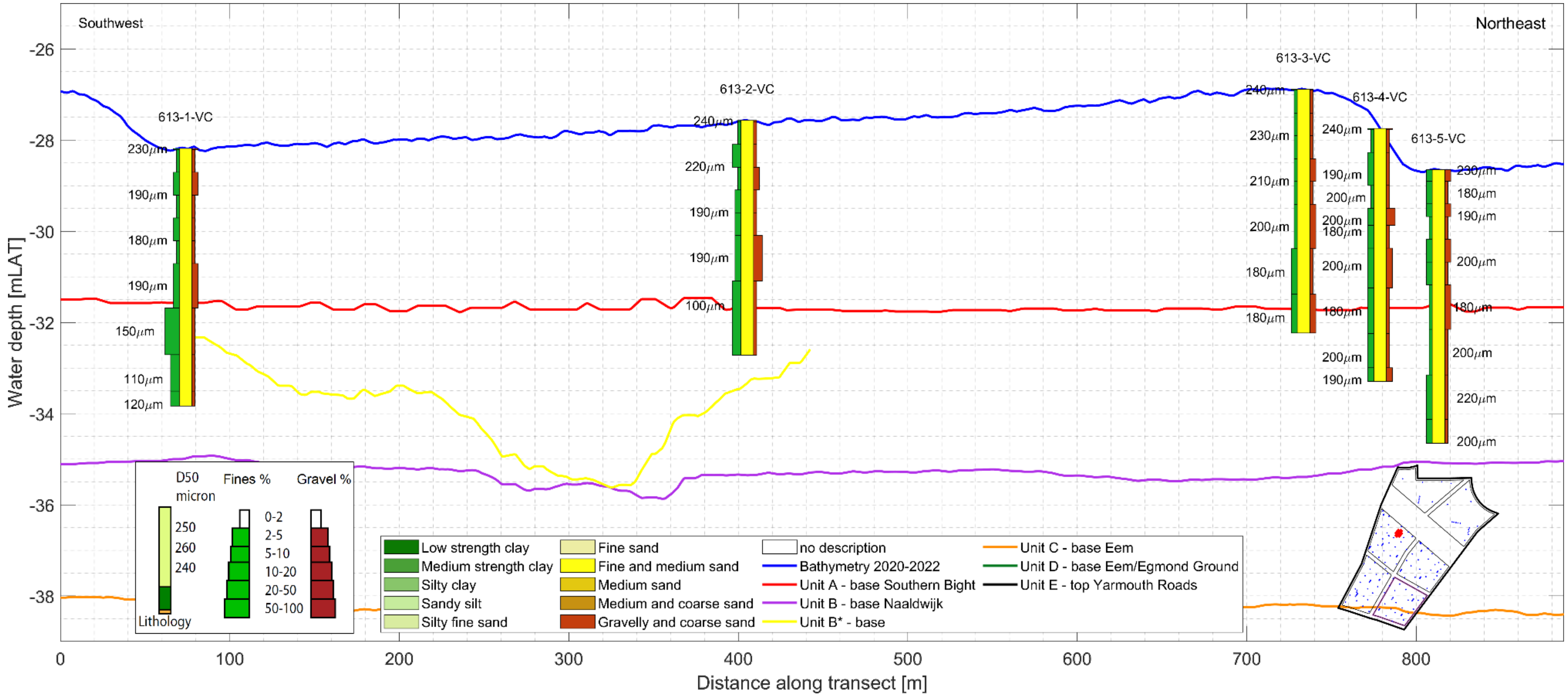

Figure C.23: Vibrocore transect 613.

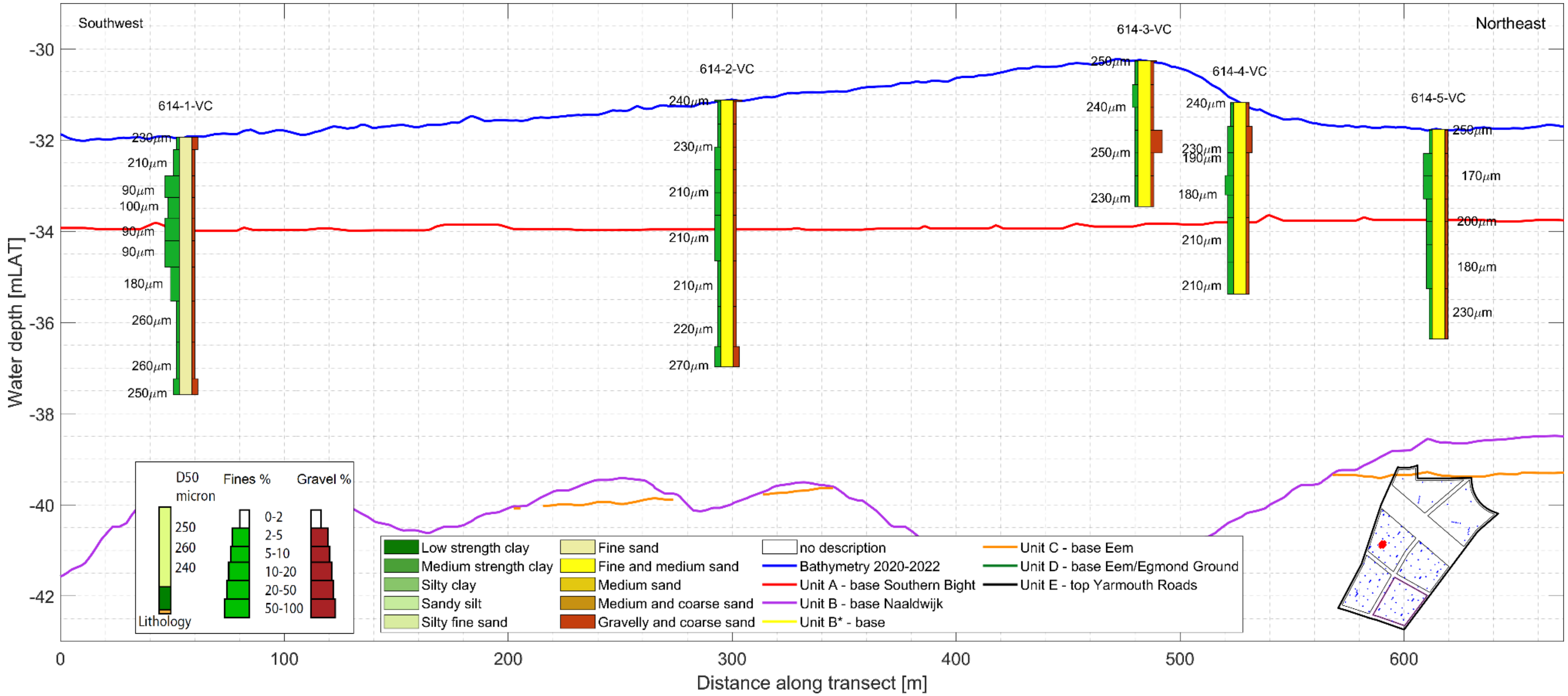

Figure C.24: Vibrocore transect 614.

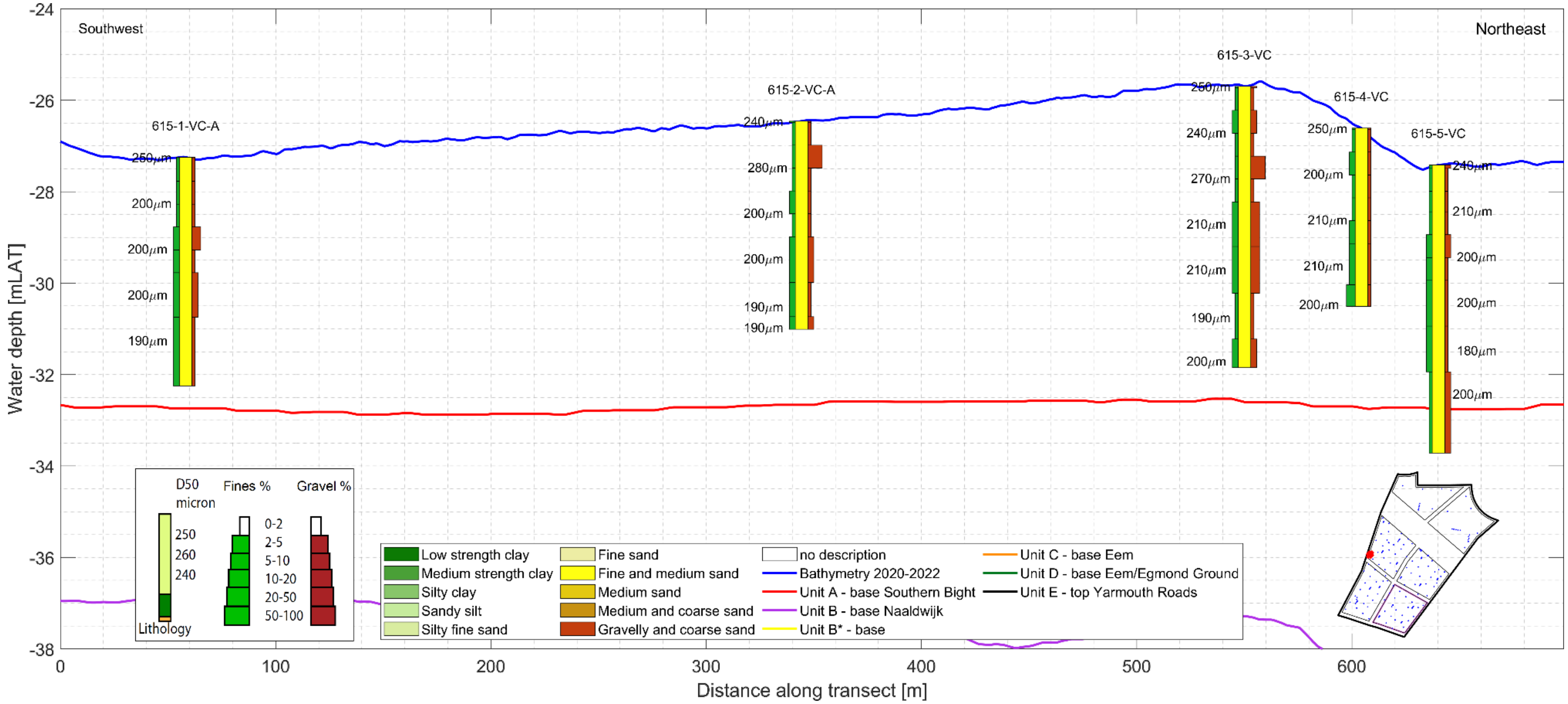

Figure C.25: Vibrocore transect 615.

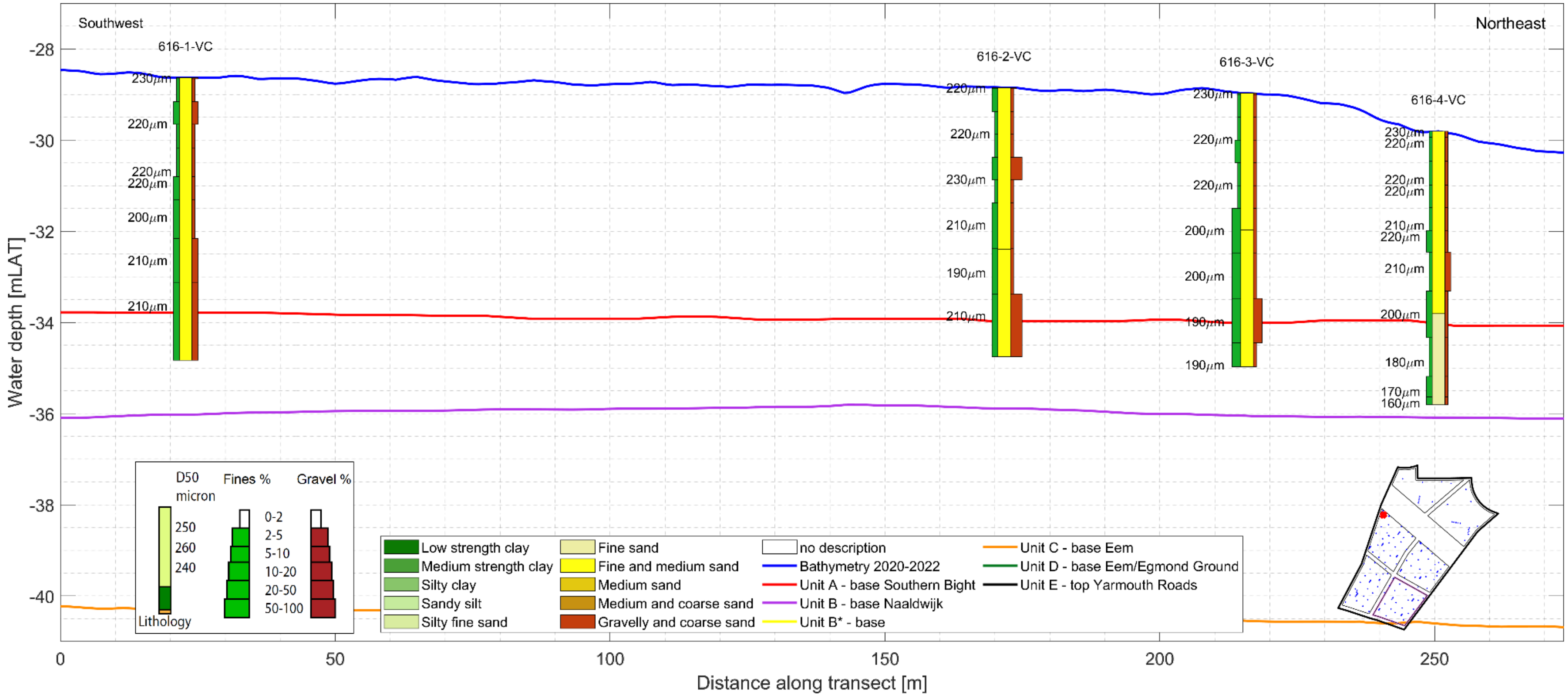

Figure C.26: Vibrocore transect 616.

Deltares

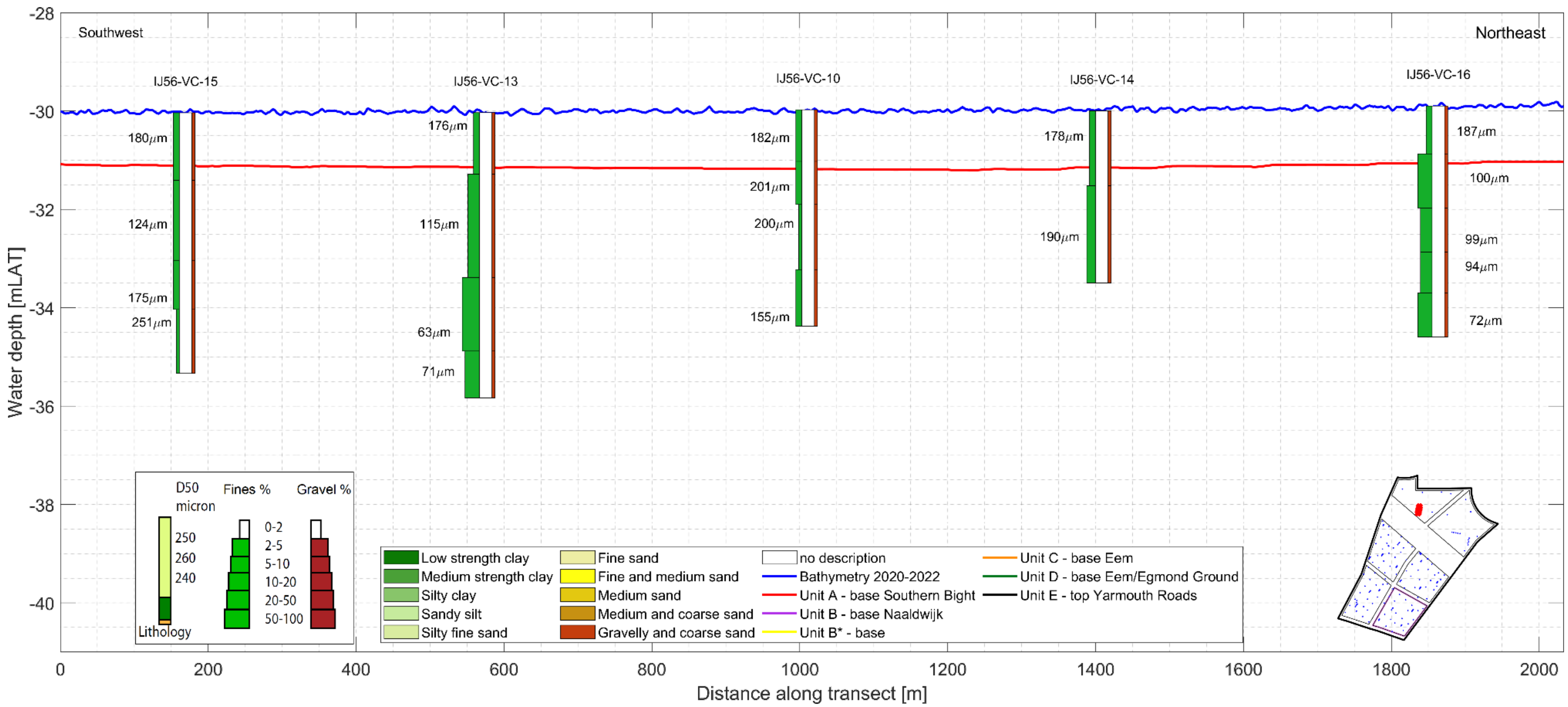

Figure C.27: Vibrocore transect 13.

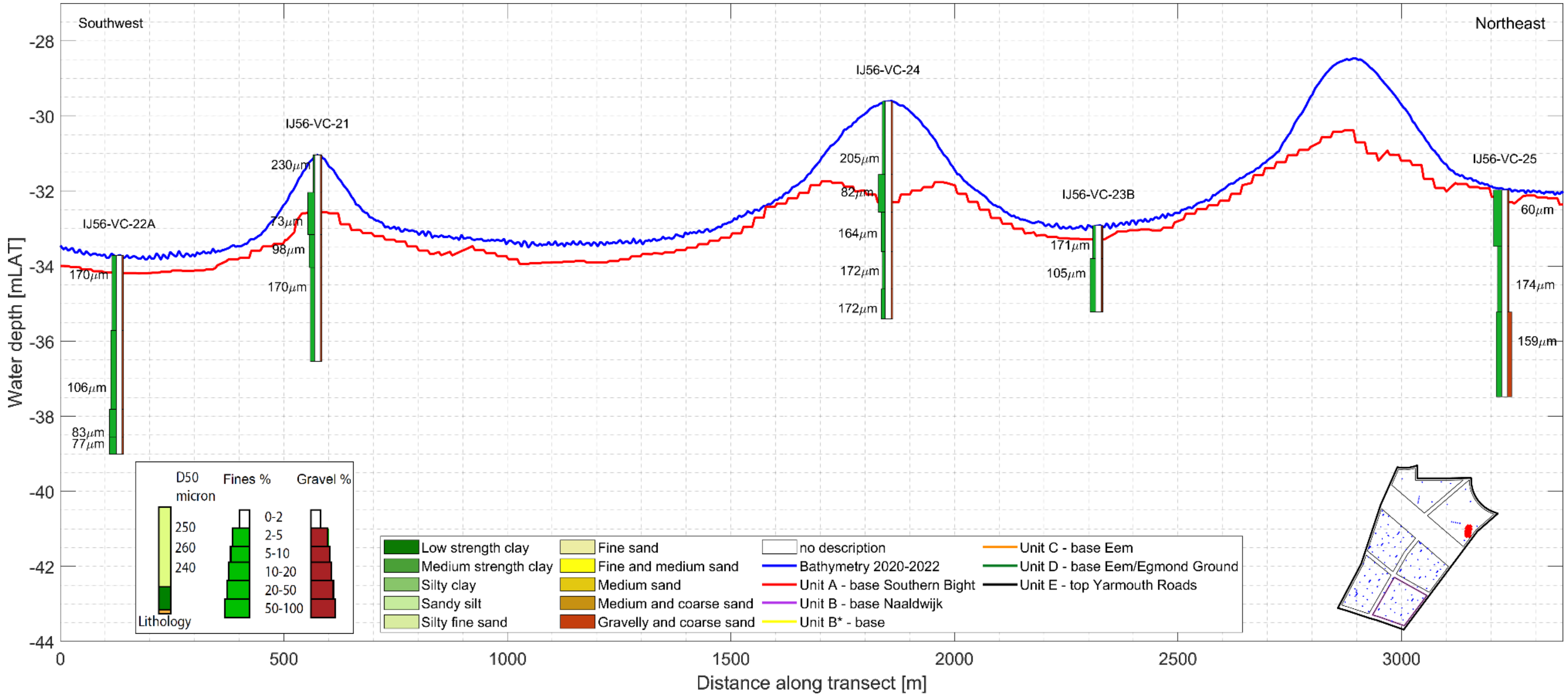

Figure C.28: Vibrocore transect 21.

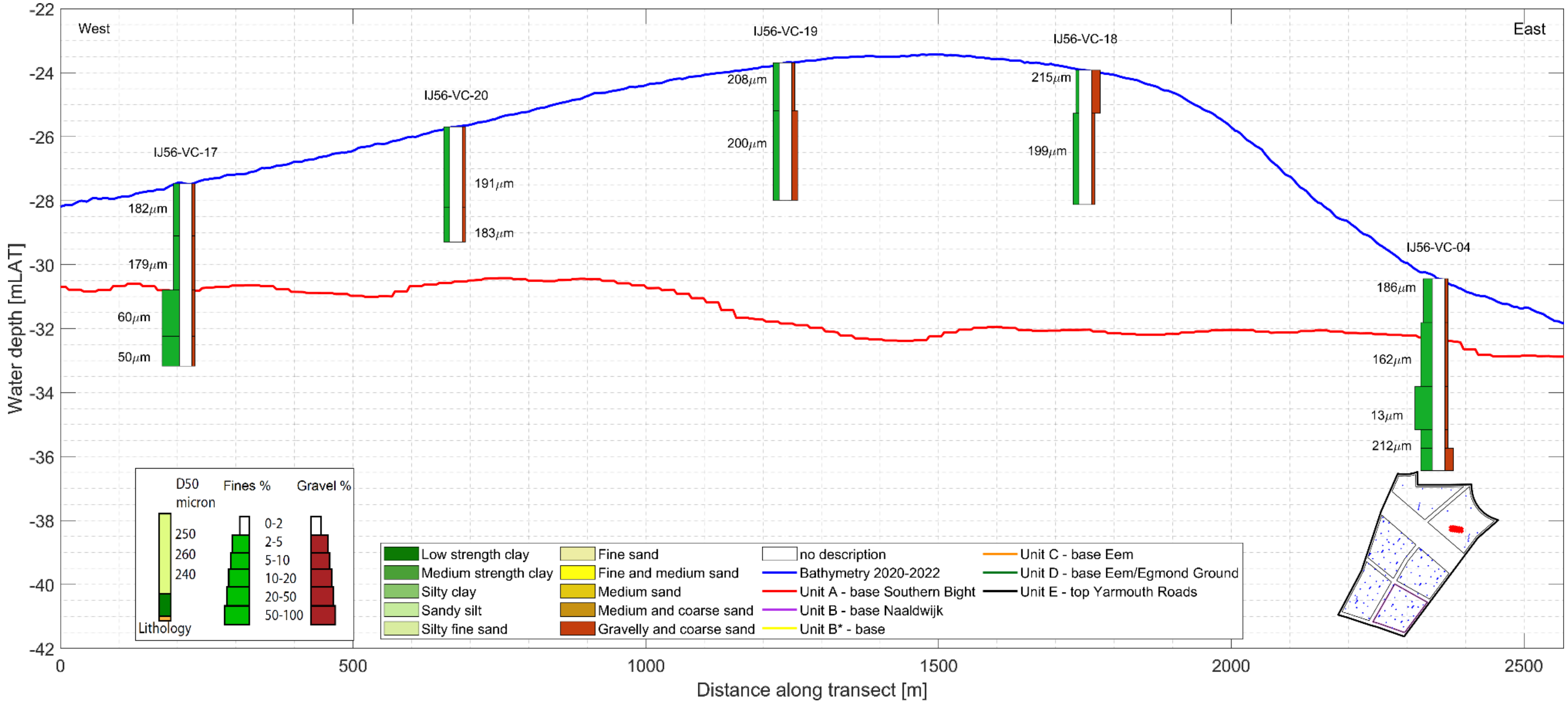

Figure C.29: Vibrocore transect 20.

D Composite bathymetries

In this appendix the overview figures of the composite bathymetries as used in the analysis are presented. A detailed description of the composite bathymetries is given in Appendix A.2.2.1 and 4.2.1. An overview of the available bathymetries is given in Section 2.2 and summarised per composite bathymetry in Table D.1.

Table D.1: Overview of composite bathymetries including sources. Numbers correspond to the sections in this appendix.

Number	Name of bathymetry	Bathymetry sources
1	Bathymetry 1976	15563, 15564, 15562(Royal Netherlands Navy - Hydrographic Office, 1980-2021)
2	Bathymetry 1992	2561 (Royal Netherlands Navy - Hydrographic Office, 1980-2021)402 (Royal Netherlands Navy - Hydrographic Office, 1980-2021)
3	Bathymetry 2002-2003	10464, 11544, 10625 (Royal Netherlands Navy - Hydrographic Office, 1980-2021)
4	Bathymetry 2013-2016	18168, 18668, 19241 (Royal Netherlands Navy - Hydrographic Office, 1980-2021)
5	Bathymetry 2020-2022	2020 survey (GEOxyz, 2021); 2022 survey (Fugro, 2022a).

D.1 Bathymetry 1976

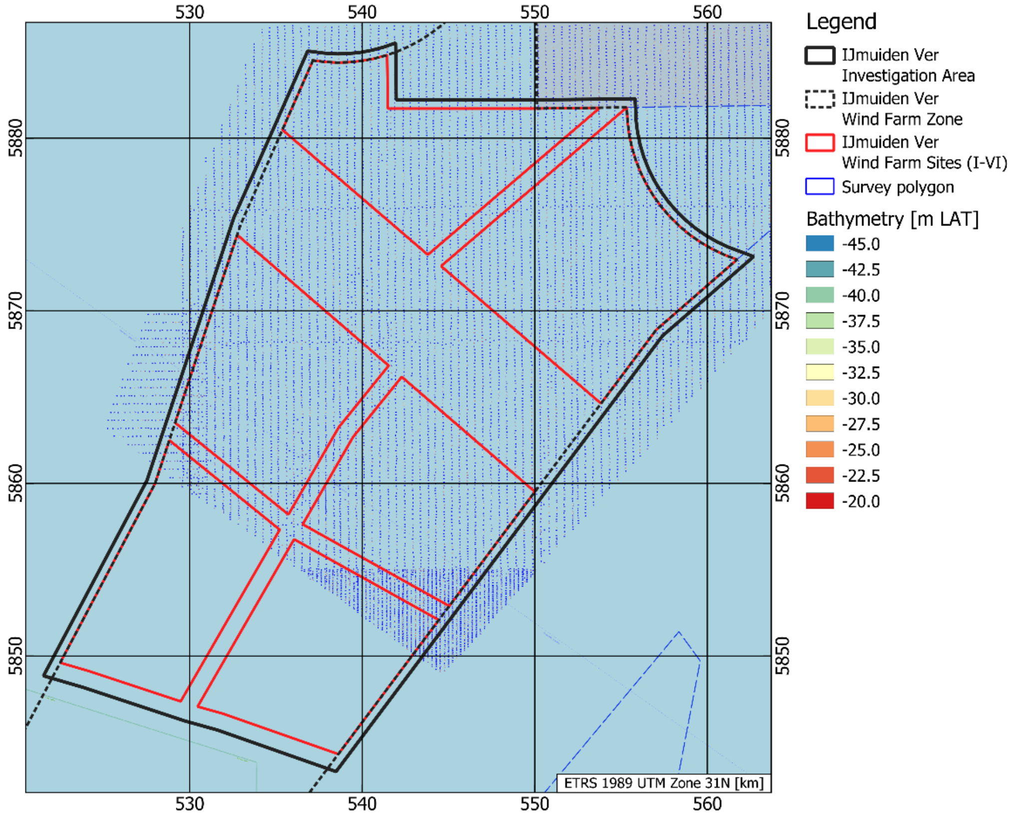

D.2 Bathymetry 1992

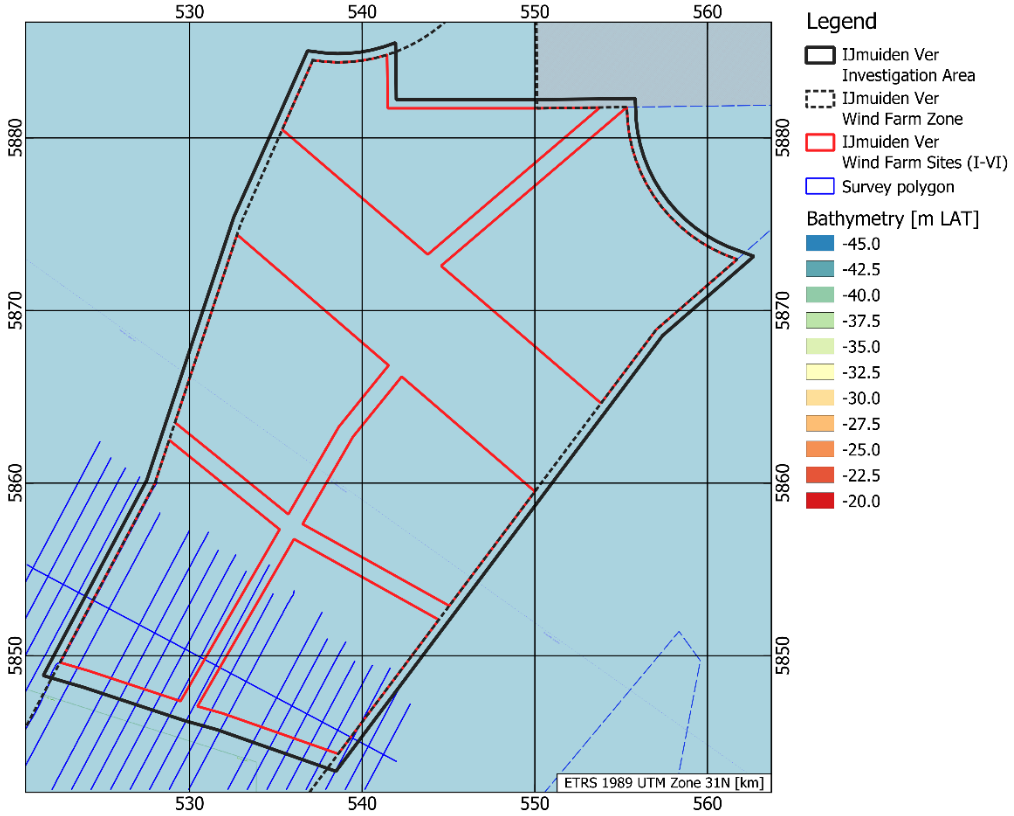

D.3 Bathymetry 2002-2003

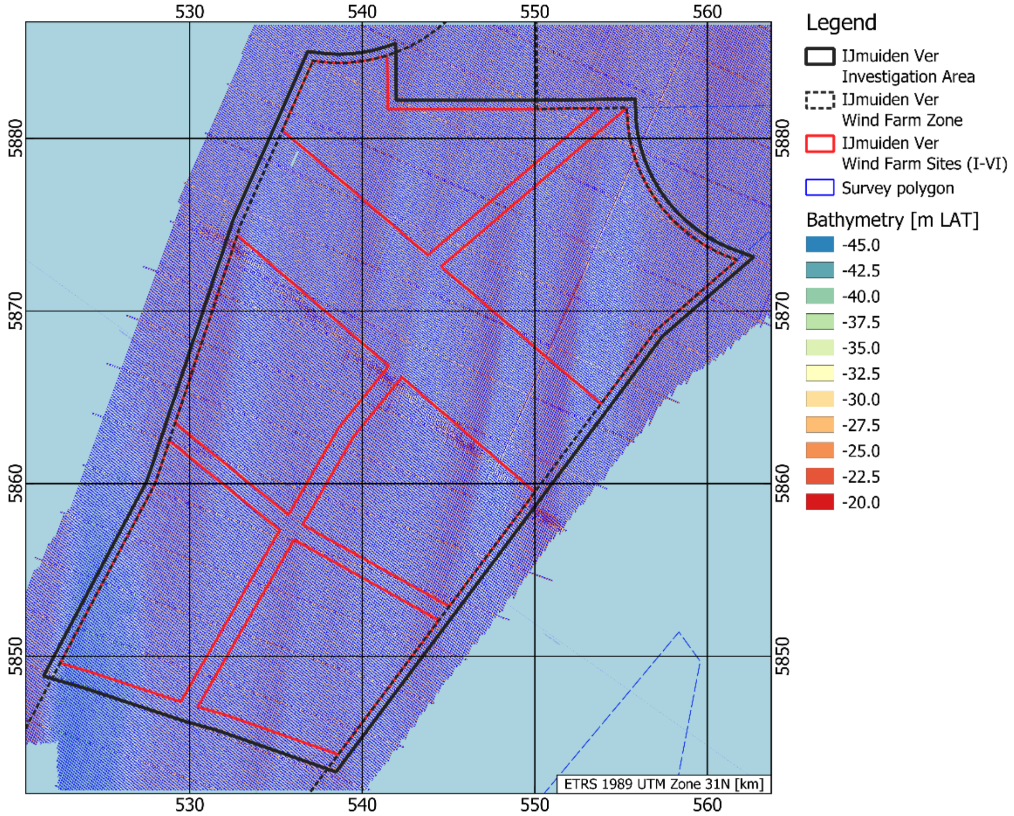

D.4 Bathymetry 2013-2016

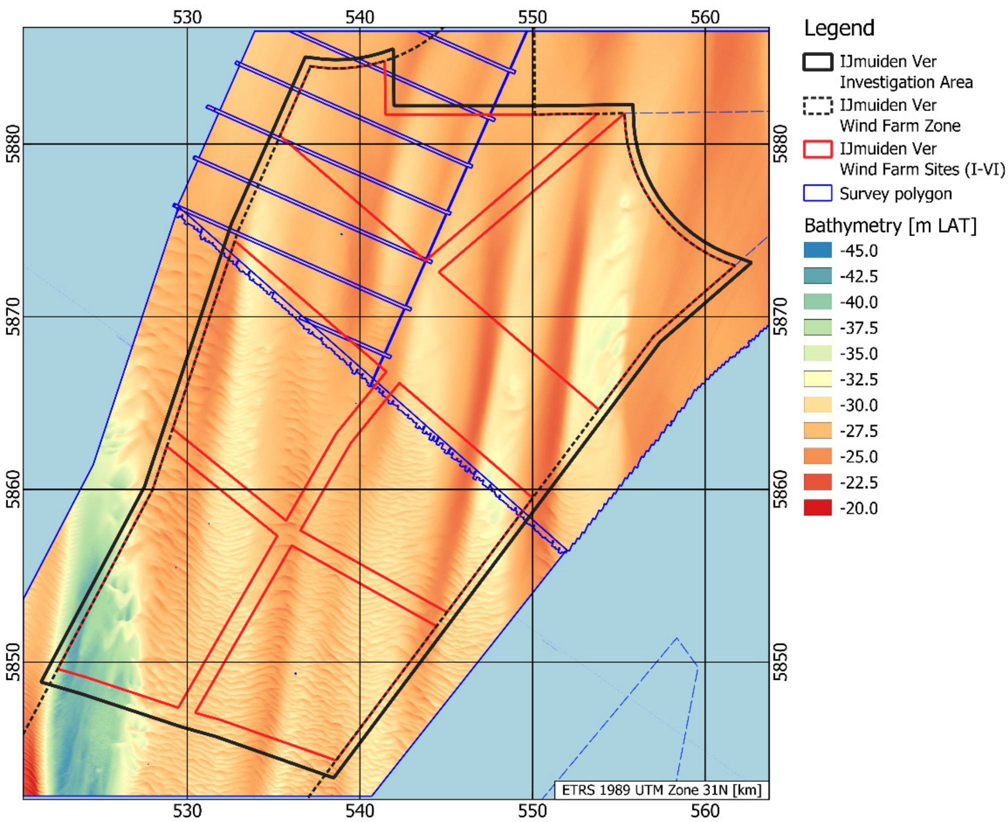

D.5 Bathymetry 2020-2022

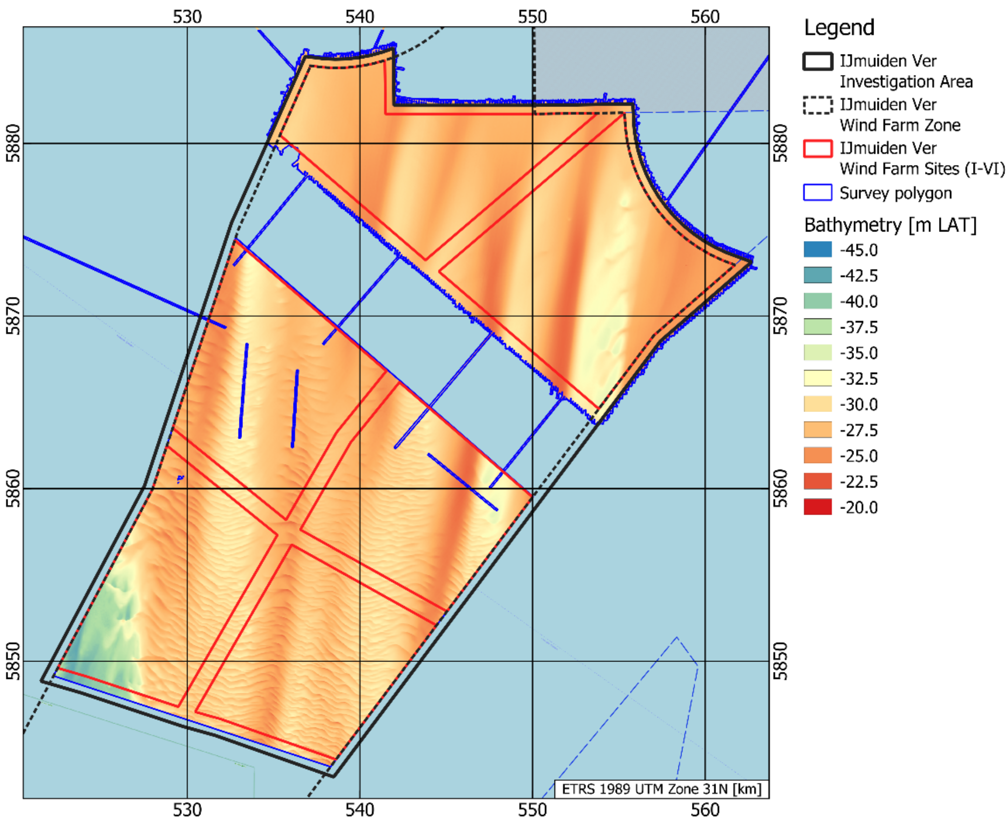

E Seabed profiles

In this appendix an overview of a number of seabed profiles in IJV is presented. This appendix contains two sections Section E.1 provides west-east seabed profiles over IJV to highlight the absence of dynamics in the large-scale seabed. Section E.2 presents all lines which have been resurveyed.

E.1 West-east transects

In the left panel of the figures the location of the profile on top of the difference in bed levels between 2020-2022 and 2013-2016 are depicted. The right panel of the figures indicate the actual measured seabed levels for all available bathymetry data. In the legend the approximate date of measurement per profile is indicated (e.g. the period over which the specific survey was performed).

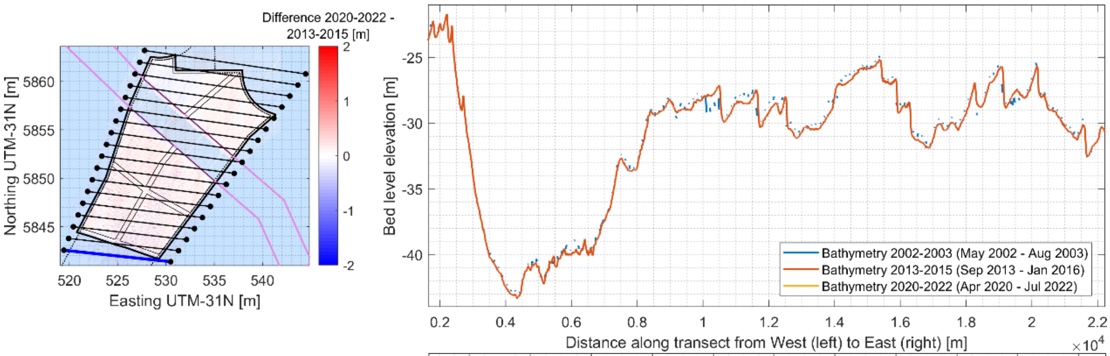

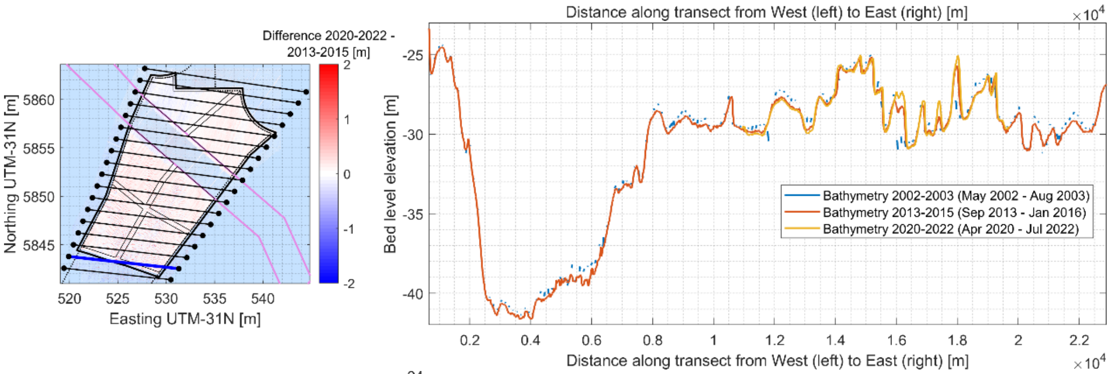

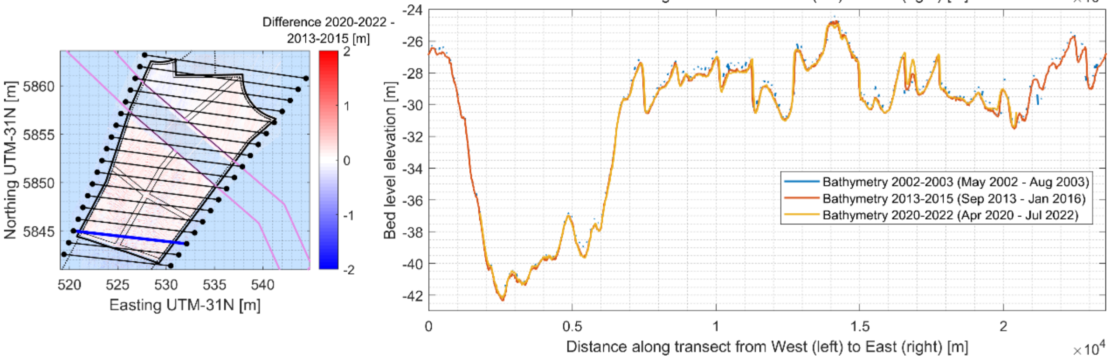

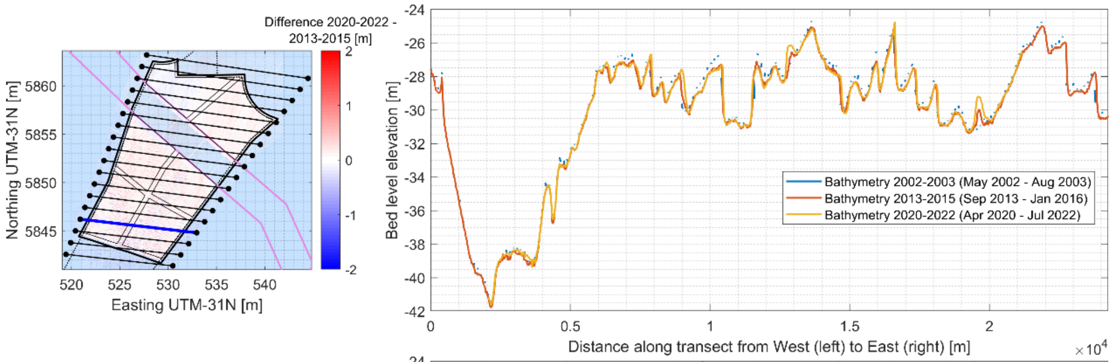
Difference 2020-2022 - 2013-2015 [m]
Northing UTM-31N [m]
Easting UTM-31N [m]
Bed level elevation [m]
Distance along transect from West (left) to East (right) [m]
×10^4
Bathymetry 2002-2003 (May 2002 - Aug 2003)
Bathymetry 2013-2015 (Sep 2013 - Jan 2016)
Bathymetry 2020-2022 (Apr 2020 - Jul 2022)

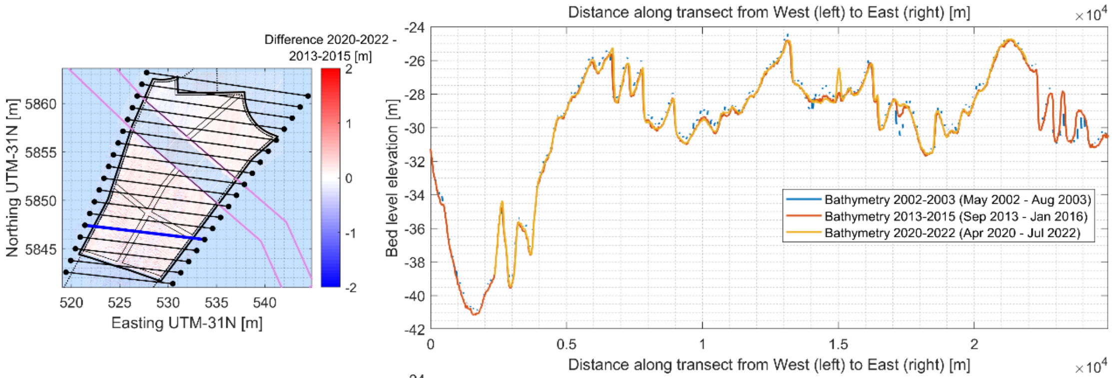
Difference 2020-2022 - 2013-2015 [m]
Northing UTM-31N [m]
Easting UTM-31N [m]
Bed level elevation [m]
Distance along transect from West (left) to East (right) [m]
×10^4
Bathymetry 2002-2003 (May 2002 - Aug 2003)
Bathymetry 2013-2015 (Sep 2013 - Jan 2016)
Bathymetry 2020-2022 (Apr 2020 - Jul 2022)

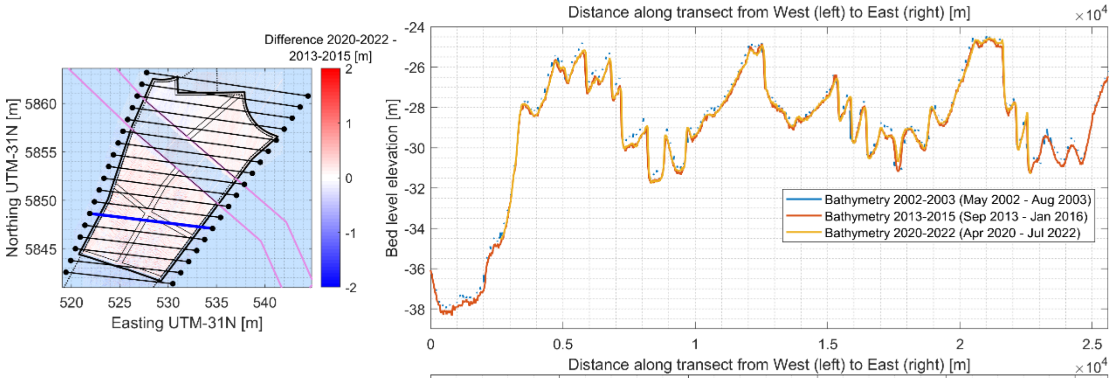
Difference 2020-2022 - 2013-2015 [m]
Northing UTM-31N [m]
Easting UTM-31N [m]
Bed level elevation [m]
Distance along transect from West (left) to East (right) [m]
×10^4
Bathymetry 2002-2003 (May 2002 - Aug 2003)
Bathymetry 2013-2015 (Sep 2013 - Jan 2016)
Bathymetry 2020-2022 (Apr 2020 - Jul 2022)

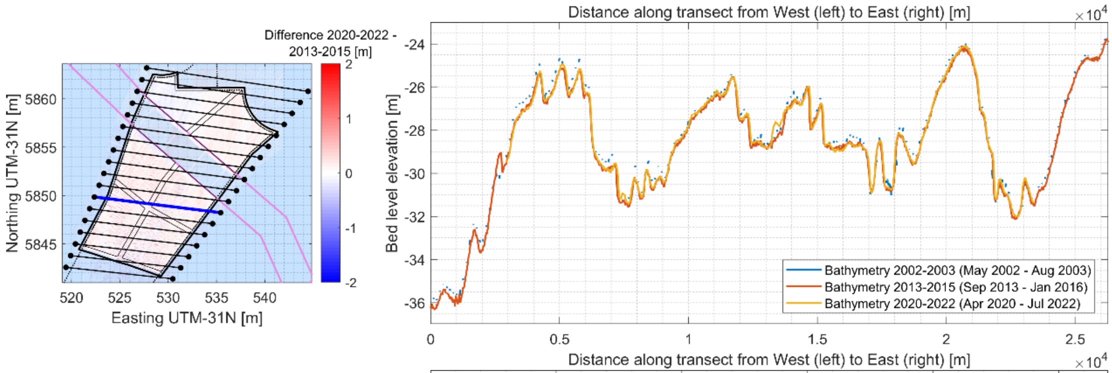
Difference 2020-2022 - 2013-2015 [m]
Northing UTM-31N [m]
Easting UTM-31N [m]
Bed level elevation [m]
Distance along transect from West (left) to East (right) [m]
×10^4
Bathymetry 2002-2003 (May 2002 - Aug 2003)
Bathymetry 2013-2015 (Sep 2013 - Jan 2016)
Bathymetry 2020-2022 (Apr 2020 - Jul 2022)

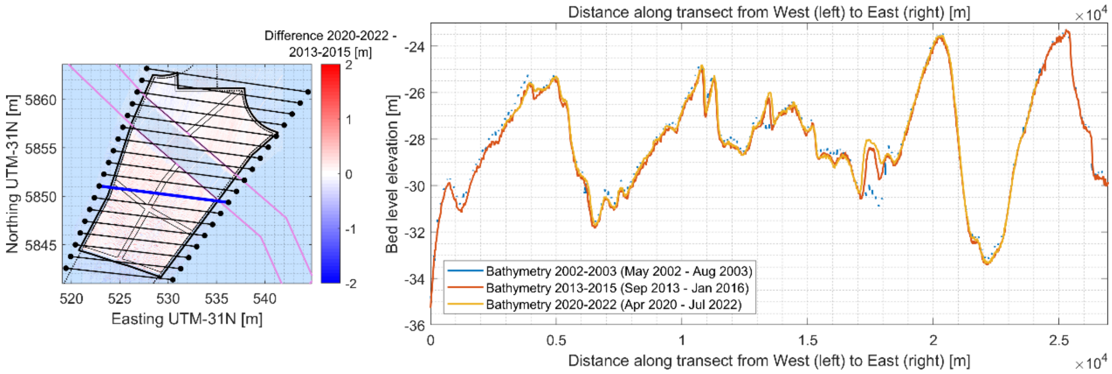
Difference 2020-2022 - 2013-2015 [m]
Northing UTM-31N [m]
Easting UTM-31N [m]
Bed level elevation [m]
Distance along transect from West (left) to East (right) [m]
×10^4
Bathymetry 2002-2003 (May 2002 - Aug 2003)
Bathymetry 2013-2015 (Sep 2013 - Jan 2016)
Bathymetry 2020-2022 (Apr 2020 - Jul 2022)

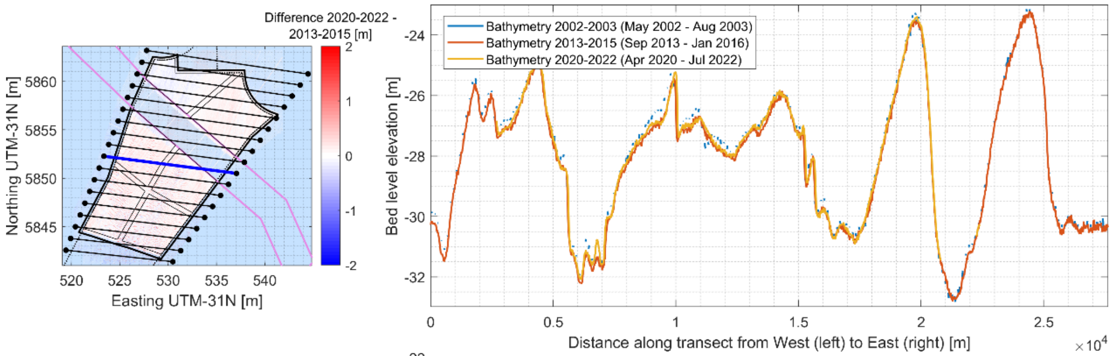
Difference 2020-2022 - 2013-2015 [m]
Northing UTM-31N [m]
Easting UTM-31N [m]
Bed level elevation [m]
Bathymetry 2002-2003 (May 2002 - Aug 2003)
Bathymetry 2013-2015 (Sep 2013 - Jan 2016)
Bathymetry 2020-2022 (Apr 2020 - Jul 2022)
Distance along transect from West (left) to East (right) [m]
×10^4

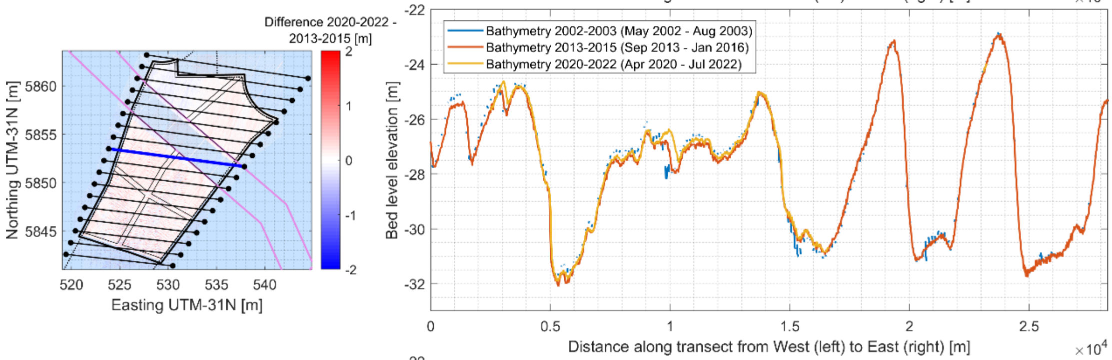
Difference 2020-2022 - 2013-2015 [m]
Northing UTM-31N [m]
Easting UTM-31N [m]
Bed level elevation [m]
Bathymetry 2002-2003 (May 2002 - Aug 2003)
Bathymetry 2013-2015 (Sep 2013 - Jan 2016)
Bathymetry 2020-2022 (Apr 2020 - Jul 2022)
Distance along transect from West (left) to East (right) [m]
×10^4

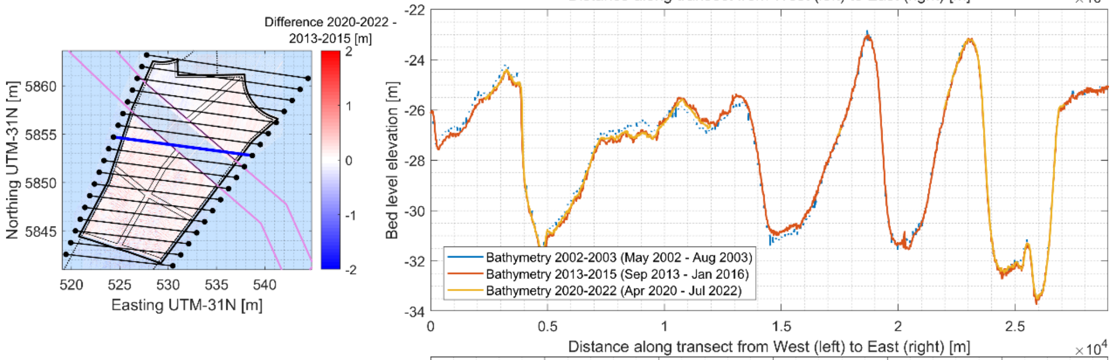
Difference 2020-2022 - 2013-2015 [m]
Northing UTM-31N [m]
Easting UTM-31N [m]
Bed level elevation [m]
Bathymetry 2002-2003 (May 2002 - Aug 2003)
Bathymetry 2013-2015 (Sep 2013 - Jan 2016)
Bathymetry 2020-2022 (Apr 2020 - Jul 2022)
Distance along transect from West (left) to East (right) [m]
×10^4

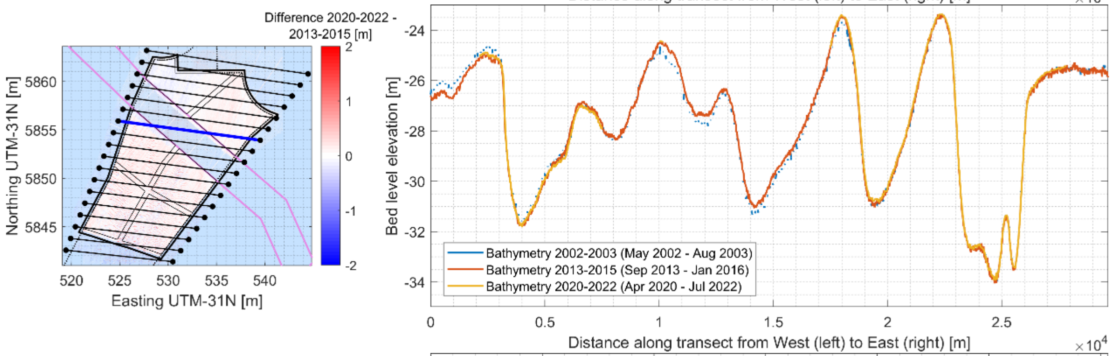
Difference 2020-2022 - 2013-2015 [m]
Northing UTM-31N [m]
Easting UTM-31N [m]
Bed level elevation [m]
Bathymetry 2002-2003 (May 2002 - Aug 2003)
Bathymetry 2013-2015 (Sep 2013 - Jan 2016)
Bathymetry 2020-2022 (Apr 2020 - Jul 2022)
Distance along transect from West (left) to East (right) [m]
×10^4

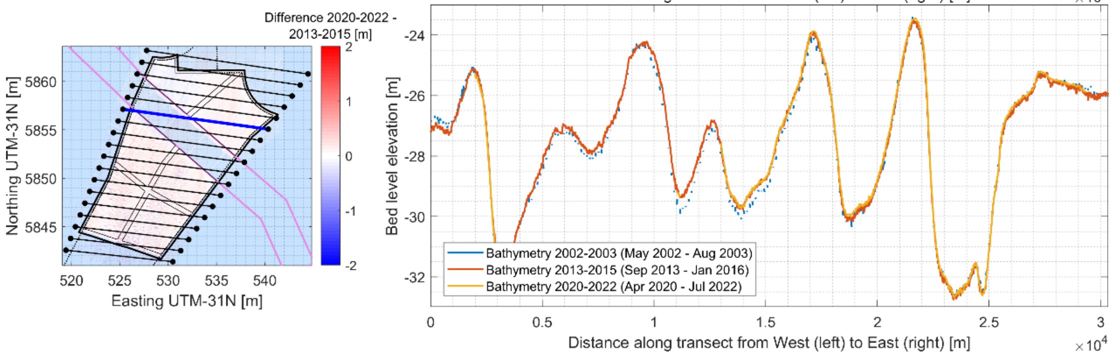
Difference 2020-2022 - 2013-2015 [m]
Northing UTM-31N [m]
Easting UTM-31N [m]
Bed level elevation [m]
Bathymetry 2002-2003 (May 2002 - Aug 2003)
Bathymetry 2013-2015 (Sep 2013 - Jan 2016)
Bathymetry 2020-2022 (Apr 2020 - Jul 2022)
Distance along transect from West (left) to East (right) [m]
×10^4

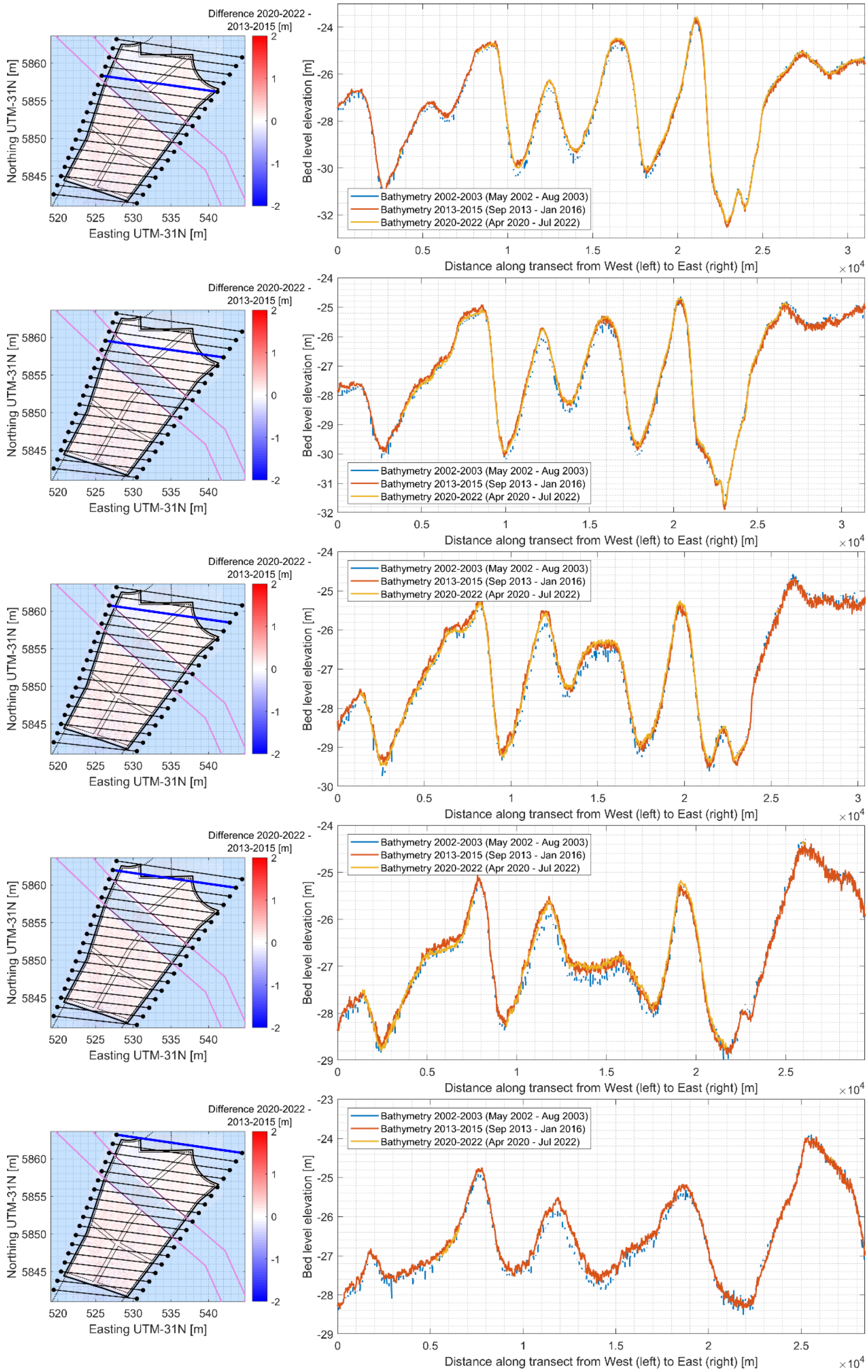
Difference 2020-2022 - 2013-2015 [m]
Northing UTM-31N [m]
Easting UTM-31N [m]
Bed level elevation [m]
Bathymetry 2002-2003 (May 2002 - Aug 2003)
Bathymetry 2013-2015 (Sep 2013 - Jan 2016)
Bathymetry 2020-2022 (Apr 2020 - Jul 2022)
Distance along transect from West (left) to East (right) [m]
Difference 2020-2022 - 2013-2015 [m]
Northing UTM-31N [m]
Easting UTM-31N [m]
Bed level elevation [m]
Bathymetry 2002-2003 (May 2002 - Aug 2003)
Bathymetry 2013-2015 (Sep 2013 - Jan 2016)
Bathymetry 2020-2022 (Apr 2020 - Jul 2022)
Distance along transect from West (left) to East (right) [m]
Difference 2020-2022 - 2013-2015 [m]
Northing UTM-31N [m]
Easting UTM-31N [m]
Bed level elevation [m]
Bathymetry 2002-2003 (May 2002 - Aug 2003)
Bathymetry 2013-2015 (Sep 2013 - Jan 2016)
Bathymetry 2020-2022 (Apr 2020 - Jul 2022)
Distance along transect from West (left) to East (right) [m]
Difference 2020-2022 - 2013-2015 [m]
Northing UTM-31N [m]
Easting UTM-31N [m]
Bed level elevation [m]
Bathymetry 2002-2003 (May 2002 - Aug 2003)
Bathymetry 2013-2015 (Sep 2013 - Jan 2016)
Bathymetry 2020-2022 (Apr 2020 - Jul 2022)
Distance along transect from West (left) to East (right) [m]
Difference 2020-2022 - 2013-2015 [m]
Northing UTM-31N [m]
Easting UTM-31N [m]
Bed level elevation [m]
Bathymetry 2002-2003 (May 2002 - Aug 2003)
Bathymetry 2013-2015 (Sep 2013 - Jan 2016)
Bathymetry 2020-2022 (Apr 2020 - Jul 2022)
Distance along transect from West (left) to East (right) [m]

E.2 Repeat survey lines

This appendix provides the seabed profiles (Appendix E.2.1), sand wave and megaripple profiles (Appendix E.2.2) and the non-exceedance curves of megaripple dimensions (Appendix E.2.2.7) for all the repeat survey lines . The survey lines are discussed in detail in Section 4.7 and Table 2.1.

E.2.1 Seabed profiles along repeat survey lines

E.2.1.1. Transect 1

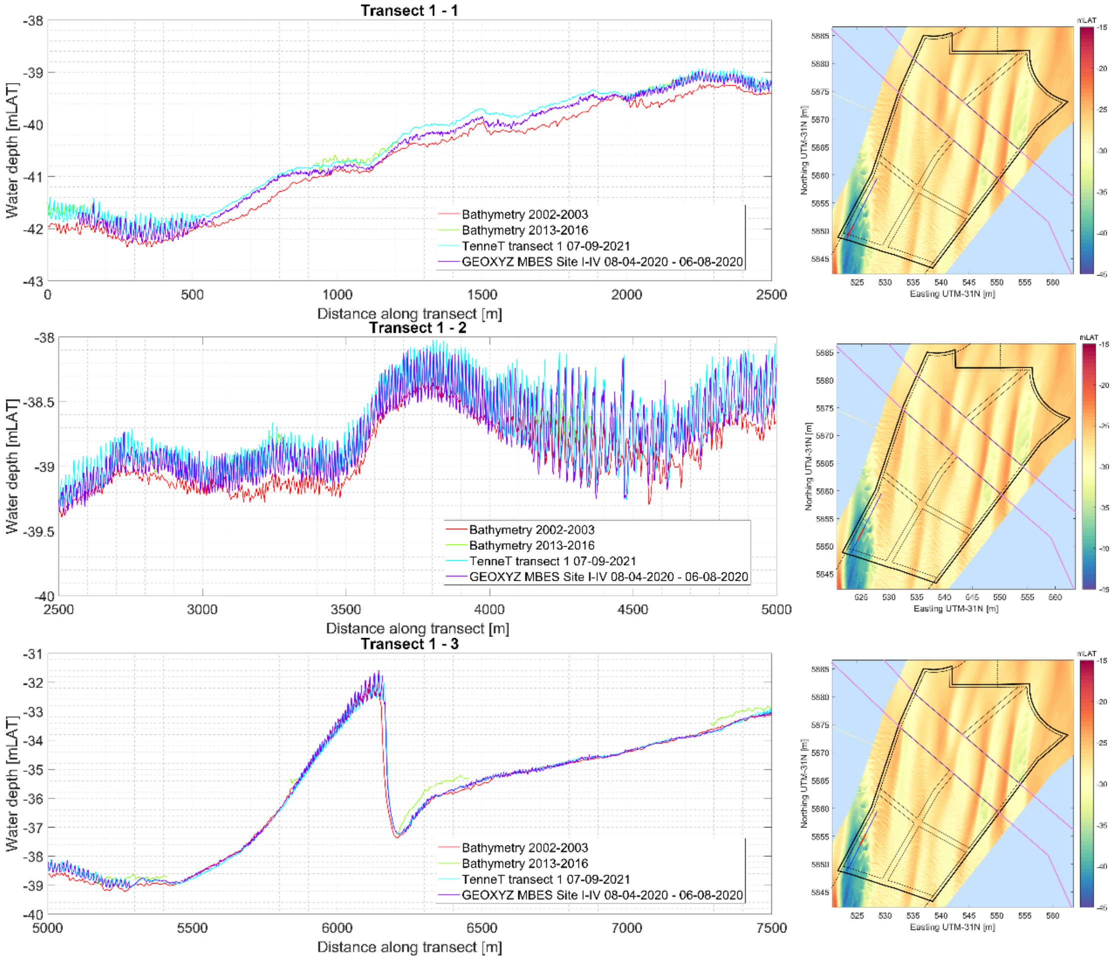

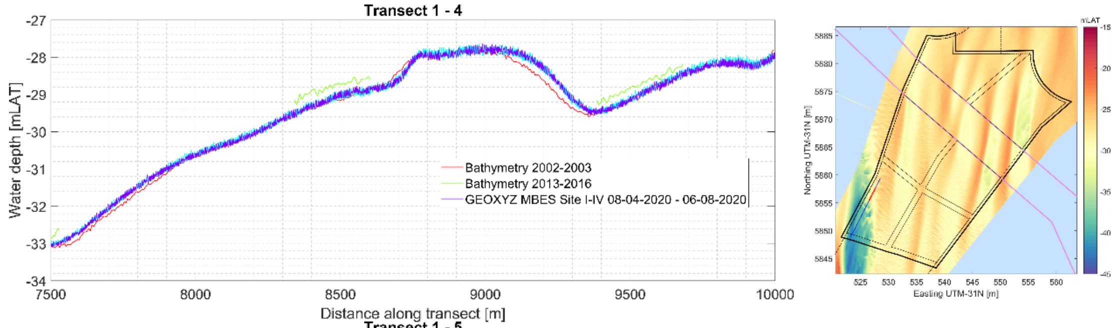

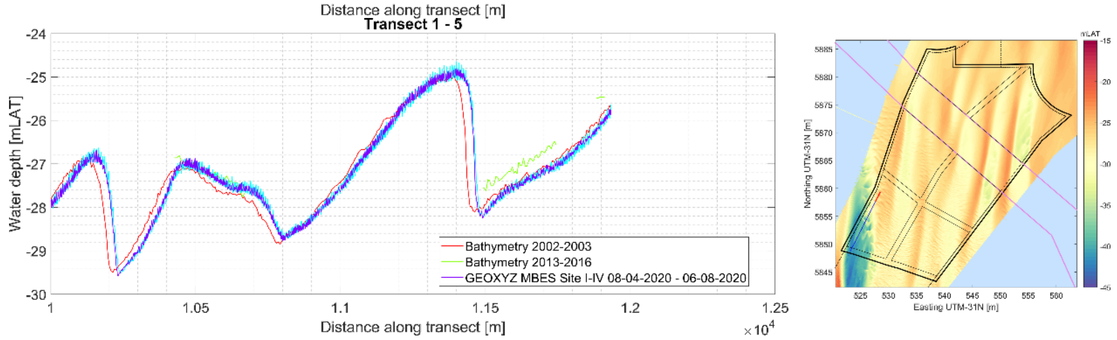

E.2.1.2. Transect 2

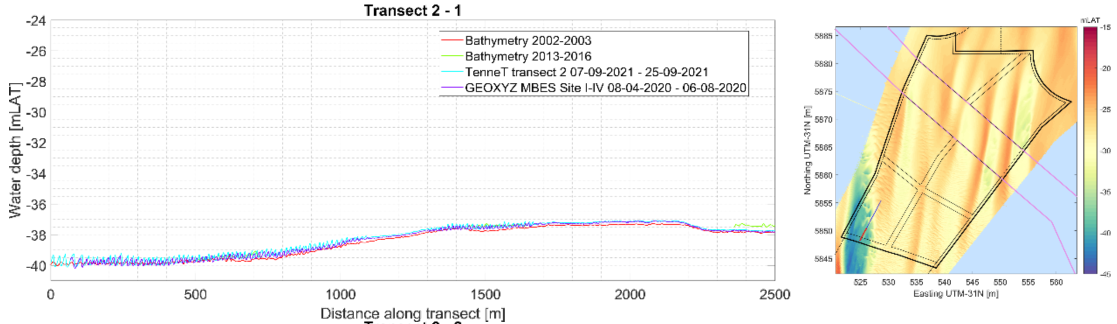

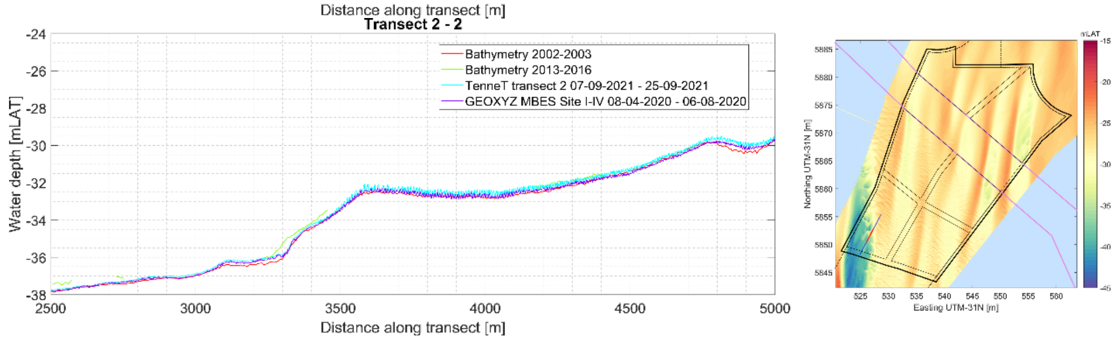

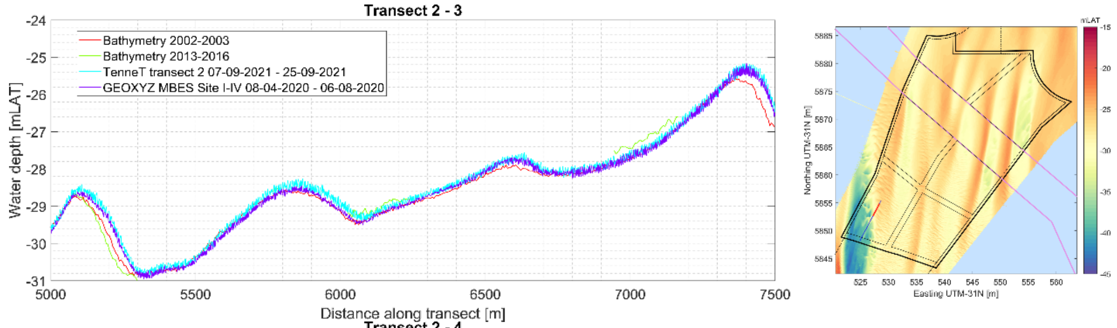

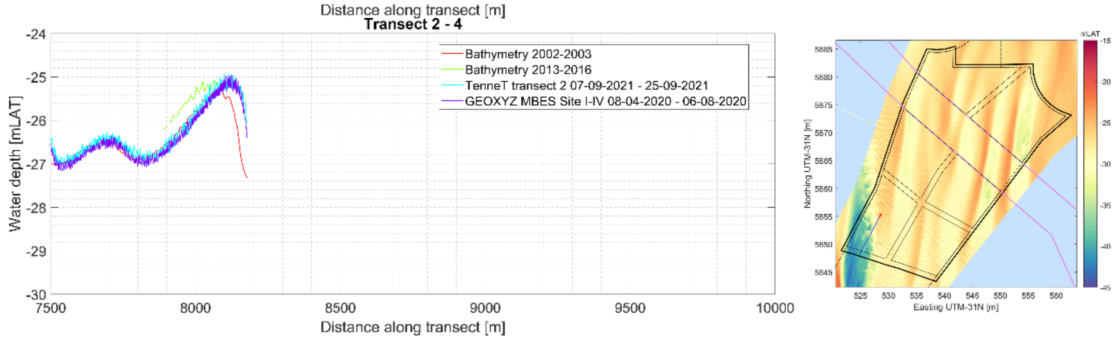

E.2.1.3. Transect 3

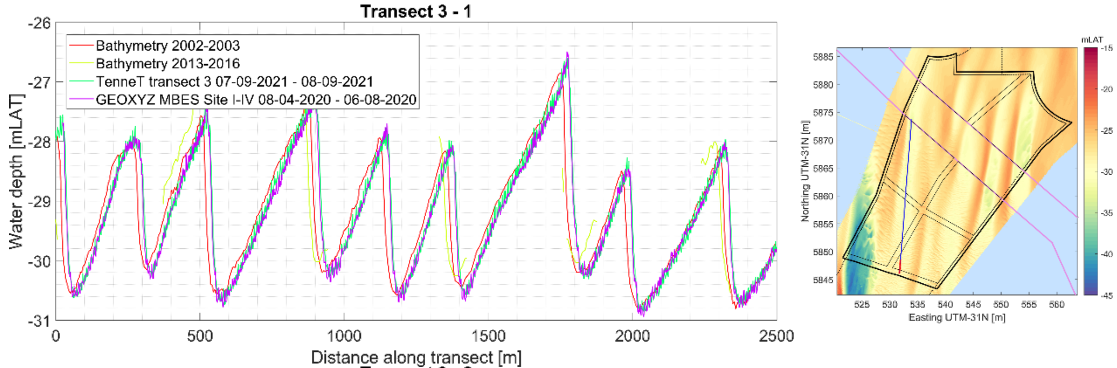

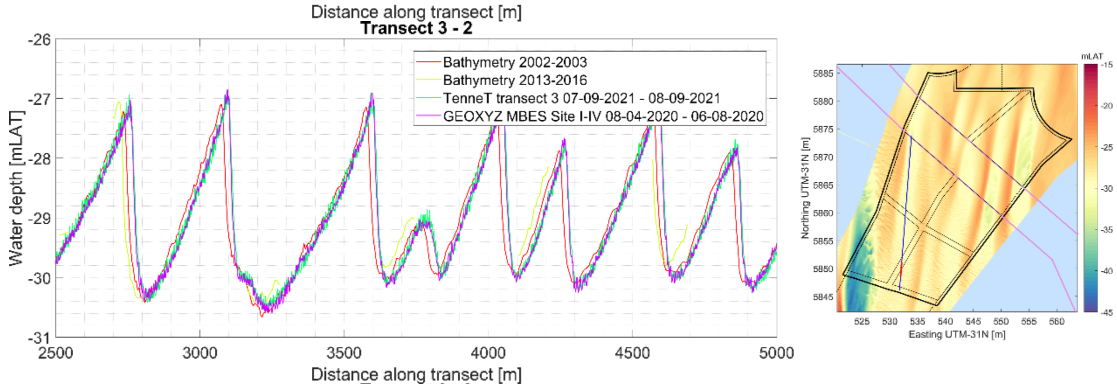

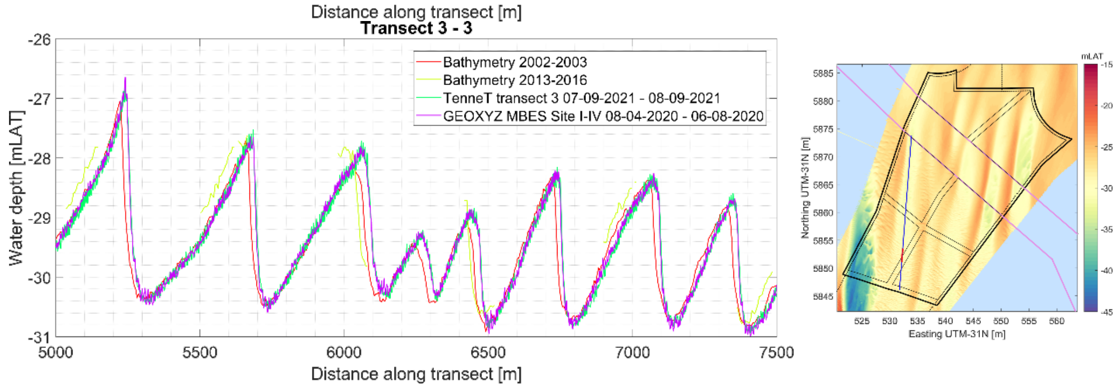

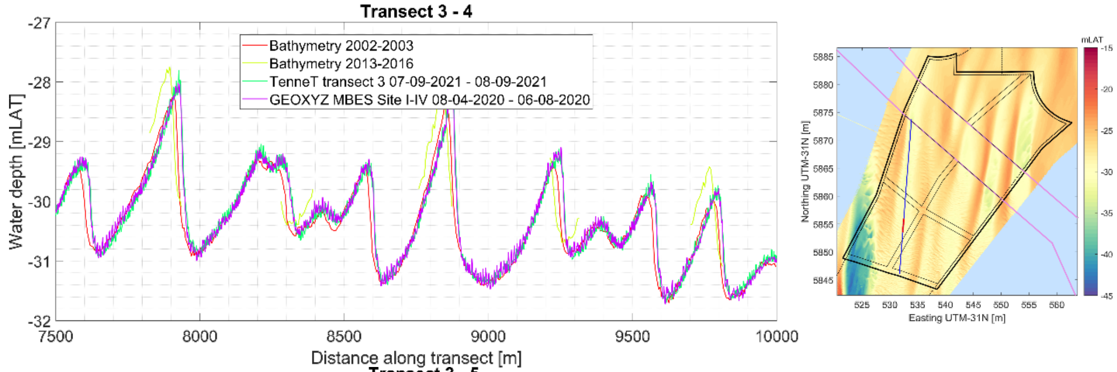
Transect 3 - 4
Bathymetry 2002-2003
Bathymetry 2013-2016
TenneT transect 3 07-09-2021 - 08-09-2021
GEOXYZ MBES Site I-IV 08-04-2020 - 06-08-2020
Water depth [mLAT]
Distance along transect [m]
Northing UTM-31N [m]
Easting UTM-31N [m]
mLAT

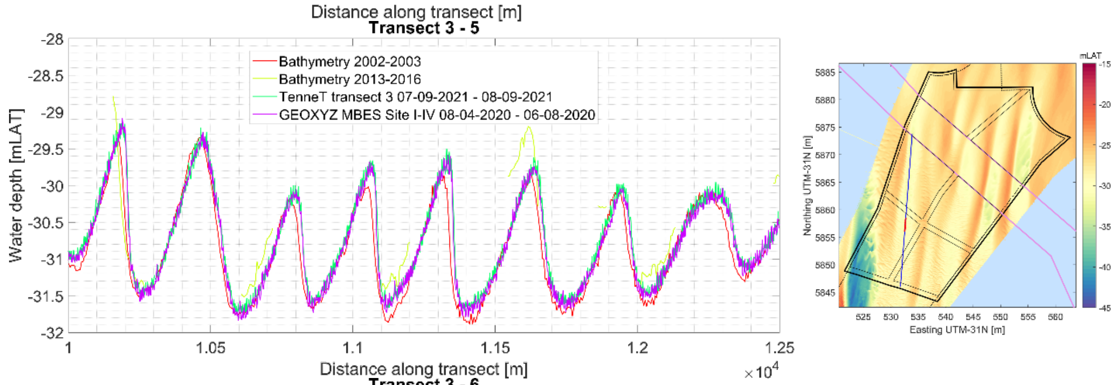
Transect 3 - 5
Bathymetry 2002-2003
Bathymetry 2013-2016
TenneT transect 3 07-09-2021 - 08-09-2021
GEOXYZ MBES Site I-IV 08-04-2020 - 06-08-2020
Water depth [mLAT]
Distance along transect [m]
Northing UTM-31N [m]
Easting UTM-31N [m]
mLAT

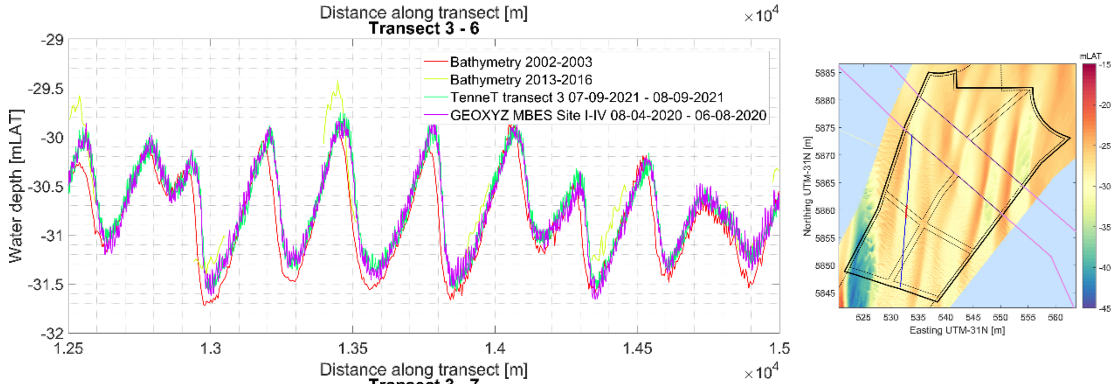
Transect 3 - 6
Bathymetry 2002-2003
Bathymetry 2013-2016
TenneT transect 3 07-09-2021 - 08-09-2021
GEOXYZ MBES Site I-IV 08-04-2020 - 06-08-2020
Water depth [mLAT]
Distance along transect [m]
Northing UTM-31N [m]
Easting UTM-31N [m]
mLAT

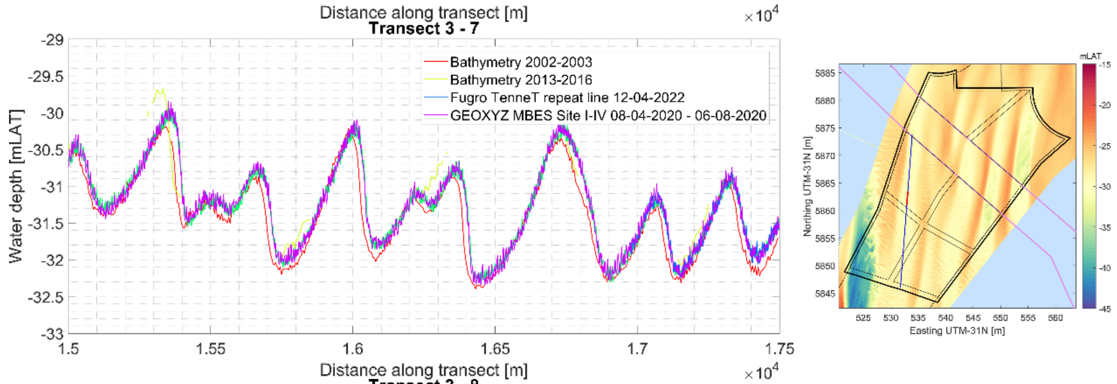
Transect 3 - 7
Bathymetry 2002-2003
Bathymetry 2013-2016
Fugro TenneT repeat line 12-04-2022
GEOXYZ MBES Site I-IV 08-04-2020 - 06-08-2020
Water depth [mLAT]
Distance along transect [m]
Northing UTM-31N [m]
Easting UTM-31N [m]
mLAT

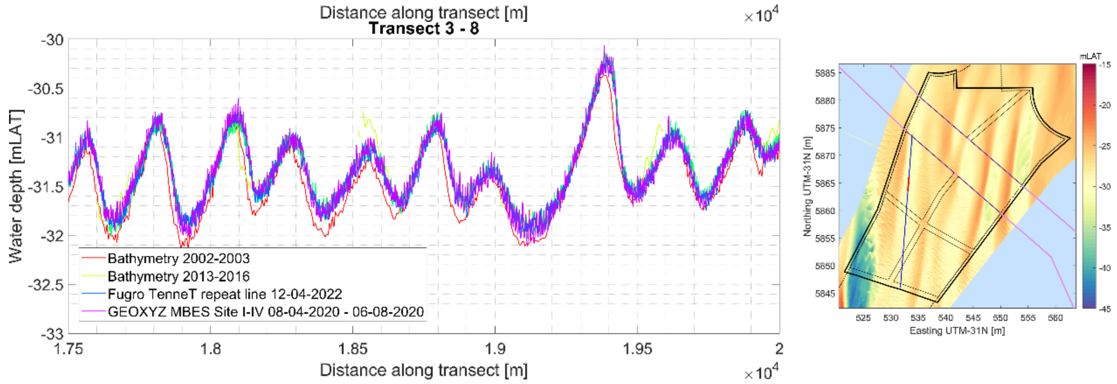
Transect 3 - 8
Bathymetry 2002-2003
Bathymetry 2013-2016
Fugro TenneT repeat line 12-04-2022
GEOXYZ MBES Site I-IV 08-04-2020 - 06-08-2020
Water depth [mLAT]
Distance along transect [m]
Northing UTM-31N [m]
Easting UTM-31N [m]
mLAT

Deltares

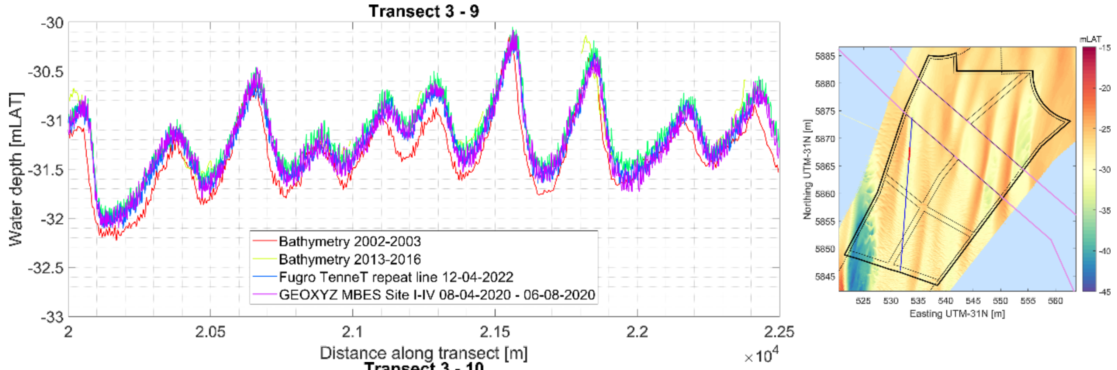
Transect 3 - 9
Water depth [mLAT]
Distance along transect [m]
×10^4
Bathymetry 2002-2003
Bathymetry 2013-2016
Fugro TenneT repeat line 12-04-2022
GEOXYZ MBES Site I-IV 08-04-2020 - 06-08-2020
Northing UTM-31N [m]
Easting UTM-31N [m]
mLAT

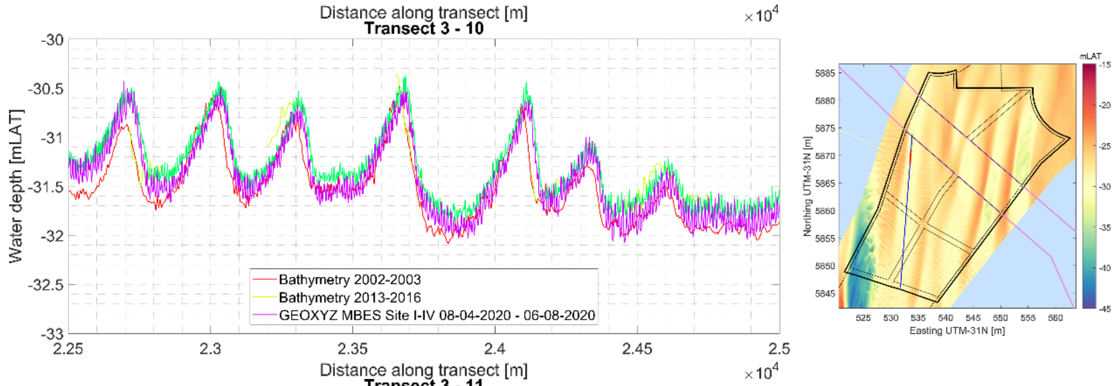
Transect 3 - 10
Water depth [mLAT]
Distance along transect [m]
×10^4
Bathymetry 2002-2003
Bathymetry 2013-2016
GEOXYZ MBES Site I-IV 08-04-2020 - 06-08-2020
Northing UTM-31N [m]
Easting UTM-31N [m]
mLAT

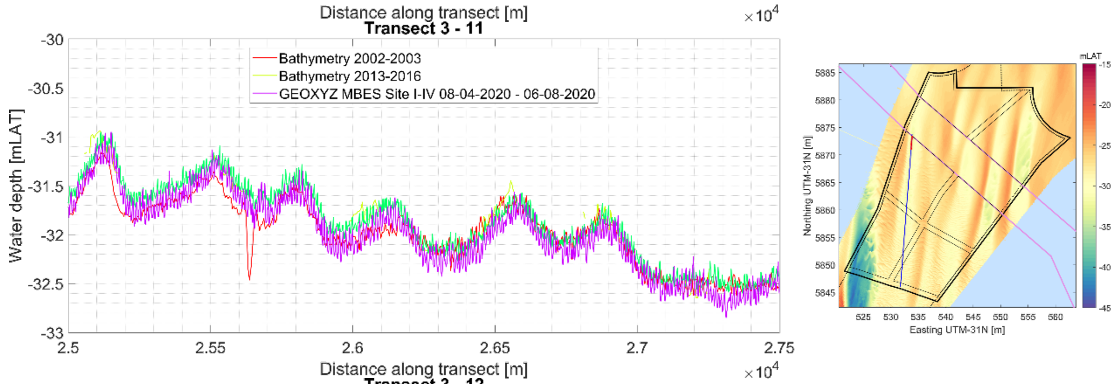
Transect 3 - 11
Water depth [mLAT]
Distance along transect [m]
×10^4
Bathymetry 2002-2003
Bathymetry 2013-2016
GEOXYZ MBES Site I-IV 08-04-2020 - 06-08-2020
Northing UTM-31N [m]
Easting UTM-31N [m]
mLAT

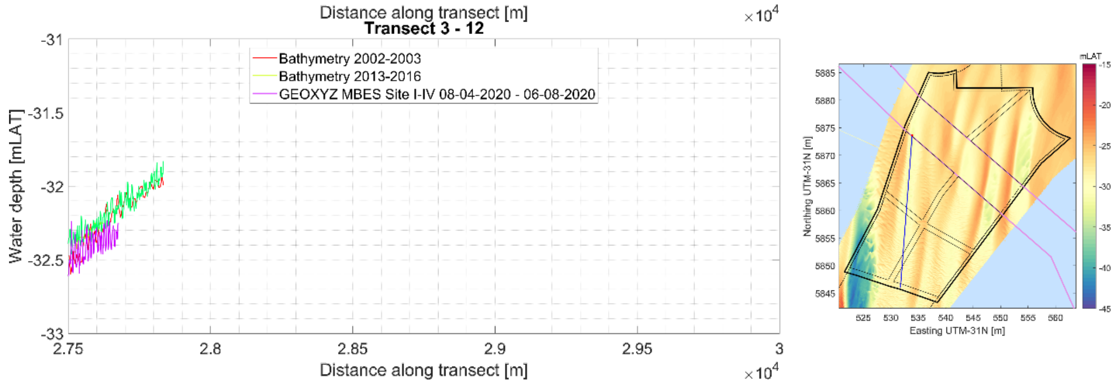
Transect 3 - 12
Water depth [mLAT]
Distance along transect [m]
×10^4
Bathymetry 2002-2003
Bathymetry 2013-2016
GEOXYZ MBES Site I-IV 08-04-2020 - 06-08-2020
Northing UTM-31N [m]
Easting UTM-31N [m]
mLAT

E.2.1.4. Transect 4

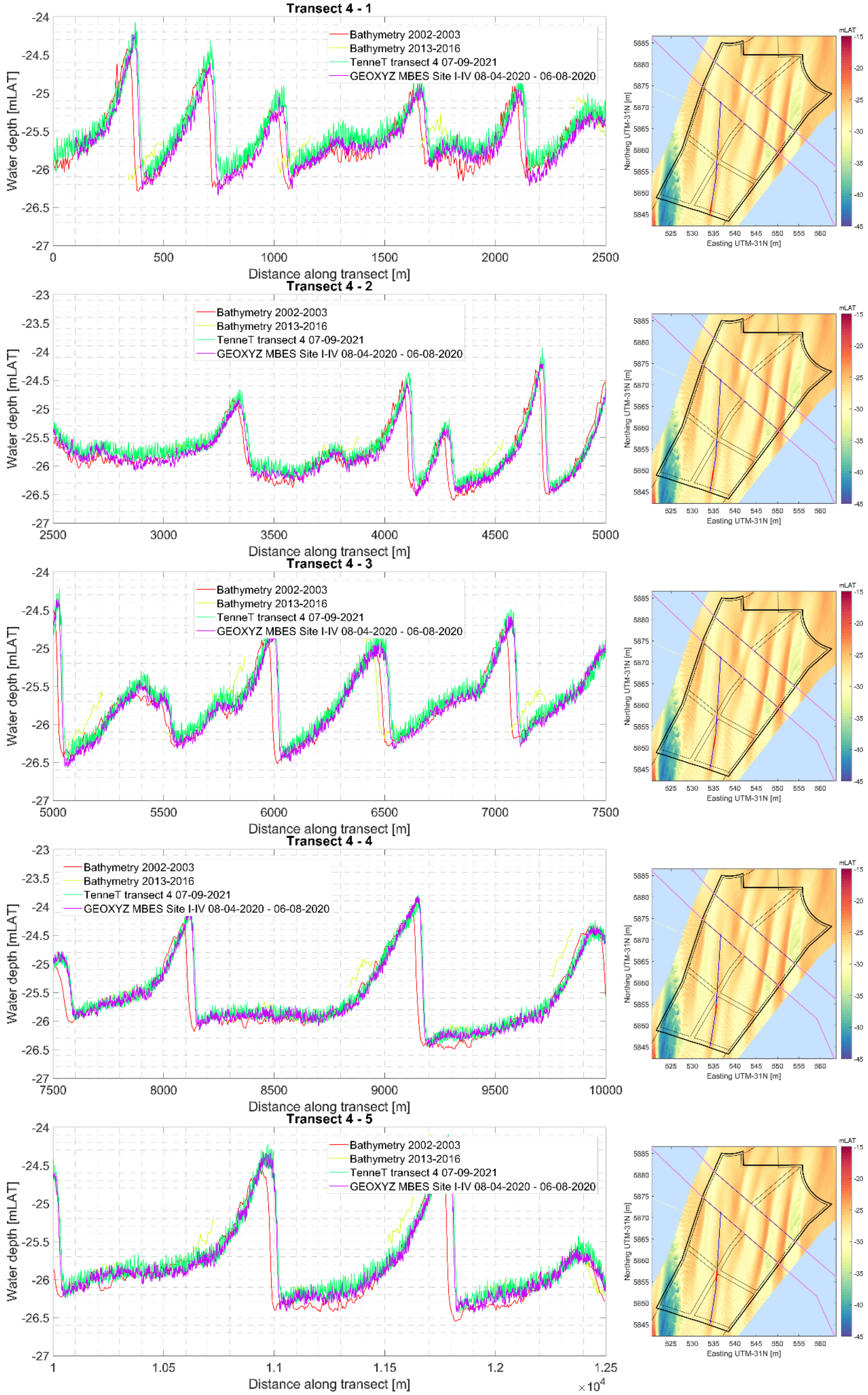

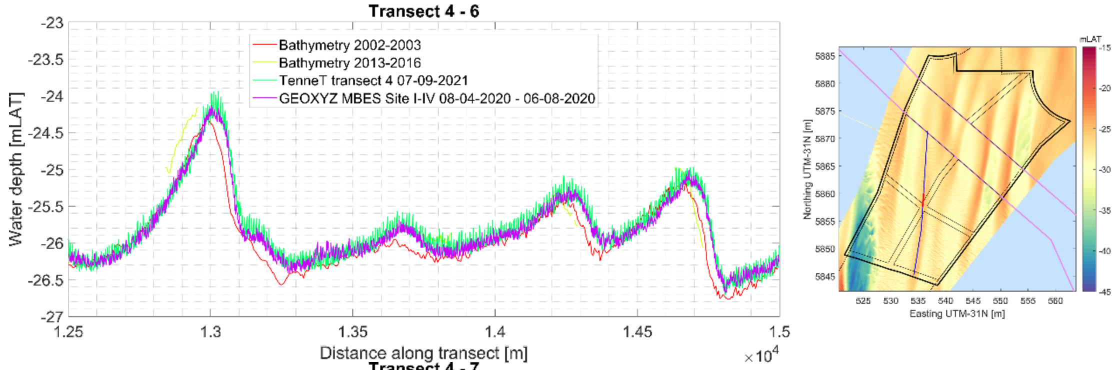
Transect 4 - 6
Bathymetry 2002-2003
Bathymetry 2013-2016
TenneT transect 4 07-09-2021
GEOXYZ MBES Site I-IV 08-04-2020 - 06-08-2020
Water depth [mLAT]
Distance along transect [m]
×10^4
Northing UTM-31N [m]
Easting UTM-31N [m]
mLAT

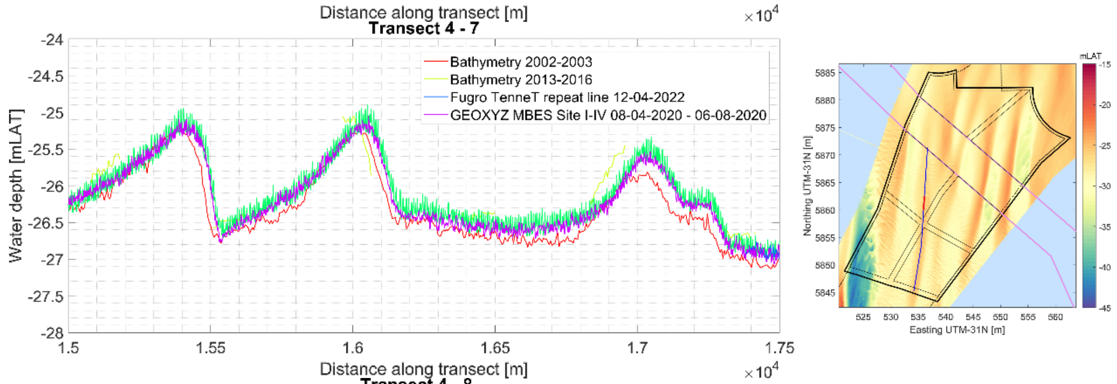
Transect 4 - 7
Bathymetry 2002-2003
Bathymetry 2013-2016
Fugro TenneT repeat line 12-04-2022
GEOXYZ MBES Site I-IV 08-04-2020 - 06-08-2020
Water depth [mLAT]
Distance along transect [m]
×10^4
Northing UTM-31N [m]
Easting UTM-31N [m]
mLAT

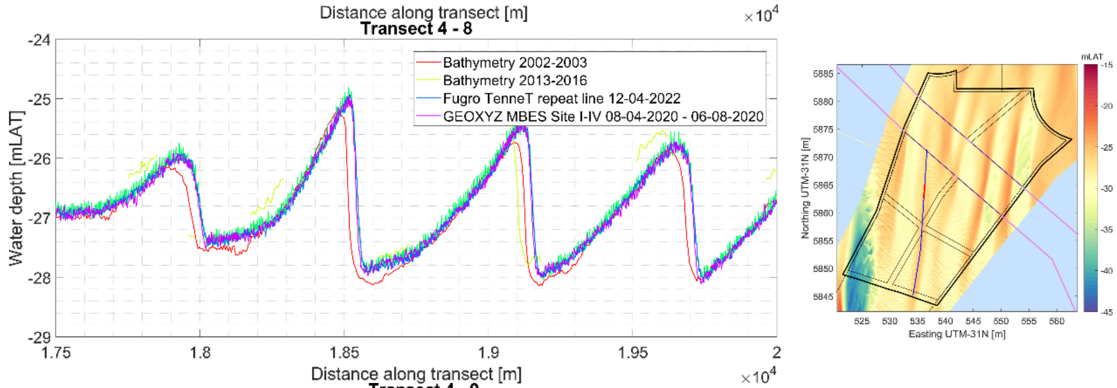
Transect 4 - 8
Bathymetry 2002-2003
Bathymetry 2013-2016
Fugro TenneT repeat line 12-04-2022
GEOXYZ MBES Site I-IV 08-04-2020 - 06-08-2020
Water depth [mLAT]
Distance along transect [m]
×10^4
Northing UTM-31N [m]
Easting UTM-31N [m]
mLAT

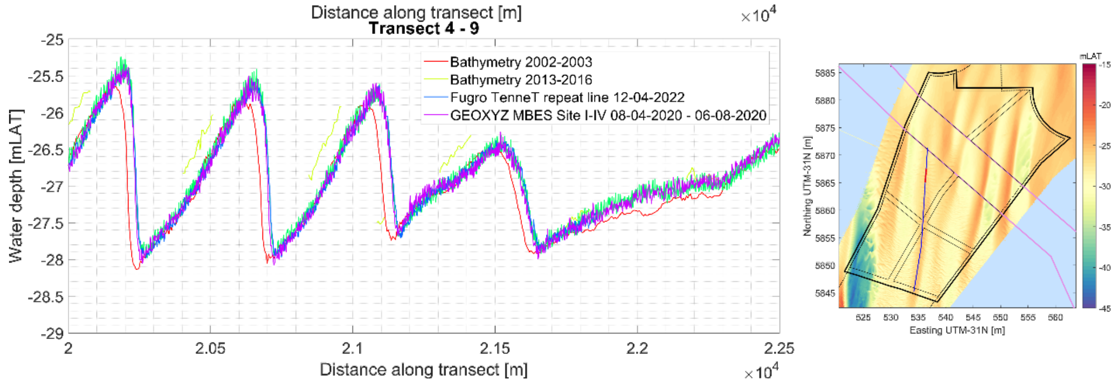
Transect 4 - 9
Bathymetry 2002-2003
Bathymetry 2013-2016
Fugro TenneT repeat line 12-04-2022
GEOXYZ MBES Site I-IV 08-04-2020 - 06-08-2020
Water depth [mLAT]
Distance along transect [m]
×10^4
Northing UTM-31N [m]
Easting UTM-31N [m]
mLAT

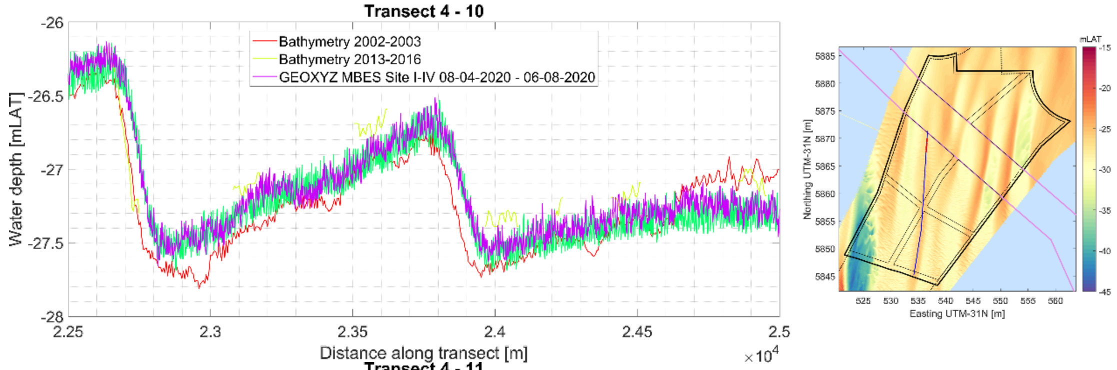
Transect 4 - 10
Bathymetry 2002-2003
Bathymetry 2013-2016
GEOXYZ MBES Site I-IV 08-04-2020 - 06-08-2020
Water depth [mLAT]
-26
-26.5
-27
-27.5
-28
2.25
2.3
2.35
2.4
2.45
2.5
Distance along transect [m]
×10^4
Northing UTM-31N [m]
Easting UTM-31N [m]
mLAT

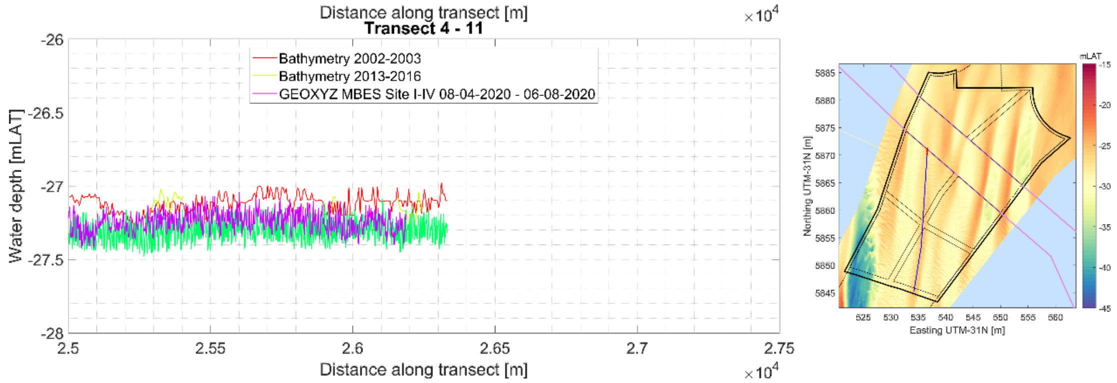
Transect 4 - 11
Bathymetry 2002-2003
Bathymetry 2013-2016
GEOXYZ MBES Site I-IV 08-04-2020 - 06-08-2020
Water depth [mLAT]
-26
-26.5
-27
-27.5
-28
2.5
2.55
2.6
2.65
2.7
2.75
Distance along transect [m]
×10^4
Northing UTM-31N [m]
Easting UTM-31N [m]
mLAT

E.2.1.5. Transect 5

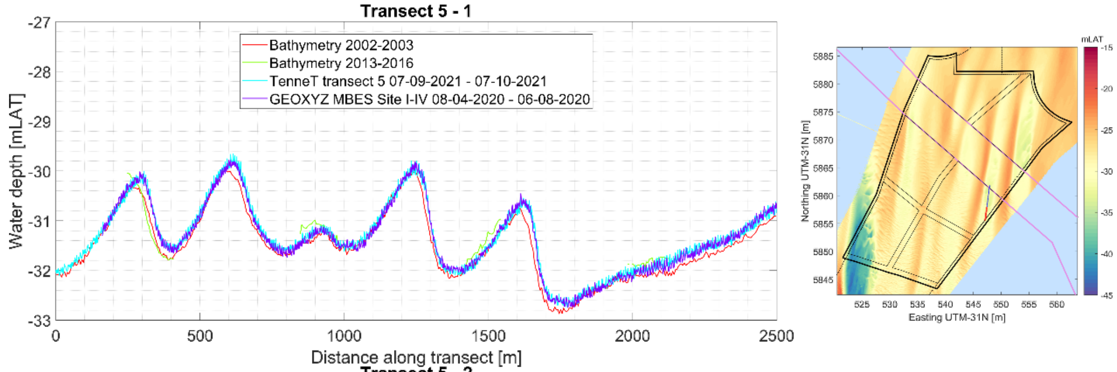

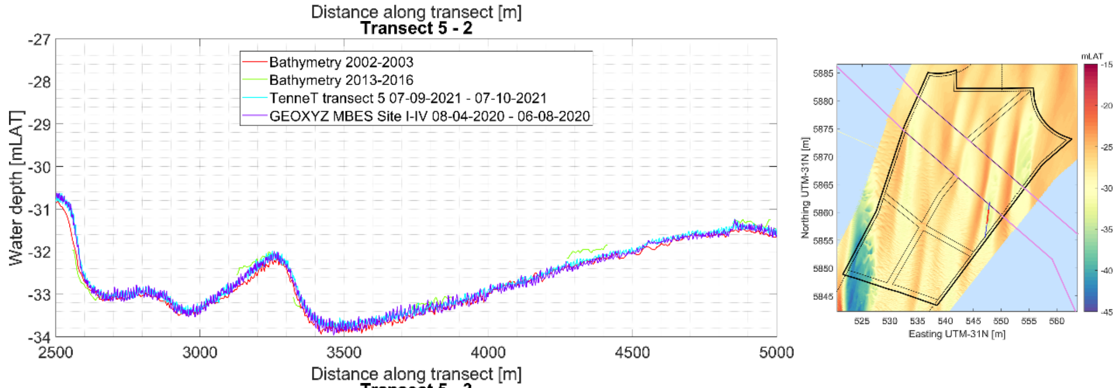

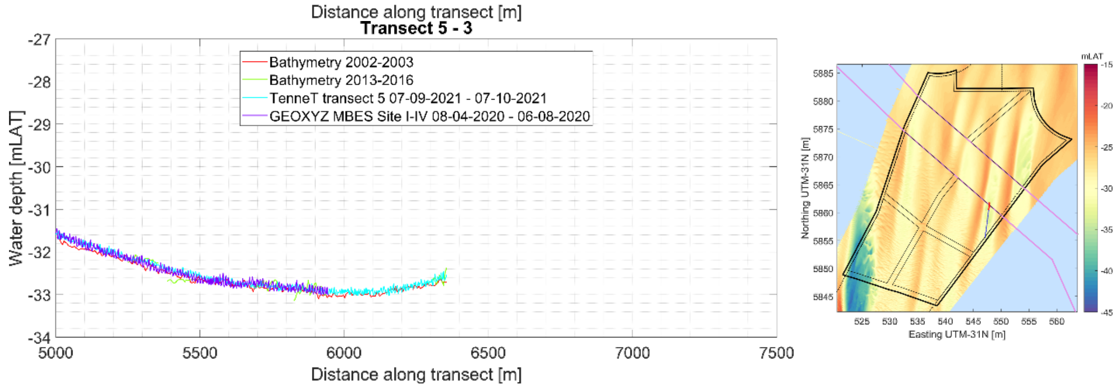

E.2.1.6. Transect 6

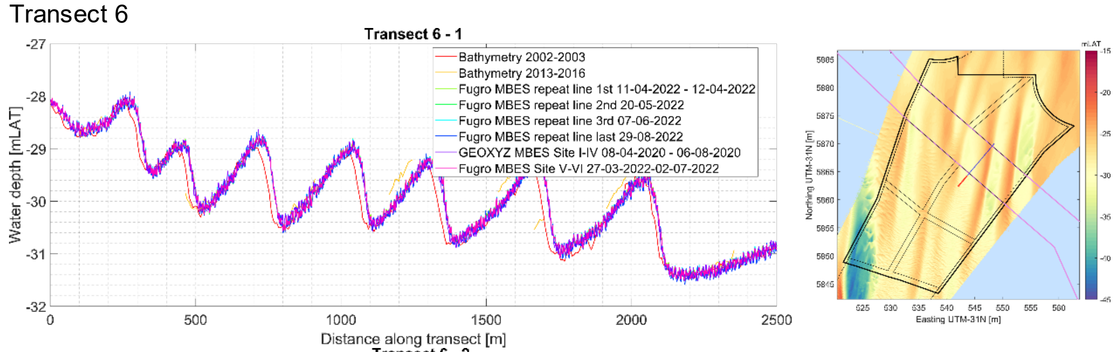

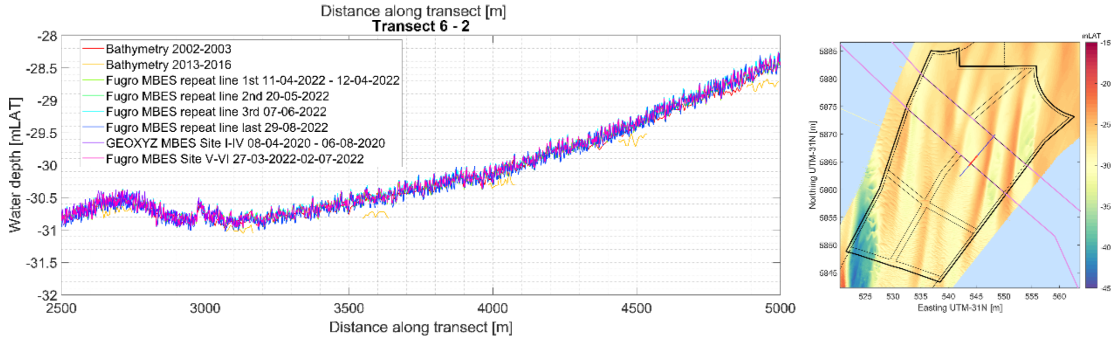

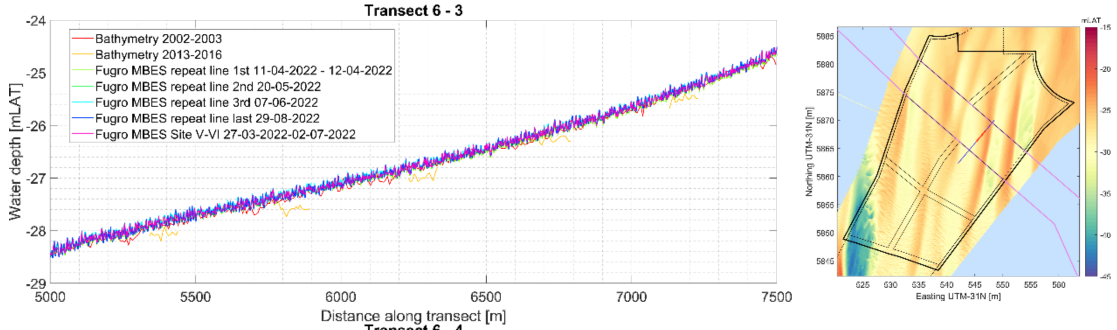
Transect 6 - 3
Bathymetry 2002-2003
Bathymetry 2013-2016
Fugro MBES repeat line 1st 11-04-2022 - 12-04-2022
Fugro MBES repeat line 2nd 20-05-2022
Fugro MBES repeat line 3rd 07-06-2022
Fugro MBES repeat line last 29-08-2022
Fugro MBES Site V-VI 27-03-2022-02-07-2022
Water depth [mLAT]
Distance along transect [m]
Northing UTM-31N [m]
Easting UTM-31N [m]
mLAT

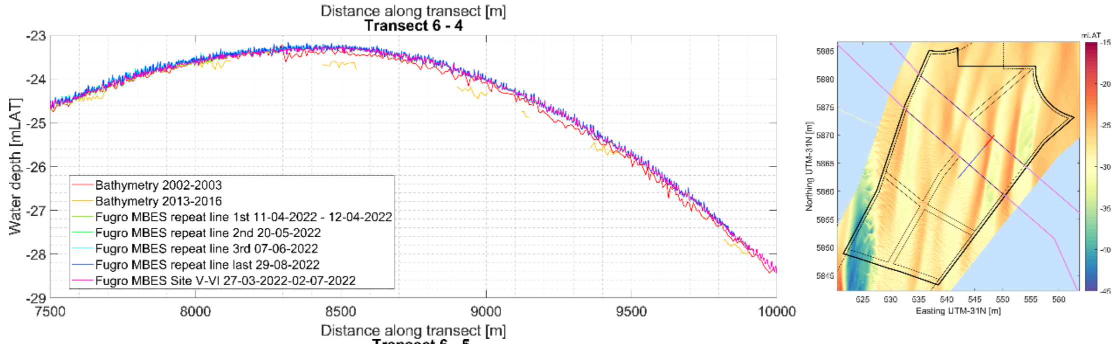
Transect 6 - 4
Bathymetry 2002-2003
Bathymetry 2013-2016
Fugro MBES repeat line 1st 11-04-2022 - 12-04-2022
Fugro MBES repeat line 2nd 20-05-2022
Fugro MBES repeat line 3rd 07-06-2022
Fugro MBES repeat line last 29-08-2022
Fugro MBES Site V-VI 27-03-2022-02-07-2022
Water depth [mLAT]
Distance along transect [m]
Northing UTM-31N [m]
Easting UTM-31N [m]
mLAT

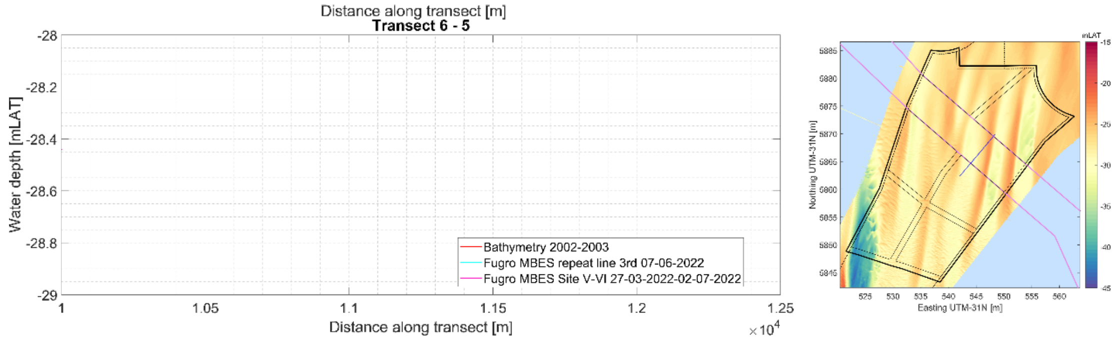
Transect 6 - 5
Bathymetry 2002-2003
Fugro MBES repeat line 3rd 07-06-2022
Fugro MBES Site V-VI 27-03-2022-02-07-2022
Water depth [mLAT]
Distance along transect [m]
Northing UTM-31N [m]
Easting UTM-31N [m]
mLAT

E.2.1.7. Transect 7

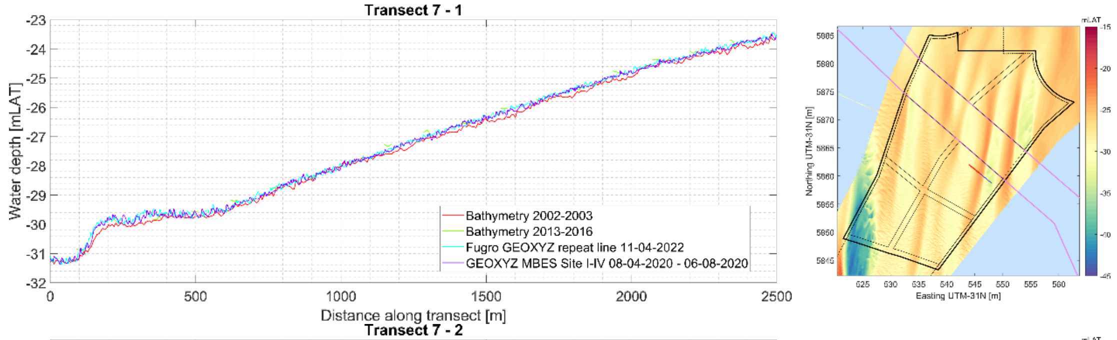

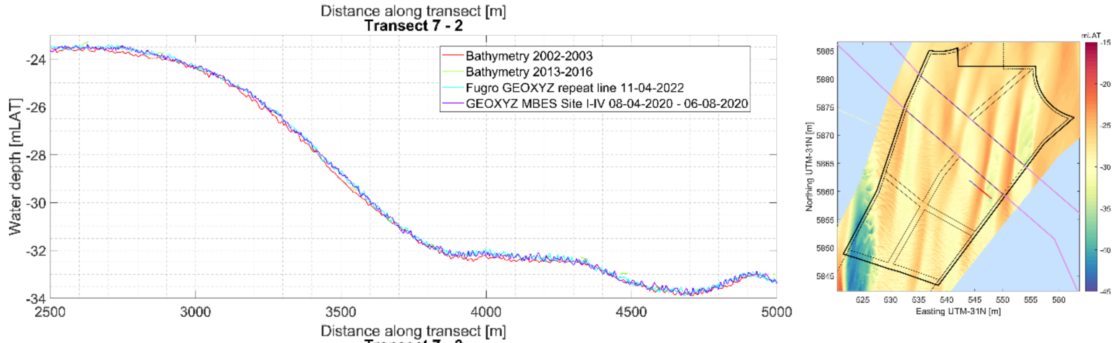

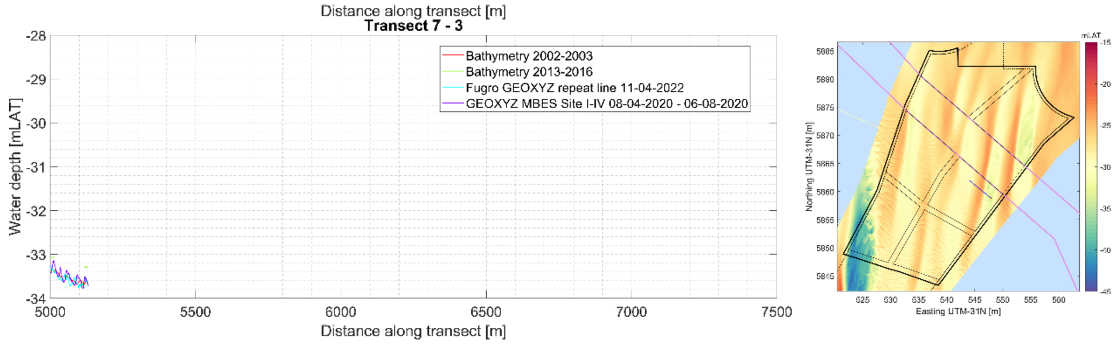

E.2.2 Sand wave and megaripple profile along repeat survey lines

E.2.2.1. Transect 1

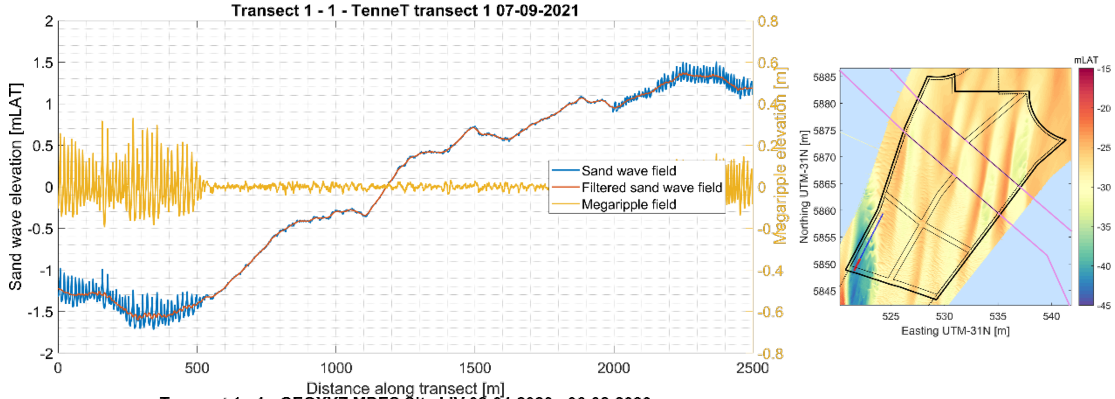

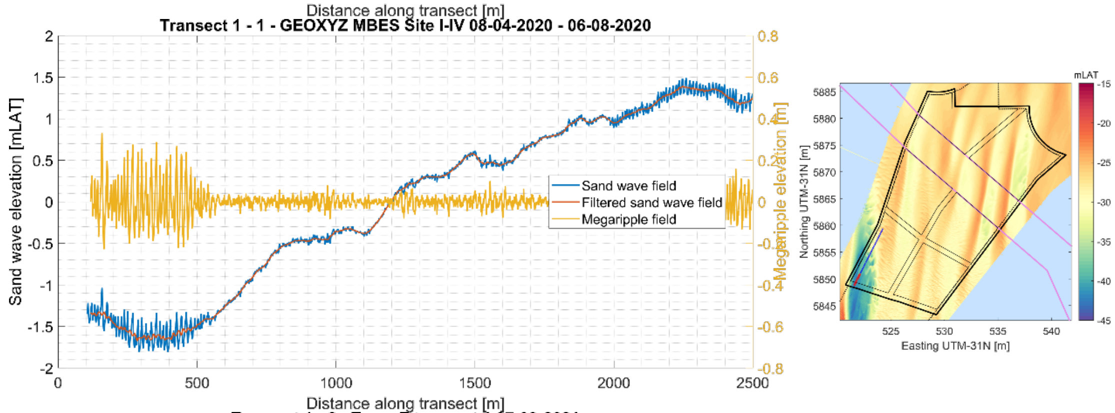

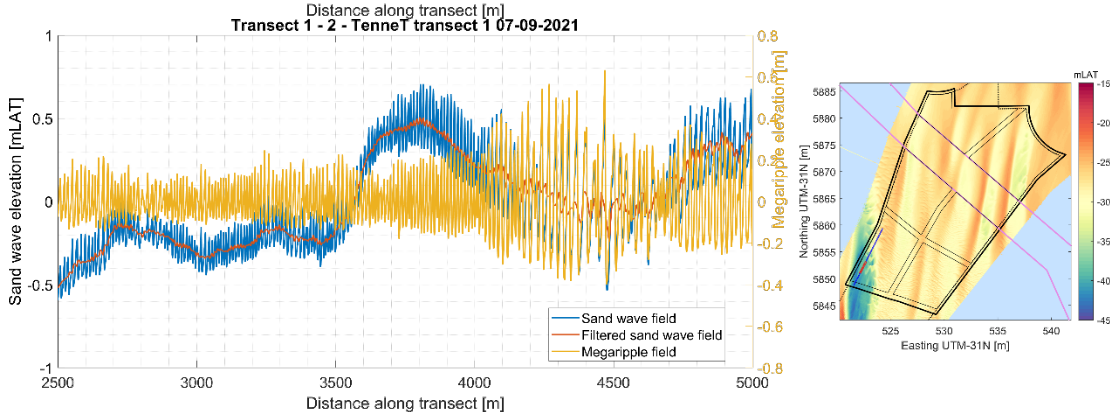

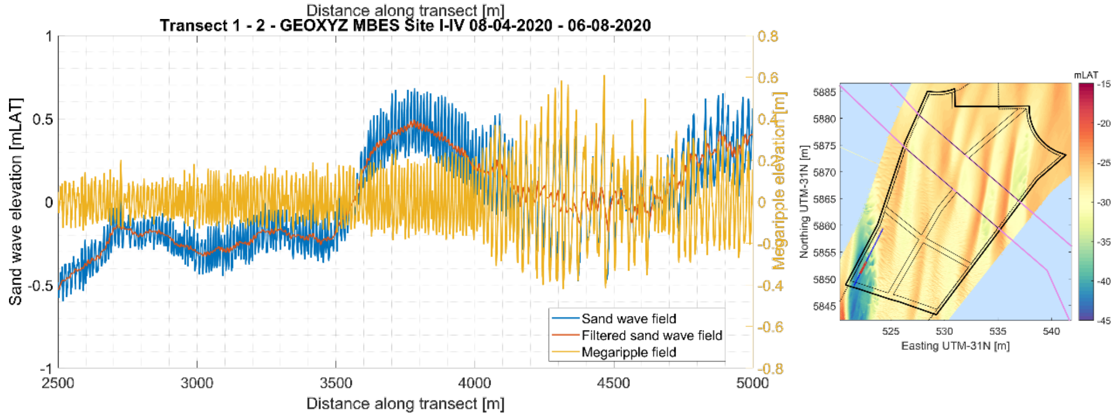

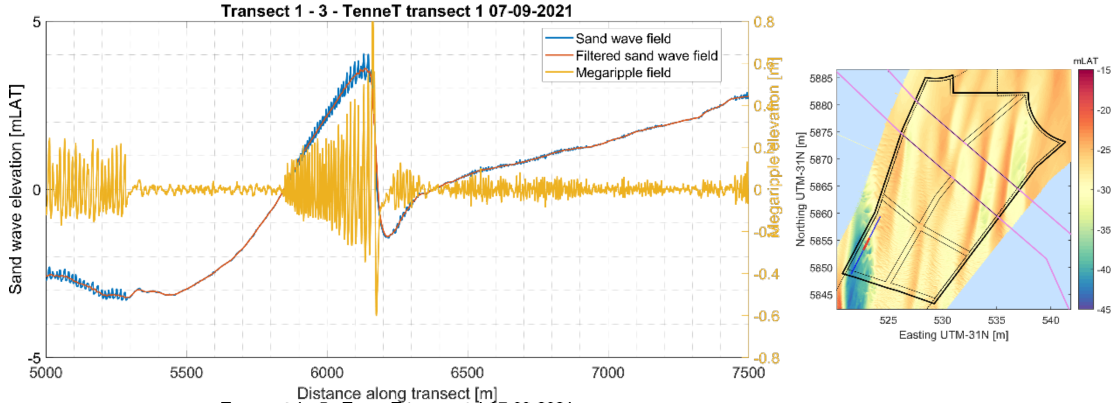
Transect 1 - 3 - TenneT transect 1 07-09-2021
Sand wave field
Filtered sand wave field
Megaripple field
Sand wave elevation [mLAT]
Megaripple elevation [m]
Distance along transect [m]
Northing UTM-31N [m]
Easting UTM-31N [m]
mLAT

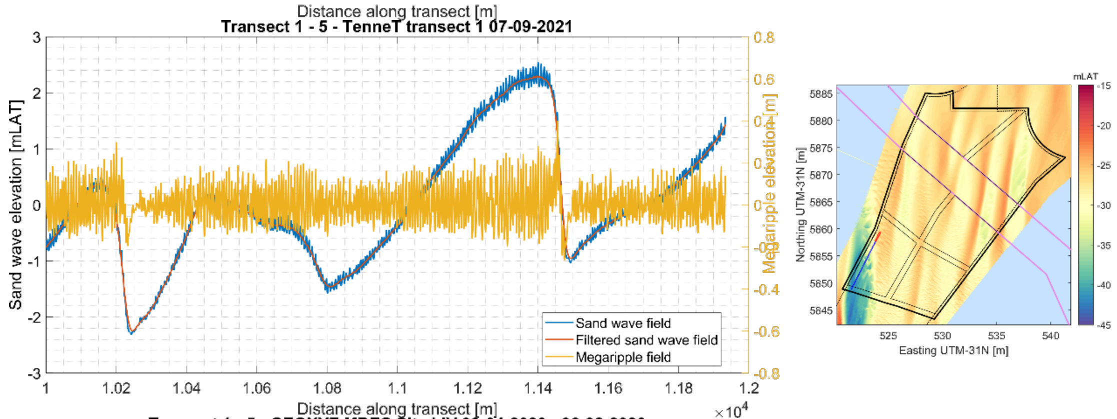
Transect 1 - 5 - TenneT transect 1 07-09-2021
Sand wave field
Filtered sand wave field
Megaripple field
Sand wave elevation [mLAT]
Megaripple elevation [m]
Distance along transect [m]
$\times 10^4$
Northing UTM-31N [m]
Easting UTM-31N [m]
mLAT

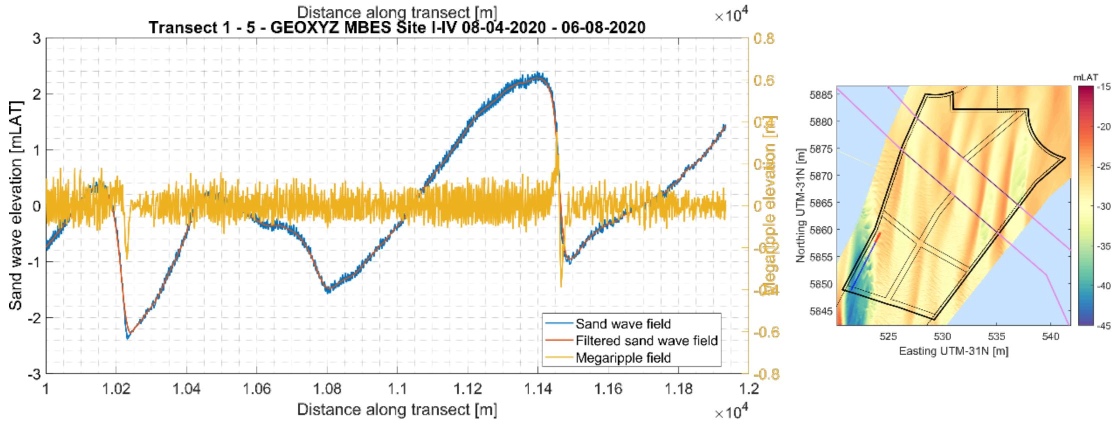
Transect 1 - 5 - GEOXYZ MBES Site I-IV 08-04-2020 - 06-08-2020
Sand wave field
Filtered sand wave field
Megaripple field
Sand wave elevation [mLAT]
Megaripple elevation [m]
Distance along transect [m]
$\times 10^4$
Northing UTM-31N [m]
Easting UTM-31N [m]
mLAT

E.2.2.2. Transect 2

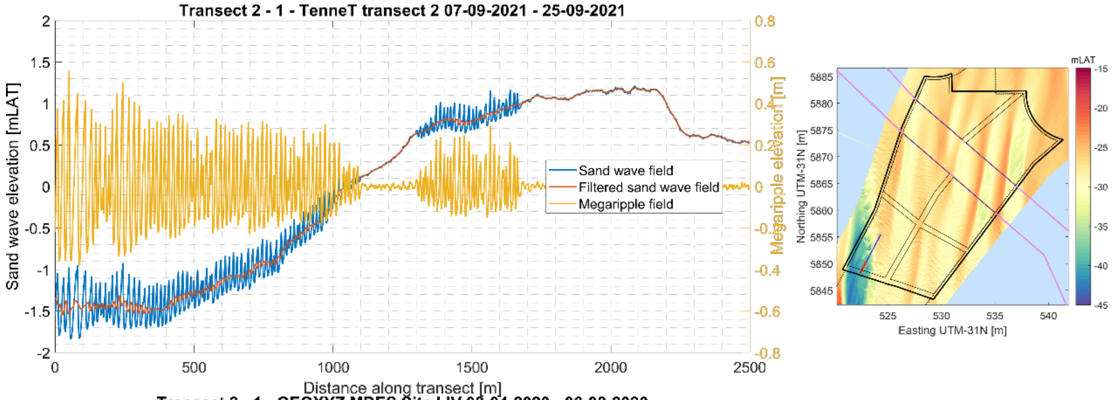

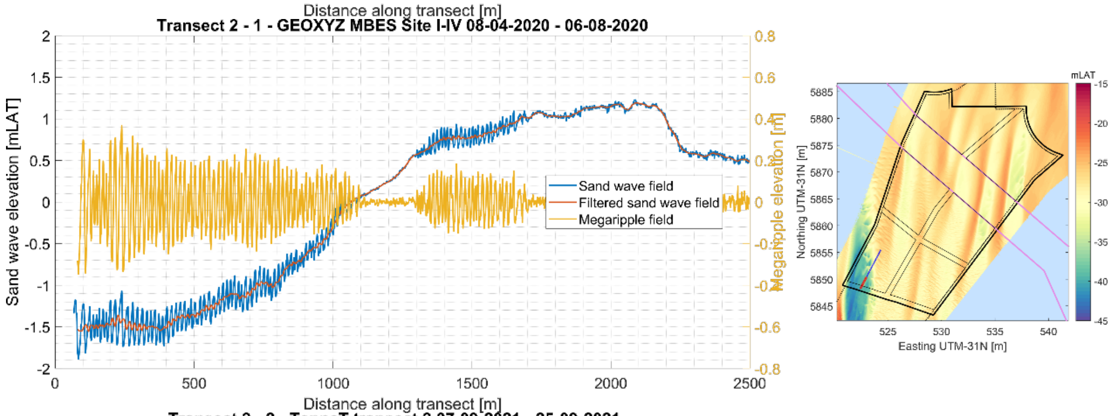

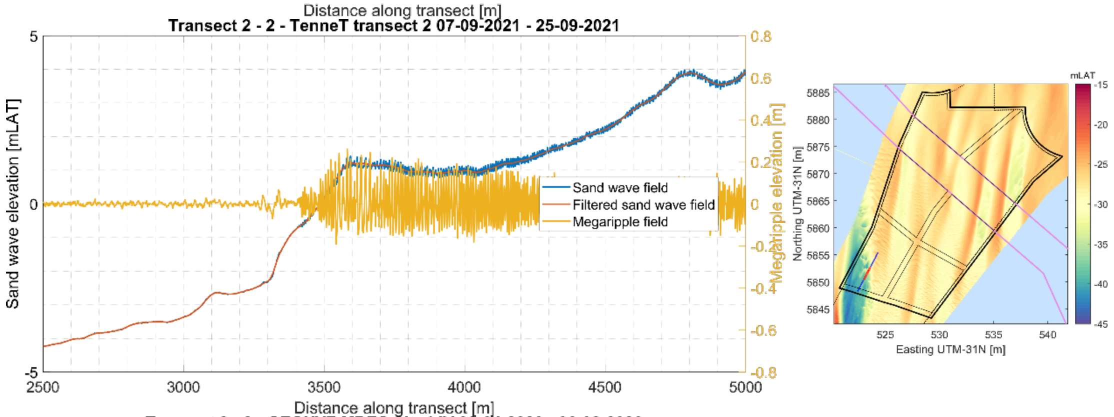

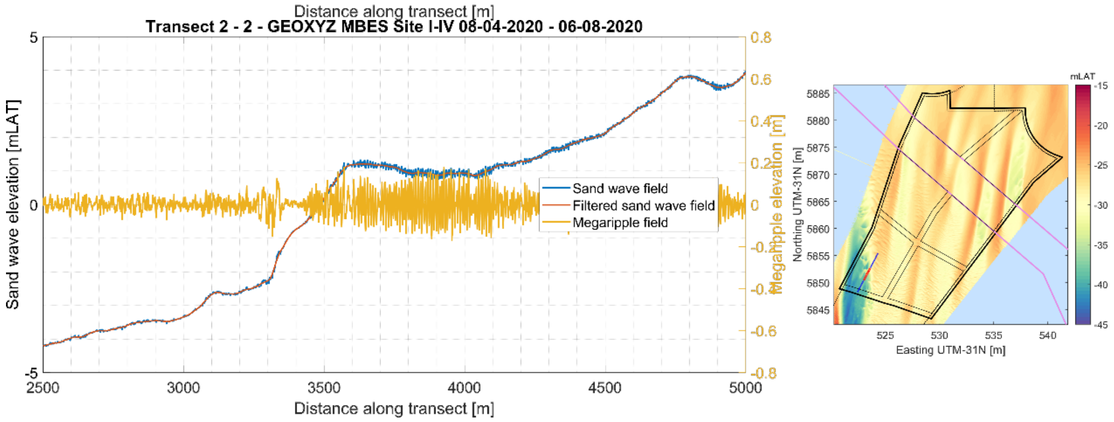

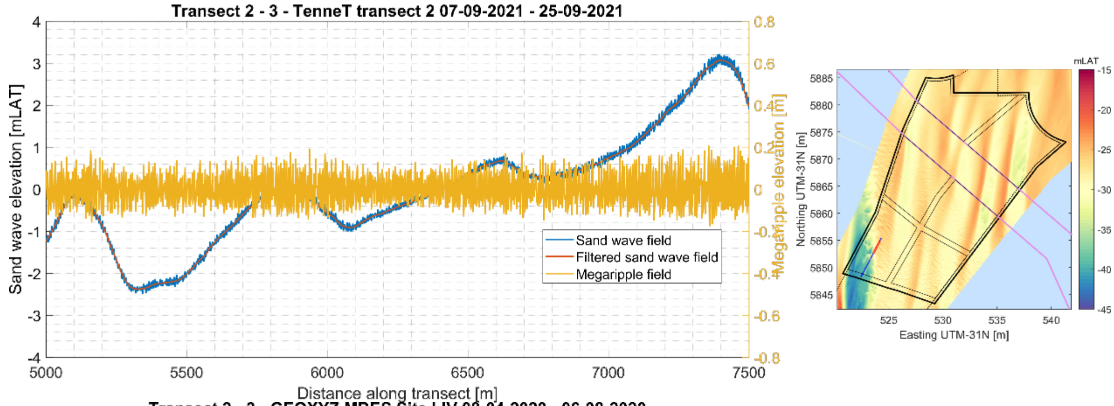
Transect 2 - 3 - TenneT transect 2 07-09-2021 - 25-09-2021
Sand wave elevation [mLAT]
Megaripple elevation [m]
Distance along transect [m]
Sand wave field
Filtered sand wave field
Megaripple field
Northing UTM-31N [m]
Easting UTM-31N [m]
mLAT

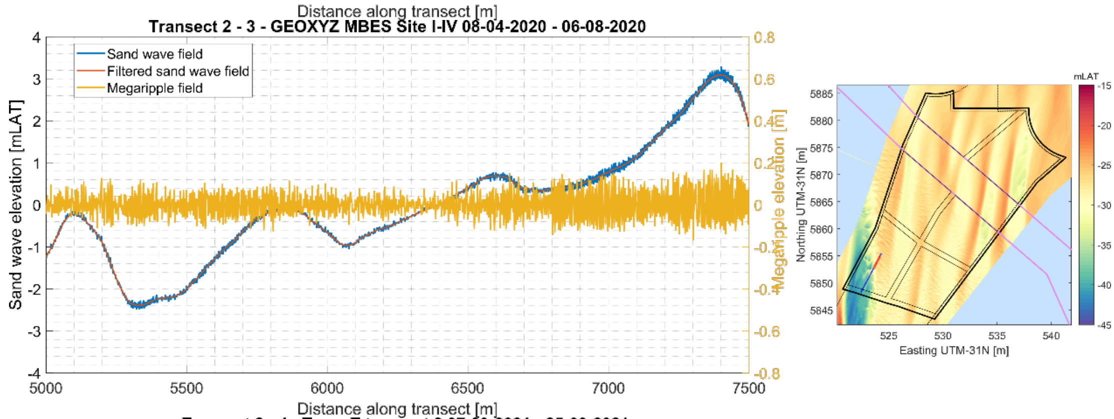
Transect 2 - 3 - GEOXYZ MBES Site I-IV 08-04-2020 - 06-08-2020
Sand wave elevation [mLAT]
Megaripple elevation [m]
Distance along transect [m]
Sand wave field
Filtered sand wave field
Megaripple field
Northing UTM-31N [m]
Easting UTM-31N [m]
mLAT

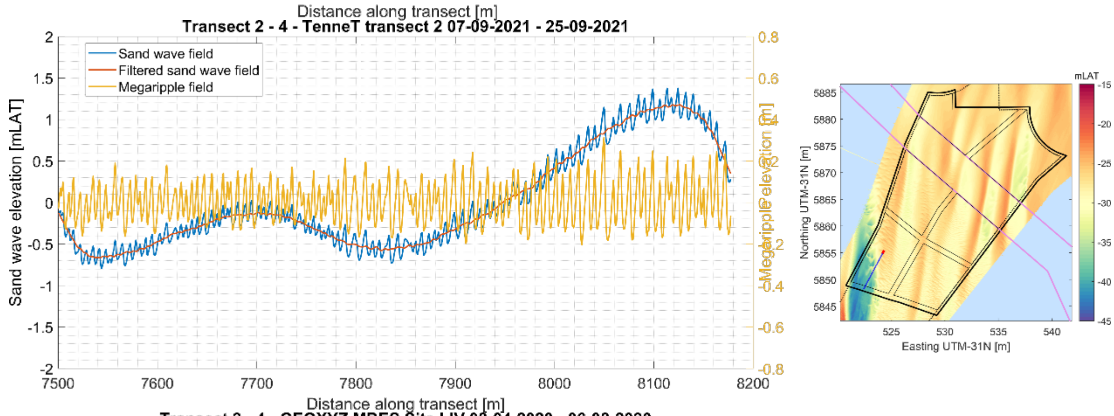
Transect 2 - 4 - TenneT transect 2 07-09-2021 - 25-09-2021
Sand wave elevation [mLAT]
Megaripple elevation [m]
Distance along transect [m]
Sand wave field
Filtered sand wave field
Megaripple field
Northing UTM-31N [m]
Easting UTM-31N [m]
mLAT

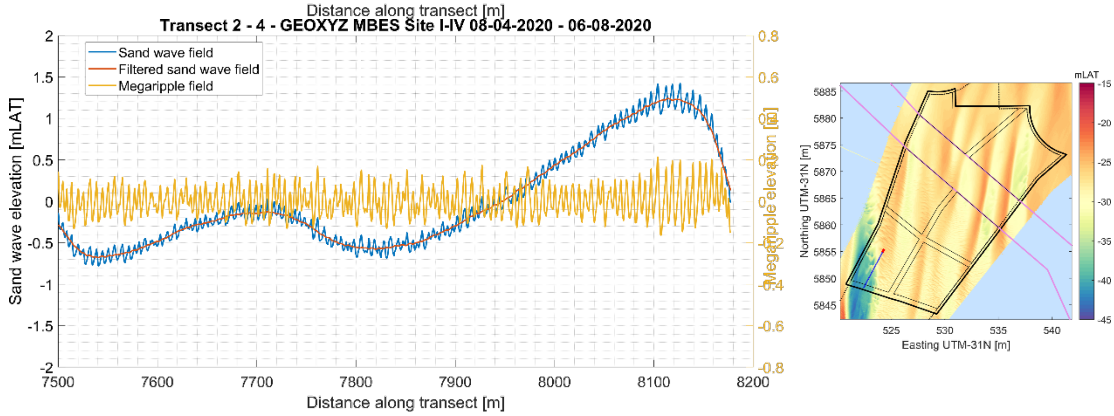
Transect 2 - 4 - GEOXYZ MBES Site I-IV 08-04-2020 - 06-08-2020
Sand wave elevation [mLAT]
Megaripple elevation [m]
Distance along transect [m]
Sand wave field
Filtered sand wave field
Megaripple field
Northing UTM-31N [m]
Easting UTM-31N [m]
mLAT

E.2.2.3. Transect 3

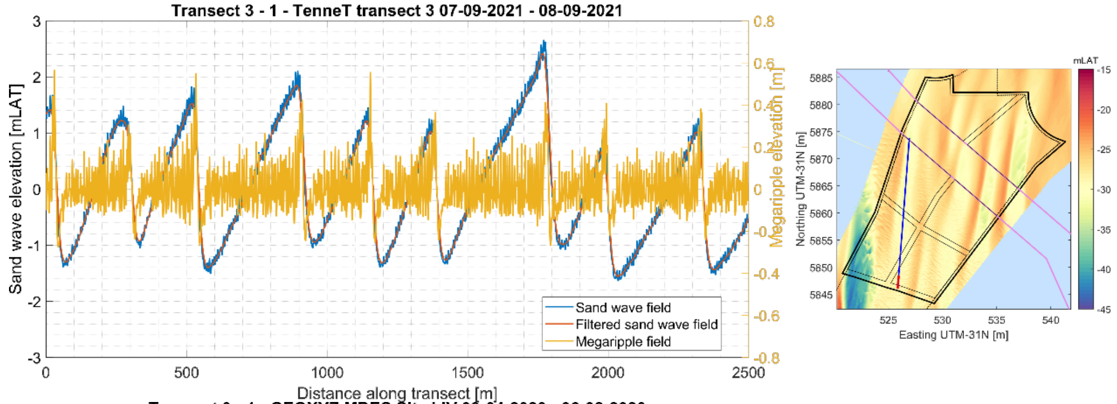

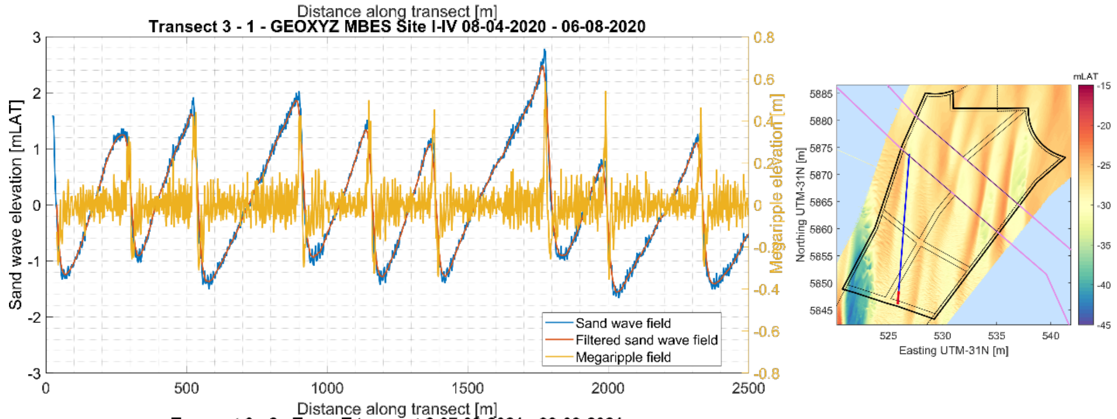

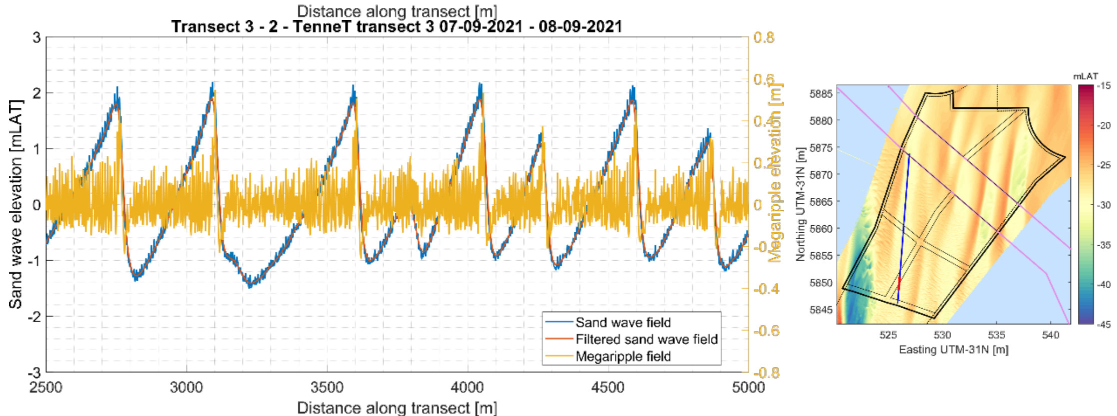

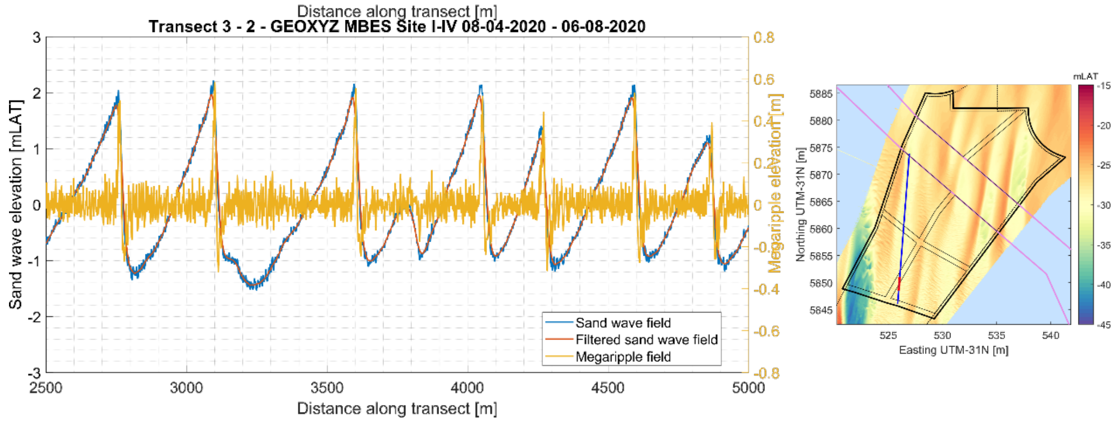

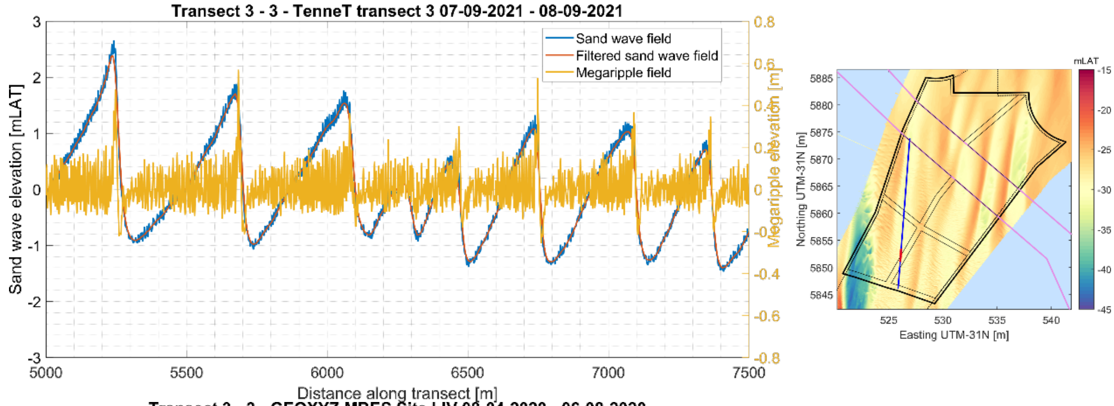
Transect 3 - 3 - TenneT transect 3 07-09-2021 - 08-09-2021
Sand wave field
Filtered sand wave field
Megaripple field
Sand wave elevation [mLAT]
Megaripple elevation [m]
Distance along transect [m]
Northing UTM-31N [m]
Easting UTM-31N [m]
mLAT

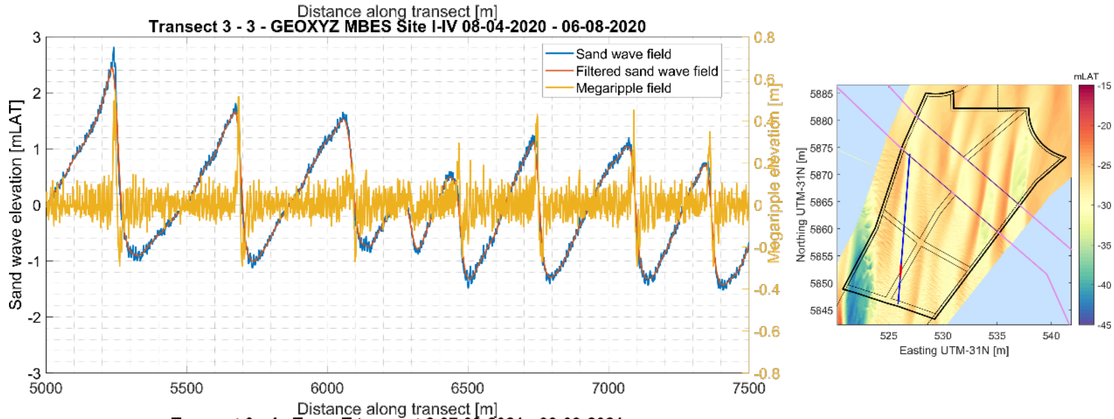
Transect 3 - 3 - GEOXYZ MBES Site I-IV 08-04-2020 - 06-08-2020
Sand wave field
Filtered sand wave field
Megaripple field
Sand wave elevation [mLAT]
Megaripple elevation [m]
Distance along transect [m]
Northing UTM-31N [m]
Easting UTM-31N [m]
mLAT

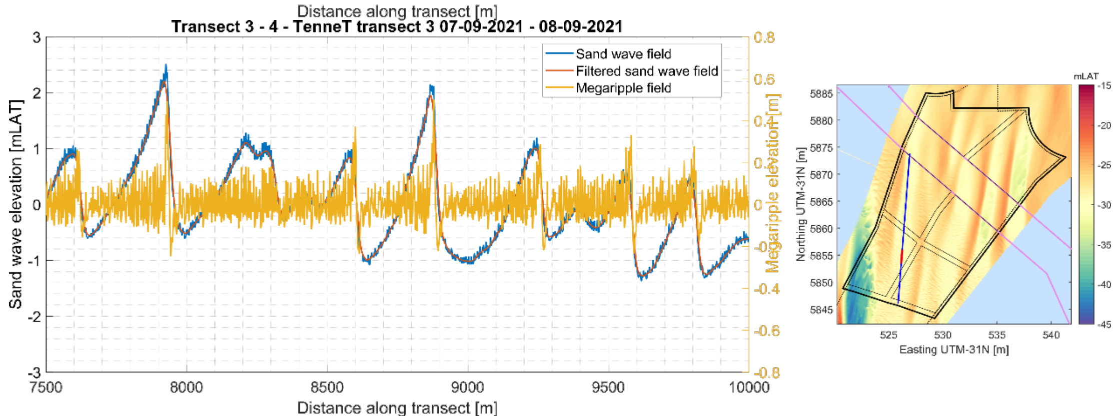
Transect 3 - 4 - TenneT transect 3 07-09-2021 - 08-09-2021
Sand wave field
Filtered sand wave field
Megaripple field
Sand wave elevation [mLAT]
Megaripple elevation [m]
Distance along transect [m]
Northing UTM-31N [m]
Easting UTM-31N [m]
mLAT

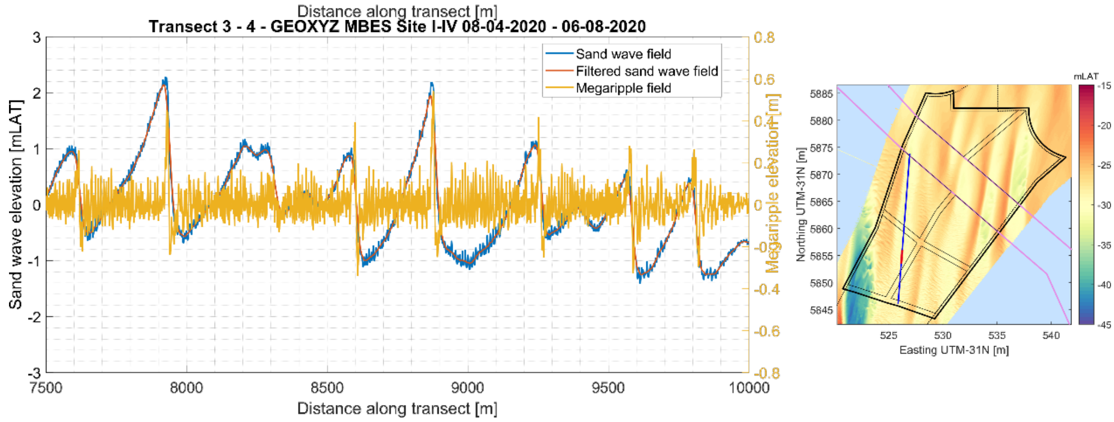
Transect 3 - 4 - GEOXYZ MBES Site I-IV 08-04-2020 - 06-08-2020
Sand wave field
Filtered sand wave field
Megaripple field
Sand wave elevation [mLAT]
Megaripple elevation [m]
Distance along transect [m]
Northing UTM-31N [m]
Easting UTM-31N [m]
mLAT

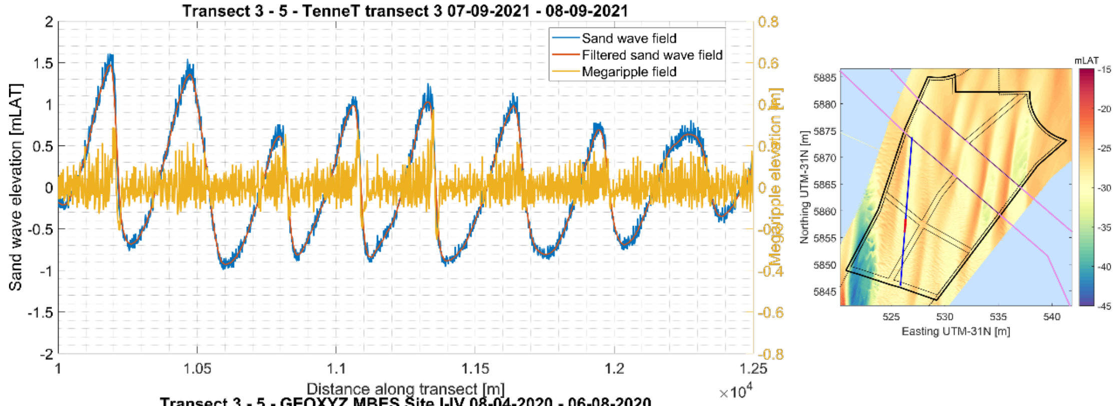
Transect 3 - 5 - TenneT transect 3 07-09-2021 - 08-09-2021
Sand wave field
Filtered sand wave field
Megaripple field
Sand wave elevation [mLAT]
Megaripple elevation [m]
Distance along transect [m]
Northing UTM-31N [m]
Easting UTM-31N [m]
mLAT

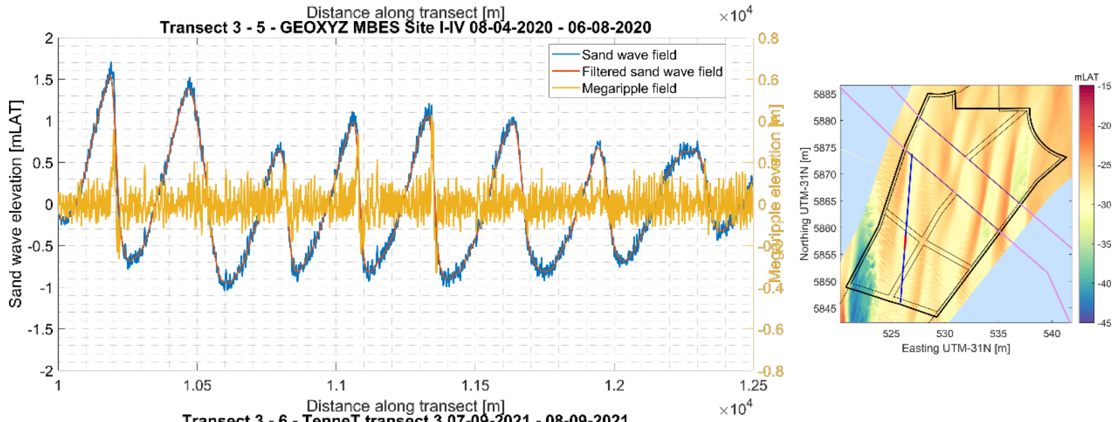
Transect 3 - 5 - GEOXYZ MBES Site I-IV 08-04-2020 - 06-08-2020
Sand wave field
Filtered sand wave field
Megaripple field
Sand wave elevation [mLAT]
Megaripple elevation [m]
Distance along transect [m]
Northing UTM-31N [m]
Easting UTM-31N [m]
mLAT

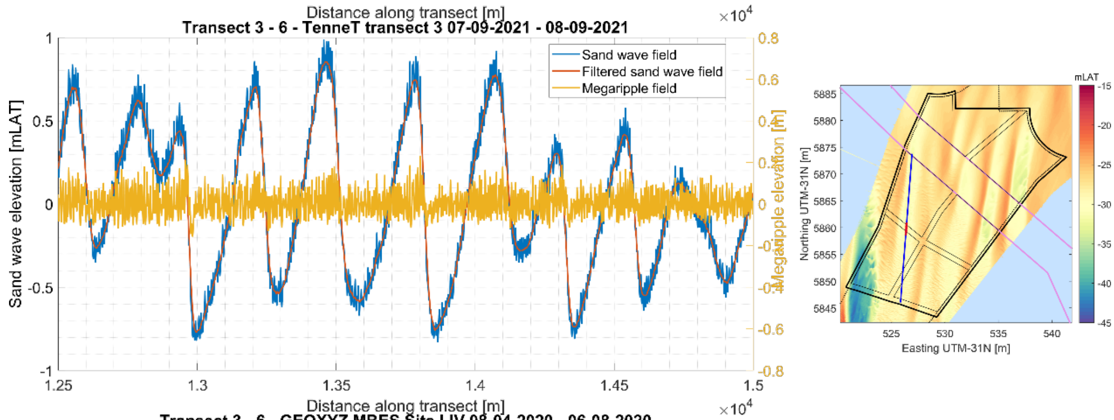
Transect 3 - 6 - TenneT transect 3 07-09-2021 - 08-09-2021
Sand wave field
Filtered sand wave field
Megaripple field
Sand wave elevation [mLAT]
Megaripple elevation [m]
Distance along transect [m]
Northing UTM-31N [m]
Easting UTM-31N [m]
mLAT

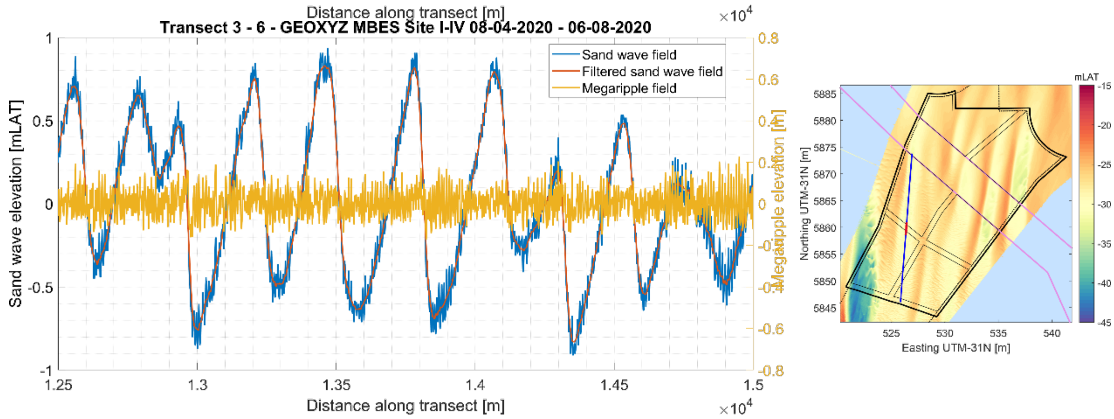
Transect 3 - 6 - GEOXYZ MBES Site I-IV 08-04-2020 - 06-08-2020
Sand wave field
Filtered sand wave field
Megaripple field
Sand wave elevation [mLAT]
Megaripple elevation [m]
Distance along transect [m]
Northing UTM-31N [m]
Easting UTM-31N [m]
mLAT

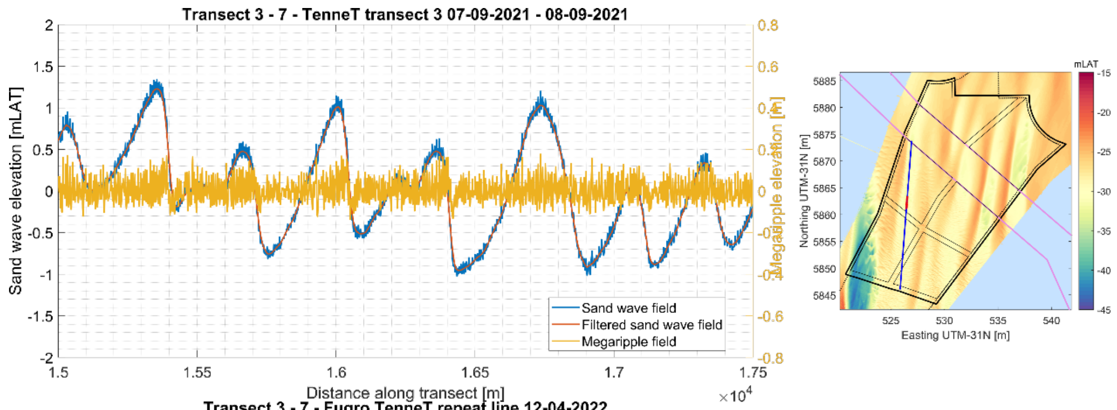
Transect 3 - 7 - TenneT transect 3 07-09-2021 - 08-09-2021
Sand wave elevation [mLAT]
Megaripple elevation [m]
Distance along transect [m]
×10^4
Sand wave field
Filtered sand wave field
Megaripple field
Northing UTM-31N [m]
Easting UTM-31N [m]
mLAT

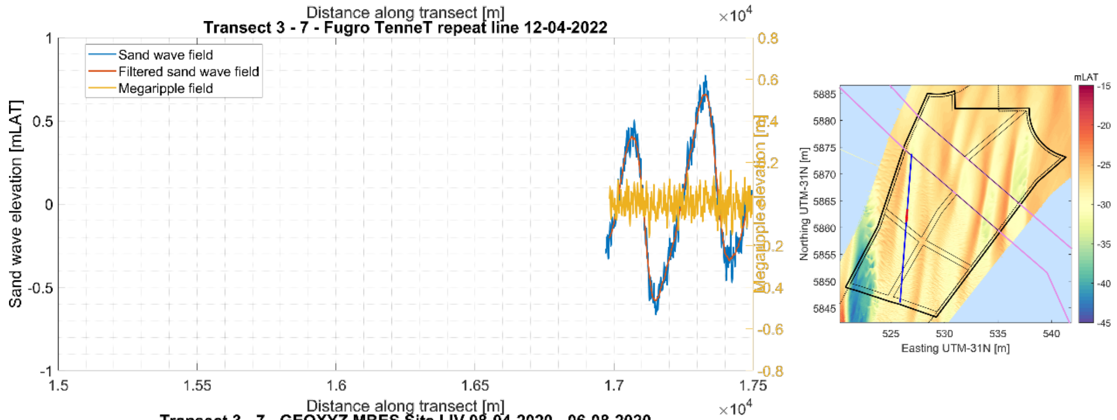
Transect 3 - 7 - Fugro TenneT repeat line 12-04-2022
Sand wave elevation [mLAT]
Megaripple elevation [m]
Distance along transect [m]
×10^4
Sand wave field
Filtered sand wave field
Megaripple field
Northing UTM-31N [m]
Easting UTM-31N [m]
mLAT

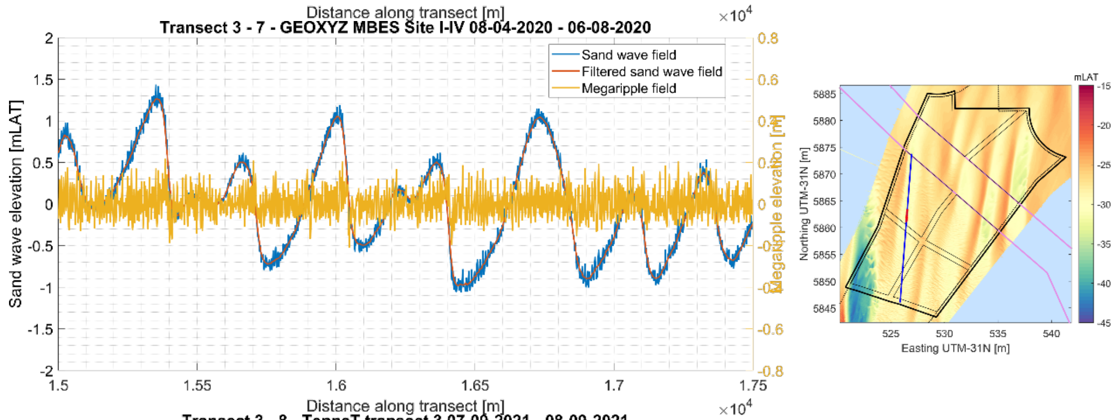
Transect 3 - 7 - GEOXYZ MBES Site I-IV 08-04-2020 - 06-08-2020
Sand wave elevation [mLAT]
Megaripple elevation [m]
Distance along transect [m]
×10^4
Sand wave field
Filtered sand wave field
Megaripple field
Northing UTM-31N [m]
Easting UTM-31N [m]
mLAT

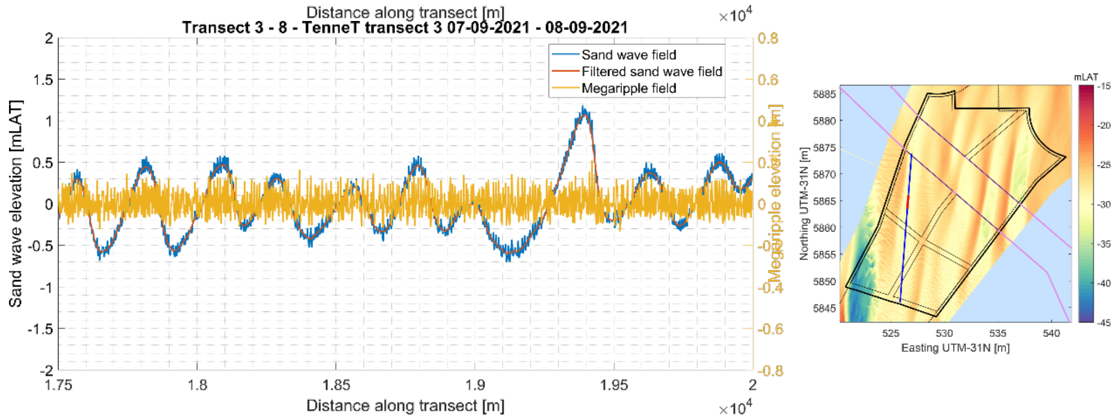
Transect 3 - 8 - TenneT transect 3 07-09-2021 - 08-09-2021
Sand wave elevation [mLAT]
Megaripple elevation [m]
Distance along transect [m]
×10^4
Sand wave field
Filtered sand wave field
Megaripple field
Northing UTM-31N [m]
Easting UTM-31N [m]
mLAT

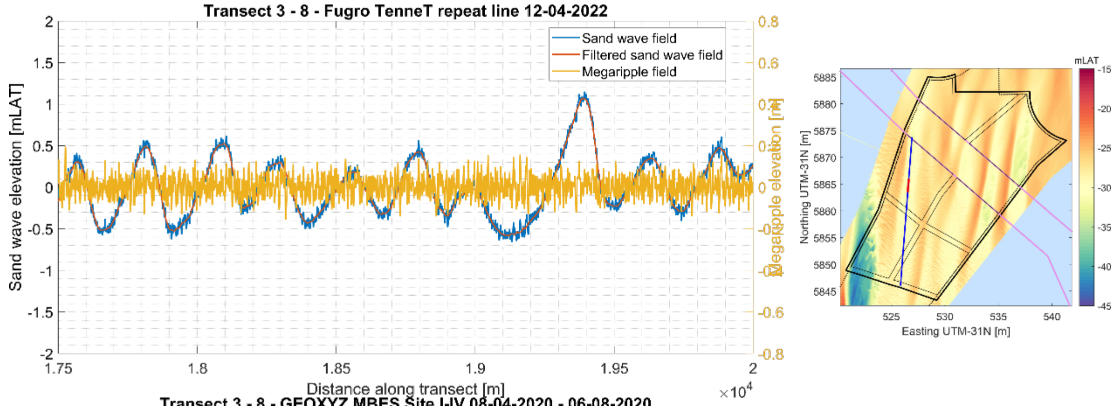
Transect 3 - 8 - Fugro TenneT repeat line 12-04-2022
Sand wave field
Filtered sand wave field
Megaripple field
Sand wave elevation [mLAT]
Megaripple elevation [m]
Distance along transect [m]
×10^4
Northing UTM-31N [m]
Easting UTM-31N [m]
mLAT

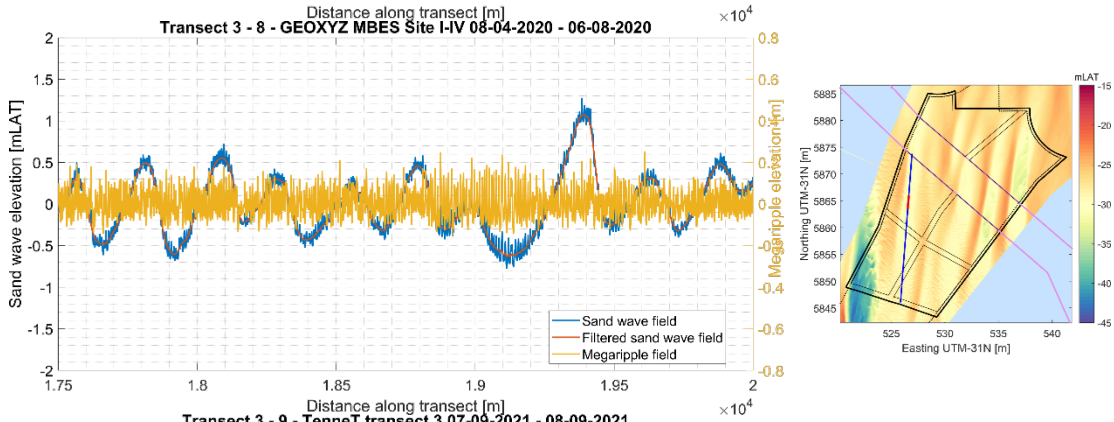
Transect 3 - 8 - GEOXYZ MBES Site I-IV 08-04-2020 - 06-08-2020
Sand wave field
Filtered sand wave field
Megaripple field
Sand wave elevation [mLAT]
Megaripple elevation [m]
Distance along transect [m]
×10^4
Northing UTM-31N [m]
Easting UTM-31N [m]
mLAT

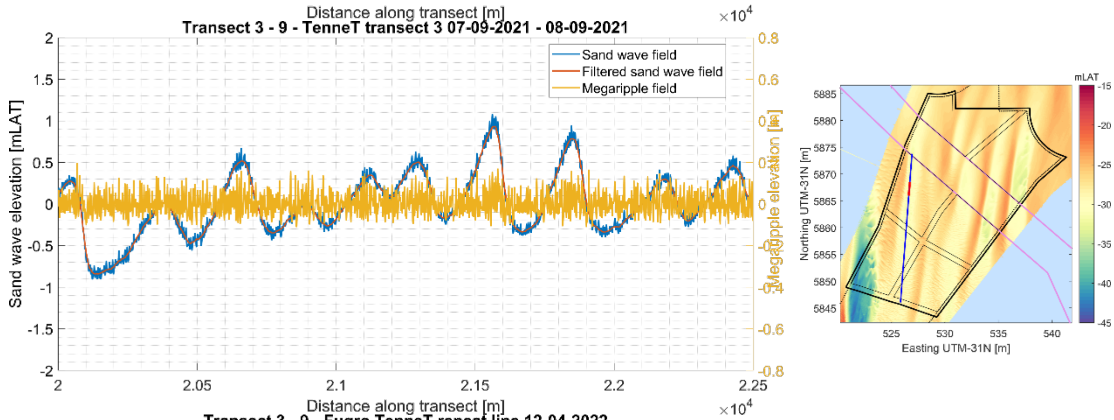
Transect 3 - 9 - TenneT transect 3 07-09-2021 - 08-09-2021
Sand wave field
Filtered sand wave field
Megaripple field
Sand wave elevation [mLAT]
Megaripple elevation [m]
Distance along transect [m]
×10^4
Northing UTM-31N [m]
Easting UTM-31N [m]
mLAT

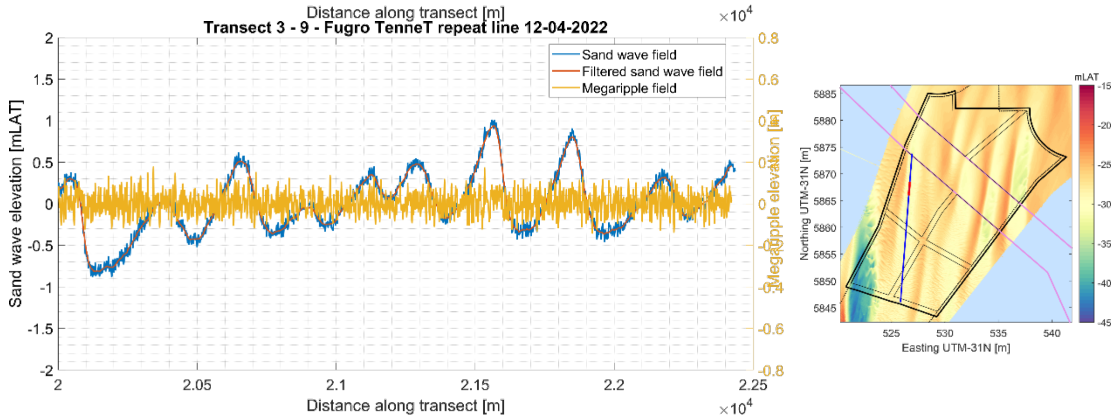
Transect 3 - 9 - Fugro TenneT repeat line 12-04-2022
Sand wave field
Filtered sand wave field
Megaripple field
Sand wave elevation [mLAT]
Megaripple elevation [m]
Distance along transect [m]
×10^4
Northing UTM-31N [m]
Easting UTM-31N [m]
mLAT

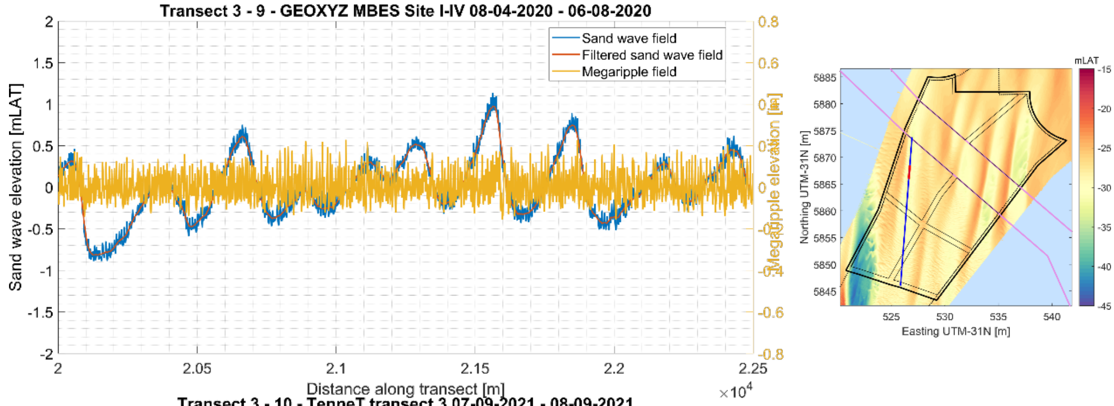
Transect 3 - 9 - GEOXYZ MBES Site I-IV 08-04-2020 - 06-08-2020
Sand wave field
Filtered sand wave field
Megaripple field
Sand wave elevation [mLAT]
Megaripple elevation [m]
Distance along transect [m]
×10^4
Northing UTM-31N [m]
Easting UTM-31N [m]
mLAT

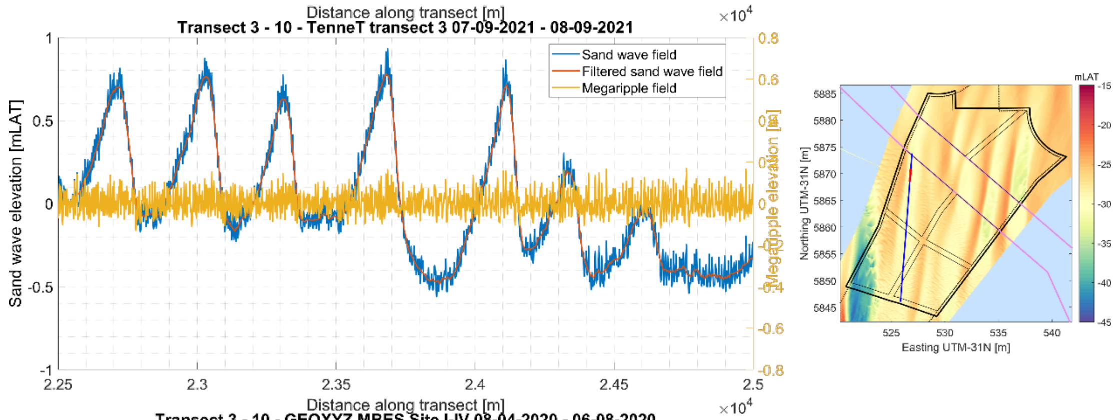
Transect 3 - 10 - TenneT transect 3 07-09-2021 - 08-09-2021
Sand wave field
Filtered sand wave field
Megaripple field
Sand wave elevation [mLAT]
Megaripple elevation [m]
Distance along transect [m]
×10^4
Northing UTM-31N [m]
Easting UTM-31N [m]
mLAT

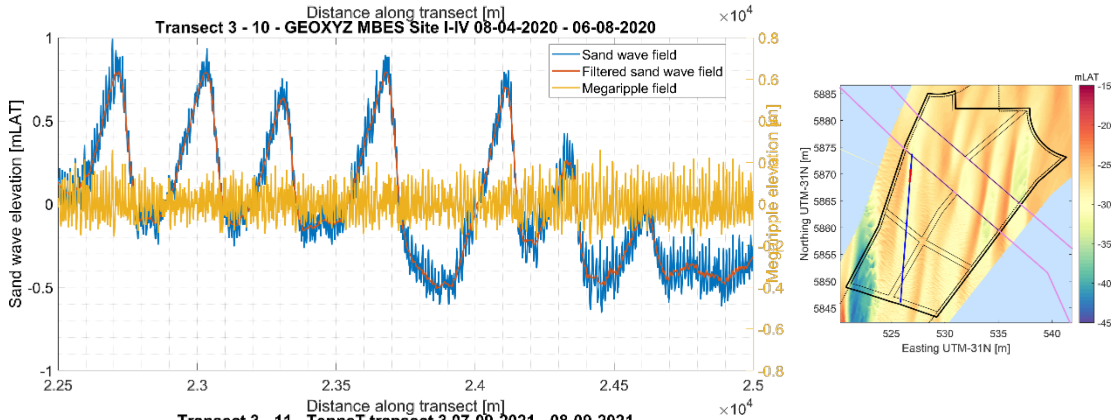
Transect 3 - 10 - GEOXYZ MBES Site I-IV 08-04-2020 - 06-08-2020
Sand wave field
Filtered sand wave field
Megaripple field
Sand wave elevation [mLAT]
Megaripple elevation [m]
Distance along transect [m]
×10^4
Northing UTM-31N [m]
Easting UTM-31N [m]
mLAT

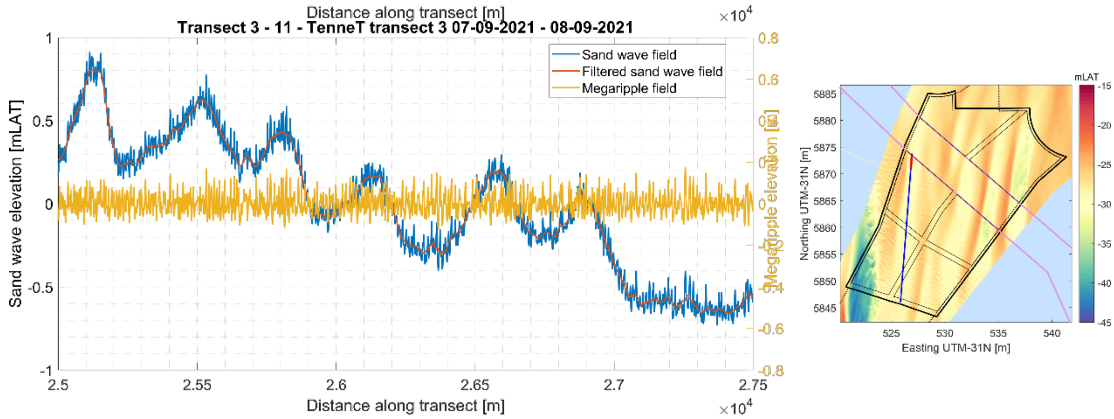
Transect 3 - 11 - TenneT transect 3 07-09-2021 - 08-09-2021
Sand wave field
Filtered sand wave field
Megaripple field
Sand wave elevation [mLAT]
Megaripple elevation [m]
Distance along transect [m]
×10^4
Northing UTM-31N [m]
Easting UTM-31N [m]
mLAT

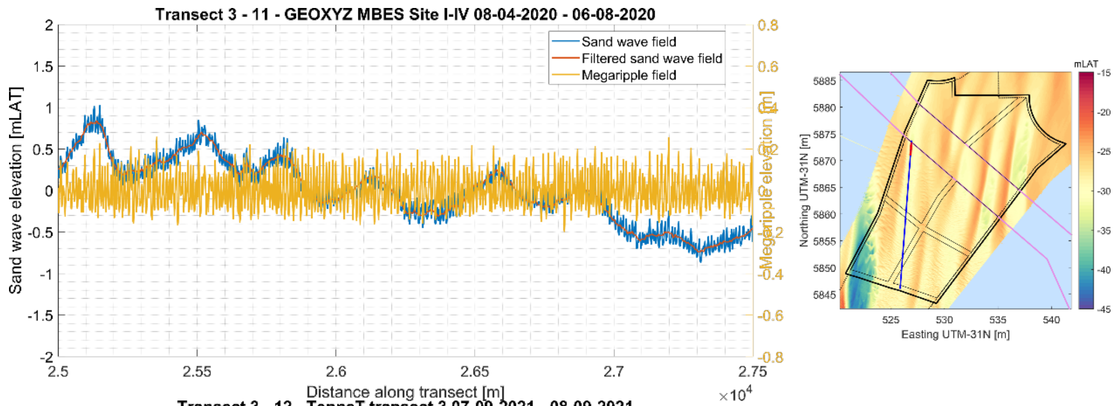
Transect 3 - 11 - GEOXYZ MBES Site I-IV 08-04-2020 - 06-08-2020
Sand wave field
Filtered sand wave field
Megaripple field
Sand wave elevation [mLAT]
Megaripple elevation [m]
Distance along transect [m]
×10^4
Northing UTM-31N [m]
Easting UTM-31N [m]
mLAT

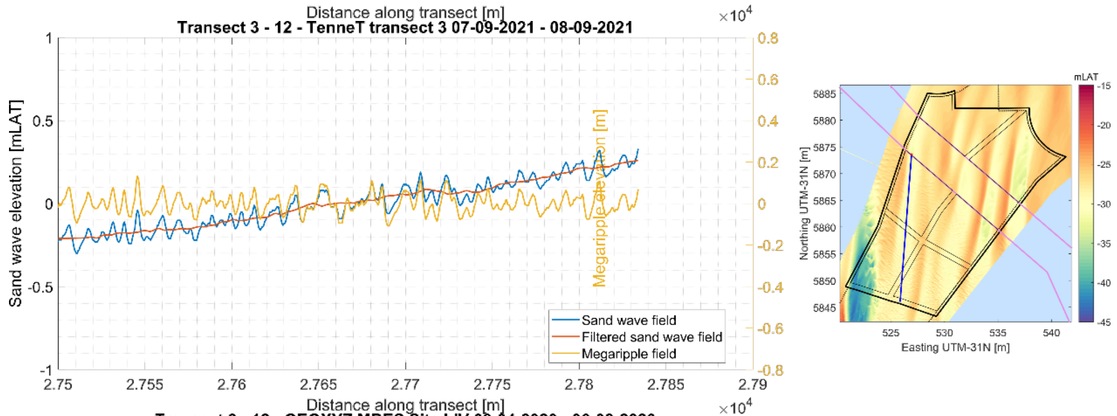
Transect 3 - 12 - TenneT transect 3 07-09-2021 - 08-09-2021
Sand wave field
Filtered sand wave field
Megaripple field
Sand wave elevation [mLAT]
Megaripple elevation [m]
Distance along transect [m]
×10^4
Northing UTM-31N [m]
Easting UTM-31N [m]
mLAT

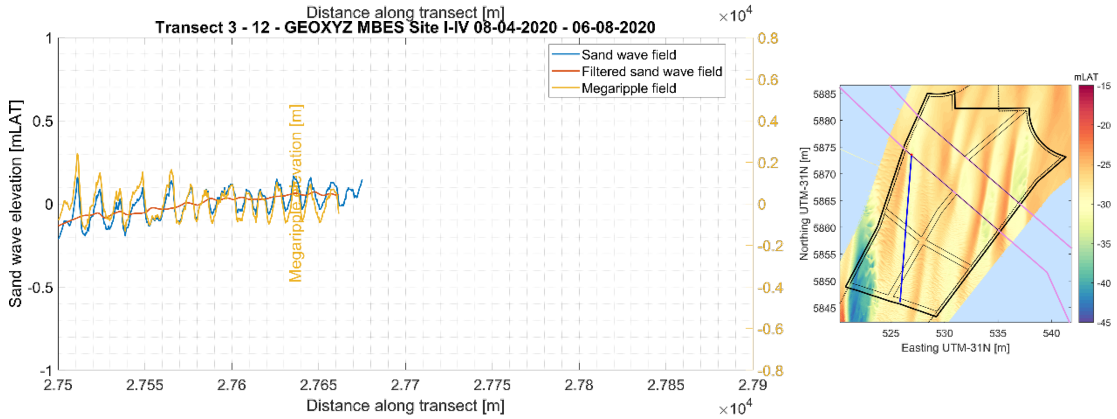
Transect 3 - 12 - GEOXYZ MBES Site I-IV 08-04-2020 - 06-08-2020
Sand wave field
Filtered sand wave field
Megaripple field
Sand wave elevation [mLAT]
Megaripple elevation [m]
Distance along transect [m]
×10^4
Northing UTM-31N [m]
Easting UTM-31N [m]
mLAT

E.2.2.4. Transect 4

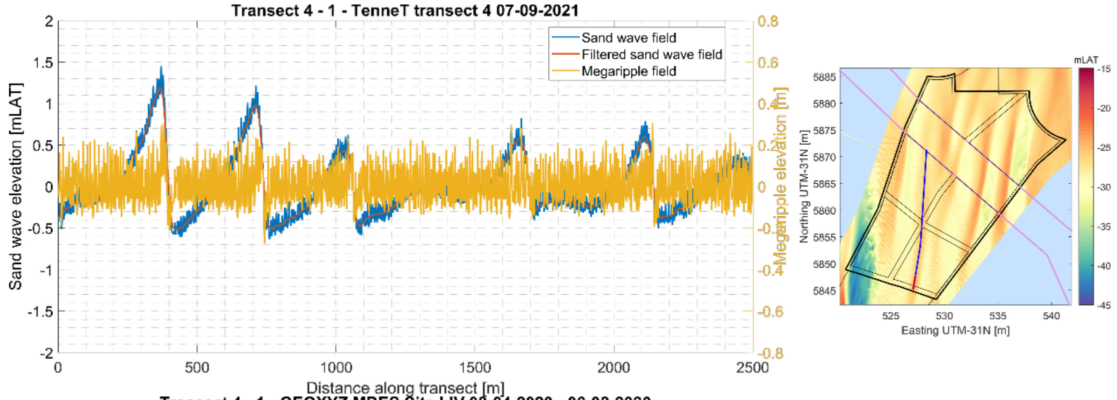

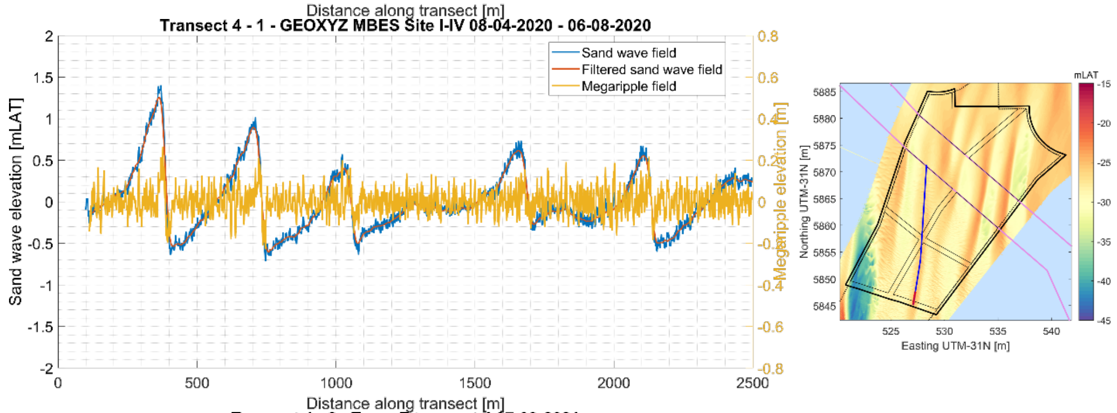

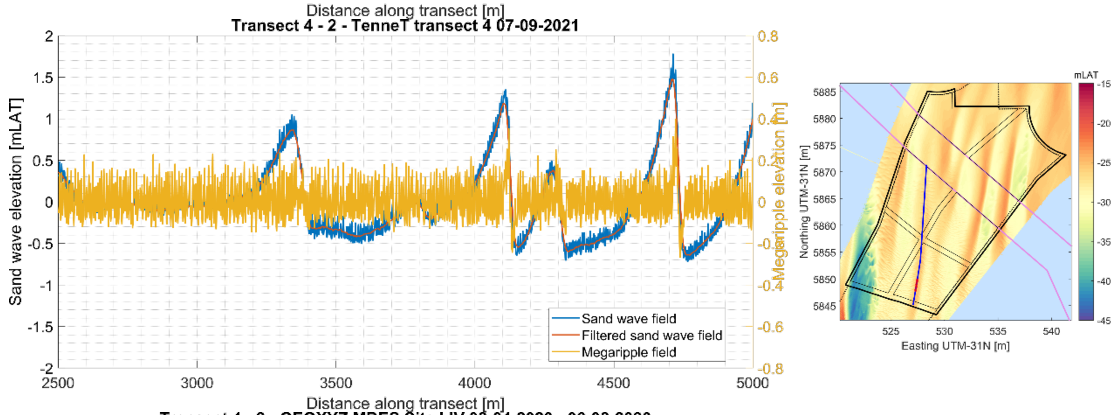

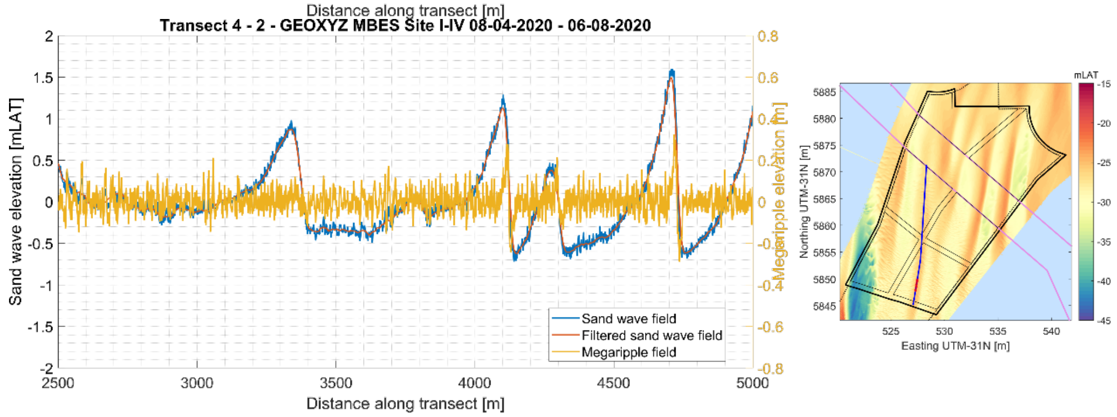

Deltares

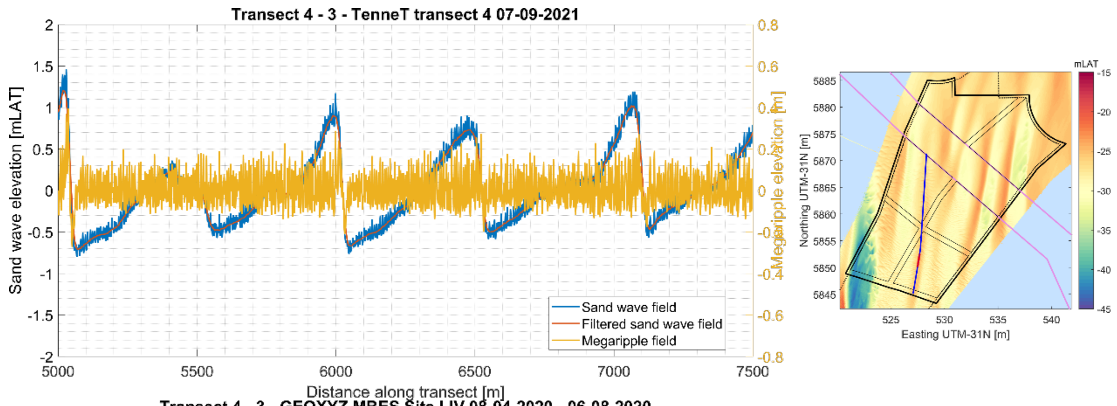
Transect 4 - 3 - TenneT transect 4 07-09-2021
Sand wave elevation [mLAT]
Megaripple elevation [m]
Distance along transect [m]
Sand wave field
Filtered sand wave field
Megaripple field
Northing UTM-31N [m]
Easting UTM-31N [m]
mLAT

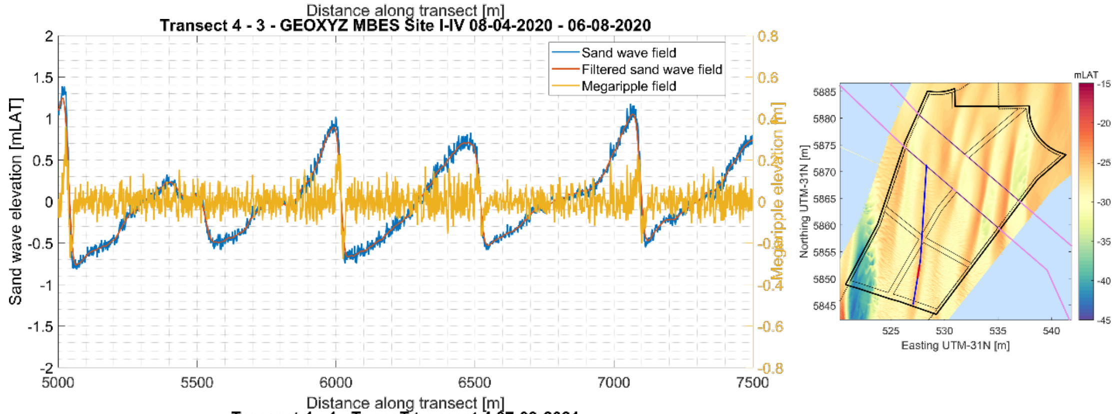
Transect 4 - 3 - GEOXYZ MBES Site I-IV 08-04-2020 - 06-08-2020
Sand wave elevation [mLAT]
Megaripple elevation [m]
Distance along transect [m]
Sand wave field
Filtered sand wave field
Megaripple field
Northing UTM-31N [m]
Easting UTM-31N [m]
mLAT

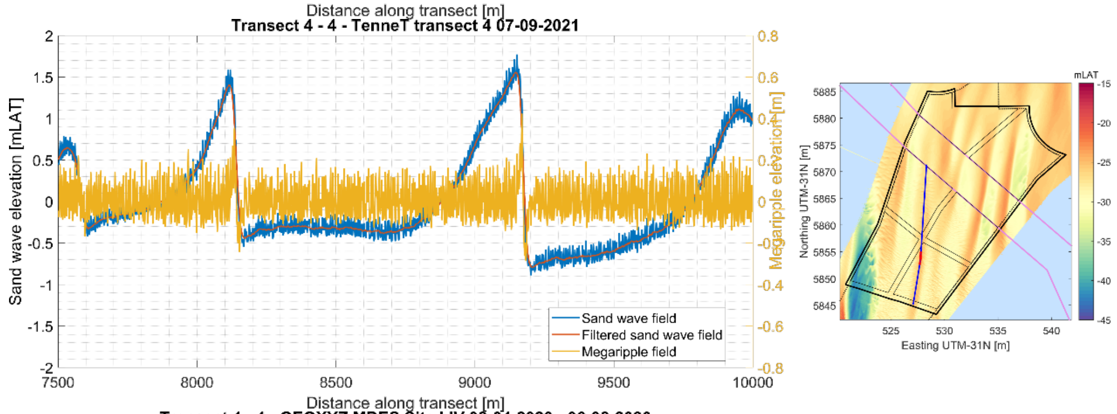
Transect 4 - 4 - TenneT transect 4 07-09-2021
Sand wave elevation [mLAT]
Megaripple elevation [m]
Distance along transect [m]
Sand wave field
Filtered sand wave field
Megaripple field
Northing UTM-31N [m]
Easting UTM-31N [m]
mLAT

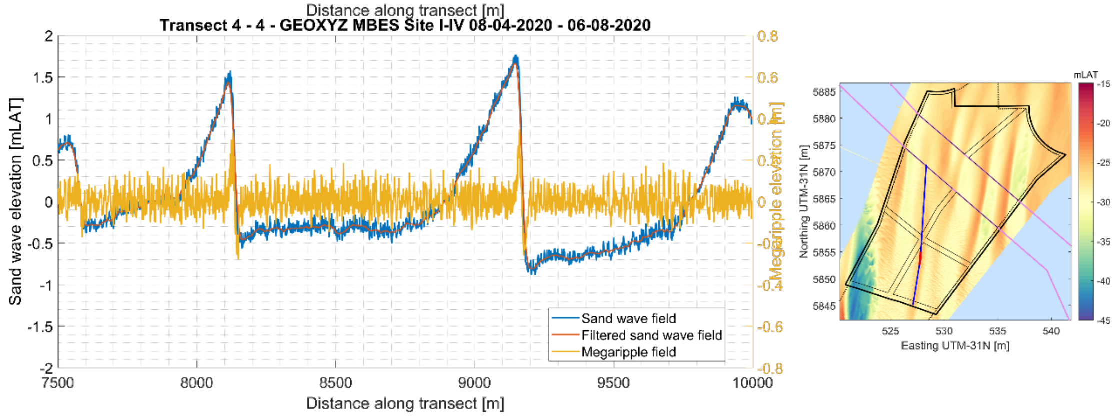
Transect 4 - 4 - GEOXYZ MBES Site I-IV 08-04-2020 - 06-08-2020
Sand wave elevation [mLAT]
Megaripple elevation [m]
Distance along transect [m]
Sand wave field
Filtered sand wave field
Megaripple field
Northing UTM-31N [m]
Easting UTM-31N [m]
mLAT

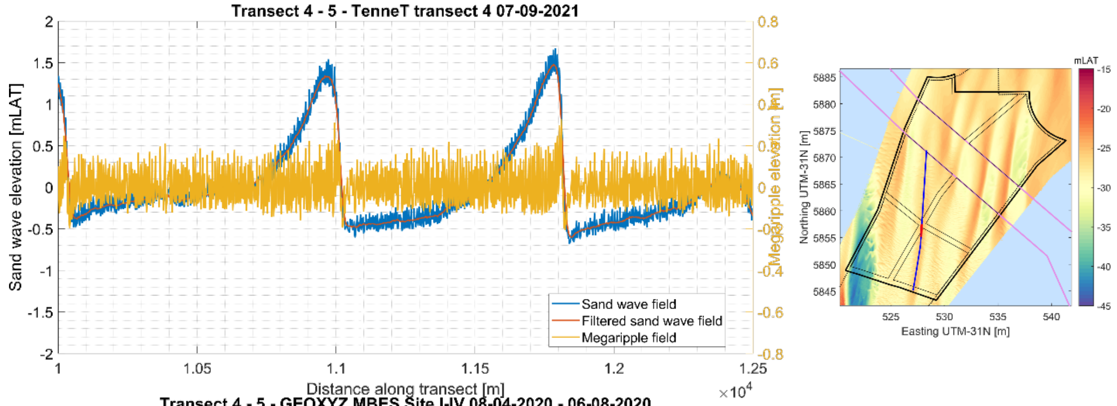
Transect 4 - 5 - TenneT transect 4 07-09-2021
Sand wave elevation [mLAT]
Megaripple elevation [m]
Distance along transect [m]
×10^4
Sand wave field
Filtered sand wave field
Megaripple field
Northing UTM-31N [m]
Easting UTM-31N [m]
mLAT

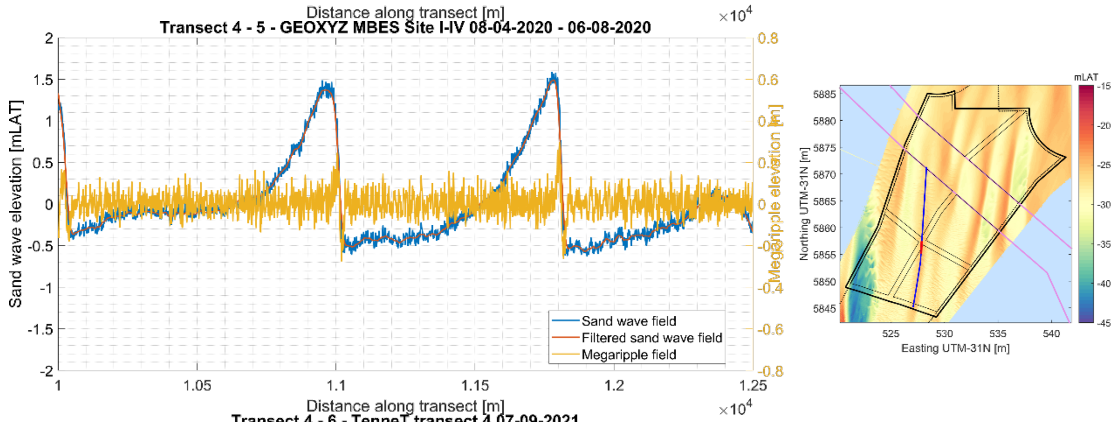
Transect 4 - 5 - GEOXYZ MBES Site I-IV 08-04-2020 - 06-08-2020
Sand wave elevation [mLAT]
Megaripple elevation [m]
Distance along transect [m]
×10^4
Sand wave field
Filtered sand wave field
Megaripple field
Northing UTM-31N [m]
Easting UTM-31N [m]
mLAT

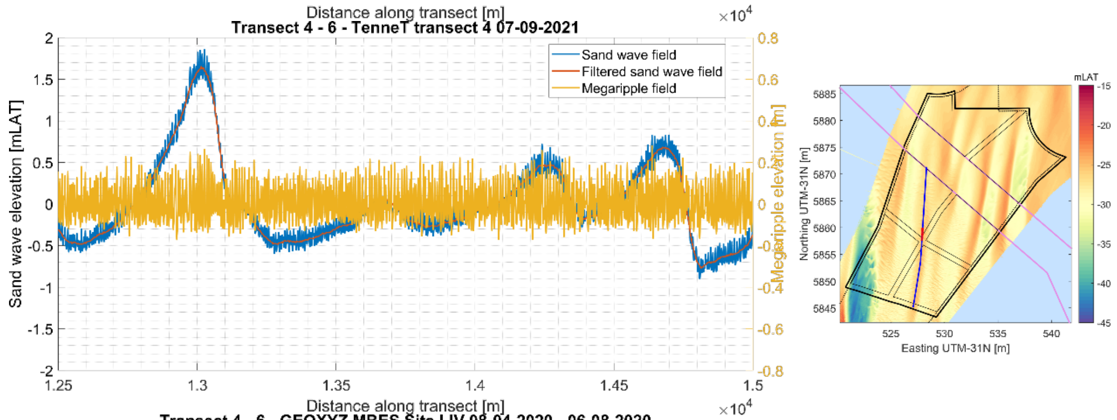
Transect 4 - 6 - TenneT transect 4 07-09-2021
Sand wave elevation [mLAT]
Megaripple elevation [m]
Distance along transect [m]
×10^4
Sand wave field
Filtered sand wave field
Megaripple field
Northing UTM-31N [m]
Easting UTM-31N [m]
mLAT

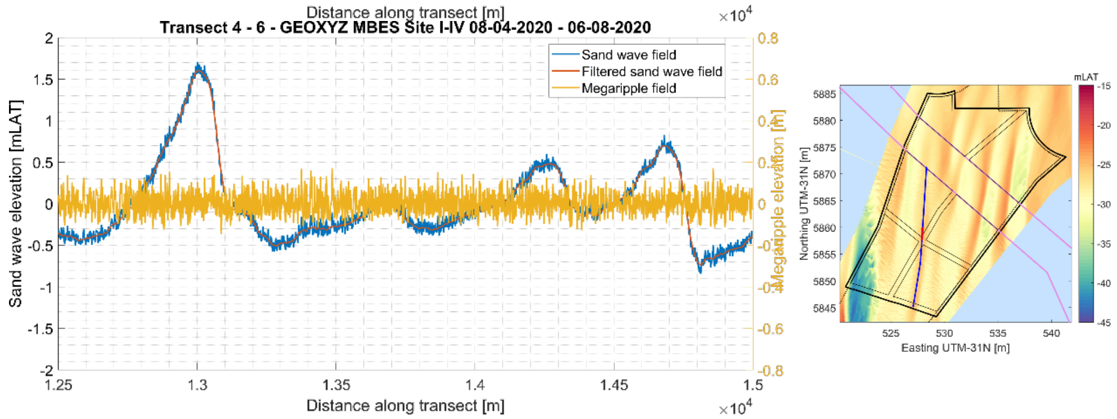
Transect 4 - 6 - GEOXYZ MBES Site I-IV 08-04-2020 - 06-08-2020
Sand wave elevation [mLAT]
Megaripple elevation [m]
Distance along transect [m]
×10^4
Sand wave field
Filtered sand wave field
Megaripple field
Northing UTM-31N [m]
Easting UTM-31N [m]
mLAT

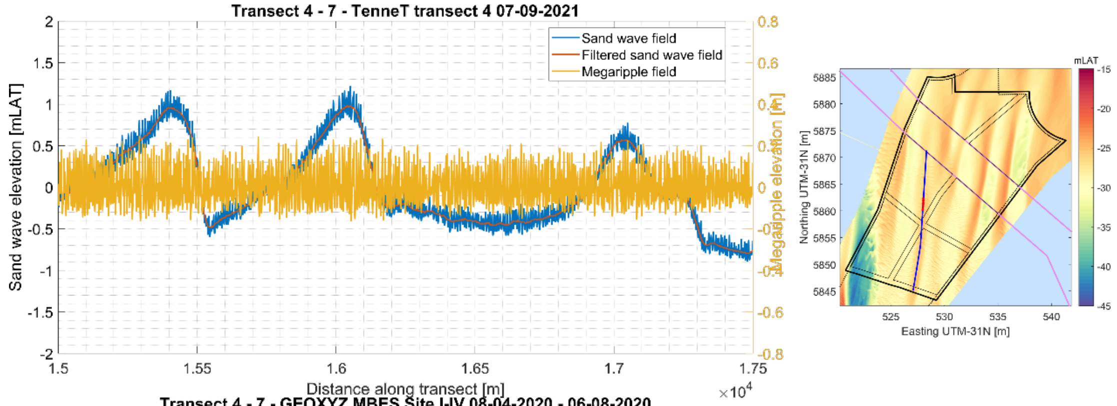
Transect 4 - 7 - TenneT transect 4 07-09-2021
Sand wave field
Filtered sand wave field
Megaripple field
Sand wave elevation [mLAT]
Megaripple elevation [m]
Distance along transect [m]
Northing UTM-31N [m]
Easting UTM-31N [m]
mLAT

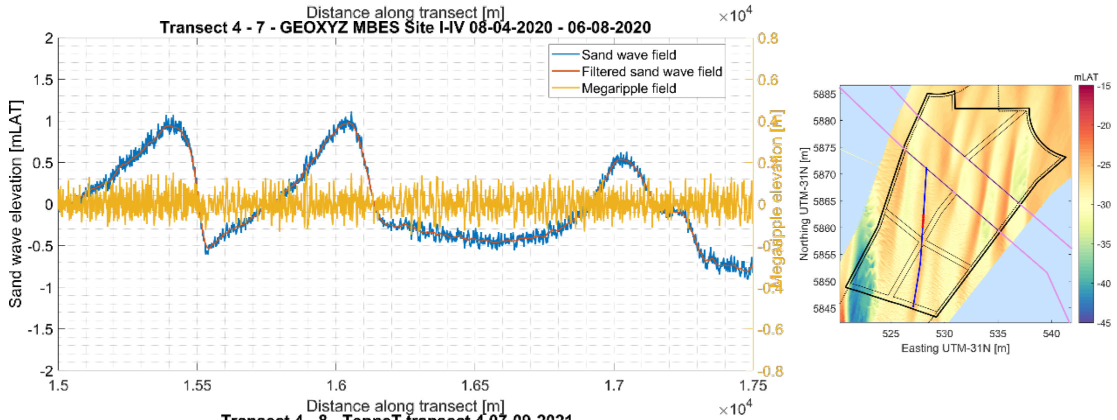
Transect 4 - 7 - GEOXYZ MBES Site I-IV 08-04-2020 - 06-08-2020
Sand wave field
Filtered sand wave field
Megaripple field
Sand wave elevation [mLAT]
Megaripple elevation [m]
Distance along transect [m]
Northing UTM-31N [m]
Easting UTM-31N [m]
mLAT

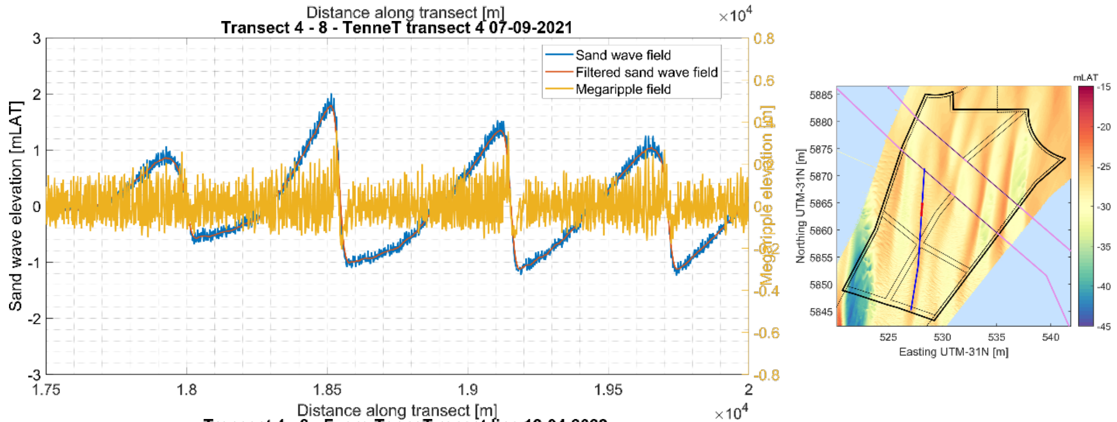
Transect 4 - 8 - TenneT transect 4 07-09-2021
Sand wave field
Filtered sand wave field
Megaripple field
Sand wave elevation [mLAT]
Megaripple elevation [m]
Distance along transect [m]
Northing UTM-31N [m]
Easting UTM-31N [m]
mLAT

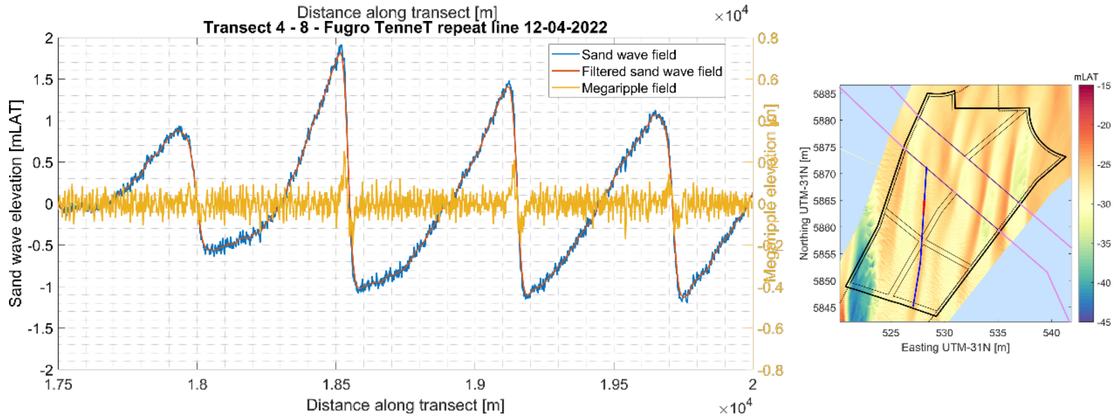
Transect 4 - 8 - Fugro TenneT repeat line 12-04-2022
Sand wave field
Filtered sand wave field
Megaripple field
Sand wave elevation [mLAT]
Megaripple elevation [m]
Distance along transect [m]
Northing UTM-31N [m]
Easting UTM-31N [m]
mLAT

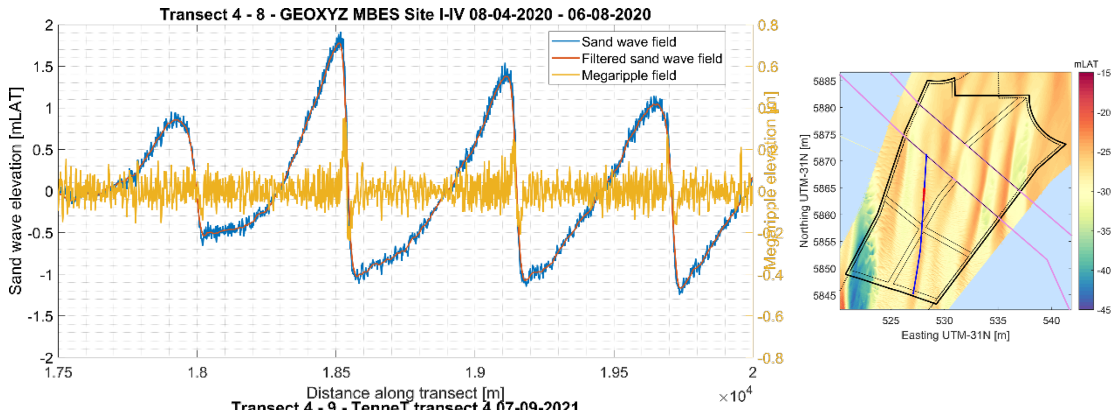
Transect 4 - 8 - GEOXYZ MBES Site I-IV 08-04-2020 - 06-08-2020
Sand wave field
Filtered sand wave field
Megaripple field
Sand wave elevation [mLAT]
Megaripple elevation [m]
Distance along transect [m]
×10^4
Northing UTM-31N [m]
Easting UTM-31N [m]
mLAT

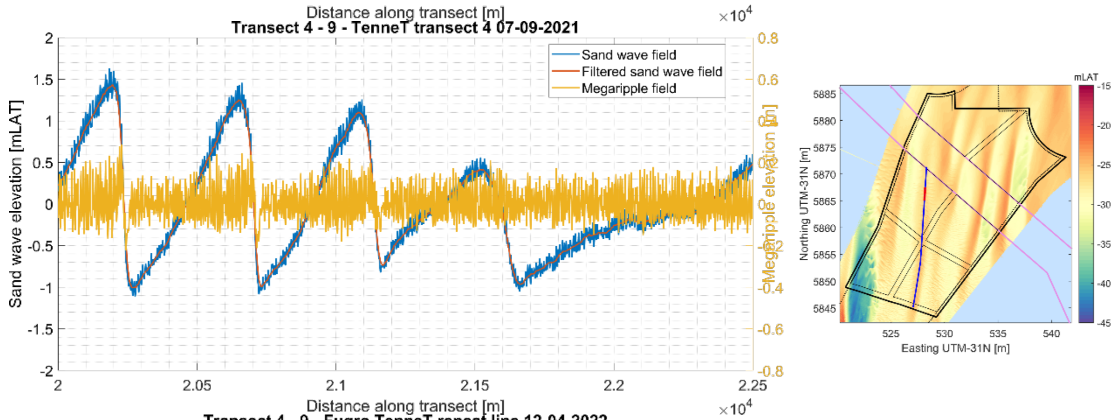
Transect 4 - 9 - TenneT transect 4 07-09-2021
Sand wave field
Filtered sand wave field
Megaripple field
Sand wave elevation [mLAT]
Megaripple elevation [m]
Distance along transect [m]
×10^4
Northing UTM-31N [m]
Easting UTM-31N [m]
mLAT

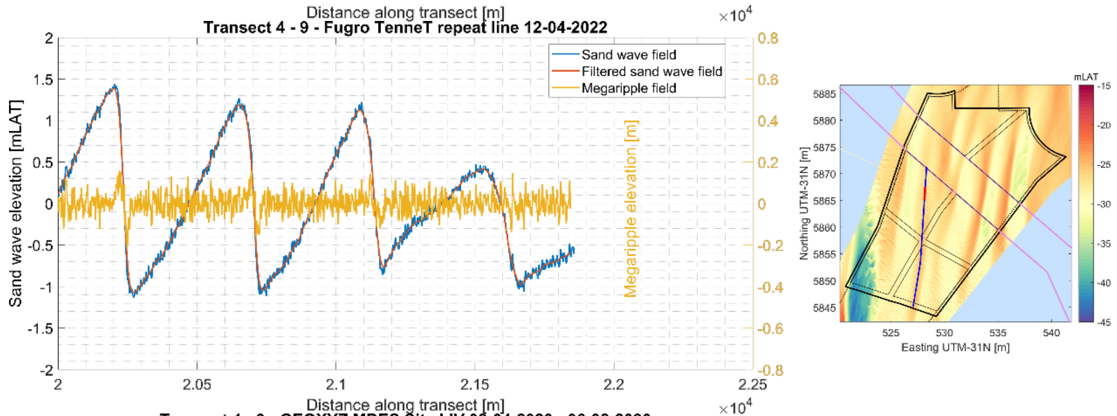
Transect 4 - 9 - Fugro TenneT repeat line 12-04-2022
Sand wave field
Filtered sand wave field
Megaripple field
Sand wave elevation [mLAT]
Megaripple elevation [m]
Distance along transect [m]
×10^4
Northing UTM-31N [m]
Easting UTM-31N [m]
mLAT

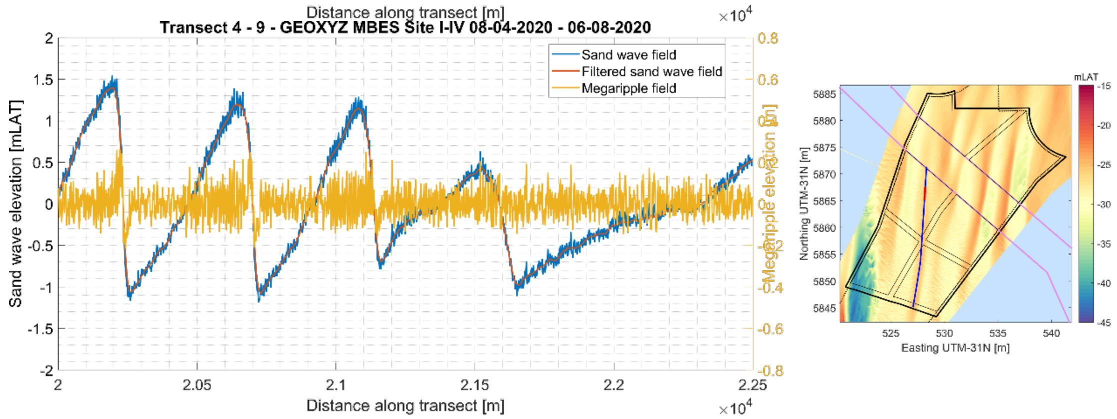
Transect 4 - 9 - GEOXYZ MBES Site I-IV 08-04-2020 - 06-08-2020
Sand wave field
Filtered sand wave field
Megaripple field
Sand wave elevation [mLAT]
Megaripple elevation [m]
Distance along transect [m]
×10^4
Northing UTM-31N [m]
Easting UTM-31N [m]
mLAT

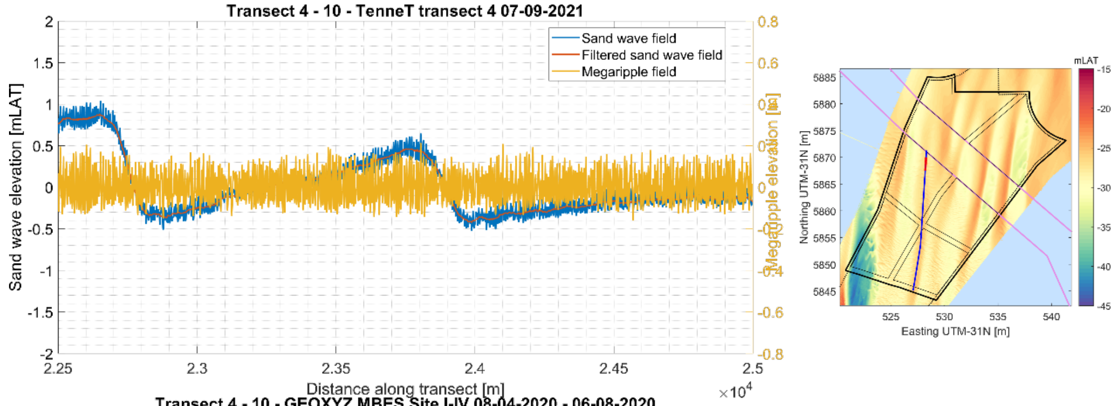
Transect 4 - 10 - TenneT transect 4 07-09-2021
Sand wave field
Filtered sand wave field
Megaripple field
Sand wave elevation [mLAT]
Megaripple elevation [m]
Distance along transect [m]
×10^4
Northing UTM-31N [m]
Easting UTM-31N [m]
mLAT

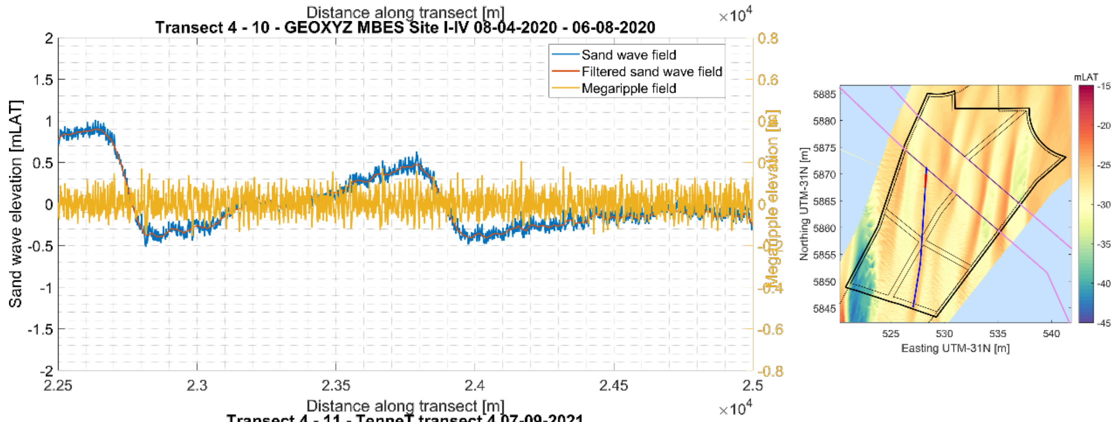
Transect 4 - 10 - GEOXYZ MBES Site I-IV 08-04-2020 - 06-08-2020
Sand wave field
Filtered sand wave field
Megaripple field
Sand wave elevation [mLAT]
Megaripple elevation [m]
Distance along transect [m]
×10^4
Northing UTM-31N [m]
Easting UTM-31N [m]
mLAT

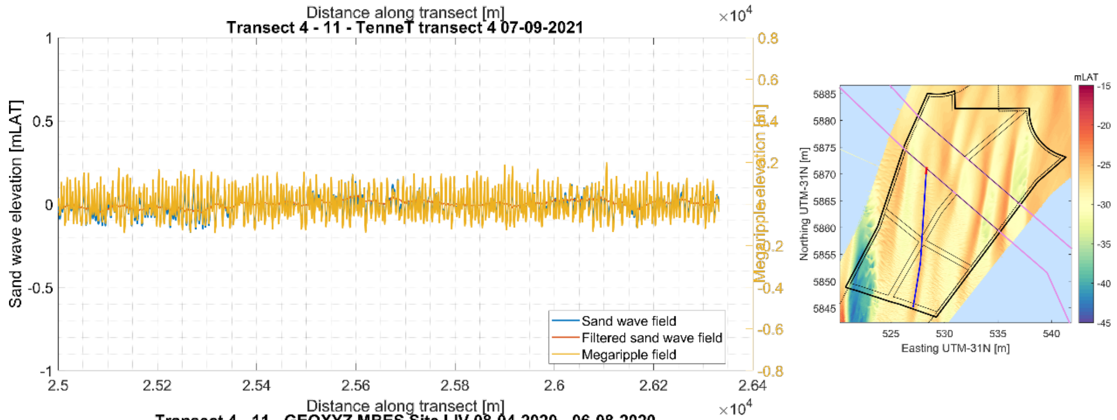
Transect 4 - 11 - TenneT transect 4 07-09-2021
Sand wave field
Filtered sand wave field
Megaripple field
Sand wave elevation [mLAT]
Megaripple elevation [m]
Distance along transect [m]
×10^4
Northing UTM-31N [m]
Easting UTM-31N [m]
mLAT

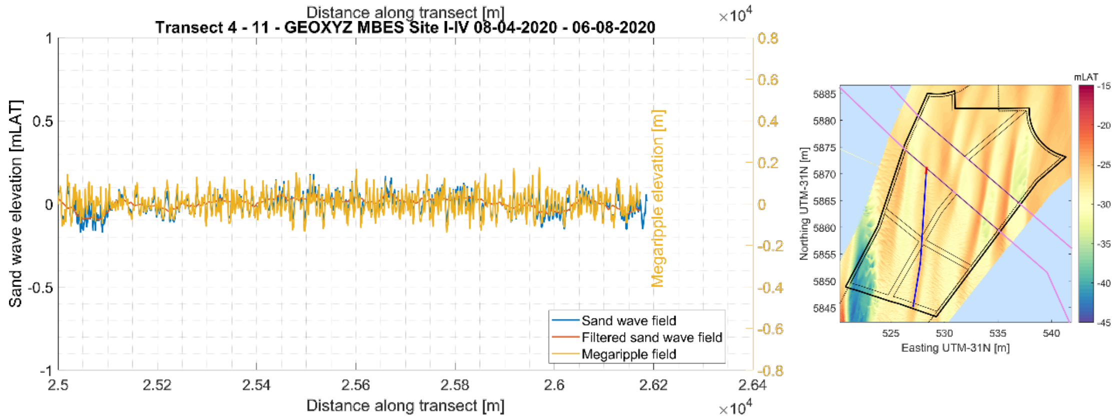
Transect 4 - 11 - GEOXYZ MBES Site I-IV 08-04-2020 - 06-08-2020
Sand wave field
Filtered sand wave field
Megaripple field
Sand wave elevation [mLAT]
Megaripple elevation [m]
Distance along transect [m]
×10^4
Northing UTM-31N [m]
Easting UTM-31N [m]
mLAT

E.2.2.5. Transect 5

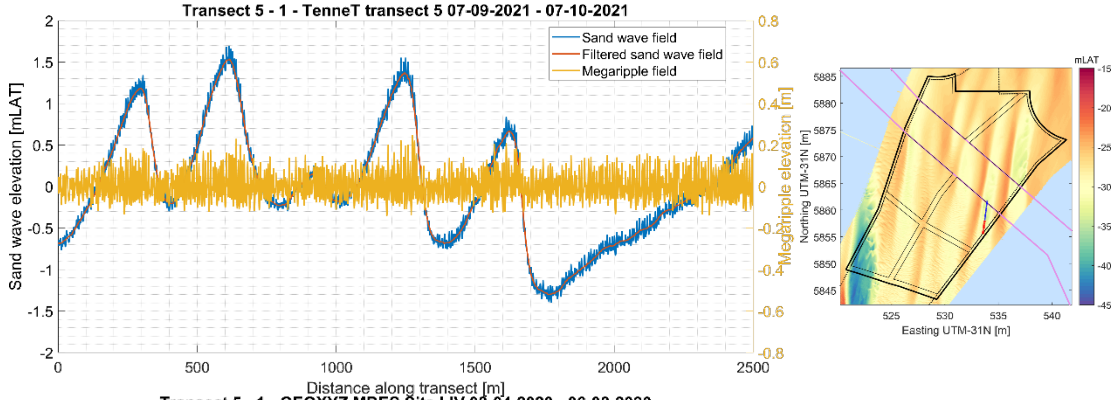

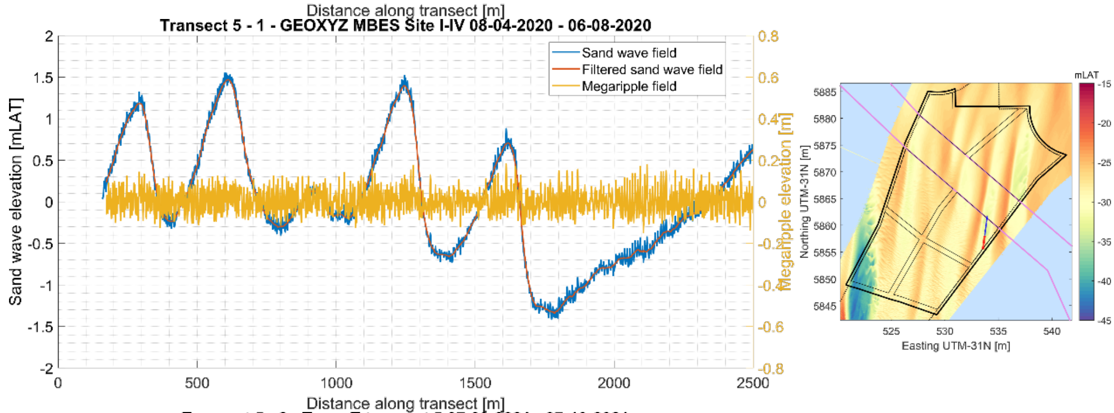

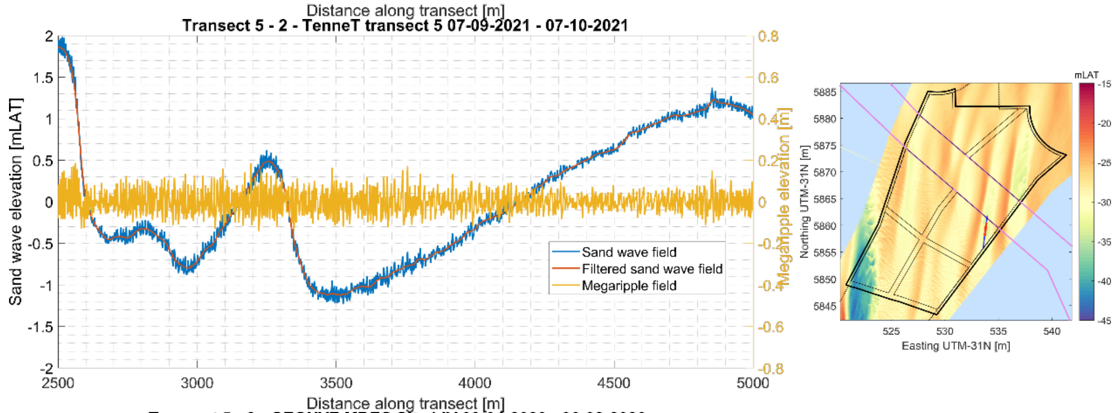

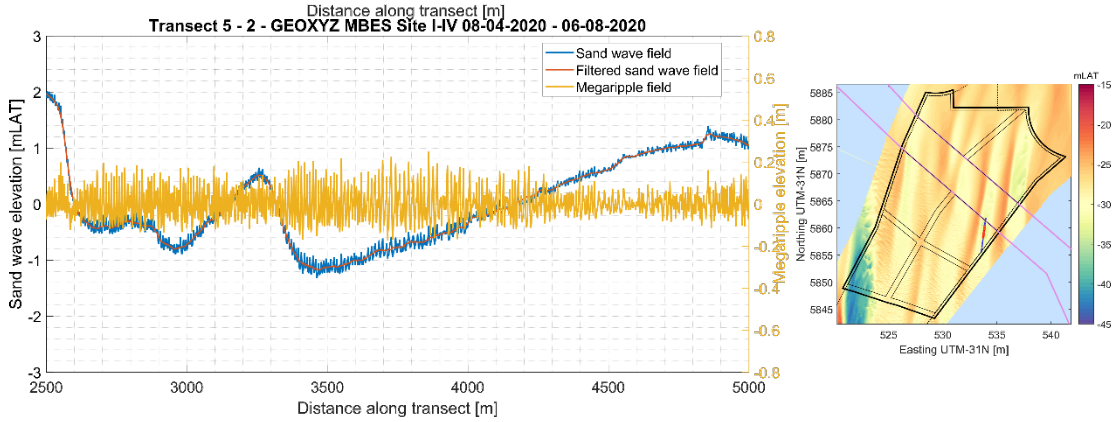

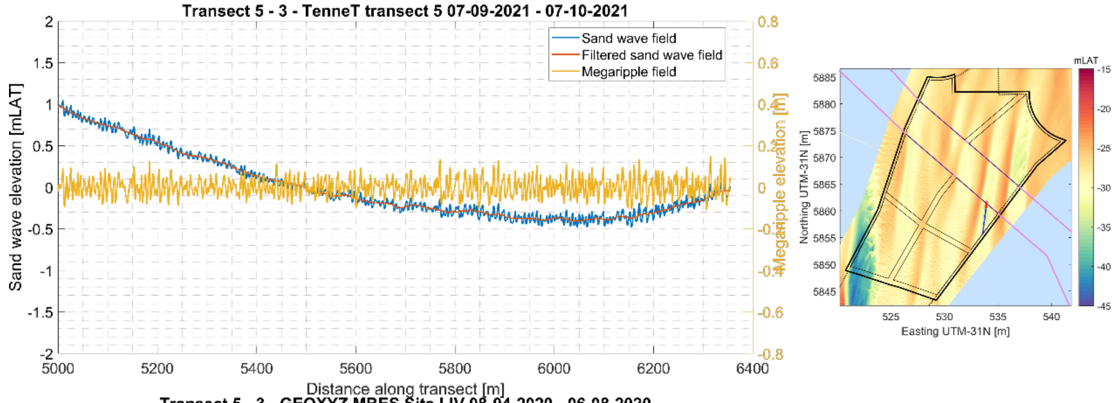

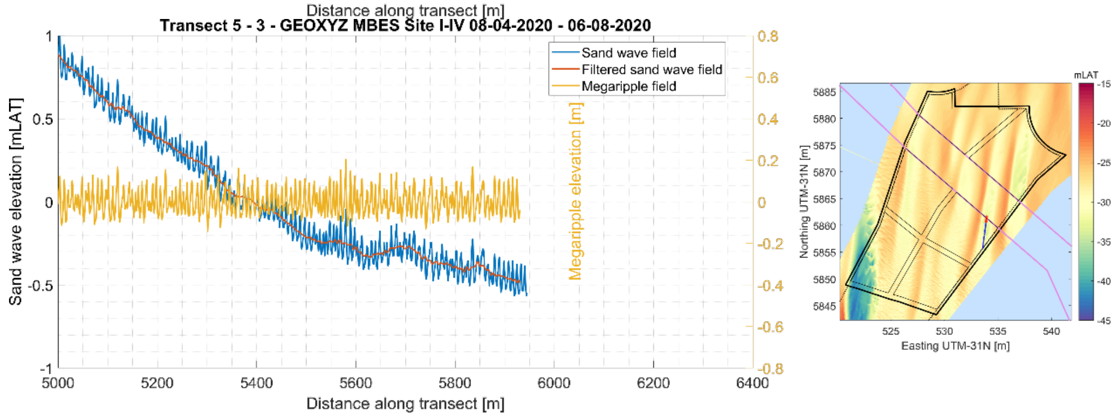

E.2.2.6. Transect 6

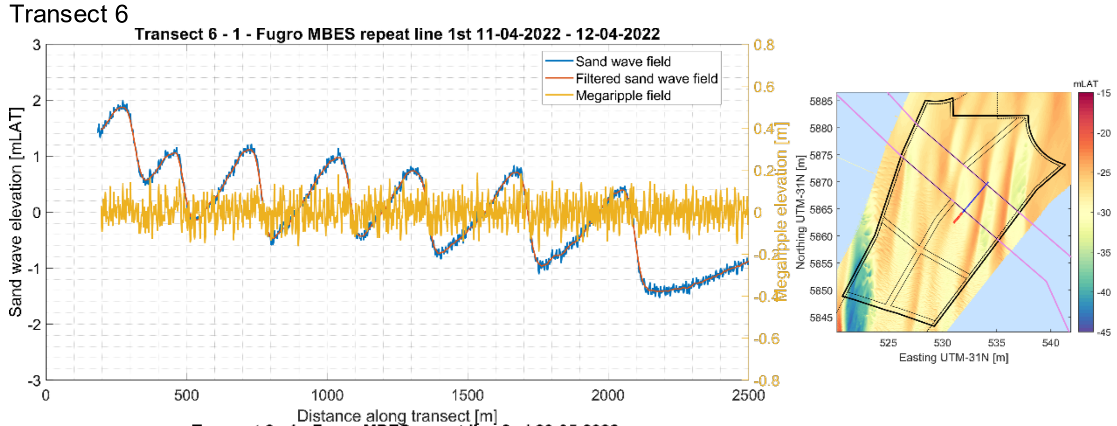

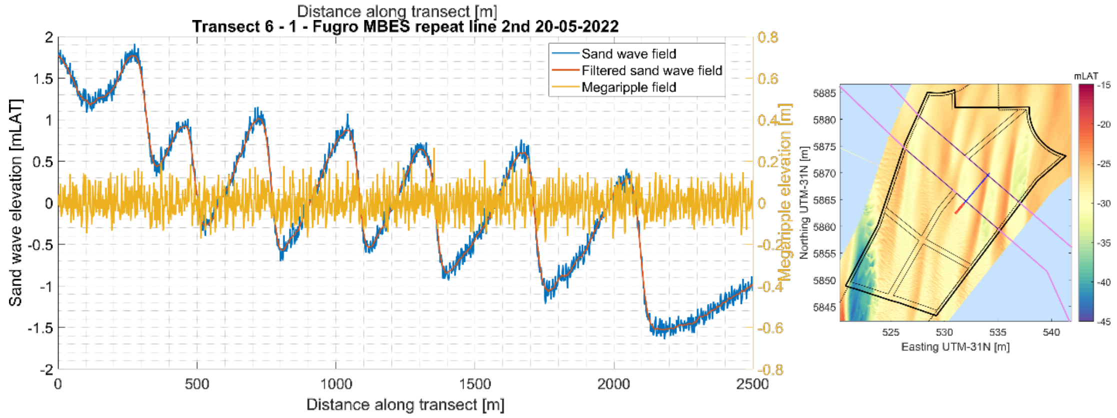

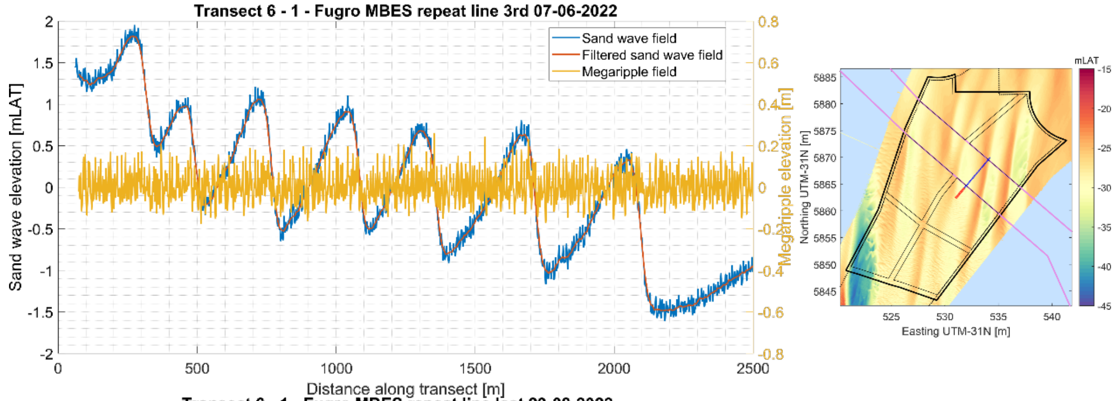
Transect 6 - 1 - Fugro MBES repeat line 3rd 07-06-2022
Sand wave field
Filtered sand wave field
Megaripple field
Sand wave elevation [mLAT]
Megaripple elevation [m]
Distance along transect [m]
Northing UTM-31N [m]
Easting UTM-31N [m]
mLAT

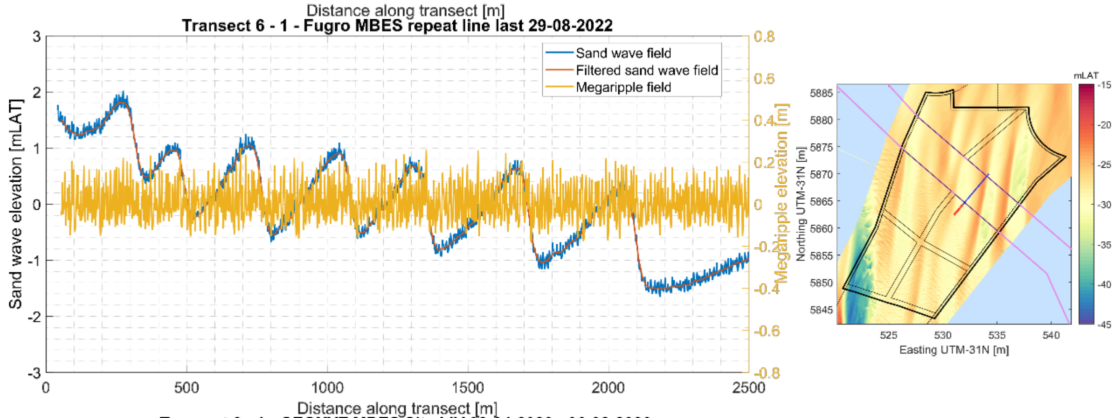
Transect 6 - 1 - Fugro MBES repeat line last 29-08-2022
Sand wave field
Filtered sand wave field
Megaripple field
Sand wave elevation [mLAT]
Megaripple elevation [m]
Distance along transect [m]
Northing UTM-31N [m]
Easting UTM-31N [m]
mLAT

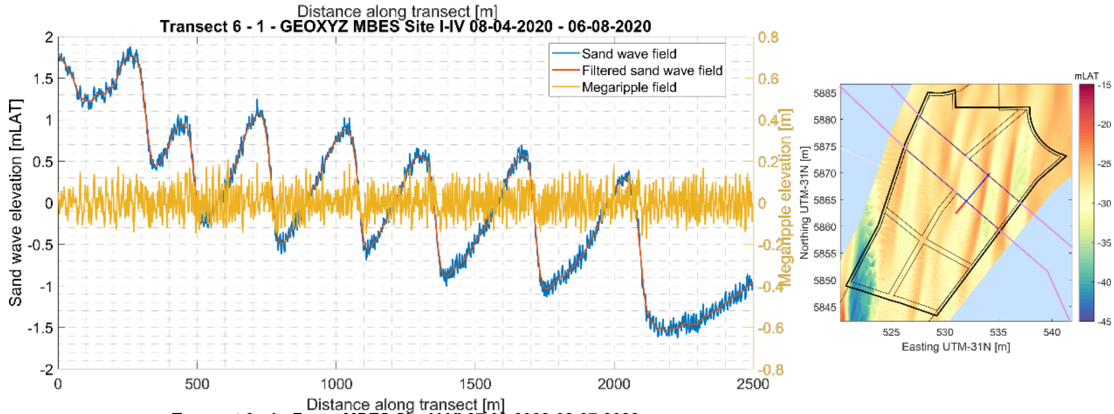
Transect 6 - 1 - GEOXYZ MBES Site I-IV 08-04-2020 - 06-08-2020
Sand wave field
Filtered sand wave field
Megaripple field
Sand wave elevation [mLAT]
Megaripple elevation [m]
Distance along transect [m]
Northing UTM-31N [m]
Easting UTM-31N [m]
mLAT

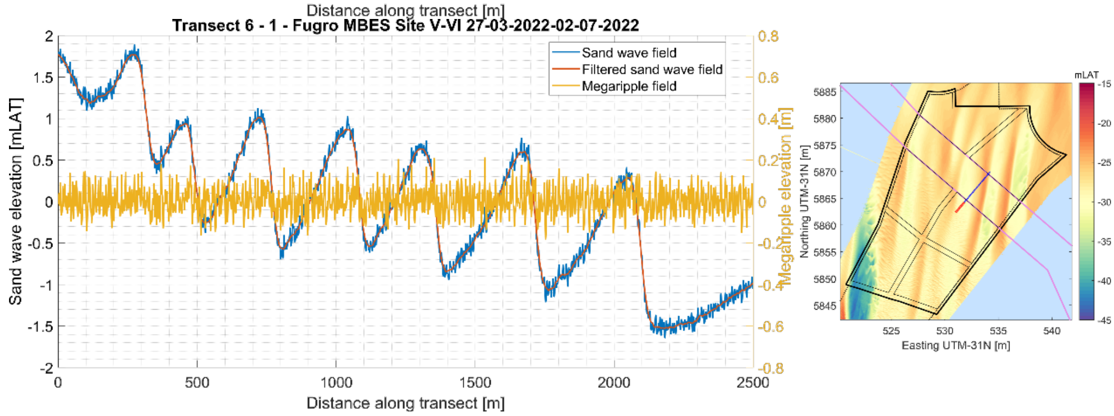
Transect 6 - 1 - Fugro MBES Site V-VI 27-03-2022-02-07-2022
Sand wave field
Filtered sand wave field
Megaripple field
Sand wave elevation [mLAT]
Megaripple elevation [m]
Distance along transect [m]
Northing UTM-31N [m]
Easting UTM-31N [m]
mLAT

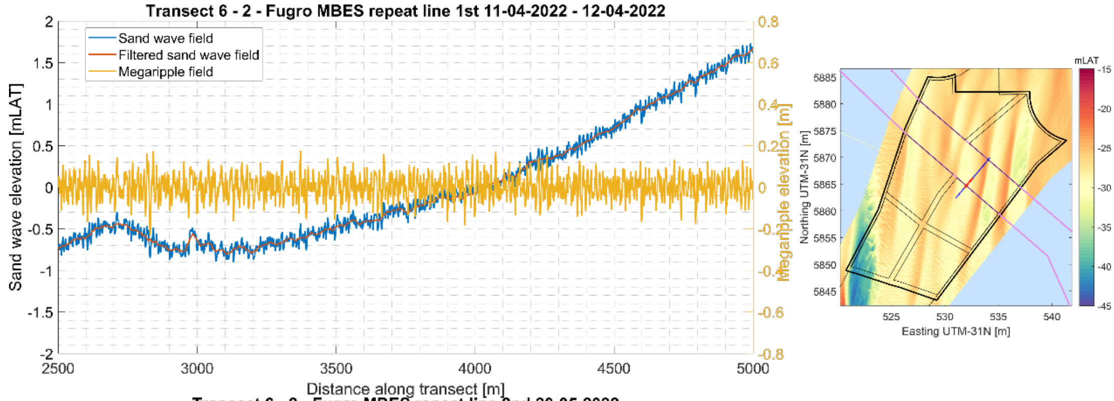
Transect 6 - 2 - Fugro MBES repeat line 1st 11-04-2022 - 12-04-2022
Sand wave field
Filtered sand wave field
Megaripple field
Sand wave elevation [mLAT]
Megaripple elevation [m]
Distance along transect [m]
Northing UTM-31N [m]
Easting UTM-31N [m]
mLAT

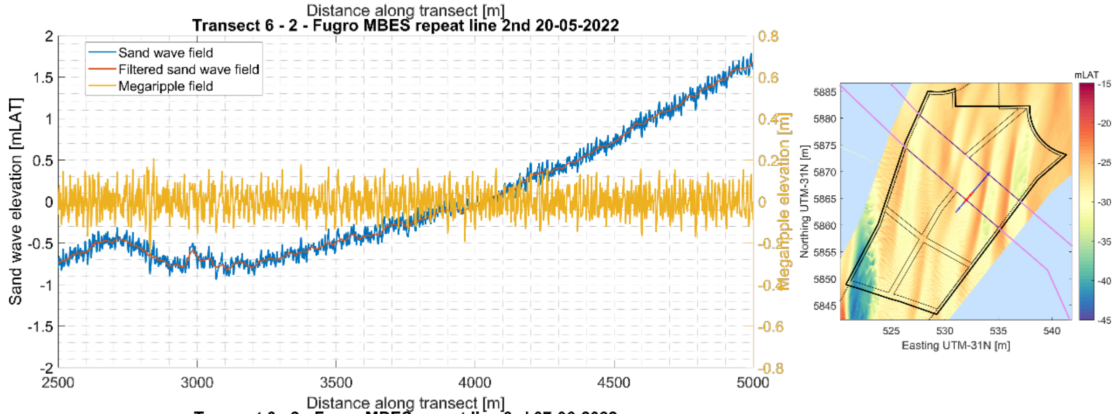
Transect 6 - 2 - Fugro MBES repeat line 2nd 20-05-2022
Sand wave field
Filtered sand wave field
Megaripple field
Sand wave elevation [mLAT]
Megaripple elevation [m]
Distance along transect [m]
Northing UTM-31N [m]
Easting UTM-31N [m]
mLAT

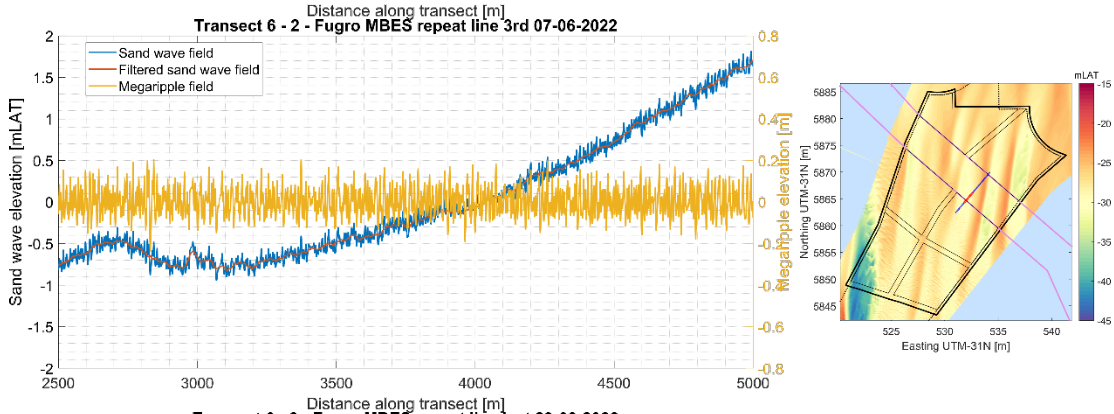
Transect 6 - 2 - Fugro MBES repeat line 3rd 07-06-2022
Sand wave field
Filtered sand wave field
Megaripple field
Sand wave elevation [mLAT]
Megaripple elevation [m]
Distance along transect [m]
Northing UTM-31N [m]
Easting UTM-31N [m]
mLAT

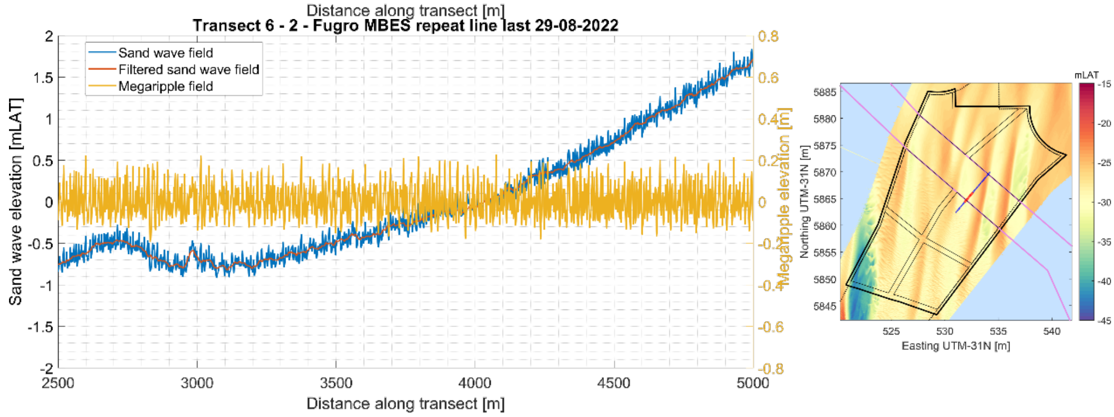
Transect 6 - 2 - Fugro MBES repeat line last 29-08-2022
Sand wave field
Filtered sand wave field
Megaripple field
Sand wave elevation [mLAT]
Megaripple elevation [m]
Distance along transect [m]
Northing UTM-31N [m]
Easting UTM-31N [m]
mLAT

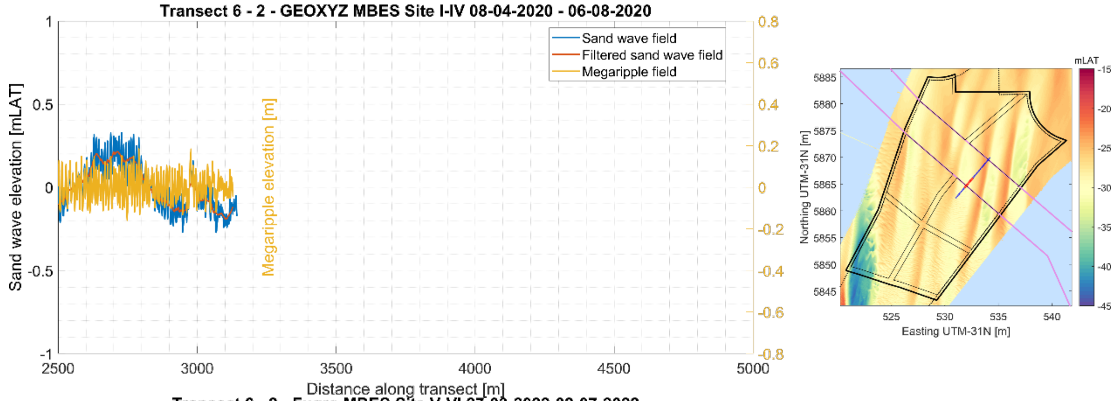
Transect 6 - 2 - GEOXYZ MBES Site I-IV 08-04-2020 - 06-08-2020
Sand wave field
Filtered sand wave field
Megaripple field
Sand wave elevation [mLAT]
Megaripple elevation [m]
Distance along transect [m]
Northing UTM-31N [m]
Easting UTM-31N [m]
mLAT

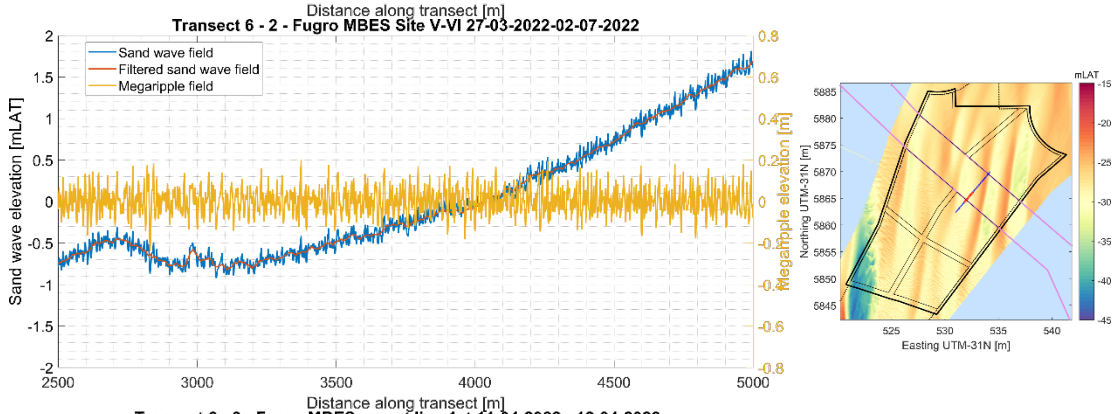
Transect 6 - 2 - Fugro MBES Site V-VI 27-03-2022-02-07-2022
Sand wave field
Filtered sand wave field
Megaripple field
Sand wave elevation [mLAT]
Megaripple elevation [m]
Distance along transect [m]
Northing UTM-31N [m]
Easting UTM-31N [m]
mLAT

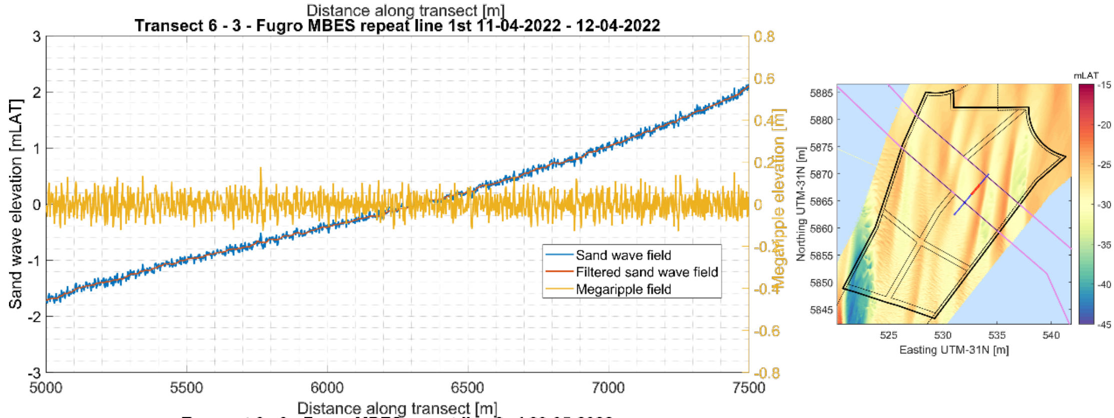
Transect 6 - 3 - Fugro MBES repeat line 1st 11-04-2022 - 12-04-2022
Sand wave field
Filtered sand wave field
Megaripple field
Sand wave elevation [mLAT]
Megaripple elevation [m]
Distance along transect [m]
Northing UTM-31N [m]
Easting UTM-31N [m]
mLAT

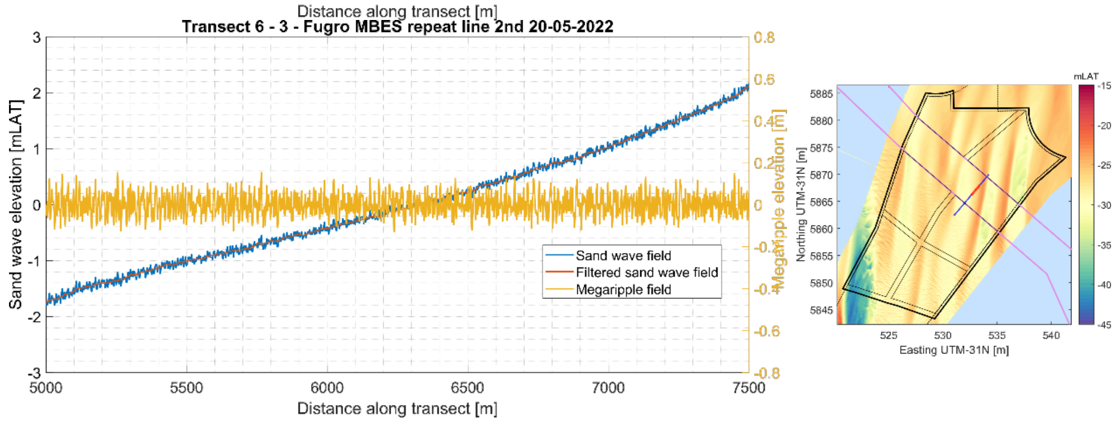
Transect 6 - 3 - Fugro MBES repeat line 2nd 20-05-2022
Sand wave field
Filtered sand wave field
Megaripple field
Sand wave elevation [mLAT]
Megaripple elevation [m]
Distance along transect [m]
Northing UTM-31N [m]
Easting UTM-31N [m]
mLAT

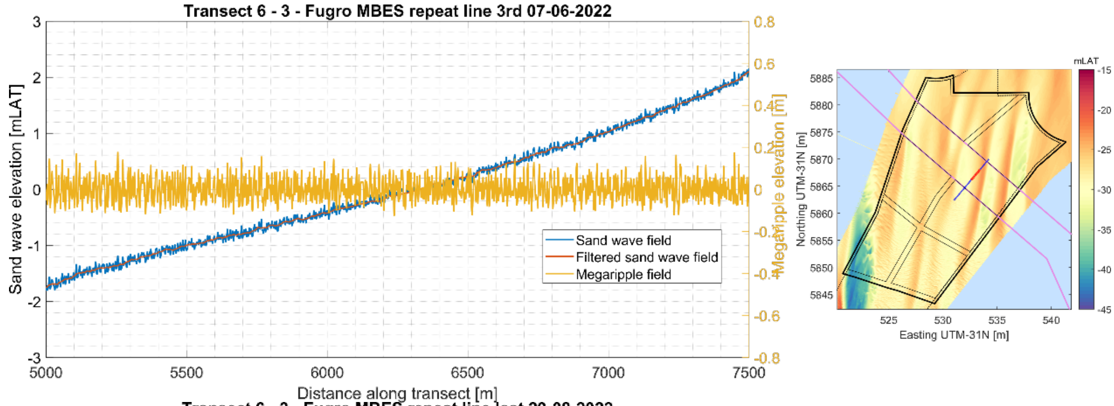
Transect 6 - 3 - Fugro MBES repeat line 3rd 07-06-2022
Sand wave elevation [mLAT]
Megaripple elevation [m]
Distance along transect [m]
Sand wave field
Filtered sand wave field
Megaripple field
Northing UTM-31N [m]
Easting UTM-31N [m]
mLAT

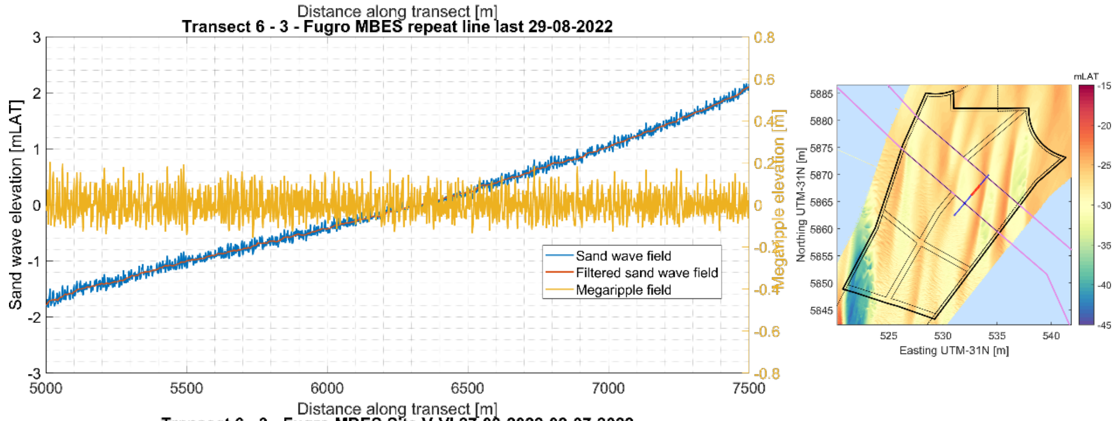
Transect 6 - 3 - Fugro MBES repeat line last 29-08-2022
Sand wave elevation [mLAT]
Megaripple elevation [m]
Distance along transect [m]
Sand wave field
Filtered sand wave field
Megaripple field
Northing UTM-31N [m]
Easting UTM-31N [m]
mLAT

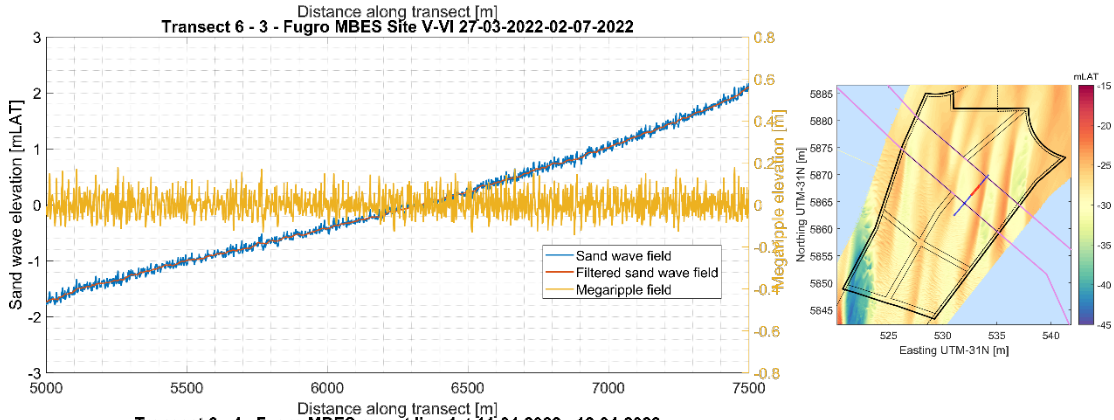
Transect 6 - 3 - Fugro MBES Site V-VI 27-03-2022-02-07-2022
Sand wave elevation [mLAT]
Megaripple elevation [m]
Distance along transect [m]
Sand wave field
Filtered sand wave field
Megaripple field
Northing UTM-31N [m]
Easting UTM-31N [m]
mLAT

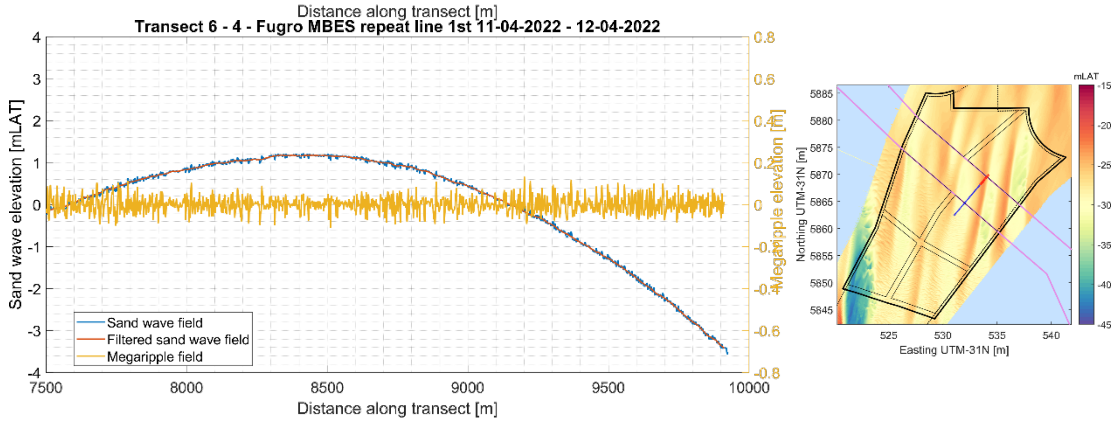
Transect 6 - 4 - Fugro MBES repeat line 1st 11-04-2022 - 12-04-2022
Sand wave elevation [mLAT]
Megaripple elevation [m]
Distance along transect [m]
Sand wave field
Filtered sand wave field
Megaripple field
Northing UTM-31N [m]
Easting UTM-31N [m]
mLAT

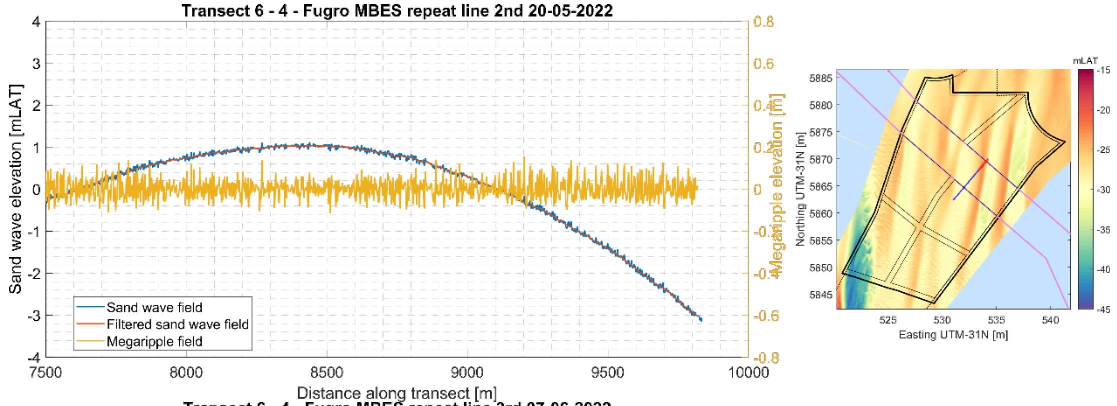
Transcect 6 - 4 - Fugro MBES repeat line 2nd 20-05-2022
Sand wave elevation [mLAT]
Megaripple elevation [m]
Distance along transect [m]
Sand wave field
Filtered sand wave field
Megaripple field
Northing UTM-31N [m]
Easting UTM-31N [m]
mLAT

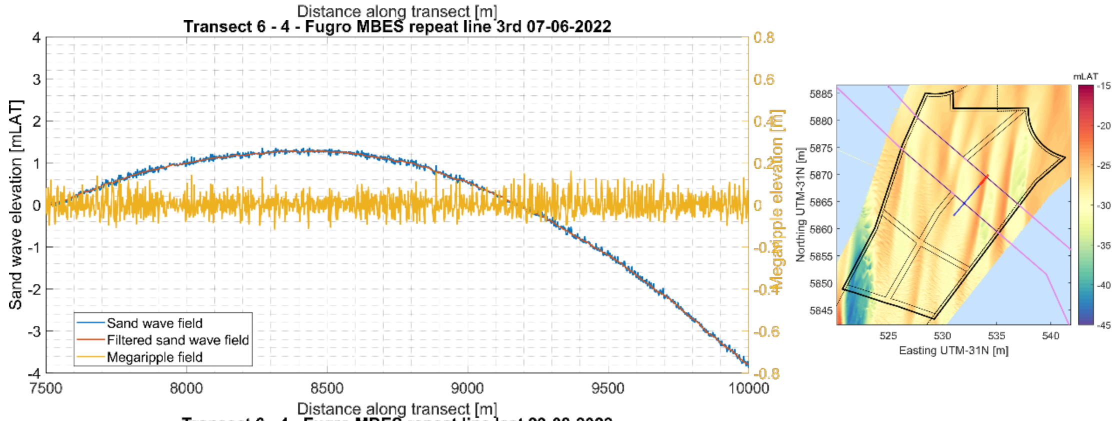
Transect 6 - 4 - Fugro MBES repeat line 3rd 07-06-2022
Sand wave elevation [mLAT]
Megaripple elevation [m]
Distance along transect [m]
Sand wave field
Filtered sand wave field
Megaripple field
Northing UTM-31N [m]
Easting UTM-31N [m]
mLAT

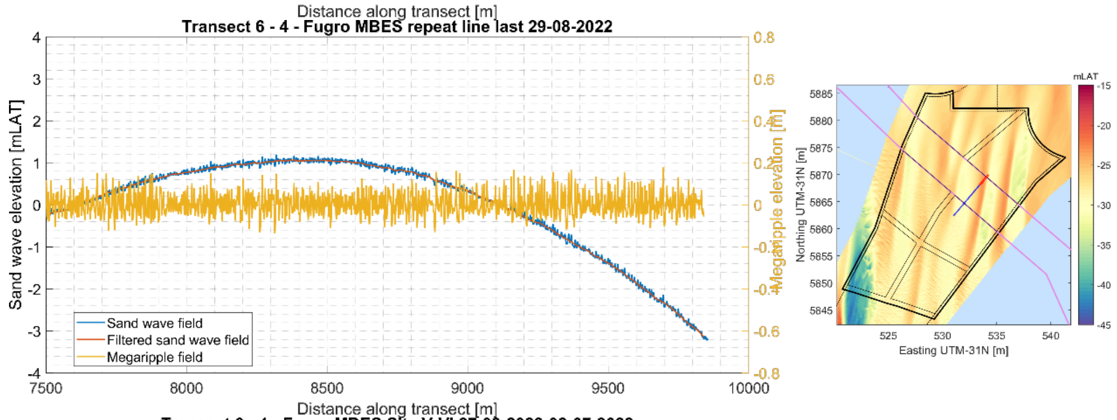
Transect 6 - 4 - Fugro MBES repeat line last 29-08-2022
Sand wave elevation [mLAT]
Megaripple elevation [m]
Distance along transect [m]
Sand wave field
Filtered sand wave field
Megaripple field
Northing UTM-31N [m]
Easting UTM-31N [m]
mLAT

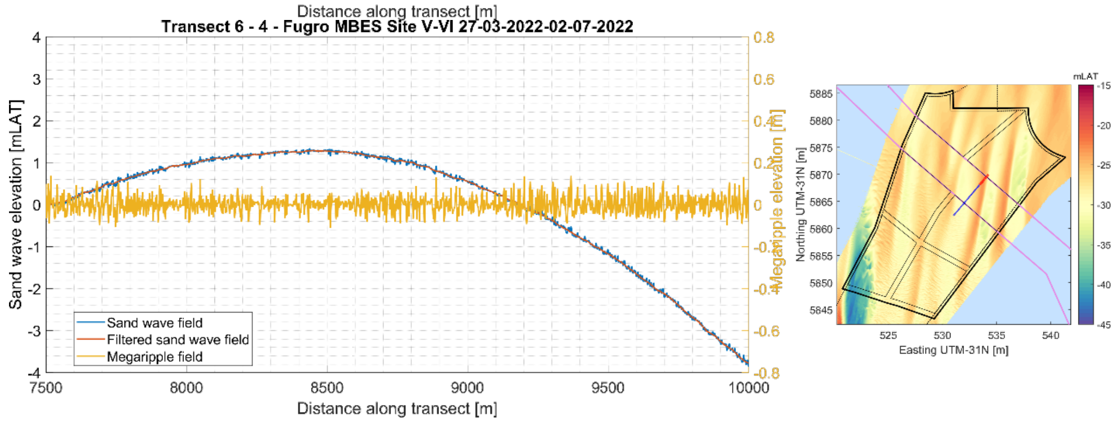
Transect 6 - 4 - Fugro MBES Site V-VI 27-03-2022-02-07-2022
Sand wave elevation [mLAT]
Megaripple elevation [m]
Distance along transect [m]
Sand wave field
Filtered sand wave field
Megaripple field
Northing UTM-31N [m]
Easting UTM-31N [m]
mLAT

E.2.2.7. Transect 7

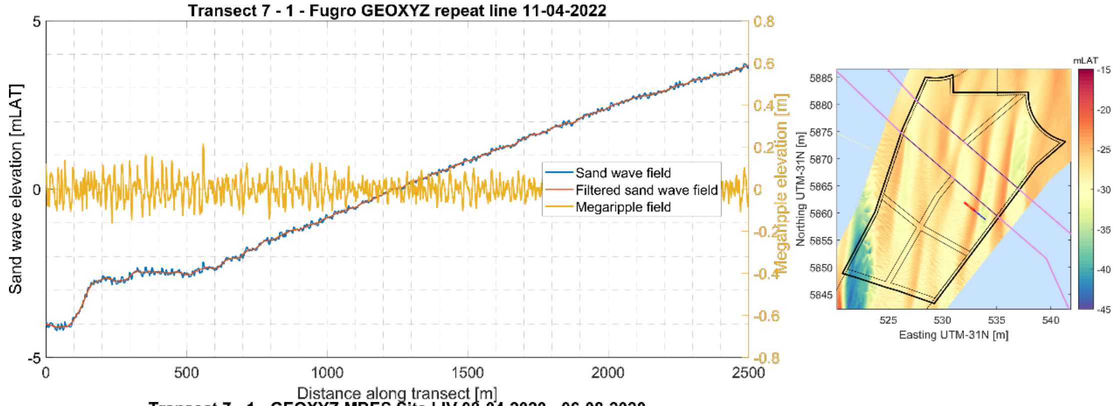

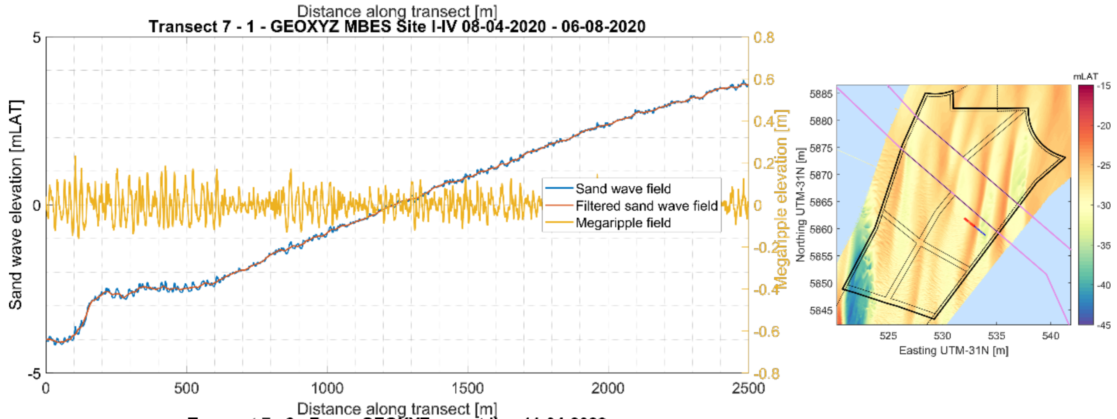

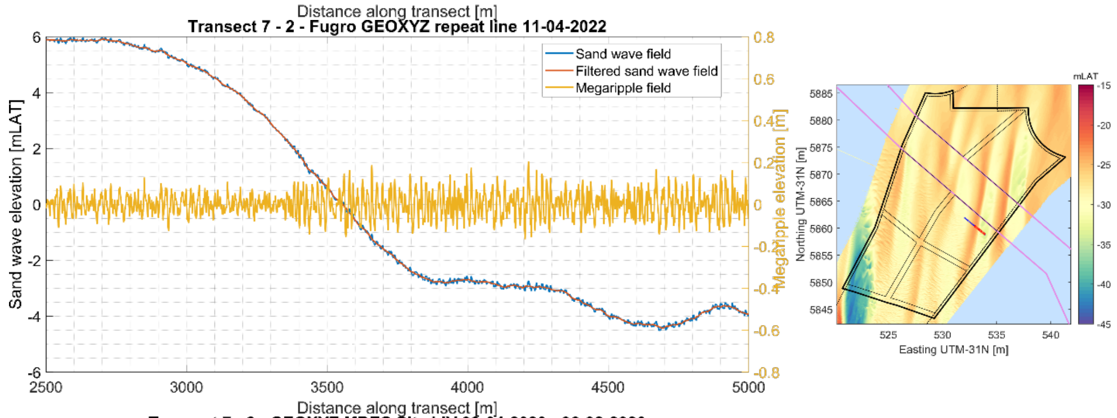

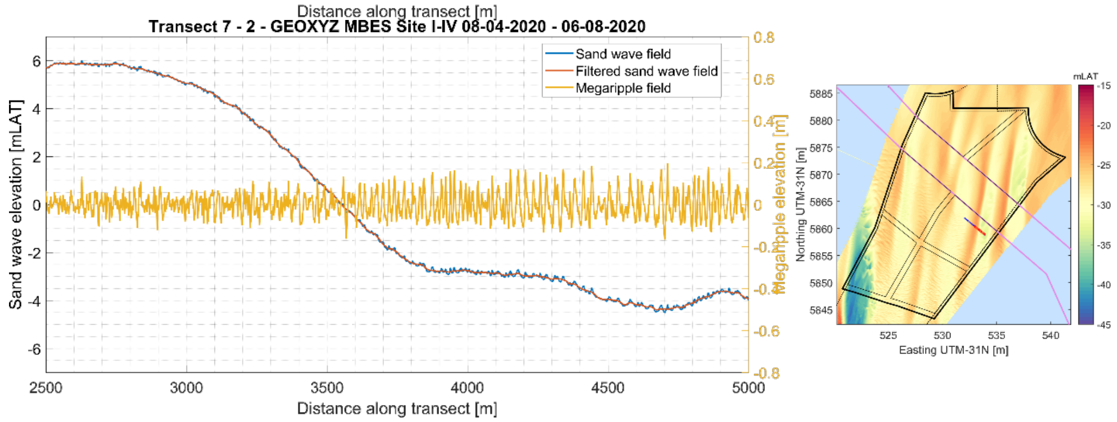

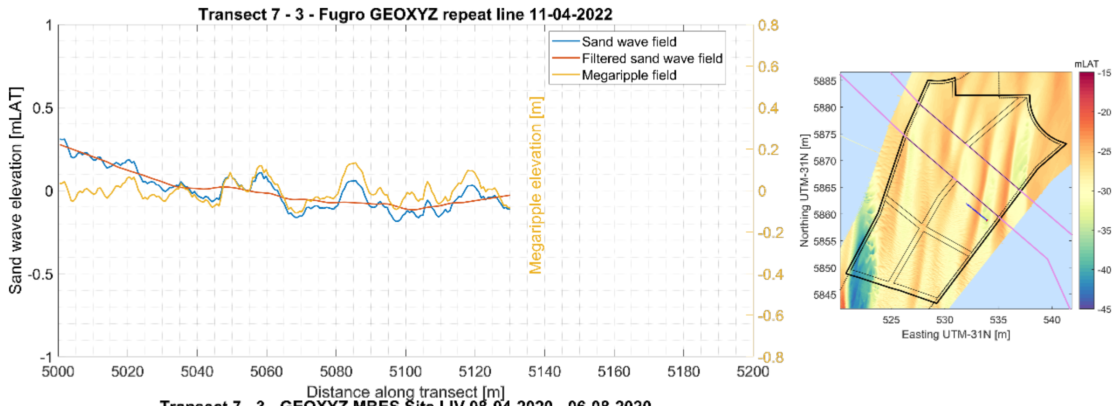

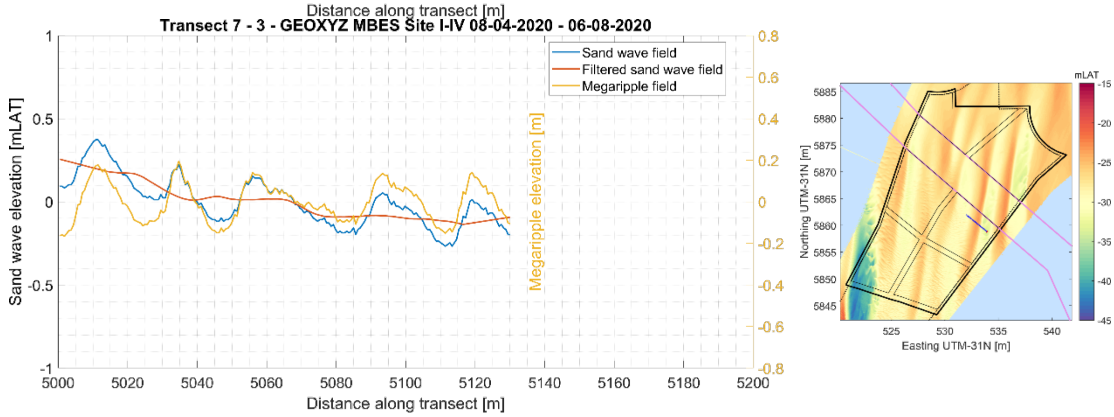

E.2.3 Non-exceedance curves of megaripple dimensions along repeat survey lines

E.2.3.1. Transect 1

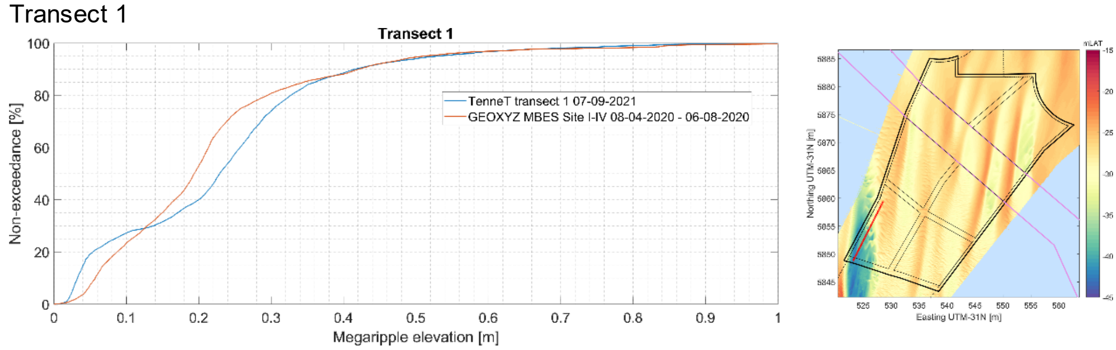

E.2.3.2. Transect 2

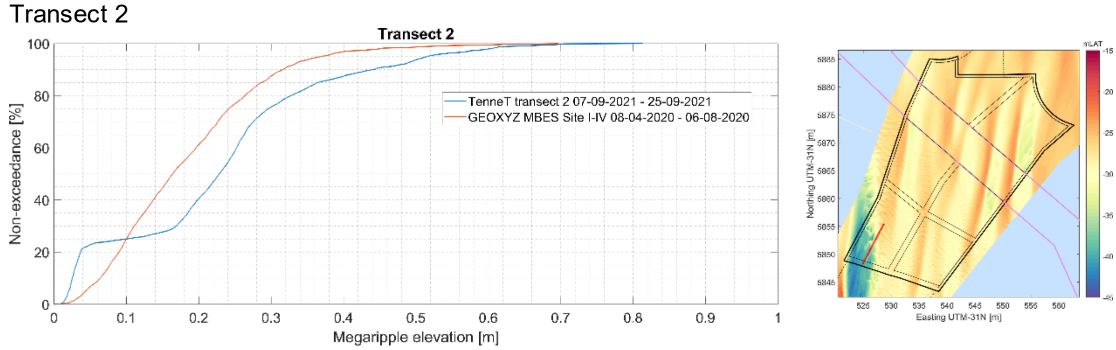

Deltares

E.2.3.3. Transect 3

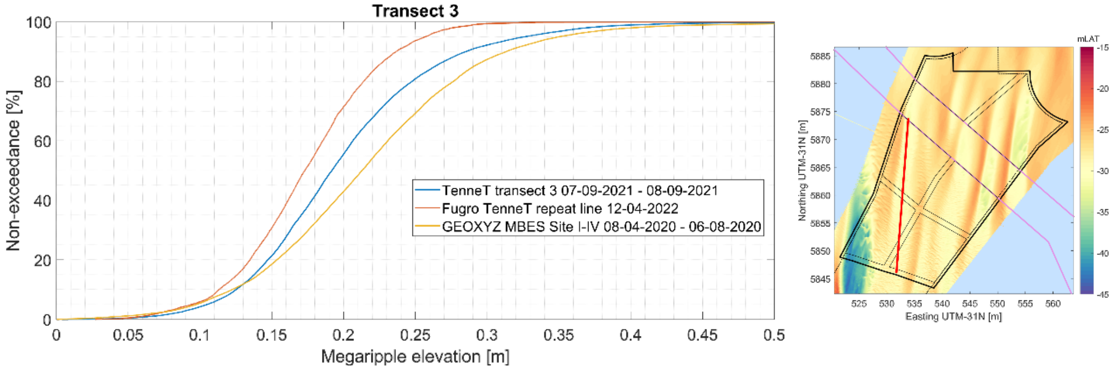

E.2.3.4. Transect 4

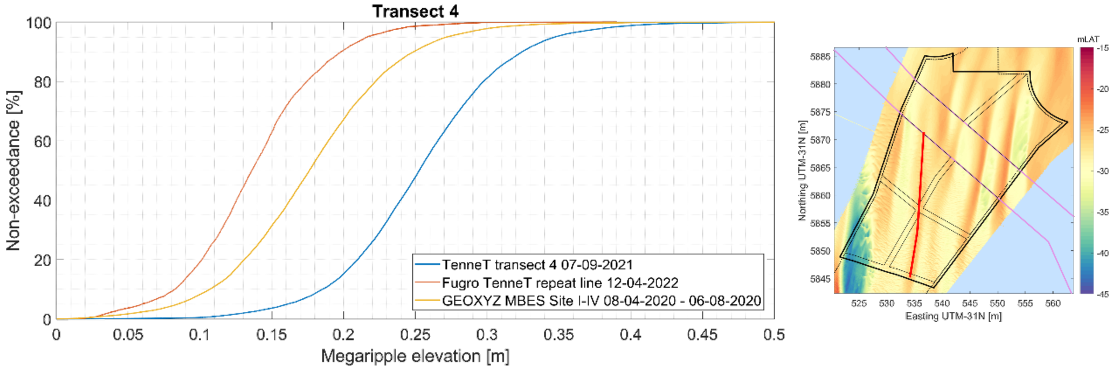

E.2.3.5. Transect 5

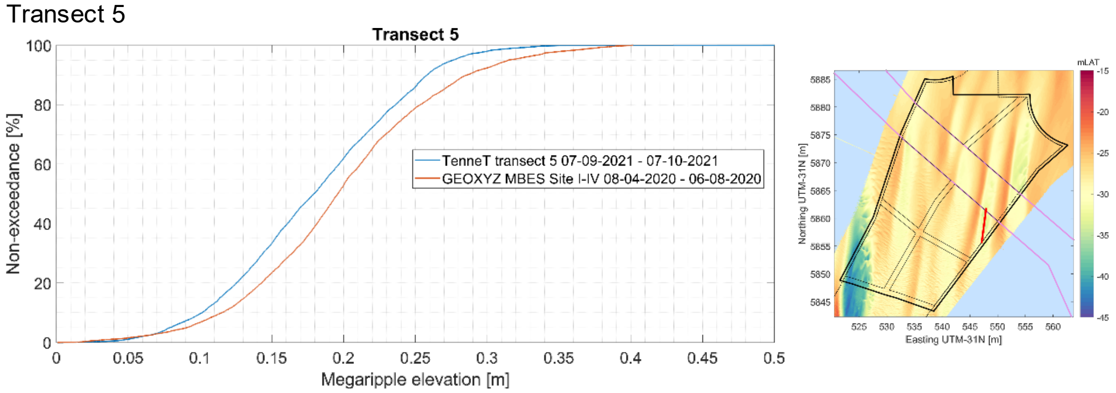

E.2.3.6. Transect 6

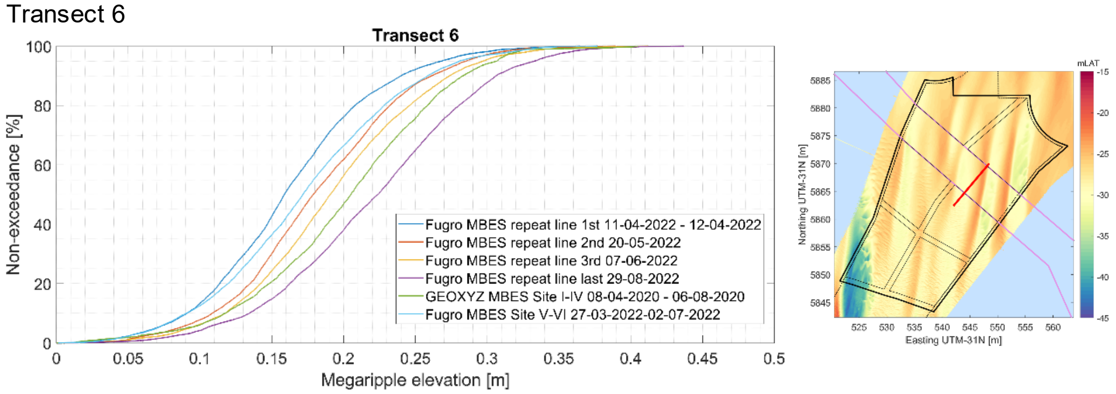

E.2.3.7. Transect 7

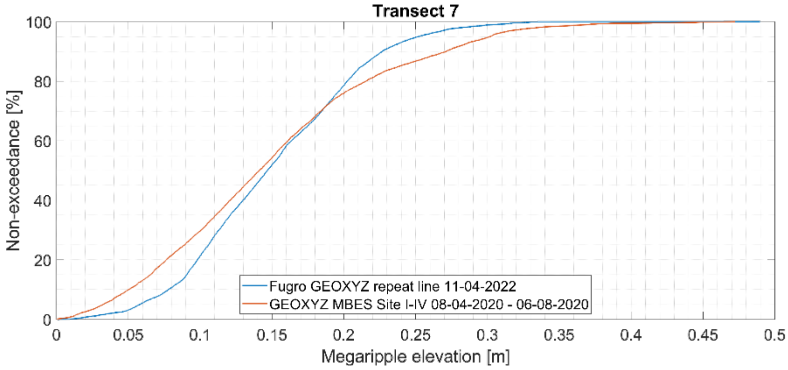

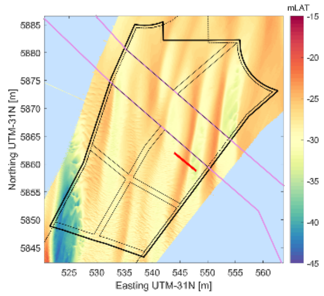

F Description of additional data

The following data are provided in GIS maps along with this report:

- Lowest SeaBed Level (LSBL) including uncertainties for time spans of 5 year over the period 2020 to 2072 (e.g. 2035);
- Highest SeaBed Level (HSBL) including uncertainties for time spans of 5 year over the period 2020 to 2072 (e.g. 2035);
- Best Estimate Bathymetry (BEB) excluding uncertainties for time spans of 5 year over the period 2020 to 2072 (e.g. 2035);
- Maximum Seabed Slopes over the period 2020 to 2072;
- Classification zones for wind farm design based on seabed lowering, rising and combined lowering and rising (for the period 2020 to 2072 only);
- Lowest Object Level (LOL) for the period 1945 to 2022;
- Best Estimate Object Level (BEOL) for the period 1945 to 2022;
- Highest Object Level (HOL) for the period 1945 to 2022.

As explained in Chapter 5, the LSBL and HSBL provide the upper and lower envelope of predicted morphological seabed level changes. But instead of a single LSBL and HSBL for the time period between 2020 and 2072, now intermediate LSBLs and HSBLs are provided. The $LSBL_{2034}$ for example provides the lower envelope to be expected in the time period between 2020 and 2034. Each subsequent LSBL provides the envelope between 2020 and a given year (e.g. the $LSBL_{2034}$ provides the lower envelope to be expected in the time period between 2020 and 2034). This is similar for the upper limit, which is provided by the HSBL.

The BEB is obtained by estimating the most probable migration rate and migration direction found in the various datasets. Based on these values the future bathymetry is predicted. The resulting bathymetry is expected to have on average the smallest overall error. In other words: when compared to the actual 2034 bathymetry the BEB_{2034} is expected to have the smallest area-averaged total difference. However, at specific locations it can differ significantly (but it is not expected to exceed the limits provided by the LSBL and HSBL).

Furthermore, the classification zones as shown in Figure 6.17, Figure 6.19 and Figure 6.20 are obtained by translating the LSBL and HSBL into possible classification zones for foundations and electricity cables. The classification of these zones is based on the predicted seabed lowering and rising.

The data files are delivered in ASCII format and GIS files for the predicted seabed levels. The ASCII files contain three columns, respectively Easting, Northing and a z-level (IJV_MOR_Deltares_XYZ_Data.zip). All map data is provided in a map package (IJV_MOR_Deltares_Map_Package.mpk). Furthermore, metadata files are delivered (IJV_MOR_Deltares_Metadata.zip).

All data points are provided in the coordinate system ETRS89 / UTM Zone 31N. The z-levels for the seabed predictions are always given in metres relative to Lowest Astronomical Tide (LAT) for each of the defined z-levels (i.e. minimum expected seabed for the LSBL-files, maximum expected seabed for the HSBL-files and most probable seabed for the BEB-files). Z-values for the slope maps are defined in degrees. The classifications for the classification zones are addressed as 1, 2, 3 or 4 corresponding to the specific classifications defined in Table A.4.

Deltares is an independent institute for applied research in the field of water and subsurface. Throughout the world, we work on smart solutions for people, environment and society.

This investigation was carried out by Deltares, commissioned by RVO, an agency of the Ministry of Economic Affairs and Climate Policy.

The information in this document is valid at the time of publishing (see month/year). Updates will be published on the website https://offshorewind.rvo.nl/ at the relevant sitemap, General Information, submap Revision Log and Q & A. In the Revision Log is indicated which versions are the latest and what the changes are in relation to previous versions. The documents can be found at the relevant sites, indicated in the List of all reports and deliverables.

Contacts
Netherlands Enterprise Agency (RVO)
Graadt van Roggenweg 200 | 3531 AH | Utrecht | The Netherlands
P.O. Box 8242 | 3503 RE | Utrecht | The Netherlands
www.rvo.nl / https://english.rvo.nl

Netherlands Enterprise Agency | February 2023